Final Report

Ground Motion Evaluation

for

Jackson Lake Dam
Minidoka Project, Wyoming

Seismotectonics and Geophysics Group
Technical Service Center
Bureau of Reclamation
Denver, Colorado

June 2003

FINAL REPORT

Ground Motion Evaluation for Jackson Lake Dam, Minidoka Project, Wyoming

Prepared by
Daniel R. H. O'Connell
Christopher K. Wood
Dean A. Ostenaa
Lisa V. Block
Roland C. LaForge

Report 2003-2

Seismotectonics and Geophysics Group
Technical Service Center
Bureau of Reclamation
Denver, Colorado

June 2003

RECLAMATION'S MISSION

The mission of the Bureau of Reclamation is to manage, develop, and protect water and related resources in an environmentally and economically sound manner in the interest of the American public.

DEPARTMENT OF THE INTERIOR'S MISSION

The mission of the Department of the Interior is to protect and provide access to our Nation's natural and cultural heritage and honor our trust responsibilities to tribes.

Prepared by:

Signature Not Verified

Daniel R.H. O'Connell — June 20, 2003 Date

Signature Not Verified

Christopher K. Wood — June 20, 2003 Date

Dean A. Ostenaa — June 20, 2003 Date

Signature Not Verified

Lisa V. Block — June 23, 2003 Date

Roland C. LaForge — June 20, 2003 Date

TSC Peer Review by:

Jon P. Ake — June 23, 2003 Date

Larry W. Anderson — June 20, 2003 Date

EXECUTIVE SUMMARY

This report provides a detailed characterization of the ground motions that might affect Jackson Lake Dam due to a large earthquake on the Teton fault. The Teton fault is an active normal fault capable of producing **M** 7+ earthquakes. The surface trace of the fault is located 12 km (7 mi) west of Jackson Lake Dam. The fault plane dips to the east, likely extending to a position below the dam. This report is based on regional seismic monitoring data, empirical site response measurements, results of previous geologic investigations, and ground motion modelling.

This report examines ground motions from the Teton fault only. While there are other sources of earthquakes in the region, previous probabilistic seismic hazard analyses by Reclamation indicate that the Teton fault is the controlling seismic source based on proximity, activity rates, and maximum earthquake magnitudes. At some locations on the dam which are more susceptible to liquefaction, ground motions from additional sources may be significant. The emphasis in the current ground motion analyses is therefore to characterize potential Teton fault earthquakes, and to investigate the effects of geologic structure on seismic wave propagation and site response. This report provides design ground motions that are intended to be used as input for engineering analyses of the dam.

Teton Fault Characterization

Scarps formed by multiple latest Quaternary surface-faulting events mark the 60-km (37-mi) long trace of the Teton fault. Maximum slip rates appear to be in the range of 2 to 5 mm/yr along sections of the fault closest to the dam. Limitations in available geomorphic data result in a factor of 2 uncertainty in these slip rate estimates, as well as uncertainty in fault segmentation models. Several alternative rupture models are therefore considered, which incorporate a range of possible scenarios. From among these models, recurrence intervals for a large (**M** ~7) surface-rupturing earthquake on the Teton fault range from about 700 years to about 2000 years, with a weighted mean of about 1180 years.

The assumed dip of the Teton fault has a substantial effect on the modeled ground motions at Jackson Lake Dam. Lower fault dips result in stronger radiation of seismic energy, greater excitation of a low-velocity crustal basin below the dam, and potentially larger seismic moment

release. No direct data is available to constrain the fault dip. Recent analyses and compilations of coseismic rupture from historical earthquakes on other normal faults suggest a preference for dips near 45°, and a range of 30° to 60°. Seismic network data indicated that few earthquakes are located on (or near) the possible downdip projections of the Teton fault. Earthquakes located east of the surface trace of the Teton fault, however, have east-dipping nodal planes that dip from 25° to 60°. While there are too few recorded earthquakes located near the Teton fault to provide a strong constraint on fault dip, the spatial distribution of earthquakes is consistent with dips of less than 50°. Focal depths from well-located earthquakes are less than 14 km (9 mi), and extend to a maximum depth of about 17 km (10 mi), providing a basis to assign maximum faulting depths for ground motion modeling.

Focal mechanisms from 773 local earthquakes indicate that the contemporary state of stress would result in primarily normal-slip for the central and northern sections of the Teton fault, and oblique left-lateral normal slip on the southern section of the Teton fault. The focal mechanism data support using a dominantly normal-slip rake to simulate ground motions associated with rupture of the central and northern segments of the Teton fault.

Effects of Geologic Structure

The geologic structure of the Jackson Lake Dam area has a large impact on potential ground motions that would result from earthquake rupture of the Teton fault. Repeated episodes of faulting, erosion and deposition have resulted in a deep basin of late Cenozoic alluvial fill underlying northern Jackson Hole, including the Jackson Lake Dam area. In addition, episodes of glacial scouring and deposition in the immediate vicinity of the dam have created a shallow basin of largely unconsolidated late Quaternary alluvium. This geologic structure is characterized by observed large-scale lateral contrasts in seismic velocity, and localized zones of low near-surface seismic velocities. This structure serves to both amplify and prolong the duration of shaking at Jackson Lake Dam.

A 3D crustal velocity model is estimated using data from 1150 of the best located earthquakes recorded by Reclamation's seismic monitoring network (out of a total of 16,000 quakes recorded between August 1986, and May 2002). The horizontal resolution of the model is 5 km (3 mi). The

3D velocity inversion revealed a laterally extensive low-velocity region east of the Teton fault that includes Jackson Lake Dam. The low-velocity region extends to depths of ~4 km (2 mi) below the dam and exhibited the lowest velocities seen in the 3D P-wave velocity model (3.4 km/s).

The inverted 3D low-velocity basin velocity (LVB) model is refined by incorporating seismic refraction data (Behrendt et al., 1968; Byrd et al., 1994), and by modeling of microearthquake ground motions at the dam. Relatively strong velocity discontinuities between the LVB velocities and the surrounding high velocity medium are required to reproduce observed strong shear-wave arrivals that follow the direct shear-wave by 3-7 s in the weak ground motion data recorded at the dam. The LVB captures radiated seismic energy over a very wide cross section. Thus the basin is a very efficient seismic collector, and sites within the basin are likely to experience substantial multipathing for sources located beneath the basin (e.g., the Teton fault).

Based on 3D modeling, peak ground motions and Arias Intensities are likely to be largest in the western half of the LVB, return to levels comparable to those on the hanging wall near the fault (but outside of the LVB), and then decrease as one moves past the dam in the S15E direction. Peak motions at hard-rock sites within the LVB east of the dam are likely to be greater than those outside of the LVB, but adjacent to the fault. In contrast to sites within the western 8 km of the LVB, the dam is likely to be subjected to less extreme amplification from the combined effects of rupture directivity and LVB amplification. However, the modeled peak velocities and Arias Intensities at the dam are larger than those at sites located adjacent to the fault on the high-velocity portion of the hanging wall (outside of the LVB). These results indicate that the dam will be subjected to amplification both because of rupture directivity and as a result of being located within the LVB. The effect of rupture directivity is smaller at the dam for fault dips of 45° to 60°.

Site Response at Jackson Lake Dam

Weak-motion site response was measured at Jackson Lake Dam using an array of seven broad-band seismometers. Key observations are the presence of substantial long-period amplification and prolonged duration of shaking beyond some transition point located between stations 13+00 and 24+00; minimal long-period amplification at stations 12+00 and less (referenced to a bedrock

site on the right abutment); and, high-frequency de-amplification on treated sections of the north embankment (referenced to a site just outside of the treated zone).

Strong ground motions at stations 13+00 and greater are expected to behave non-linearly. The observed weak-motion site response must be modified to account for non-linear soil behavior. The observed site response at station 24+00 is consistent with the 2D and 3D response of a shallow, low-velocity sedimentary basin, and likely results from the generation of surface waves, converted phases, and interface waves. 2D synthetic seismogram modeling of the site response data show that the extended ground motion durations observed at the surface are likely associated with a mixture of refracted S-waves, and horizontally propagating surface and interface waves. The 2D synthetic seismograms show that there is a critical distance range from the southern margin of the glacial scour, on which the concrete section of the dam is founded, where peak horizontal acceleration responses are likely to be amplified relative to most of the embankment section of the dam. These results indicate that 1D computer codes for modelling nonlinear soil behavior at the dam will need to be modified to account for 2D and 3D effects.

Ground Motion Modeling

Ground motion simulations of the Teton fault for multiple rupture scenarios were performed using kinematic rupture models of the fault, and propagation of seismic waveforms through the 3D model. A hybrid procedure was used to incorporate high frequencies and purely empirical Green's functions were also used to simulate ground motions to ascertain the sensitivity of ground motion estimates to source and propagation approximations. These simulations provided a range of possible ground motions, and provided constraints on parameters having the most significant effect.

The combined influences of rupture directivity and the LVB amplify rock input motions at the dam. The resulting motions are more like a soil site than a typical rock site. Based on ground motion simulations for the northern Teton fault (dips of 35° and 45°), the mean and 84th-percentile acceleration responses for periods > 0.35 s exceed empirical predictions for rock. For a fault dip of 35°, the mean and 84th-percentile acceleration responses exceed empirical predictions for soil on the south abutment for periods > 1 s. For a fault dip of 45°, the mean and 84th-

percentile acceleration response exceed empirical predictions for soil on the south abutment for periods > ~1.5 s. Of particular note is that mean peak horizontal velocities exceed 90 cm/s for all dip scenarios. Hanging wall LVB amplification increases ground motions at Jackson Lake Dam in a way that is similar to the extreme ground motion effects of rupture directivity; In addition, the LVB produces extended duration of strong ground shaking at the dam, which is an effect that is not typically associated with rupture directivity.

Based on ground motion modelling and empirical site response data, ground motions at Jackson Lake Dam will have greater amplification, duration, and Arias Intensities than would be predicted using generic empirical ground motion attenuation relationships. We therefore recommend that the ground motions provided in this report be used directly for engineering analyses. However, if empirical relationships are used for engineering analyses, then magnitude proxies of the seismic loads should be **M** 8 for the rock ground motions, and **M** 9 for the soil ground motions. These recommended proxy magnitudes for soil sites are much larger than the moment magnitudes of all-segment and northern segment rupture scenarios of the Teton fault, but specifically account for the extended durations and amplifications of ground motions observed at the dam. The most likely scenarios for soil response and nonlinear soil calculations indicate rock ground motion durations of at least 80 seconds and soil durations possibly as long as 180 s for the embankment portion of the dam.

Ground motions are likely to vary substantially over the 1.5 km span of the dam, both along the dam's axis and in the upstream-downstream direction. That is because the low soil S-wave velocities result in wavelengths nearly equal to the dam's width at 1 Hz. In addition, the southern portion of the dam will shake less strongly and for shorter durations than the rest of the dam because it overlies more competent soils and rock. Consequently, the largest strains resulting from differential motions along the axis of the dam are likely to be located in the embankment section extending from stations 12+00 to 32+00.

Table of Contents

Section	Title	Page
	EXECUTIVE SUMMARY	**III**
1.0	**INTRODUCTION**	**1**
1.1	Introduction	1
1.2	Objectives and Scope	2
1.2.1	Teton Fault Source Characterization	3
1.2.2	Seismicity Analyses	4
1.2.3	Hanging Wall Crustal Velocity Structure	4
1.2.4	Empirical Site Response	4
1.2.5	Ground Motion Estimation for Jackson Lake Dam	5
1.3	Jackson Lake Dam	6
1.3.1	Geologic Setting of the Dam	8
1.3.2	Previous Seismic Hazard and Ground Motion Studies	10
1.4	Acknowledgements	11
2.0	**TETON FAULT- SOURCE CHARACTERIZATION**	**13**
2.1	Introduction	13
2.1.1	Primary Data Sources	16
2.2	Late Quaternary Faulting on the Teton Fault	17
2.2.1	Quaternary Chronology of Faulted Deposits Along the Teton Fault	17
2.2.2	Distribution of Late Quaternary Fault Scarps and Surface Rupture	20
2.2.2.1	Relationship of the Late Quaternary Fault to Older Structures	25
2.2.2.2	Fault Dip	28
2.2.3	Slip Rate and Along-Strike Variations in Displacement	30
2.2.3.1	Age(s) and Number of Faulting Events	34
2.2.4	Segmentation	36
2.3	Potential Fault Rupture Models	37
2.3.1	Unsegmented, with Variable Displacement Along Strike.	38
2.3.2	Two Independent Fault Segments with Overlapping Rupture.	38
2.3.3	Three Independent Fault Segments.	39
2.3.4	Implications for Ground Motion Models	39
3.0	**SEISMICITY ANALYSES**	**41**
3.1	Hypocenter-Velocity-Station Correction Inversion	44
3.1.1	Procedure	44
3.1.2	Improvement in Residuals	45
3.1.3	New Velocity Model and Station Corrections	45
3.1.4	Final Earthquake Locations	49
3.2	Focal Mechanisms	49
3.3	Earthquake Recurrence	61
3.4	Catalog Development	62
3.4.1	Jackson Lake Network Catalog	62
3.4.1.1	Declustering	62
3.4.2	Pre-Jackson Lake Network Catalog	65

3.5 Recurrence Calculations 71
3.6 Earthquake Recurrence Discussion 71
3.7 Summary and Conclusions 80
4.0 HANGING WALL CRUSTAL VELOCITY STRUCTURE 85
4.1 3D Velocity Model Development Using Seismic Refraction Data. 87
4.2 3D Velocity Model Development Using LVB Seismograms. 91
4.2.1 Synthetic Seismogram Modeling of the 19 April 2001 M 1.4 Earthquake 92
4.2.2 Synthetic Seismogram Modeling of the 29 Sep. 1996 M 1.6 Earthquake 94
4.2.3 Synthetic Seismogram Modeling of the 15 Nov. 2001 M 2.9 Earthquake 103
4.3 Comparison of 3D Velocity Model to the Seismic Refraction Data 106
4.4 Seismic LVB Responses to Teton Fault Earthquakes: Influence of LVB Structure 109
4.5 Structural Interpretation of Hanging Wall Geology and Geophysics 118
4.6 Conclusions 120
5.0 SITE RESPONSE 125
5.1 Weak-Motion Site Response 125
5.1.1 Instrumented Sites 127
5.1.2 Initial Data Recording System 132
5.1.3 Upgraded Data Recording System 134
5.2 Observations 134
5.2.1 Waveform Data Results 135
5.2.2 Spectral Ratio Method 138
5.2.3 Average Spectral Ratios 139
5.3 Weak-Motion Impulse Response Functions 145
5.3.1 Impulse Response Functions for JLD2 and JLD3 148
5.3.2 Bedrock Motions with Weak-Motion Site Response Included 151
5.4 2D Finite-Difference Site Response Modeling 158
5.4.1 Previous Work 158
5.4.2 Site-Specific Model 160
5.5 Summary and Conclusions. 182
6.0 GROUND MOTION MODELING 185
6.1 Overall Approach 185
6.1.1 Green's Function For Linear Ground Motions. 187
6.1.2 Nonlinear Soil Ground Motions. 187
6.2 Source Parameterization 189
6.3 Linear Wave Propagation Methods 195
6.3.1 Low-Frequency 3D Green's Functions. 195
6.3.1.1 Viscoelastic 3D Finite-Difference Calculations 197
6.3.2 High-Frequency Empirical Green's Functions. 197
6.4 Linear Ground Motion Simulations 206
6.4.1 Idealized Fault Rupture Geometries. 206
6.4.2 Forward Calculations of Low-Frequency 3D Ground Motions. 206
6.4.3 Broadband Hybrid Ground Motions. 216
6.4.3.2 Northern Teton Fault Segment - 35° Dip 218
6.4.3.3 Northern Teton Fault Segment - 45° Dip. 226
6.4.3.4 Northern Teton Fault Segment - 60° Dip. 234

6.4.4 Comparison of Linear Ground Motions for Varying Fault Dips. 238
6.5 Ground Motions for Dynamic Analyses of the Concrete Portion of Jackson Lake Dam. 245
6.6 Inputs for Nonlinear Ground Motion Calculations 264
6.6.1 Nonlinear Compacted Soil Zone Results 275
6.6.2 Nonlinear Soil Mix Wall Results 275
6.6.3 Discussion of Nonlinear Results 282
6.7 Ground Motion Summary 285
7.0 ANALYSIS OF ESTIMATED GROUND MOTIONS 291
7.1 Strong Ground Motions From the 1979 M 6.5 Imperial Valley Earthquake 292
7.2 Performance of the Kinematic Rupture Model 305
7.2.1 Validation Ground Motion Modeling Approach: Green's Functions 307
7.2.2 Kinematic Rupture Model Test: Northridge Ground Motions 311
7.3 Alternative Ground Motion Synthesis Approach of Frankel (1995) 330
7.4 Ground Motions From Larger Regional Earthquakes 335
7.4.1 Rock Site JLDW 340
7.4.2 Soil Site JLD3 362
7.5 Ground Motion Synthesis with Local Broadband Empirical Green's Functions 373
7.5.1 Simulated Ground Motions Using the 11 July 1998 M2.9 EGF's 383
7.5.2 Simulated Ground Motions Using the 20 November 2002 M 3.2 EGF 393
7.5.3 Influence of EGF Location on Long-Period Responses 397
7.6 Comparison to Broadband Hybrid Ground Motions From Section 6. 401
7.7 Discussion. 409
8.0 CONCLUSIONS 417
8.1 Teton Fault Slip Rates 418
8.2 Teton Fault Dip 419
8.3 3D Crustal Velocity Structure 420
8.4 Soil Site Response 422
8.5 Ground Motion Estimation 425
8.6 Rock Ground Motions for the Concrete Section 436
8.7 Rock Ground Motion Time Histories 437
8.8 Recommended Acceleration Seismograms for Nonlinear Soil Analyses 450
8.9 Appropriate Use of Ground Motions 453
9.0 REFERENCES 459

List of Figures

Figure No.	Title	Page
Figure 1-1:	Map showing location of Jackson Lake Dam and late Quaternary trace of Teton fault.	2
Figure 1-2:	Schematic sections through Jackson Lake Dam at stations 12+00, 24+00, and 31+00.	7
Figure 1-3:	Generalized geologic cross section along the axis of Jackson Lake Dam.	9
Figure 2-1:	Regional tectonic map of the northwestern Wyoming and Jackson Lake Dam region.	14
Figure 2-2:	Map of the Teton Range-Jackson Hole region showing the generalized late Quaternary trace of the Teton fault in relationship to Jackson Lake Dam.	15
Figure 2-3:	Map of fault traces defined by late Quaternary fault scarps along the Teton fault.	22
Figure 2-4:	Schematic geologic cross section of the Teton Range and Jackson Hole depicting a vertical offset of ~6 km on the Teton fault copied from Smith et al. (1993).	26
Figure 2-5:	Various interpretations of the Teton Range and Teton normal fault from 1938 through 1974 (Figure 6 of Lageson, 1992).	27
Figure 2-6:	Schematic geologic cross section depicting late Quaternary Teton fault versus basin structure to east of fault.	28
Figure 2-7:	Estimated vertical slip rates along the Teton fault.	33
Figure 2-8:	Shoreline intervals for Bearpaw Bay shorelines.	37
Figure 3-1:	Map showing the distribution of JLSN seismographic stations.	42
Figure 3-2:	Map showing the distribution of Jackson Lake Dam site-response seismographs.	43
Figure 3-3:	Histograms of arrival time residuals.	45
Figure 3-4:	Plan views of P-wave velocities for elevations (relative to mean sea level) of -5 km to 2 km.	46
Figure 3-5:	Plan view of the final locations of 4642 events relocated in the 3D velocity model from the joint inversion.	50
Figure 3-6:	Histogram of the final earthquake elevations (with respect to mean sea level, e.g., 0 km).	51
Figure 3-7:	West-east depth sections of earthquake locations.	53
Figure 3-8:	T-axes azimuths from the 303 focal mechanisms with < 5º T-axis solution variability	54
Figure 3-9:	T-axes azimuths from the 773 focal mechanisms with < 20º T-axis solution variability	55
Figure 3-10:	"Pure" nodal planes from focal mechanisms with < 5º T-axis solution variability	57
Figure 3-11:	"Pure" strike-slip and oblique dip-slip nodal planes from focal mechanisms with < 5º T-axis solution variability	58
Figure 3-12:	"Pure" nodal planes from focal mechanisms with < 20º T-axis solution variability	59
Figure 3-13:	"Pure" strike-slip and oblique dip-slip nodal planes from focal mechanisms with < 20º T-axis solution variability	60
Figure 3-14:	Epicenters from Jackson Lake Seismic Network, magnitude > 2.0, June	

1986 - December 2001 63
Figure 3-15a Latitude vs. time, unfiltered JLSN catalog. 66
Figure 3-15b Longitude vs. time, unfiltered JLSN catalog 66
Figure 3-16a Latitude vs. time, declustered JLSN catalog. 67
Figure 3-16b Longitude vs. time, declustered JLSN catalog. 67
Figure 3-17: JLSN earthquakes identified as being clusters by declustering algorithm. 68
Figure 3-18: JLSN earthquakes identified as independent events by declustering algorithm. 69
Figure 3-19: 1963 - June 1986 epicenters, from NCDEC. 70
Figure 3-20: Declustered earthquakes used in recurrence calculations using the combined catalogs. 72
Figure 3-21a Incremental recurrence curve for JLSN catalog. 74
Figure 3-21b Cumulative recurrence curve for JLSN catalog. 74
Figure3-22a Incremental recurrence curve for combined catalogs. The ellipse shows the approximate rate of M ~6.7-7.2 earthquakes on the Teton fault based on Section 2 75
Figure 3-22b Cumulative recurrence curve for combined catalogs. 75
Figure 3-23a Example soil-site hazard curves for random seismicity at Jackson Lake Dam. 78
Figure 3-23b Example rock-site hazard curves for random seismicity at Jackson Lake Dam. 78
Figure 4-1: Plan view of the P-wave 3D velocity model with the embedded hanging wall LVB at 2 km elevation. 86
Figure 4-2: P-wave travel-time plots for lines 1-4 from Behrendt et al. (1968). 88
Figure 4-3: Line 2 gravity and seismic refraction interpretation reproduced from Behrendt et al. (1968). 90
Figure 4-4: S-wave velocity depth cross section A-B (see Figure 4-1). 95
Figure 4-5: Radial-component JLDW seismogram from the M 1.4 normal-faulting earthquake on 19 April 2001. 96
Figure 4-6: Synthetic radial-component-seismogram record section for the 19 April 2001 earthquake. 97
Figure 4-7: 2D ray-tracing slices through the 3D S-wave velocity model. 98
Figure 4-8: S-wave velocity-depth cross section C-D (see Figure 4-1) used to model the 29 Sep. 1996 M 1.6 earthquake. 100
Figure 4-9: Line 4 traveltimes and interpretations reproduced from Behrendt et al. (1968) 101
Figure 4-10: Radial-component JLDW observed seismogram from the M 1.6 normal-faulting earthquake on 29 Sep. 1996. 102
Figure 4-11: S-wave velocity-depth cross section E-F (see Figure 4-1) used to model the 15 Nov. 2001 M 2.9 earthquake. 104
Figure 4-12: Observed and synthetic radial-component JLDW seismograms the M 2.9 normal-faulting earthquake on 15 Nov. 2001. 105
Figure 4-13: (A) P-wave travel-time plot for lines 2 from Behrendt et al. (1968) and (B) corresponding slice of the 3D P-wave velocity model.107
Figure 4-14: (A) Line 2 interpretation from Behrendt et al. (1968) and (B) corresponding slice of the 3D P-wave velocity model. 108
Figure 4-15: Plan view of the P-wave 3D velocity model with embedded Jackson Hole LVB at elevation 2 km. 110
Figure 4-16: E15S horizontal component < 1 Hz 3D finite-difference RGF's moment-time

histories at JLDW for a point-source at the northeast corner of the Teton fault 111
Figure 4-17: N15E horizontal component < 1 Hz 3D finite-difference RGF's moment-time histories at JLDW for a point-source at the northeast corner of the Teton fault 112
Figure 4-18: E15S horizontal component < 1 Hz 3D finite-difference RGF's moment-time histories at JLDW for a point-source at the southeast corner of the Teton fault 113
Figure 4-19: N15E horizontal component < 1 Hz 3D finite-difference RGF's moment-time histories at JLDW for a point-source at the southeast corner of the Teton fault 114
Figure 4-20: Simulated peak motion characteristics for a M 7.1 earthquake on the Teton fault. 116
Figure 5-1: Jackson Lake Dam section showing locations of site response seismometers JLDW-JLD7..... 128
Figure 5-2: Profiles across Jackson Lake Dam at stations 12+00, 24+00, and 31+00 (Stelma, 1996) showing location of site response seismometers JLD2 through JLD6..... 129
Figure 5-3: Compressional and shear wave velocity profiles for the soil column underlying the north dike of Jackson Lake Dam, as determined by crosshole velocity measurements (Sirles, 1986). 130
Figure 5-4: M 3.2 earthquake located near Driggs Idaho. 136
Figure 5-5: M 3.1 earthquake located 34 km southeast of the Jackson Lake Dam in the Gros Ventre Range..... 137
Figure 5-6: Spectral ratios relative to JLDW for 29 earthquakes recorded by the RefTek instrumentation initially deployed at seven sites (JLDW through JLD7). 141
Figure 5-7: Spectral ratios relative to JLDW for 24 earthquakes recorded by the upgraded instrumentation deployed at sites JLDW, JLD2, JLD3, and JLD5... 142
Figure 5-8: Spectral ratios relative to JLD3 for 29 earthquakes recorded by the initial deployment of RefTek instruments..... 144
Figure 5-9: Average spectral ratios relative to JLDW for 29 earthquakes recorded by the initial deployment of RefTek instruments 146
Figure 5-10: Average spectral ratios relative to JLDW for 29 earthquakes recorded by the upgraded instrumentation deployed at stations JLDW, JLD2, JLD3 and JLD5..... 147
Figure 5-11: (A) Unwrapped phase at JLD2 relative to JLDW for 7 representative earthquakes. (B) Impulse response functions constructed from the average spectral ratio, and from individual or average relative phases. 149
Figure 5-12: Tabas E-W acceleration and velocity waveforms (solid lines) convolved with several realizations of the JLD2 weak-motion impulse response functions (dashed lines). 150
Figure 5-13: (A) Unwrapped phase at JLD3 relative to JLDW for 7 representative earthquakes. (B) Impulse response functions constructed from the average spectral ratio, and from individual or average relative phases. 152
Figure 5-14: Tabas E-W acceleration and velocity waveforms (solid) convolved with several realizations of the JLD3 weak-motion impulse response functions

(dashed). 153
Figure 5-15: Bedrock input motions (solid lines), and bedrock motions convolved with JLD2 weak-motion response (dotted lines). 154
Figure 5-16: Bedrock input motions (solid lines), and bedrock motions convolved with JLD3 weak-motion response (dotted lines). 155
Figure 5-17: Bedrock input motions (left), and motions convolved with JLD2 weak-motion site response (right). 157
Figure 5-18: Bedrock input motions (left), and motions convolved with JLD3 weak-motion site response (right). 159
Figure 5-19: Simulation of Lomnitz et al.'s (1999) soil response. 161
Figure 5-20: Simple 2D S-wave velocity model of the glacial scour basin beneath the dam 163
Figure 5-21: 1D S-wave velocity profile from the middle of the 2D glacial scour basin 164
Figure 5-22: Simple 2D S-wave Qs model of the glacial scour basin beneath the dam 165
Figure 5-23: Horizontal 2D finite-difference acceleration record section z = 0 m 166
Figure 5-24: Horizontal 2D finite-difference acceleration record section z = 10 m 168
Figure 5-25: Horizontal 2D finite-difference acceleration record section z = 20 m 169
Figure 5-26: Horizontal 2D finite-difference acceleration record section z = 30 m 170
Figure 5-27: Horizontal 2D finite-difference acceleration record section z = 40 m 171
Figure 5-28: Horizontal 2D finite-difference acceleration record section z = 50 m 172
Figure 5-29: Vertical 2D finite-difference acceleration record section z = 0 m 174
Figure 5-30: Vertical 2D finite-difference acceleration record section z = 10 m 175
Figure 5-31: Vertical 2D finite-difference acceleration record section z = 20 m 176
Figure 5-32: Vertical 2D finite-difference acceleration record section z = 30 m 177
Figure 5-33: Vertical 2D finite-difference acceleration record section z = 40 m 178
Figure 5-34: Vertical 2D finite-difference acceleration record section z = 50 m 179
Figure 6-1: Plan view of the ground motion P-wave 3D velocity model at elevation 2 km. 186
Figure 6-2: High-frequency approximation to the Kostrov slip-velocity function. 192
Figure 6-3: Two cross sections of the ground motion P-wave 3D velocity model with orientations as labeled. 196
Figure 6-4: Epicenters of the EGFs with P-wave 3D velocity model at elevation 2 km. 199
Figure 6-5: E15S-component S-wave normal-dip-slip polarities and 0.8-1.5 Hz amplitudes at JLDW for a 35° fault dip. 201
Figure 6-6: N15E-component S-wave normal-dip-slip polarities and 0.8-1.5 Hz amplitudes at JLDW for a 35° fault dip. 203
Figure 6-7: Vertical-component S-wave normal-dip-slip polarities and 0.8-1.5 Hz amplitudes at JLDW for a 35° fault dip. 204
Figure 6-8: Low-frequency (< 1 Hz) E15S-component velocity waveforms for a full Teton fault rupture with a 35° fault dip. 208
Figure 6-9: Low-frequency (< 1 Hz) N15E-component velocity waveforms for a full Teton fault rupture with a 35° fault dip. 209
Figure 6-10: Low-frequency (< 1 Hz) vertical-component velocity waveforms for a full Teton fault rupture with a 35° fault dip. 210
Figure 6-11: Low-frequency (< 1 Hz) horizontal peak velocity, acceleration, and Arias intensity profiles for a full Teton fault rupture with a 35° dip (black curves). 211
Figure 6-12: Low-frequency (< 1 Hz) E15S-component velocity waveforms for a full Teton fault rupture with a 60° fault dip. 213

Figure 6-13: Low-frequency (< 1 Hz) N15E-component velocity waveforms for a full Teton fault rupture with a 60° fault dip. 214
Figure 6-14: Low-frequency (< 1 Hz) vertical-component velocity waveforms for a full Teton fault rupture with a 60° fault dip. 215
Figure 6-15: Low-frequency (< 1 Hz) horizontal peak velocity, acceleration, and Arias intensity profiles for a full Teton fault rupture with a 60° dip (black curves). . 217
Figure 6-16: JLDW rock site mean downstream horizontal PSA response spectra for a 35°-dipping northern Teton fault segment (solid). 219
Figure 6-17: JLDW rock site 84% quantile downstream horizontal PSA response spectra for a 35°-dipping northern Teton fault segment (solid). 220
Figure 6-18: JLDW rock site PSA response spectra for a 35°-dipping northern Teton fault segment for all hypocenters. 222
Figure 6-19: JLDW rock site central hypocenter PSA response spectra for a 35°-dipping northern Teton fault segment (black). 223
Figure 6-20: JLDW rock site northern hypocenter PSA response spectra for a 35°-dipping northern Teton fault segment (black). 224
Figure 6-21: JLDW rock site southern hypocenter PSA response spectra for a 35°-dipping northern Teton fault segment (black). 225
Figure 6-22: JLDW rock site PSA response spectra for a 45°-dipping northern Teton fault segment using all hypocenter positions. 227
Figure 6-23: JLDW rock site mean downstream horizontal PSA response spectra for a 45°-dipping northern Teton fault segment (solid). 228
Figure 6-24: JLDW rock site 84% quantile downstream horizontal PSA response spectra for a 45°-dipping northern Teton fault segment (solid). 229
Figure 6-25: JLDW rock site central hypocenter PSA response spectra for a 45°-dipping northern Teton fault segment (black). 230
Figure 6-26: JLDW rock site southern hypocenter PSA response spectra for a 45°-dipping northern Teton fault segment (black). 231
Figure 6-27: JLDW rock site northern hypocenter PSA response spectra for a 45°-dipping northern Teton fault segment (black). 232
Figure 6-28: JLDW rock site PSA response spectra for a 60°-dipping northern Teton fault segment using all hypocenter positions. 235
Figure 6-29: JLDW rock site central hypocenter PSA response spectra for a 60°-dipping northern Teton fault segment (black). 236
Figure 6-30: JLDW rock site southern hypocenter PSA response spectra for a 60°-dipping northern Teton fault segment (black). 237
Figure 6-31: JLDW rock site northern hypocenter PSA response spectra for a 60°-dipping northern Teton fault segment (black). 239
Figure 6-32: JLDW rock site mean PSA horizontal response spectra for a 60°-dipping northern Teton fault segment. 240
Figure 6-33: JLDW rock site 84% quantile PSA horizontal response spectra for a 60°-dipping northern Teton fault segment. 241
Figure 6-34: JLDW rock site ratios of 35°-to-60°-dipping northern Teton fault segment PSA response spectra. 242
Figure 6-35: JLDW rock site ratios of 45°-to-60°-dipping northern Teton fault segment PSA response spectra. 243

Figure 6-36: JLDW rock site ratios of 35°-to-45°-dipping northern Teton fault segment PSA response spectra. 244
Figure 6-37: JLDW rock site PSA response spectra corresponding to the mean acceleration seismograms. 251
Figure 6-38: JLDW rock site mean acceleration seismograms for dynamic analyses of Jackson Lake Dam. 252
Figure 6-39: JLDW rock site mean velocity seismograms for dynamic analyses of Jackson Lake Dam. 253
Figure 6-40: JLDW rock site mean displacement seismograms for dynamic analyses of Jackson Lake Dam. 254
Figure 6-41: JLDW rock site PSA response spectra corresponding to the 84 percentile acceleration seismograms. 255
Figure 6-42: JLDW rock site 84 percentile acceleration seismograms for dynamic analyses of Jackson Lake Dam. 256
Figure 6-43: JLDW rock site 84 percentile velocity seismograms for dynamic analyses of Jackson Lake Dam. 257
Figure 6-44: JLDW rock site 84 percentile displacement seismograms for dynamic analyses of Jackson Lake Dam. 258
Figure 6-45: Llolleo, Chile, acceleration seismograms for dynamic analyses of the concrete section of Jackson Lake Dam. 260
Figure 6-46: Llolleo, Chile, velocity seismograms for dynamic analyses of Jackson Lake Dam. 261
Figure 6-47: Llolleo, Chile, displacement seismograms for dynamic analyses of Jackson Lake Dam. 262
Figure 6-48: Response spectra corresponding to the Lloleo acceleration seismograms. 263
Figure 6-49: East horizontal component microearthquake velocity seismograms for JLDW and JLD3. 265
Figure 6-50: Time-frequency for the JLDW east-component seismogram from Figure 6-49. 266
Figure 6-51: Time-frequency for the JLD3 east-component seismogram from Figure 6-49. 267
Figure 6-52: NOAH velocity-density depth model for the compaction region. 269
Figure 6-53: NOAH velocity-density depth model for the soil mix wall region. 270
Figure 6-54: Mean JLDW E15S rock motion velocity (a) and acceleration (b) convolved with the JLD3 soil response transfer function. 272
Figure 6-55: 84% JLDW E15S rock motion velocity (a) and acceleration (b) convolved with the JLD3 soil response transfer function. 273
Figure 6-56: Tabas E15S rock motion velocity (a) and acceleration (b) convolved with the JLD3 soil response transfer function. 274
Figure 6-57: Time-domain compacted soil responses for JLD3 response input motions. 276
Figure 6-58: Compacted soil acceleration response spectra for JLD3 response input motions. 277
Figure 6-59: Time-domain compacted soil responses for rock response input motions. 278
Figure 6-60: Compacted soil acceleration response spectra for rock response input motions. 279
Figure 6-61: Time-domain soil mix wall responses for JLD3 response input motions. 280

Figure 6-62: SMW soil acceleration response spectra for JLD3 response input motions. 281
Figure 6-63: Time-domain soil mix wall responses for rock response input motions. 283
Figure 6-64: SMW soil acceleration response spectra for rock response input motions. 284
Figure 7-1: Map view of the Imperial Valley area from Archuleta (1984). 293
Figure 7-2: El Centro Array station E06 acceleration seismograms. 295
Figure 7-3: El Centro Array station E06 velocity seismograms. 297
Figure 7-4: El Centro Array station E06 pseudo-acceleration response spectra. 298
Figure 7-5: El Centro Array station E07 acceleration seismograms. 299
Figure 7-6: El Centro Array station E07 velocity seismograms. 300
Figure 7-7: El Centro Array station E07 pseudo-acceleration response spectra. 301
Figure 7-8: El Centro Array station EMO acceleration seismograms. 302
Figure 7-9: El Centro Array station EMO velocity seismograms. 303
Figure 7-10: El Centro Array station EMO pseudo-acceleration response spectra. 304
Figure 7-11: Plan view of observed peak velocities and accelerations from the M 6.7 1994 Northridge earthquake. 306
Figure 7-12: S-wave velocity profile from a 3D randomization of a 2D velocity model for the top 2 km of the crust. 310
Figure 7-13: First example of a synthetic three-component SV scattering function. 312
Figure 7-14: Another example of a synthetic three-component SV scattering function. 313
Figure 7-15: Effective stress distribution that produced the best-fitting Northridge ground motions 314
Figure 7-16: Slip-velocity distribution that produced the best-fitting Northridge ground motions 315
Figure 7-17: Rise-time distribution that produced the best-fitting Northridge ground motion 316
Figure 7-18: Slip distribution that produced the best-fitting Northridge ground motion 317
Figure 7-19: Fractional-rupture-velocity distribution that produced the best-fitting Northridge ground motion 319
Figure 7-20: Rupture time distribution that produced the best-fitting Northridge ground motion 320
Figure 7-21: Observed and simulated peak horizontal component velocities and accelerations as labeled for station RSS (Rinaldi). 321
Figure 7-22: Observed and simulated peak horizontal component velocities and accelerations as labeled for station SYL (Sylmar). 322
Figure 7-23: Observed and simulated peak horizontal component velocities and accelerations as labeled for station NHL (Newhall). 323
Figure 7-24: Observed and simulated peak horizontal component velocities and accelerations as labeled for station U56. 324
Figure 7-25: Observed and simulated peak horizontal component velocities and accelerations as labeled for station PARD. 325
Figure 7-26: Observed and simulated peak horizontal component velocities and accelerations as labeled for station PDM (Pacoima Dam downstream station). 326
Figure 7-27: Observed and best-fitting Northridge horizontal PSA response spectra. 327
Figure 7-28: Statistical synthetic PSA results. 329
Figure 7-29: Example of relative slip-velocity function. 333

Figure 7-30: Map showing the location of the regional EGF earthquakes relative to the dam. 337
Figure 7-31: Site JLDW velocity seismograms from the 21 Apr. 2001 M 5.2 Idaho earthquake. 341
Figure 7-32: Site JLDW Fourier velocity spectra from the 21 Apr. 2001 M 5.2 Idaho earthquake. 342
Figure 7-33: Site JLDW acceleration response spectra from the 21 Apr. 2001 M 5.2 Idaho earthquake. 343
Figure 7-34: Subevent sum M 7.1 northern Teton fault earthquake simulation JLDW vertical response before long-period correction. 344
Figure 7-35: M 7.1 northern Teton fault earthquake simulation JLDW vertical response. 346
Figure 7-36: Subevent sum M 7.1 northern Teton fault earthquake simulation JLDW north response before long-period correction. 347
Figure 7-37: M 7.1 northern Teton fault earthquake simulation JLDW north response. 348
Figure 7-38: Subevent sum M 7.1 northern Teton fault earthquake simulation JLDW east response before long-period correction. 349
Figure 7-39: M 7.1 northern Teton fault earthquake simulation JLDW east response. 350
Figure 7-40: Site JLDW velocity seismograms from the 24 Nov. 2000 M 4.6 Yellowstone earthquake. 352
Figure 7-41: Site JLDW Fourier velocity spectra from the 24 Nov. 2000 M 4.6 Yellowstone earthquake. 353
Figure 7-42: Site JLDW acceleration response spectra from the 24 Nov. 2000 M 4.6 Yellowstone earthquake. 354
Figure 7-43: Subevent sum M 7.1 northern Teton fault earthquake simulation JLDW vertical response before long-period correction. 356
Figure 7-44: M 7.1 northern Teton fault earthquake simulation JLDW vertical response. 357
Figure 7-45: Subevent sum M 7.1 northern Teton fault earthquake simulation JLDW north response before long-period correction. 358
Figure 7-46: M 7.1 northern Teton fault earthquake simulation JLDW north response. 359
Figure 7-47: Subevent sum M 7.1 northern Teton fault earthquake simulation JLDW east response before long-period correction. 360
Figure 7-48: M 7.1 northern Teton fault earthquake simulation JLDW north response. 361
Figure 7-49: Site JLD3 velocity seismograms from the 21 Apr. 2001 M 5.2 Idaho earthquake. 363
Figure 7-50: Site JLD3 Fourier velocity spectra from the 21 Apr. 2001 M 5.2 Idaho earthquake. 364
Figure 7-51: Site JLD3 acceleration response spectra from the 21 Apr. 2001 M 5.2 Idaho earthquake. 365
Figure 7-52: Subevent sum M 7.1 northern Teton fault earthquake simulation JLD3 vertical response before long-period correction. 367
Figure 7-53: M 7.1 northern Teton fault earthquake simulation JLD3 vertical response. 368
Figure 7-54: Subevent sum M 7.1 northern Teton fault earthquake simulation JLD3 north response before long-period correction. 369
Figure 7-55: M 7.1 northern Teton fault earthquake simulation JLD3 north response. 370
Figure 7-56: Subevent sum M 7.1 northern Teton fault earthquake simulation JLD3 east response before long-period correction. 371

Figure 7-57: M 7.1 northern Teton fault earthquake simulation JLD3 east response. 372
Figure 7-58: Site JLD3 velocity seismograms from the 24 Nov. 2000 M 4.6 Yellowstone earthquake. 374
Figure 7-59: Site JLD3 Fourier velocity spectra from the 24 Nov. 2000 M 4.6 Yellowstone earthquake. 375
Figure 7-60: Site JLD3 acceleration response spectra from the 24 Nov. 2000 M 4.6 Yellowstone earthquake. 376
Figure 7-61: Subevent sum M 7.1 northern Teton fault earthquake simulation JLD3 vertical response before long-period correction. 377
Figure 7-62: M 7.1 northern Teton fault earthquake simulation JLD3 vertical response. 378
Figure 7-63: Subevent sum M 7.1 northern Teton fault earthquake simulation JLD3 north response before long-period correction. 379
Figure 7-64: M 7.1 northern Teton fault earthquake simulation JLD3 north response. 380
Figure 7-65: Subevent sum M 7.1 northern Teton fault earthquake simulation JLD3 east response before long-period correction. 381
Figure 7-66: M 7.1 northern Teton fault earthquake simulation JLD3 north response. 382
Figure 7-67: Epicenters of the three "broadband" EGF local earthquakes with P-wave 3D velocity model at elevation 2 km. 384
Figure 7-68: Site JLDW velocity seismograms and Fourier spectra from the M 2.9 11 July 1998 earthquake 385
Figure 7-69: Site JLDW velocity seismograms and Fourier spectra from the M 3.2 20 November 2002 earthquake 386
Figure 7-70: Site JLDW velocity seismograms and Fourier spectra from the M 3.7 29 January 2002 earthquake 387
Figure 7-71: Focal mechanism for the M 2.9 EGF on 11 July 1998. 388
Figure 7-72: JLDW 84% quantile acceleration response spectra for the 11 July 1998 EGF 389
Figure 7-73: JLDW velocity seismograms for the best-fitting 84% quantile acceleration response spectra for the 11 July 1998 EGF 390
Figure 7-74: JLDW acceleration seismograms for the best-fitting 84% quantile acceleration response spectra for the 11 July 1998 EGF 391
Figure 7-75: JLDW displacement seismograms for the best-fitting 84% quantile acceleration response spectra for the 11 July 1998 EGF 392
Figure 7-76: JLDW mean and 84% quantile northern Teton fault segment acceleration response spectra using the M 3.2 20 Nov. 2002 EGF 394
Figure 7-77: JLDW 84% quantile acceleration response spectra for the 20 Nov. 2002 EGF 395
Figure 7-78: JLDW velocity seismograms for the best-fitting 84% quantile acceleration response spectra for the 20 Nov. 2002 EGF 396
Figure 7-79: JLDW acceleration seismograms for the best-fitting 84% quantile acceleration response spectra for the 20 Nov. 2002 EGF 398
Figure 7-80: JLDW displacement seismograms for the best-fitting 84% quantile acceleration response spectra for the 20 Nov 2002 EGF 399
Figure 7-81: JLDW PSA ratios of the M 3.2 EGF ground motions to the M 2.9 EGF ground motions 400
Figure 7-82: JLDW PSA ratios of the M 3.7 EGF ground motions to the M 2.9 EGF

ground motions 402
Figure 7-83: JLDW rock site mean downstream horizontal PSA response spectra for a 35°-dipping northern Teton fault segment (solid). 404
Figure 7-84: JLDW rock site hybrid Section 6 84% quantile downstream horizontal PSA response spectra for a 35°-dipping northern Teton fault segment (solid). 405
Figure 7-85: JLDW rock site hybrid Section 6 PSA response spectra for a 35°-dipping northern Teton fault segment for all hypocenters. 406
Figure 7-86: Schematic plan and cross section views of the low-velocity basin boundary configuration for Jackson Lake Dam. 407
Figure 7-87: Differential displacements between sites JLD3 and JLD2 for a M 7.1 northern Teton fault segment earthquake. 415
Figure 8-1: Mean downstream horizontal JLDW rock site PSA response spectra for a 35°-dipping northern Teton fault segment (solid). 429
Figure 8-2: 84% quantile downstream horizontal JLDW rock site PSA response spectra for a 35°-dipping northern Teton fault segment (solid). 430
Figure 8-3: Mean downstream horizontal JLDW rock site PSA response spectra for a 45°-dipping northern Teton fault segment (solid). 431
Figure 8-4: 84% quantile downstream horizontal JLDW rock site PSA response spectra for a 45°-dipping northern Teton fault segment (solid). 432
Figure 8-5: Mean JLDW rock site PSA horizontal response spectra for a 60°-dipping northern Teton fault segment. 433
Figure 8-6: 84% quantile JLDW rock site PSA horizontal response spectra for a 60°-dipping northern Teton fault segment. 434
Figure 8-7: Northern Teton fault segment mean rock synthetic ground motion acceleration time histories. 438
Figure 8-8: Northern Teton fault segment mean rock synthetic ground motion velocity time histories. 439
Figure 8-9: Northern Teton fault segment mean rock synthetic ground motion displacement time histories. 440
Figure 8-10: Northern Teton fault segment mean rock synthetic ground motion acceleration response spectra. 441
Figure 8-11: Northern Teton fault segment 84% quantile rock synthetic ground motion acceleration time histories. 442
Figure 8-12: Northern Teton fault segment 84% quantile rock synthetic ground motion velocity time histories. 443
Figure 8-13: Northern Teton fault segment 84% quantile rock synthetic ground motion displacement time histories. 444
Figure 8-14: Northern Teton fault segment 84% quantile rock synthetic ground motion acceleration response spectra. 445
Figure 8-15: Llelleo Valparaiso, Chile, proxy for a Northern Teton fault segment rock ground motion acceleration time histories. 446
Figure 8-16: Llelleo Valparaiso, Chile, proxy for a Northern Teton fault segment rock ground motion velocity time histories. 447
Figure 8-17: Llelleo Valparaiso, Chile, proxy for a Northern Teton fault segment rock ground motion displacement time histories. 448

Figure 8-18: Llelleo Valparaiso, Chile, proxy for a Northern Teton fault segment rock ground motion acceleration response spectra. 449

List of Tables

Table No.	Title	Page
Table 2-1:	Teton Fault - Event Data	35
Table 2-2:	Teton Fault Rupture Scenario Summary	40
Table 3-1:	Station corrections from the hypocenter-velocity-station correction inversion.	48
Table 3-2:	Number of Different Focal Mechanisms for < 5º T-axis Azimuth Variability.	56
Table 3-3:	Number of Different Focal Mechanisms for < 20º T-axis Azimuth Variability.	56
Table 3-4a:	Completeness Periods and Event Counts Used in Recurrence Calculations, JLSN Catalog	73
Table 3-4b:	Completeness Periods and Event Counts Used in Recurrence Calculations, JLSN and 1963-1986 Catalog	73
Table 3-5a:	Recurrence Parameters, JLSN Catalog	76
Table 3-5b:	Recurrence Parameters, Combined Catalogs	76
Table 3-6a:	JLSN Catalog: Return Periods, Observed and Maximum Likelihood, with Upper and Lower Bounds at 95% Confidence	77
Table 3-6b:	Combined Catalogs: Return Periods, Observed and Maximum Likelihood, with Upper and Lower Bounds at 95% Confidence	77
Table 4-1:	Best-Estimates of Relationships between P-wave Velocity and Vs, r, Qp, and Qs.	93
Table 5-1:	RefTek Data Collection Summary	135
Table 6-1:	Empirical Green's Function Earthquake Information	198
Table 6-2:	JLDW Rock Ground Motion Parameters: 35°-Dipping Northern Teton Fault Segment.	218
Table 6-3:	JLDW Rock Ground Motion Parameters: 45°-Dipping Northern Teton Fault Segment.	226
Table 6-4:	JLDW Rock Ground Motion Parameters: 60°-Dipping Northern Teton Fault Segment.	234
Table 6-5:	Ground Motion Input Scenarios for Nonlinear Soil Calculations	268
Table 7-1:	Regional EGF Earthquake Locations	335
Table 7-2:	21 April 2001 EGF Focal Mechanism Nodal Plane Estimates	336
Table 7-3:	Regional EGF Earthquake Simulation Parameters	340
Table 7-4:	Local Broadband Empirical Green's Function Earthquake Information	373
Table 7-5:	JLDW Rock Ground Motion Parameters: 35°-Dipping Northern Teton Fault Segment.	401
Table 8-1:	Ground Motion Parameters for a 35°-Dipping Northern Teton Fault Segment.	427
Table 8-2:	Ground Motion Parameters for a 45°-Dipping Northern Teton Fault Segment.	428
Table 8-3:	Ground Motion Parameters for a 60°-Dipping Northern Teton Fault Segment.	428
Table 8-4:	Rock PHA for the Concrete Section, PHA Range 1.	436
Table 8-5:	Rock PHA for the Concrete Section, PHA Range 2.	437
Table 8-6:	Ground Motion Time History Annual Exceedence Probabilities	450

Appendices

Appendix	Title
A	Teton Fault Section and Fault Scarp Slip Rate Data
B	Hypocenter-Velocity-Station Correction Inversion
C	3D P-Wave Velocity Model Plots
D	3D Empirical Green's Function Plots
E	3D Nonlinear Soil Response Plots
F	Final Report - Nonlinear Wave Propagation in One and Two Dimensions - by R.J. Archuleta and Kenichi Tsuda
G	Review Comments by Dr. Paul Somerville

Plates

1 Partial reproduction of the gravity, geologic and seismic refraction map from Behrendt et al. (1968).

1.0 INTRODUCTION

1.1 Introduction

This report is a detailed characterization of the ground motions that might affect Jackson Lake Dam due to a large earthquake on the Teton fault. Advances in the understanding of strong ground motions over the past decade have accrued due to the recording of several large earthquakes and research efforts to understand the seismic source, propagation, and site effects that produce and influence recorded ground motions. These efforts have lead to the development of improved methods of estimating and predicting strong ground motions at sites such at Jackson Lake Dam. These new data and approaches highlight the importance of geologic structure, basin geometry and properties, and site response to at-site ground motion estimation. Prior approaches to estimating ground motions at Jackson Lake Dam (USBR, 1987, Wong et al., 2000) relied on either simplified approaches or empirical data approaches that did not extensively incorporate these factors.

The surface trace of the Teton fault lies along the western shore of Jackson Lake, about 12 km (7 mi) west of Jackson Lake Dam (Figure 1-1). Late Quaternary fault scarps, formed by multiple Holocene surface faulting events, are present along about 60 km (37 mi) of the fault trace. The fault dips to the east forming a deep basin of late Cenozoic alluvial fill. Jackson Lake Dam was constructed on the eastern margin of this basin. At the damsite, largely unconsolidated late Quaternary alluvium ranges in thickness from zero on the south abutment to nearly 500 ft under the northern section of the dam. Although there are numerous earthquakes and potential seismic sources in the region, previous engineering analyses of Jackson Lake Dam by Reclamation have assumed that the Teton fault is the controlling seismic source for analyses of the dam based on proximity, activity rates, and maximum earthquake magnitudes. This assumption appears to be confirmed by results from a preliminary probabilistic hazard analyses (Wong et al., 2000). Thus, the primary focus of this study is on developing ground motions for large earthquakes on the Teton fault.

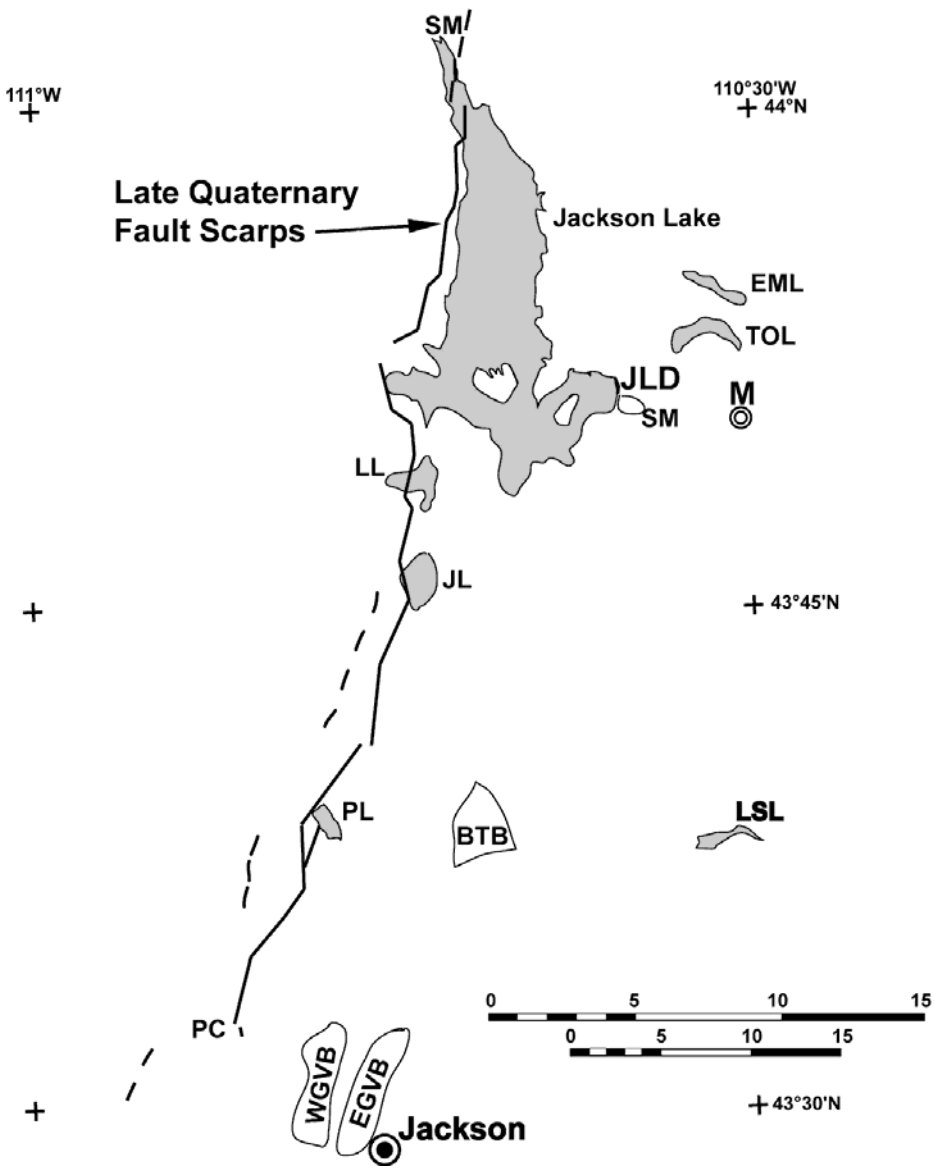

Figure 1-1: Map showing location of Jackson Lake Dam and late Quaternary trace of Teton fault. SM-Steamboat Mountain; EML-Emma Matilda Lake; TOL-Two Ocean Lake; JLD-Jackson Lake Dam; M-Moran; LL-Leigh Lake; JL-Jenny Lake; PL-Phelps Lake; BTB-Blacktail Butte; LSL-Lower Slide Lake; PC-Phillips Canyon; WGVB-West Gros Ventre Butte; EGVB-East Gros Ventre Butte.

1.2 Objectives and Scope

The objective of the Dam Safety investigations at Jackson Lake Dam is to reach a decision addressing whether or not additional modifications to the dam are reasonably required in accordance with the Reclamation Safety of Dams Act. The objective of this report is to provide estimates of the site-specific ground motions that might affect Jackson Lake Dam as a result of a large earthquake on the Teton fault. These ground motion results are intended as inputs for

engineering analyses of the stability of the dam during large earthquakes as part of an overall risk assessment for Jackson Lake Dam. Because the foundation of the dam consists of a varied thickness of unconsolidated alluvium and the site is located on the margin of a large structural basin, particular emphasis in the current ground motion analyses is to investigate aspects of seismic wave propagation and site response on estimates of ground motions at the site.

Within this study are embedded several major subtasks that are required as inputs to various phases of the ground motion analyses. These include 1) geologic source characterization of the Teton fault, 2) analyses of seismicity in the region of the Teton fault and Jackson Lake Dam, 3) analyses of the crustal basin velocity structure and seismic response, 4) empirical site response analyses based on specific foundation conditions and recorded data at Jackson Lake Dam, and 5) development of ground motions from the Teton fault for Jackson Lake Dam considering the integrated results of the previous tasks. As a final step, these results are portrayed in a simplified probabilistic framework to facilitate their input to Reclamation risk assessments for Jackson Lake Dam. Analyses of data from the Jackson Lake Seismic Network (JLSN) and from site-response instrumentation operated at Jackson Lake Dam between 1996-2002 in conjunction with the JLSN are major inputs to all of these subtasks.

1.2.1 Teton Fault Source Characterization. This task includes the compilation of geologic data on the distribution and rate of paleoearthquakes on the Teton fault. Quaternary fault scarps and faulted Quaternary deposits define the length of surface rupture associated with past earthquakes on the Teton fault. These data also provide information on the size, age and frequency of faulting events, and on the geometry of individual fault planes associated with paleoearthquakes on the fault. For ground motion analyses, the objective is to describe the constraints imposed by the available data on the location (coordinate information), orientation (strike and dip), and slip characteristics (slip per event) of fault planes associated with potential earthquakes on the Teton fault. For probabilistic analyses, it is necessary to describe the extent, size, ages, and frequency of paleoearthquakes along the fault, or to describe the behavior of the fault in terms of a slip rate and various models of earthquake occurrence. For both ground motion and probabilistic analyses, it is necessary to consider potential alternative models of fault behavior and the uncertainties in descriptive data and fault models. The scope of the present

investigation consists of a brief review and compilation of data from previous studies that have been conducted on the Teton fault. No new data collection or significant re-analyses of existing data have been conducted.

1.2.2 Seismicity Analyses. As part of this task, seismicity recorded by the JLSN between 1986-2002 were reanalyzed to provide refined regional (network-scale) velocity models, locations, magnitudes, focal mechanisms and recurrence information. The large and spatially diverse seismicity catalog from the JLSN provide a rich data set that were used to improve the regional velocity models used for preliminary locations of earthquakes within the JLSN. Improved earthquake locations allow enhanced discrimination of specific earthquakes that might be associated with the Teton fault and related structures and more reliable characterization of stress and slip regimes. Stress and slip information are primary inputs to describing the earthquake source and the velocity models are a primary input for evaluating seismic radiation from the source. Recurrence analyses are used in characterizing the probability of ground motions at the site.

1.2.3 Hanging Wall Crustal Velocity Structure.

Rupture directivity can be a significant issue for sites where fault planes have moderate- to shallow-dips and fault rupture extends beneath the site of interest. For scenarios in which the Teton fault dips less than about 50°, significant fault rupture on the northern and central sections of the Teton fault would include rupture at depth directly beneath or adjacent to the damsite. The impacts of 3D crustal velocity structure are also substantial, and to model these effects, data from a mini-array of three-component digital broadband stations operated in the vicinity of the dam in conjunction with the JLSN from October 1995 to May 2001 is used. Through waveform and traveltime modeling, the geometry and extent of the low-velocity basin surrounding the damsite area can be further resolved, and P- and S-wave velocities, and attenuation (Qp and Qs) characteristics defined to support the rock and soil ground motion simulations for the site.

1.2.4 Empirical Site Response.

Bedrock ground motions propagating from the Teton fault will be considerably modified by the near-surface soil column underlying much of Jackson Lake Dam. Recordings of strong ground shaking at the dam that could be used to directly estimate this effect do not exist. As a practical matter, since nearby large earthquakes occur infrequently, only the weak-motion recordings from smaller, more frequently occurring earthquakes are available. Ground motions from moderate-magnitude local earthquakes were recorded by three-component broadband velocity seismometers at six locations at Jackson Lake Dam. Recordings from the six sensors were compared to a reference location near the right abutment in order to estimate the weak-motion site response.

Computer codes for estimating the strong-motion site response are commonly based on one-dimensional models. These codes tend to underestimate the observed duration of shaking at Jackson Lake Dam. In order to partially account for the two and three-dimensional character of the observed weak-motion site response, yet employ available one-dimensional codes for estimating non-linear site response, a hybrid approach was used. This approach incorporates the longer durations observed from the weak-motion response to modify the input motions for use in one-dimensional computer codes.

1.2.5 Ground Motion Estimation for Jackson Lake Dam.

The influences of large-scale crustal velocity structure and source radiation on rock and soil ground motions at Jackson Lake Dam are the focus of this section. Ground motions are synthesized for the rock site station JLDW for a variety of magnitudes and source geometries to quantify peak ground motions scaling and variability associated with earthquake rupture scenarios postulated for earthquakes on the Teton fault. The uncertainties in fault dip are accounted for by considering multiple values of dip for each fault segment; thus as fault dip decreases, fault area and moment increase. A total of six fault segment and dip scenarios are considered when simulating ground motions. Rupture of the northern segment of the fault for dips of 35° and 45° involves fault rupture directly beneath the dam. It is necessary to determine how strongly rupture directivity may influence peak ground motions and ground motion variability at the dam for all of these near-source earthquake scenarios. Impacts of 3D crustal velocity structure are substantial and much of the modeling effort is devoted to accounting for the influences of 3D

velocity heterogeneity on ground motion amplitudes and durations, and evaluating the influence of fault dip uncertainties on ground motion characteristics

1.3 Jackson Lake Dam

Jackson Lake Dam is located on the South Fork of the Snake River about 48 km (30 mi) north of Jackson, Wyoming. The dam and reservoir provide water storage for the Minidoka Project, an irrigation project along the Snake River in southeastern Idaho. The dam and reservoir were left as inholdings when the Grand Teton National Park was initially established in 1929.

Jackson Lake Dam was originally constructed by the Bureau of Reclamation in 1907, rebuilt in 1911 and enlarged in 1916. The resultant dam was a composite structure consisting of a short (south) embankment section on the right abutment adjacent to Signal Mountain, a short combined concrete spillway and outlet works section across the former channel of the Snake River, and a long embankment section that extended north across the Pilgram Creek alluvial fan. By the mid-1970's it was recognized that aspects of the original construction were potentially susceptible to earthquake-induced failure. Initial modifications to the concrete section were completed in 1977, but since much of the original embankment sections were constructed with hydraulic fill methods and minimal foundation treatments, more extensive investigations and analyses were required. Following these studies of potential earthquake hazards, foundation conditions, and alternatives, additional modifications were completed to the dam by 1989. These modifications included major changes to roadways that sit atop the south embankment and concrete section, widening of the south embankment, further modifications to the concrete sections of the dam, and complete reconstruction of the north embankment with extensive strengthening of the underlying foundation. Strengthening of the north embankment foundation was accomplished through dynamic compaction along the entire length of the dam and through construction of variably-sized SMW (concrete-soil mix walls) at the upstream and downstream toes of the embankment from the concrete section north to approximately station 29+00 (Stelma, 1996) (Figure 1-2).

The present dam has a total crest length of about 1500 m (4920 ft) at elevation 2066.7 m (6780.5 ft). The dam impounds a reservoir containing 7.7 x 10^8 m^3 (624,000 acre-ft) at the normal operating pool elevation of 2060.4 m (6760 ft).

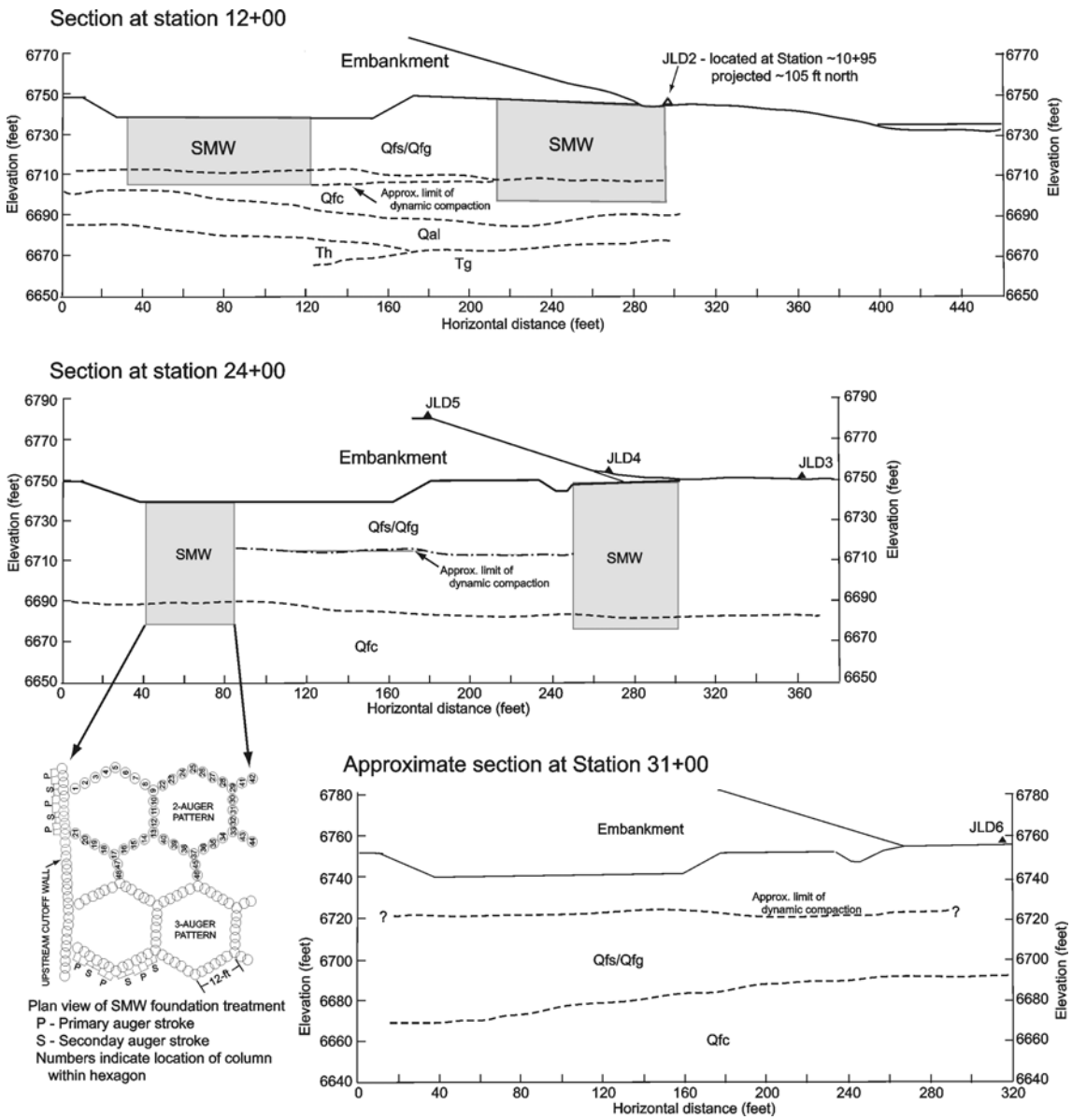

Figure 1-2: Schematic sections through Jackson Lake Dam at stations 12+00, 24+00, and 31+00. Extent of SMW treatment is shown by shaded boxes and in plan view sketch. Extent of dynamic compaction treatment zone is indicated by dot-dash line. Positions of seismographs sensors used to evaluate site response are indicated with triangles and labels. Sections and geologic data are modified from Stelma (1996). See text and Figure 1-3 for geologic legend and explanation.

1.3.1 Geologic Setting of the Dam. The right (south) abutment of Jackson Lake Dam is founded on the northern edge of Signal Mountain, a west-tilted block of early- to pre-Quaternary volcanic rocks and sediments capped by a thin veneer of young glacial deposits. Signal Mountain and Blacktail Butte (located further south in Jackson Hole) delineate the approximate western limit of pre-Quaternary rocks within Jackson Hole adjacent to the Teton fault (Figure 1-1 and Plate 4-1). West of these areas and extending nearly to the Teton fault, lies a thick sequence of Quaternary glacial deposits and alluvium; east of these areas are older Cenozoic alluvial deposits and weakly consolidated Mesozoic sedimentary rocks (Love et al., 1992). Quaternary glaciers flowing into Jackson Hole headed on the Yellowstone/Absaroka source area north and east of Jackson Lake Dam (e.g. Pierce and Good, 1992). Thick lobes of ice flowing through the damsite area excavated deep scour troughs that rapidly filled with alluvial and lacustrine deposits as the glaciers retreated (Pierce and Good, 1992; Smith et al., 1993). Jackson Lake Dam is located on one edge of a deep glacial scour trough that lies north of Signal Mountain. This trough probably extends several kilometers west of the dam beneath Jackson Lake, but probably bifurcates to the east and northeast in the damsite area. Near the present damsite, ice lobes flowing west, up the present Snake River, and west-southwest through the Emma Matilda Lake area joined. Thus, the northern extent of the scour trough is not well defined and likely extends well beyond the northern end of Jackson Lake Dam. As a result, the south embankment and concrete sections of Jackson Lake Dam are founded on variably compacted to over-compacted glacial deposits and Huckleberry Ridge Tuff while the north embankment section of the dam is constructed on a northward-thickening wedge of post-glacial alluvium and lacustrine units deposited on top of a compact glacial deposit (Figure 1-3; USBR, 1987). At the northern end of the dam, these relatively unconsolidated post-glacial deposits reach a thickness of about 180 m (600 ft). The presence of the glacial scour trough, and the large velocity contrast between the post-glacial alluvial fill and the underlying, older units are significant factors for estimation of ground motions at the site.

Material properties of the uppermost section of the post-glacial alluvial fill were derived from extensive drilling along the footprint of the dam that was done in conjunction with design and construction of the modification (Lockhart, 1986; Stelma, 1986; USBR, 1987). A limited number

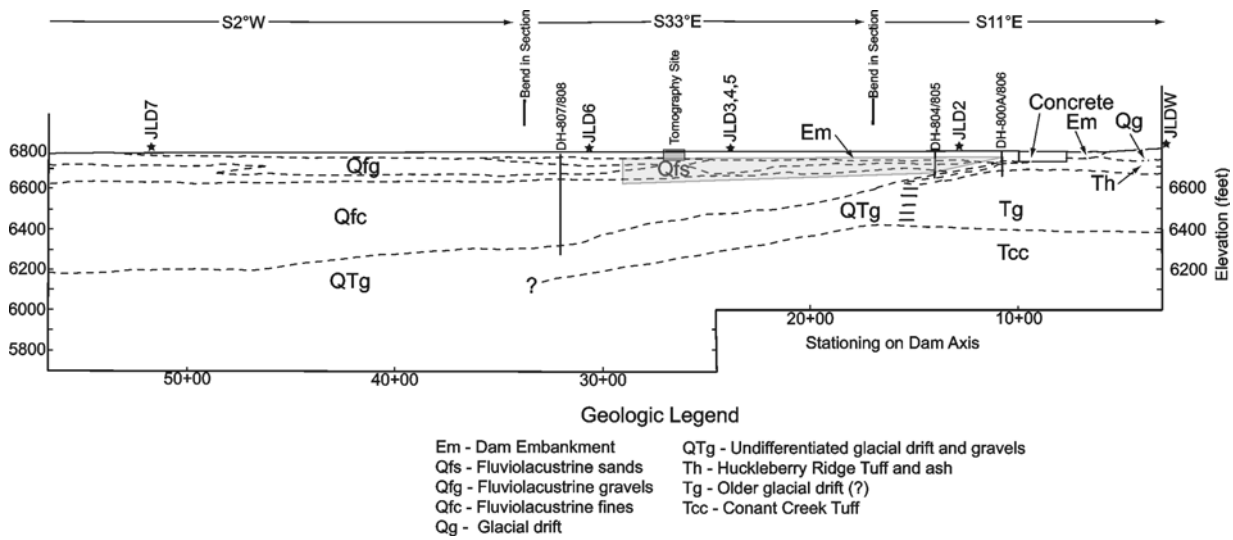

Figure 1-3: Generalized geologic cross section along the axis of Jackson Lake Dam. Foundation treatment consisting of SMW (shaded area) along the upstream and downstream toe of the embankment extended from the concrete section north to station 29+00 (see Figure 1-2). Dynamic compaction foundation treatment was completed beneath the embankment section north of the concrete section from about station 11+00 to about JLD7. Drillholes with geophysical logs (Sirles, 1986) are shown and labeled. Tomography site (Wright, 1990) is shown with grey box. Seismometer sites are shown with stars and labels. Geologic data compiled and modified from Gilbert et al. (1983), Lockhart (1986), USBR (1986), and Stelma (1996). View to east, looking downstream.

of drillholes penetrated the entire section. As part of these investigations, the alluvial fill beneath the northern embankment was described as three complexly interbedded subunits (USBR, 1987).

"The subunit termed gravel (Qfg) of the fluviolacustrine sediments consits of predominantly coarse sand and gravel, but may include some oversize, as indicated by drilling conditions observed while advancing the boreholes. Deposits of the subunit are saturated, loose, unconsolidated, and range from nonstratified to poorly stratified. Wash cuttings returned from the Qfg consist of fragments of quartzite and other metamorphics and some volcanics.

The subunit termed sand (Qfs) of the fluviolacustrine sediments consists of predominantly fine-grained sand but includes variable amounts of the medium and coarse sand fractions. The Qfs is saturated, loose, unconsolidated, and poorly stratified. Deposits of the Qfs subunit may contain a variable range of organic matter varying from less than 1 up to 5 percent.

The subunits termed fines (Qfc) of the fluviolacustrine sediments is composed of clay, silt, and very fine-grained sand. The Qfc is soft, unconsolidated, and ranges from thinly bedded to laminated, with minor and scattered sand and gravel lenses."

In contrast to the fluviolacustrine deposits that underlie Jackson Lake Dam, other deposits in the foundation (Figure 1-3) are much more consolidated and hard. The contrast in material properties is shown by a limited suite of geophysical investigations (Sirles, 1986; Wright, 1990) which provides geophysical properties that can be directly used in modeling of ground motions at the site and interpretation of site response data gathered from instruments at the dam. These data are discussed in more detail in Sections 5 and 6 in conjunction with site response and ground motion modeling.

1.3.2 Previous Seismic Hazard and Ground Motion Studies. No formal investigations of seismic hazards or ground motions are documented in association with the original dam construction in the early 1900's. In support of the modification studies of Jackson Lake Dam in the late 1970's and early 1980's, Reclamation conducted extensive seismic hazard analyses to develop earthquake loadings that were used in developing modification designs for the dam. These seismic hazard studies (Gilbert et al., 1983) included the first compilation and recognition of the extent of late Quaternary fault scarps along the Teton fault and established an MCE (Maximum Credible Earthquake) of M_L7.5 for the Teton fault as the most significant seismic source for Jackson Lake Dam. Gilbert et al. also identified other local and regional earthquake sources of potential significance, provided assessments for potential surface faulting at the site, coseismic subsidence and tilting of the damsite and reservoir basin which could lead to differential elevation changes and seiche waves in the reservoir, and seismically-induced landslides around the reservoir. Seismic loadings and ground motions for the Teton fault used in analyses of the proposed modifications were developed with input from a consultant board that provided review of the proposed modification designs and are documented in numerous technical memoradums (USBR, 1987). Details of the input motions varied slightly based on needs for individual analyses, but most were based on a time history record for the MCE that used a modified Pacoima-Taft record with a peak acceleration between 0.57-0.75 g and durations of 20-38 seconds as the input bedrock motions. Based on inputs from the consultant board, these

motions were propagated through the alluvial fill beneath the embankment sections and resultant free-field motions at the toe of the embankment sections ranged between 0.25 - 0.36 g.

Based on recommendations contained in Gilbert et al. (1983) the Jackson Lake Seismic Network (JLSN) was established in 1986. Wood (1986) describes the initial configuration and operation of the network. Data from the JLSN used in analyses for this report are discussed in Section 3.

Recently, Wong et al. (2000) completed a preliminary probabilistic seismic hazard analyses for Jackson Lake Dam and other nearby Reclamation dams. Their analyses provided input bedrock motions which included the hazard contributions from both the Teton fault as well as numerous other nearby and regional seismic sources. For return periods of 10,000 and 50,000 years respectively, the estimated peak horizontal accelerations were 0.89 and 1.19 g, and the 1.0 sec spectral accelerations were 0.91 and 1.42 g. Review of the results in Wong et al. indicate that for all return periods greater than about 100-200 years, the Teton fault is the dominant contributor to input bedrock ground motions at the Jackson Lake Dam site.

1.4 Acknowledgements

Completion of this report has been a collaborative effort on the part of several individuals in the Seismotectonics and Geophysics Group. Lisa Block conducted the joint-velocity hypocenter inversions described in Section 3.1 and Appendix A. Roland LaForge performed the recurrence analyses in Sections 3.3 - 3.6. Dan O'Connell was responsible for focal mechanism analyses in Section 3.2, basin modeling in Section 4, and ground motion analyses in Section 6. Dean Ostenaa developed the source characterization for the Teton fault in Section 2, compiled initial drafts of introductory and summary sections, and assembled the overall report framework and text from the other contributors. Chris Wood conducted seismicity analyses of JLSN data, compiled the catalogue used in recurrence analyses, conducted the site response analyses in Section 5, and has had overall responsibility for operations of the JLSN since its inception. Jerry Wright provided overall management and direction to these efforts. Ralph Archuleta and Kenichi Tsuda of the University of California, Santa Barbara, constructed nonlinear soil models and performed nonlinear soil calculations. Robert Graves of URS Corp, Pasadena, performed the 3D finite-difference reciprocity Green's function calculations.

Internal peer review of drafts of this report were provided by Jon Ake and Larry Anderson of the Seismotectonics and Geophysics Group. Paul Somerville of URS Corp, Pasadena, reviewed the initial draft report and provided many helpful comments and suggestions. Ralph Archuleta hosted the meeting for the initial review at the Institute for Crustal Studies and provided many helpful comments and suggestions. Bob Smith provided supplementary information for several of his publications concerning seismotectonics and crustal structure in the study area. Fabian Bonilla provided the nonlinear soil software NOAH, Peng Cheng Liu provided the 3D viscoelastic variable grid-spacing finite-difference program nuf3d, Robert Graves provided the 3D viscoelastic finite-difference program emod3d, and Shawn Larson provided the 2D viscoelastic finite-difference program e3d. We acknowledge the use of The Generic Mapping Tools (Wessel, P., and W. H. F. Smith, New, improved version of Generic Mapping Tools released, EOS Trans. Amer. Geophys. U., vol. 79 (47), pp. 579, 1998).

Seismicity data were provided by the Jackson Lake Seismic Network, the University of Utah Seismograph Stations, the Northern California Earthquake Data Center, the Northern California Seismic Network, U.S. Geological Survey, Menlo Park, the Berkeley Seismological Laboratory, University of California, Berkeley, and the Advanced National Seismic System.

2.0 TETON FAULT- SOURCE CHARACTERIZATION

2.1 Introduction

The Teton fault is one of several major late Quaternary faults within the Intermountain Seismic Belt region surrounding Jackson Lake Dam. These faults include the Centennial, Hebgen Lake, and Madison Range normal faults to the north and west of the dam, as well as the seismically active Yellowstone Caldera and the Star Valley and Greys River faults to the south near the Snake River Range (Figure 2-1). In addition to these earthquake sources, there are numerous other late Quaternary faults and potential seismic sources in the region surrounding Jackson Lake Dam (Wong et al., 2000; Machette et al., 2001). The surface trace of the Teton fault lies along the western shore of Jackson Lake, within about 12 km (7 mi) of Jackson Lake Dam and dips to the east potentially extending beneath the damsite if fault dips are less than ~ 45° (Figure 2-2). Late Quaternary fault scarps, the product of multiple Holocene surface faulting events, are present along about 60 km (37 mi) of the fault trace. Previous engineering analyses by Reclamation at Jackson Lake Dam have assumed that the Teton fault is the controlling seismic source for analyses of the dam based on proximity and maximum earthquake magnitudes, and this assumption appears to be confirmed by results from a preliminary probabilistic hazard analyses (Wong et al., 2000).

In this section the seismic source characteristics of the Teton fault are provided. The initial task in this assessment is to delineate the extent of rupture associated with past earthquakes on the Teton fault as shown by late Quaternary fault scarps and faulted Quaternary deposits. These data also provide information on the age and frequency of faulting events, and on the geometry of individual fault planes associated with paleoearthquakes on the fault. For ground motion analyses, the objective is to describe the constraints imposed by the available data on the location (coordinate information), orientation (strike and dip), and slip characteristics (slip per event) of fault planes associated with potential earthquakes on the Teton fault. For probabilistic analyses, it is necessary to describe the extent, size, ages, and frequency of paleoearthquakes along the fault, or to describe the behavior of the fault in terms of a slip rate and various models of earthquake occurrence. For both ground motion and probabilistic analyses, it is necessary to consider

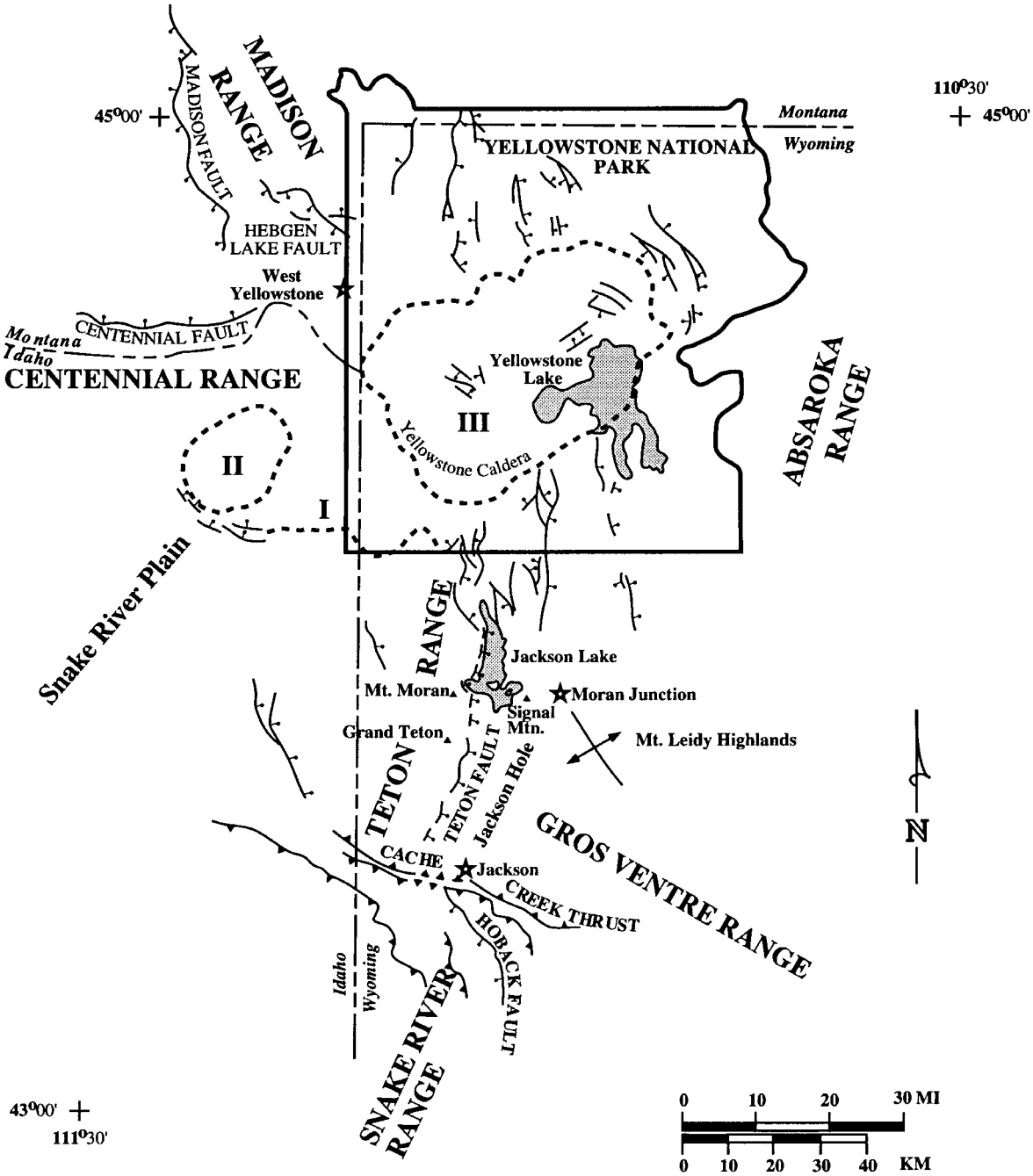

Figure 2-1: Regional tectonic map of the northwestern Wyoming and Jackson Lake Dam region. Ages of Yellowstone calderas (outlined with dashes): I = 2.0 Ma, II = 1.2 Ma, and III = 0.6 Ma. Normal faults shown with hachured symbol on downthrown side; thrust faults with barbs on overthrust block. Figure from Smith et al. (1993b).

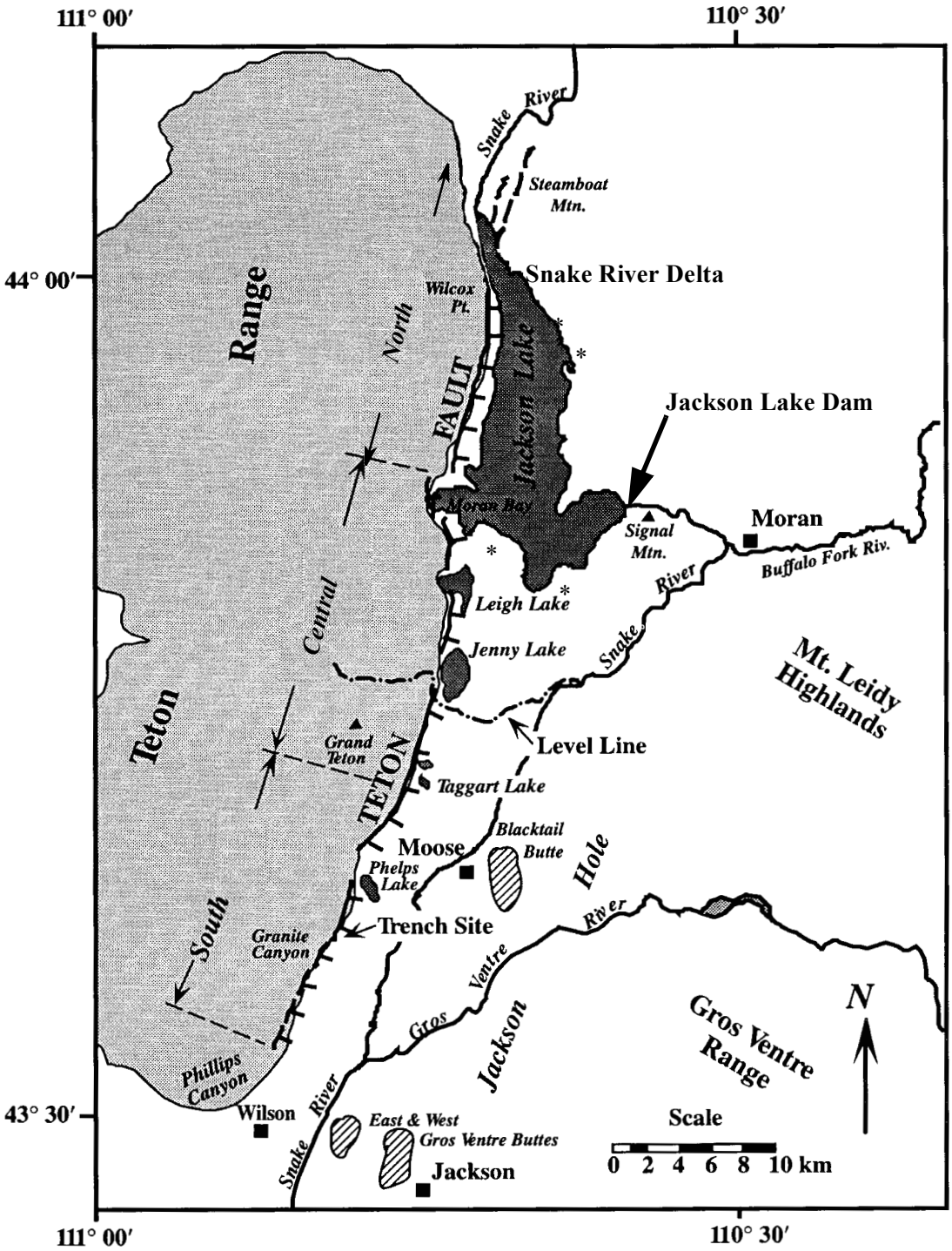

Figure 2-2: Map of the Teton Range-Jackson Hole region showing the generalized late Quaternary trace of the Teton fault in relationship to Jackson Lake Dam. Approximate boundaries of sections of the Teton fault are indicated with arrows along the fault. Approximate locations where submerged shorelines of Jackson Lake date paleoseismic events are shown with *around the margins of Jackson Lake. "Trench Site" is the Granite Creek site of Byrd et al. (1994) and Byrd (1995). Cross-hachured areas are outcrops of Paleozoic rocks in Jackson Hole. Figure slightly modified from Smith et al. (1993b).

potential alternative models of fault behavior and the uncertainties in descriptive data and fault models.

2.1.1 Primary Data Sources. There are three primary sources of data for the seismic source characterization of the Teton fault: 1) previous Reclamation seismic hazard studies, 2) research studies by the University of Utah, and 3) research and mapping projects by the U.S. Geological Survey. Although some of these studies have been quite extensive and limited areas studied in great detail, overall, the Teton fault has been mapped in only moderate detail and there is relatively little detailed information available on the paleoseismic history of the fault. Of particular importance is the lack of a detailed fault map coupled with detailed mapping and dating of the Holocene to late Pleistocene deposits in which fault scarps are found.

Several previous Reclamation seismic hazard studies have addressed the Teton fault in some detail. Seismotectonic studies for Jackson Lake Dam by Gilbert et al. (1983) summarized previous studies, produced the first map which depicted the extent of fault scarps along the Teton fault, and developed slip-rate estimates based on the estimated offsets of the 2-Ma old Huckleberry Ridge tuff and late Quaternary deposits along the range front. As part of a seismotectonic study for Grassy Lake Dam, Ostenaa et al. (1993) mapped fault scarps along the northern section of the Teton fault in greater detail and evaluated evidence for fault activity along several potential traces of the Teton fault north of Jackson Lake. Based on data from these studies, Ostenaa and Gilbert (1988) described some potential geometric controls on the segmentation of the Teton fault. Most recently, Wong et al. (2000) compiled fault activity and slip rate data for many faults in the region as part of a preliminary probabilistic hazard evaluation for Jackson Lake Dam and several other Reclamation dams in the region.

Research by the University of Utah since the 1980's has resulted in several significant contributions to understanding the paleoseismic history of the Teton fault. Field investigations extended the mapping and provided additional offset measurements of late Quaternary fault scarps (Susong et al., 1987; Byrd, 1995). Geophysical investigations in Jackson Lake identified potential fault traces in the lake sediments (Smith et al., 1993a). At one site, Granite Creek, trench investigations provided detail on the Holocene displacement history of the fault (Byrd et al., 1994). A level line across Jackson Hole has provided a basis for repeated measurements of

deformation in the basin. Results of these field investigations, including models of fault behavior and segmentation, and analyses of leveling results are presented in several publications (Byrd et al., 1994; Smith et al., 1993b; Sylvester et al., 1991).

Mapping by J.D. Love of the U.S Geological Survey provided the earliest descriptions of the magnitude and recency of faulting on the Teton fault (e.g., Love and Montagne, 1956; Love and Reed, 1971; Leopold and Love, 2002). Compilation geologic maps of the Grand Teton National Park (Love et al., 1992) and the State of Wyoming (Love and Christiansen, 1985) provide a framework for the overall structure and geologic setting of the fault. Ongoing studies of the Quaternary glacial history of the Yellowstone - Teton region provide much of the chronologic data for evaluating the age of fault scarps and resulting estimates of slip rates (Pierce and Good, 1992). Detailed geoarcheology studies of sites submerged by Jackson Lake Reservoir yielded evidence of the ages and amount of offset for multiple Holocene earthquakes on northern and central sections the Teton fault (Pierce and Good, 1992; Connor, 1998). Results of previous studies for the Teton fault and other faults in the region have been compiled in a database which provides slip rate and other fault characterization data (Machette et al., 2001).

2.2 Late Quaternary Faulting on the Teton Fault

2.2.1 Quaternary Chronology of Faulted Deposits Along the Teton Fault. The Quaternary chronology of faulted deposits, together with the amounts of faulting, is the data from which estimates of faulting rates are derived. To the extent that there are large gaps in the detailed understanding of the ages of deposits along the fault, there will also exist significant uncertainty in the rates and chronology of faulting and earthquake recurrence. While there is a broad understanding of the geomorphic history and ages of the faulted Quaternary deposits along the front of the Teton Range (e.g., Love et al., 1992), there has been relatively little detailed mapping and chronology developed for most sites where fault scarps have been mapped. In general, four broad groups of late Quaternary (past 140 ka) deposits are clearly faulted: 1) glacial deposits in Jackson Hole related to ice lobes which primarily sourced from the highland areas of the Yellowstone Park area to the north and northeast, 2) glacial deposits related to local glaciers flowing out of the Teton Range, 3) deposits along glaciated drainages that post-date the major deglaciation of the Teton Range glaciers and Yellowstone ice sheet, and 4) colluvial deposits that

blanket the slopes of the Teton Range front between major drainages. Each of these four groups includes several different types of deposits and can potentially include deposits with ages that span as much as 20,000 to 40,000 years.

The first broad group of deposits includes extensive deposits associated with oldest well-documented glaciation in Jackson Hole, termed the Munger (Bull Lake? or glaciation 2 of Love et al., 1992), as well as deposits of younger, Pinedale glaciers that entered Jackson Hole. The volume of ice flowing into Jackson Hole at the peak of the Munger glaciation was of such extent that all of Jackson Hole was filled with ice (e.g., Love and Reed, 1971; Love et al., 1992; Pierce and Good, 1992). Based on correlation to dated glacial deposits at West Yellowstone and to the marine oxygen-isotope stage record, the age of this glaciation is thought to be about 130,000 - 170,000 ka (Pierce and Good, 1992). Although no fault scarps are mapped in deposits of the Munger glaciation along the Teton fault, at Timbered Island and Windy Point, these deposits are apparently tilted towards the fault, indicative of significant cumulative displacement.

The last and most recent large-scale glaciation in Jackson Hole, the Pinedale, consisted of at least two phases (Pierce and Good, 1992; Connor, 1998). During both phases of the Pinedale glaciation, ice lobes flowed into Jackson Hole from highland areas to the north and northeast and built large end moraines and outwash surfaces in Jackson Hole south of Jackson Lake. Related moraines and recessional deposits are present on both the west and east shores of Jackson Lake. Along the west shore of Jackson Lake, some of these deposits straddle the trace of the Teton fault (Love et al., 1992; Pierce and Good, 1992; Ostenaa et al., 1993). Glaciers from the Teton Range apparently extended only a relatively short distance out from the range front and made relatively small contributions to the ice lobes in the main valley. However, the detailed history of individual sequences derived from the range-front glaciers and the deposits of the main valley ice lobes has not yet been described. Moraines constructed by Pinedale-age range-front glaciers also cross the Teton fault in several areas and are clearly faulted (Gilbert et al., 1983; Love et al., 1992).

The older phase of the Pinedale glaciation in Jackson Hole is termed the Burned Ridge. There are no direct ages in Jackson Hole on deposits of this phase and the age of the Burned Ridge is estimated by correlation to the marine oxygen-isotope stage record. This correlation suggests an age range of about 35,000 to 72,000 years ago (Pierce and Good, 1992; Connor, 1998). No Teton

fault scarps occur directly on the Burned Ridge deposits of the major ice lobe in Jackson Hole, but these deposits have been tilted westward by displacement on the fault (e.g., Love and Montagne, 1956; Byrd, 1995). The full extent of Burned Ridge phase deposits from range-front glaciers is unclear. It is possible that some of the older range-front glacial deposits on which fault scarps are present are in fact correlative to the Burned Ridge phase. However, no detailed mapping has been done to substantiate or refute this.

The younger phase of the Pinedale glaciation in Jackson Hole had two positions defined by deposits of the ice lobes: a maximum advance (Hedrick Pond) and a recessional stand (Jackson Lake) (Pierce and Good, 1992; Good and Pierce, 1997; Connor, 1998). Radiocarbon ages on materials recovered from drill holes at Jackson Lake and ages on samples from the Yellowstone Lake area (source area for the ice lobes) indicate the ice lobes had retreated from the Jackson Lake area by about 15,000 ^{14}C yr B.P., an age roughly equivalent to 17,000 to 18,000 calendar years (Pierce and Good, 1992; Good and Pierce, 1997; Connor, 1998). Thus, the ages of the moraines associated with the Jackson Lake recession and Hedrick Pond maximum advance are older, possibly in the range of 20,000 to 35,000 years ago.

The second broad group of deposits that are significant to evaluating the paleoseismic history of the Teton fault are the glacial deposits from glaciers flowing out of the Teton Range. Ages for these deposits along the Teton fault are inferred based on correlation to the Jackson Lake and Hedrick Pond deposits. Deglaciation of Teton Range glaciers is generally inferred to be broadly synchronous with deglaciation of the Yellowstone ice sheet, but there are no published studies that confirm this. In the Moran Bay area and other sites on the west side of Jackson Lake, glaciers from the Teton Range appear to have merged with the ice lobes that sourced in the Yellowstone area to the north and northeast. The absence of significant end moraines from the range-front glaciers in these areas appears to suggest that deglaciation of the Teton Range was mostly in phase with, or possibly slightly preceded, retreat of the ice lobes that sourced in the Yellowstone area. At many sites along the range front, there is clearly a sequence of glacial deposits, which may or may not reflect significant age differences, but detailed mapping and descriptions of these sites are generally lacking. Thus, the age of range-front glacial deposits faulted along the Teton fault is assumed to be similar to ages inferred for the Jackson Lake and Hedrick Pond deposits, or

about 20,000 to 35,000 years ago. The Teton Range is assumed to have been essentially deglaciated by about 17,000 to 18,000 years ago.

The third broad group of deposits are inset within the glacial deposits that flank most drainages of the Teton Range. These deposits are related to the deglaciation and post-Pinedale processes in these drainages, and spans a time interval that appears to include several large faulting events on the Teton fault. In the steeper drainages this includes debris flows and avalanche deposits that may be related to the smaller scale post-Pinedale glaciers that were limited to the higher elevations in these drainages. In other areas, there are alluvial fan and fluvial deposits. With two exceptions, detailed chronologies for these deposits have not been developed for sites along the Teton fault. In the Jackson Lake area, Pierce and Good (1992) and Connor (1998) developed a detailed post-glacial geomorphic framework for several archaeological sites. The chronology for this framework is supported by several radiocarbon ages and archaeological dating of sites as old as about 8000 years. In the Granite Creek area, radiocarbon ages from a trench excavated across a fault scarp indicate that some of the post-glacial deposits along Granite Creek are in the range of 4000 to 8000 years (Byrd et al., 1994; Byrd, 1995). However, in other areas, portions of these deposits could be as old as 17,000 - 18,000 years, the estimated time of major deglaciation in Jackson Hole.

The fourth broad group consists of large areas of undifferentiated fan and colluvial deposits that exist between the major drainages along the Teton range front (e.g., Love et al., 1992). In some areas, fault scarps are present on these deposits, but in other areas these deposits appear to post-date the most recent surface faulting. No specific studies have been done to define a chronology for these deposits. Limited areas within these deposits are likely historic, while other areas possibly are synchronous in age with the glacial sequences discussed above. A tentative age range from 0 - 17,000 years is assigned to these sites.

2.2.2 Distribution of Late Quaternary Fault Scarps and Surface Rupture. Late Quaternary fault scarps are recognized along approximately 60 km (38 mi) of the Teton fault (Gilbert et al., 1983; Ostenaa et al., 1993; Smith et al., 1993b; Byrd et al., 1994; Byrd, 1995; Machete et al., 2001). These scarps can be followed nearly continuously along the steep front of the Teton Range from near Phillips Canyon, at the southern end of the fault, to the east side of

Steamboat Mountain, located at the north end of Jackson Lake (Figure 2-2). Gaps in the mapped continuity of the scarps are mostly associated with areas of active drainages and lakes. A notable exception is western Moran Bay of Jackson Lake, where there is an approximately 2-km stepover in the scarps, and no evidence of faulting in the glacial or post-glacial sediments beneath Moran Bay (Smith et al., 1993a).

Quaternary displacement on the Teton fault has clearly extended beyond the limits of the fault scarps mapped along the range front, as shown by the range front and structural relief at the southern end of the range (e.g., Love and Reed, 1971; Lageson, 1987) and by numerous fault traces and offset of 2 Ma year old Huckleberry Ridge tuff at the northern end of the fault (e.g., Love et al., 1992). However, existing studies have not identified evidence of surface rupture on these faults at the northern and southern ends of the range in the past approximately 15 ka (e.g., Ostenaa et al., 1993; Gilbert et al., 1983).

In previous studies, the scarps along the Teton fault were compiled on 1:62,500 scale base maps (Gilbert et al., 1983; Sussong et al., 1987; Smith et al., 1993b; Love et al., 1992), with the exception of the northern section of the fault, which was compiled on a 1:24,000 scale base map (Ostenaa et al., 1993). While the locations of many fault scarps along the Teton Range have been noted, the mapping in most areas has not been of sufficient detail to also identify a narrow range of ages for the deposits faulted at each site along the fault. Thus, for purposes of slip rate estimation and fault characterization, the offsets measured on these scarps are combined with broad age ranges based on regional correlations.

For purposes of ground motion modeling and seismic hazard calculations, the existing mapping of the fault scarps has been used as a basis to develop representations of the fault that can be used in these models. In these models, faults are depicted as planar structures, defined by a surface trace with a strike and dip, and by the depth of seismogenic fault rupture. The surface trace and strike are well defined by the distribution of fault scarps along the Teton fault. The dip of the fault is only poorly constrained by surface geology, limited subsurface data and structural models, and observational information from historical earthquakes. The depth of seismogenic fault rupture is defined by earthquake data from local and regional seismic networks, geophysical data and models, and historical earthquakes.

A somewhat simplified characterization of the surface fault geometry (Figure 2-3) is presented here for use in different ground motion and seismic hazard models. This characterization consists of 29 fault traces with varied strike and geometrical relations. Fault traces are defined based on changes in strike or discontinuities in the fault scarps. In this characterization (Appendix A, Table A-1), individual fault traces range in length from < 1 km to about 5 km and the location of each fault trace is generally within about 0.1 km of actual trace of the fault scarps.

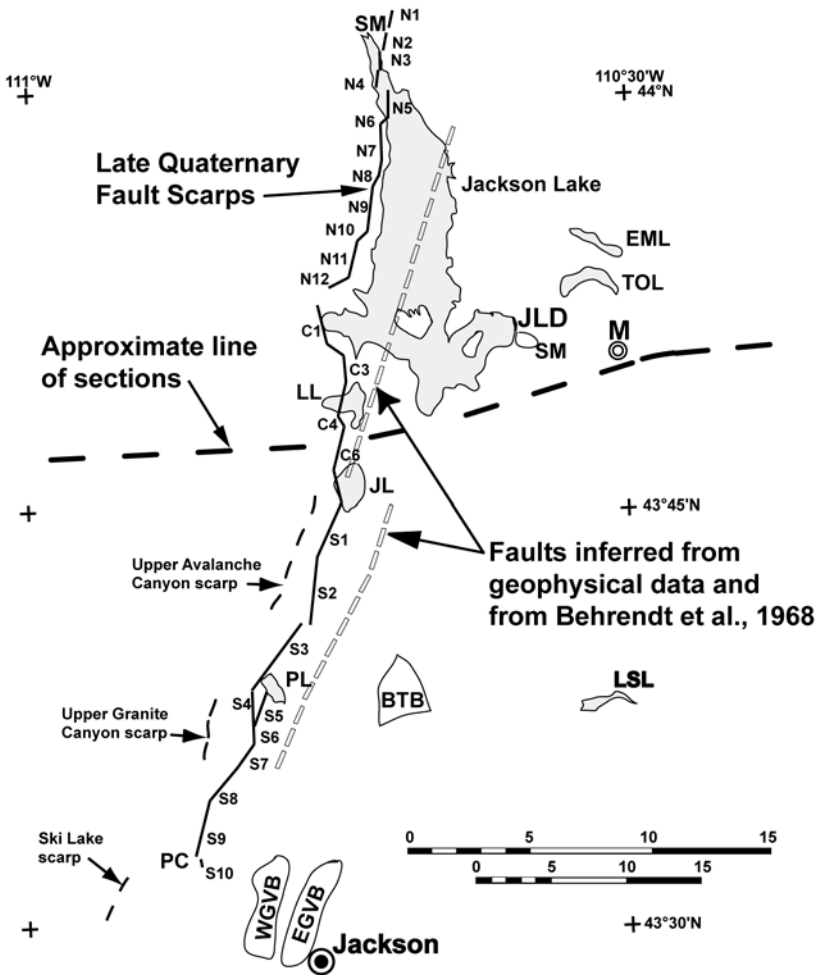

Figure 2-3: Map of fault traces defined by late Quaternary fault scarps along the Teton fault. Scarp and slip rate data for each trace are tabulated in Appendix A, Table A-2. Letter number combinations, N1, N2, etc., designate different fault traces in Appendix A, Table A-1. Dashed traces west of fault scarps are high-angle, 60-80°, faults mapped within Teton Range (Love et al., 1992) that coincide with scarps in Avalanche and Granite Canyons (Gilbert et al., 1983). Open box dashed fault traces east of fault scarps are approximate locations of buried, 35°-dipping faults defined by geophysical data (Behrendt et al., 1968). Sections across basin are shown in Figure 2-4,-5 and -6. SM- Steamboat Mountain, EML-Emma Matilda Lake, TOL-Two Ocean Lake, JLD-Jackson Lake Dam, M-Moran, LL-Leigh Lake, JL-Jenny Lake, PL-Phelps Lake, BTB-Blacktail Butte, LSL-Lower Slide Lake, PC-Phillips Canyon WGVB-West Gros Ventre Butte, EGVB-East Gros Ventre Butte.

For discussion purposes, it is convenient to consider the Teton fault as consisting of three major sections, termed northern, central, and southern (Figure 2-2). Names used for the fault sections in this report are generally consistent with Smith et al. (1993), Byrd et al. (1994) and Byrd (1995), but differ slightly from terminology used by Machete et al. (2001). However, it is not clear from the existing data on the fault whether or not these fault sections behave independently as separate fault rupture segments and earthquake sources or whether the entire fault ruptures in single earthquake events (e.g., Ostenaa and Gilbert, 1988; Smith et al., 1993b; Byrd et al., 1994; Machette et al., 2001).

The northern section of the fault (traces N1 - N12) consists predominantly of longer fault traces that strike between N-S and N10°E that alternate with short fault traces that strike about N30-65°E. In most cases, these shorter traces act as right steps to the overall trace of the fault, although a significant left step must be present beneath the northern end of Jackson Lake. Mapped fault scarps make sharp bends at these steps (Ostenaa et al., 1993). At Moran Bay, there is a substantial discontinuity in the scarps. The fault trace as defined by scarps both north and south of Moran Bay bends sharply around the bay, but does not join and there is an approximately 2-km gap in the scarps in this area. Further, geophysical surveys that cross potential projections of the fault in Moran Bay show no evidence of faulting in the sediments beneath the bay (Smith et al., 1993a).

The central section of the fault (traces C1 - C7) displays a more regular sawtooth pattern, defined by somewhat longer traces that strike about N10°E, which alternate with traces only slightly shorter that strike NW. The overall effect of the NW-striking traces is a left-stepping arrangement along this section of the fault. Throughout this central section, existing mapping indicates that the fault scarps have a high degree of continuity. In map view, the scarps have large bends and reentrants that are unrelated to steep topography which they traverse, indicating that individual fault traces have significantly disparate strikes. South of Jenny Lake the overall strike of the Teton fault becomes more northeasterly than on the central or northern sections of the fault north of Jenny Lake and the overall strike of the fault traces between Jenny and Taggart Lakes (traces C8-C9) is somewhat transitional between the fault traces north of Jenny Lake and those south of Taggart Lake. The fault trace geometry in this area is also somewhat transitional as well, but the

continuity of the surface fault scarps on fault traces C8 to C9, which extend south of Taggart Lake, is very high and similar to those on the central and northern sections of the fault.

The Taggart Lake area has been generally considered as the northern end of the southern fault section (e.g., Smith et al., 1993; Byrd et al., 1994; Machete et al., 2001) Fault scarps along this section of the fault define two arcuate to wedge-shaped traces, a northern group which is set back slightly and centered on Phelps Lake (traces S1-S4), and a southern, more curved wedge in the Teton Village to Phillips Canyon area (traces S5-S7). South of Taggart Lake, overall, the fault scarps appear to be more discontinuous than along other sections of the fault, particularly in the areas near Phelps Lake and the Jackson Hole Ski area. While there are several prominent fault scarps in these areas, such as near Teton Village, Granite Creek, and north of Phelps Lake, there are also several discontinuities or gaps in the scarps. Whether these discontinuities reflect incomplete surface rupture along this section of the fault or destruction of the fault scarps by erosion and deposition is unclear based on the existing mapping. The only site on the Teton fault where fault scarps have been trenched is at Granite Creek, along trace S4 (Byrd et al. (1994); Byrd (1995).

South of Jenny Lake is the only area along the fault where mapping has shown clear evidence of left-lateral offsets along the fault (Smith et al., 1993b; Byrd, 1995). Ostenaa and Gilbert (1988) suggested that left-lateral offsets along the more northeasterly striking sections of the fault were consistent with nearly E-W oriented extension affecting the fault as a whole, and not necessarily indicative of fault segmentation. Also, along the southern section of the fault, there appears to be some evidence for late Quaternary displacement along discontinuous, subparallel, high-angle faults within the range as shown by apparent short, fault scarps that coincide with the traces of these faults in Avalanche and Granite Canyons (Gilbert et al., 1983) and southwest of Phillips Canyon near Ski Lake (Love et al., 1992; Machete et al., 2001).

Because of the overall irregularity of the fault trace, we have used simplified representations of the Teton fault geometry in ground motion models described in subsequent sections of this report. For 2 or 3 plane representations of the fault, the planar fault sections used in the models are typically within about 1 km of the surface trace defined by the fault scarps, but locally may be as much as about 2 km from the surface trace defined by the fault scarps in areas where there are

large re-entrants in the scarps such as near Moran Bay. Characterization of the Teton fault as a single planar fault over the entire length of the fault scarps, inevitably leads to discrepancies of 5 km or more between the surface location of the single planar fault and the surface trace defined by the fault scarps. This discrepancy arises because overall average strike of the southern portion of the fault differs by more than 20º from the overall average strike of the central and northern portions of the fault (e.g., Figure 2-2 or 2-3). Thus, in ground motion modeling discussed in the following section of this report, the fault is displayed as two simplified planes, or simplified rupture segments. The northern rupture segment as used in the ground motion modeling consists of the northern and central fault sections discussed above, extending from the east side of Steamboat Mountain to just south of Taggart Lake (Figure 2-2 or 2-3). The southern rupture segment coincides with the southern fault section and extends from just south of Taggart Lake to Phillips Canyon.

2.2.2.1 Relationship of the Late Quaternary Fault to Older Structures. Most previous investigations of the Teton fault have recognized some linkage between the late Cenozoic deformation and earlier tectonic events in the area (e.g., Love and Reed, 1968, Lageson, 1992; Smith et al., 1993; Byrd et al., 1994). This has led to several differing views on the structure of the Teton fault. It appears that the strongest case for direct linkage between the Teton fault and preexisting structure can be made on the southern section of the fault where it appears that the fault has responded to the north-dipping Cache Creek thrust (e.g., Lageson, 1991). However, further north along the fault, the influence of this structure is diminished by its increased depth. As discussed subsequently in Section 4, geophysical characteristics of the basin differ substantially between the northern and southern portions of the basin. Some differences in perceptions of the structure of the Teton fault are the result of portraying the structure at different locations along the fault. Notably, sections based on Behrendt et al. (1968) which are drawn through the area between Jenny Lake and Jackson Lake, reflect a substantially differing structural setting from that present on the southern Teton fault nearer the Cache Creek thrust as discussed by Lageson (1992). Significant differences exist in previously published sections regarding the width and number of traces associated with the Teton fault, and the dip of fault planes considered to be part of the Teton fault (see Figures 2-4 and 2-5).

For this study, the late Quaternary trace of the Teton fault is defined by the fault scarps on Quaternary deposits along the range front. These data provide the surface location of the fault trace associated with the most recent cycle(s) of earthquake activity. In contrast, the Teton fault(s) defined by geophysical data (e.g., Behrendt et al., 1968) reflect subsurface characteristics of bedrock units and structure that may or may not be associated with recent earthquake activity. The geophysical data allow development of structural models which portray the cumulative effects of the entire history of movement on the Teton fault and other structures. The faults defined by geophysical data such as Behrendt et al. (1968), and data discussed subsequently in Section 4, define elements of the basin structure through which seismic energy radiates to reach the site of interest (Jackson Lake Dam). Thus, for the present investigation, it is important to distinguish the elements of structural interpretation which are significant to the seismogenic fault rupture from those which are significant to the overall composite structure of the basin. From this perspective, it appears that the late Quaternary trace of the Teton fault, on which the most recent series of earthquake-related surface ruptures have occurred, is not the trace which bounds the major basin that underlies northern Jackson Hole and contains a thick sequence of lower velocity, lower

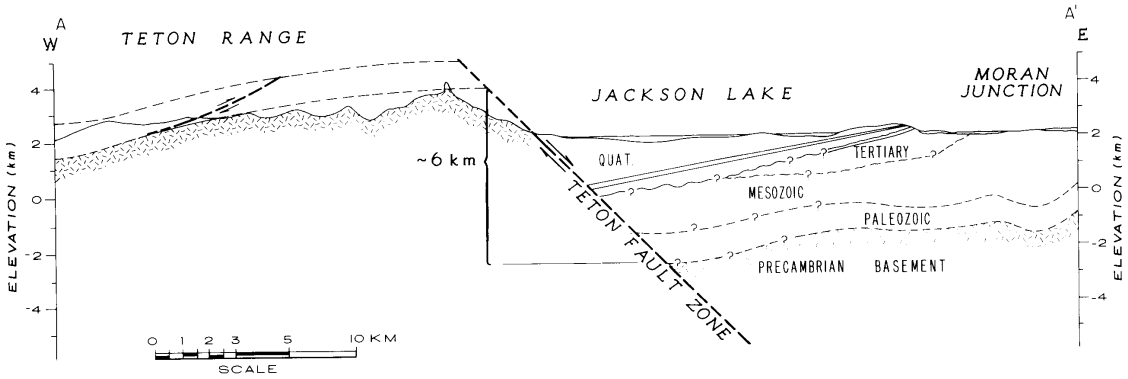

Figure 2-4: Schematic geologic cross section of the Teton Range and Jackson Hole depicting a vertical offset of ~6 km on the Teton fault copied from Smith et al. (1993). The vertical displacement is estimated based on the offset of the Cambrian Flathead Sandstone exposed on top of Mt. Moran to its projected depth beneath Jackson Hole. The subsurface configuration of Mesozoic and Paleozoic sediments beneath Jackson Hole is based on a projection of limited outcrop data and well data taken from Love et al. (1992), Behrendt et al. (1968), and Tibbetts et al. (1969). Section is vertically exaggerated. Fault dip as shown is this section is about 60°.

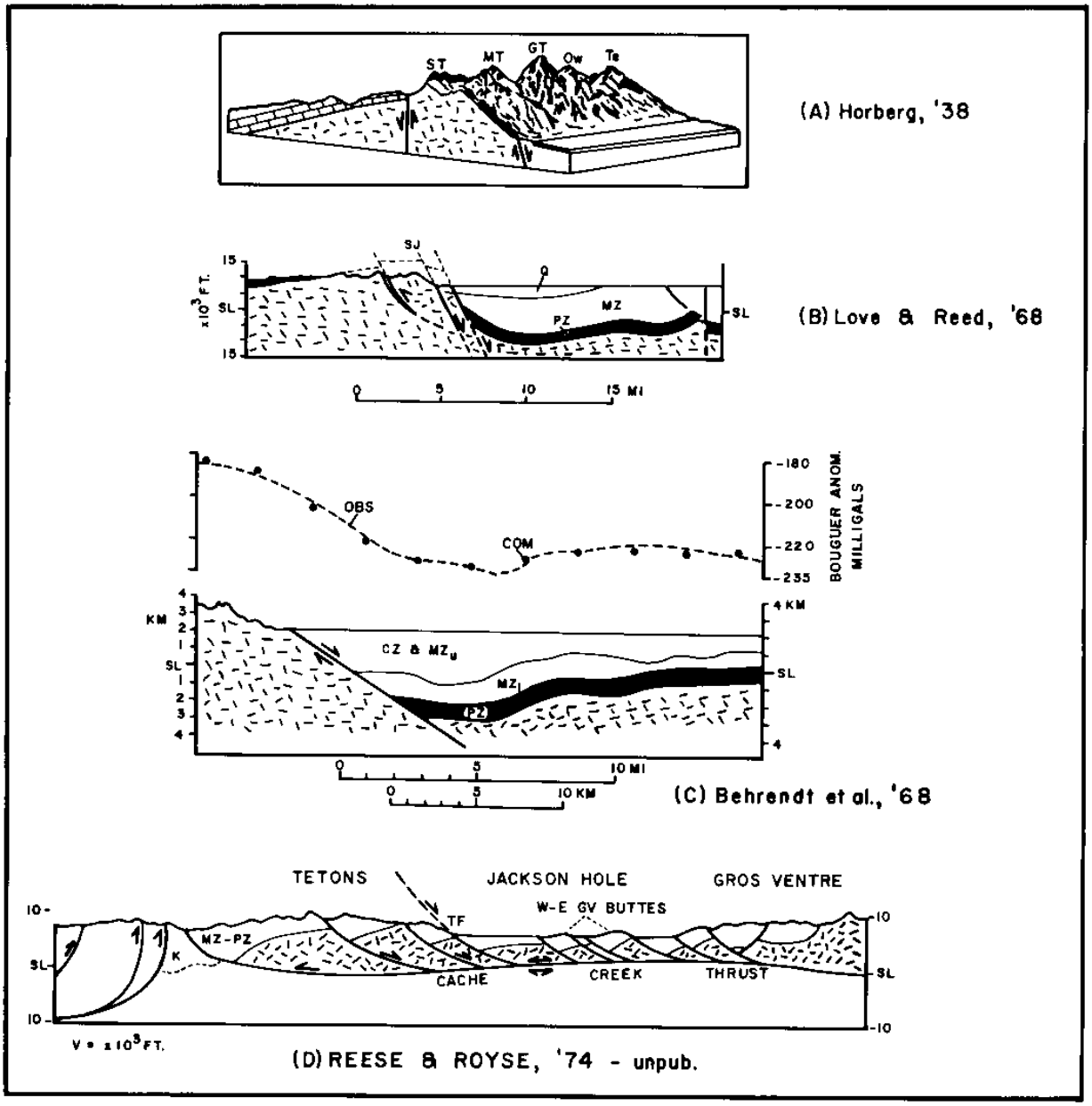

Figure 2-5: Various interpretations of the Teton Range and Teton normal fault from 1938 through 1974 (Figure 6 of Lageson, 1992). ST=South Teton; MT=Middle Teton; GT=Grand Teton; OW=Mount Owen; Te=Mt. Teewinot; SJ= Mt. St. John; TF=Teton normal fault; GV Buttes=Gros Ventre Buttes; OBS=observed gravity; COM=computed gravity. Rock units: Q=Quaternary deposits; CZ=Cenozoic rocks; K=Cretaceous rocks; MZu=Upper Mesozoic rocks; MZ=Mesozoic rocks; MZl=Lower Mesozoic rocks; MZ-PZ=Mesozoic and Paleozoic rocks, undivided; PZ=Paleozoic rocks; and Random hachures=Precambrian basement rocks.

density sediment (Figure 2-6). This further implies that the dip of the late Quaternary fault trace may not be the same as the major, basin bounding structure (Figure 2-6).

For purposes of the present study, the trace of the Teton fault defined by fault scarps on late Quaternary deposits is used as the site of the fault plane on which co-seismic rupture occurs.

2.2.2.2 Fault Dip. Available information on the dip of the Teton fault was reviewed by Byrd et al. (1994) and Byrd (1995), who concluded that the dip of the seismogenic fault lies between 45-75º. This range was derived primarily from regional information on the dip of faults associated with large normal-fault earthquakes and from limited geophysical information in the northern portion of Jackson Hole (see Byrd et al., 1994 and Byrd, 1995 for details). Most estimates compiled by Byrd et al. (1994) were within the range of 45-75º, with the notable exception of Behrendt et al. (1968) who showed a dip of 35º for the Teton fault. However, as noted in the section above, the fault of Behrendt et al. is not coincident with the late Quaternary

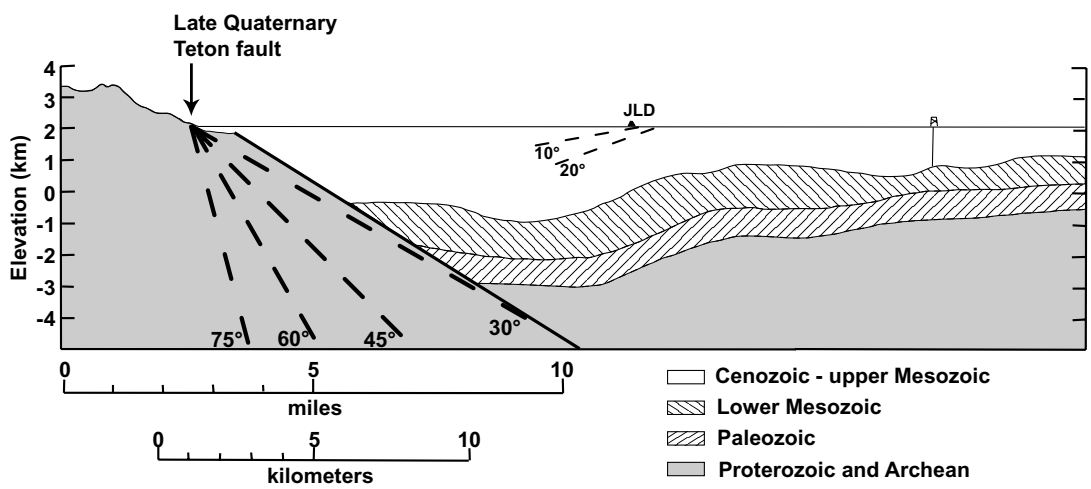

Figure 2-6: Schematic geologic cross section depicting late Quaternary Teton fault versus basin structure to east of fault. The subsurface configuration of Mesozoic and Paleozoic sediments beneath Jackson Hole is based Behrendt et al. (1968). Note that western basin boundary fault (Teton fault of Behrendt et al., 1968) dips about 35º east and is offset about 1-2 km from the trace of the late Quaternary Teton fault. Possible subsurface projections of the late Quaternary Teton fault are shown with thick dashed lines for dip ranges of 30-75º. Thin dashed lines beneath JLD (Jackson Lake Dam) show projected positions of Huckleberry Ridge Tuff, 10º, and Conant Creek Tuff, 20º, which have been rotated westward by late Cenozoic movement on the Teton fault.

fault trace and more likely reflects an older, basin-bounding structure(s) rather than indicating the dip of the late Quaternary seismogenic fault.

Along the late Quaternary fault trace, the fault exposed in the trench at Granite Creek had a dip of 75-85º based on the 2-m high exposure in the trench (Byrd, 1995). Near-surface steepening of fault planes in surficial alluvium has long been recognized and dips from the trench exposures are clearly oversteepened. The fault scarps along the Teton fault traverse several areas of significant relief which potentially could be used to estimate fault dip over elevation ranges of 50 - 300 m. However, the surface trace of the fault is very irregular, consisting of fault planes with multiple orientations, and many step-overs. This complex geometry, combined with the relative lack of detail associated with the existing compilations of fault scarps, has thus far frustrated any attempts to use the fault scarp data to generate a meaningful estimate of fault dip.

Evidence from historical normal-faulting earthquakes in the western United States, notably the 1959 Hebgen Lake and 1983 Borah Peak earthquakes, indicates that fault planes that ruptured during these earthquakes likely had dips near 45º (e.g., Smith and Arabasz, 1991). Further compilations of data from large normal-faulting earthquakes suggests that there is marked preference for dips near 45º, but with significant spread over a range of 30-60º (Thatcher and Hill, 1991; Collettini and Sibson, 2001). There appears to be little seismological evidence for fault dips of less than 30º in association with historical normal-faulting earthquakes.

The evidence from the historical earthquakes indicates that a preferred dip of about 45º, and a range of 30-60º should be considered as the likely range of dips associated with fault rupture on the late Quaternary trace of the Teton fault. The dips of buried faults within the basin, such as the fault trace defined by Behrendt et al. (1968) are probably lower than the currently active fault trace. Most models of fault basin evolution suggest that these intrabasin faults likely have dips that are less than the currently active fault due to rotation on the hangingwall block (e.g., Buck, 1993; Wernicke, 1995; Lavier et al., 1999). Thus, the 35º dip of the Teton fault as shown by Behrendt et al. (1968) is further evidence that the lower bound on the for the presently active trace of the Teton fault is probably greater than 30º.

2.2.3 Slip Rate and Along-Strike Variations in Displacement. There are four types of data that allow estimates of slip rates for the Teton fault: 1) estimated stratigraphic offsets of the pre-Cenozoic bedrock units and late Cenozoic volcanic units, 2) detailed topographic maps and profiles across fault scarps on late Quaternary deposits, 3) measured displacements from the trench across the fault scarp at Granite Creek, and 4) estimates of slip based on submerged shorelines beneath Jackson Lake. Not all of these data are directly comparable because of differences in the way these estimates are derived. Further, not all investigators have been clear in stating whether their slip rates or displacement values represent vertical estimates or displacement along a fault of unspecified dip. Despite these difficulties, the first type of data provide long-term values for large sections of the fault because outcrop data are compiled from a large region and combined into a single cross section. The scarp profile and trench data provide estimates of slip at specific locations along the fault that reflect the behavior through the last several faulting episodes at specific points along the fault. Combinations of these point data can be used to derive averaged values along the length of the fault. Estimates of slip rate derived from the submerged shorelines beneath Jackson Lake again represent a set of averaged values for a large section of the fault, but have the advantage the areal variations in the shoreline deformation can be described and related to the displacement on the fault.

A significant source of uncertainty for slip rate estimates derived from the pre-Cenozoic and late Cenozoic rock units is related to the dip of the fault and the width and number of fault traces that may comprise the fault zone. The potential for slip on multiple fault traces and effects of rotation through time greatly complicate these estimates and their reliability. Because outcrop data must be projected to the estimated fault location, even vertical displacement estimates are sensitive to the assumed fault dip and width. Thus, these estimates should be considered only as providing very loose constraints on contemporary slip rates. Byrd et al. (1994) summarized previous displacement estimates for the Teton fault, which ranged between 2 and 11 km of total slip.

Estimates of the total displacement for the central portion of the Teton fault range from about 6 km (4 mi) (Smith et al., 1993b) to about 10 km (6 mi) (Love, 1977). These values are based the estimated stratigraphic offset of Precambrian and Cambrian rock units in the central portions of Jackson Hole (Figure 2-4). The age of initial displacement on the Teton fault is not known with

certainty, but appears to be near the time of deposition of the Conant Creek Tuff based on the concordancy of dip between this unit and older, underlying units in Jackson Hole (Gilbert et al., 1983; Smith et al., 1993b). Based on these relations, an age for initial movement on the Teton fault of about 5 to 6 Ma is commonly assumed, yielding long-term average slip rates of about 1-2 mm/yr (e.g. Gilbert et al., 1983; Smith et al., 1993b). Somewhat lower rates could be derived based on the Byrd et al. (1994) preferred displacement value of 2.5 - 3.5 km.

Similar long-term slip rates can be derived from the estimated offset of the Conant Creek Tuff and Huckleberry Ridge Tuff in the northern portion of Jackson Hole. Offset is estimated based on the observed westward tilt of outcrops in the area (e.g., Figure 2-6). Vertical offset of the 4-6 Ma yr old Conant Creek Tuff may be on the order of 5 km (3 mi) suggesting a long-term rate of about 1 mm/yr (Pierce and Good, 1992). Leopold and Love (2002) suggest that uplift on the Teton fault was in two phases, the most recent of which post-dated deposition of the Huckleberry Ridge Tuff. Projections of the 2-Ma yr old Huckleberry Ridge Tuff suggest vertical offset on the order of 2400 - 2800 m (Gilbert et al., 1983) and resultant slip rate estimates of 1.25 mm/yr ± 20% (Pierce and Good, 1992). The southernmost outcrops of these tuffs in Jackson Hole are located near Jackson Lake Dam, but outcrops north of the dam and east of Jackson Lake are faulted by several other subsidiary faults which also probably contribute to the observed tilts. Thus, while topographic relief on the Teton Range diminishes to the north along the west shore of Jackson Lake, presumably indicating decreasing displacement on the fault, observed tilt on outcrops of the Huckleberry Ridge Tuff does not diminish to the north (see data in Gilbert et al., 1983, Figures D-2 and D-3). However, if some displacement of the Huckleberry Ridge Tuff resulted from displacement on other subparallel traces of the Teton fault, the estimated vertical displacement derived from the tilt of Huckleberry Ridge Tuff outcrops may be considerably less.

As discussed previously, there is little data on the actual dip of the Teton fault, which Byrd (1995) estimated to be 45-75º. For this range of dips, the difference between the true slip and the vertical slip rate would be between about 10-40 per cent, with vertical slip underestimating true slip. Love and Montagne (1956) suggested that the westward tilt of alluvial surfaces in Jackson Hole south of Jenny Lake was due to movement on the Teton fault. Based on boundary element models, Byrd et al. (1994) estimated that the westward tilt interpreted in surfaces in the Love and Montagne

(1956) profiles was consistent with a minimum of 110-125 m dip-slip displacement on the Teton fault over a depth range of 0-15 km and dips of 45-75º. Based on the surface ages of 25,000 to 75,000 years used by Byrd et al. (1994) in their analyses, the minimum slip rate for the fault south of the Jenny Lake area would be 1.5 - 5 mm/yr. However, their analysis did not account for the pre-existing depositional slopes of the surfaces towards the Teton fault, which likely would reduce the slip rate estimate substantially.

Estimates of late Quaternary vertical slip on the Teton fault from scarp profiles (e.g., Bucknam and Anderson, 1979) have been made at about 17 sites along the length of the fault (Appendix A, Table A-2). These profiles provide measured estimates of the vertical component of fault slip; which must then be increased for the dip of the fault to obtain a true estimate of slip. At most sites this adjustment is probably relatively small because the near surface dip of the fault is probably 60-75º based on exposures from the trench at Granite Creek.

An additional source of uncertainty arises from the potential for a lateral component of slip on the fault. At most sites, there are insufficient geomorphic data to determine whether a lateral component of slip is present or absent. However, a some sites along the fault, particularly where the fault has a marked NE strike, it appears that significant left-lateral slip may be present (e.g., Smith et al., 1993b). At a few of these sites, detailed topographic surveys of the offset landforms permit estimates of the lateral slip component and appear to indicate that at least locally, lateral and vertical slip components may be nearly equal (Smith et al., 1993b; Byrd, 1995). At these sites, estimates based solely on the vertical offset from the scarp profiles may be as much as 40 per cent too low. However, the largest source of uncertainty in the calculated slip rate is introduced by the lack of data on the age of the deposits on which the scarp profiles are measured. At several of the sites where scarp profiles have been measured, there is a factor of 2 to 3 uncertainty in the age of the faulted deposits (Appendix A, Table A-2).

Vertical slip rates on the Teton fault are largest in the central section of the fault, and decrease towards both ends (Figure 2-7 and Appendix A, Table A-2). The overall pattern of displacement along the fault is only weakly correlated to the topographic expression of the range (Byrd, 1995), except along the northern part of the range where the topographic expression of the range mimics

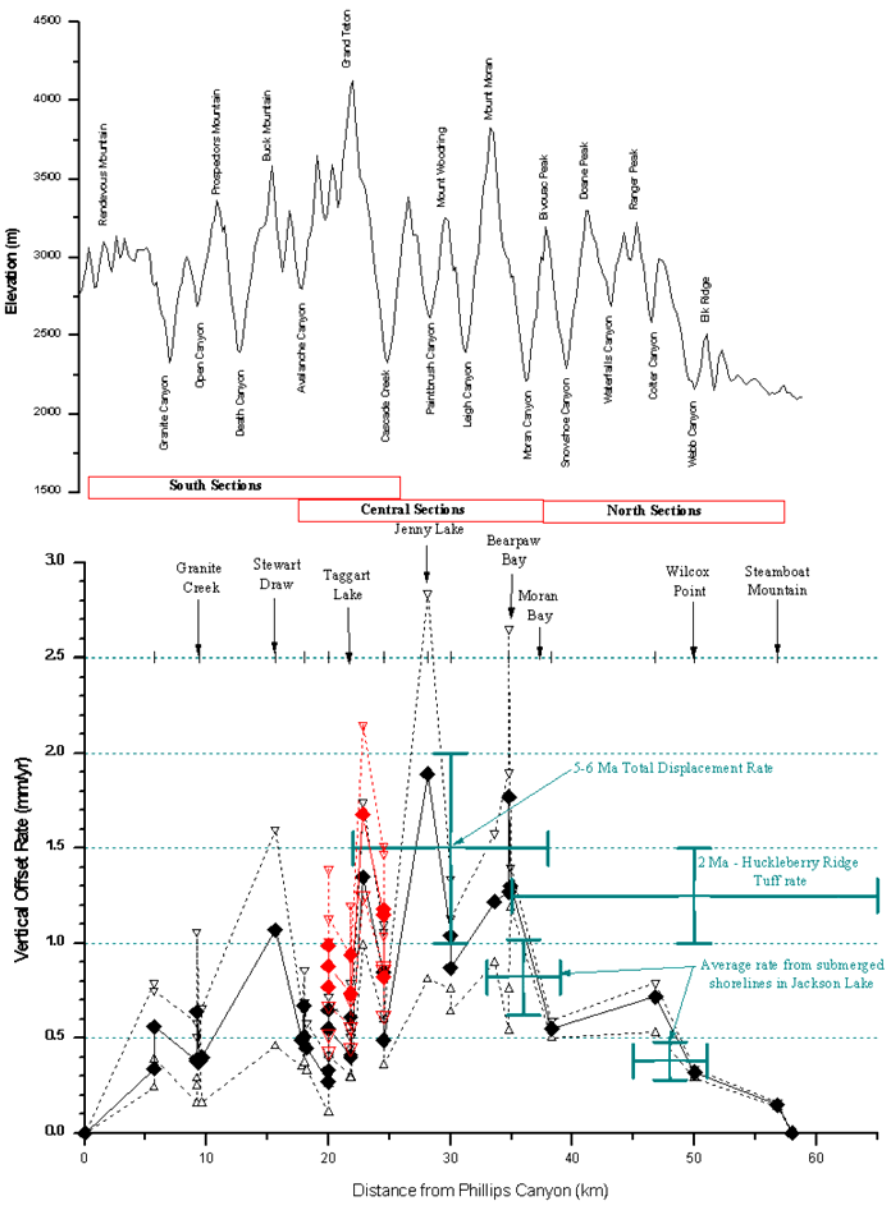

Figure 2-7: Estimated vertical slip rates along the Teton fault. Upper graph shows range profile footwall block along a line about 2-3 km west of late Quaternary fault trace. Major peaks are labeled above the profile; major canyons are labeled below the profile. Fault sections and selected geographic locations are shown between graphs; for complete data see Appendix A, Table A-2. Slip rate data are shown in lower graph: diamonds show slip rates from scarp profiles; filled symbols are mid-range values, open symbols depict uncertainty in rate, primarily due to uncertainty in age of the faulted deposits. Red symbols show effects of considering lateral component of offset on slip rate. Blue bars show rates derived from other records. Vertical extent of bars shows uncertainty in slip rate estimate. Horizontal bars depict areal extent of applicability of the rate information along the fault.

the pattern of slip along the fault. Vertical slip rates along the southern section of the fault, south of the Taggart Lake area, appear to mostly lie in the range of 0.3 - 1 mm/yr. However, along this section of the fault, there are several sites where the lateral separation appears to be nearly as large as the vertical offset (Smith et al., 1993b). In the central section of the fault, from the Jenny Lake area to Moran Bay, most vertical slip rates are in the range of 1 - 2 mm/yr, and may be as high as 2.5 - 3 mm/yr. The highest slip rate estimates are all obtained from scarp profiles along the crest of moraines constructed by Teton Range glaciers. These types of sites are potentially susceptible to secondary deformation which could enhance the size of the scarps, and have very large uncertainties in their ages as well (Appendix A, Table A-2). North of Moran Bay, vertical slip rates are again in the range of 0.3 - 0.7 mm/yr for a >10-km-long section of the fault along the west shore of Jackson Lake. Vertical displacement appears to gradually decrease over the northernmost 10 km of fault length and dies out on the east side of Steamboat Mountain.

Previous studies that characterized slip rate on the Teton fault have used basically the same data discussed above. Machette et al. (2001) placed most sections of the Teton fault in a slip rate category of 0.2-1 mm/yr. The northernmost section of the fault near Steamboat Mountain was listed as <0.2 mm/yr and the central section as 1-5 mm/yr. Wong et al. (2000) included four weighted slip rate values between 0.5-4 mm/yr. Values of 1.5 and 2 mm/yr received 70 per cent of the weight in their model.

For this study, we note that slip rates vary substantially along the length of the fault and are strongly dependent on the assumed dip of the fault. Uncertainty in the ages of the faulted late Quaternary deposits contributes substantial uncertainty, as does the need to account for observations of lateral displacements at several sites along the fault. Despite these factors, it appears clear that the maximum slip rate for the late Quaternary Teton fault occurs along the section of the fault just west and south of Jackson Lake, and is probably near 2 mm/yr, but could be as large as 5 mm/yr if the fault dip is low. Slip rates appear to taper to zero over distances of 5 to 10 km at each end of the fault (Figure 2-7).

2.2.3.1 Age(s) and Number of Faulting Events. Detailed information on the age, number, and extent of faulting events along the Teton fault is generally lacking. Limited information is available from two areas located about 25-40 km apart (Table 2-1): 1) a trench on

Table 2-1: Teton Fault - Event Data

Fault Section	Site Name	Geomorphic Setting and Type of Evidence	Age of Faulting Events (thousands of years)	Number of Faulting Events	Inferred Average Return Period (thousands of years)	Estimated Vertical Displacement per Event (m)	Data Source
North Teton* (N5? to N9?)	Snake River Delta	Snake River, Lizard and Arizona Creek fan-delta alluvium and pre-reservoir Jackson Lake shorelines. Backflooded delta deposits and beaches constructed across Snake River alluvium. Landforms from secondary deformation.	~ 2 ~4	2 subsidence* or strong ground shaking events in the past 4,000 years.	~2 since 4 ka	>0.7 from delta backflooding for MRE; earlier event uncertain.	Pierce and Good, 1992; Connor, 1998
North and/or Central Teton (N11 to C4?)	South Jackson Lake - east of Bearpaw Bay and east of Spaulding Bay	Submerged pre-reservoir Jackson Lake shorelines	all younger than 17	Ten subsidence events in the past 17,000 years	1.6 - 2.1 over past 17 ka	>1.4 from spacing of shorelines east of Bearpaw Bay; >0.8 from spacing of shorelines east of Spaulding Bay.	Pierce and Good, 1992; Connor, 1998
South Teton S-5 and S6	Granite Creek	Trench exposure of faulted post-glacial deposits.	~ 4 ~7.9	2 displacement events in the past 8,000 years	~ 4 since 8 ka	~ 2 ± 0.8 (1.3 @ 4 ka and 2.8 @ 7.9 ka)	Byrd, 1995; Byrd et al., 1994; Smith et al., 1993a,b;

* The post-earthquake position of shorelines relative to lake level is controlled by the relative subsidence of the outlet of Jackson Lake and the pattern of subsidence along the fault (See Figure 18 of Connor, 1998). Subsidence of the southern end of the lake, and/or the outlet area, resulting from a displacement event on the central section of the fault, could result in stranding or apparent "uplift" of shoreline features in the Snake River Delta area, even if no associated displacement were to occur on the northern section of the fault.

the southern section of the fault near Granite Creek (Byrd, 1995; Byrd et al., 1994; Smith et al., 1993b) and 2) from shorelines of the pre-reservoir Jackson Lake (Pierce and Good, 1992; Connor, 1998).

Results from trenching at Granite Creek indicate two surface faulting events, one about 4000 years ago and an earlier event about 7900 years ago (Byrd, 1995). These data appear to suggest intervals of nearly 4000 years between faulting events on the southernmost portion of the fault.

Adjacent to the northern end of the fault, near Bearpaw and Spaulding Bays in Jackson Lake, submerged shorelines appear to indicate 8 to 10 earthquakes since deglaciation about 17,000-18,000 years ago (K. Pierce, personal comm., 2002). This implies average intervals between earthquakes of less than 2000 years for at least the central portion of the fault adjacent to Bearpaw and Spaulding Bays. The apparent submergence, based on the spacing of the submerged shorelines, is relatively uniform over the entire record (Figure 2-8), although no specific ages have been obtained for any of these shorelines. Data from shorelines near the Snake River delta at the north end of Jackson Lake indicate a submergence event on the delta about 2000 years ago, and a strong ground shaking event about 4000 years ago (Pierce and Good, 1992). These are presumed to be related to faulting events on the northern section of the fault, although the extent of fault rupture associated with these events is not constrained and could involve rupture on the central section of the fault as well. Shoreline submergence results from changes in lake levels that are a complex product of subsidence at the shoreline site and subsidence and/or base level changes at the natural outlet of Jackson Lake (Pierce and Good, 1992; Conner, 1998). Thus, the shoreline data are difficult to relate to specific faulting scenarios along the Teton fault.

2.2.4 Segmentation. The existing data are not sufficient to determine whether the Teton fault is segmented (Machette et al., 2001). As summarized above, there is only limited data available on the age of individual faulting events, mostly from sites near the ends of the fault (Table 2-1). The fault geometry lends itself to subdividing into fault sections, which some investigators have also used as a basis for segmentation. For example, Smith et al. (1993b) suggested that the fault consisted of 2 or 3 segments based primarily on strike changes and geophysical data. However, Ostenaa and Gilbert (1988) noted that the fault geometry was consistent with rupture along entire fault length.

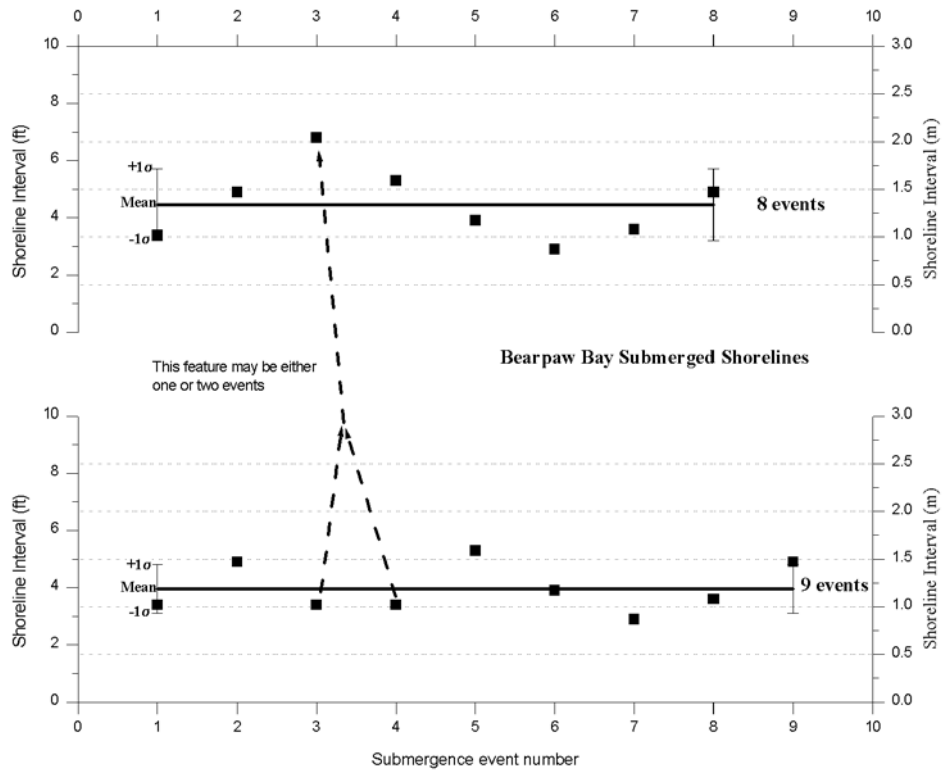

Figure 2-8: Shoreline intervals for Bearpaw Bay shorelines. Solid bar shows mean and 1s variation for event shoreline interval based on either 8 (upper panel) or 9 (lower panel) submergence events. Data from K. Pierce (personal communication, 2002).

2.3 Potential Fault Rupture Models

Based on the existing geologic data, three general groups of potential rupture models are proposed for the Teton fault. Of these models the first is considered somewhat more plausible, primarily because of its simplicity, while the second and third models are considered less plausible. One of the strongest constraints on faulting behavior comes from the submerged shoreline data from Jackson Lake. This data appears to imply that the displacements for each of the faulting events on this part of the fault are relatively similar, and provide a data point for the approximate average frequency of submergence events during the past ~17,000 years. The extent to which the models honor these data is the primary discriminant amongst the models.

General fault geometry is described in the previous section. The only difference in fault geometry for each of the models is in the length and amount of displacement along strike. Potential linkage

of the Teton fault with the Beula-Herring Lake faults, as proposed by Wong et al. (2000), is not considered in this analyses because of the apparent lack of evidence for surface rupture on these faults (Ostenaa et al., 1993), the much smaller long-term slip rates on these faults compared to the northern section of the Teton fault, and the 30+ km distance for the closest approach of these faults to Jackson Lake Dam. Slip rates on the northern section of the Teton fault appear to be mostly in the range of 0.3 - 0.7 mm/yr and decrease to the north (Figure 2-7 and Appendix A, Table A-2). They are nearly an order of magnitude greater than long-term slip rates for the Buela - Herring Lake faults (see data tabulation in Wong et al., 2000).

2.3.1 Unsegmented, with Variable Displacement Along Strike. This type of fault rupture model appears to provide the most simple reconciliation of the limited data for individual faulting events along the Teton fault. In this model rupture extends over nearly the entire length of fault, up to 58 km for the largest events and ~40-45 km for slightly smaller events. The displacement pattern varies along strike as shown by variations in slip rate (e.g., Figure 2-7). Displacement near Moran Bay is ~1.5 m as indicated by average spacing of submerged shorelines in Jackson Lake. Maximum displacement is ~4.5 m on sections of the fault near Bearpaw Bay and Jenny Lake. For some events, rupture does not extend fully to the south end of the fault which could account for differences in the age of the most recent event at the Granite Creek trench site versus the age of apparent faulting events from submerged shorelines on the Snake River delta in Jackson Lake. This model would appear to imply nucleation of most ruptures on the central and northern sections of the fault. On average, for this model there is one faulting event about every 1700-2000 years based on the number of submerged shorelines in Jackson Lake (i.e., there have been 8-10 large surface faulting earthquakes in the past 17,000-18,000 years on the Teton fault). Thus, about half of the faulting events would not include full rupture of the southern 10 - 15 km of the fault (fault sections S3-S10 on Figure 2-3), including the Granite Creek trench site (Byrd et al., 1994; Byrd, 1995). Earthquake magnitudes for these events would likely be somewhat smaller than for events that involve the entire fault length.

2.3.2 Two Independent Fault Segments with Overlapping Rupture. In the second fault rupture model, the northern and southern sections of the fault behave independently, but have overlapping rupture on the central section of the fault. Individual earthquake magnitudes

would be somewhat smaller in this model, but the total number of large earthquakes on the fault over a given time interval might be larger than in the first model. A northern fault segment would rupture between the area of Taggart Lake and Steamboat Mountain, with displacement of ~1.5 - 2 m along much of the 35-40 km length. Maximum displacement would be in the area between Jenny Lake and Bearpaw Bay. A southern fault segment would rupture between Phillips Canyon and Bearpaw Bay. Displacement would be ~2 m along much of the segment with maximum displacements in the Taggart Lake to Jenny Lake area. Total rupture length would be ~35 km. On average, this model implies one faulting event every 2000 years on the northern segment, and one faulting event every 4000 years on the southern segment. Thus, over a time of 17,000-18,000 years, possibly 12-14 large surface-faulting earthquakes might originate on the Teton fault.

2.3.3 Three Independent Fault Segments. This model implies that individual fault ruptures on the Teton fault would be limited in length to about 20-25 km, and hence typical magnitudes would be somewhat smaller than in either of the previous two models, but significantly more large earthquakes would need occur. The northern, central, and southern sections of the fault each rupture as independent fault segments with negligible overlap. Rupture on the northern segment would extend between Steamboat Mountain and Moran Bay, a distance of ~20 km. Maximum displacement would be ~1.5 - 2 m along the western shore of Jackson Lake. Rupture on the central segment of the fault would extend between Taggart Lake and Moran Bay, a distance of ~25 km. Displacement would either be ~1.5 - 2 m along much of the length of the fault, or 2-3 times that if events are somewhat less frequent. Rupture on the southern fault segment would extend between Phillips Canyon and Taggart Lake, a distance of about 22 km. Displacement would be ~2 m along much of the fault segment. On average, there is one faulting event every 2000 years on the northern fault segment, one faulting event every 1700 years on the central segment of the fault, and one faulting event every 4000 years on the southern segment of the fault. This would imply that over a period of 17,000-18,000 years, the Teton fault would be the potential site of 20-25 large surface rupturing earthquakes.

2.3.4 Implications for Ground Motion Models. The general lack of specific paleoseismic event data for the Teton fault implies that potential ground motion models based on specific fault slip geometries need to consider a broad range of scenarios. At present there is

insufficient data to reliably discriminate amongst these potential scenarios. The existing geologic data appear to be permissive of paleoseismic events associated with surface rupture lengths of ~20 to ~60 km and individual slip events of 1.5 - > 5 m. If most paleoseismic events have somewhat shorter rupture lengths and smaller individual slip, the average frequency of events will be much shorter and earthquake magnitudes will be somewhat smaller. As outlined in the Sections 2.3.1 to 2.3.3 and summarized in Table 2-2, the average intervals between large surface-rupture events on the Teton fault could be as low as several hundred years or as long as a few thousand. What appears to be the most simple model of fault rupture on the Teton fault, i.e, an unsegmented model, suggests that large events involve most of the fault area with average return intervals of about 1700 to 2000 years. If the fault is segmented to any extent, the average return interval for large events decrease significantly. Because Jackson Lake Dam is located nearly astride the likely boundary of the northern and central sections of the fault, rate and event data for these sections of the fault appear to be most significant to the ground motion evaluations for the damsite. For use in simplified probabilistic analyses, the unsegmented scenario could be weighted 0.5, the two segment scenario weighted 0.3, and the three segment scenario 0.2, leading to a mean average return interval of about 1180 years.

Table 2-2: Teton Fault Rupture Scenario Summary

Fault rupture scenario	Number of fault rupture segments	Estimated number of paleoearthquakes in past 17-18 ka.	Average earthquake return interval (ka)	Typical rupture length (km)	Typical paleoearthquake magnitude* (M_w)
Unsegmented, with variable displacement along strike	1	8 - 10	~1850	45 - 60	7.1
Two independent fault segments with overlapping rupture	2	12 - 14	~1350	35 - 40	6.9
Three independent fault segments	3	20 - 25	~800	20 - 25	6.7

*Typical magnitude for 45° fault dip and 16 km rupture depth from fault-area relationships of Wells and Coppersmith (1994).

3.0 SEISMICITY ANALYSES

In this section, we describe analyses of data from the Jackson Lake Seismic Network (JLSN) to develop three-dimensional (3D) velocity models of the crust, earthquake locations, focal mechanisms, and an earthquake catalogue for recurrence analyses. It is necessary to develop a 3D velocity model of the crust to accurately locate earthquakes, to determine focal mechanisms, to perform earthquake declustering for earthquake recurrence analyses, and to estimate ground motion responses in the vicinity of Jackson Lake Dam.

Figure 3-1 shows the geographic distribution of JLSN stations. The network initially consisted of 16 short-period (1 Hz) vertical-component (Geotech model S-13) seismographic stations. An additional four stations were installed in 1990 to improve monitoring coverage, bringing the total to 20 stations. Prior to Oct. 2000, the network used analog telemetry between station sites and communications collection facilities located in the field. The analog signals were relayed to Denver over dedicated phone circuits and digitized using a real-time computer system equipped with a 12-bit digitizer. Data were time-stamped in Denver using either GPS- or GOES-based timing systems. From Oct. 2000 to Oct. 2002, the data were digitized at the communications collection facilities in the field using 16-bit digitizers equipped with GPS time-keeping systems, and then relayed to Denver via local Frame Relay links to Reclamation's wide-area network. This change greatly improved signal-to-noise ratios by reducing analog data transfers to relatively short transmission paths via FM radio between the seismographic stations and the field communications collection facilities. Seven digital broadband three-component velocity seismographs were installed from 1996 to 2001 on-or-near Jackson Lake Dam to provide site response recordings of local earthquakes (Figure 3-2). Four of the site-response stations operated intermittently until the end of Oct. 2002. A detailed description of the original (16-station) short-period seismographic network and instrumentation is found in Wood (1988). The site-response instrumentation is described in Chapter 5 of this report.

From 1986 through 2002, more than 16,000 local earthquakes were recorded by the seismic network, ranging in magnitude from 0.5 to 4.7. Of these earthquakes, about 1,550 were greater than magnitude 2.0. Earthquakes of this size and larger were typically recorded clearly on most of

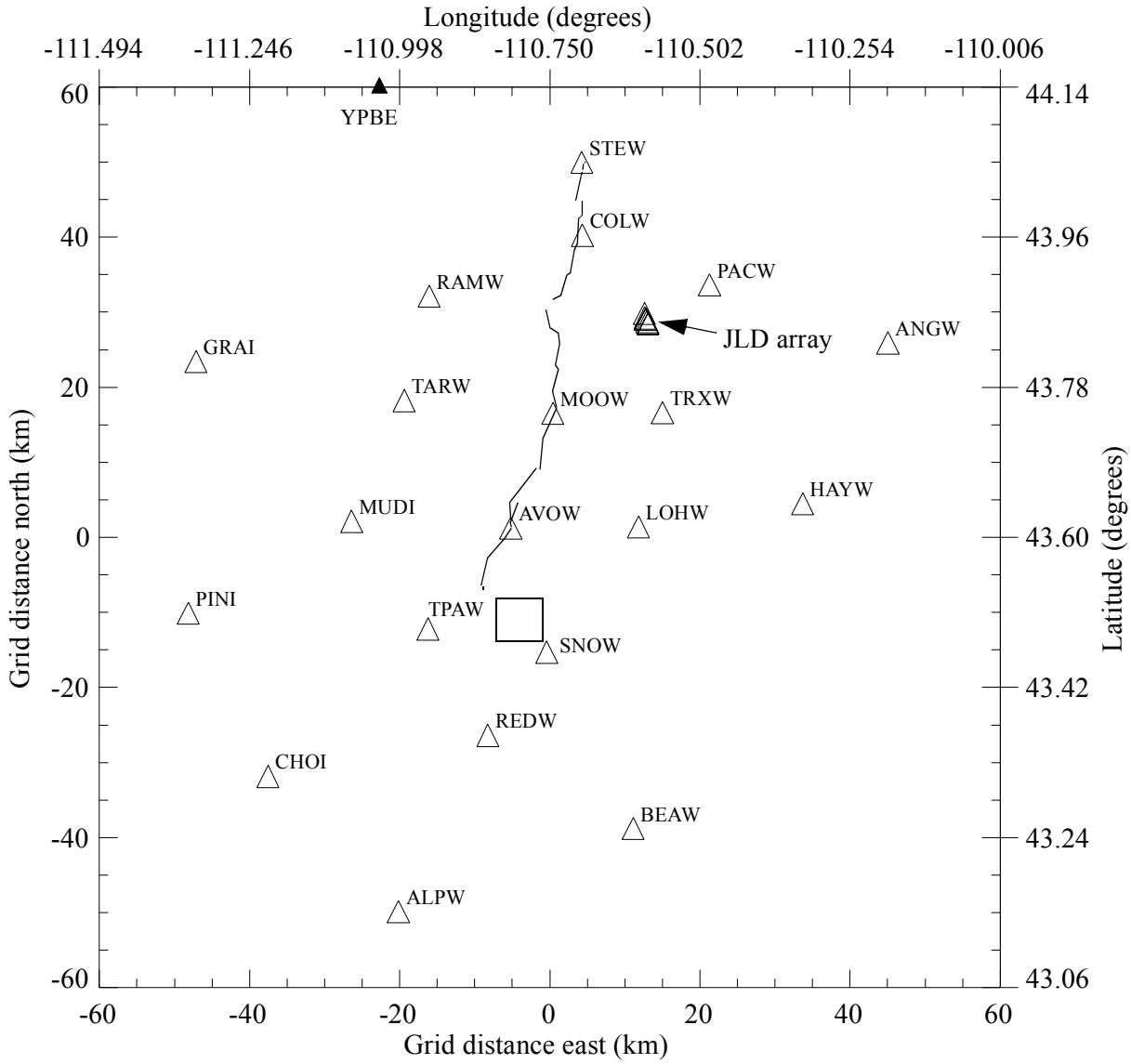

Figure 3-1: Map showing the distribution of JLSN seismographic stations. The filled triangle is station YPBE from the University of Utah Yellowstone seismic network. JLSN stations are open triangles labeled with four-letter station names, the Jackson Lake Dam site response array is the cluster of triangles labeled JLD array, the line segments show the surface traces of the Teton fault, and the town of Jackson is the square. The map coordinates are the Cartesian grid coordinates used in the 3D velocity-hypocenter inversion.The origin of the cartesian grid is 43.6°N, 110.75°W.

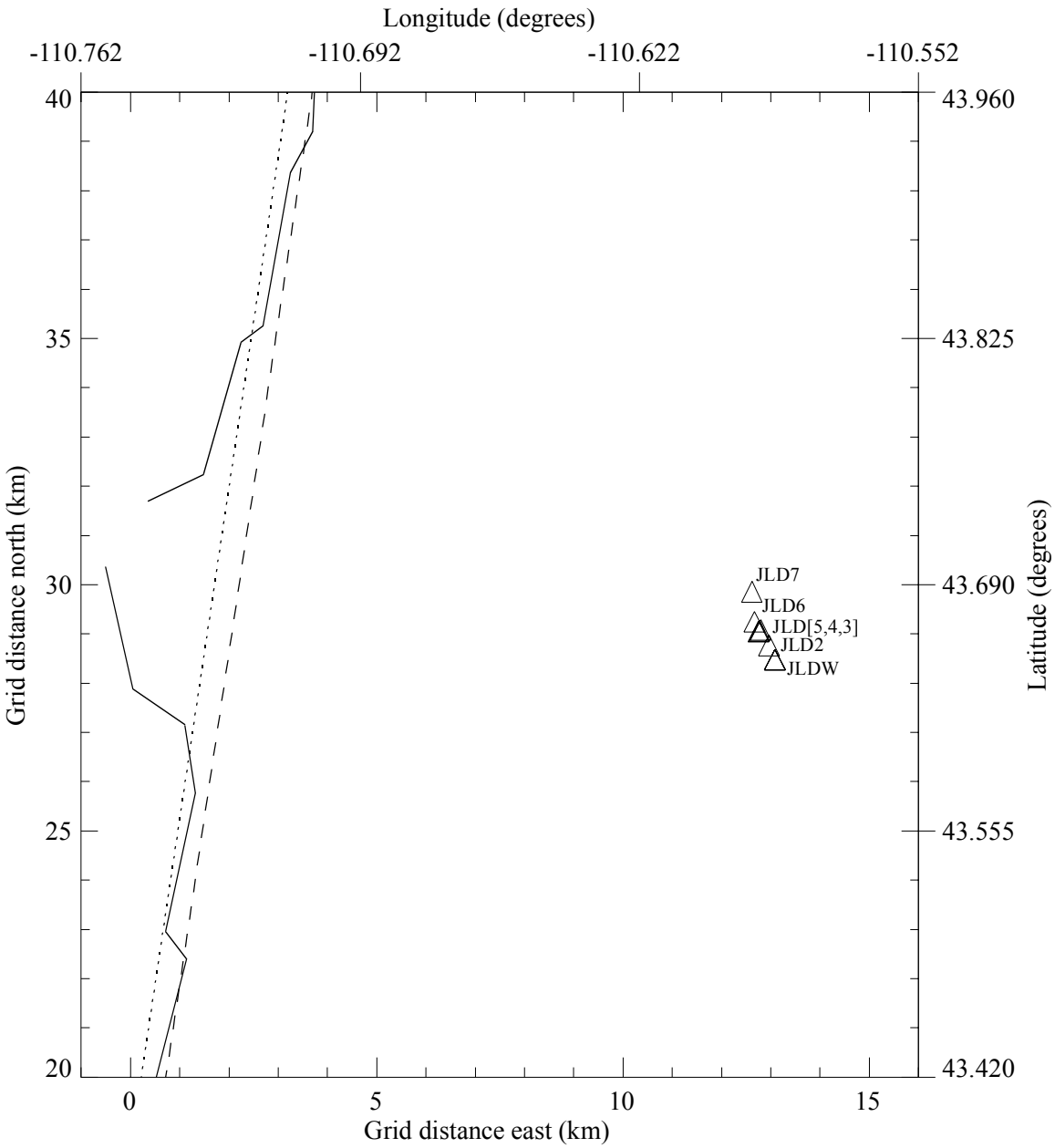

Figure 3-2: Map showing the distribution of Jackson Lake Dam site-response seismographs. Jackson Lake Dam site-response stations are labeled triangles; the designation JLD[5,4,3] refers to station JLD5 on the dam crest, station JLD4 on the eastern dam toe, and station JLD3 located east of the treated foundation zone. The solid line segments show the surface traces of the Teton fault. The dotted line shows the idealized position of the Teton fault used in Section 6 to synthesize ground motions at station JLDW. The dashed line shows that the credible eastern limit for an idealized position of the Teton fault is about 0.5 km closer to the dam than the Teton fault position used in Section 6. The map coordinates are the Cartesian grid coordinates used in the 3D velocity-hypocenter inversion.The rock reference station, JLDW, is located furthest from the idealized Teton fault surface traces at distances of 11.2-to-11.7 km due east of the fault traces Station JLD7 as located near the northern end of the dam, and is the closest station to the Teton fault at distances of 10.4-to-10.9 km due east of the idealized Teton fault surface traces. Station JLD2 is the station near the dam that is furthest from the Teton fault at distances of 11.1-to-11.6 km due east of the fault traces.

the stations in the seismic network. All earthquakes were automatically processed in real time. Phase arrivals for all local earthquakes equal or greater than magnitude 2, along with selected smaller earthquakes, were subsequently interactively picked and reprocessed. Routine processing included phase picking, magnitude estimation, 1-D hypocenter location, focal mechanism determination, and seismic moment estimation.

3.1 Hypocenter-Velocity-Station Correction Inversion

3.1.1 Procedure. A joint hypocenter-velocity-station correction inversion was performed using arrival times from a subset of 1150 earthquakes with well-constrained hypocenters. These events were selected from all events recorded between August, 1986, and May, 2002, having initial locations within the region bounded by the Jackson Lake seismic network. The events were selected using the following criteria: number of stations with arrival times ≥ 12, maximum azimuthal gap ≤ 160°, and distance from epicenter to the nearest recording station divided by the focal depth ≤ 2. The number of events included in the inversion was further reduced using a spatial distribution criteria, in order to limit spatially redundant data and thereby reduce computation time. These 1150 events provided 18,117 P-wave arrival times. S-wave arrival times were not included in the inversion because of a lack of spatially-distributed three-component stations and significant uncertainty about S-wave arrival times determined solely from vertical component seismographs.

Earthquake hypocenters, P-wave velocities, and station corrections varied simultaneously during the inversion. Initially, P-wave velocities were only allowed to vary vertically, and subsequently they were allowed to vary in three dimensions. Station corrections were only included for those stations located outside the 3D velocity grid and for stations JLD2 to JDL7, located on soil sites near Jackson Lake Dam. Arrival times from 40 quarry explosions provided some constraints during the inversion. The z coordinates of these events were fixed at the known elevation of the quarry, while the (x,y) coordinates and origin times varied. Details of the inversion procedure are included in Appendix B.

Following the inversion, 4642 events were relocated with the final 3D P-wave velocity model and station corrections. These events were selected from all recorded events using the following

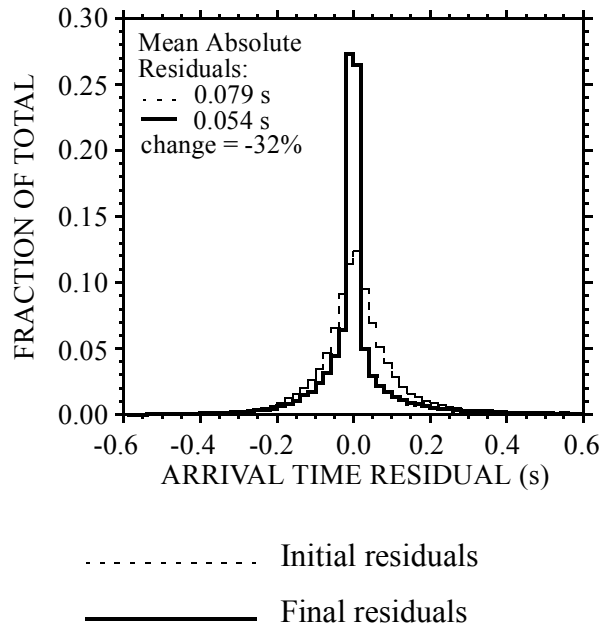

Figure 3-3: Histograms of arrival time residuals. Initial (dashed lines) and final (solid lines) are P-wave residual histograms from 4642 events relocated with the new model from the hypocenter-velocity-station correction inversion.

criteria: number of stations with arrival times ≥ 6, maximum azimuthal gap ≤ 225°, and distance from epicenter to the nearest recording station ≤ 20 km.

3.1.2 Improvement in Residuals. The 3D P-wave velocity model and corresponding station corrections obtained from the hypocenter-velocity-station correction inversion provide a much better fit to the data than that obtained with the original model. For all relocated events, the mean absolute P-wave arrival time residual decreased by 32% (Figure 3-3).

3.1.3 New Velocity Model and Station Corrections. Horizontal slices through the final 3D P-wave velocity model are shown in Figure 3-4. Although velocities were allowed to vary during the inversion from +2 to -16 km elevation (relative to mean sea level), only cross sections at and above -5 km elevation are presented because of a lack of significant horizontal velocity variations below that depth. The discrete-node velocity model (with linearly-interpolated velocities between nodes) used during the inversion was interpolated onto 1 km x 1 km x 1 km constant-velocity pixels for plotting. Pixels that are not crossed by at least one ray path are not

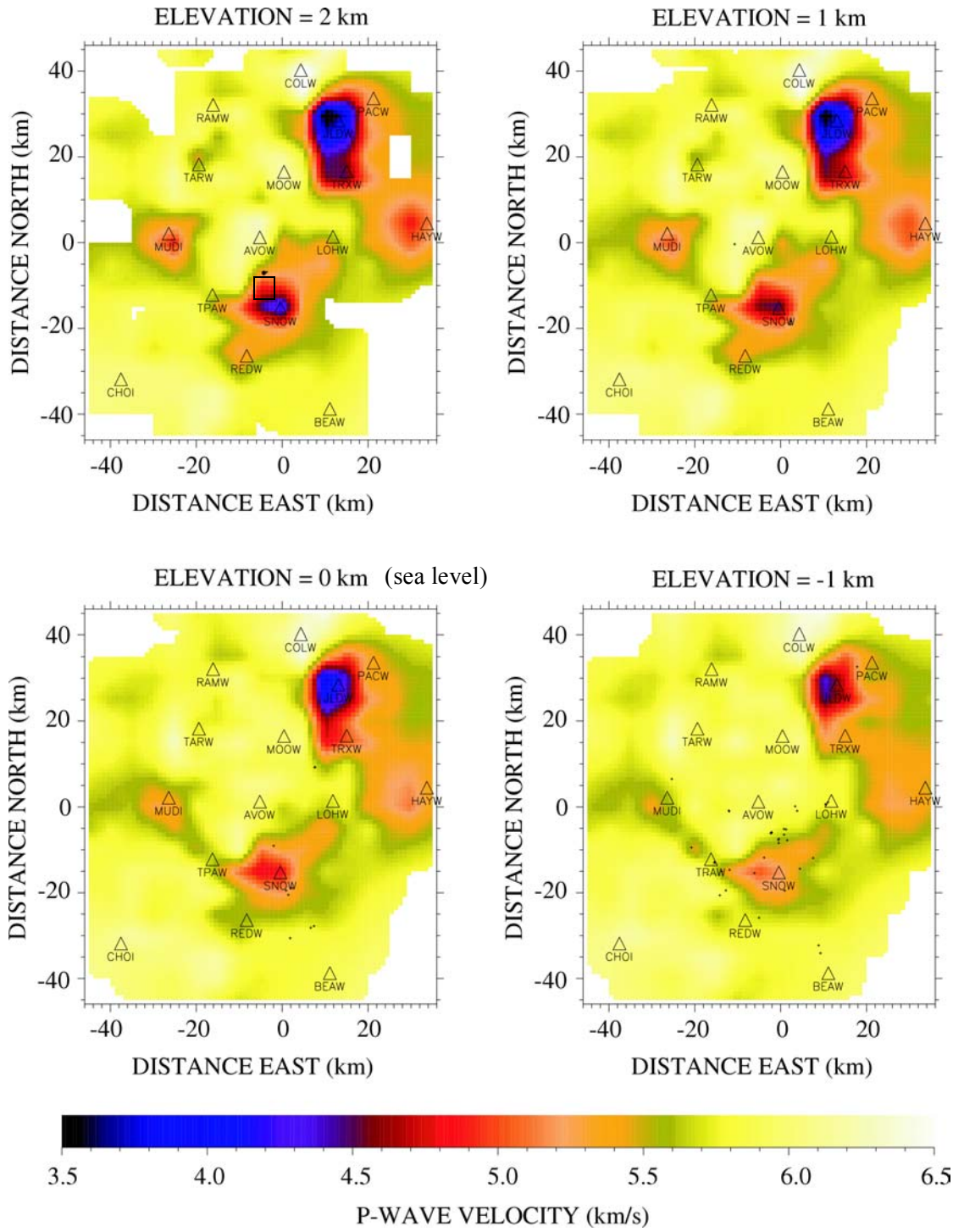

Figure 3-4: Plan views of P-wave velocities for elevations (relative to mean sea level) of -5 km to 2 km. Triangles are seismographic stations. Black pluses are hypocenters within 0.5 km of each the plotted elevation. Regions where velocities are not constrained by ray coverage are shaded white. The town of Jackson, Wyoming, is the black square in the 2 km elevation plot. The plots are continued on the next page.

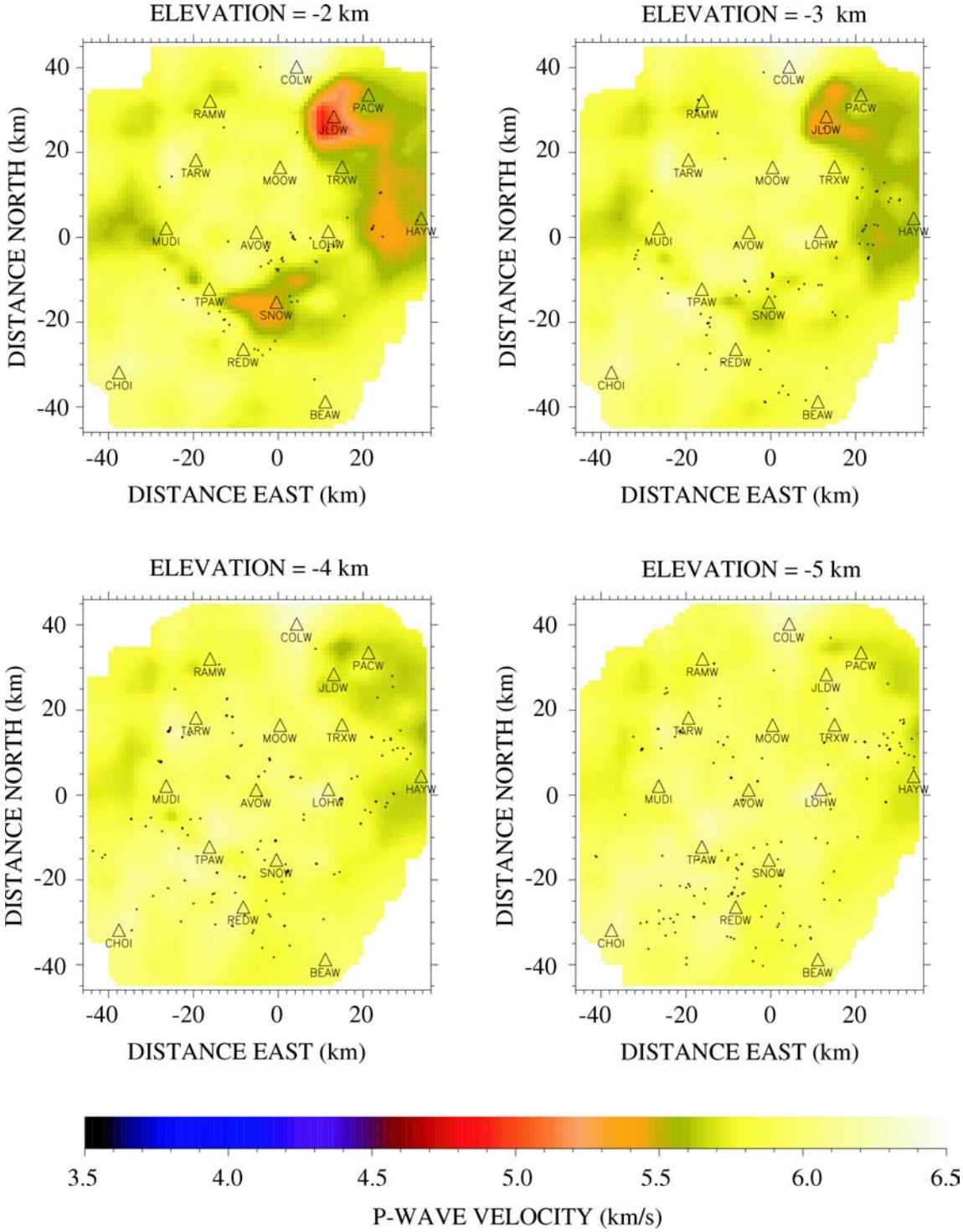

Figure 3-4 continued.

plotted (e.g., these pixels are white). The seismic stations that lie within the 3D velocity grid are shown on the plan-view constant elevation plots for reference. The final locations of the events used in the inversion that occur within 0.5 km of each cross section are also plotted.

Four P-wave low-velocity anomalies are centered near seismic stations JLDW (at Jackson Lake Dam), MUDI, SNOW, and HAYW. The relatively low P-wave velocities occur from the ground surface to at least -2 km elevation. The anomaly around station JLDW, which has the lowest velocities (as low as 3.4 km/s), disappears between -2 and -3 km elevation (between 4.1 and 5.1 km depth). While the shallowest velocities may be vertically smeared due to insufficient ray coverage, the lower boundaries of the velocity anomalies are fairly well-constrained by the data.

The P-wave station corrections obtained from the joint inversion are listed in Table 3-1. Station corrections were included only at stations located outside the 3D velocity grid and at stations JLD2 to JLD7, located on soil sites near Jackson Lake Dam (Figures 3-1 and 3-4). A positive

Table 3-1: Station corrections from the hypocenter-velocity-station correction inversion.

STATION NAME	P-WAVE STATION CORRECTION (s)
ALPW	-0.157
ANGW	0.007
GRAI	0.326
PINI	-0.025
STEW	0.102
YPBE	0.022
JLD2	0.036
JLD3	0.041
JLD4	0.026
JLD5	0.053
JLD6	0.043
JLD7	0.031

station correction indicates that velocities along ray paths going to the station are lower than that given by the velocity model, while a negative station correction indicates relatively high velocities. For a station that is located outside the 3D velocity grid, the station correction reflects cumulative velocity variations between the edge of the grid and the station. For stations JLD2 to JLD7, which are located on soil sites within the 3D velocity grid, the positive station corrections indicate that the shallow local velocities are lower than those given by the velocity model. The relative size of the station corrections at stations JLD2 to JLD7 is not solely indicative of the relative velocities of materials beneath these stations because the velocity model also varies laterally across these stations. The velocities in the model decrease from station JLD2 on the south to station JLD7 near the northern end of Jackson Lake Dam.

3.1.4 Final Earthquake Locations. The final locations of the 4642 events relocated in the new model are plotted in Figure 3-5. The locations of earthquakes occurring beyond the perimeter of the seismic network are much less well-constrained than those occurring within the network. The seismicity is distributed throughout the network, with some epicenters concentrated in several distinct clusters. A generally low seismicity rate is associated with the northern two-thirds of the Teton fault, a result typical of many western U.S. normal faults (Smith and Arabasz, 1991).

A histogram of the elevations of the final event locations is presented in Figure 3-6. The median event elevation is -4.9 km (with respect to mean sea level). Very few earthquakes occur below -12 km elevation.There is a slight tendency for earthquake elevations to deepen from the north toward the south (Figure 3-7). Earthquakes tend to cluster closer to a Teton fault dipping 35° than for a dip of 60° along the northern segment of the Teton fault (depth cross sections with north coordinates of 20 km and 40 km in Figure 3-7), but the earthquake locations are too diffuse near the Teton fault to draw strong conclusions about fault dip solely from the earthquake locations.

3.2 Focal Mechanisms

Focal mechanisms were estimated for 4600 earthquakes from the 4642 events relocated using the 3D velocity model; the 42 blast events were ignored. Based on the criteria used for event selection and relocation, these earthquakes had reasonable seismographic station coverage. Focal

mechanisms were estimated using P-wave first motions and SV/P amplitude ratios from vertical component seismograms in an approach similar to Kisslinger (1980) and Kisslinger et al. (1981), as updated and improved by Anderson and O'Connell (1998) and O'Connell and Unruh (2000), and further improved as described here. A simulated-annealing, downhill-simplex algorithm

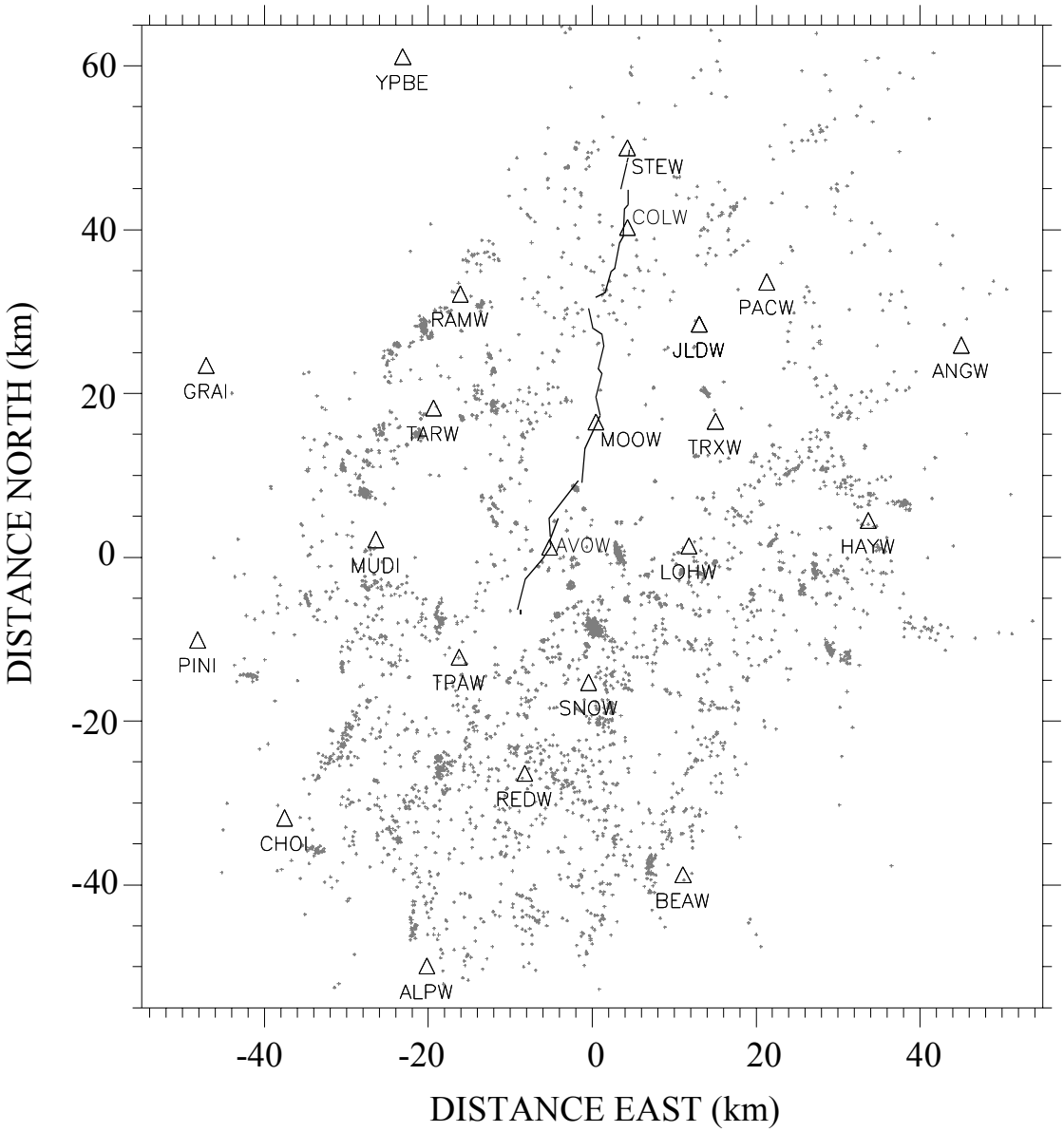

Figure 3-5: Plan view of the final locations of 4642 events relocated in the 3D velocity model from the joint inversion.Triangles are seismographic stations and small grey pluses are the epicenters. The crooked lines show the surface traces of the Teton fault. Station YPBE is part of the Yellowstone seismographic network operated by the University of Utah.

(Press et al., 1992) was used to calculate double-couple focal mechanisms. The starting simplex was constructed to have a normal-faulting node, two strike-slip nodes, and an oblique reverse-faulting node. The first simulated annealing solution was then perturbed four more times to sequentially substitute each of the initial four simplex nodes (one normal, two strike-slip, and one reverse) into the "final" solution simplex to produce four additional focal mechanism solutions. P-wave first motions were weighted 10 times more than SV/P ratio misfits and an L1 norm was used to calculate total misfits. The 20% of the SV/P amplitude ratios with the worst misfit were ignored because SV/P can become unrealistically large near nodal positions. SV/P data from stations at distances greater than 100 km were always ignored in the inversion. SV/P data in the 50 km to 100 km range were linearly downweighted from one to zero, respectively. One second P-wave windows and 5 second S-wave windows were used to calculate integral displacement amplitudes. The velocity seismograms are high-pass filtered with a one pole Butterworth filter at one Hz and double integrated to estimate long-period displacement levels. This method of calculating displacement integral amplitudes was compared to spectral fitting procedures to displacement spectra, and found to be more stable than spectral approaches. A total

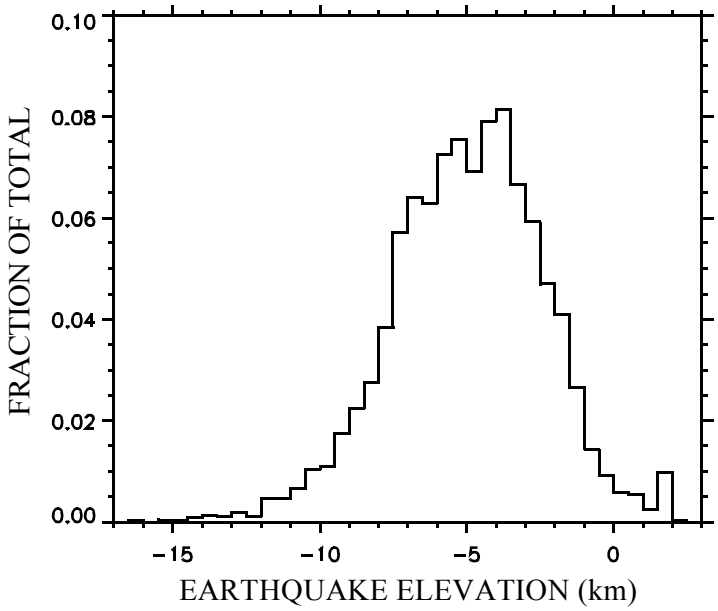

Figure 3-6: Histogram of the final earthquake elevations (with respect to mean sea level, e.g., 0 km). The histogram was constructed using the 4642 events relocated in the 3D velocity model from the joint inversion.

of 28 "temperature" levels were used in the simulated annealing inversions, with a maximum of 90 function evaluations at each "temperature". The starting "temperature" was set to a value corresponding to 60 misfitting first motions and decreased using the following temperature schedule, $T = T_0(1-k/K)^{\alpha}$, where T_0 is the initial temperature, K is the total number of function evaluations, and k is the cumulative number of function evaluations so far, and α is set to two. At large "temperatures", the process occasionally accepts models associated with increases in functional misfit to inhibit convergence to a local minima. As T tends toward zero, the inversion reduces to a simple downhill simplex algorithm (Press et al., 1992). Take-off angles and azimuths were calculated using the 3D P-wave velocity model curved ray paths. S waves were assumed to follow the same ray paths as the P waves.

Given the large number of earthquakes, numerical criteria were used to determine the subset of earthquakes with well-constrained focal mechanisms. A minimum of 8 P-wave first motions, and a total of at least 12 P-wave first motions and SV/P amplitude ratios were required to retain an earthquake for focal mechanism analysis. Since five candidate focal mechanism solutions were available for each earthquake, a criteria for a robust solution is that one of the five focal mechanism solutions fit the data distinctly better than the other four solutions, or that all five solutions fit nearly equally well and are essentially the same. Any solution that had a likelihood 2/3 or greater of the best-fitting solution was considered to fit the data equally well as the "best-fitting" solution. If the *T*-axis azimuths of nearly-equally-fitting solutions varied either < 5° or <20°, the solutions were considered similar and well constrained. Two scenarios were used for the T-axis variability criteria to evaluate sensitivity to this criteria. A 5° *T*-axis azimuth variability cutoff yields 307 focal mechanisms, but is probably too conservative, and limited the geographic distribution and density of focal mechanisms (Figure 3-8). A 20° *T*-axis azimuth variability cutoff produces 773 focal mechanisms and a more detailed distribution of focal mechanisms, but may include a small percentage of focal mechanisms that are not well constrained or are even erroneous (Figure 3-9); *T*-axes standard deviations are slightly larger when *T*-axis variability is allowed to be < 20° (compare Figures 3-9 and 3-8), but the overall pattern is very similar.

The focal mechanisms where divided into five focal mechanism classes based on *T*- and *P*-axis plunges (T_p and P_p, respectively), as defined in Tables 3-2 and 3-3. For the well-constrained focal

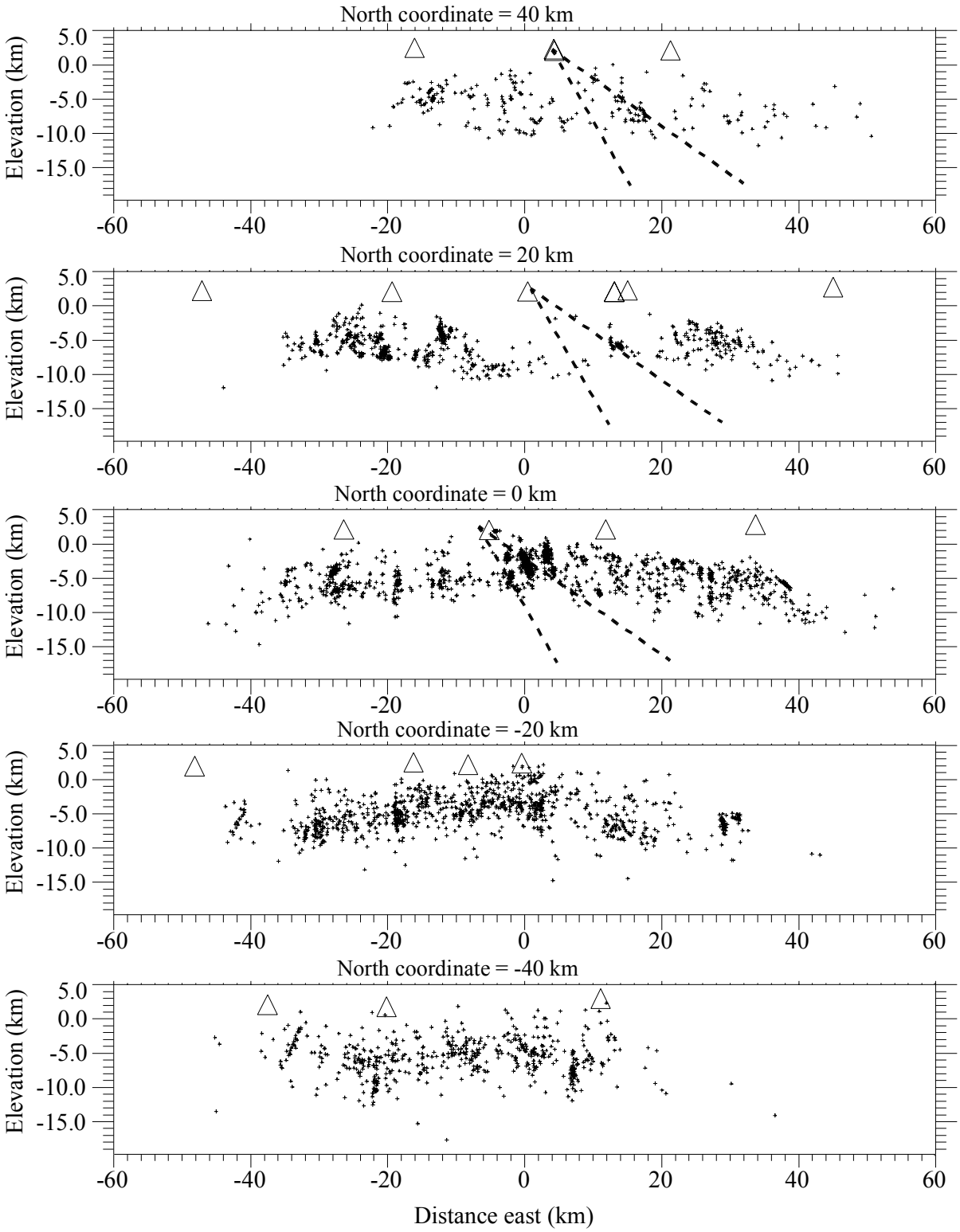

Figure 3-7: West-east depth sections of earthquake locations. Earthquakes located within 10 km of the north coordinate (as defined in Figure 3-5) are included in the section as small plus symbols as are seismographic stations as triangles. Where the Teton fault intersects the depth section the fault is shown with dips of 35° and 60° as dashed lines.

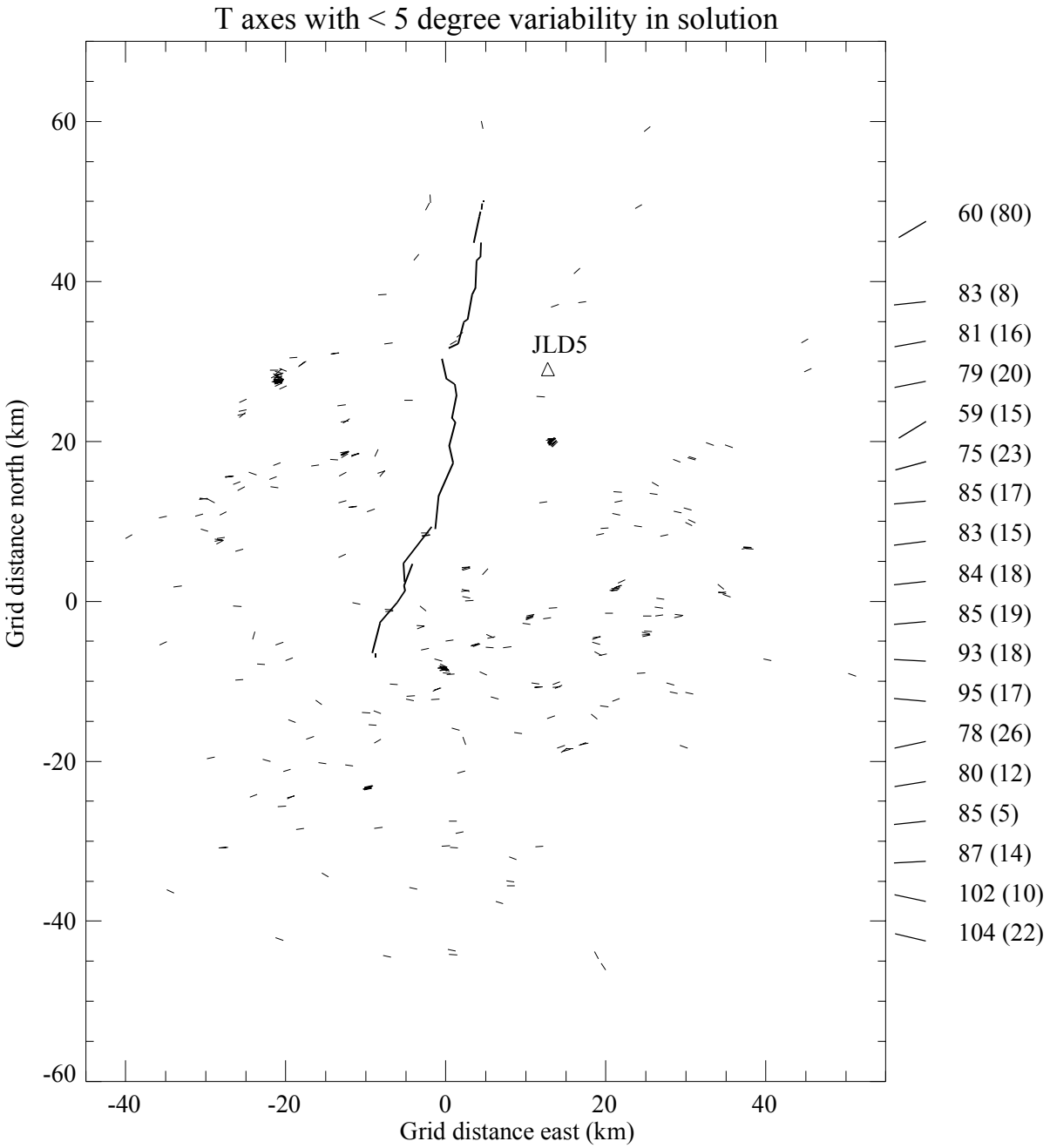

Figure 3-8: *T*-axes azimuths from the 303 focal mechanisms with < 5° *T*-axis solution variability. Each *T* axis is plotted as a 1 km line segment. The thick discontinuous black line segments are the surface traces of the Teton fault. Line segments to the right of the figure show median *T*-axis orientations for east-west regions that are 5-km-wide in the north-south extent labeled by the median *T*-axis azimuth values in degrees east of north and standard deviations in parenthesis. The grid origin corresponds to 43.6°N, 110.75°W. The triangle labeled JLD5 shows the location of the tallest section of Jackson Lake Dam, where site response station JLD5 was located.

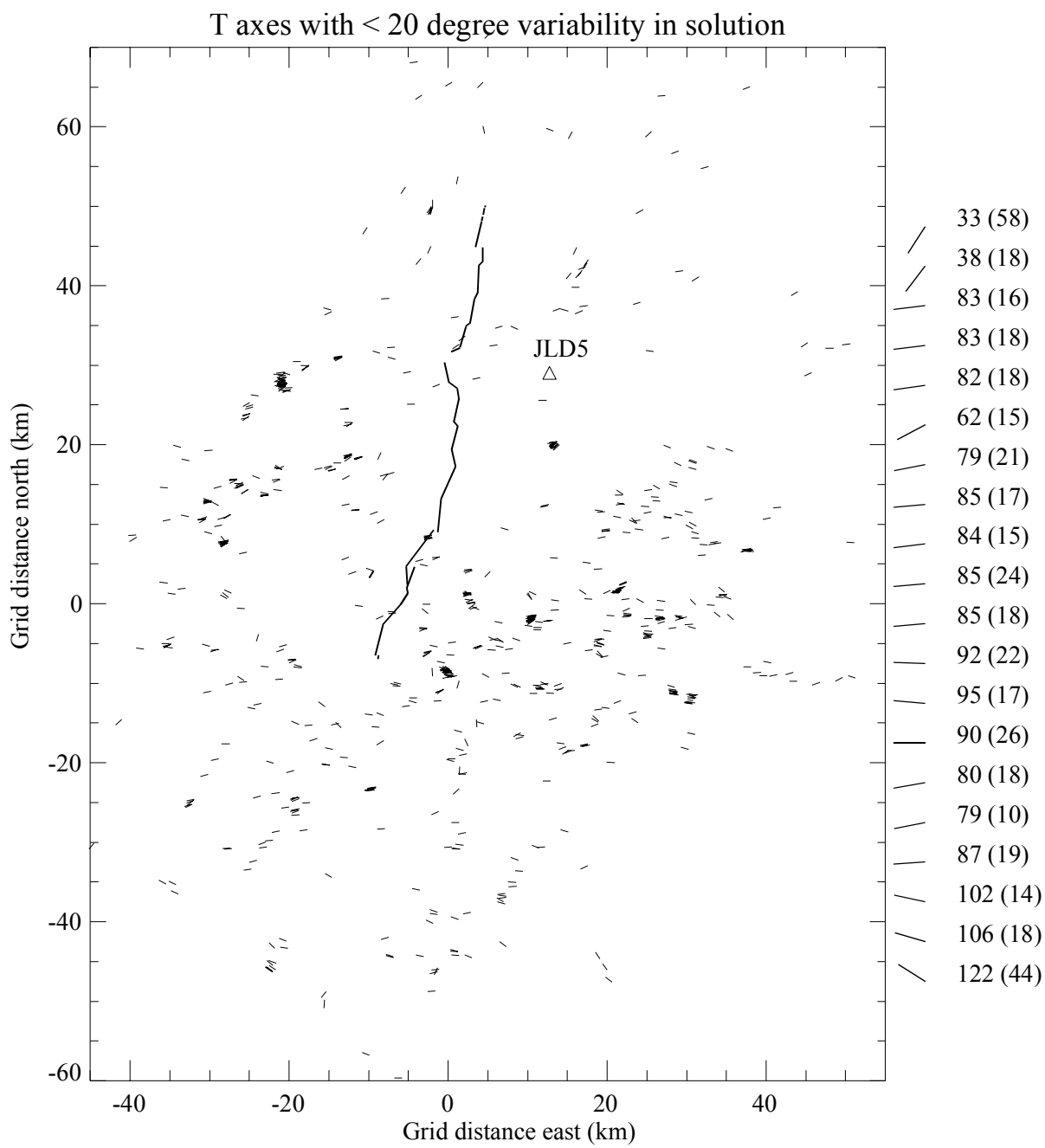

Figure 3-9: *T*-axes azimuths from the 773 focal mechanisms with < 20° *T*-axis solution variability. Each *T* axis is plotted as a 1 km line segment. The thick discontinuous black line segments are the surface traces of the Teton fault. Line segments to the right of the figure show median *T*-axis orientations for east-west regions that are 5-km-wide in the north-south extent labeled by the median *T*-axis azimuth values in degrees east of north and standard deviations in parenthesis. The grid origin corresponds to 43.6°N, 110.75°W. The triangle labeled JLD5 shows the location of the tallest section of Jackson Lake Dam, where site response station JLD5 was located.

Table 3-2: Number of Different Focal Mechanisms for < 5° *T*-axis Azimuth Variability.

Strike-slip.	Normal.	Reverse.	Oblique Normal.	Oblique Reverse.
$T_p \geq 30$ & $P_p \leq 30$	$T_p > 60$	$P_p > 60$	$P_p \leq 30$ & $T_p \geq 30$ & $T_p \leq 60$	$T_p \leq 30$ & $P_p \geq 30$ & $P_p \leq 60$
160	59	2	69	10

Table 3-3: Number of Different Focal Mechanisms for < 20° *T*-axis Azimuth Variability.

Strike-slip.	Normal.	Reverse.	Oblique Normal.	Oblique Reverse.
$T_p \geq 30$ & $P_p \leq 30$	$T_p > 60$	$P_p > 60$	$P_p \leq 30$ & $T_p \geq 30$ & $T_p \leq 60$	$T_p \leq 30$ & $P_p \geq 30$ & $P_p \leq 60$
368	172	3	169	34

mechanisms with < 5° *T*-axis azimuth variability, these five focal mechanism classes accounted for 300 of the 307 total focal mechanisms. Figure 3-10 shows the "pure" mechanisms (first three columns of Table 3-2). Figure 3-11 shows the "pure" strike slip and oblique mechanisms (first column and last two columns in Table 3-2). For the less well-constrained focal mechanisms with < 20° *T*-axis azimuth variability, these five focal mechanism classes accounted for 746 of the 773 total focal mechanisms, and are plotted in Figure 3-12 for "pure" mechanisms (first three columns of Table 3-3) and "pure" strike slip and oblique mechanisms in Figure 3-13 (first column and last two columns in Table 3-3).

The strike-slip, normal-slip, and oblique normal-slip focal mechanisms represent > 92% of the focal mechanisms and occur throughout the study area (Figures 3-10 to 3-13). Consequently, the *T*-axes orientations provide the most consistent picture of stress orientation (Figures 3-8 and 3-9). *T*-axes are nearly uniformly orientated almost east-west from north grid coordinate -35 km to 40 km. *T*-axes azimuths turn more northerly along the northernmost 10 km of the Teton fault (Figure 3-9), possibly reflecting the influence of the Yellowstone region on stresses in the northern portion of the study area. South of -40 km north grid distance, *T*-axes azimuths increasingly trend southerly in the southward direction (Figure 3-9). The northeast deflection of the *T*-axes at the northern limits of the grid and the southeast deflection of the *T*-axes at the southern limits of the

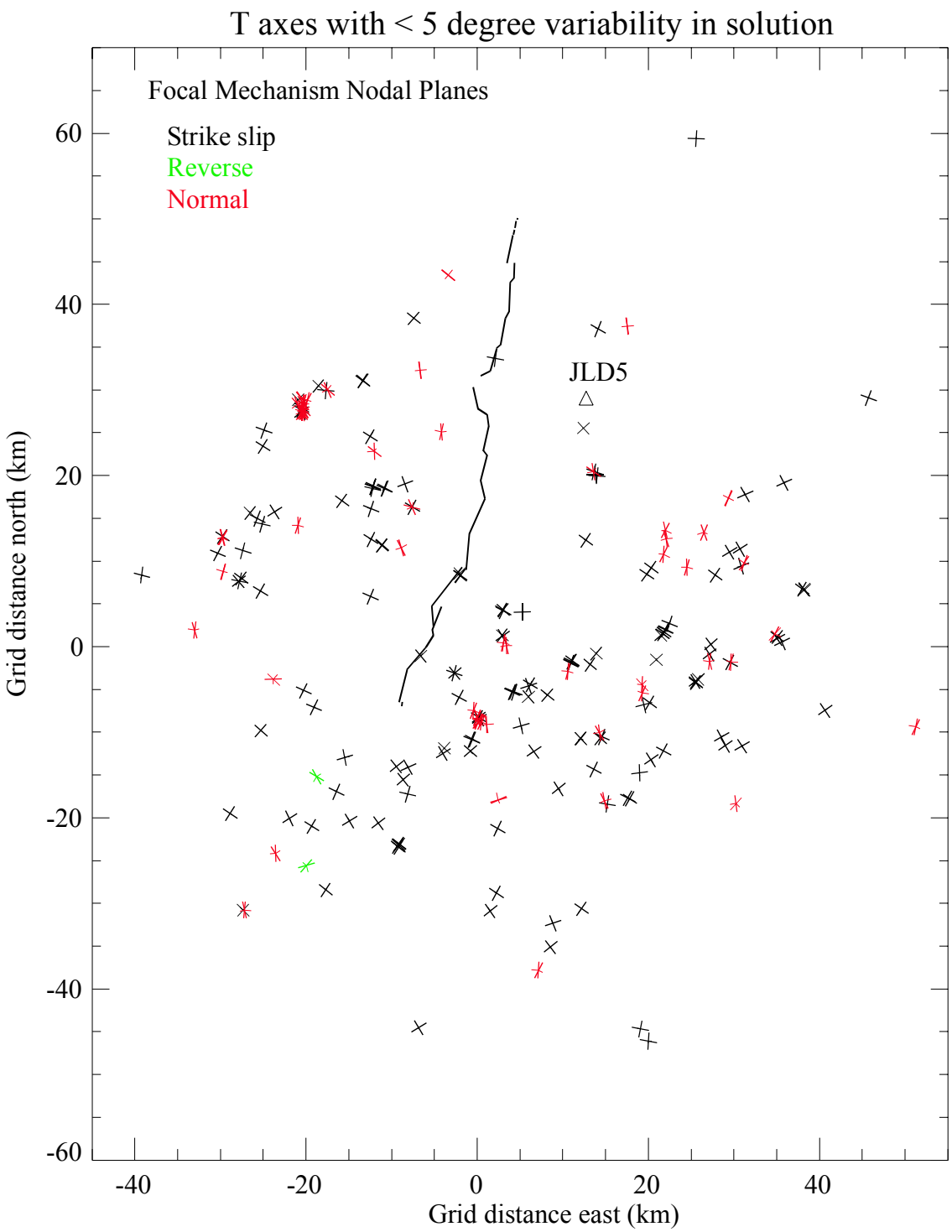

Figure 3-10: "Pure" nodal planes from focal mechanisms with < 5° T-axis solution variability. The long axes show nodal plane strikes, color-coded by focal mechanism (see legend on plot) as defined in Table 3-2. The short orthogonal lines show dip directions for the normal and reverse mechanisms; dip lines are half nodal strike lengths for a dip of zero and have zero length for a dip of 90°. The grid origin corresponds to 43.6°N, 110.75°W. The thick discontinuous black line segments are the surface traces of the Teton fault. The triangle labeled JLD5 shows the location of the tallest section of Jackson Lake Dam, where site response station JLD5 was located.

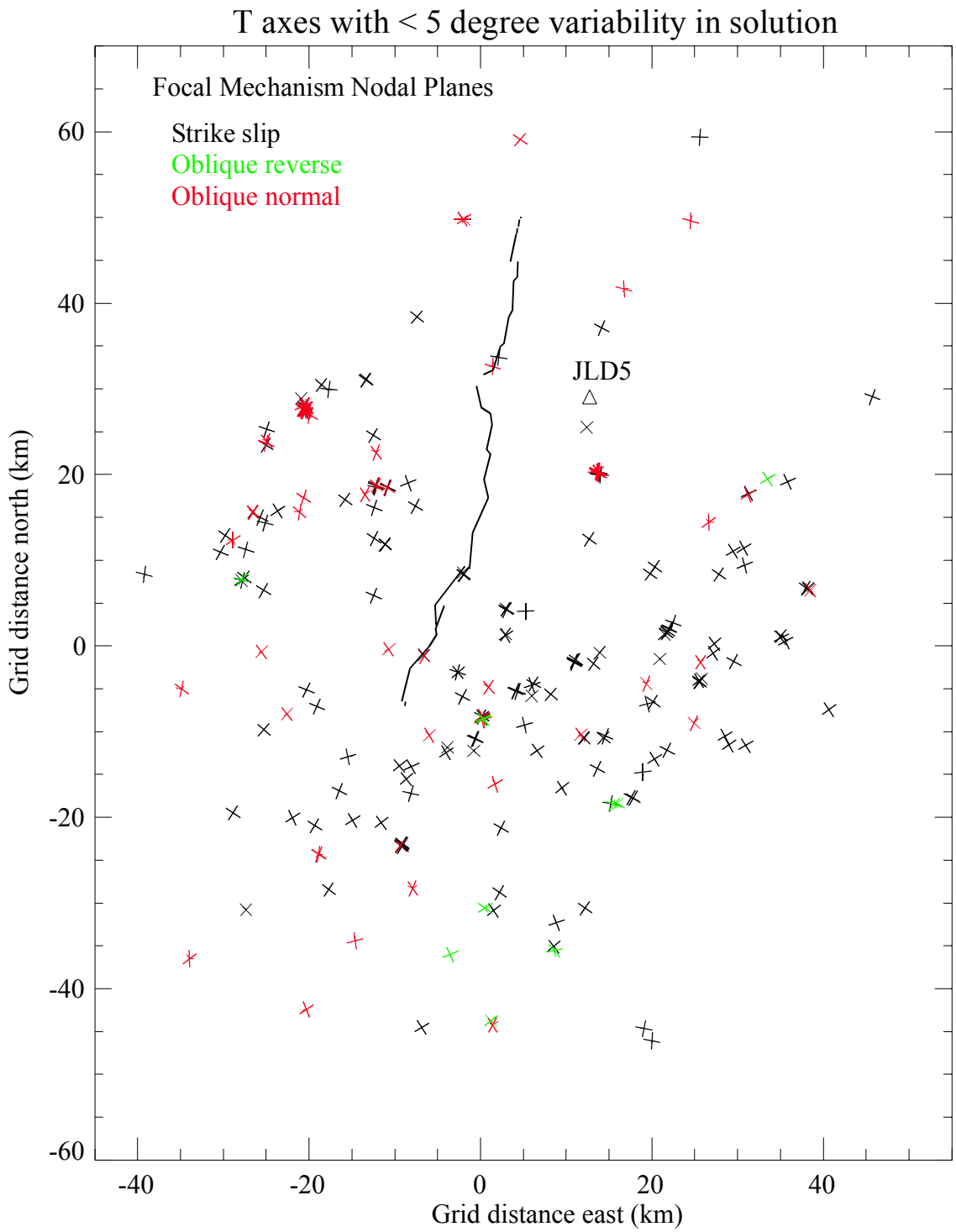

Figure 3-11: "Pure" strike-slip and oblique dip-slip nodal planes from focal mechanisms with < 5° T-axis solution variability. See Table 3-2 for focal mechanism definitions and Figure 3-10 for plot description.

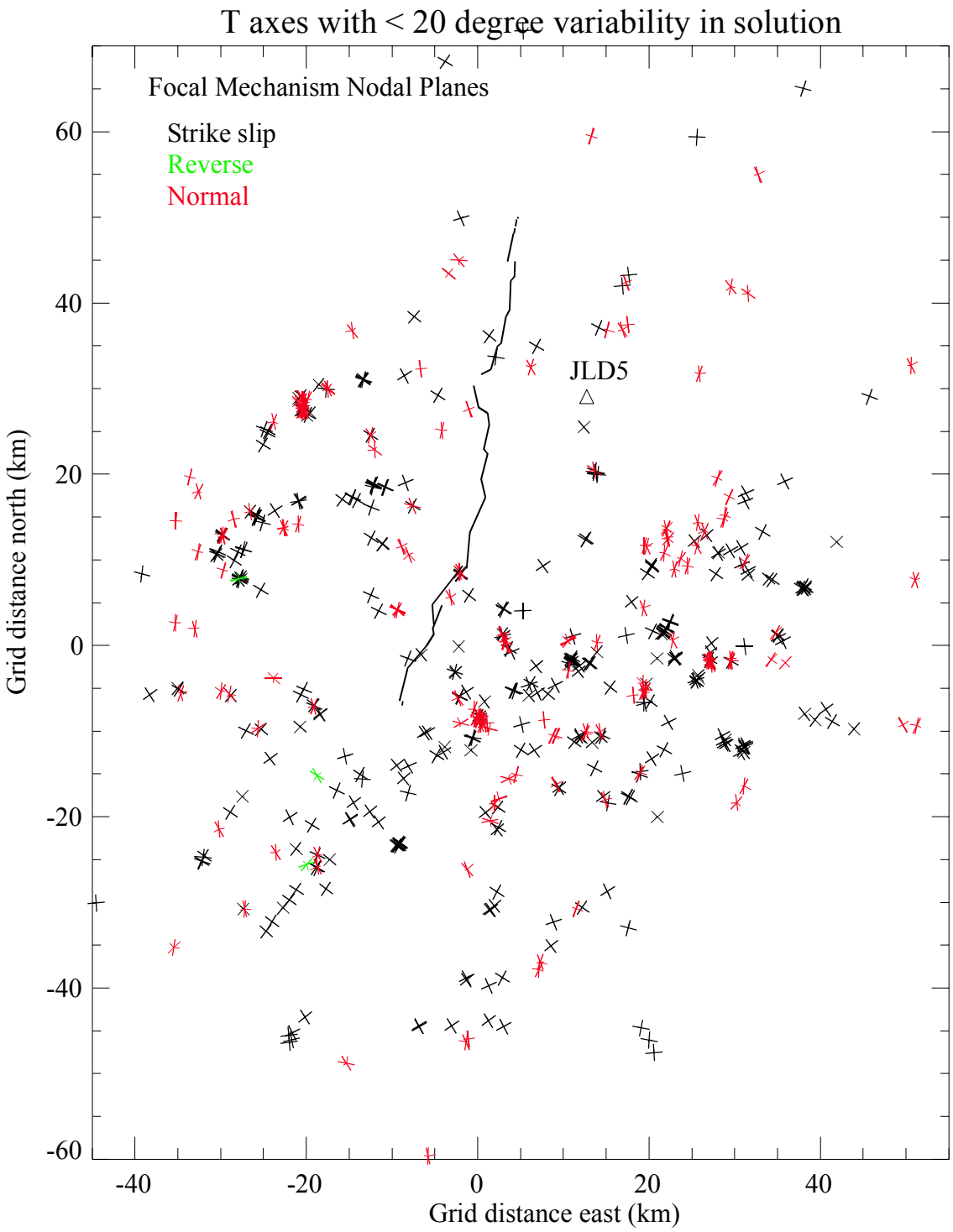

Figure 3-12: "Pure" nodal planes from focal mechanisms with < 20° T-axis solution variability. The long axes show nodal plane strikes, color-coded by focal mechanism (see legend on plot) as defined in Table 3-3. The short orthogonal lines show dip directions for the normal and reverse mechanisms; dip lines are half nodal strike lengths for a dip of zero and have zero length for a dip of 90°. The grid origin corresponds to 43.6°N, 110.75°W. The thick discontinuous black line segments are the surface traces of the Teton fault. The triangle labeled JLD5 shows the location of the tallest section of Jackson Lake Dam, where site response station JLD5 was located.

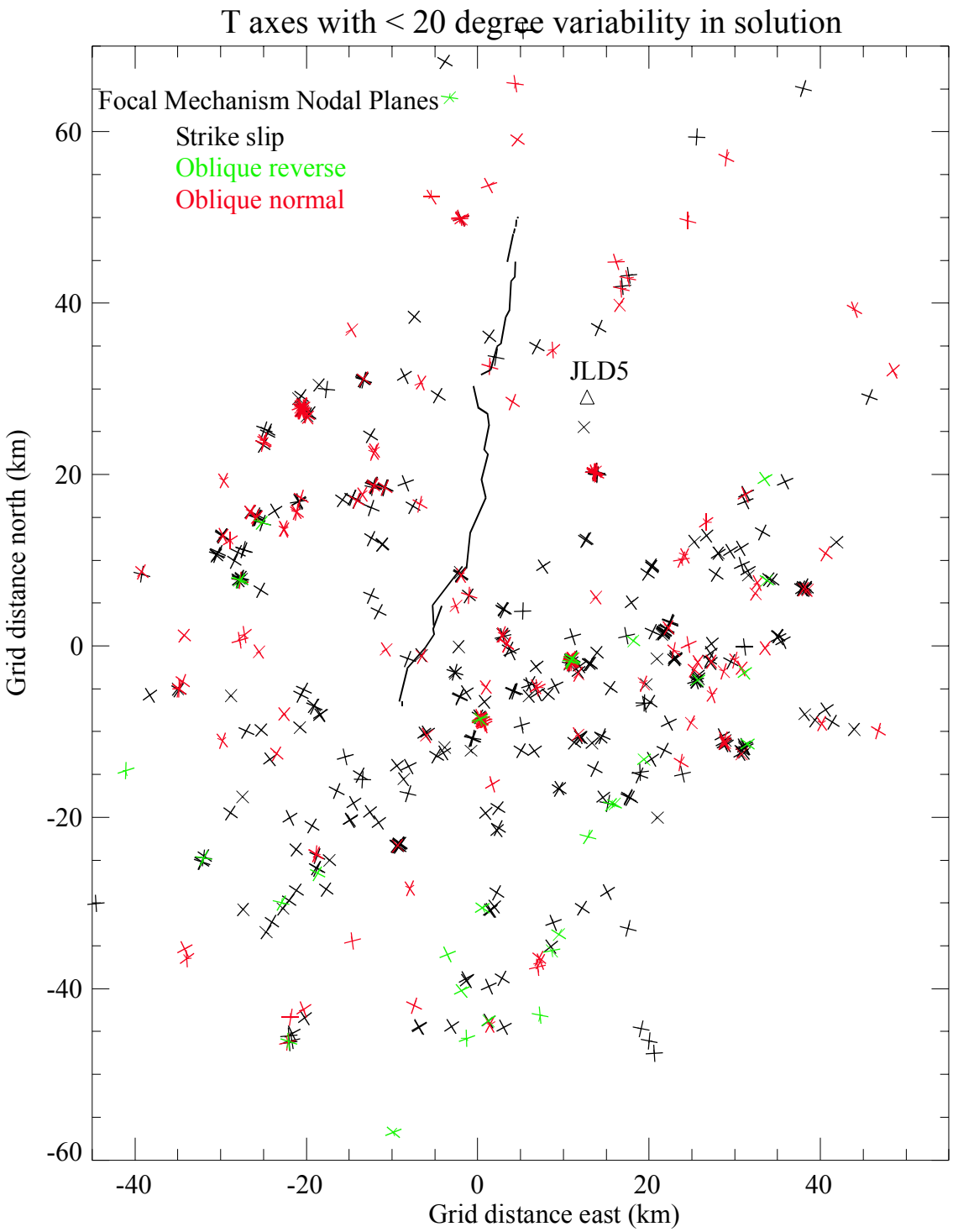

Figure 3-13: "Pure" strike-slip and oblique dip-slip nodal planes from focal mechanisms with < 20º T-axis solution variability. See Table 3-3 for focal mechanism definitions and Figure 3-12 for plot description.

grid roughly maintain the *T*-axes normal to the overall parabolic distribution of seismicity east of the Snake River Plain described in Anders et al. (1989). The reverse and oblique reverse solutions are mostly confined to the region south of 15 km north grid coordinates, and may reflect stress heterogeneity in the stepover region between the Teton fault and normal faults south of the Teton fault (e.g., Grand Valley fault and Star Valley fault). Consistent with field observations discussed in Section 2, the *T*-axes and nodal planes indicate primarily normal-slip on the central and northern sections of the Teton fault, and oblique left-lateral normal slip on the southern section of the Teton fault. The focal mechanism data, particularly the *T*-axes orientations, support using a dominantly normal-slip rake to simulate ground motions associated with rupture of the central and northern segments of the Teton fault.

The relative paucity of earthquakes that could be associated with the Teton fault at depth do not provide strong constraints on fault dip. Focal mechanism solutions of earthquakes located east of the surface trace of the Teton fault dips have east-dipping nodal planes that dip from 25° to 60°. There are too few earthquakes located east of the Teton fault, with far too limited spatial coverage to provide a strong constraint on fault dip, although the spatial distribution of earthquakes is consist with dips of < 50° (Figure 3-7). As discussed in Section 4, detailed waveform modeling of two earthquakes suggest that the Teton fault dips < 50°, if the earthquakes are actually located on the Teton fault. Waveform modeling of more of the earthquakes located east of the Teton fault may provide better constraints on Teton fault dip at depth than are currently available.

3.3 Earthquake Recurrence

This section describes the development of earthquake recurrence parameters for the Jackson Lake region. There are two data sets available for this purpose; the Jackson Lake Seismic Network (JLSN) catalog (June, 1986 - December, 2001), and the historic record for this region prior to the network's installation in 1986 (1963 - May, 1986). Two sets of recurrence parameters were developed, one with just the JLSN data and one with the combined JLSN - pre-1986 information. Because few, if any, earthquakes in either catalog have been positively associated with a known fault, this seismicity represents "random" or "background" earthquakes, and any further analysis using the parameters developed here pertain only to such seismic activity.

The procedure consisted of declustering both catalogs in order to qualify as a Poissonian process; one that is random in space and time. Log-normal maximum likelihood magnitude-frequency curves were then fit to the data. Formal uncertainties in recurrence parameter values and seismicity rates were also computed and are presented below.

3.4 Catalog Development

3.4.1 Jackson Lake Network Catalog.

The JLSN catalog, with a lower magnitude cutoff of 2.0, consists of 1547 earthquakes (Figure 3-14). The seismicity has a roughly uniform geographic distribution, with decreased activity in the vicinity of the Teton Range and the basin containing Jackson Lake. The largest event is a M_c (coda magnitude) 4.7 event that occurred on December 28, 1993 (labeled along the right side of Figure 3-14). There are a number of spatial earthquake clusters, the most notable being a swarm in the southwest corner of Figure 3-14. This cluster does not represent a typical mainshock-aftershock sequence, but a series of about 100 events that occurred between November 10 and November 17, 1992. The largest magnitude was 4.0.

3.4.1.1 Declustering. In order to model earthquake occurrence as a random process, the catalogs must approximate random space-time characteristics. However, due to the existence of foreshock-mainshock-aftershock sequences and swarms, the raw data set cannot be considered to have "random" or Poissonian characteristics. It is therefore necessary to identify and delete "dependent" events from swarms and foreshock-mainshock-aftershock sequences. A declustering algorithm based on Reasenberg (1985) was used for this purpose. This technique, with some modifications, was used by Savage and dePolo (1993) to search for foreshocks in the Nevada seismicity catalog. The algorithm used in this report is based on these two papers, with some additional appropriate modifications. The major details are described below.

Any cluster identification scheme must establish criteria for deciding whether neighboring events in the catalog are "dependent" on or "independent" in time and space. To determine spatial dependence, a "mainshock" is defined, with a magnitude-dependent source radius based on the circular crack model described in Kanamori and Anderson (1975) and a stress drop of 30 bars (a reasonable stress drop for an extensional environment, see Spudich et al., 1999). The radius of the

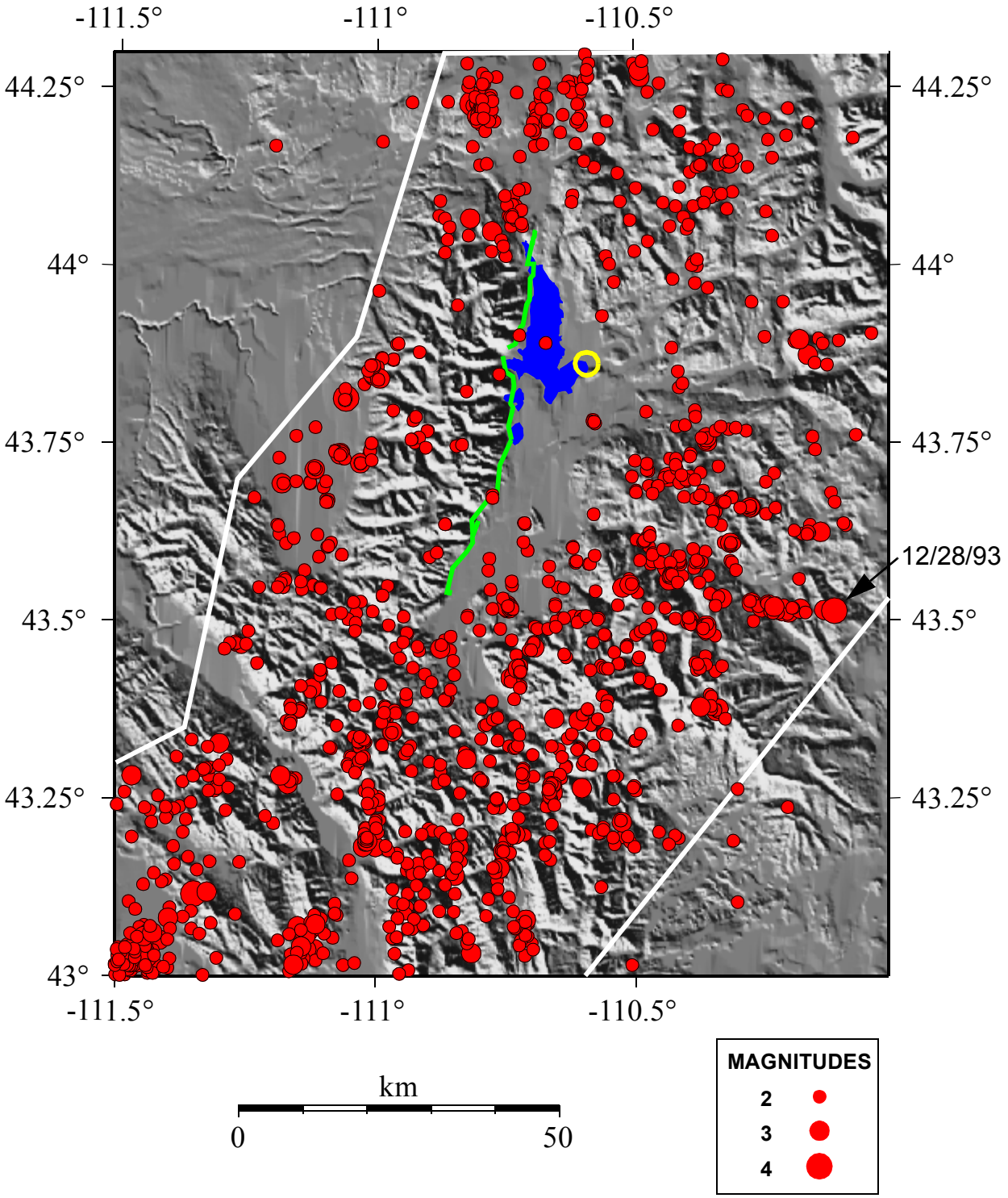

Figure 3-14: Epicenters from Jackson Lake Seismic Network, magnitude ≥ 2.0, June 1986 - December 2001. Surface traces of the Teton fault are shown in green. Location of Jackson Lake Dam shown as yellow circle. Boundaries of recurrence study area shown in white. The arrow points to the location of M_c 4.7 event of Dec. 28, 1993.

next event in time is defined as its circular crack radius times a factor Q. If the distance between the two epicenters is less than the sum of the two radii, the two events are considered spatially dependent. Temporal dependence is judged by an application of Omori's Law, which describes the exponential temporal decay of aftershocks. The aftershock sequence is modeled as a time-dependent Poisson process, with the Omori constants taken from the "generic Utah model" of Arabasz and Hill (1996). These constants were derived from 10 mainshock-aftershock sequences from the Intermountain Seismic Belt (ISB) in Utah, and are assumed to be representative of aftershock sequences occurring in the study area.

The "look-ahead" time criterion is a function of the Omori constants, the magnitude of the mainshock, the detection threshold magnitude, the confidence probability, and the time between the two events. Since the "look-ahead" time, τ, is proportional to the time difference, upper and lower bounds must be placed on it. If the time difference is less than τ, the two events are considered temporally dependent. If both spatial and temporal criteria are satisfied, the two events are considered dependent. If the magnitude of the second event exceeds that of the first, it is considered the new mainshock.

Because Reasenberg (1985) applied this technique to a catalog resulting from a spatially and temporally uniform seismograph network, it was not necessary to be concerned with changes in earthquake location capabilities through time. During the time span of the JLSN catalog, (1986-2001) we use earthquakes of magnitude 2 and greater, and it was assumed that the catalog is complete down to this magnitude level for the period of network operation. The hypocentral precision was estimated to be 10 km. This means that in judging distance criteria, two events were spatially linked if less than 10 km apart. For a given cluster an "equivalent" event was calculated as the moment-weighted mean of latitude, longitude, and origin time. In contrast to Reasenberg (1985), "equivalent" magnitudes, derived by summing the seismic moment of groups of a cluster and finding a new magnitude, were not computed. In our judgement, for purposes of hazard estimation it is more important to retain accurate magnitude estimates than to conserve the seismic moment of the catalog. All other declustering parameters were set to the values recommended in Reasenberg (1985).

Space-time plots of the raw and declustered catalog are shown in Figures 3-15 and 3-16. The "a" figures shows latitude vs. time; the "b" figures longitude vs. time. The plots for the unfiltered catalog show many clusters, the most prominent being the 1992 sequence. The plots of the declustered catalog show a much more "random" appearance. There is still a trace of the 1992 swarm in Figure 3-16b, but it is clear from these figures that the great majority of the events have been removed. The events identified as being members of clusters are shown in Figure 3-17. The events that appear to be solitary are actually two or more events at the same location.

Out of a total of 1547 events in the **M** > 2 JLSN earthquake catalog, 791 events were identified as being members of a total 229 clusters. The number of "independent" earthquakes is 984. The declustered JLSN catalog is shown in Figure 3-18.

3.4.2 Pre-Jackson Lake Network Catalog.

Earthquakes that occurred in the study region prior to installation of the JLSN were also analyzed. These were taken from the Northern California Earthquake Data Center (NCEDC), which compiles earthquake data from a variety of sources. A total of 155 events of magnitude 2 and greater, spanning 1963 to June 1986, were extracted. These data are of lower location accuracy than the JLSN data, due to the sparseness and heterogeneity of seismograph station deployment that predates the installation of the JLSN. Listed magnitudes are either local magnitude (M_L), coda magnitude (M_c), body wave magnitude (M_b), or unknown. This mix of scales signifies probable incompatibility between the values presented. Due to the complexities involved and the scope of this project, no attempt was made to fit the pre-network magnitudes to a common scale, or calibrate them to the JLSN magnitudes.

The pre-network events are plotted in Figure 3-19. The spatial pattern appears similar to the JLSN data (Figure 3-14). The largest event is a M_c 5.1 event that occurred at the top of Figure 3-19 on March 30, 1973.

Declustering was performed on the pre-network catalog, using the same algorithm as described above. Completeness was assumed to magnitude 4, and location precision was estimated to be 20

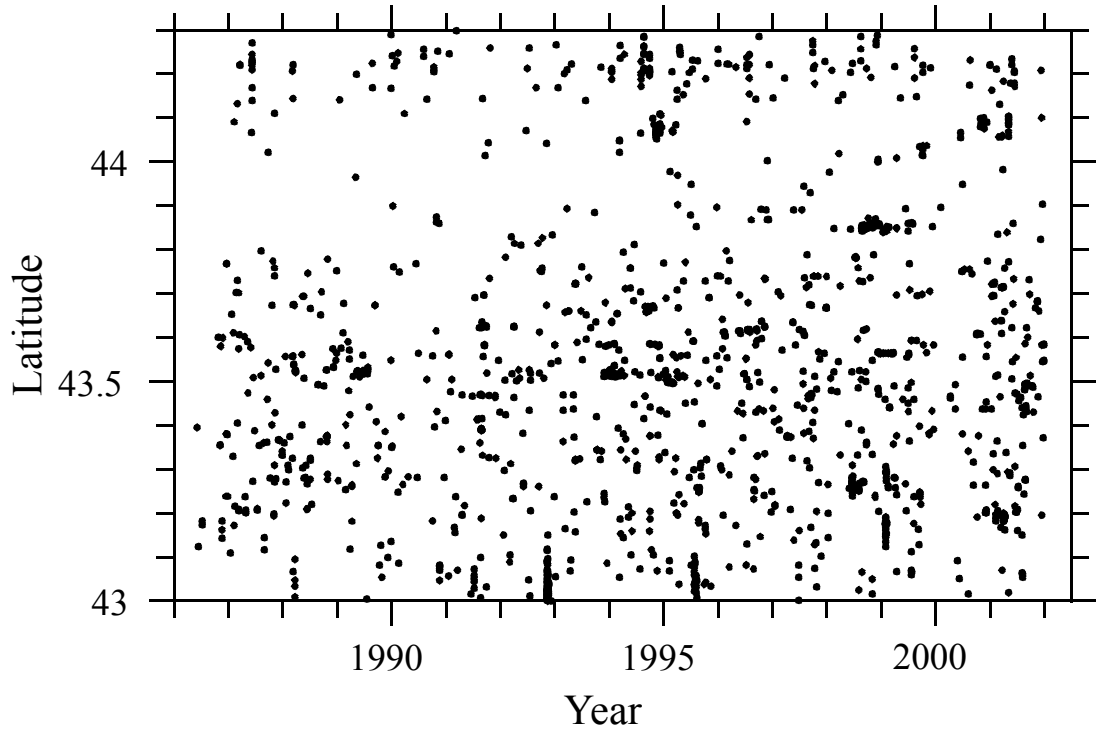

Figure 3-15a: Latitude vs. time, unfiltered JLSN catalog.

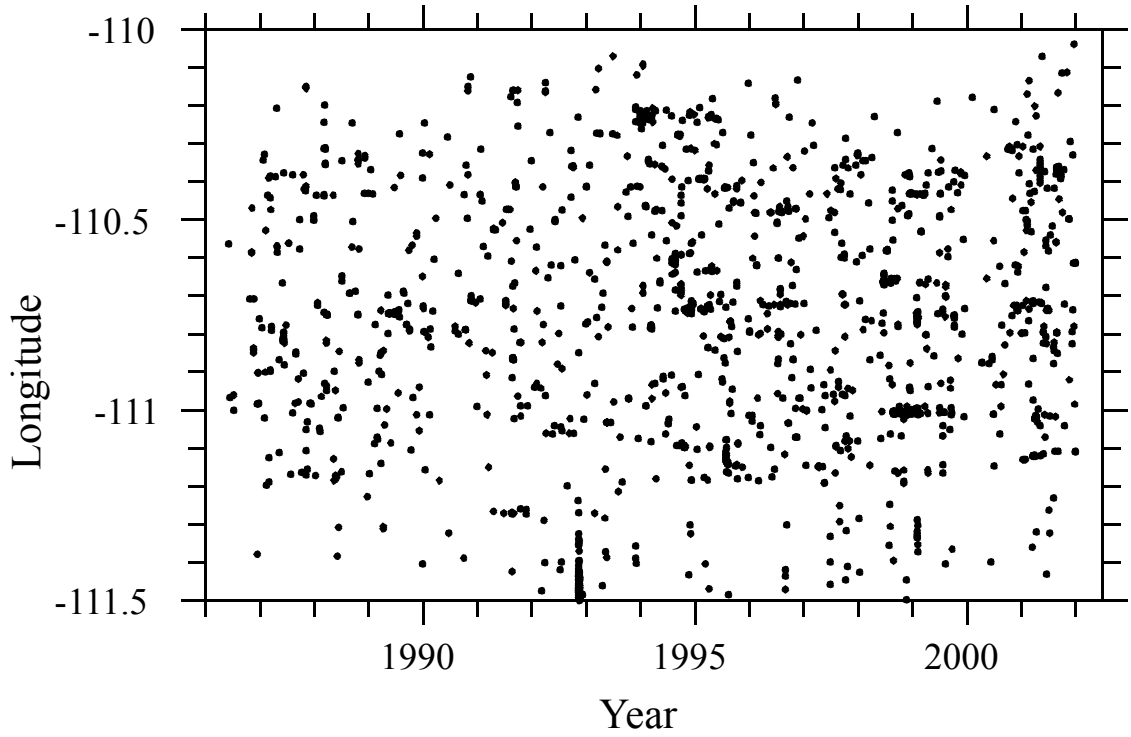

Figure 3-15b: Longitude vs. time, unfiltered JLSN catalog.

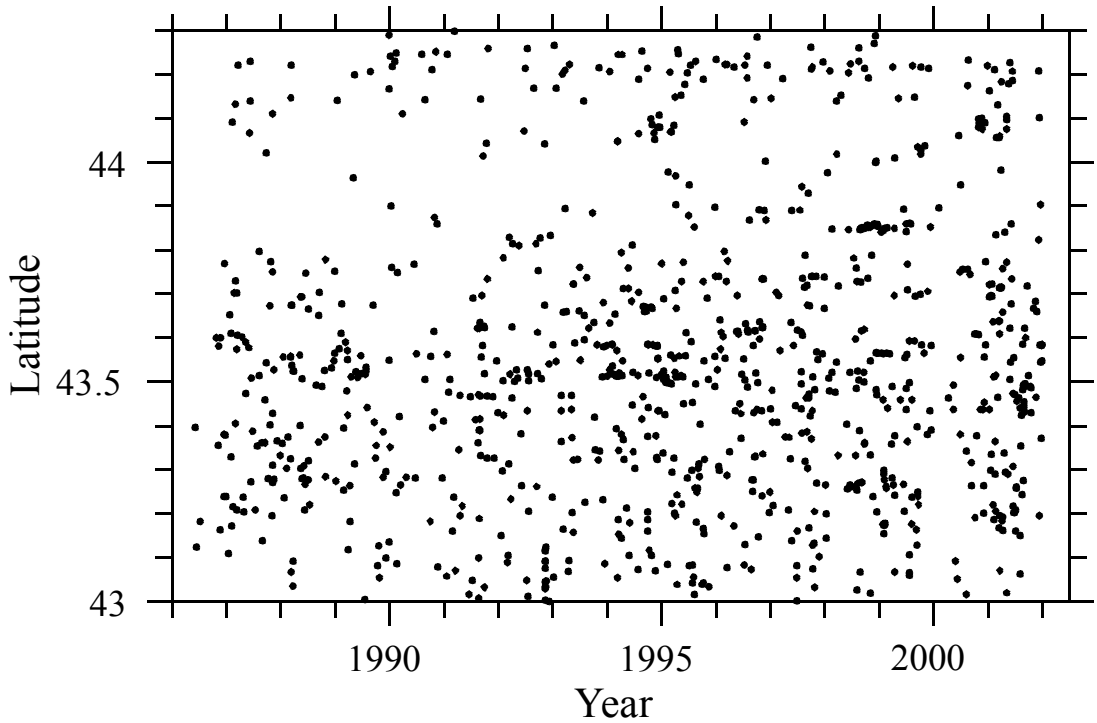

Figure 3-16a: Latitude vs. time, declustered JLSN catalog.

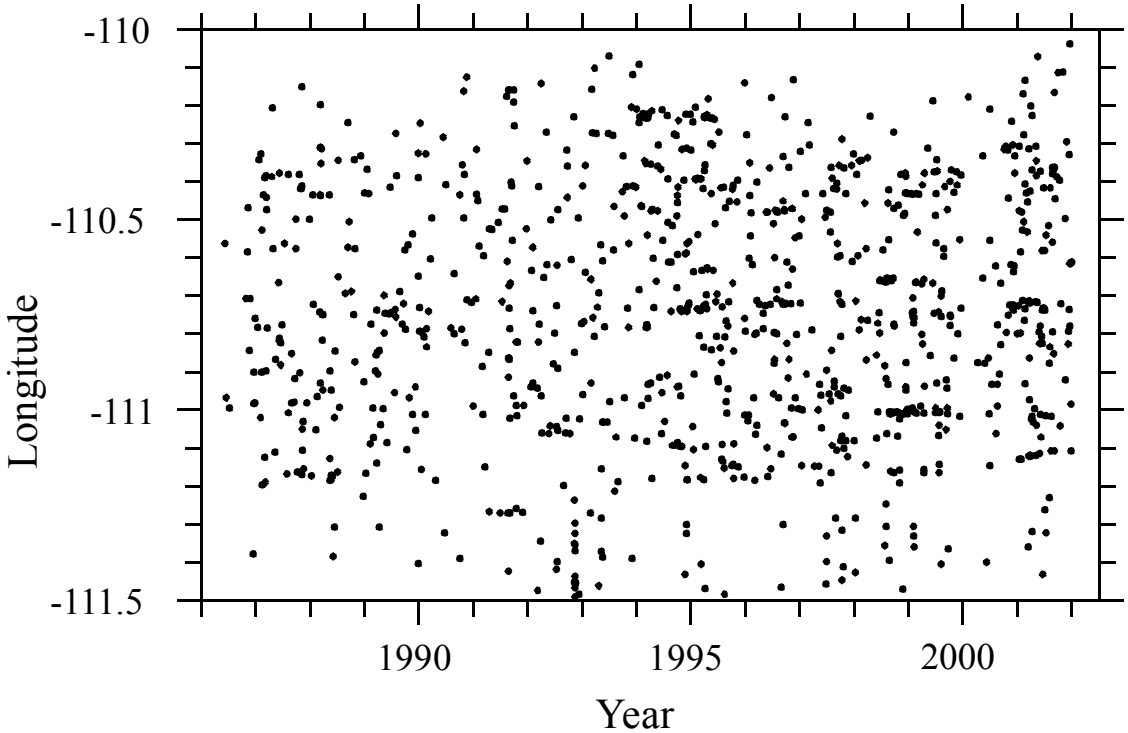

Figure 3-16b: Longitude vs. time, declustered JLSN catalog.

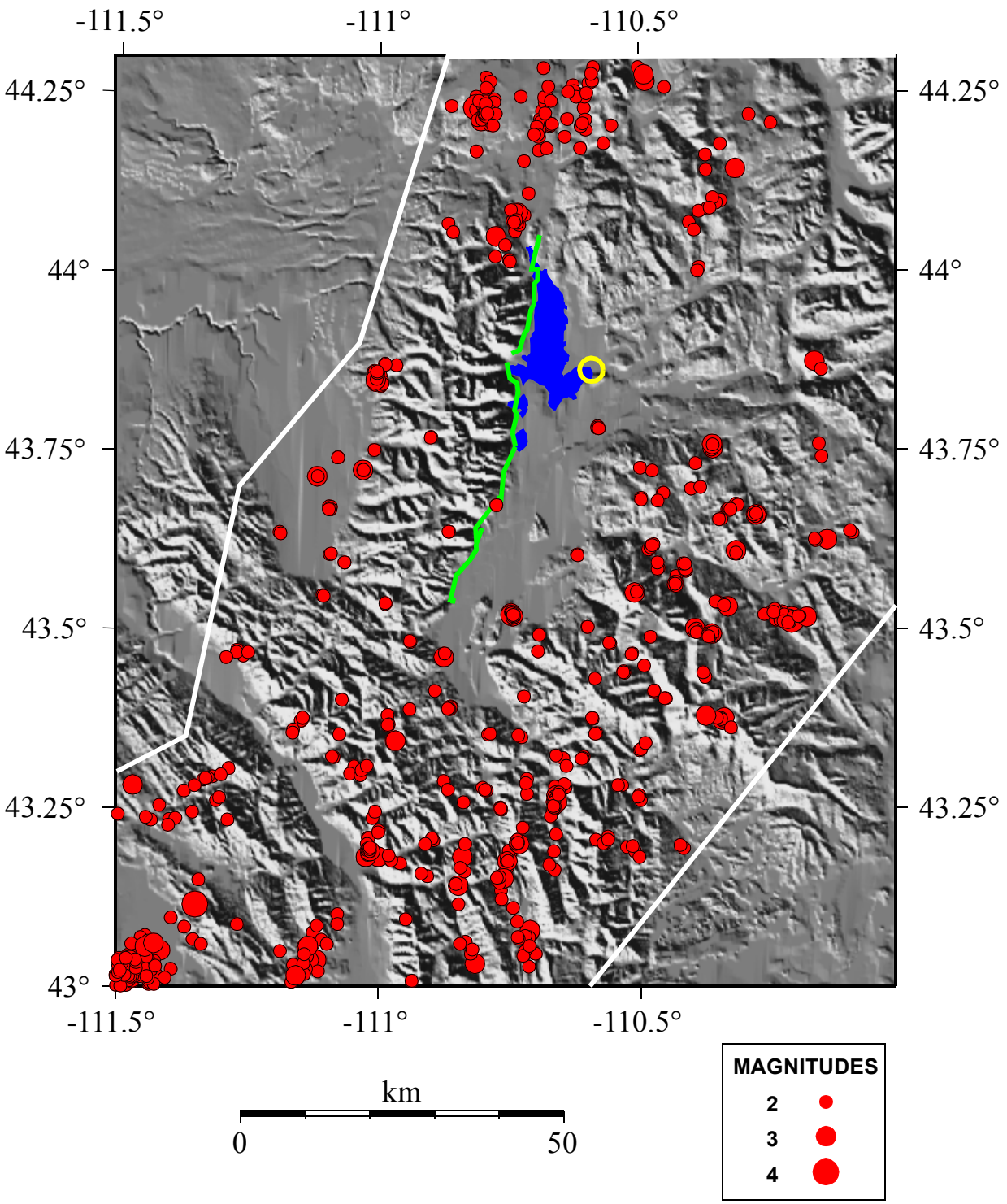

Figure 3-17: JLSN earthquakes identified as being clusters by declustering algorithm.See Figure 3-14 for plot details.

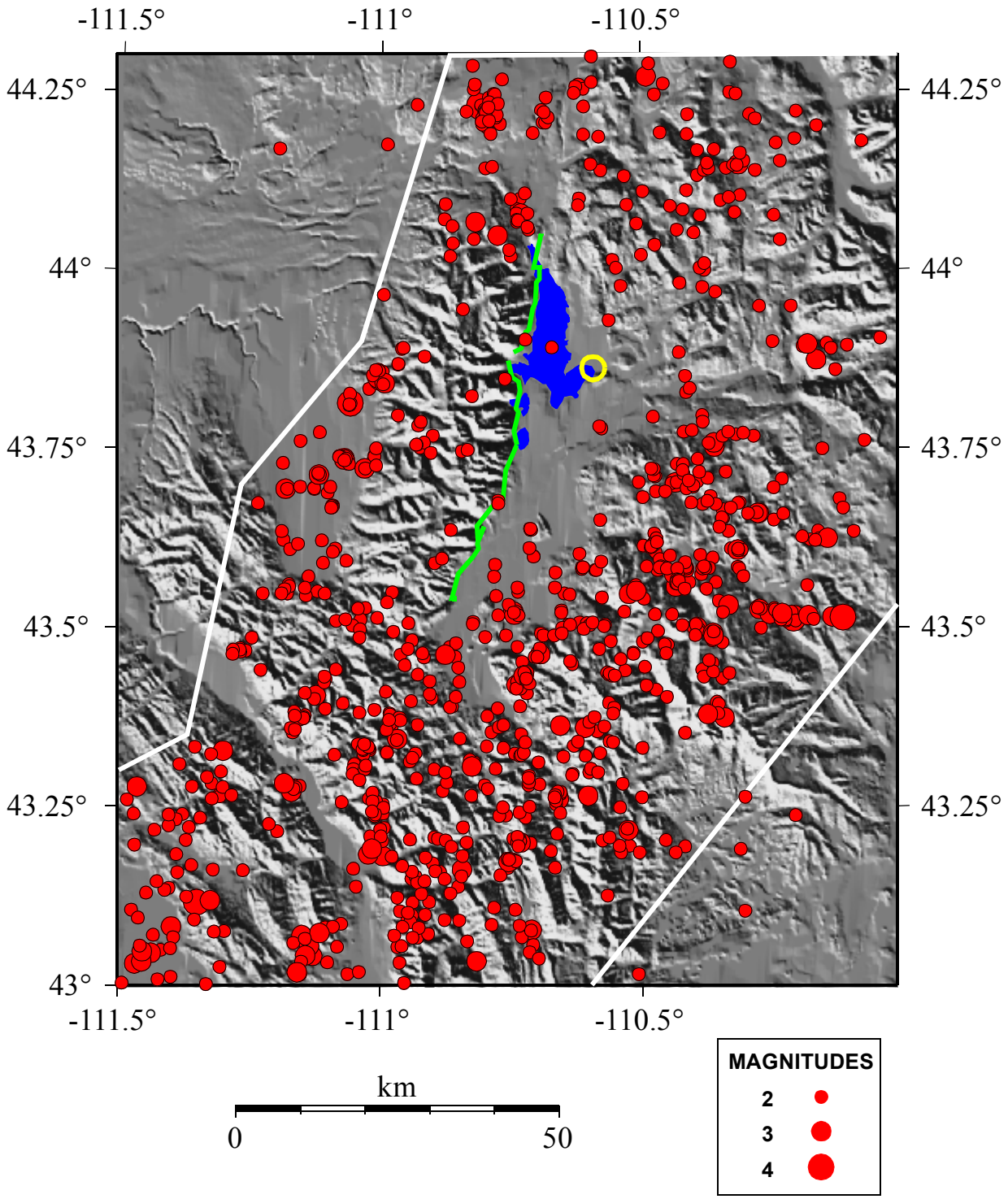

Figure 3-18: JLSN earthquakes identified as independent events by declustering algorithm.See Figure 3-14 for plot details.

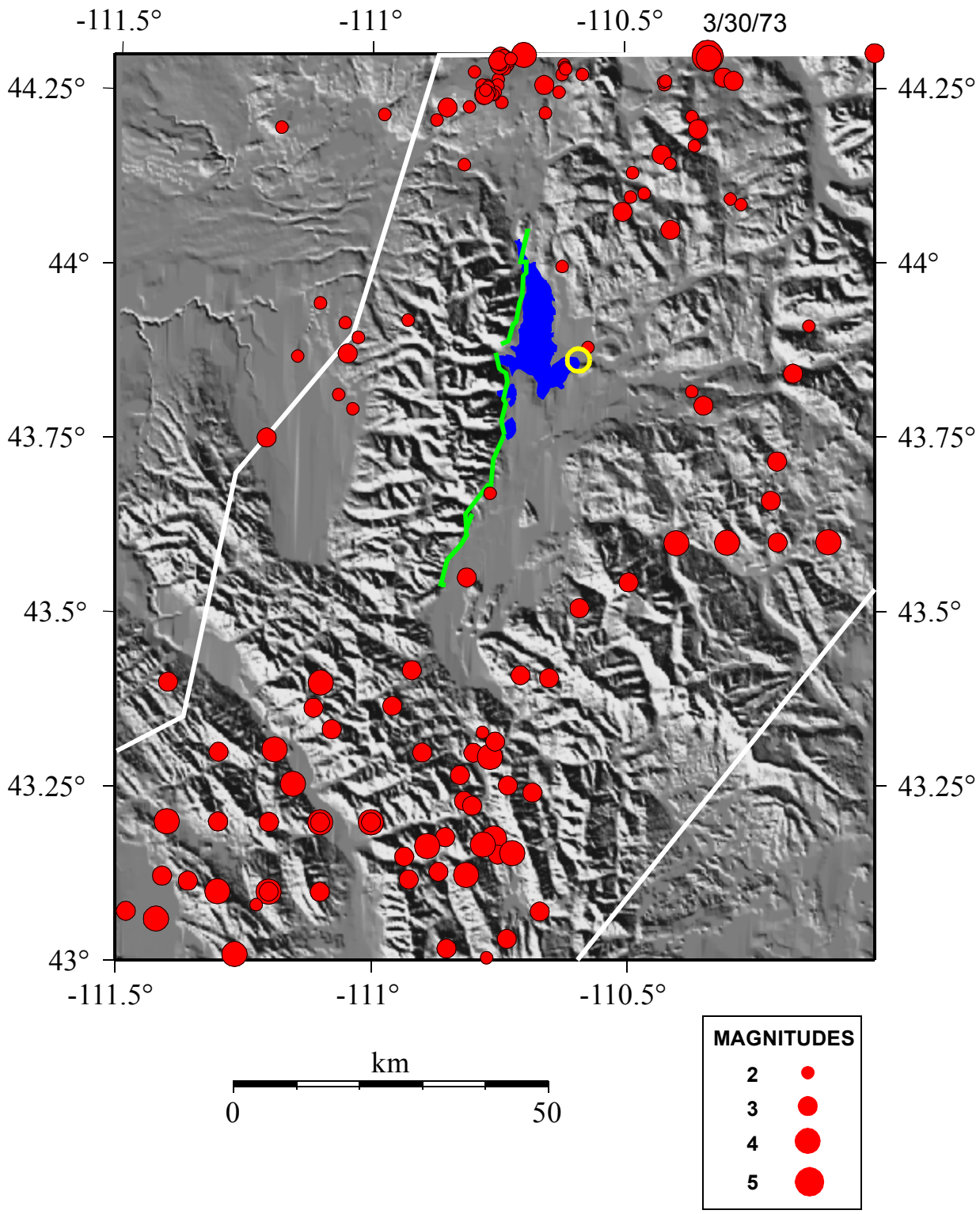

Figure 3-19: 1963 - June 1986 epicenters, from NCDEC. See Figure 3-14 for plot details.

km, in contrast to the 10 km assumed for the JLSN catalog. Of the 25 events of magnitude 4 or greater, 5 clusters and 18 independent events were identified.

3.5 Recurrence Calculations

Earthquake recurrence statistics were computed from the JLSN data set (1986-2001), and the combined pre-network - JLSN data set (1963-2001) shown in Figure 3-20. The maximum likelihood method (Weichert, 1980) was used, which accounts for unequal observation periods for different magnitude ranges. Data variances were computed as outlined in Weichert (1980). Recurrence parameter and seismicity rate uncertainties and confidence bounds were calculated using the method of Bollinger et al. (1989). A spacing of 0.5 magnitude unit was used. Tables 3-4a and 3-4b give the completeness periods and event counts for each data set, for the recurrence area shown in the seismicity figures (see Figure 3-14).

Incremental and cumulative recurrence curves for each data set are shown in Figures 3-21 and 3-22. Recurrence parameters *a* and *b* in the Gutenberg-Richter relation Log (N) = *a* - *b*(M), and their uncertainties, are listed in Tables 3-5a and 3-5b. The "*a*" values have been normalized to km^2/year, based on an area of 12,872 km^2. Tables 3-6a and 3-6b give observed and computed return periods for the different magnitude intervals, along with 95% confidence bounds on the maximum likelihood rates.

3.6 Earthquake Recurrence Discussion

Recurrence parameters for the Jackson Lake area have been computed using two data sets: JLSN data, and a combined catalog consisting of JLSN data and earthquakes recorded prior to installation of the JLSN. Each set has its advantages: the JLSN results are from high quality data that are self-consistent in location accuracy and magnitude computation, but cover a relatively short time span. The combined catalog results offer a longer time span (38 years vs. 15 years) and include more moderate (magnitude 4 and 5) events, but magnitude determinations for pre-JLSN events were computed using at least four different magnitude formulas, are of indeterminate quality, and their compatibility with JLSN magnitude values is unknown. Further use of these relations, for example in a probabilistic ground motion analysis, should incorporate both results.

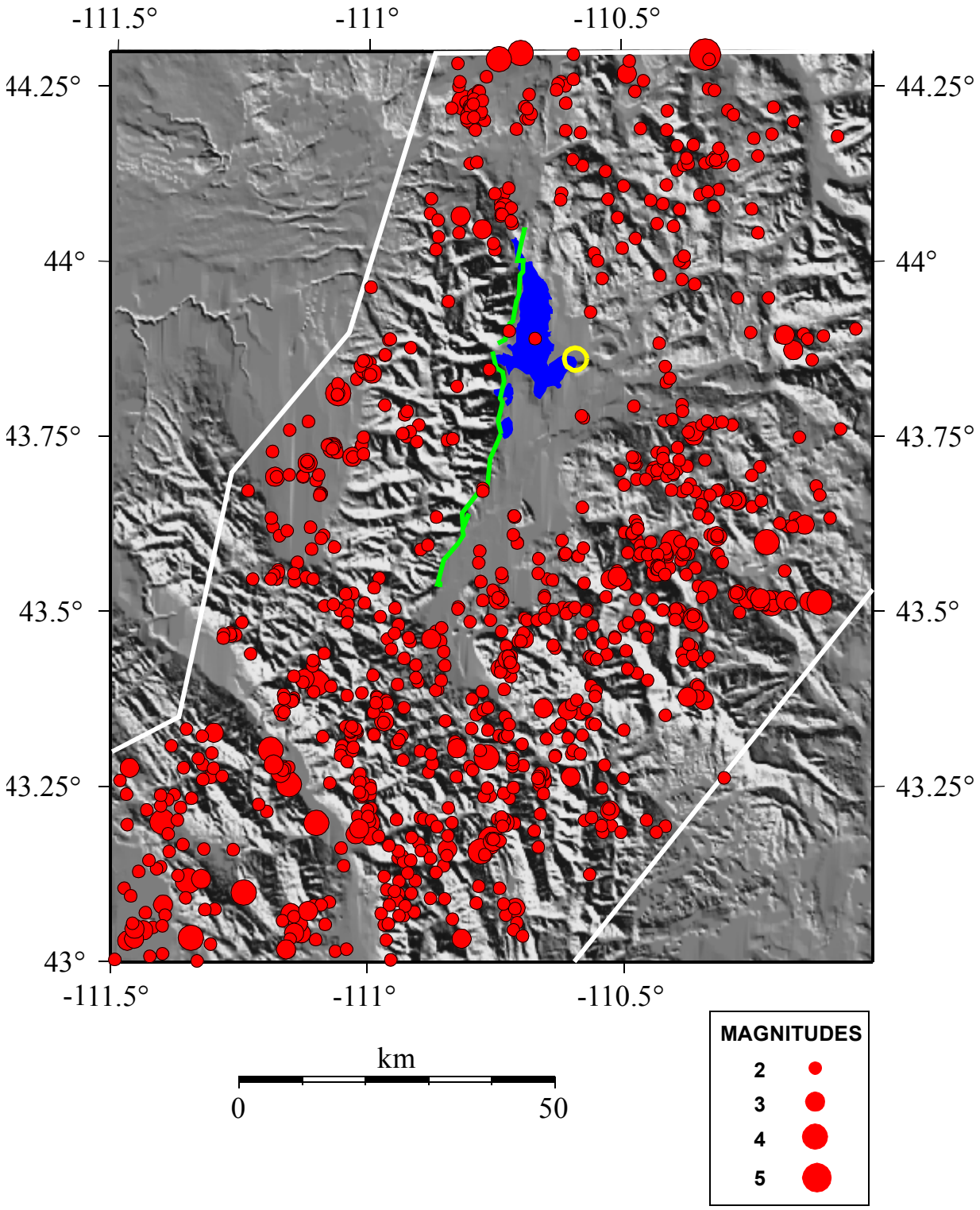

Figure 3-20: Declustered earthquakes used in recurrence calculations using the combined catalogs. See Figure 3-14 for plot details.

Table 3-4a: Completeness Periods and Event Counts Used in Recurrence Calculations, JLSN Catalog

Magnitude Range	Completeness Period	Number of Earthquakes
2.0 - 2.5	6/1986 - 12/2001	704
2.5 - 3.0	6/1986 - 12/2001	196
3.0 - 3.5	6/1986 - 12/2001	64
3.5 - 4.0	6/1986 - 12/2001	10
4.0 - 4.5	6/1986 - 12/2001	4
4.5 - 5.0	6/1986 - 12/2001	1
5.0 - 5.5	6/1986 - 12/2001	0
5.5 - 6.0	6/1986 - 12/2001	0
6.0 - 6.5	6/1986 - 12/2001	0

Table 3-4b: Completeness Periods and Event Counts Used in Recurrence Calculations, JLSN and 1963-1986 Catalog

Magnitude Range	Completeness Period	Number of Earthquakes
2.0 - 2.5*	6/1986 - 12/2001	704
2.5 - 3.0*	6/1986 - 12/2001	196
3.0 - 3.5*	6/1986 - 12/2001	64
3.5 - 4.0*	6/1986 - 12/2001	10
4.0 - 4.5	1/1963 - 12/2001	19
4.5 - 5.0	1/1963 - 12/2001	3
5.0 - 5.5	1/1963 - 12/2001	1
5.5 - 6.0	1/1963 - 12/2001	0
6.0 - 6.5	1/1963 - 12/2001	0

* JLSN only

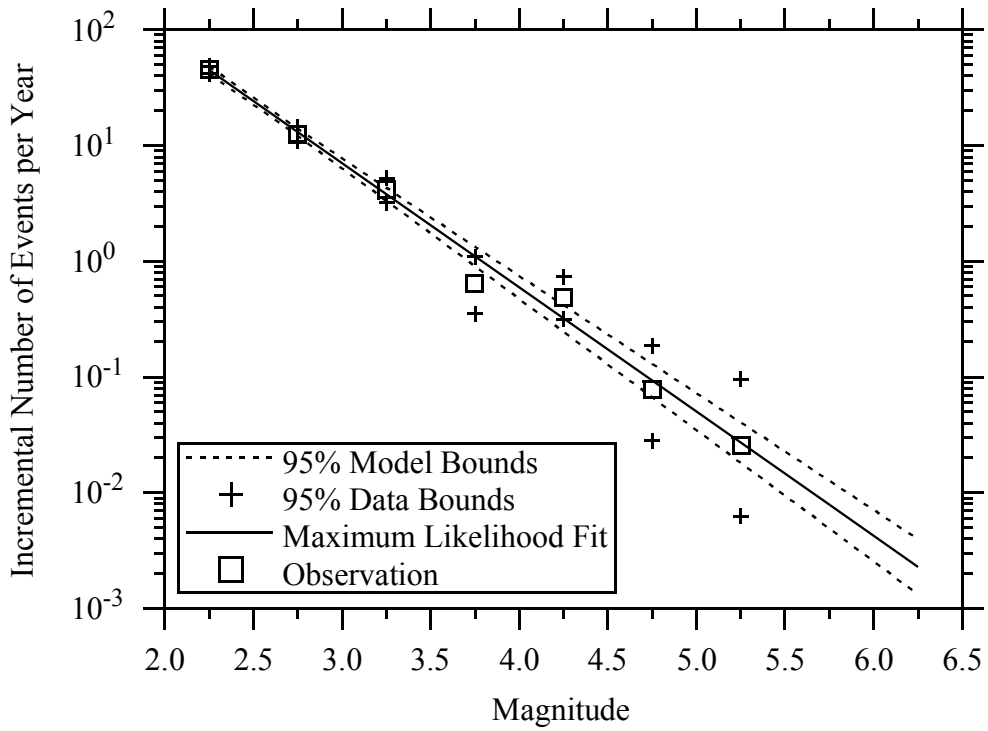

Figure 3-21a: Incremental recurrence curve for JLSN catalog.

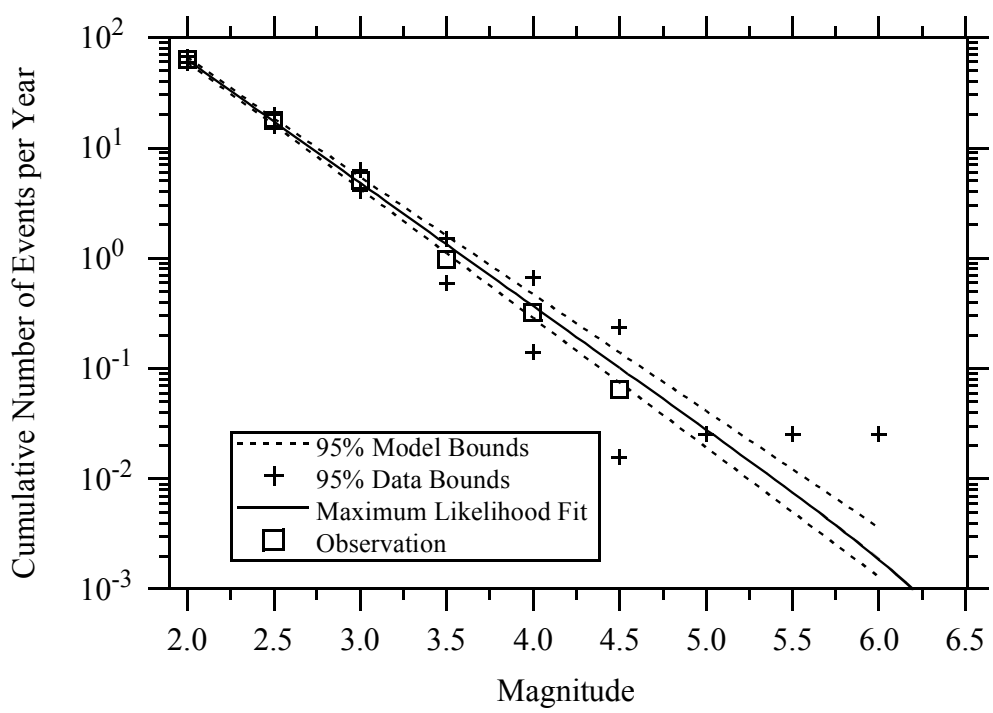

Figure 3-21b: Cumulative recurrence curve for JLSN catalog.

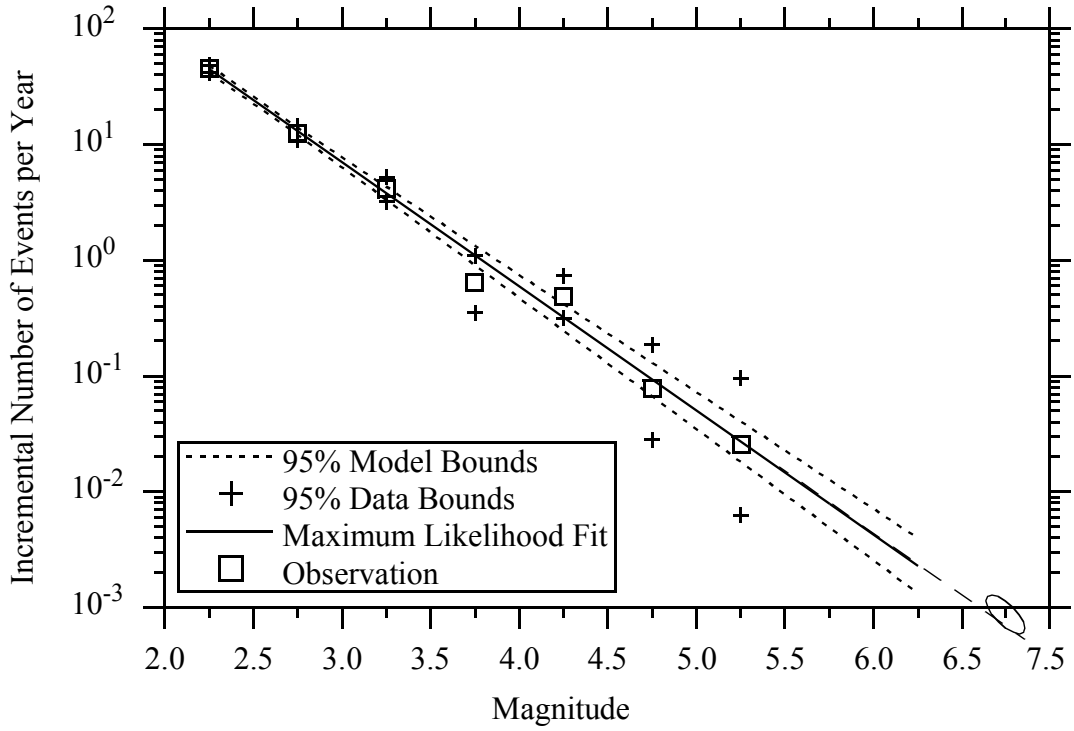

Figure 3-22a: Incremental recurrence curve for combined catalogs. The ellipse shows the approximate rate of **M** ~6.7-7.2 earthquakes on the Teton fault based on Section 2.

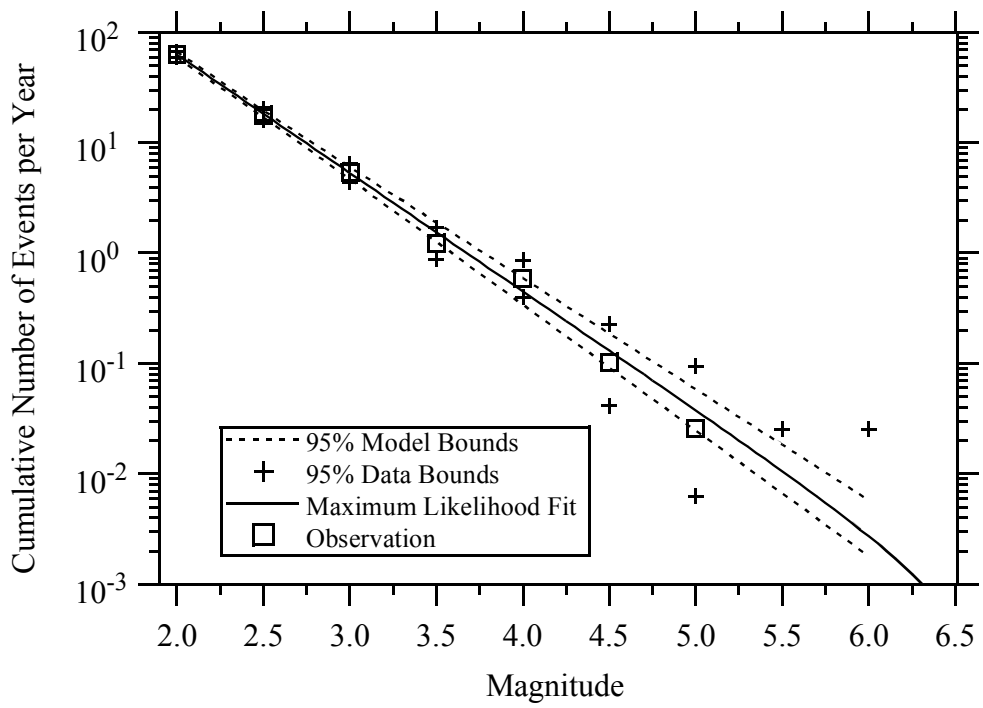

Figure 3-22b: Cumulative recurrence curve for combined catalogs.

Recurrence information from each relation, however, give a fairly consistent picture of recurrence rates of potentially hazardous randomly occurring earthquakes. The JLSN relation gives median return periods of 36 and 635 years for events greater than magnitude 5.0 and 6.0, respectively (with an upper limit of 6.5), while the combined catalog relation gives return periods of 27 and 434 years. Averaged results indicate 31 and 515 years, respectively.

Gilbert et al. (1983) obtained a recurrence relation for the Jackson Lake area which gave an (cumulative) *a* value of 0.86, and a *b* value of 1.31. This gives return periods of 38 years for magnitude ≥ 5.0 and 776 years for magnitude ≥ 6.0; similar to the results presented here. Wong et al. (2000) computed recurrence for a larger area of the ISB that extends from the southern Yellowstone area south to the Utah border. They obtained a cumulative *a* value of -1.6 (scaled to km^2/yr) and a *b* value of 0.79. When scaled to our study area, this results in 27 years for magnitude ≥ 5.0 and 170 years for magnitude ≥ 6.0. The higher activity rate for magnitude 6 events results from the inclusion of a more active section of the ISB to the south of the Jackson Lake area, and the lower *b* value. Piety et al. (1986) computed earthquake recurrence for the ISB from 41°N to 44°N, using a method similar to that used in this report. The results were very close to those obtained by Wong et al. (2000). Arabasz et al. (1980) computed recurrence for the ISB in Utah, based on the historic record through 1978. Their results indicated 30 years for magnitude ≥ 5.0 and 158 years for magnitude ≥ 6.0, similar to the Wong et al. (2000) recurrence values.

Table 3-5a: Recurrence Parameters, JLSN Catalog

Parameter (std. dev.)	Incremental	Cumulative
a (σ)	0.057 (.094)	-0.081 (.066)
b (σ)	1.115 (.038)	1.115 (.030)

Table 3-5b: Recurrence Parameters, Combined Catalogs

Parameter (std. dev.)	Incremental	Cumulative
a (σ)	-0.045 (.080)	-0.164 (.078)
b (σ)	1.072 (.032)	1.0722 (.032)

Table 3-6a: JLSN Catalog: Return Periods, Observed and Maximum Likelihood, with Upper and Lower Bounds at 95% Confidence

Magnitude Range	Return Period (yrs) (observed)	Return Period (yrs) (maximum likelihood)	Lower Bound	Upper Bound
2.0 - 2.5	0.02	0.02	0.02	0.02
2.5 - 3.0	0.08	0.08	0.07	0.09
3.0 - 3.5	0.24	0.29	0.25	0.33
3.5 - 4.0	1.56	1.04	0.82	1.31
4.0 - 4.5	3.90	3.74	2.72	5.14
4.5 - 5.0	15.6	13.5	9.03	20.2
5.0 - 5.5	not observed	48.7	29.9	79.4
5.5 - 6.0	not observed	176	99.2	312
6.0 - 6.5	not observed	635	329	1228

Table 3-6b: Combined Catalogs: Return Periods, Observed and Maximum Likelihood, with Upper and Lower Bounds at 95% Confidence

Magnitude Range	Return Period (yrs) (observed)	Return Period (yrs) (maximum likelihood)	Lower Bound	Upper Bound
2.0 - 2.5	0.02	0.02	0.02	0.02
2.5 - 3.0	0.08	0.08	0.07	0.08
3.0 - 3.5	0.24	0.26	0.23	0.30
3.5 - 4.0	1.56	0.90	0.75	1.10
4.0 - 4.5	2.04	3.11	2.39	4.04
4.5 - 5.0	13.0	10.7	7.66	14.9
5.0 - 5.5	38.8	36.7	24.5	55.0
5.5 - 6.0	not observed	126	78.5	203
6.0 - 6.5	not observed	434	251	749

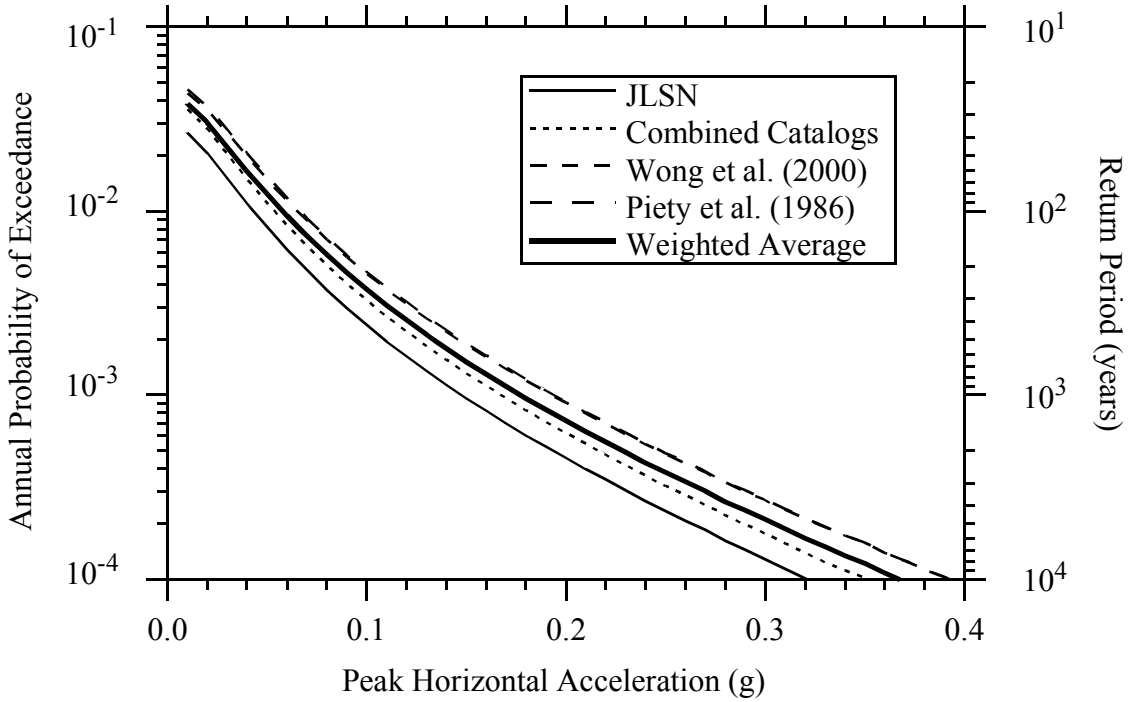

Figure 3-23a: Example soil-site hazard curves for random seismicity at Jackson Lake Dam. The three curves show differences due to different recurrence relations.

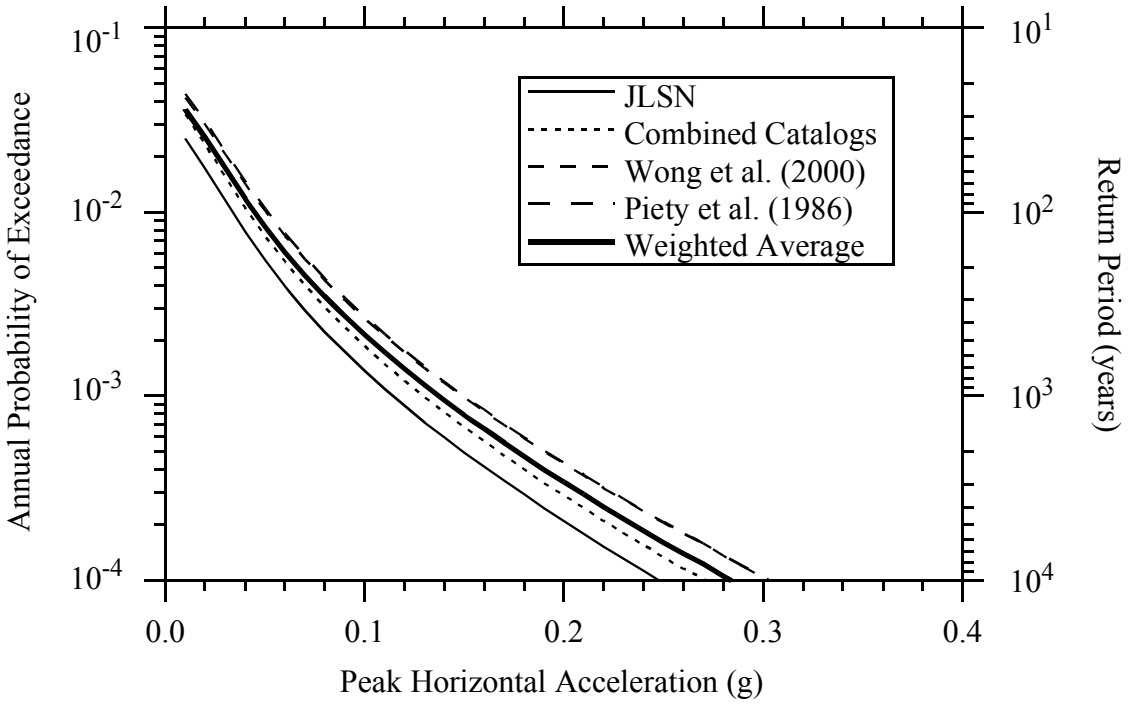

Figure 3-23b: Example rock-site hazard curves for random seismicity at Jackson Lake Dam. The three curves show differences due to different recurrence relations.

These comparisons show that for magnitude ≥ 5.0 events rates in the Jackson Lake area are about the same as in the ISB to the south, but for magnitude ≥ 6.0 events they are about 30% of the other ISB value. To show how this impacts probabilistic ground motion hazard results, Figures 3-23a and 3-23b shows example hazard curve for peak horizontal acceleration at Jackson Lake Dam for soil (Figure 3-23a) and rock (Figure 3-23b) site conditions. The four hazard curves were produced using the two recurrence curves developed in this report, the recurrence relation of Wong et al. (2000), and that of Piety et al. (1986). The soil and rock attenuation functions used are from Spudich et al. (1999). (These examples are for purposes of comparison only, and should not be used for engineering applications). Figures 3-23a and 3-23b show that the other two recurrence results gives larger ground motions; at a return period of 10,000 years in Figure 3-23a, the Wong et al. (2000) recurrence produces about 17% higher soil and rock ground motions than given by the average of the two relations developed in this report.

It is doubtful if sound physical arguments could be made as to why seismic activity is lower between 43N and 43.5N than in other parts of ISB. When observed as a whole, the ISB does form a recognizable band of seismicity, but within that band the distribution of seismicity is quite heterogeneous (e.g., Arabasz and Smith, 1980). The lower rate for M ≥ 6 events is in part due to the higher b-value computed here, compared to the other ISB recurrence calculations. This value appears to be real, and not the result of incomplete reporting of the smaller magnitudes (Figure 22a,b). On the other hand, there are uncertainties associated with the recurrence figures presented in this report. For example, the coda magnitude has not been calibrated to a "true" local or moment magnitude scale, and the pre-network catalog contains significant errors in earthquake locations, and several different magnitude scales. For the hazard curves shown in Figures 23a and b, we therefore weight the Wong et al. (2000) and Piety et al. (1986) relations equally with those computed for this report. The weighted hazard curves are shown in these figures. At a return period of 10,000 years, this results in 8% higher ground motions for the rock relations, and 10% higher for the soil relations, over the averaged recurrence relations for the JLSN area presented in this report.

3.7 Summary and Conclusions

The Jackson Lake Seismographic Network recorded 1150 well-located earthquakes between August, 1986, and May, 2002, that provided the basis for inverting for 3D P-wave crustal velocity structure near Jackson Lake Dam. The 3D P-wave velocity-hypocenter-station-correction inversion provided information necessary to locate earthquake for earthquake recurrence investigations, to constrain focal mechanisms for seismotectonic investigations, and to determine the large-scale 3D crustal P-wave velocity structure required to estimate seismic loads at Jackson Lake Dam. The 3D P-wave velocity model and corresponding station corrections obtained from the hypocenter-velocity-station correction inversion provide a much better fit to the data than that obtained with the 1D original velocity model. For all relocated events, the mean absolute P-wave arrival time residual decreased by 32%. The 3D velocity inversion revealed a low-velocity region east of the Teton fault that includes Jackson Lake Dam. The low-velocity region extends to depths of ~4 km below the dam, has the lowest velocities in the 3D P-wave velocity model (3.4 km/s), and has the largest spatial extent of any of the low-velocity regions in the 3D velocity model (Figure 3-4). While the shallowest velocities may be vertically smeared due to insufficient ray coverage, the lower boundaries of the velocity anomalies are fairly well-constrained by the data. For the Jackson Lake Dam site-response stations JLD2 to JLD7, which are located on soil sites within the 3D velocity grid, the positive station corrections indicate that the shallow local velocities are lower than those given by the 3D velocity model. The velocities in the 3D model decrease from station JLD2 on the south to station JLD7 near the northern end of Jackson Lake Dam. These results are consistent with geophysical measurements discussed in Section 5, that show extremely low-velocity materials beneath the dam that increase in thickness toward the north.

Relatively few earthquakes are located near the possible downdip projections of the Teton fault; many more earthquakes are located in the footwall side of the Teton fault. The same seismicity behavior is associated with other normal faults in the ISB, particularly the Wasatch fault system in Utah (Smith and Arabasz, 1991), the only other predominantly normal-faulting region in the ISB with sufficient seismographic station coverage to locate earthquakes with uncertainties < 5 km. Most earthquakes are < 14 km deep, but seismicity does extend to a maximum depth of ~17 km, providing a basis to assign maximum faulting depths for ground motion modeling in Section 6.

Reasonably well-constrained focal mechanisms were obtained for 773 earthquakes located by the JLSN using P-wave first motions and SV/P amplitude ratios from vertical component seismograms. The strike-slip, normal-slip, and oblique normal-slip focal mechanisms represent > 92% of the focal mechanisms and occur throughout the study area (Figures 3-10 to 3-13). *T*-axes are nearly uniformly orientated almost east-west from north grid coordinate -35 km to 40 km. Both the northeast deflection of the *T*-axes at the northern limits of the grid and the southeast deflection of the *T*-axes at the southern limits of the grid, roughly maintain the *T*-axes normal to the overall parabolic distribution of seismicity east of the Snake River Plain described in Anders et al. (1989). The reverse and oblique reverse solutions are mostly confined to the region south of 15 km north grid coordinates, and may reflect stress heterogeneity in the stepover region between the Teton fault and normal faults south of the Teton fault (e.g., Grand Valley fault and Star Valley fault). Consistent with field observations discussed in Section 2, the *T*-axes and nodal planes indicate primarily normal-slip on the central and northern sections of the Teton fault, and oblique left-lateral normal slip on the southern section of the Teton fault. The focal mechanism data, particularly the *T*-axes orientations support using a dominantly normal-slip rake to simulate ground motions associated with rupture of the central and northern segments of the Teton fault.

The relative paucity of earthquakes that could be associated with the Teton fault at depth do not provide strong constraints on fault dip. Focal mechanism solutions of earthquakes located east of the surface trace of the Teton fault dips have east-dipping nodal planes that dip from 25° to 60°. There are too few earthquakes located east of the Teton fault, with far too limited spatial coverage to provide a strong constraint on fault dip, although the spatial distribution of earthquakes is generally consistent with dips of < 50°. Waveform modeling of more of the earthquakes located east of the Teton fault may provide better constraints on Teton fault dip at depth than are currently available.

Earthquake recurrence parameters were developed for the Jackson Lake region. Two data sets were used; the Jackson Lake Seismic Network (JLSN) catalog (June, 1986 - December, 2001) with a lower magnitude cutoff of 2.0 to ensure catalog completeness, and the historic record for this region prior to the network's installation in 1986 (1963 - May, 1986). Two sets of recurrence parameters were developed, one with just the JLSN data and one with the combined JLSN -

pre-1986 information. Because no earthquakes in either catalog have been positively associated with a known fault, this seismicity represents "random" or "background" earthquakes, and any further analysis using the earthquake recurrence parameters developed here pertain only to such seismic activity. The earthquake catalogs were declustered to produce a total of 984 independent events in the JLSN catalog and 18 independent events in the pre-JLSN catalog.

Each earthquake dataset has its advantages: the JLSN results are from high quality data that are self-consistent in location accuracy and magnitude computation, but cover a relatively short time span. The combined catalog results offer a longer time span (38 years vs. 15 years) and include more moderate (magnitude 4 and 5) events, but magnitude determinations for pre-JLSN events were computed using at least four different magnitude formulas, are of indeterminate quality, and their compatibility with JLSN magnitude values is unknown. Further use of these relations, for example in a probabilistic ground motion analysis, should incorporate both results. Recurrence information from each relation, however, give a fairly consistent picture of recurrence rates of potentially hazardous randomly occurring earthquakes. The JLSN relation gives median return periods of 36 and 635 years for events greater than magnitude 5.0 and 6.0, respectively (with an upper limit of 6.5), while the combined catalog relation gives return periods of 27 and 434 years. Averaged results indicate 31 and 515 years, respectively.

Gilbert et al. (1983) obtained a recurrence relation for the Jackson Lake area which gives return periods of 38 years for magnitude ≥ 5.0 and 776 years for magnitude ≥ 6.0; similar to the results presented here. Wong et al. (2000) computed recurrence for a larger area of the ISB that extends from the southern Yellowstone area south to the Utah border. When scaled to our study area, this results in 27 years for magnitude ≥ 5.0 and 170 years for magnitude ≥ 6.0. The higher activity rate for magnitude 6 events in Wong et al. (2000) results from the inclusion of a more active section of the ISB to the south of the Jackson Lake area, and their lower *b* value. Piety et al. (1986) computed earthquake recurrence for the ISB from 41°N to 44°N, using a method similar to that used in this report. The results were very close to those obtained by Wong et al. (2000). Arabasz et al. (1980) computed recurrence for the ISB in Utah, based on the historic record through 1978. Their results indicated 30 years for magnitude ≥ 5.0 and 158 years for magnitude ≥ 6.0, similar to the Wong et al. (2000) recurrence values.

Hazard curves for peak horizontal acceleration were computed, using a single attenuation function and the recurrence relations developed in this report, and those of Wong et al. (2000) and Piety et al. (1986). A weighted curve was calculated, with the results of the two recurrence relations developed here and those of the other ISB relations weighted equally. The computed ground motions of the averaged relations, at a 10,000 year return period, are 10% or less higher than those computed from the relations developed in this report.

This section has focused on analyses related to seismicity. The 3D P-wave velocity model developed in this section serves as the basis for the more detailed crustal velocity structure modeling necessary to estimate ground motions at Jackson Lake Dam, as presented in the next section.

4.0 HANGING WALL CRUSTAL VELOCITY STRUCTURE

The 3D velocity-hypocenter inversion (see Section 3) used 1150 earthquakes recorded by the Jackson Lake Seismic Network to delineate a 3-to-4-km-deep low-velocity "basin" in the hanging wall of the east-dipping Teton fault, but could not resolve details of the velocity structure portion of the hanging wall containing Jackson Lake Dam. Previous studies (Behrendt et al., 1968, Tibbetts et al., 1969; Byrd et al., 1994) used seismic refraction and gravity data to delineate a geophysical "basin" consisting of low-velocity (surface P-wave velocities of ~2.2 km/s), low-density (densities of 2.3 g/cm^3) Cenozoic and Mesozoic rocks. Low velocities in the hanging wall begin 1-2 km east of the surface scarp of the Teton fault, extend east of Jackson Lake Dam, and extend east of the likely eastern limit of the Teton fault at depth. The geophysical measurements of P- and S-wave velocities in the vicinity of the dam by Sirles (1986) provide the only direct measurements of S-wave velocities within the low-velocity portion of the hanging wall.

In this section, a low-velocity basin (LVB) in the hanging wall is defined in terms of its internal velocity properties, particularly the large impedance contrasts between the LVB and the surrounding high-velocity basement rocks, because these are the crustal properties that have the strongest influence on ground motion responses at the dam. The LVB extends beyond the geographic confines of the hanging wall located directly above the fault surface (compare Figure 4-1 to Plate 1), and encompasses a wide variety of stratigraphic units that happen to have similar velocities: All the sedimentary units in the LVB have velocities that are much lower than surrounding basement rocks. Although the LVB consists of Cenozoic and Mesozoic sedimentary stratigraphic units, designation of the LVB shown as in Figure 4-1 reflects long-standing geophysical practice (e.g., Boore, 1970, Boore et al., 1971), which focuses on defining the velocity (not stratigraphic) properties of the crust for the purposes of ground motion modeling. No attempt is made here to associate specific stratigraphic units with velocity features in the LVB, since this is not necessary for the purposes of ground motion estimation at the dam.

Rupture of the northern segment of the Teton fault for shallow dips of 35° and 45° would involves fault rupture directly beneath the dam (Figure 4-1). Thus, it is important to determine how strongly rupture directivity may influence peak ground motions and ground motion variability at

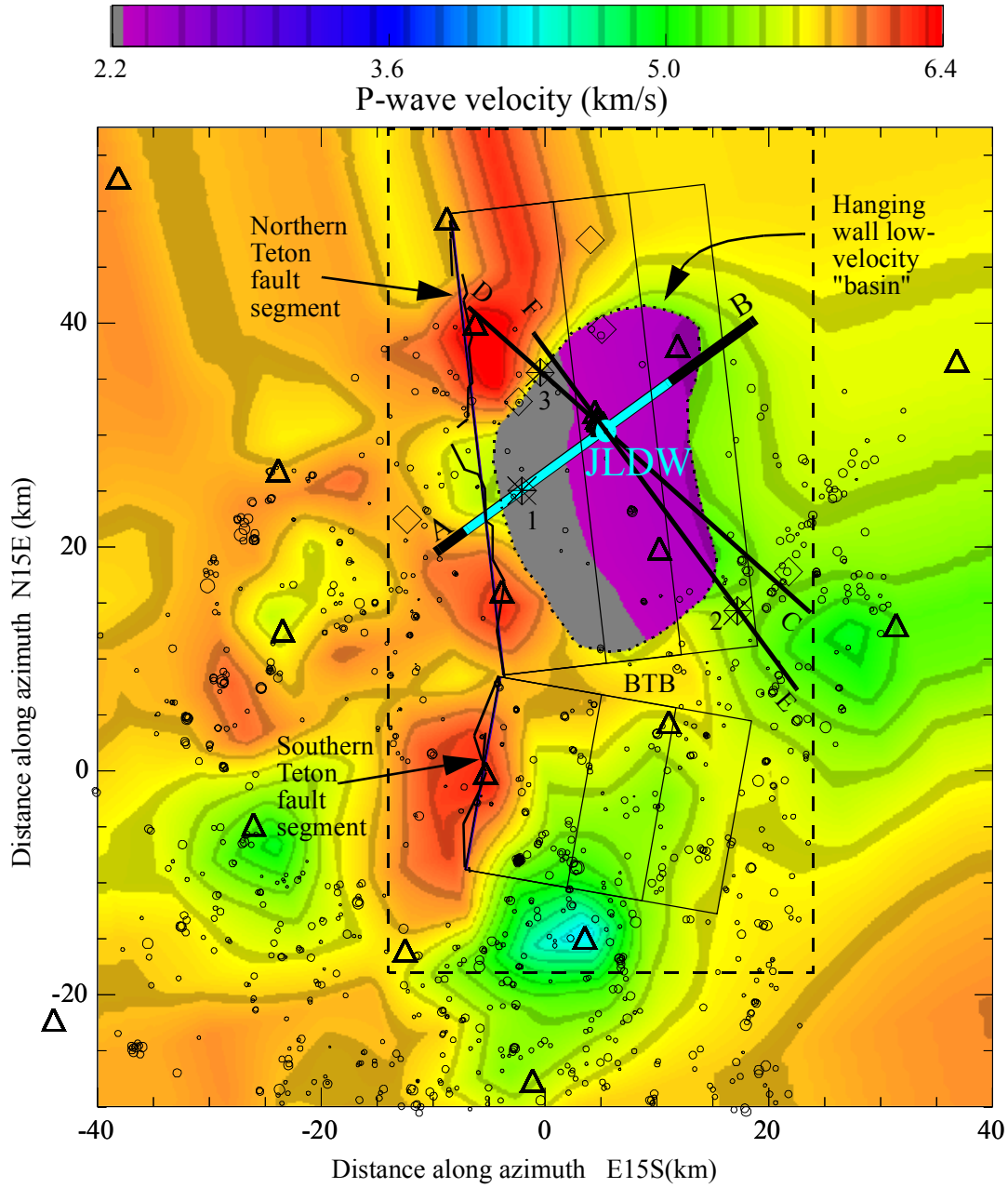

Figure 4-1: Plan view of the P-wave 3D velocity model with the embedded hanging wall LVB at 2 km elevation. The LVB is "closed"; it's surrounded by high-velocities everywhere (in depth and plan views). Black circles are earthquake epicenters, triangles are JLSN seismographic stations, numbered stars show epicenters of the three earthquakes used for 2D finite-difference waveform modeling, and diamonds are empirical Green's function (EGF) epicenters used in Section 6. The plan projection of the idealized geometries of the two primary (northern and southern) segments of the Teton fault for dips of 35°, 45°, and 60° are the solid rectangles (detailed surface scarps to the left are the short, irregular line segments). The 2D S-wave velocity cross section in Figure 4-4 is the thick black line labeled A -B (Figure 4-5 is the cyan portion of the line). Profile C-D corresponds to Figure 4-8 and profile E-F corresponds to Figure 4-11. Blue circle is the JLDW rock site station. The dashed rectangle shows the limits of the 3D finite-difference grid. Blacktail Butte is denoted by BTB.

the dam for these near-source earthquake scenarios. Impacts of 3D crustal velocity structure on ground motion amplitudes and durations are substantial (Frankel, 1993). Much of the modeling effort is devoted to accounting for the influences of 3D velocity heterogeneity, particularly hanging wall LVB velocity structure, on ground motion amplitudes and durations. It is necessary to constrain S-wave velocities within the hanging wall LVB to estimate ground motions at the dam. A mini-array of seven three-component digital broadband stations with a long-axis aperture of 1.6 km oriented along the axis of the dam was operated from October 1995 to May 2001 to record site responses within the Jackson Lake LVB, particularly on or near the dam. One site (station JLDW) was located near Signal Mountain, about 0.2 km south of the dam, on ~1 km/s S-wave-velocity over-compacted glacial till (Sirles, 1986) to serve as a "rock" reference site. However, because JLDW was located within the hanging wall LVB, it recorded secondary S-wave and surface wave arrivals originating at the LVB margins. Waveform modeling of direct S-waves and later secondary arrivals from microearthquake seismograms from the seven-station mini-array near the dam was used to constrain LVB S-wave velocities and LVB margin geometry. This section presents waveform and traveltime modeling results used to constrain P- and S-wave velocities, and attenuation (Qp and Qs) characteristics within the hanging wall LVB to support rock and soil ground motion simulations presented in Section 6 and soil and site response investigations in Section 5.

4.1 3D Velocity Model Development Using Seismic Refraction Data.

LVB velocity structure was derived from the 3D velocity-velocity model (Section 3), reinterpretation of existing seismic refraction data, and 2D finite-difference waveform modeling of three microearthquakes (MEQ) located near the perimeter of the LVB, and recorded on broadband stations near the middle of the LVB. Four seismic refraction lines were shot in 1964 and 1965 by Behrendt et al. (1968) to study P-wave velocity structure in the LVB east of the Teton fault (e.g., Jackson Hole). Plate 1 from Behrendt et al. (1968) shows the shot and recording geometries of the seismic refraction lines. The recording geometries for lines 1-3 consisted of six geophone arrays with 0.5-km spacings between geophones (line 4 used 0.2-km spacings between geophones) and 1-3 km gaps in geophone coverage along the lines (Plate 1 and Figure 4-2).

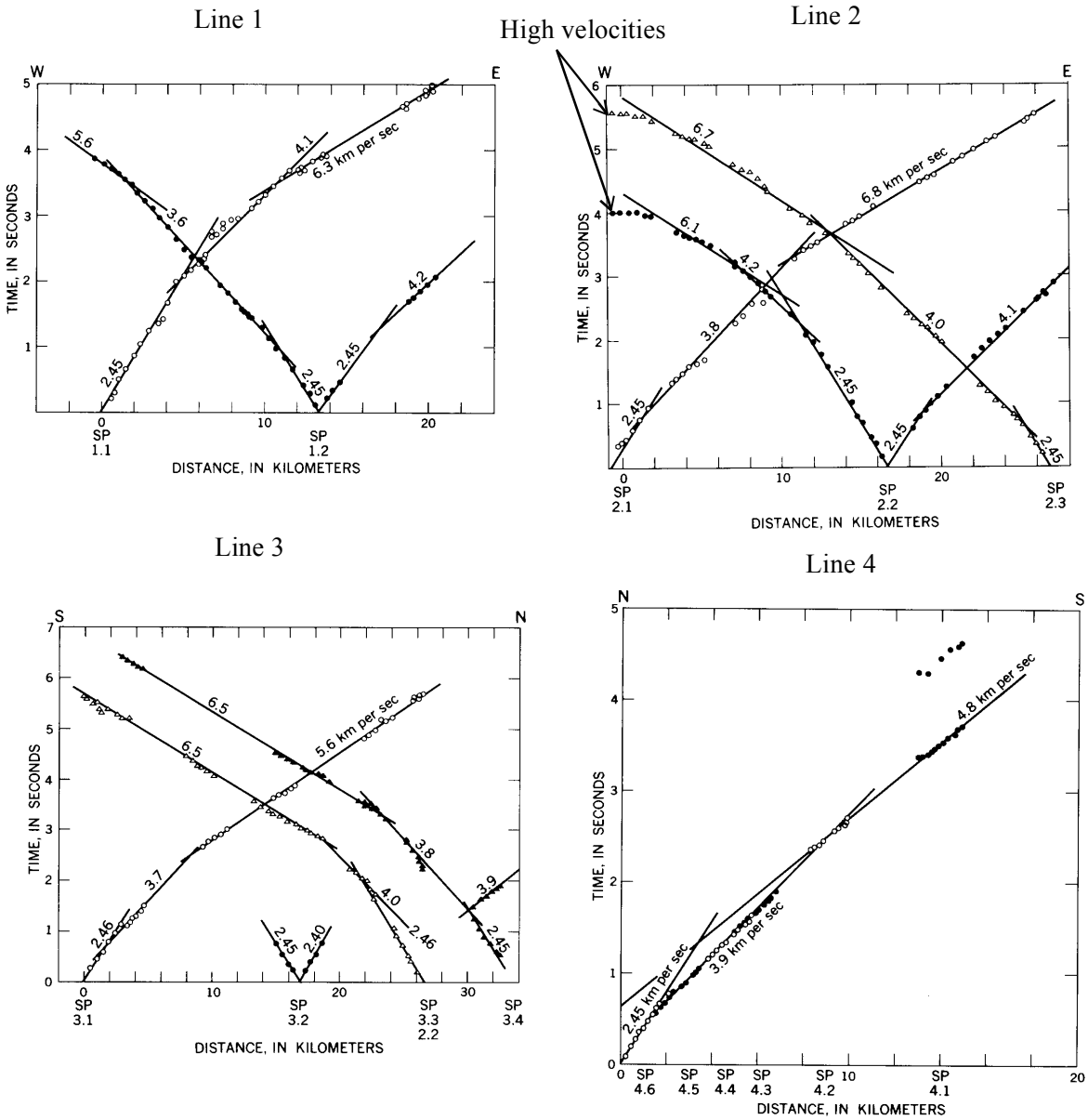

Figure 4-2: P-wave travel-time plots for lines 1-4 from Behrendt et al. (1968). The circles and triangles are the traveltime observations and the straight line segments are the constant-velocity-layer velocity interpretations from Behrendt et al. (1968) labeled in km/s; SP are shotpoint numbers from Plate 1. Note that most traveltime branches have 1-3 km traveltime gaps that make it impossible to distinguish between gradient and constant velocity layer interpretations of the traveltimes < 3 s (which constrain velocity structure within the LVB). The western portion of line 2, located ~1 km north of Jenny Lake, shows very-high apparent velocities for shotpoints 2.2 and 2.3 as show by the arrows.

There are three published traveltime interpretations of line 2 (Behrendt et al., 1968; Tibbetts et al., 1969; Byrd et al., 1994); none of these published interpretations included amplitude modeling of refraction data waveforms. Inevitably there are an infinite number of velocity models that can satisfy the traveltime data, but a finite class of velocity models that can satisfy band-limited amplitude data. This study attempts to satisfy the traveltime constraints represented by the seismic refraction data, but focuses on developing velocity models that reproduce the dominant < 4 Hz phases of three-component seismograms recorded in the interior of the LVB; producing a 3D velocity model that can reproduce ground motion observations most relevant to strong motions within the LVB is the focus of this investigation. In this subsection the seismic refraction interpretations are presented and discussed in relation to the 3D velocity model developed using LVB-edge MEQ seismograms in Section 4.2.

It is useful for illustration to start with the results of Behrendt et al. (1968). Behrendt et al. (1968) and Tibbetts et al. (1969) used forward modeling and delay-time analyses of line 2 travel times, and gravity modeling, to infer velocities and thicknesses of constant-velocity layers (Figure 4-3). Lines 1-3 have very crooked and discontinuous recording geometries (Plate 1). Consequently neither of the dip lines (lines 1 and 2) is normal to the structural strike and strike 3 is not parallel to structural strike (Plate 1). However, line 2 in particular, provides valuable constraints on the characteristics of the western boundary of the LVB. The very high apparent velocities on the western travel-time branch of shotpoint 2.2 (noted on Figure 4-2) unequivocally establishes that the LVB begins 1-2 km east of the surface scarp of the Teton fault, as discussed in detail below, and that there is a strong velocity contrast between LVB material and surrounding basement rocks. The reversed traveltime curves provided by shotpoints 2.1 and 2.2 place strong constraints on the maximum depth of the LVB. The initial slopes of the travel-times curves establish that the near-surface (depth) till P-wave velocities of 2.2-to-2.45 km/s measured by Sirles (1986) south of Jackson Lake Dam, are representative of shallow P-wave velocities throughout the LVB. This suggests that the near-surface till S-wave velocities of ~1.0 km/s measured by Sirles (1986) are also likely to be representative of near-surface till S-wave velocities throughout the LVB. Finally, it is clear from the seismic refraction data that P-wave velocities increase with depth, although the refraction lines are too crooked and discontinuous to make an unequivocally distinction between

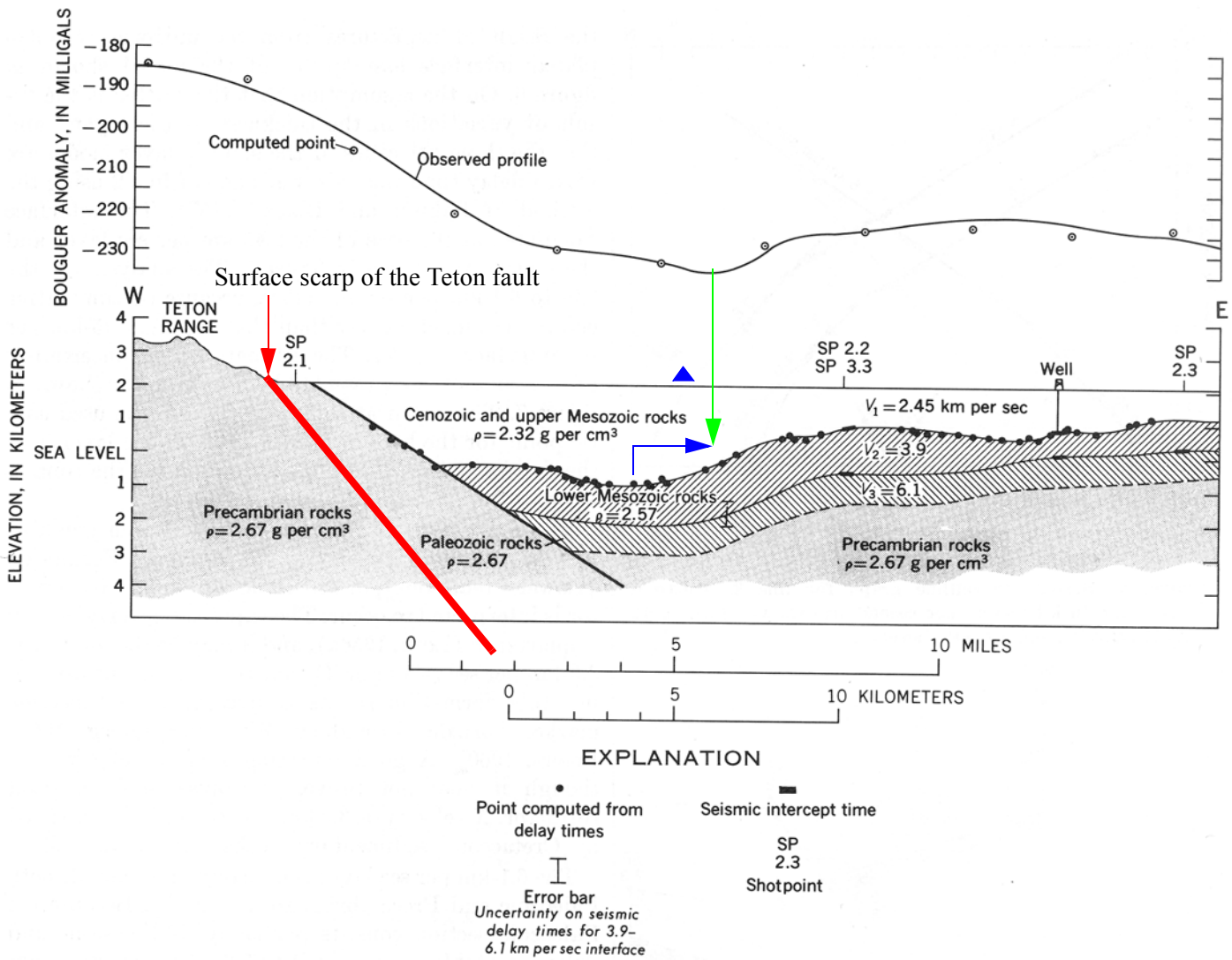

Figure 4-3: Line 2 gravity and seismic refraction interpretation reproduced from Behrendt et al. (1968).The red arrow and line show the approximate position of the surface scarp and depth (for an arbitrarily selected 50° dip) of the Teton fault (from Section 2), and the blue triangle shows the projected position of Jackson Lake Dam. The vertical green arrow indicates the minimum observed gravity location and the blue arrow points from where the maximum LVB depth is in the model to where the maximum LVB depth is indicated by the gravity data.

constant velocity and vertical-velocity-gradient interpretations of the traveltime data. However, as shown in the next section, constant-velocity layers do not reproduce strong secondary arrivals observed on MEQ seismograms in the interior of the LVB.

Behrendt et al. (1968) assume the scatter in travel-times about fitted apparent velocities in Figure 4-2 is the result of variations in the thicknesses of the assumed constant velocity layers and use the delay time analysis method of Pakiser and Black (1957) to produce the detailed layer depth variation estimates of Figure 4-3. However, the gravity data in Figure 4-4 and Plate 1 indicate that the deepest portion of the LVB is likely located near or slightly east of Jackson Lake Dam, in contrast to the inferred LVB geometry inferred by Behrendt et al. (1968) in Figure 4-3. In contrast to Behrendt et al. (1968) and Tibbetts et al. (1969), Byrd et al. (1994) allowed velocity gradients in their ray-tracing velocity inversions of the traveltimes from line 2. They found evidence for vertical and horizontal velocity gradients. Unfortunately, Byrd et al. (1994) do not report the vertical or horizontal velocity gradients for their models, although from circular ray arcs in their Figure 9, it is clear that they found significantly non-zero vertical velocity gradients.

4.2 3D Velocity Model Development Using LVB Seismograms.

Three microearthquakes located near the perimeter of the LVB (Figure 4-1) were recorded by the site-response stations in the vicinity of Jackson Lake Dam. Signal-to-noise levels in the seismograms were adequate to use the seismograms in trial-and-error waveform modeling to constrain P- and S-wave velocity structure within the LVB. Earthquakes located close to the perimeter of the LVB were selected because they produced strong secondary arrivals associated with secondary S-waves and surface waves generated at the large-velocity contrast between the low-velocity sediments and surrounding basement rocks. The 2D version of the elastic finite-difference program E3D (Larsen and Grieger, 1998), which includes viscoelastic capabilities implemented using the approach of Robertsson et al. (1994), was used to calculate the seismic response of a double-couple point source for 2D velocity slices intersecting the earthquakes and station JLDW. The JLSN provided the earthquake location and focal mechanism constraints necessary to minimize trade-offs between velocity structure, earthquake locations, and focal mechanisms. Grid spacings of 0.032 km were used to allow modeling of seismograms to a maximum frequency of 4 Hz given minimum S-wave velocities of ~1 km/s (> 6 points per

wavelength sampling at 4 Hz to minimize grid dispersion in a fourth-order finite-difference code, e.g., Moczo et al., 2000). The observed seismograms were rotated to provide a radial horizontal component seismogram to compare with synthetic radial seismograms from the 2D P-SV finite-difference modeling. The observed seismograms were low-pass-filtered at the lowest possible frequencies as allowed by signal-to-noise levels, to focus on fitting seismogram frequencies most likely to be strongly influenced by 3D deterministic velocity structure; as frequencies increase above 5 Hz, seismogram coherence is expected to decrease substantially because velocity heterogeneity in the crust (Frankel and Clayton, 1986) strongly perturbs body-wave phase as the mean free path increases (Spetzler and Snieder, 2001). The 2D synthetic seismograms are corrected using the approach of Vidale and Helmberger (1987) to approximate a point-source and corresponding 3D geometric spreading.

The velocity inversion results of Byrd et al. (1994) suggested that linear-velocity-gradient models for the LVB were most consistent with the seismic refraction data. Consequently, the trial-and-error forward modeling effort focused on developing linear-velocity-gradient velocity models for the LVB embedded in the 3D velocity model obtained from a progressive velocity-hypocenter inversion (Section 3, Figure 4-1). Constant-velocity-layer models similar to Behrendt et al. (1968) were also evaluated. One of the modeling requirements was to develop relationships to predict S-wave velocities, densities, Qp, and Qs, based on P-wave velocities. The model relationships used with the P-wave model in Figure 4-1 are shown in Table 4-1.

4.2.1 Synthetic Seismogram Modeling of the 19 April 2001 M 1.4 Earthquake. This earthquake occurred beneath the western margin of the LVB about 3.2 km below the surface (event 1 on Figure 4-1). First-motions from the JLSN indicate a normal-faulting focal mechanism with dips of 40-50 degrees for the east-dipping nodal plane. As indicated in Figure 4-4, depth uncertainties of ~1 km allow for Teton fault dips of 35-60 degrees, assuming the earthquake is located on the Teton fault. A small horizontal velocity gradient that makes the western-most LVB velocities 10% slower than the eastern-most LVB velocities was imposed to produce the minimum velocities along the western margin of the LVB in the 3D velocity model (Figures 4-1 and 4-4). The geometry of the LVB is similar to Behrendt et al.'s (1968) in Figure 4-3, but the deepest portion of the LVB is allowed to extend several km further east beneath the dam,

Table 4-1: Best-Estimates of Relationships between P-wave Velocity and Vs, ρ, Qp, and Qs.

Let Vp = P-wave velocity (km/s),
Vp_{max} = Maximum P-wave velocity in the 3D model (km/s),
Vp_{min} = Minimum P-wave velocity in the 3D model (km/s),
$Vp_{range} = Vp_{max} - Vp_{min}$ (km/s),
Vs = S-wave velocity (km/s),
Vp/Vs_{max} = Maximum Vp/Vs ratio in the 3D model = 2.2,
Vp/Vs_{min} = Minimum Vp/Vs ratio in the 3D model = 1.73,
$Vp/Vs_{range} = Vp/Vs_{max} - Vp/Vs_{min} = 0.47$,
ρ = density (g/cm^3),
Qp = P-wave attenuation quality factor,
Qs = S-wave attenuation quality factor,

Then:

$$Vs = Vp/([(Vp_{max} - Vp)/Vp_{range}]^3 * Vp/Vs_{range} + Vp/Vs_{min}),$$

$$\rho = (Vp_{max} - Vp)/Vp_{range} * -0.45 + 2.75,$$

$$Qp = (Vp_{max} - Vp)/Vp_{range} * 350 + 50,$$

$$Qs = (Vs_{max} - Vs)/Vs_{range} * 180 + 20.$$

These relationships were used to generate Vs, ρ, Qp, and Qs for the "best-fitting" 2D finite-difference grids in this section and the 3D finite-difference grids used to calculate ground motions in Section 6.

consistent with the gravity observations in Figure 4-3 and Plate 1. The 2D synthetic seismograms reproduces the relative amplitudes and travel-times of the direct P- and S-waves and the LVB-edge S-wave (Figure 4-5). Several Vs, Qp, and Qs relationships with P-wave velocity were tested before arriving at the relationships listed in Table 4-1. The synthetic seismogram also does a reasonable job of reproducing the total duration of ground motion; a relatively low Qs of 20 is used near the surface to reproduce observed durations and amplitude decays observed at JLDW.

A synthetic radial-component record section is shown in Figure 4-6 to illustrate the characteristics of the LVB-edge S-wave observed at station JLDW. The largest amplitudes are found in the western portion of the LVB closest to the hypocenter. However, the LVB-edge S-wave attains a peak velocity at the dam of 33% of the maximum velocity observed on the surface. These large LVB-edge S-wave amplitudes occurs at the dam because the dam is located ~10 km from the western LVB margin, in the distance range where a caustic develops due to the critical refraction/reflection of the LVB-edge S-wave along the east-dipping margin of the western LVB. Using JLDW as the source position and invoking reciprocity, the ray paths in Figure 4-7b illustrate the consequences of the geometry of the western margin of the LVB on ground motion amplification at the dam. Refraction/reflection along the western LVB boundary produces focusing (e.g., near zero wavefront curvature) that counteracts geometric spreading sufficiently to make the LVB-edge S-wave amplitude larger than the direct S-wave, even though the LVB-edge wave has propagated along a path distance that is nearly twice the propagation distance of the direct S wave. Figure 4-7a shows that the LVB captures radiated seismic energy over a very wide cross section. Thus, the LVB is a very efficient seismic collector, and sites within the LVB are likely experience substantial multipathing for sources located beneath the LVB (e.g., the Teton fault).

4.2.2 Synthetic Seismogram Modeling of the 29 Sep. 1996 M 1.6 Earthquake. This earthquake is located about 7 km northwest of station JLDW (the epicenter is event 3 in Figure 4-1) at a depth of 5-6 km (Figure 4-8). First-motions from the JLSN indicate a normal-faulting focal mechanism with dips of 47 degrees for the east-dipping nodal plane. Depth uncertainties of ~1 km allow for Teton fault dips of 40-50 degrees, assuming the earthquake is located on the Teton fault. The small magnitude and substantial long-period site noise required modeling to a maximum

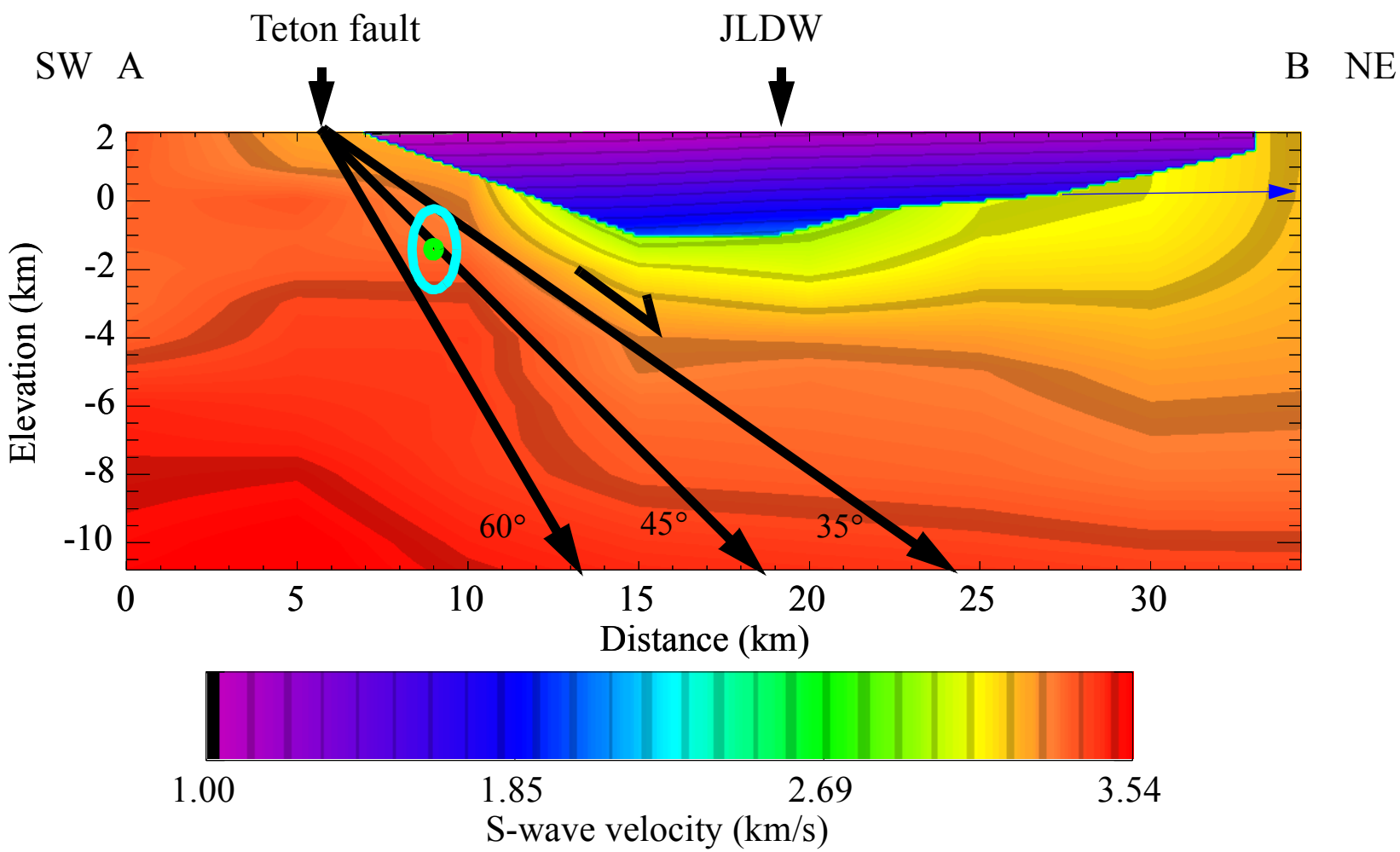

ure 4-4: *S*-wave velocity depth cross section A-B (see Figure 4-1). The model was derived from trial-and-error *P-SV* 2D finite-difference waveform modeling of the observed rock-site radial seismogram from the 19 April 2001 **M** 1.4 earthquake (Figure 4-5). The hypocenter is the green circle and the cyan ellipse shows the hypocenter location uncertainty. The range of allowable dips for the Teton fault are indicated by the black arrows labeled 35° and 60°; a black arrow labeled 45° is also provided. Note that the LVB is located ~1-2 km east of the surface scarp of the Teton fault. Seismic refraction data and gravity data clearly establish that a shallow a high-velocity (*P*-wave velocities > 6 km/s) and high-density body (> 2.6 g/cm^3) is located between the Teton fault scarp and the LVB (Behrendt et al., 1968, Tibbetts et al., 1969; and Byrd et al., 1994). The blue arrow indicates that low velocities probably continue to the northeast with thicknesses of ~2 km.

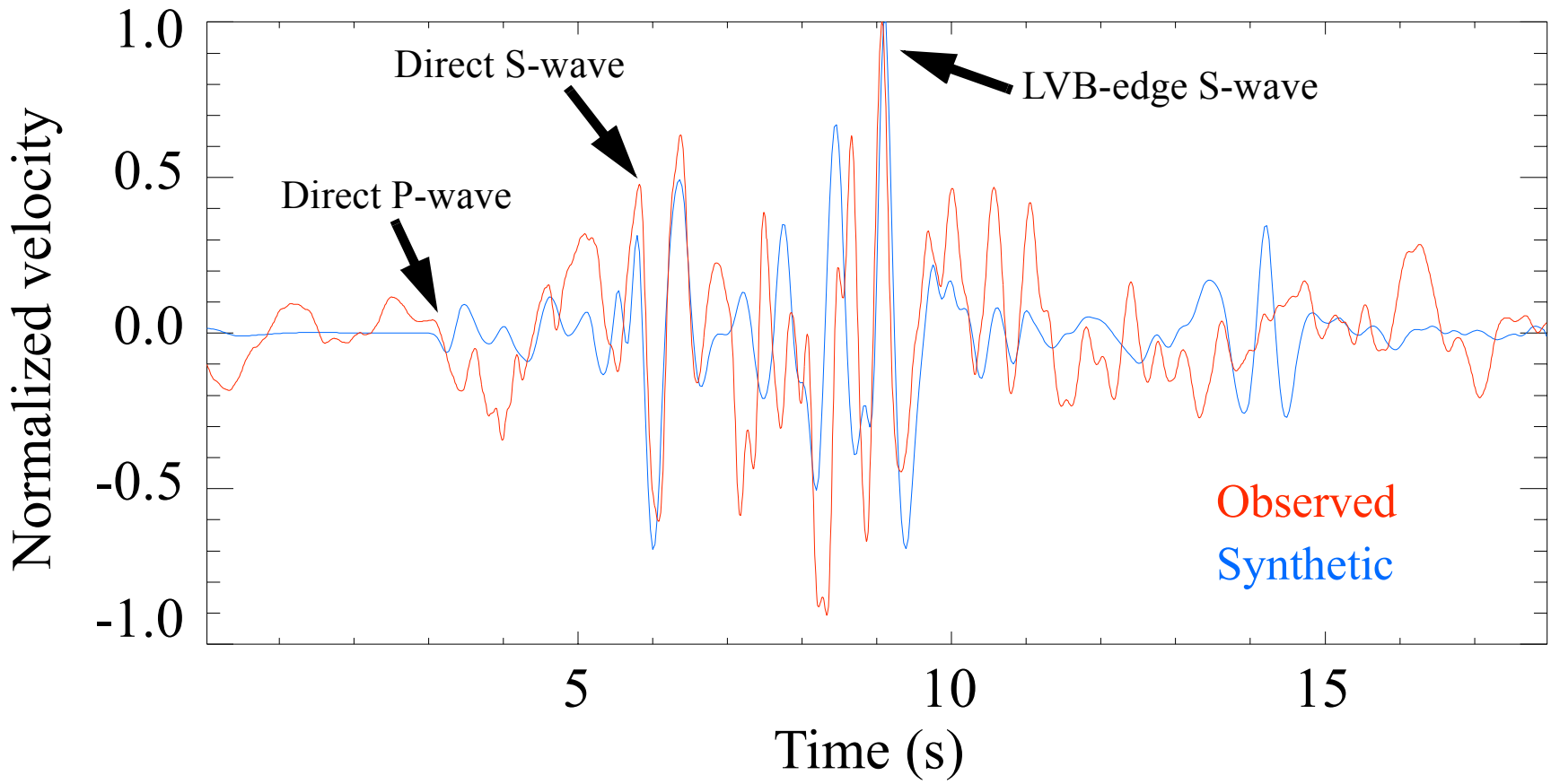

Figure 4-5: Radial-component JLDW seismogram from the **M** 1.4 normal-faulting earthquake on 19 April 2001. Seismograms are band-pass filtered from 0.5 Hz to 2 Hz; observed in red and synthetic in blue. This earthquake was located at a depth of 3.2 km below the LVB margin (epicenter is event 1 on Figure 4-1). The LVB-edge arrival from the western margin of the LVB is a critically reflected/refracted *S*-wave as indicated in the synthetic radial component record section in Figure 4-6 and by the rays in Figure 4-7. This secondary *S*-wave arrival is the largest amplitude arrival at this site and has an amplitude 33% of the largest S-wave amplitude recorded within the LVB, even though the JLDW rock site is located ~10 km from the western-edge of the LVB.

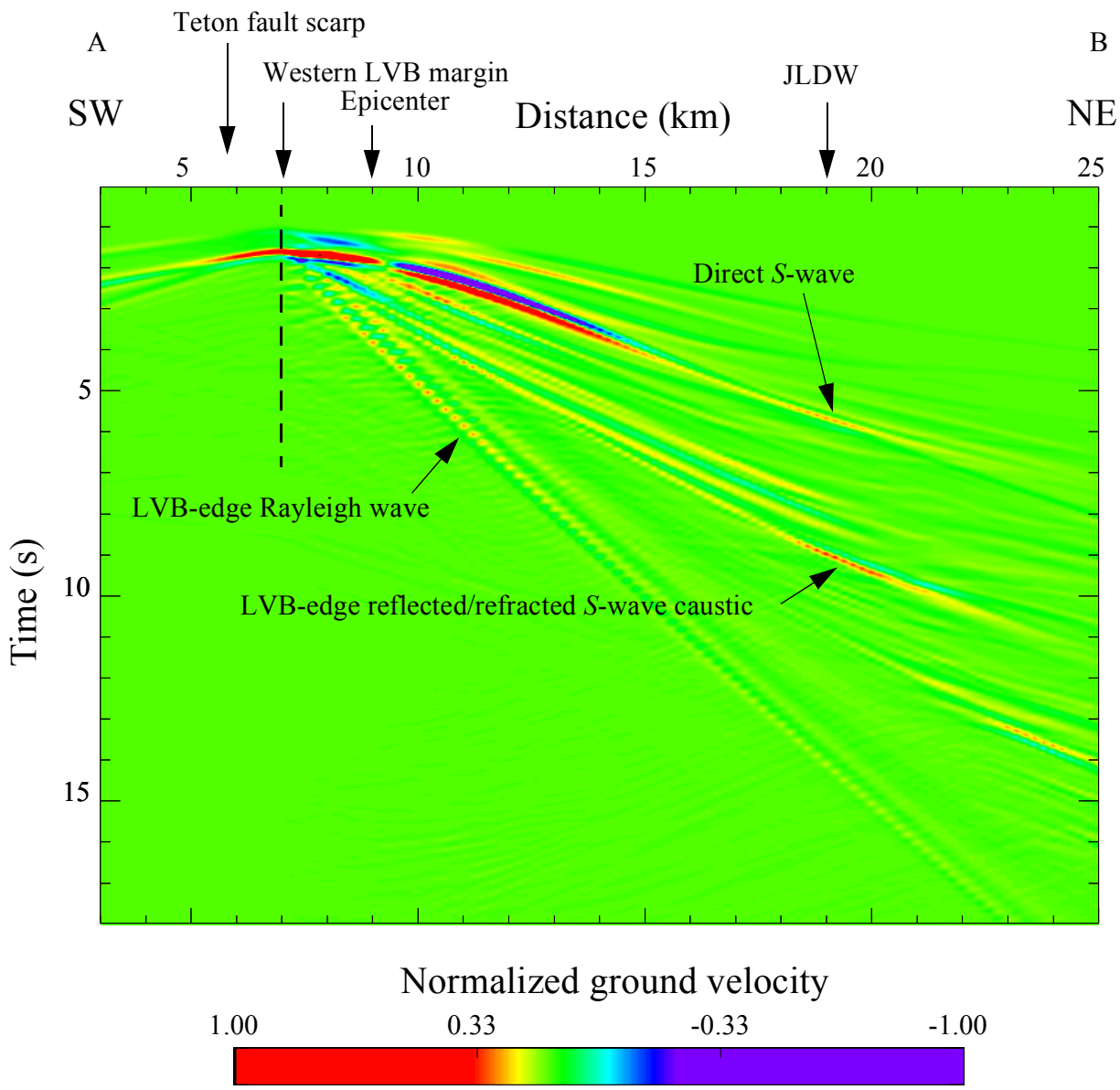

Figure 4-6: Synthetic radial-component-seismogram record section for the 19 April 2001 earthquake. The record section has the same orientation as Figure 4-4 and is represented by the cyan portion of A-B in Figure 4-1. Labels and arrows show the locations of the rock site, epicenter, and surface scarp of the Teton fault. Note the secondary S-wave and surface wave arrivals generated at the western LVB edge (denoted by the dashed vertical line).

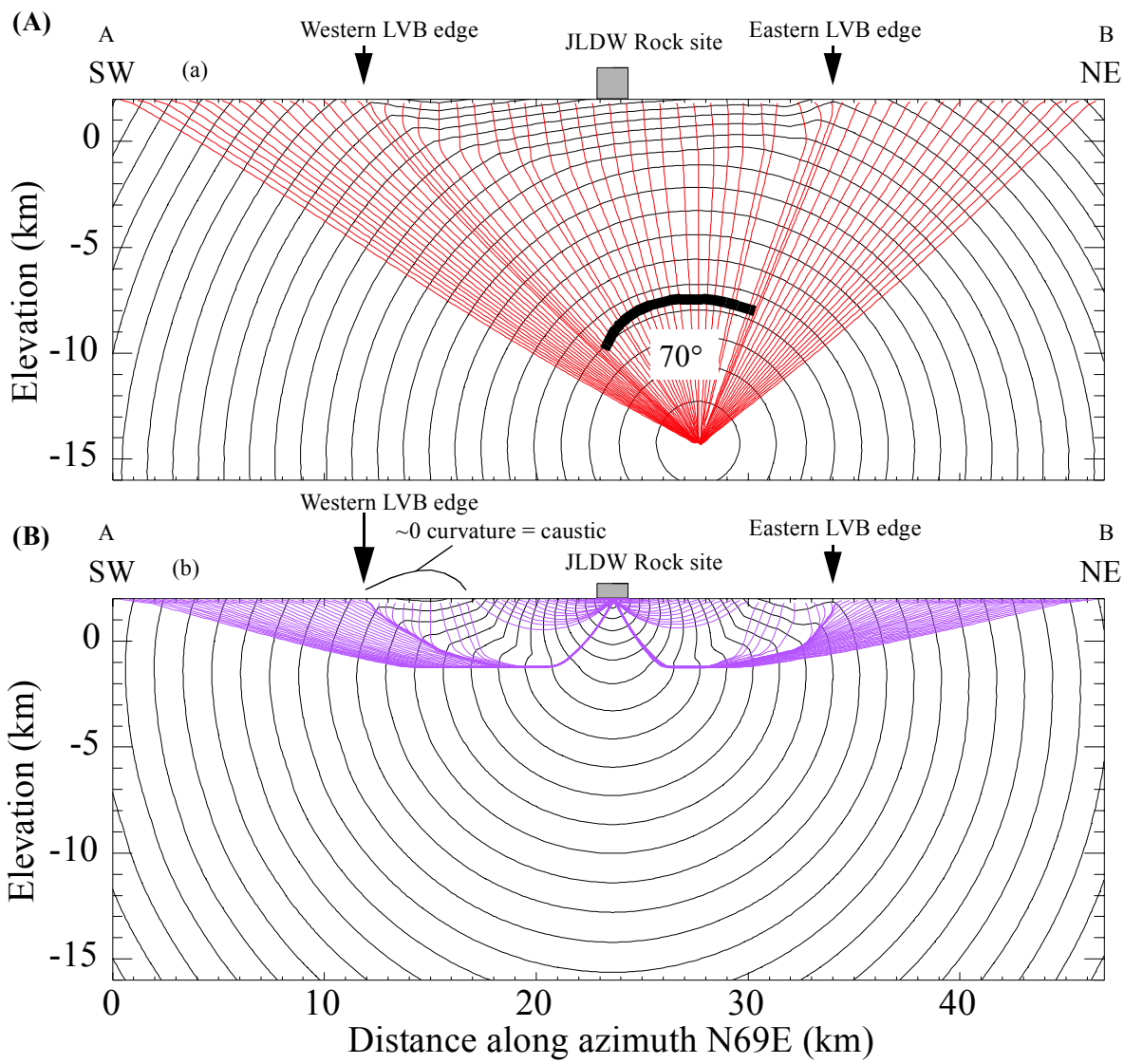

Figure 4-7: 2D ray-tracing slices through the 3D S-wave velocity model. (A) Black curves are isochrones and red curves are S-wave first-arrival ray paths from a hypocenter near the bottom of the Teton fault and east of the rock site (filled square). Rays emitted over a 70° arc from the source are captured by the LVB. (B) Purple rays are first S-wave arrivals from JLDW to positions within and outside the LVB (a reciprocity visualization). Note the first-arrival path between the western LVB-edge and the rock site is a refracted path along the large-velocity discontinuity between the LVB and the high-velocity basement rocks. Figure 4-6 shows large amplitudes associated with a triplication caustic for LVB-edge S-waves propagating to sites located between 9-11 km from the western margin of the LVB. The isochrone on the ~5-km-wide region on the western margin of the LVB has nearly zero curvature resulting in a caustic at the dam.

frequency of 4 Hz to obtain sufficient signal-to-noise ratios to model the direct S-wave and LVB-edge S-wave arrivals. The focus for modeling this earthquake was on varying the northwestern boundary dip and position (Figure 4-8), so no attempt was made to model the southeastern portion of the model in Figure 4-8, since it had little effect on the JLDW seismograms for this earthquake.

This is an important earthquake because it occurs close to line 4 of Behrendt et al. (1968) and provides constraints on the geometry of the northwestern boundary of the LVB (Plate 1 and Figure 4-9). The strongest lateral gravity gradient is located along the northwest boundary of the LVB (Plate 1 and Figure 4-9b). As noted by Behrendt et al. (1968), this requires the northwest LVB boundary to have a steep dip and for the LVB to have it's maximum depth within the northwestern portion of the LVB (Figure 4-8). Several LVB boundary dips were used to calculate synthetic seismograms, only velocity models with steep LVB boundary dips were able to reproduce the observed amplitude ratios and time-differences between the direct S-wave and the LVB-edge S-wave on the radial seismogram (Figure 4-10).

Several Hertz reverberations persist for > 20 s in the observed seismograms (Figure 4-10). Frankel and Clayton (1986) showed that correlated-random (fractal) crustal velocity variations are necessary to explain seismic coda. To ascertain the importance of short-wavelength correlation on the waveform duration, a 2D fractal velocity randomization of the low-velocity-LVB portion of Figure 4-8 was employed using an anisotropic von-Karman autocorrelation function in the wavenumber domain, $P(k_r)$, of the form

$$P(k_r) \approx \frac{a_z a_x}{\left((a_z k_z)^2 + (a_x k_x)^2\right)} \tag{4-1}$$

where a_x and a_z are the horizontal and vertical correlation distances, respectively, and k_x and k_z are the horizontal and vertical wavenumbers, respectively. Values of a_x = 0.5 km and a_z =0.35 km were used because the deposits in the LVB are likely to vary more rapidly in depth than in the horizontal dimension (e.g., normal to bedding structures). A standard deviation of 9% was used which produced very long synthetic high-frequency coda durations (Figure 4-10). This suggests that either the actual velocity variability is better represented by standard deviations < 9% and/or that near-surface Qs is < 20. Since empirical Green's function were used to represent > 1 Hz site

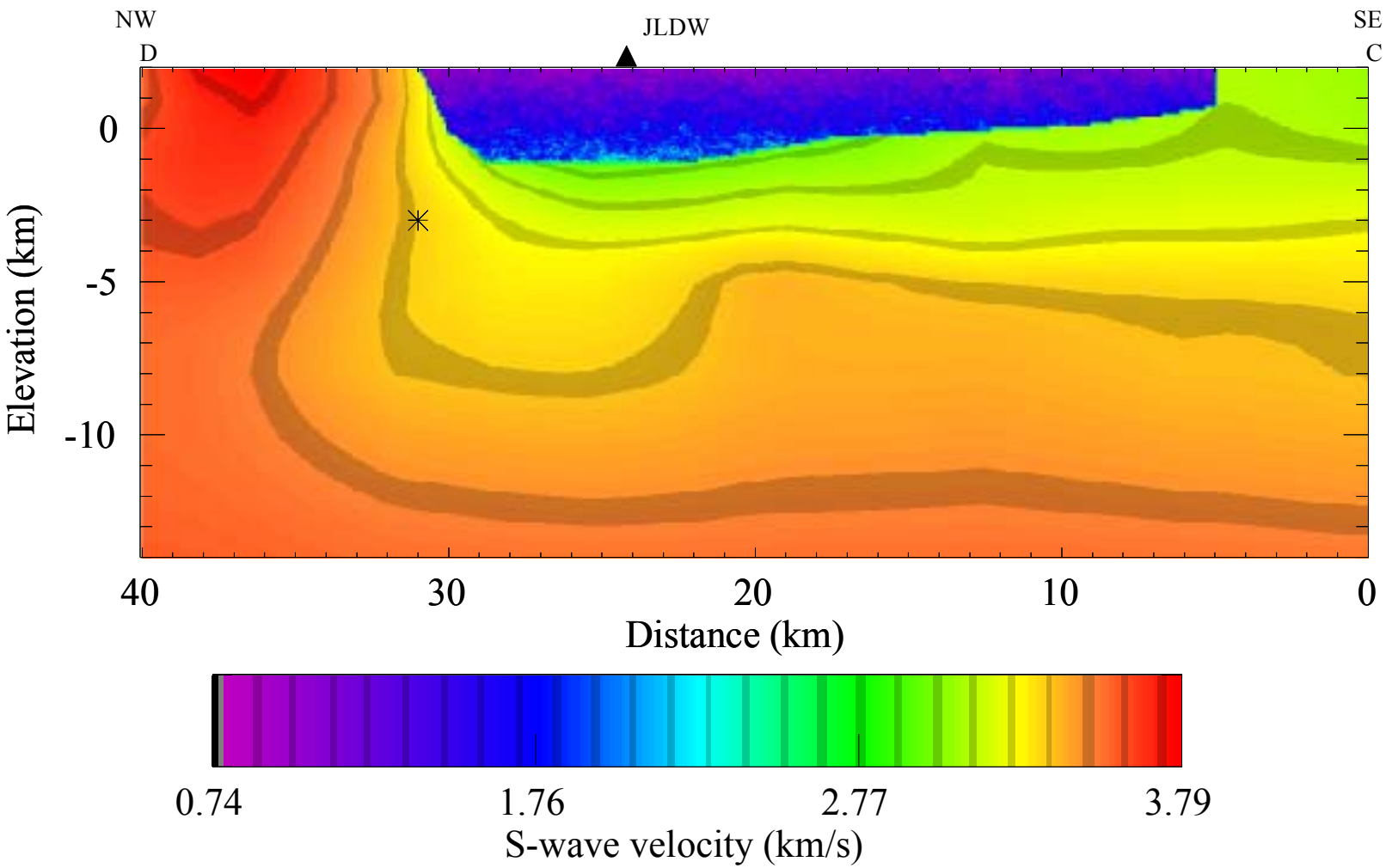

Figure 4-8: S-wave velocity-depth cross section C-D (see Figure 4-1) used to model the 29 Sep. 1996 **M** 1.6 earthquake. The hypocenter is the black star and station JLDW is the black triangle.

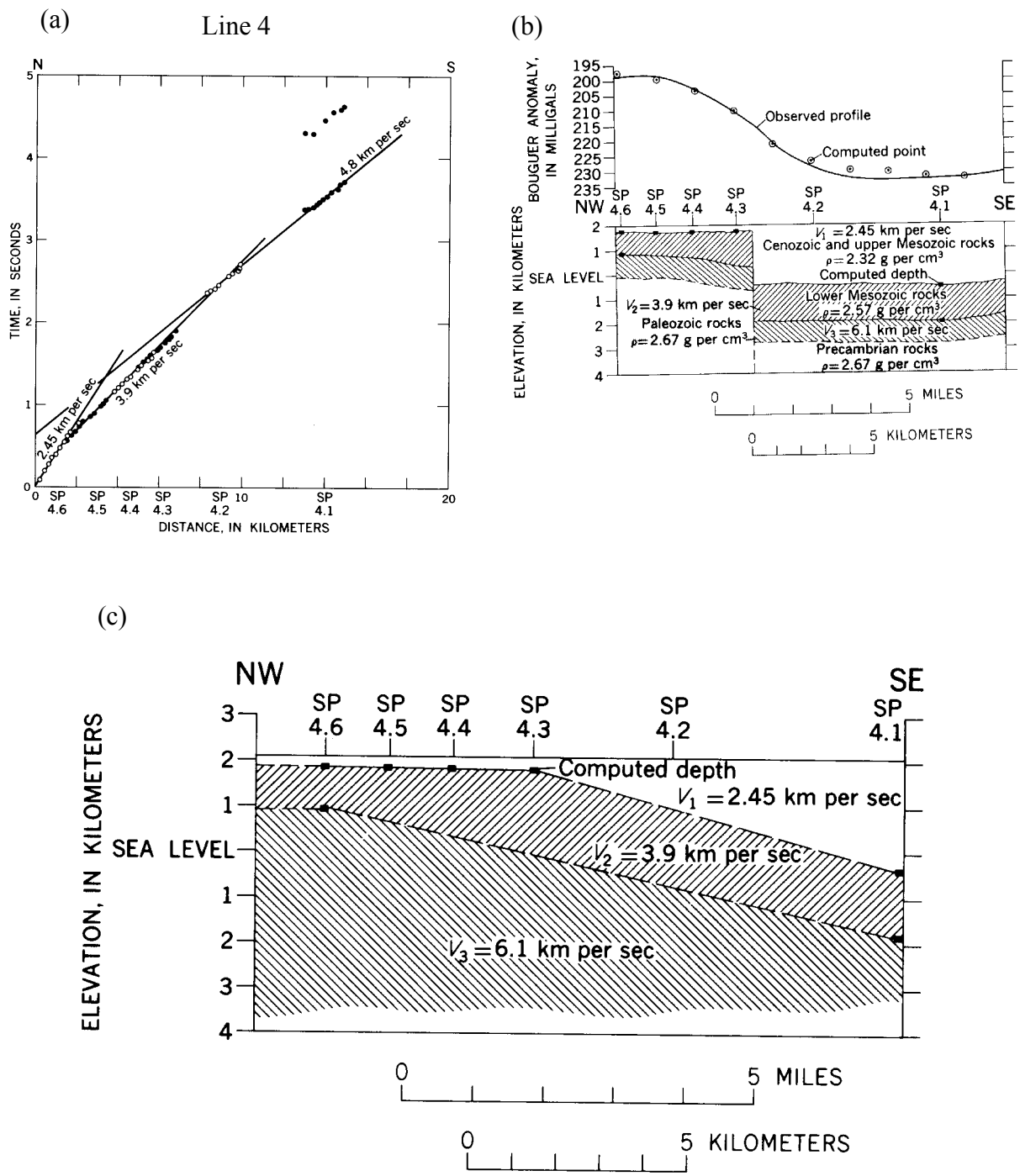

Figure 4-9: Line 4 traveltimes and interpretations reproduced from Behrendt et al. (1968). (a) Unreversed traveltimes from line 4 (see Plate 1 for shotpoint locations). (b) Behrendt et al.'s (1968) Bouguer-anomaly observations and 2D line integral gravity model for line 4 based on the model in (c). (c) P-wave velocity model from Behrendt et al. (1968) estimated using time-depth method and velocities from lines 1-3.

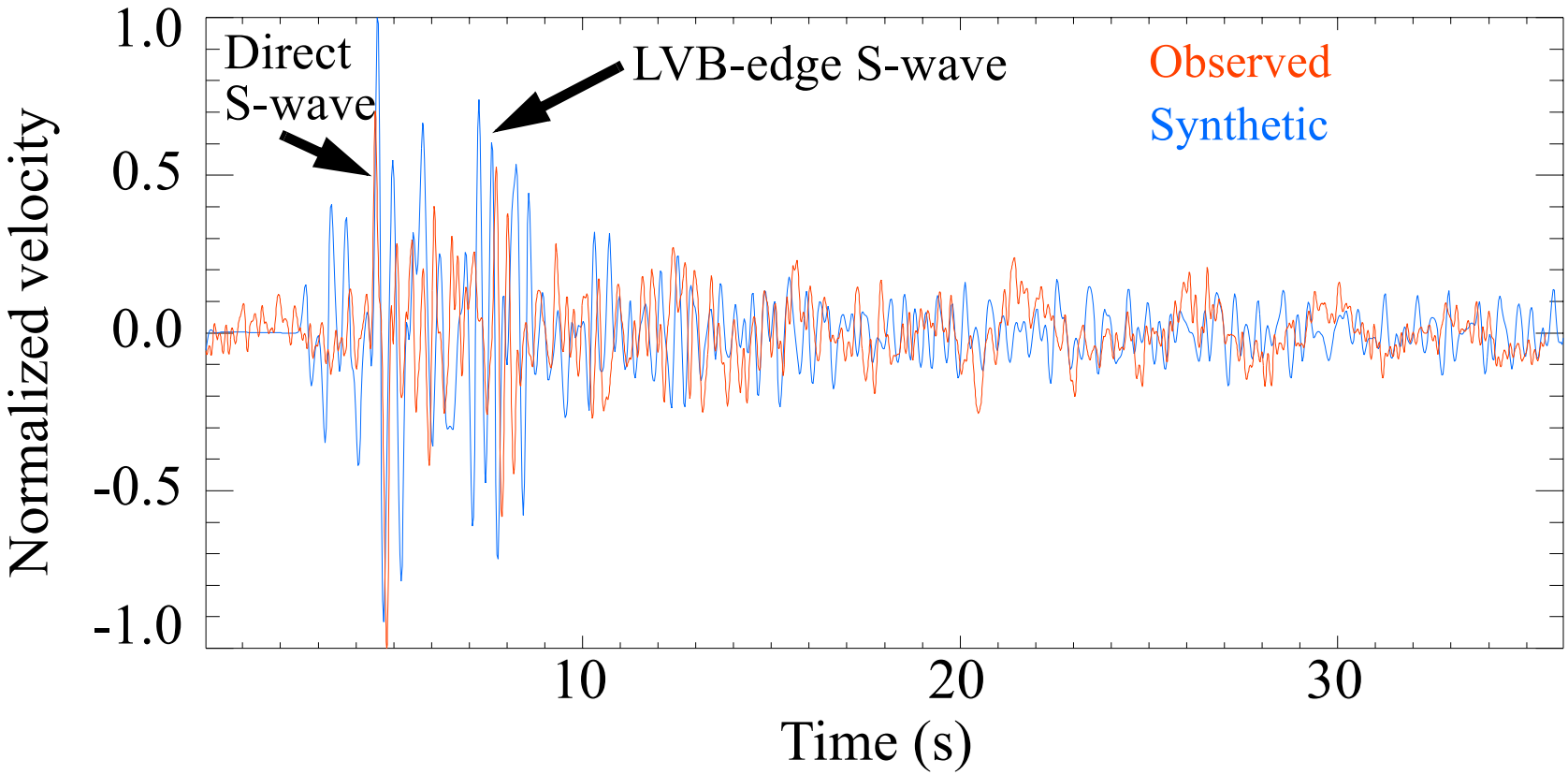

gure 4-10: Radial-component JLDW observed seismogram from the **M** 1.6 normal-faulting earthquake on 29 Sep. 1996. The epicenter is event 3 on Figure 4-1. This earthquake was located at a depth of 6 km below the northwest portion of the LVB margin. Both the observed and synthetic seismograms were band-pass filtered from 0.5 Hz to 4 Hz. The amplitude of the secondary *S*-wave arrival is smaller than the direct S-wave arrival because the site is located about 6 km from the LVB edge closest to the hypocenter, too close to develop a critically reflected/refracted S-wave at the site. Because of long-period site noise and relatively small event magnitude, it was necessary to model to a maximum frequency of 4 Hz. In contrast to Figures 4-4, a 9% standard deviation fractal randomization of the velocities in the LVB was used to modify the 2D velocity model. This resulted in synthetic high-frequency durations more consistent with the observed data.

responses in Section 6, further comparisons of correlated-random velocity variations and variability of synthetic seismogram responses were not pursued.

4.2.3 Synthetic Seismogram Modeling of the 15 Nov. 2001 M 2.9 Earthquake. This earthquake is located about 20 km SSE of station JLDW (the epicenter is event 2 in Figure 4-1) at a depth of ~8 km (Figure 4-11). P-wave first-motions from the JLSN indicate a oblique-normal-faulting focal mechanism with a dip of 57 degrees for the east-dipping nodal plane. This earthquake is located too far east of the surface trace of the Teton fault to be associated with the fault. The magnitude of 2.9 allowed for modeling to lower frequencies (< 1.5 Hz) than the other two events. The focus for modeling this earthquake was on varying the southeastern boundary dip and position (Figure 4-11), so no attempt was made to model the northwestern portion of the model in Figure 4-11, since it had little effect on the JLDW seismograms for this earthquake. This model was developed prior to the modeling presented in Section 4.2.2.

The synthetic 2D seismogram provides good amplitude agreement with the observed direct S-wave and LVB-edge S-wave; the synthetic LVB-edge surface wave amplitude is a bit smaller than the observed amplitude (Figure 4-12). The synthetic LVB-edge S-wave arrives about 0.5 s later than the observed LVB-edge S-wave, but the synthetic and observed direct S-waves and LVB-edge surface waves arrival times are the same. Minor adjustments to the hypocenter location would likely reduce the arrival time discrepancies. Overall, the good agreement between the amplitudes of the observed and synthetic radial seismograms in Figure 4-12 indicates that the position and dip of the southern LVB margin in Figure 4-11 and the LVB velocities between the southeastern LVB margin and station JLDW are reasonable. The 9% standard deviation fractal velocity randomizations within the LVB imposed in the same manner as the 29 Sep. 1996 earthquake modeling increased synthetic durations. However, the synthetic duration is shorter than the observed duration, which probably reflects the lack of 3D multipathing in the 2D model, and the greater distance of this earthquake (> 20 km) from JLDW relative to the 29 Sep. 1996 earthquake (~7 km from JLDW). Durations using the 3D model are more consistent with the observed data as discussed in Section 4.4.

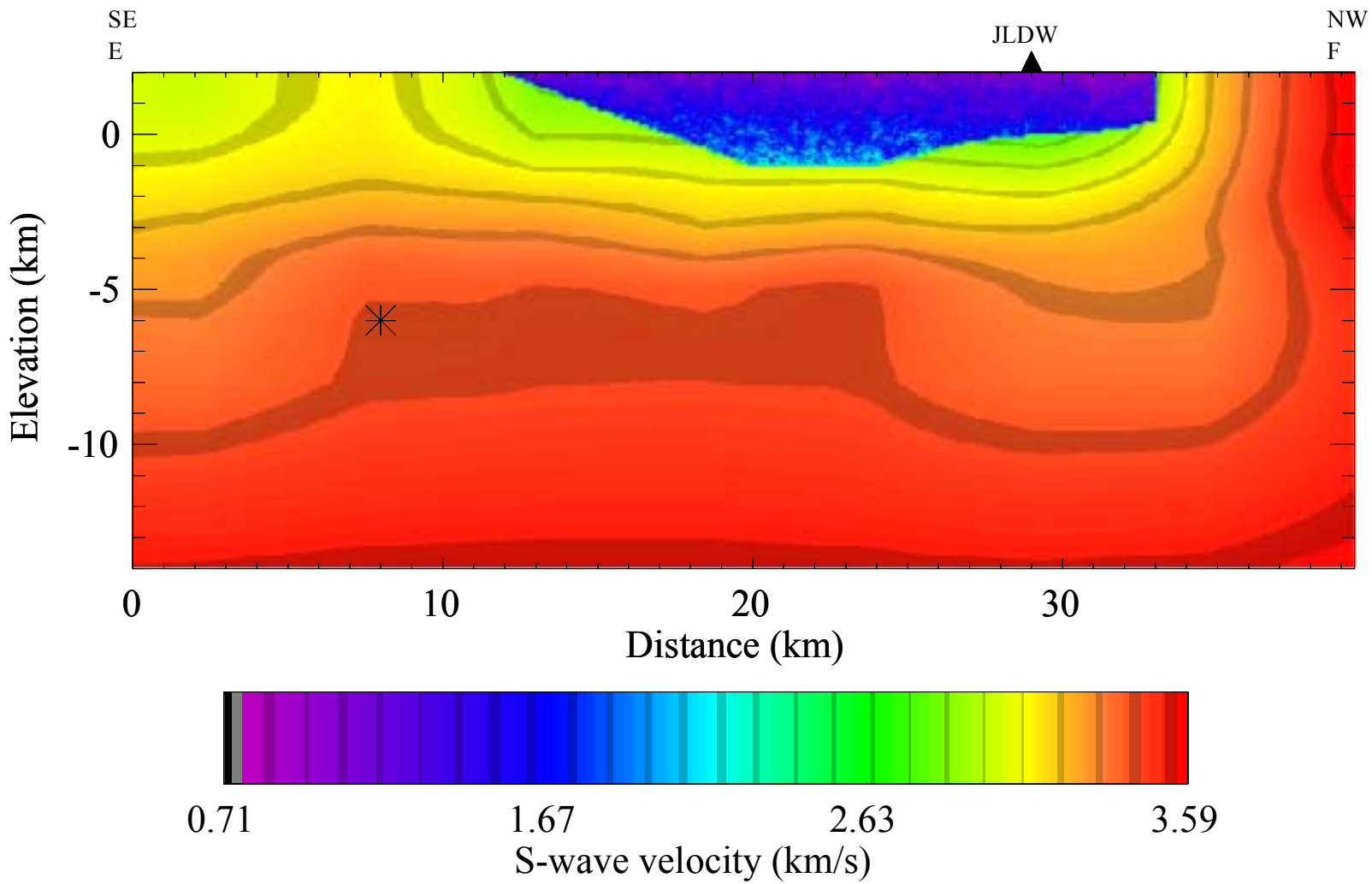

Figure 4-11: S-wave velocity-depth cross section E-F (see Figure 4-1) used to model the 15 Nov. 2001 **M** 2.9 earthquake. The hypocenter is the black star and station JLDW is the black triangle.

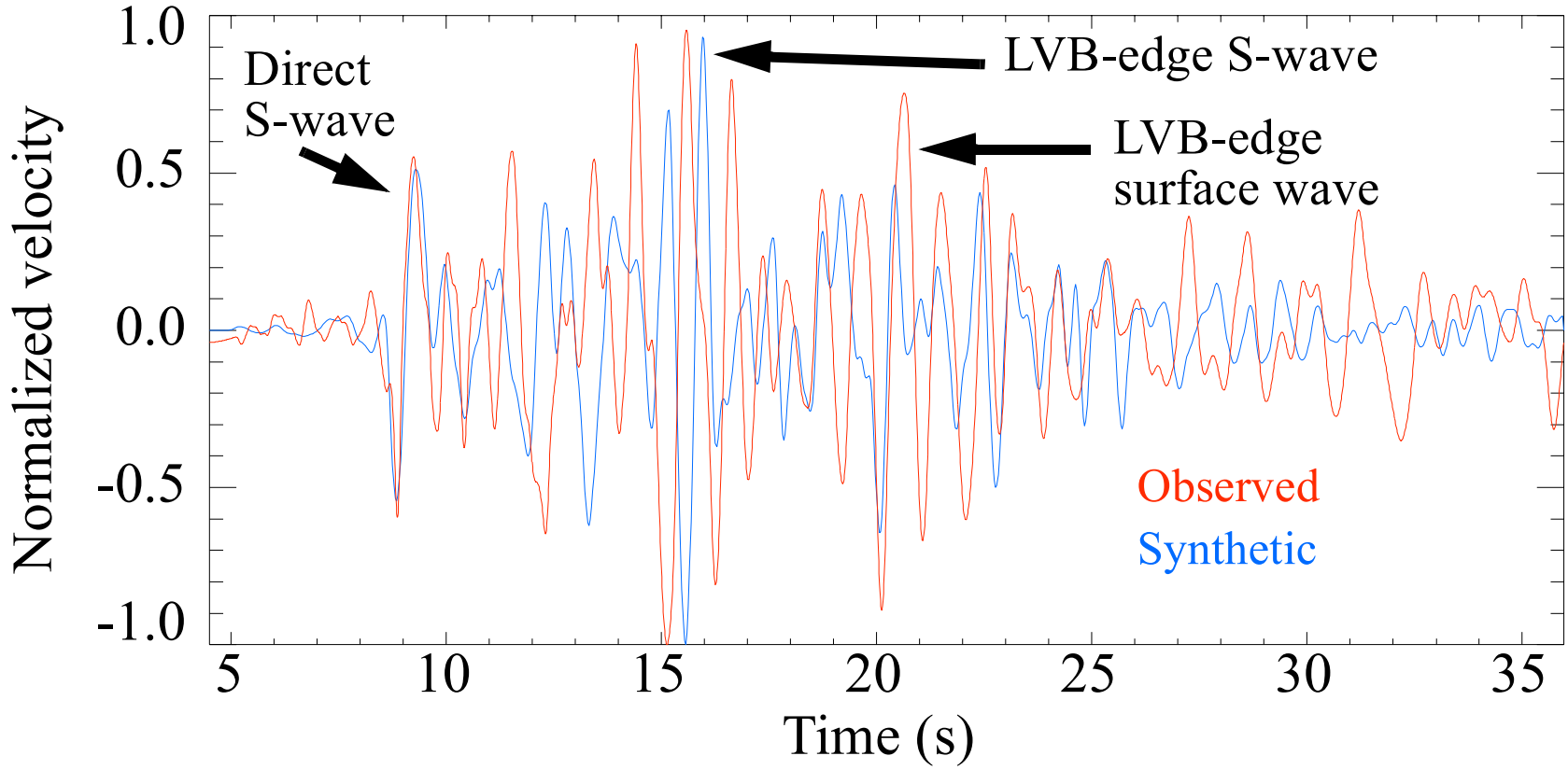

Figure 4-12: Observed and synthetic radial-component JLDW seismograms the **M** 2.9 normal-faulting earthquake on 15 Nov. 2001. (Epicenter is star 2 on Figure 4-1. Both seismograms were band-pass filtered from 0.5 Hz to 1.5 Hz. This earthquake was located at a depth of 8 km, within 4 km of the southeast corner of the LVB margin. Both the LVB-edge S-wave and the LVB-edge surface wave amplitudes are larger than the direct S-wave and are reasonably well reproduced by the blue 2D synthetic seismogram. The 2D velocity model does not reproduce the extended duration of the surface waves observed after 30 s. In contrast, the 3D finite-difference Green's functions include the multipathing necessary to reproduce observed durations (see Figures 4-18 and 4-19).

4.3 Comparison of 3D Velocity Model to the Seismic Refraction Data

The 3D P-wave velocity model reproduces the line 2 P-wave traveltimes of Behrendt et al. (1968) well, except for the eastern portion of the travel time data (Figure 4-13), where it is clear that the low-velocities would need to be continued to the east in the 3D model to match the refraction data. The truncation of the LVB east of the dam in the 3D velocity model is probably not a substantial issue for using the 3D model to estimate ground motions at the dam because the Teton fault interacts most strongly with the western portion of the LVB. However, it would be prudent to use several earthquakes located east of the dam recorded at station JLDW to constrain the eastward extent of the LVB.

The 3D velocity model produces a refracted traveltime branch on the west of shotpoint 2.1 that is about 0.1 s too late. As shown in Figure 4-14b, the bottom of the western portion of the LVB is probably 0.2-0.3 km too deep to precisely reproduce the traveltimes in the 2-10 km distance range in Figure 4-13. While the 3D velocity model actually fits the high apparent velocities observed for distances < 2 km in Figure 4-13, the model lacks the 0.1-0.2(?) km thickness of low-velocity near-surface material (moraines, talus, etc.) that likely comprise the near-surface materials between the LVB and the scarp of the active Teton fault. If the depths to the bottom of the western portion of the LVB in the 3D model were modified to reproduce the travel-time curve more closely in the 2-to-10-km distance range, the veneer of low-velocity near-surface materials that probably exist for distances < 2 km would also need to be added to the 3D velocity model to reproduce the observed shotpoint 2.2 western-branch traveltime curve in the < 10 km distance range. Since a grid spacing of 0.2 km was used in the 3D velocity model to calculate ground motions at the dam, these discrepancies in traveltimes all approach the resolution limit of the discrete 3D velocity model and are probably not significant for calculating < 1 Hz synthetic ground motion responses at the dam.

The 3D velocity model has a horizontal velocity gradient that increases velocities in the eastward direction. Whereas Behrendt et al. (1968) substantially decreased the thickness of low-velocity sediments east of JLDW, the 3D velocity model simply increases the average velocities of the sediments eastward, instead of decreasing sediment thicknesses eastward as rapidly as Behrendt

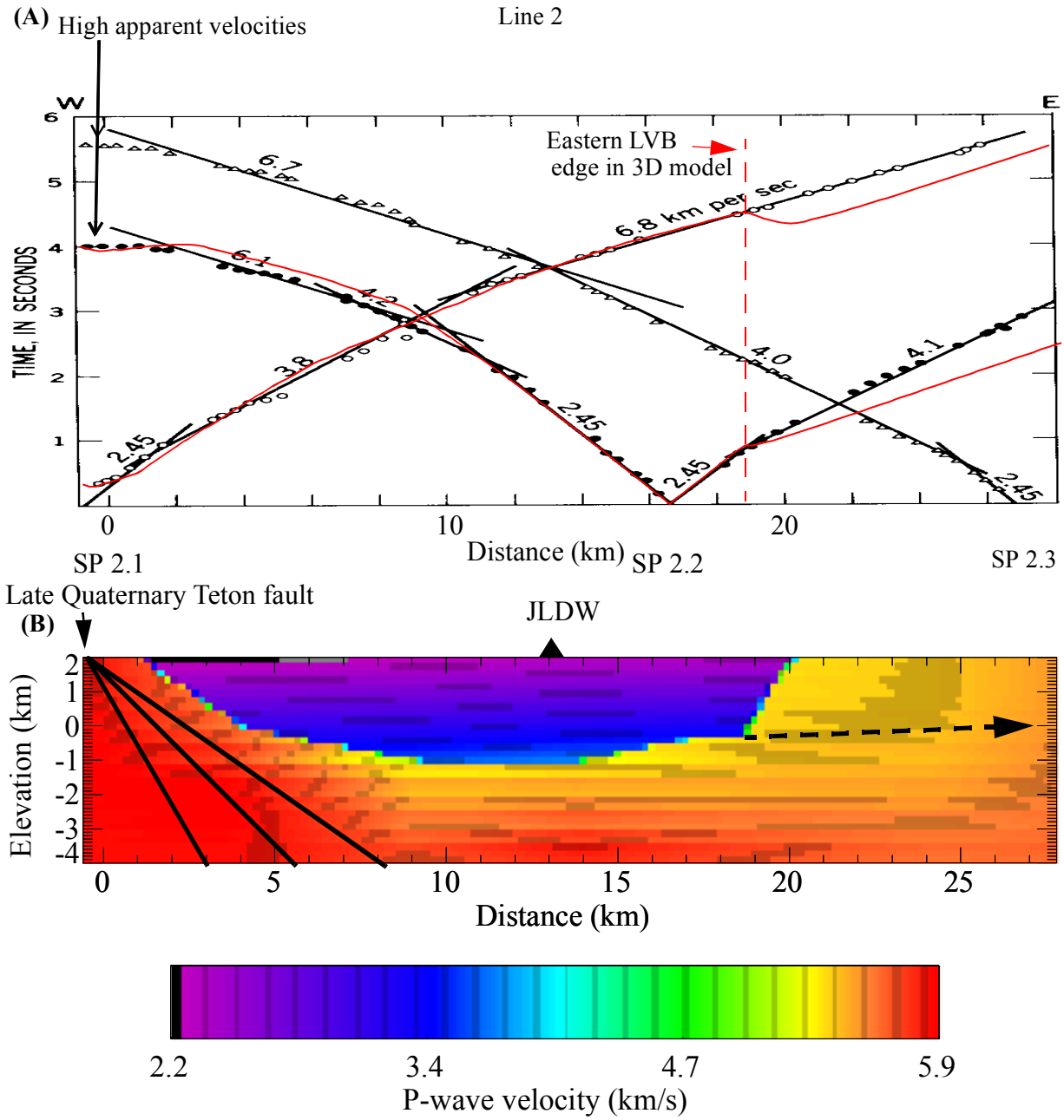

Figure 4-13: (A) P-wave travel-time plot for lines 2 from Behrendt et al. (1968) and (B) corresponding slice of the 3D P-wave velocity model. Labeling of (A) is as in Figure 4-2. The western portion of line 2 located ~1 km north of Jenny Lake shows very-high apparent velocities for shotpoints 2.2 and 2.3 as show by the black arrows. The red curves on line 2 are P-wave travel-time curves from the 3D velocity model (Figure 4-1) for shotpoints 2.1 and 2.2. The 0.1 s delay on the ~6.1 km/s apparent velocity western traveltime branch for shotpoint 2.2 suggests that the deepest portion of the LVB in the 3D model is 0.2-0.3 km too deep to fit the refraction data (see Figure 4-14). The lack of a travel-time advance in the refraction data along the eastern traveltime branch from shotpoint 2.2 indicates that the LVB continues east of the limit indicated by the 3D model, as shown by the dashed black arrow in (B); the refraction data show that ~2-km-thick low velocities persist to at least the eastern limit of line 2. The Teton fault is shown for dips of 35°, 45°, and 60° by the black lines in (B).

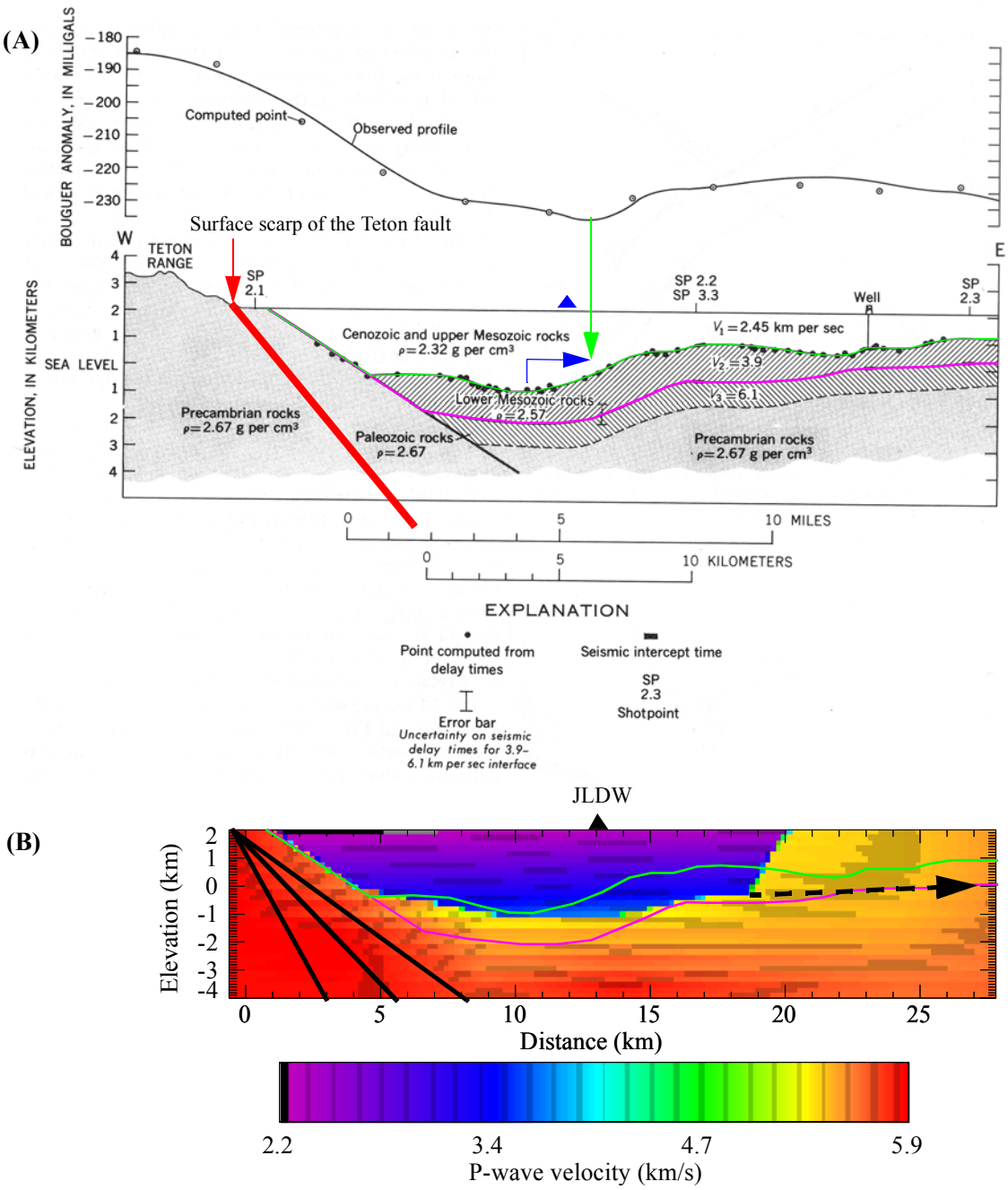

Figure 4-14: (A) Line 2 interpretation from Behrendt et al. (1968) and (B) corresponding slice of the 3D P-wave velocity model. Labeling of (A) is as in Figure 4-3. The lack of a travel-time advance in the refraction data along the eastern traveltime branch from shotpoint 2.2 (Figure 4-13) indicates that the LVB continues east of the limit indicated by the 3D model, as shown by the dashed arrow in (b); the refraction data show that ~2-km-thick low velocities persist to at least the eastern limit of line 2. The green curves in (A) and (B) are the Behrendt et al. (1968) interfaces between slow sediments and faster Mesozoic rocks and the magenta curves in (A) and (B) are Behrendt et al.'s interface between Mesozoic rocks and basements rocks. There is strong agreement in the depth to a significant velocity contrast between the Behrendt et al. (1968) model and the 3D model for the portion of the LVB west of JLDW, but east of the JLDW, the 3D model places the strong velocity contrast near the interface between Mesozoic rocks and basements rocks in model of Behrendt et al. (1968).

et al. (1968). The 3D velocity model is consistent with the findings of Byrd et al. (1994) that significant vertical and horizontal velocity gradients exist within the LVB. The 3D velocity model is consistent with the total thickness of lower density rocks within the LVB, particularly with the relatively small increase of gravity east of the dam (except for the fact that the LVB is artificially truncated to the east, as indicated in Figure 4-15). Specifically, it appears likely that the dam is located over the deepest portion of the LVB, as indicated by the observed gravity in Figure 4-14a. The time delay between the LVB-edge S-waves and the direct S-waves in the two earthquakes (events 1 and 3) also support having JLDW located over the deepest portion of the LVB.

It would be necessary to model more earthquake responses at JLDW from earthquakes located east of the dam to better constrain the eastern extent of the LVB velocity model. Since the eastern portion of the LVB is located furthest from the Teton fault, it is less likely to produce LVB responses that are as strongly amplified at the dam as the LVB-edge S-wave produced along the western margin of the LVB. This issue is discussed in more detail in the next section.

4.4 Seismic LVB Responses to Teton Fault Earthquakes: Influence of LVB Structure

To illustrate the importance of the 3D velocity structure on seismic responses at the dam, low-frequency (< 1 Hz) reciprocity Green's functions (RGF) calculated using the 3D velocity-density model (for use in Section 6) are discussed here. As indicated in Figure 4-15, there are three portions of the LVB margin that are located 10-to-14 km from the dam and likely to produce high-amplitude, critically reflected/refracted LVB-edge S-waves at the dam. Two of the three portions of the LVB margin in the critical distance range from the dam are located along the eastern end of the LVB where LVB structure is most uncertain. For instance, the strongest S-wave horizontal arrivals at the dam for a point-source located at the base a 35-degree-dipping Teton fault at the northeast corner of the fault (Figures 4-16 and 4-17) are the LVB-edge S-waves produced along the northeast corner of the LVB (see F8 in Figure 4-15). However, if the northeastern edge of the LVB is actually located more than 14 km from the dam, the LVB edge will not produce high-amplitude LVB-edge S-waves at the dam. Instead the response may be more like those found in Figures 4-18 and 4-19 for a point source at the southeast corner of a 35-degree-dipping Teton fault, where total durations are much longer, and LVB-edge S-wave amplitudes do not always exceed direct S-wave amplitudes. However, the amplitudes of the secondary arrivals are rather

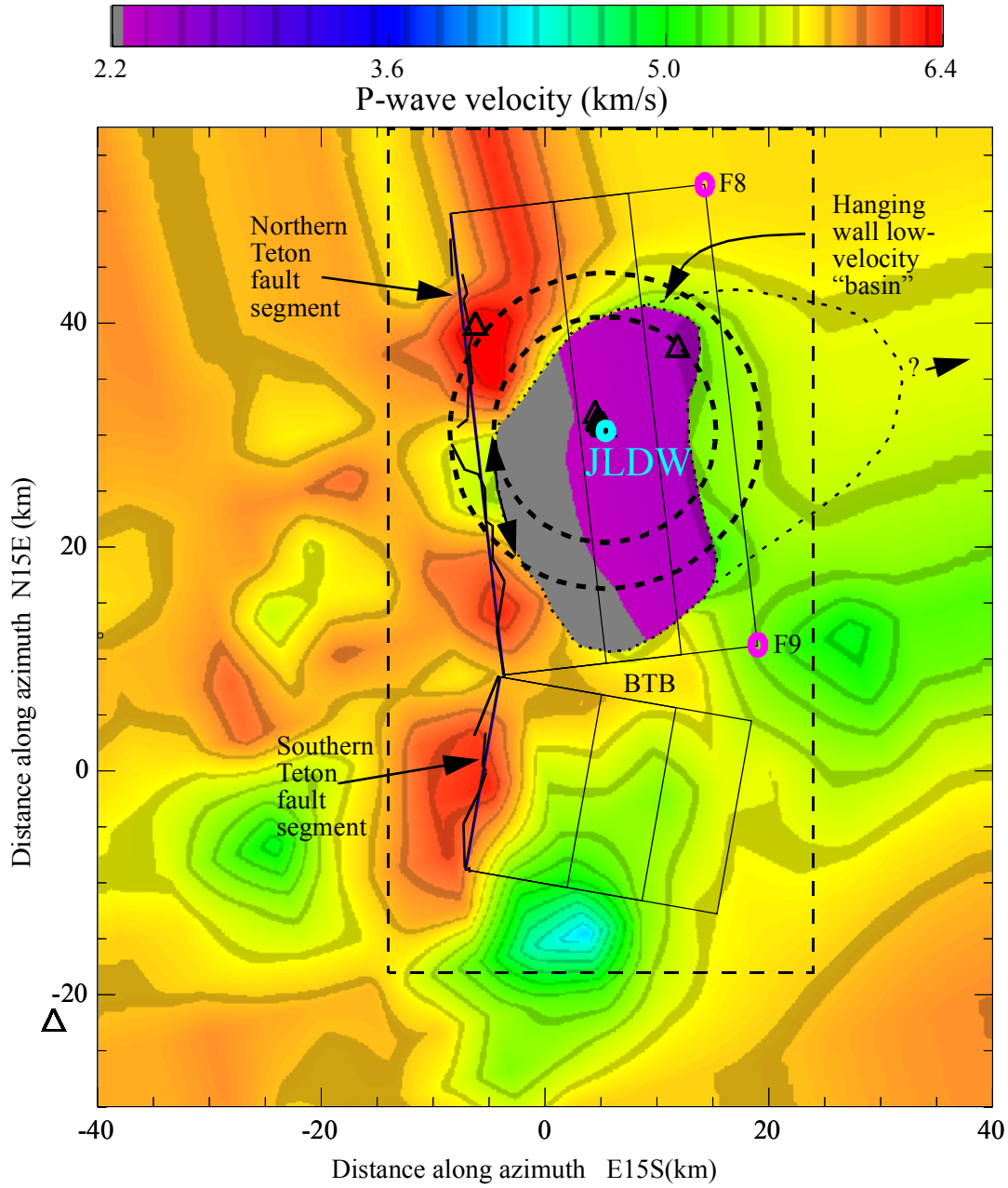

Figure 4-15: Plan view of the P-wave 3D velocity model with embedded Jackson Hole LVB at elevation 2 km. The postulated LVB is "closed"; it's surrounded by high-velocities everywhere (in depth and plan views), however as indicated by the short-dashed black curve, question mark, and arrow, the eastern portion of the LVB is likely to extend well beyond the LVB indicated in the 3D velocity model.The plan projection of the idealized geometries of the two primary (northern and southern) segments of the Teton fault for dips of 35°, 45°, and 60° are the solid rectangles (surface trace to the left). Blue circle is the JLDW rock site station. The dashed rectangle shows the limits of the 3D finite-difference grid. Numbered magenta circles are point-source positions for Figures 4-16 and 4-17 (F8) and 4-18 and 4-19 (F9). Blacktail Buttes is denoted by BTB. The region between the thick dashed lines indicates the distance range from station JLDW that strong LVB-edge S-wave arrivals are produced. The double arrow line indicates the portion of the western LVB that acts as a strong secondary source of S-waves at the dam.

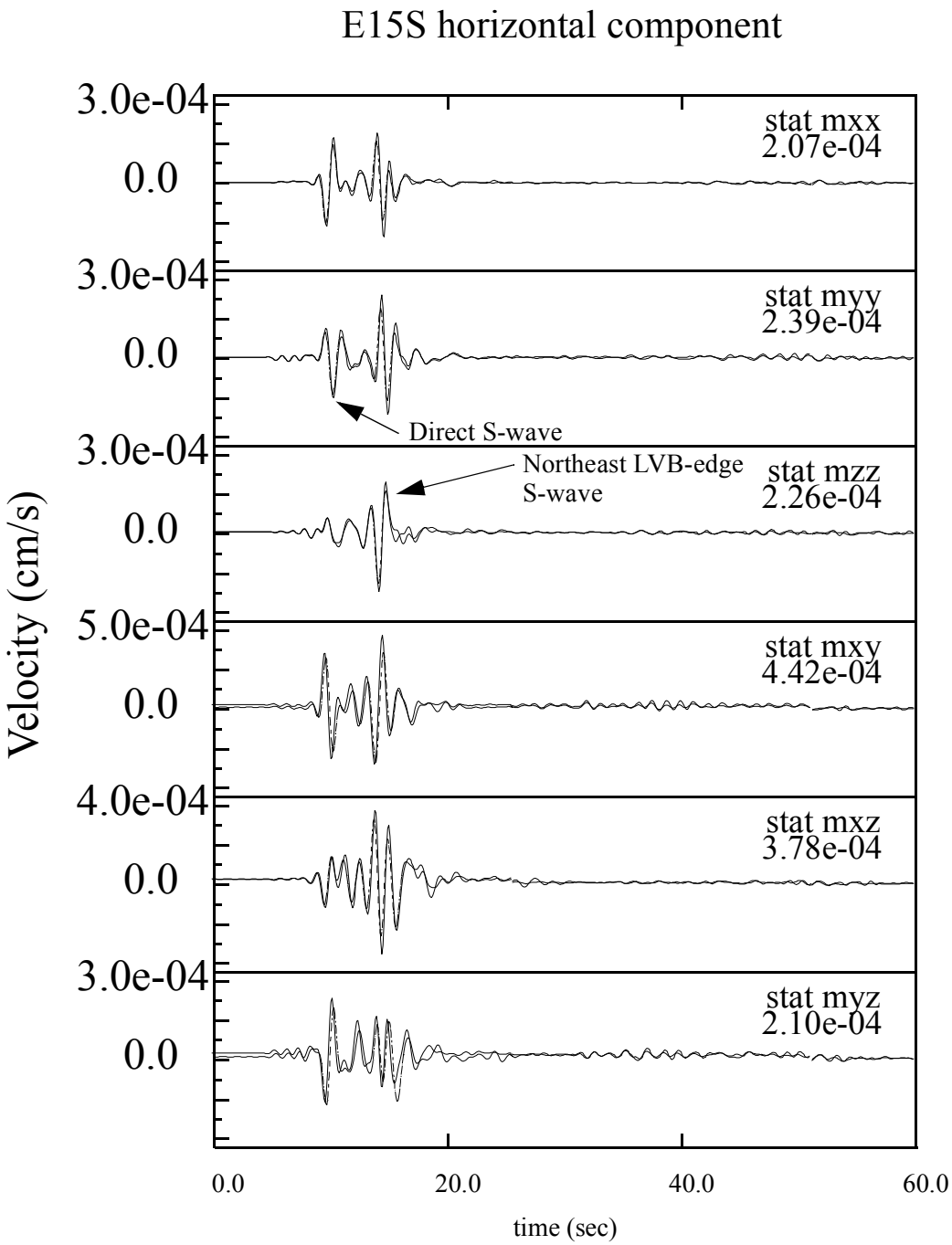

Figure 4-16: E15S horizontal component < 1 Hz 3D finite-difference RGF's moment-time histories at JLDW for a point-source at the northeast corner of the Teton fault. The point-source has a moment of 10^{20} dyne-cm (magenta circle labeled F8 on Figure 4-15). The mxx, mzz, and mxz moment components are most relevant for normal-faulting ground motions associated with the Teton fault. There are two seismograms shown for each moment component to illustrate the differences between the Graves (1996) and Graves and Day (2003) approaches to accounting for attenuation. The Graves and Day (2003) approach was used for all calculations in this report.

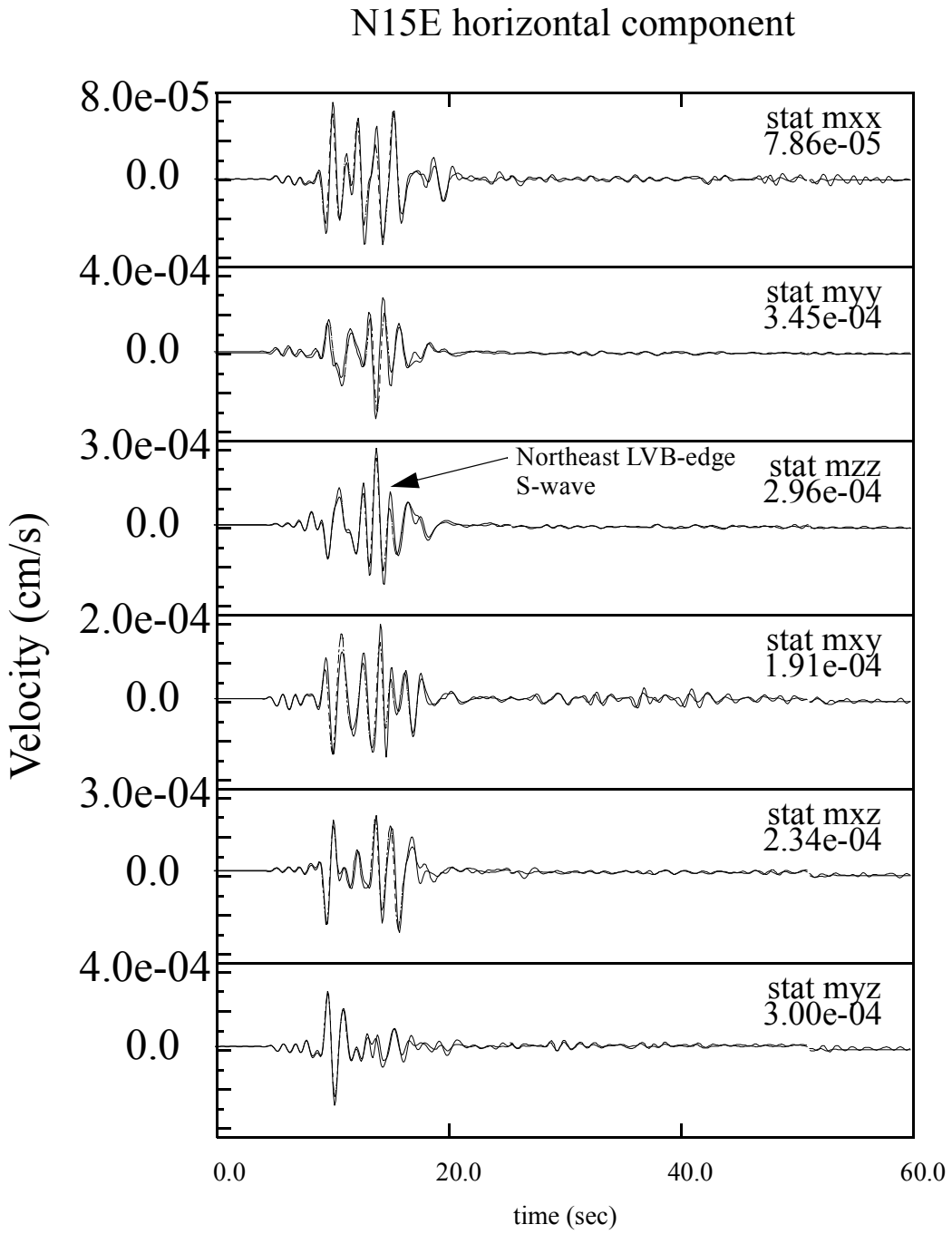

Figure 4-17: N15E horizontal component < 1 Hz 3D finite-difference RGF's moment-time histories at JLDW for a point-source at the northeast corner of the Teton fault. The point-source has a moment of 10^{20} dyne-cm (magenta circle labeled F8 on Figure 4-15). The mxx, mzz, and mxz moment components are most relevant for normal-faulting ground motions associated with the Teton fault. There are two seismograms shown for each moment component to illustrate the differences between the Graves (1996) and Graves and Day (2003) approaches to accounting for attenuation. The Graves and Day (2003) approach was used for all calculations in this report.

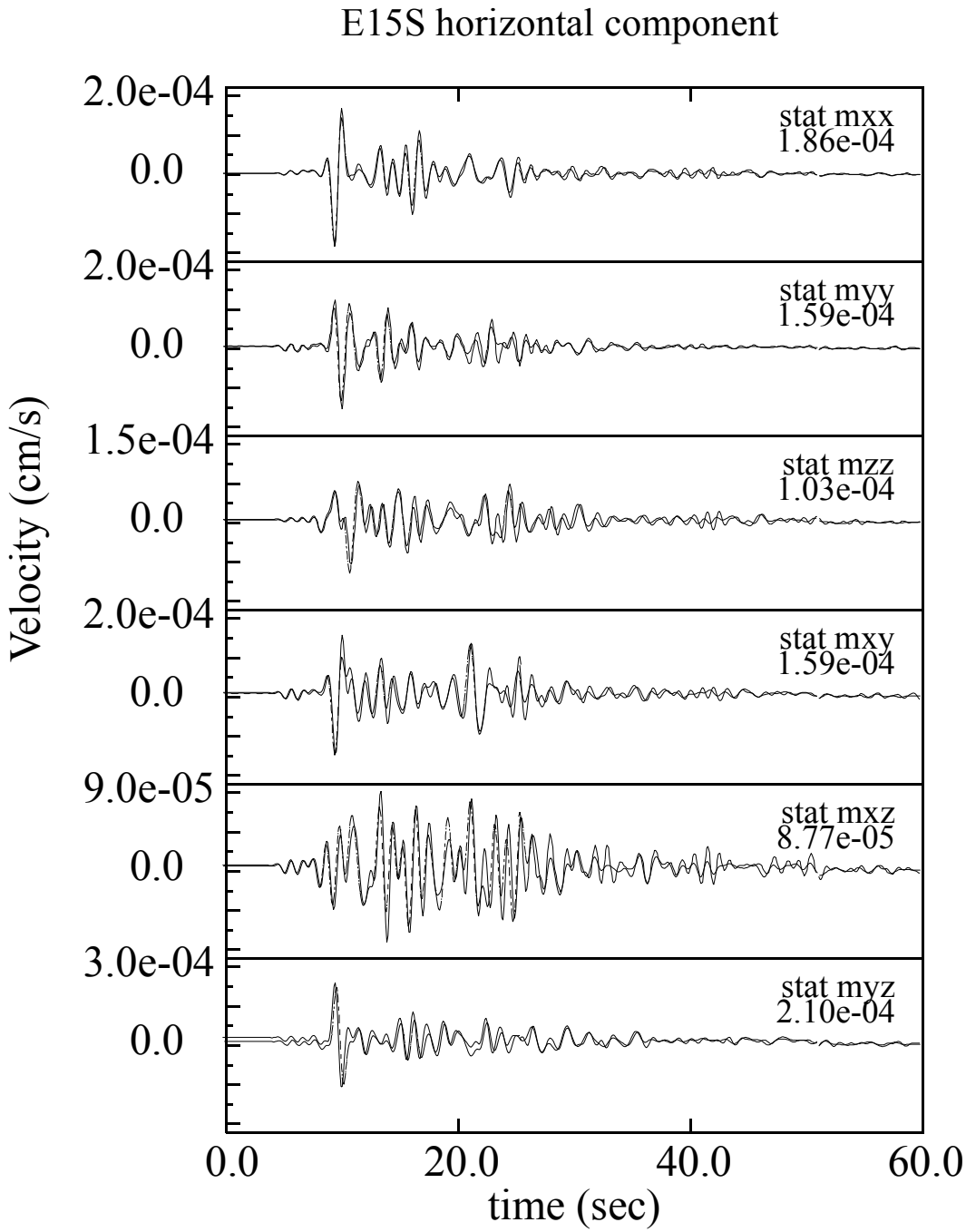

Figure 4-18: E15S horizontal component < 1 Hz 3D finite-difference RGF's moment-time histories at JLDW for a point-source at the southeast corner of the Teton fault. The point-source has a moment of 10^{20} dyne-cm (magenta circle labeled F9 on Figure 4-15). The mxx, mzz, and mxz moment components are most relevant for normal-faulting ground motions associated with the Teton fault. Note the longer duration of these moment responses relative to Figure 4-16. There are two seismograms shown for each moment component to illustrate the differences between the Graves (1996) and Graves and Day (2003) approaches to accounting for attenuation. The Graves and Day (2003) approach was used for all calculations in this report.

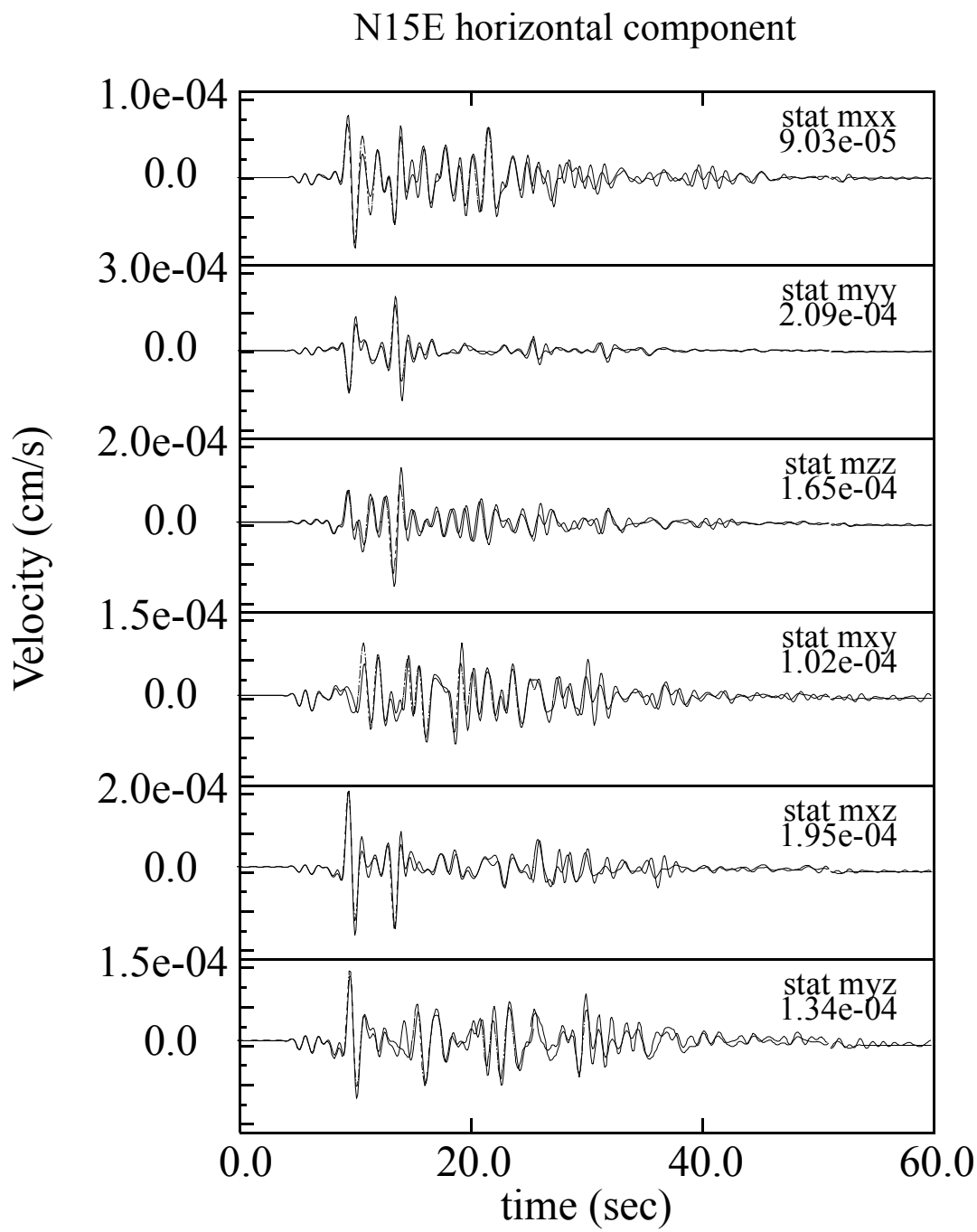

Figure 4-19: N15E horizontal component < 1 Hz 3D finite-difference RGF's moment-time histories at JLDW for a point-source at the southeast corner of the Teton fault. The point-source has a moment of 10^{20} dyne-cm (magenta circle labeled F9 on Figure 4-15). The mxx, mzz, and mxz moment components are most relevant for normal-faulting ground motions associated with the Teton fault. Note the longer duration of these moment responses relative to Figure 4-17. There are two seismograms shown for each moment component to illustrate the differences between the Graves (1996) and Graves and Day (2003) approaches to accounting for attenuation. The Graves and Day (2003) approach was used for all calculations in this report.

remarkable considering that the direct S-wave propagation distance is less than the half propagation distances of most LVB-edge S-waves. A nearly 10-km-long region of the along western margin of the LVB (Figure 4-15) provides a large secondary source dimension which explains why the amplitudes of LVB-edge S-waves are nearly comparable to direct S-wave amplitudes in (Figures 4-18 and 4-19). The longer durations in Figures 4-18 and 4-19 relative to Figures 4-16 and 4-17 also reflect the fact that the southern end of the LVB is located > 15 km from the dam, allowing LVB-edge surface waves to fully develop between the southern LVB-edge and the dam. If the LVB is extended further east and northeast, then the responses at the dam for seismic energy radiated from the northeast portion of the fault will likely be much longer than in Figures 4-16 and 4-17, but LVB-edge S-wave amplitudes should be somewhat reduced.

These results illustrate some of the sensitivities of seismic responses at the dam to assumed 3D velocity structure. To provide an overview of the influence of the 3D LVB on strong motion responses, E15S profiles of ground motion attributes, including Arias Intensities, are shown in Figure 4-20 for a kinematic simulation of a **M** 7.1 earthquake on the northern segment of a 35°-dipping Teton fault that extends to 16 km depth. Arias Intensity is a ground motion parameter that quantifies the potential destructiveness of an earthquake as the integral of the square of the acceleration-time history (Kayen and Mitchell, 1997). Arias Intensity correlates will with several commonly used engineering demand measures of structural performance, liquefaction, and seismic slope stability (Kayen and Mitchell, 1997). The kinematic rupture model for Figure 4-20 uses a different random seed to generate the asperity distribution than the rupture models used to produce Figure 6-11. The substantial differences in peak velocities and accelerations between Figures 4-20 and 6-11 illustrate the sensitivity of ground motions to details of fault rupture in the near fault region.

Peak ground motions and Arias Intensities are largest in the western half of the LVB, return to peak levels comparable to the hanging wall near the fault, at the position of the dam, and decrease past the dam in the E15S direction. Peak motions in the LVB east of the dam are less than peak motions on the hard-rock sites (> 3 km/s S-wave velocities) located west of the LVB adjacent to the fault. Unlike the western 8 km of the LVB, the dam is not subjected to extreme amplification associated with combined effects of rupture directivity and LVB amplification. However, the peak

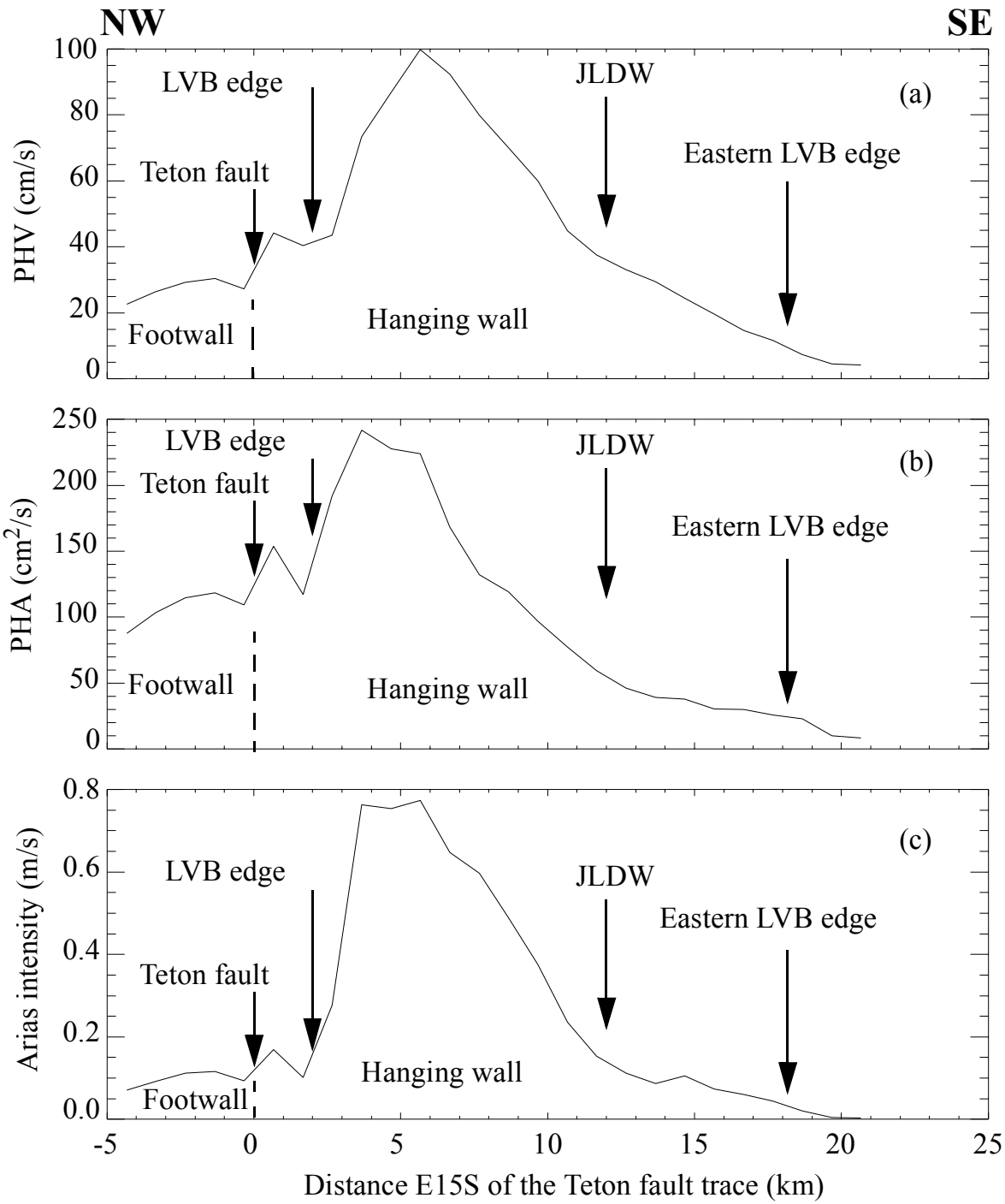

Figure 4-20: Simulated peak motion characteristics for a **M** 7.1 earthquake on the Teton fault. Long-period (**< 1 Hz**) peak horizontal velocities (PHV) (a), peak horizontal accelerations (PHA) (b), and Arias Intensities (c) for a profile of sites oriented E15S through the JLDW from a 3D finite-difference simulation of a **M** 7.1 normal-faulting earthquake on the northern Teton fault segment with a 35°-dip extending to 16 km depth. The hypocenter was located at 15 km depth, 2 km from the south end of the fault segment. The Jackson Lake LVB is located on the hanging wall, 2 km from the surface trace of the Teton fault.

velocities and Arias intensities at the dam are larger than at sites located adjacent to the fault on the high-velocity portion of the hanging wall, indicating that the dam is subjected to amplification associated with rupture directivity; rupture directivity is smaller at the dam for fault dips of 45° and 60°, as shown in Section 6. Amplification at the dam is a result of it being located in the LVB. Note that high-velocity hard-rock footwall peak horizontal velocities (PHV) are < 1/4 of the largest PHV's in the LVB (1/16th of the LVB's peak kinetic energy), footwall peak horizontal accelerations (PHA) are < 1/2 of maximum LVB PHA's, and footwall Arias Intensities are < 1/7th of the maximum LVB Arias Intensities. PHA's, PHV's, and Arias Intensities diminish to values less than high-velocity footwall site values about 3 km east of the dam, indicating the absence of rupture directivity for sites locate > 15 km east of the fault. The results in Figure 4-20 represent but one kinematic rupture simulation, so it's important to not over interpret the results. However, Figure 4-20 provides a good schematic example of systematic spatial variations of strong motions relative to the surface scarp of the Teton fault and the LVB. Section 6 presents detailed calculations focused on quantifying strong motion responses at JLDW.

Stirling et al. (2002) postulate that rock site observations of balanced rocks may provide paleo ground motion information. Stirling et al. (2002) compared observed balanced-rock-site amplifications with observed soil-site responses. They found that 1 Hz rock site responses were half those of soil sites. Yet Stirling et al. (2002) concluded that since 10 Hz responses were comparable, rock sites responses were not substantially different than soil sites. However, Stirling et al. (2002) fail to acknowledge that peak velocities (~ 1 Hz response) provide better correlations with earthquake damage than peak accelerations (~10 Hz responses) (EERI, 1994). Also, ground motion durations and thereby, integral measures, such as Arias Intensity, that correlate much better than peak accelerations with earthquake damage (Kayen and Mitchell, 1997), will be lowest at rock sites (see Figure 4-20c). Given all these caveats about Stirling et al. (2002), and the low-frequency ground motion results in Figure 4-20, is it reasonable to expect normal-faulting, near-fault footwall proxies for paleo-ground motions to have any relevance to ground motions in hanging wall LVBs adjacent to normal faults? Probably not, given the contrast between low Arias Intensities adjacent to the fault in the footwall, and Arias Intensities seven times larger in the LVB at sites located > 5 km from the fault (Figure 4-20c). It is clear that footwall paleo ground motion proxies are not realistic ground motion proxies for hanging wall ground motions for typical

normal fault crustal velocity geometries, including the crustal velocity structure adjacent to the Teton fault.

4.5 Structural Interpretation of Hanging Wall Geology and Geophysics

The late-Quaternary surface scarp of the Teton fault is located ~1-2 km west of the western margin of the LVB as constrained by seismic refraction and gravity data (Figures 4-13 to 4-15). Line 2 shotpoint 2.1 is located about ~0.5 km east of the Teton fault scarp (Figure 4-14). The high-apparent velocities near shotpoint 2.1, the high-apparent velocities that extend 3 km east of the western edge of line 2 for shotpoint 2.2 travel-times, and gravity modeling of Lavin and Bonini (1957), Behrendt et al. (1968), and profile 2 of Byrd et al. (1994) clearly show that high velocities and high densities persist at shallow depths ~1-2 km east of the surface scarp of the Teton fault in the vicinity of Jenny Lake (Figures 4-13 and 4-14). The gravity interpretations of Byrd et al. (1994) for profiles north (profile 1) and further south of Jenny Lake (profile 3) fail to satisfy maximum gravity observations located immediately east of the surface scarp of the Teton fault, because low-density LVB sediments with thickness of ~2 km are extended west by Byrd et al. (1994) to abut the present-day Teton fault scarp. A more parsimonious interpretation of Byrd et al.'s (1994) gravity profiles 1 and 3 would extend high-density material 1-2 km east of the late-Quaternary surface scarp of the Teton fault to satisfy the maximum gravity amplitudes observed immediately **east** of the Teton fault scarp on each of the profiles. Thus, it appears that the low-velocity, low-density LVB begins >1 km east of the late-Quaternary scarp of the Teton fault for most of the length of the northern Teton fault segment (Figure 4-15). This means that both the footwall and hanging wall in the vicinity of the Teton fault consist of relatively high-density and high-velocity materials; the LVB does not represent the hanging wall interface of the active Teton fault. This has some important ground motion and rupture dynamic implications that are discussed in Section 6.

The high-velocity, high-density structure on each side of the Quaternary surface trace of the Teton fault was noted by Behrendt et al. (1968) and Byrd et al. (1994), among others. Several investigators have postulated the existence of a second normal fault bounding the western margin of the LVB (Lavin and Bonini, 1957; Behrendt et al., 1968; Tibbetts et al., 1969). Byrd et al. (1994) discount the existence of a normal fault bounding the LVB (e.g., > 1 km east of the late-

Quaternary Teton fault scarp), and appeal to the existence of a Laramide or older structure high-density body along the northern 40 km of the Teton fault to explain the high gravity amplitude observations east of the mapped surface trace of the Teton fault. An enigmatic aspect of the postulated normal fault several km east of the late Quaternary scarp of the Teton fault, is it's lack of apparent Quaternary activity (Gilbert et al., 1983; Susong et al., 1987; Smith et al., 1993; Byrd et al., 1994; Byrd, 1995) and it's relatively shallow dip of about 30 degrees (Behrendt et. al. 1968, Figure 4-14). The 10-degree, west-side-down tilt of the Teton Range in response to normal-faulting, as inferred by Byrd et al. (1994) from paleomagnetic data, provides a mechanical explanation for the westward migration of the Teton fault into the Teton Range and the existence of multiple normal faults. A westward tilt of 10 degrees would take a 40-degree east-dipping normal fault and rotate it to 30 degrees. Mandl (2000, p. 333-334) showed that as a normal fault approaches 30 degrees it become mechanically impossible to continue normal fault growth, particularly if fault growth is controlled by processes below 10 km. Consequently, in response to the westward tilting in the vicinity of the Teton Range, the Teton fault jumped west several km and initiated a new more steeply dipping (>> 35°), east-dipping normal-fault in its present position.

Buck (1993) showed isostatic responses make it likely that normal faults will tend to rotate toward shallower dips as total fault displacement increases. Collettini and Sibson (2001) use worldwide focal mechanism data from **M** > 5.5 earthquakes to show that the most common normal fault dips are 40-to-45 degrees, substantially lower dips than would be ascribed to normal faults based on simple faults mechanics of Anderson (1951) of 60-to-75 degrees. Thus, even if the initial dip of the late-Quaternary scarp of the Teton fault was 60° several m.y. ago, the results of Buck's (1993) analyses indicate that the present dip of the active Teton fault is likely be < 50 degrees. The preponderance of normal faulting dips ≤ 50 degrees (76%) in Collettini and Sibson (2001) also suggests that the dip of the currently active trace of the Teton fault is likely to be ≤ 50°. As noted in Section 2, there appears to be a third set of normal faults developing west of the primary late-Quaternary Teton fault scarps shown on Figure 4-15. These western-most normal faults have relatively small late-Quaternary scarp heights of < 10 m, but steep dips of ~75°, consistent with the development of new normal faults at high angles predicted by fault mechanics (e.g., Anderson, 1951).

Westward tilt of the Teton Range (Byrd et al., 1994) and isostatically-driven progressive fault rotation toward shallower dips with fault displacement (Buck, 1993) explains the existence and current orientations of all three "Teton" faults, a now inactive ~30°-dipping relic Teton fault bordering the western margin of the LVB, the currently late-Quaternary-active range-front-bounding Teton fault that has produced multiple surface-rupturing earthquakes in the past 17-18 ka (Section 2), and an incipient steeply-dipping Teton fault developing several km west of the range front that is characterized by relatively small-offset fault scarps (Section 2). In summary, the existence of three "Teton" faults, each offset from its neighbor by several km in the east-west direction, is consistent with fault mechanics, all the geophysical and geological data, including the lack of Quaternary activity on the eastern fault, and expected isostatic responses. The ground motion investigations in the report focus exclusively on earthquake rupture scenarios on the range-front Teton fault (Figure 4-15); earthquake scenarios are not considered for the other two "Teton" faults because the easternmost fault shows no signs of late-Quaternary activity (Gilbert et al., 1983; Susong et al., 1987; Smith et al., 1993; Byrd et al., 1994; Byrd, 1995) and the western most fault is located further from the dam, and would produce smaller ground motions at the dam.

The horizontal offset of the hanging wall LVB several km east of the presently-active Teton fault is typical of most normal faults in the Wasatch fault zone region of the intermontane seismic belt (ISB) (Zoback, 1983). It may be that fault rotation and migration of normal faults into the footwall (into range fronts) may be the norm in the ISB. Zoback (1983) only reports three cases in a sample of 23 normal faults in the Wasatch fault zone that consists of a single normal fault bounding the hanging-wall LVB. The rest of the normal fault hanging wall LVB in Zoback (1983) contained at least one normal fault embedded in the LVB.

4.6 Conclusions

The refraction data and MEQ waveform modeling indicate that nearly linear vertical and horizontal velocity gradients characterize the LVB generally referred to as Jackson Hole, consistent with the seismic refraction interpretations of LVB velocity structure of Byrd et al. (1994). Behrendt et al.'s (1968) and Tibbetts et al. (1969) interpretations of the refraction data used constant velocity layers with strong velocity discontinuities within the LVB; these models fail to reproduce strong broadband arrivals that follow direct S-waves by ~3-6 s. These arrivals

are composed of S-waves and surface waves produced at the LVB margins. The 3D velocity model of the LVB developed in this section is similar to the velocity model of Byrd et al. (1994) and reproduces observed seismograms from three earthquakes located near the edges of the LVB quite well. The paucity of strong S-P conversions on vertical-component seismograms from station JLDW, also argues against the existence of strong velocity discontinuities internal to the LVB, postulated by Behrendt et al. (1968). Geophysical P- and S-wave velocity logs near station JLDW (Sirles, 1986) provided near-surface S-wave velocity estimates that where consistent with observed LVB-edge S-wave and surface wave travel-times to the LVB rock site.

The 2D finite-difference waveform modeling presented in this section shows that earthquake seismograms recorded at station JLDW inside the LVB can constrain LVB margin locations and dip geometries using earthquakes located near LVB edges, and independent constraints on earthquake locations and focal mechanisms provided by a large-scale Jackson Lake seismographic network. The JLSN provided the data necessary to constrain earthquake locations, focal mechanisms, and large-scale 3D P-wave velocity structure, and made it possible to model broadband earthquake recordings in the LVB to constrain Jackson Lake LVB P- and S-wave velocity structure. The gravity data in Behrendt et al. (1968) and Byrd et al. (1994) provided valuable information to interpolate LVB margin structure between constraints provided by the 2D finite-difference modeling and seismic refraction data, but interpretation of the gravity data is intrinsically non-unique.

While the 3D model of the LVB appears to provide a good representation of western LVB velocity structure close to the Teton fault, the 3D LVB model is clearly artificially truncated east of the dam (Figure 4-13). It would be necessary to perform 2D or 3D seismogram modeling of LVB recordings of earthquakes east of the dam to constrain the LVB velocity structure > 8 km east of the dam. It's logical that eastern LVB velocity structure is less important than western LVB structure, because the Teton fault interacts more strongly with the western LVB. It is not clear how significantly the artificial truncation of the LVB influences estimated ground motions at the dam. For instance, the LVB-edge S-wave amplitudes in Figures 4-16 and 4-17 may be overestimated, but the total ground motion durations may be underestimated if the eastern margin

of the LVB extends > 4-to-5 km further east than indicated in Figure 4-15. This issue probably warrants further investigation.

The seismogram modeling of microearthquakes shows that 3D velocity-model Green's functions are necessary to simulate ground motions within the LVB, not just to obtain realistic durations, but to include the constructive interference effects of coherent secondary sources, like LVB-edge *S*-waves. Empirical Green's functions may underestimate 1-4 Hz responses because the coherent LVB-edge S-waves are probably not adequately represented by the eight empirical Green's functions used in Section 6. As Figure 4-20 shows, near-surface ground motion amplitudes may be very large along the western margin of the LVB due to rupture directivity. Thus, material nonlinearity may occur at the LVB edges; nonlinearity may modify LVB-edge *S*-wave and surface contributions to LVB ground motions. It may be important to conduct 2D P-SV plane-wave experiments using nonlinear finite-difference or finite-element codes to ascertain if near-surface, LVB-edge nonlinearity substantially influences ground motion durations and amplitudes within the LVB.

Since the majority of ground motions used to develop ground motion attenuation relations are from California, it's important to recognize the significant differences between the crustal velocity structure near the Teton fault and typical California crustal velocity structure. Near-surface P-wave velocities are ~6 km/s near the surface adjacent to the Teton fault. In southern California, P-wave velocities of 6 km/s are typically not encountered until depths of 5-10 km (Hauksson and Haase, 1997). High basement velocities extending to near the surface in the vicinity of the Teton fault translates into very large velocity contrasts between the LVB and surrounding basement rocks, particularly along the western half of the LVB. Thus, even though LVB S-wave velocities are similar to California "rock" or NEHRP site class B S-wave velocities (> 720 m/s), the JLDW rock site behaves more like California stiff-soil site with S-wave velocities of 300-to-600 m/s, than a California "rock" site. The large velocity contrasts between the LVB and the basement rock makes the LVB a strong collector of radiated seismic energy (Figure 4-7a), which produces unusually long observed durations at JLDW (Section 5), long synthetic ground motion durations (Figures 4-16 and 4-17) and amplification of ground motions within the LVB (Figure 4-20).

Seismographic network monitoring by the JLSN for over 16 years was necessary to record a large number of earthquakes and associated arrival time data to constrain 3D crustal velocity structure. Since earthquakes tend to cluster in space and time (Section 3), a long duration of seismic monitoring was required to begin to fill the 3D volume of the crust with earthquakes. It's necessary to have earthquakes distributed throughout the 3D crustal volume to obtain reasonable constraints (ray-path coverage) on 3D velocity structure. The five-year duration of broadband site-response monitoring was critical to obtaining earthquakes located on-or-near the Teton fault, given the relatively low-rate of seismicity observed on the Teton fault trace and other major ISB normal faults; one of the earthquakes used in the seismogram modeling of LVB velocity structure occurred in Sep. 1996 and another occurred in Nov. 2001. Longer duration broadband three-component monitoring of site responses increases the probability of recording larger-magnitude earthquakes that could provide the data necessary for modeling seismograms to lower frequencies than could be accomplished with the site-response data available for this study. The configuration of the JLSN provided the supplemental data necessary to constrain earthquake locations and focal mechanisms; seismogram modeling cannot constrain LVB velocity structure when there are too many unconstrained parameters, like earthquake locations, focal mechanisms, and large-scale 3D velocity structure. The absence of three-component broadband seismographic stations on the periphery of the LVB limited resolution of the characteristics of LVB boundary structure and precluded absolute amplitude calibration of LVB responses.

The 3D velocity model developed here provides a basis to use 3D finite-difference methods to synthesize strong ground motions at Jackson Lake Dam. It would be prudent to investigate the significance of several aspects of the 3D model on ground motion predictions at the dam. Modeling of broadband site-response recordings of earthquakes located east of the dam would help constrain the extent and velocity structure of the eastern limits of the LVB. Longer duration broadband site response and seismographic network monitoring would likely provide larger-magnitude earthquake recordings with sufficient signal-to-noise properties to allow 3D (instead of 2D) finite-difference seismogram modeling of LVB structure for frequencies on the order of 1 Hz.

This section has focused on the 3D velocity structure of the Jackson Hole LVB and seismic responses at the ~1 km/s near-surface S-wave velocity station JLDW, located just south of

Jackson Lake Dam. A portion of the dam is located on a very-low-velocity (VLV) glacial scour basin, with near-surface S-wave velocities < 100 m/s. The next Section focuses on empirical and synthetic seismogram analyses of the seismic responses of the VLV glacial scour basin and the reference rock station JLDW.

5.0 SITE RESPONSE

Bedrock ground motions propagating from the Teton fault will be modified by the soil column underlying much of Jackson Lake Dam. Recordings of strong ground shaking at the dam that would be needed to directly estimate this effect do not exist. As a practical matter, since nearby large earthquakes occur infrequently, only the weak-motion recordings from smaller, more frequently occurring earthquakes are available. We use this information, in conjunction with the material properties of the soil column (including drill-hole logs and seismic velocity profiles), to predict how these materials are likely to behave during M ~7 earthquakes on the Teton fault to develop realistic input motions for use in non-linear soil response models of strong ground shaking. The theoretical predictions are constrained by observations from weak-motion recordings made at the dam.

5.1 Weak-Motion Site Response

This section describes measurement of the weak-motion site response at Jackson Lake Dam. Ground motions from moderate-magnitude local earthquakes were recorded by three-component broadband velocity seismometers at six locations on the dam and one location on the right abutment. Seismometers were deployed in an array along the axis of the dam, and in a linear array trending perpendicular to the dam. In order to estimate the weak-motion site response, recordings were compared to reference sites using the method of spectral ratios.

Ground motions on the north dike at stations 24+00 (JLD3, JLD4, and JLD5), 30+95 (JLD6), and 52+00 (JLD7) are amplified in the frequency range of 0.2 to 1.5 Hz, in comparison to the right abutment (JLDW). The duration of ground shaking in this frequency band is substantially prolonged. Ground motions at station 13+00 (JLD2) are not similarly amplified over this frequency range, nor are the durations appreciably prolonged. Shallow sedimentary basins can generate surface waves and converted body waves which result in this type of extended duration site response. Low-velocity fluviolacustrine sands, gravels and a northward thickening wedge of fines overlie higher-velocity glacial drift and gravels below the north dike (for stations greater than 14+00), which effectively produces a low-velocity sedimentary basin structure.

The amplification and prolonging of durations observed at station 24+00 (JLD3) were not observed at station 13+00 (JLD2), consistent with the higher shear-wave velocities measured in the soil column there. The transition in site response observed between stations 13+00 and 24+00 may occur close to station 14+00 based on the low shear-wave velocity observed at DH-804/805 (Sirles, 1986).

High-frequency (>1.0 Hz) ground motions recorded directly above the treated embankment foundation at station 24+00 (JLD4) are observed to be lower in amplitude than outside of the treated zone (JLD3), consistent with the higher shear-wave velocities obtained from the dynamic compaction and Soil Mix Wall (SMW) treatments (Wright, 1990). However, for frequencies below 1.0 Hz, substantial amplification and prolonging of duration are observed both inside and outside of the treated zone.

Poorly consolidated sands and gravels underlie much of the north dike of Jackson Lake Dam, and the site response to strong shaking is expected to be non-linear, in contrast to the observed weak motion response. However, both the weak and strong motion responses are influenced by the same shallow depositional basin structure underlying the dam.

While the observed weak motion site response (amplification and prolonging of duration) is consistent with that of a shallow closed basin (2-D and 3-D response), it is not easily explained by a vertically-propagating shear-wave in a horizontally stratified soil column (1-D response). The response of a one-dimensional soil column is difficult to reconcile with the observed response on the dam, which appears to be characterized by surface waves and converted body-waves.

Available computer codes for estimating non-linear site response are based on propagating an incident body wave through a 1-D soil column. These codes will tend to underestimate the observed duration of shaking at Jackson Lake Dam because they do not fully account for the 2-D and 3-D response of the local sedimentary basin (converted phases, surface waves, etc.). In order to better account for the two or three-dimensional character of the observed weak-motion site response, yet employ available one-dimensional codes for estimating non-linear site response, we have used a hybrid approach. This approach incorporates the longer durations observed in the

weak motion data to modify the input motions for use in one-dimensional nonlinear computer codes.

5.1.1 Instrumented Sites. Seven three-component, broad-band velocity seismometers were intermittently deployed at Jackson Lake Dam over a six-year period. Three to six seismometers were deployed at localities along the north dike, and one was deployed on the right abutment as a reference site. These sites are labeled JLDW, and JLD2 through JLD7 (see Figure 5 1), and are described as follows:

JLDW: Located on Huckleberry Ridge Tuff on the right abutment, about 450 ft (140 m) from the south dike (approx. Station 03+00). This site is located in an old quarry that was used to provide rip rap for the dam. The Huckleberry Ridge Tuff appears to be about 70 to 100 ft (20-30 m) thick at this locality.

JLD2: Toe of the north dike 300 ft (100 m) to the left of the concrete section at about station 13+00, near where the roadway diverges from the top of the north dike. The seismometer is about 10 feet (3 m) downstream of the downstream Soil Mix Wall (SMW). Figure 5-2 shows a cross-section of the dam near JLD2. Shear velocity profiles for the nearest drill hole pairs DH-800A/806 and DH-804/805 are shown in Figure 5-3. The profile for DH-800A/806, which has higher velocities, appears to be more representative for JLD2 because of the similarity of the observed site response to JLDW.

JLD3: Downstream from the toe of the north dike, at Station 24+00. This site is about 100 ft (30 m) downstream from the break in slope at the base of the embankment. It is located about 30 ft (10 m) away from the edge of the downstream SMW (Figure 5-2). No velocity profiles are available for JLD3-5, however the similarity of profiles at DH-804/805 and DH-807/808 (Figure 5-3) for the upper 100 feet (30 m) suggests that the velocity profile at JLD3-5 would be similar, at least for the upper 100 feet.

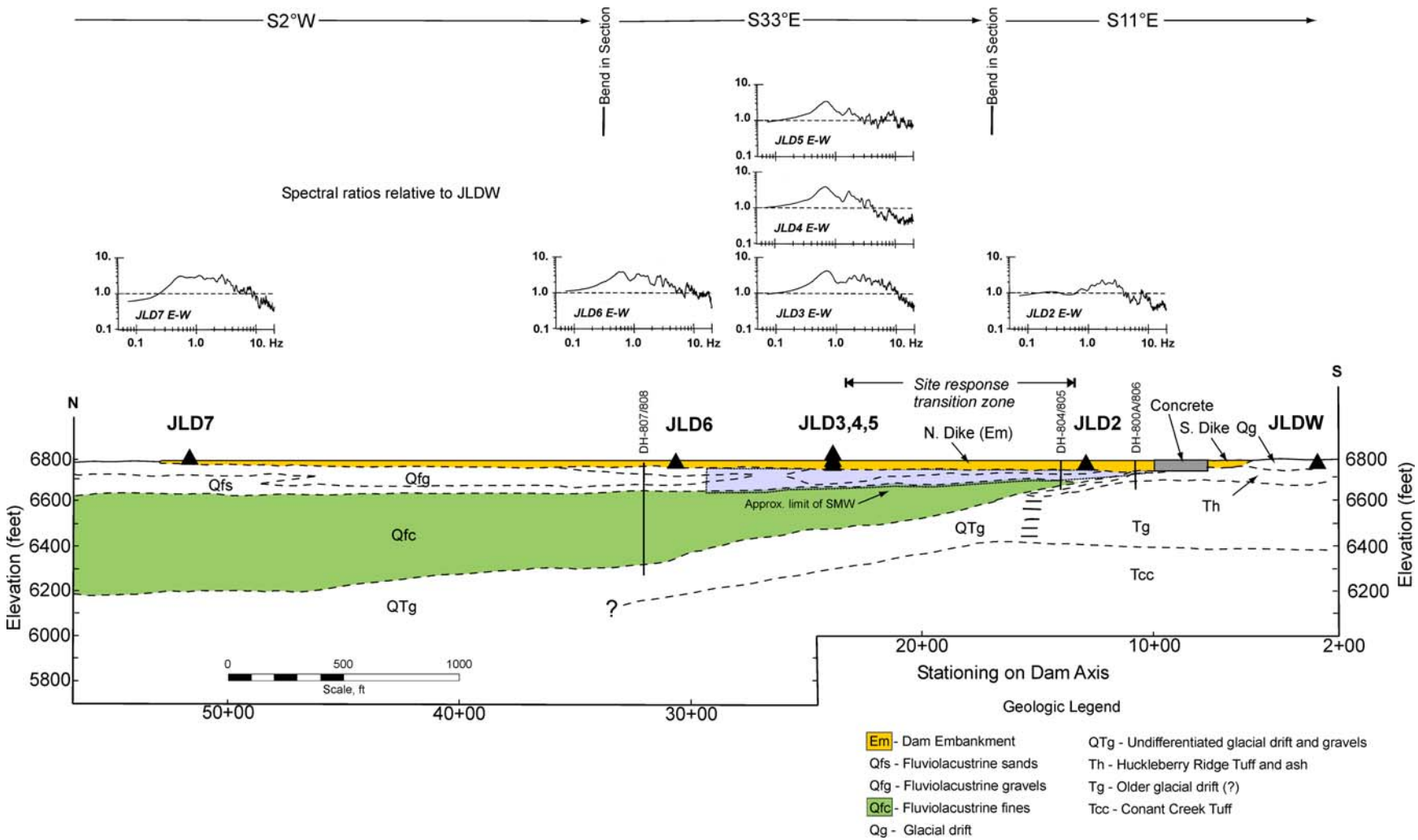

Figure 5-1: Jackson Lake Dam section showing locations of site response seismometers JLDW-JLD7. Average spectral ratios relative to JLDW measured from weak-motion data are also shown (east-west component). JLD3 through JLD7 exhibit amplification for frequencies between 0.2 and 1.0 Hz, whereas JLD2 does not. Transition between JLD2 and JLD3 response may occur as soon as DH-804/805 (stn. 14+00) since Qfs/Qfg shear-wave velocities measured there are much lower than measured at DH-800A/806, but are similar to shear velocities measured at DH-807/808. See Section 1.3.1 for additional discussion of site geology

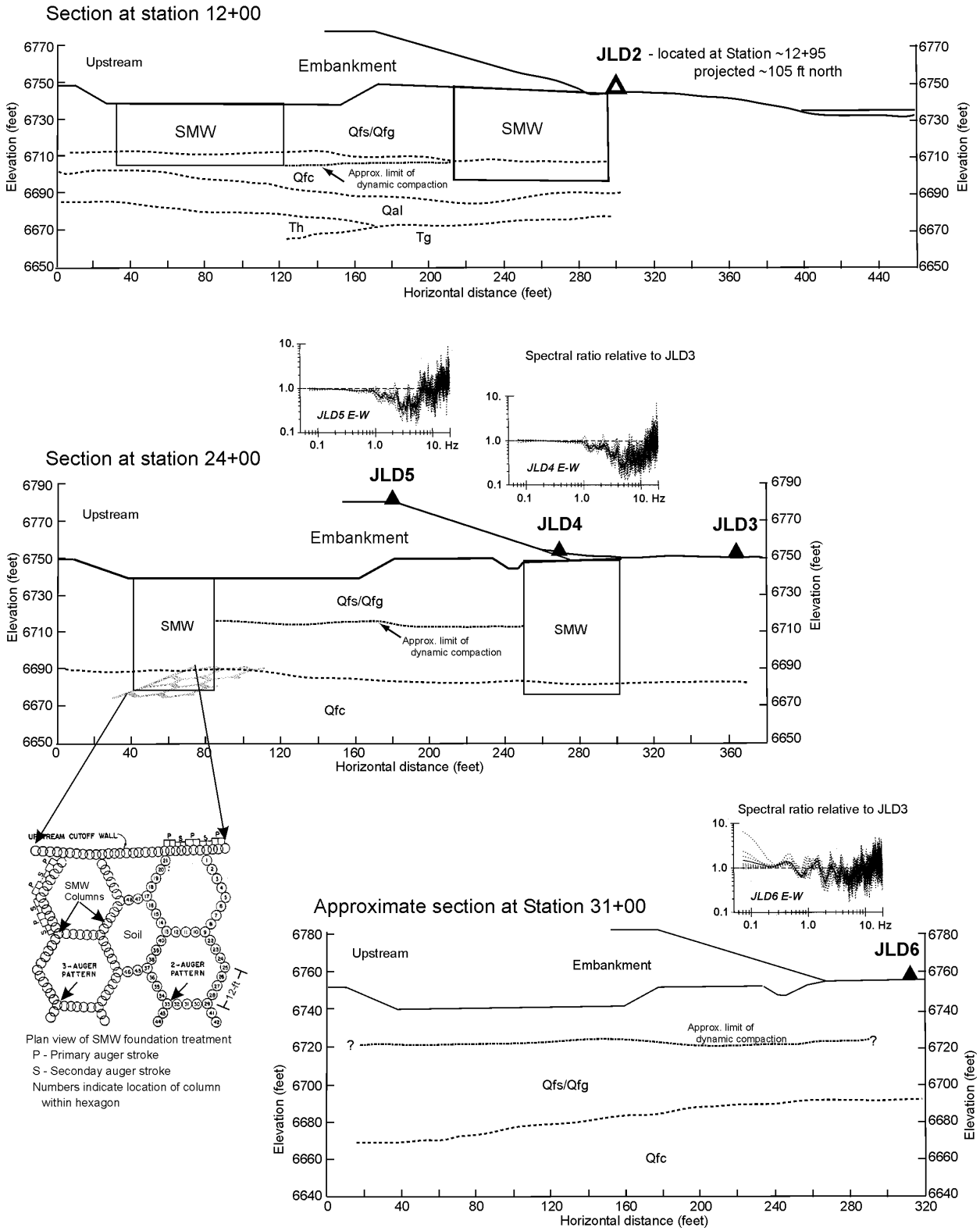

Figure 5-2: Profiles across Jackson Lake Dam at stations 12+00, 24+00, and 31+00 (Stelma, 1996) showing location of site response seismometers JLD2 through JLD6. Single-event spectral ratios relative to JLD3 are shown, indicating a de-amplification effect of foundation treatment for frequencies above 1.0 Hz.

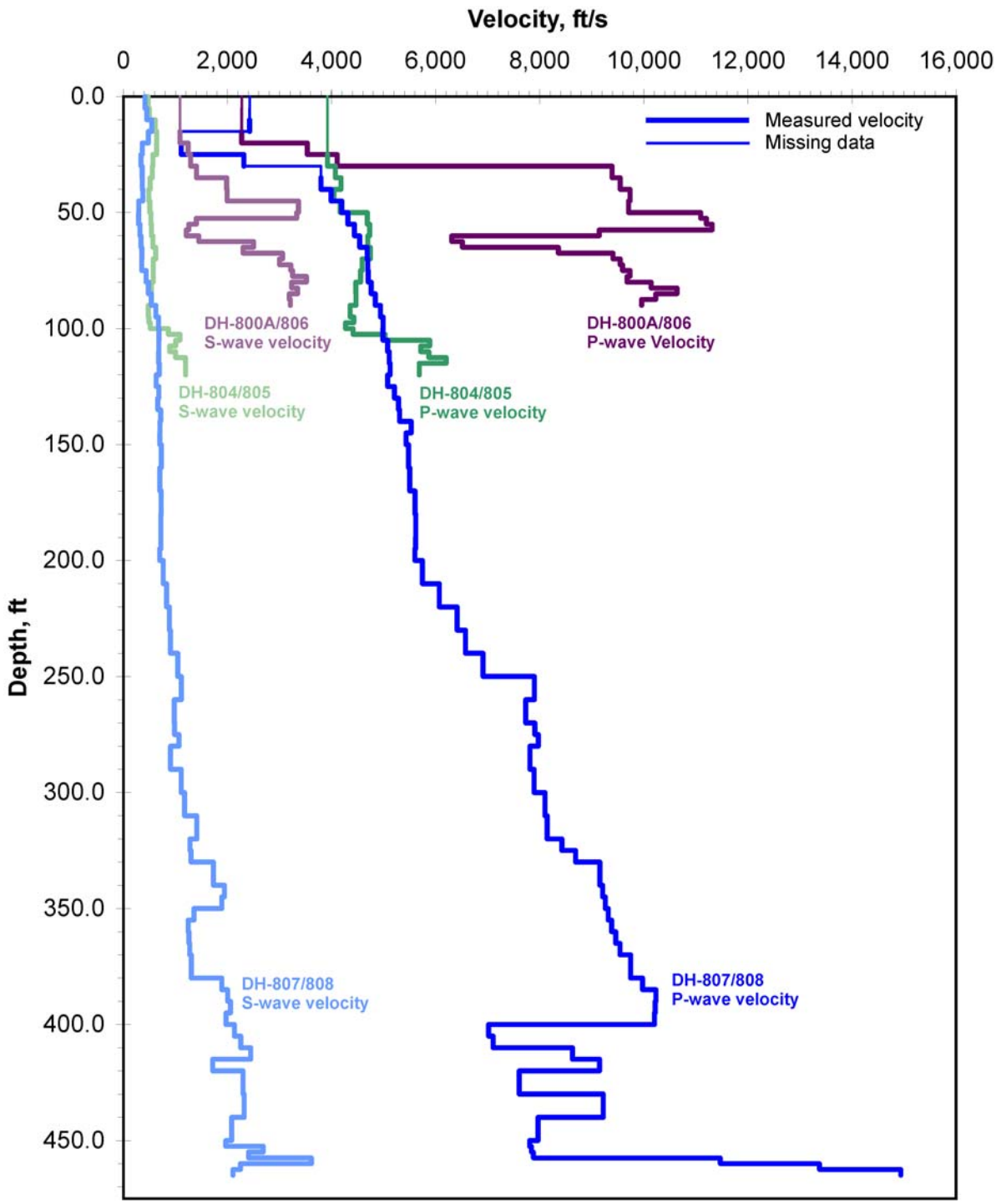

Figure 5-3: Compressional and shear wave velocity profiles for the soil column underlying the north dike of Jackson Lake Dam, as determined by crosshole velocity measurements (Sirles, 1986). See Figure 5-1 for location of drill holes. Zero-level for profiles is approximately the level of the upstream toe of the north dike. For DH-800A/806, which was drilled from the crest of the dike, the profile reported by Sirles (1986) was shifted by 25 feet. The other profiles were drilled from the upstream toe

JLD4: Toe of the north dike at Station 24+00. This site is located at the downstream edge of the embankment. The top of the downstream SMW lies a few feet below the site (Figure 5-2).

JLD5: Crest of the north dike at Station 24+00. This site is located at the downstream edge of the roadway on the crest of the dike (Figure 5-2).

JLD6: Toe of the north dike at Station 30+95. This site is located 57 ft (17 m) downstream from the embankment, about 20 ft (6 m) outside of the limit of the Stage I dynamic compaction zone (Figure 5-2). DH-807/808 is near JLD6. The velocity profile is shown in Figure 5-3.

JLD7: Toe of the north dike at Station 52+00. This site is located 5 ft (2 m) downstream from the embankment. The Stage I dynamic compaction zone extends approximately to station 52+00, and JLD7 is near the boundary, perhaps up to 10 ft (3 m) outside of the compaction zone. Groundwater encountered just below the ground surface prevented placement of the seismometer vault much beyond or downstream from this point. No shear-wave velocity profile is available at JLD7.

Initially, each seismometer (Guralp model CMG-40T) was installed below grade on a 2-ft (0.5 m) diameter plaster pad covered by a lightweight plastic vault. The pad for JLDW was cemented onto an outcrop of Huckleberry Ridge Tuff. The top of each vault was buried about 6 in (15 cm) below grade, and covered with soil for thermal stability. Conduit was extended from the seismometer vaults to nearby fiberglass instrumentation enclosures that served to house digital event recorders and other equipment.

Flooding problems during the spring snowmelt and runoff eventually required abandonment of many of the subsurface vaults. While the vaults, seismometers and cables were watertight, they were not designed for long term immersion and eventually leaked or corroded. Flowing water was observed just a few inches below the ground surface at stations JLD3, JLD6, and JLD7. These vaults flooded on several occasions, requiring uncovering, draining, cleaning, and resealing.

Because of flooding problems, the seismometers at stations JLD2, JLD3, JLD5 and JLD6 were eventually relocated above ground, to the inside of nearby fiberglass instrumentation enclosures. The data logging instrumentation was also upgraded. The above ground enclosures did not provide the thermal stability of the subsurface vaults, but the seismometers remained dry. These fiberglass enclosures also housed the strong-motion instrumentation for the dam. Each fiberglass enclosure was bolted to a 5-ft x 5-ft x 6-in concrete pad that had been poured on grade. The relocated seismometers from JLD2, JLD3, and JLD5 were placed on the concrete pads, inside of the enclosures. The subsurface vault for JLDW remained dry, and the seismometer there was not relocated. The seismometers for JLD4 and JLD7 were eventually removed because there were no adjacent strong-motion enclosures to relocate the seismometers into.

5.1.2 Initial Data Recording System. Instrumentation for the initial deployment consisted of Guralp CMG-40T seismometers attached to 16-bit digital event recorders (RefTek Model A72-06), each with an internal 1-Gbyte disk drive. Identical instrumentation was installed at seven sites (JLDW and JLD2-7). The RefTek recorders have unity and x32 gain inputs for each component, providing a nominal 120 dB dynamic range. Reference timing was obtained from GPS receivers attached to each digital event recorder. Seismometer calibration was obtained from the manufacturer. Differences in the calibrated response for all the sensors used in this study were minor, apart from an overall gain factor.

The Guralp CMG-40T sensors used in this study had a corner frequency of 30 seconds (velocity output), which allowed for adequately recording motions in the frequency range of engineering interest (0.2 to 2 Hz). However, background noise for unfiltered seismograms was typically dominated by long period (> 6 seconds) microseisms. In contrast, the predominant frequency content of small local earthquakes was typically greater than 1 Hz.

The broad-band frequency response of the seismometers thus had a significant impact on the triggering algorithm used by the RefTek digital event recorders because they lacked any provision for adequate high-pass filtering of the data stream used for event detection. Only local events producing amplitudes much greater than the background long-period microseismic noise could be consistently recorded. High-frequency local earthquake waveforms riding on top of the low-

frequency microseisms were not consistently detected, resulting in reduced efficiency of data collection.

Each of the RefTek digital event recorders at the dam operated independently of one other, and from the regional seismic network. This had a further limitation on the efficiency of event detection and recording because it prevented real-time correlation of triggers from the individual stations in declaring an event trigger. Correlation of station triggers provides a powerful tool for earthquake event detection in seismic networks. But correlation was not possible at the time of recording, and hence numerous noise triggers were recorded because noise and seismic triggers were not readily distinguished by the event recorders. The resulting low ratio of seismic triggers to noise triggers required considerable post-processing efforts to retrieve usable data.

Because seismic noise levels tended to vary substantially between the seven sites due to differences in proximity to highway traffic, wind and water noise, site conditions, etc., smaller events would rarely trigger all event recorders simultaneously. Instead, only a subset of the digital event recorders might trigger for any particular event. Operating seven separate GPS receivers for each event recorder also proved to be less reliable because of intermittent temperature related failures of some receivers. Trigger levels for the individual recorders were adjusted to capture the greatest number of local events

Approximately 60,000 individual station triggers were obtained from the seven sites at the dam, the vast majority being noise triggers unrelated to earthquakes. This volume of data required an automated method for post processing. Post-processing of the individual station triggers initially consisted of correlating similar trigger times, and combining the separate station triggers into an event trigger if at least three of the seven stations had triggered. However, it soon became apparent that most of these event triggers were also noise, albeit correlated between stations (e.g., from highway traffic). After thoroughly examining a subset of the digital event recorder triggers, it appeared that most seismic triggers recorded at the dam resulted from local earthquakes that had also been well-recorded by the regional seismic network. The seismic network was thus used to establish specific time windows for seismic events for the remainder of data recorded by the event recorders. Consequently, only triggers from stations at the dam which also correlated with the origin times of local earthquakes as determined by the regional seismic network were considered.

These potential triggers were reviewed by hand, and if confirmed to be seismic in origin, were merged into the waveform data from the seismic network for further processing. This process resulted in a data set consisting of about 270 local earthquakes with epicentral distance ranging between 5 and 110 km, and magnitude ranging between 1.2 and 3.9.

5.1.3 Upgraded Data Recording System. Technology advances allowed for site response data to be collected much more reliably and with far less effort needed for post-processing. The 16-bit RefTek digital event recorders and stand-alone Guralp sensors were replaced by 24-bit digital-output broadband seismometers (Guralp DM-24). Real-time continuous digital data telemetry via frame relay was extended to the dam. The continuous data streams from four seismometers at the dam (JLDW, JLD2, JLD3, and JLD5) were automatically merged into the data streams for the regional seismic network data acquisition system. Common time stamping was provided by a single GPS receiver located at the dam.

The upgraded instrumentation allowed for more reliable data collection because any earthquake that triggered the regional seismic network would automatically trigger simultaneous data recording from all the site-response sensors at the dam. Over the 8-month period that the upgraded instrumentation collected data, about 150 local earthquakes were recorded, with magnitude ranging between 1.0 and 3.6. This rate of data collection using the upgraded system was thus about three times greater than obtained using the RefTek system. All data were recorded on a common time base, and the seismic traces from the network stations were automatically merged with the site response stations, which greatly reduced the time needed for routine analysis tasks.

A final benefit of the improved system was to allow for long codas (> 90 seconds) to be recorded. Post-trigger waveforms on the RefTek system were limited to 60 seconds to prevent overrunning of the storage system from noise triggers. In contrast, the upgraded system allowed for improved estimates of duration and spectral amplification by recording longer codas.

5.2 Observations

From 1996 through 1999, using the initial RefTek recording system, approximately 270 local earthquakes were recorded by one or more site-response instruments. Of these earthquakes, just 6

were simultaneously recorded by all seven instruments (Table 5-1). The upgraded recording system was installed and became operational in October, 2000, and included four of the previous seven sites (JLDW, JLD2, JLD3, and JLD5). Data was acquired more rapidly and reliably, with 150 events simultaneously recorded on all four instruments over the next eight months. In June, 2001, a minor equipment failure halted the flow of data from JLD2, JLD3, and JLD5, and it was not possible to carry out the necessary repairs. However, data continued to be collected from JLDW along with the regional seismic network until December, 2002, when all recording of the seismic network ceased.

Table 5-1: RefTek Data Collection Summary

RefTeks triggered simultaneously.	Number of local earthquakes.
7	6
6+	14
5+	65
4+	136

5.2.1 Waveform Data Results. From the velocity waveforms recorded by the site response instruments, several characteristics of the weak-motion site response are apparent. Long period ground motions (1.0 to 5.0 seconds) are amplified and prolonged on the north dike of the dam, compared to bedrock motions on the right abutment.

Figure 5-4A shows a typical waveform recorded by the upgraded instrumentation, and is from an **M** 3.2 earthquake located near Driggs, Idaho (epicenter approximately 45 km west of the dam). The uncorrected, unfiltered east-west velocity waveforms (95-second time window) for JLDW, JLD2, JLD3 and JLD5 are shown in Figure 5-4A. Figure 5-4B shows the same data, but bandpass-filtered between 0.2 and 1.0 Hz. In both the unfiltered and filtered data, JLDW and JLD2 have similar waveforms, with some enrichment in high-frequency (> 1.0 Hz) ground motions at JLD2 after the direct S-wave. In contrast, ground motions at JLD3 and JLD5 have considerably more long-period (> 1 s) energy, with several phases arriving 40 seconds after the direct S-wave that considerably extend the duration of shaking. While the amplitude of long-period shaking for this event decreases by a factor of two within 10 seconds for the direct S-wave

at JLDW and JLD2, it takes nearly 50 seconds for a similar decrease to be seen at JLD3 and JLD5.

Figure 5-4C shows the instrument-corrected Fourier amplitude spectrum of east-west displacement for JLDW, and the spectral ratios (referenced to JLDW) for JLD2, JLD3, and JLD5. The methodology is described in Section 5.2.2. Spectral ratios for JLD3 and JLD5 for this event reach a value of about 5 at a frequency of 0.7 Hz; below 0.2 Hz, the ratios are near unity. The spectral ratio for JLD2 does not exhibit a similar long-period peak; the ratio is near unity for frequencies below about 1.0 Hz, and there are numerous peaks and valleys above 1.0 Hz.

Figure 5-5 shows another example, this time for an **M** 3.1 earthquake located 34 km southeast of the Jackson Lake Dam in the Gros Ventre Range. This earthquake was recorded by the initial

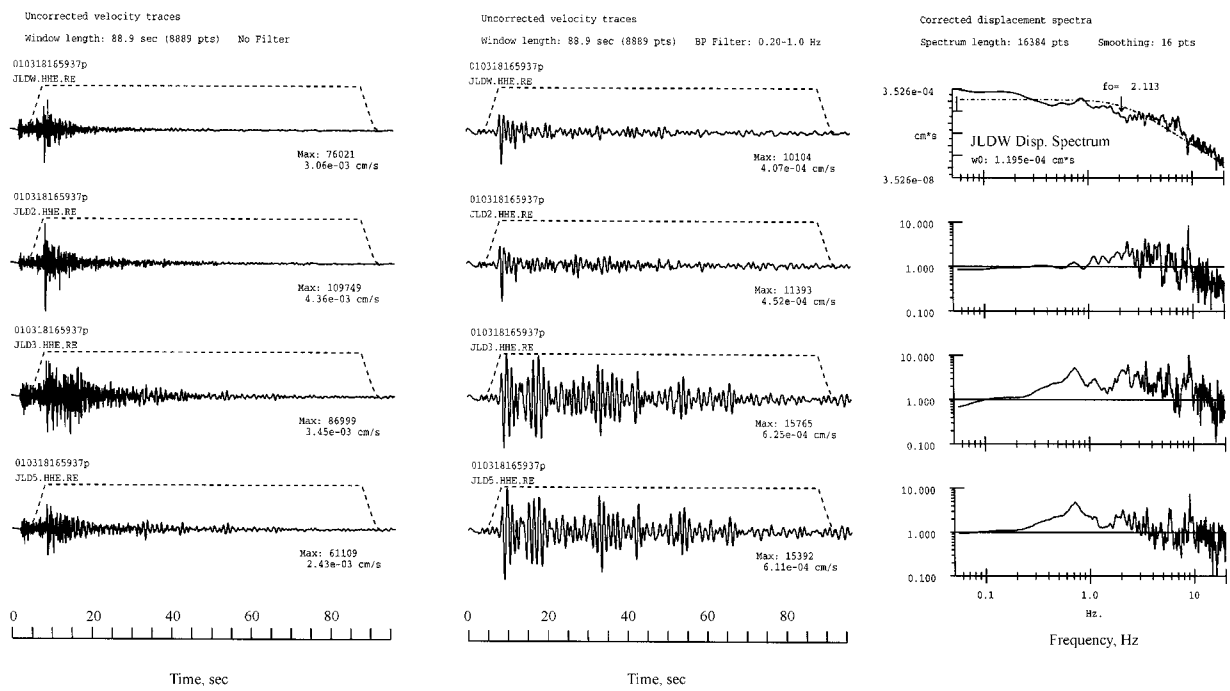

(A) Unfiltered velocity (East-West) (B) Filtered velocity: 0.2 - 1.0 Hz (C) Spectral ratio (rel. to JLDW)

Figure 5-4: M 3.2 earthquake located near Driggs Idaho. Epicentral distance is 45 km. (A) Unfiltered, uncorrected velocity; (B) Bandpass filtered 0.2 – 1.0 Hz, uncorrected velocity; (C) Corrected Fourier amplitude spectrum of displacement (JLDW), and spectral ratios referenced to JLDW. Prolonged duration of shaking for frequencies less than 1.0 Hz is clear in (B). JLD2 has a spectral ratio near unity for f < 1Hz. JLD3 and JLD5 show pronounced amplification for f < 1Hz.

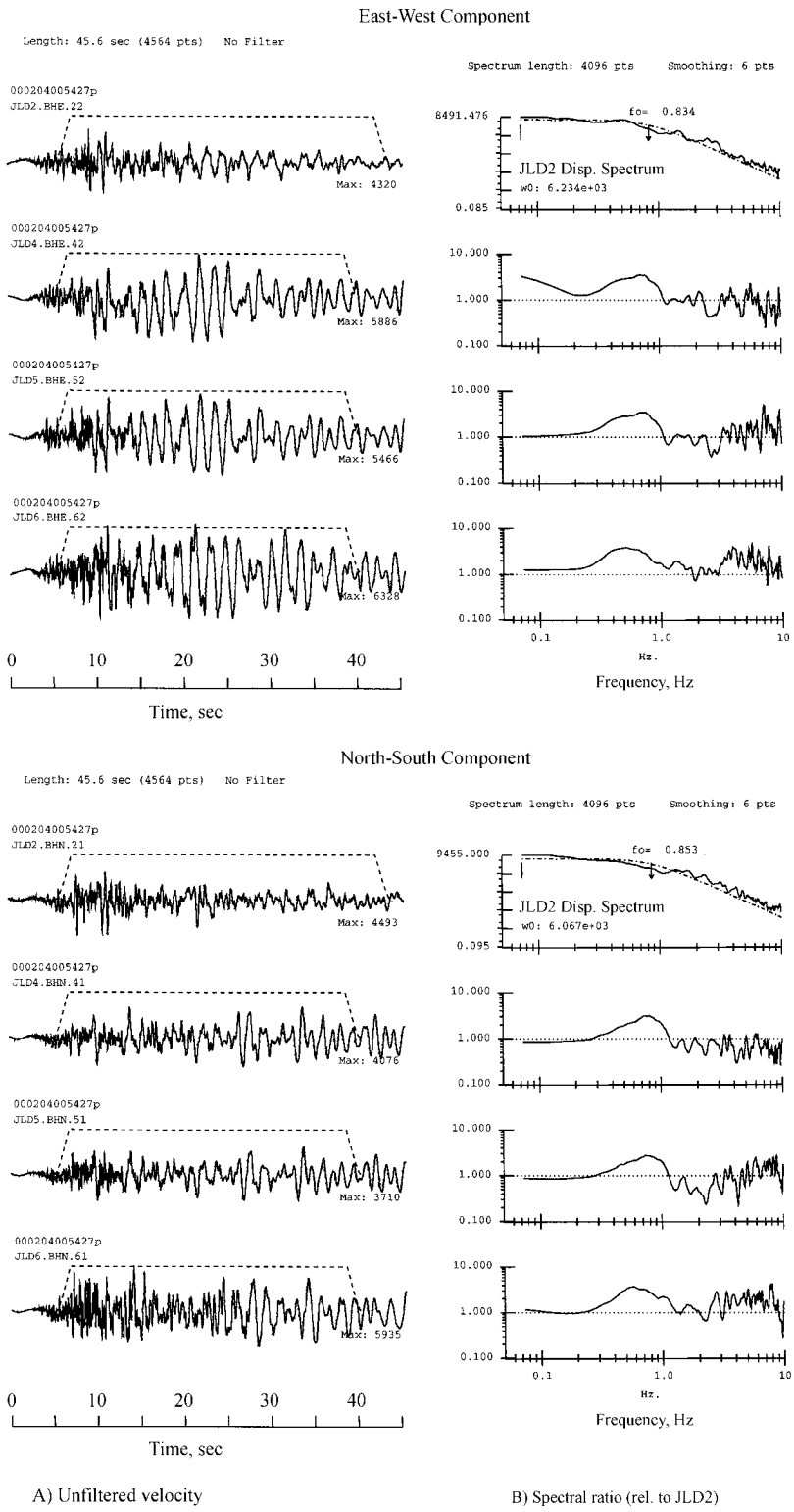

Figure 5-5: M 3.1 earthquake located 34 km southeast of the Jackson Lake Dam in the Gros Ventre Range. (A) Unfiltered velocity waveforms; (B) Corrected Fourier amplitude spectrum of displacement (JLD2), and spectral ratios referenced to JLD2. Amplification of <1.0 Hz frequencies relative to JLD2 is readily seen in the unfiltered velocity traces.

instrumentation (which relied on the RefTek digital event recorders), and has a shorter data window (40 seconds) than the first example. While the low-pass filtered direct S-wave pulse has a similar shape on JLDW, JLD2, JLD4 and JLD5, the waveforms are markedly dissimilar after the first few seconds. The amplitude actually increases about 5 seconds after the direct S arrival at JLD4 and JLD5, and large amplitude phases continue to appear up through the end of the data window some 35 seconds later. The amplitudes of the band-pass filtered seismogram at JLD4 and JLD5 are about a factor of 2 to 3 times greater than observed at JLDW or JLD2.

Prolonged duration of shaking is commonly attributed to basin response (e.g., Osborne and Taber, 2000), since a soil column by itself does not lead to appreciable increases in duration on soil sites compared to rock sites (Bommer and Martinez-Pereira, 1999).

5.2.2 Spectral Ratio Method. We used the method of spectral ratios (Borcherdt, 1970; Field et al., 1992; Field and Jacob, 1995) to evaluate weak motion site response. The Fourier amplitude spectra of the S-wave and coda at seismometer sites on the dam were compared to nearby reference sites. This method assumes that the earthquake source and propagation effects are nearly the same for all sites. This assumption appears to be satisfied since the overall dimension of the array is less than 2 km, while typical epicentral distances for the events analyzed are 20 km or more, and the source dimension of the earthquakes was small. We calculated spectral ratios separately for the vertical, north-south and east-west components of motion at each of the 6 sites on the dam (JLD2-7) referenced to the right abutment site JLDW. We also computed spectral ratios using other selected subsets of stations and reference stations (e.g., JLD3-7 referenced to JLD2, and JLD4-7 referenced to JLD3).

Fourier amplitude spectra for the direct-S and coda were calculated for each event using the following procedure. First, each data trace was de-meaned and box-car windowed, starting about 1 second before the picked direct S arrival for that station. A time-domain Hanning (cosine) taper was then applied to the initial and final 10% of the window (Bartlett, Parzan, and Blackmann-Harris tapers were also tried but made little difference). The start time of the pre-S part of the window was selected so that the taper reached a value of one by the time of the S arrival. The mean was removed (again) from the tapered trace, zero-padded to the next power of two, and Fourier transformed using an FFT. The amplitude and phase were further smoothed in the

frequency domain by using a 3 to 25-point triangular window, depending on the length of the FFT. The smoothed spectra were then corrected for instrument response, using calibration data provided by the manufacturer, converted to displacement, and corrected for relative gain between instruments. The phase spectra were also unwrapped.

The response of the Guralp sensors used throughout this study was nominally flat to velocity between 30 seconds and 50 Hz, and the data were sampled at 100 Hz, however, we have focused on a 20-second to 20 Hz bandwidth for the spectral ratios to maintain good signal to noise ratios.

Ratios of the smoothed spectra for specific events were computed using the following procedure. First, if the window length of the reference trace differed from that of the comparison trace, a further correction equal to the square-root of the ratio of the input data window lengths was applied to the Fourier amplitude spectrum. Next, the ratios of the amplitude spectra were computed, and logarithms taken. The difference between the unwrapped phases of the comparison and reference station was also computed.

Mean spectral ratios were computed by taking the mean of the logarithms of the spectral ratios for the selected events, with the vertical and two horizontal components treated separately.

We considered but did not implement the cross-spectral ratio method of Safak (1991; 1997) for computing spectral ratios. There have been questions raised about the accuracy of the cross-spectral approach because of signal-induced noise such as scattering (Field et al., 1992). While those concerns were addressed by Safak (1997), the examples presented by Safak (1997) comparing both methods indicate that differences between the two methods are likely less than other sources of uncertainty. Thus, we have chosen to use the direct method of computing spectral ratios. We also did not use the generalized inverse method of computing site response spectra (Andrews, 1986) since it also appeared to offer minimal advantage over the direct spectral ratio method (Field and Jacob, 1995).

5.2.3 Average Spectral Ratios. Station spectral ratios were obtained by averaging, for each of the three components of motion, the single-event spectral ratios. Averages for the vertical and two horizontal components of motion were determined separately for each station.

Figure 5-6 shows the spectral ratios for the east-west and north-south components of motion for the 29 events that were well recorded at JLDW through JLD7. The spectral ratios are referenced to JLDW, and both individual and average station spectra are shown. It is apparent from Figure 5-6 that stations JLD2-JLD7 are amplified by a factor of 2 to 5 at various frequency bands ranging from 0.2 to 4.0 Hz, referenced to JLDW. For both the north-south and east-west components of motion, there is a similar broad pattern of amplification. The site amplification observed at JLD2 differs from JLD3-7 in at least one important respect. At JLD2, the amplification is for frequencies above 1.0 Hz, whereas at JLD3 through JLD7, the site amplification is for frequencies above 0.2 Hz. Thus stations JLD3-7 show much more broadband amplification than does JLD2, relative to JLDW.

The spectral ratios for JLD3-JLD7 at low frequencies (0.2 to 0.1 Hz) consistently show site amplification of about a factor of 3 to 5, referenced to JLDW. In comparison, the spectral ratio for JLD2 in this frequency range is approximately unity. Thus JLD2 has relatively little long-period site amplification, with respect to JLDW, which is in contrast to the amplification observed at JLD3-7.

JLD2 is located at station 13+00, about 15 feet (5 m) downstream from the toe of the north embankment. The underlying soil column at JLD2 consists of a thin layer of fluviolacustrine fines overlying gravels and Pliocene rocks. JLD2 is also located at the edge of the SMW zone underlying the south half of the north dike. In contrast, at JLD3-7, the underlying soil column consists of about a 100-ft (30 m) thick layer of poorly consolidated sands and gravels overlying a 200 to 400 ft (60 to 120 m) thick layer of fluviolacustrine fines. While JLD4 and 5 are also within the SMW zone (see Figure 5-2), the pattern of long-period amplification persists, apparently the result of a thicker column of lake deposits and a position further within the sedimentary basin.

Figure 5-7 shows the average spectral ratios for the east-west and north-south components of motion at JLD2, JLD3 and JLD5, relative to JLDW, for 24 earthquakes recorded by the upgraded instrumentation. The upgraded system allowed for consistently recording longer time windows at 24-bit resolution, and thus provided data recorded at the best fidelity, although at a smaller number of locations. The same pattern of long-period amplification at JLD3 and JLD5 (with little

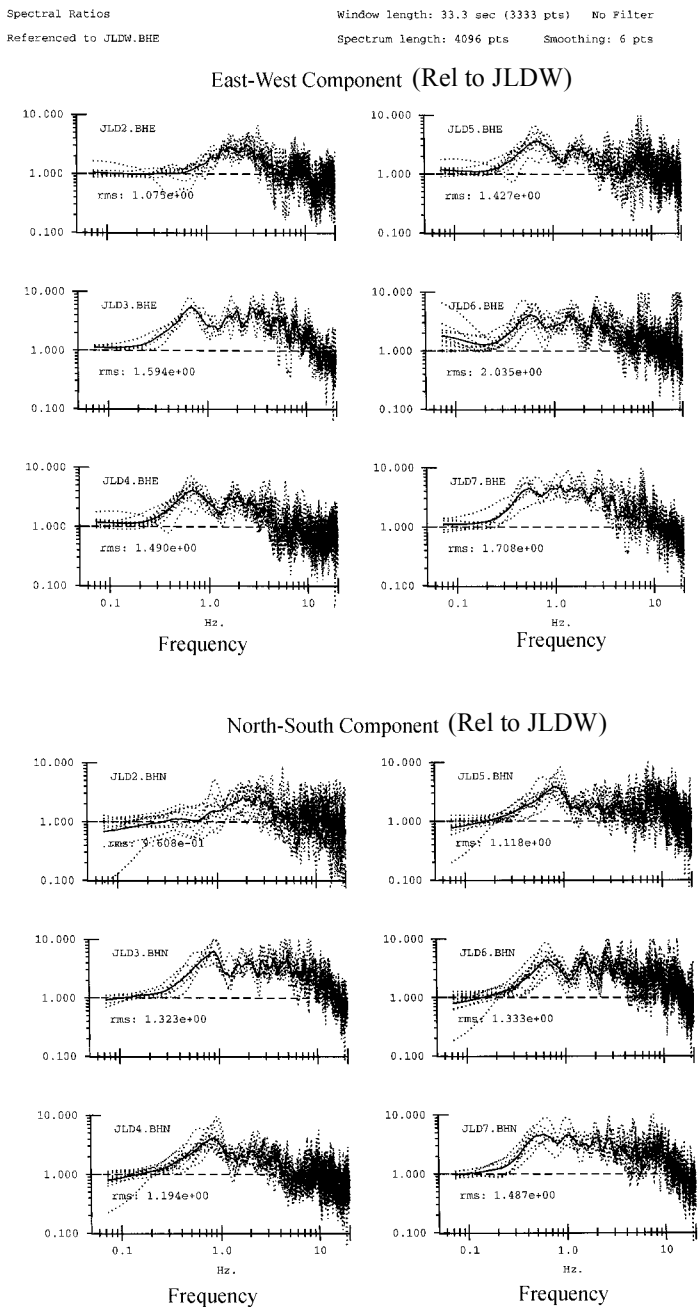

Figure 5-6: Spectral ratios relative to JLDW for 29 earthquakes recorded by the RefTek instrumentation initially deployed at seven sites (JLDW through JLD7). Solid line indicates average of individual spectral ratios; dashed lines are spectra from individual events. At low frequencies (f < 1 Hz), the observed spectral ratios are consistent between earthquakes, which occur at several different azimuths. The east-west and north-south spectral ratios are also similar for each sensor location. JLD3 through JLD7 exhibit a consistent pattern of low-frequency (0.3 to 1.0 Hz) amplification, with a spectral peak at about 0.8 Hz.

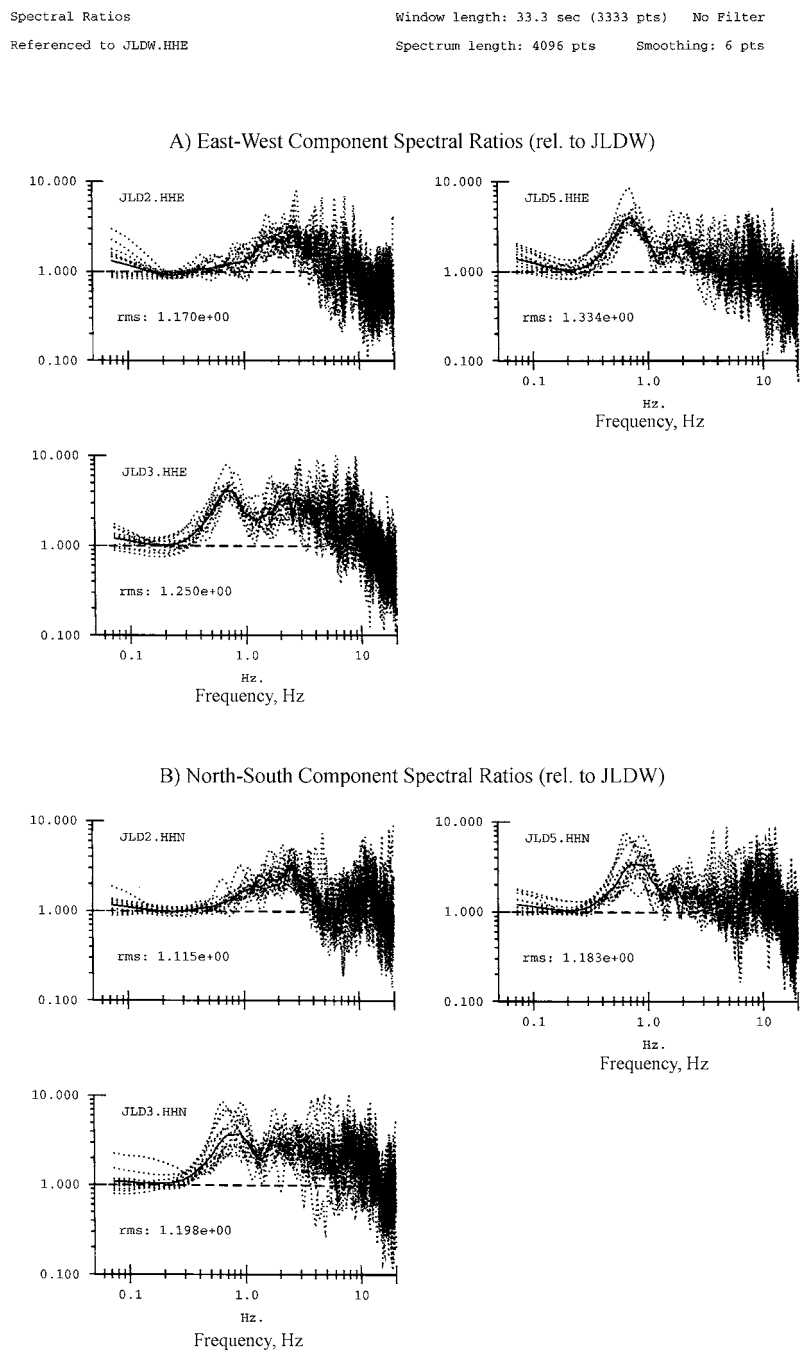

Figure 5-7: Spectral ratios relative to JLDW for 24 earthquakes recorded by the upgraded instrumentation deployed at sites JLDW, JLD2, JLD3, and JLD5. The upgraded instrumentation allowed data to be recorded with a wider dynamic range and spectral resolution than could be achieved with the RefTek instrumentation. Solid line indicates average of individual spectral ratios; dashed lines are spectra from individual events. At low frequencies ($f < 1$ Hz), spectral ratios are consistent between earthquakes, which occur over a range of azimuths and epicentral distances. As with the RefTek data, JLD3 and JLD5 exhibit low frequency amplification with respect to JLDW, whereas JLD2 does not.

or no long-period amplification at JLD2), that was seen in the earlier data is also readily apparent in the data collected by the upgraded instrumentation.

Average spectral ratios may also be used to compare the response of the five stations on the north dike (JLD3-7) that overly a 300-500 ft (90-150 m) thick column of fluviolacustrine deposits (Figure 5-1). Figure 5-8A shows spectral ratios at JLD4 through JLD7, referenced to JLD3, for the east-west component of motion. Figure 5-8B shows corresponding spectra for the north-south component of motion.

JLD3, JLD4 and JLD5 form a 177-ft (54 m) linear profile perpendicular to the north dike embankment at station 24+00 (see Figure 5-2). JLD3 is located 95 feet from the downstream edge of the north dike embankment, outside of the zone of dynamic compaction, and in other circumstances would be chosen as our "reference" soil site. JLD4 is 93 feet from JLD3, at the edge of the embankment, and overlies the downstream soil mix wall. JLD5 is 84 feet from JLD4 (177 feet from JLD3), and is at the crest of the embankment. The spectral ratios for JLD4 referenced to JLD3 show de-amplification for frequencies above 1 Hz; below 1 Hz, the spectral ratio is near unity. A similar pattern is seen for JLD5 referenced to JLD3, although the de-amplification above 1 Hz is less pronounced. The strongest de-amplification relative to JLD3 is seen at JLD4, which is consistent with the higher seismic velocities of the treated foundation (soil mix wall and dynamic compaction). A more limited de-amplification at JLD5 is consistent with the higher seismic velocities in the embankment and in the underlying dynamically compacted foundation, relative to JLD3, and the amplification typically observed at the crest of dams relative to the toe due to simple geometric focusing. However, at longer periods (>1 second), the response is similar at all three sites (JLD3, 4 and 5).

JLD6 is 20 feet (6 m) outside of the zone of dynamic compaction, and 57 feet (17 m) from the downstream edge of the embankment at station 30+95. The soil mix walls do not extend this far north, stopping at about station 29+00. JLD7 is 5 feet from the downstream edge of the embankment at station 52+00, and is located about 10 feet outside of the zone of dynamic compaction. Relative to JLD3, there is some long-period amplification at JLD6, and alternating amplification and de-amplification at frequencies above 1 Hz. JLD7 shows even greater long-

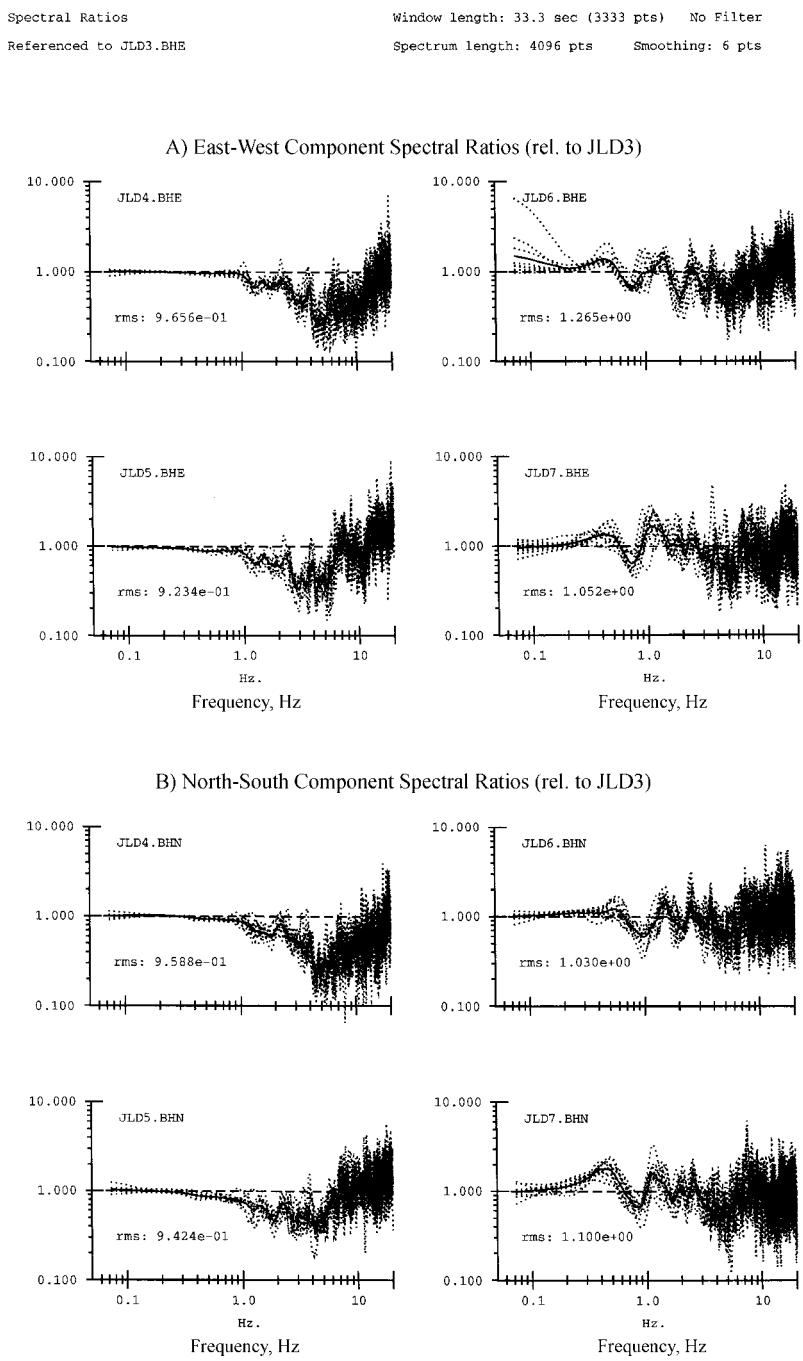

Figure 5-8: Spectral ratios relative to JLD3 for 29 earthquakes recorded by the initial deployment of RefTek instruments. Solid line indicates the average of individual spectral ratios. JLD4 and JLD5 exhibit a de-amplification effect relative to JLD3 for frequencies between about 1 and 10 Hz, which is consistent with the higher velocities achieved through foundation treatment (dynamic compaction and the Soil Mix Wall). Below 1 Hz, little meaningful difference is seen; each of stations JLD3, JLD4 JLD5 are amplified relative to JLDW.

period amplification than JLD6, relative to JLD3. This pattern is consistent with a deepening soil column at JLD6 and JLD7 relative to JLD3 (Figure 5-1).

Average spectral ratios relative to JLDW for all data recorded by the RefTek instrumentation are shown in Figure 5-9 and Figure 5-10. Stations JLD3 through JLD7 consistently show a spectral ratio amplification in the frequency range of 0.2 to 1.0 Hz, referenced to JLDW. In contrast, JLD2 shows no such long-period amplification.

There is a considerable difference in site amplification observed between JLD2 and JLD3-5, which are located about 1100 ft (340 m) apart, along the axis of the north dike. This difference has the potential to lead to significant axial strains between these two points. The magnitude of the strain will depend on the sharpness of the transition. From JLD3-5 to JLD7, which are 2800 ft (850 m) apart, there is relatively little difference in site response; long-period amplification is observed even though the soil column is deepening. JLD6, midway between JLD3-5 and JLD7, shows the same pattern. Thus there appears to be a point between JLD2 and JLD3-5 at which a sharp rather than gradual transition to long-period amplification may take place. It is not clear from the site-response data where the precise position of this transition is located, however shear wave profiles (Figure 5-3) suggest the transition may be closer to station 14+00.

5.3 Weak-Motion Impulse Response Functions

The previous sections provide a qualitative description of the observed weak-motion site response at Jackson Lake Dam. Key observations are the presence of substantial long-period amplification and prolonged duration of shaking beyond some transition point located between JLD2 and JLD3-5; minimal long-period amplification at JLD2 referenced to JLDW; and, high-frequency de-amplification at JLD4 and JLD5 referenced to JLD3.

To apply these findings to simulations of strong ground shaking from the Teton Fault, we have generated weak-motion site impulse response functions at stations 13+00 (JLD2) and 24+00 (JLD3) that are based on the observed average amplitude spectral ratio and the relative phase for average or specific earthquakes. For the amplitude part of the impulse response, we use the average spectral ratios described in the previous section (Figure 5-10). For the phase response, we selected several representative events and extracted the single-event relative phase response (the

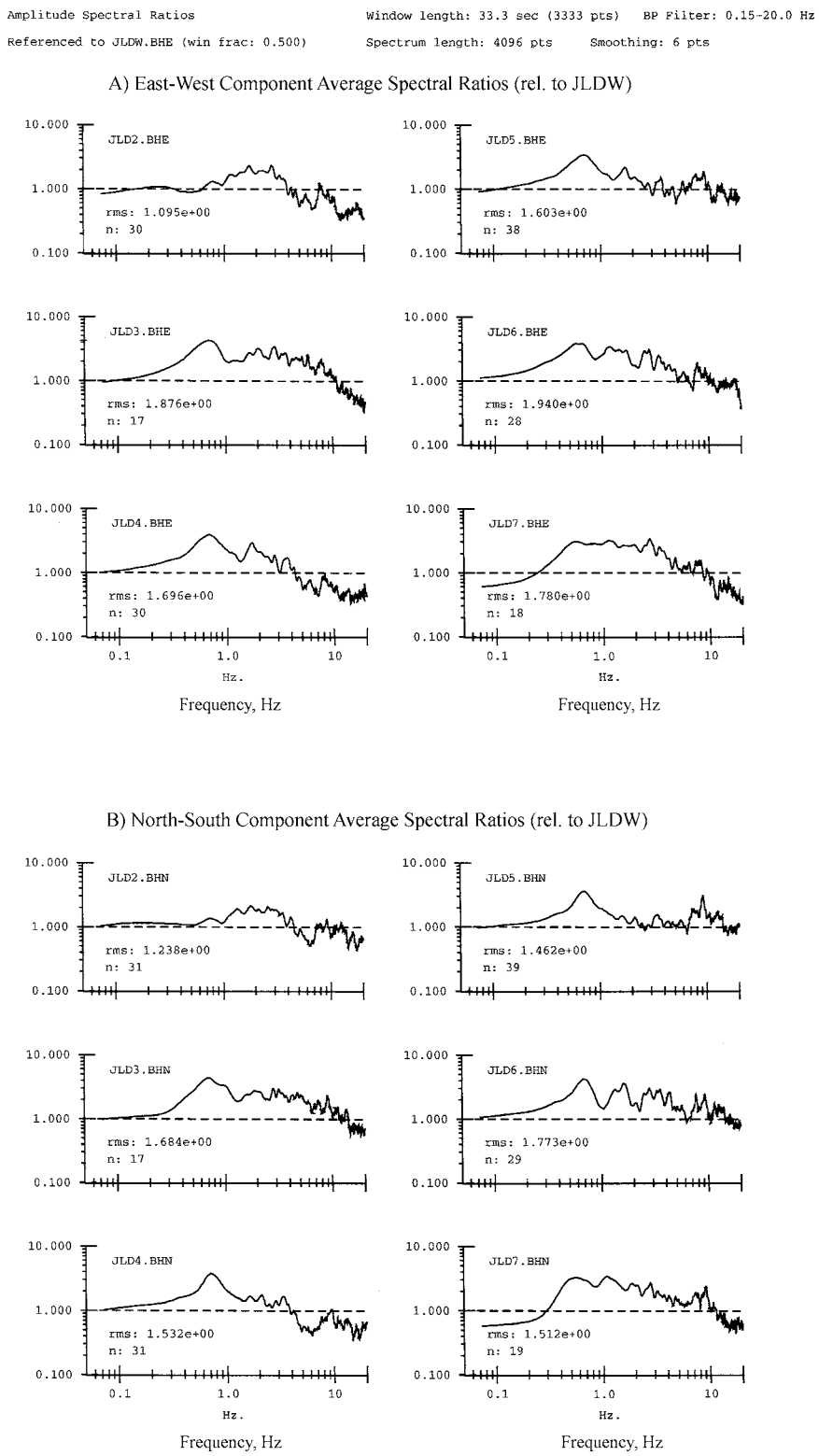

Figure 5-9: Average spectral ratios relative to JLDW for 29 earthquakes recorded by the initial deployment of RefTek instruments.

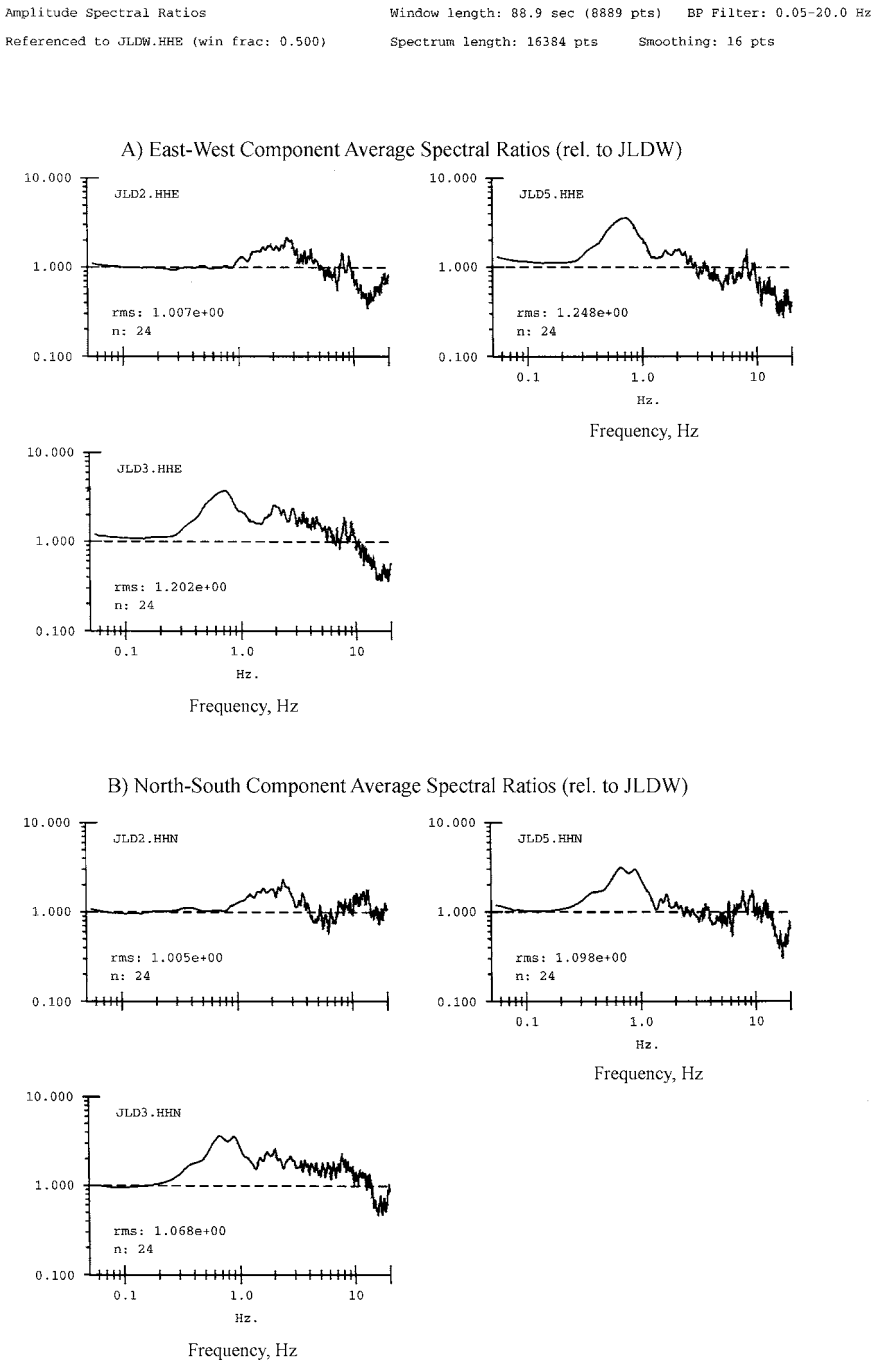

Figure 5-10: Average spectral ratios relative to JLDW for 29 earthquakes recorded by the upgraded instrumentation deployed at stations JLDW, JLD2, JLD3 and JLD5. JLD3 (station 24+00) exhibits broadband (0.2 to 10 Hz) amplification relative to the bedrock reference site JLDW, with the greatest amplification occurring in the 0.3 to 1.0 Hz range. JLD2 exhibits limited amplification between 1 and 4 Hz relative to JLDW, but the low-frequency (< 1.0 Hz) spectral ratio is near unity. The spectral ratio estimates from this data set are preferred over those obtained using the RefTek instrumentation because of the greater recording fidelity achieved. These spectral ratio estimates are therefore assumed to best characterize weak-motion site response on the north dike from the available data set.

difference in phase between JLDW and JLD2 or JLD3), and also the average relative phase response. The generated weak-motion impulse response functions are neither causal nor minimum phase.

For this study, the relative phase spectrum is used primarily as a means to generate a suitable weak-motion impulse response function, and little physical meaning is attached. Given the 1000-ft (300 m) separation between JLDW and JLD2, and the 2400-ft (730 m) separation between JLDW and JLD3, the observed waveforms are expected to exhibit little coherency at high frequencies. The only correction made for propagation delay for phases traveling between the two stations was to line up the time windows on the picked S-wave arrival time at each site. Because the relative phases exhibit a common trend only for the lowest frequencies, we did not attach much significance to the average of the phase responses from multiple events. The average phase response tended towards an arbitrary value for frequencies greater than about 1 Hz, which results in a tendency to compress the impulse response function in time (with corresponding magnification of amplitude). This effect is greater at JLD3, where substantial low-frequency energy arrives in later phases, than at JLD2.

5.3.1 Impulse Response Functions for JLD2 and JLD3. Figure 5-11A shows the unwrapped relative phase spectra for seven selected events recorded at JLD2, as well as the average relative phase spectrum for all 24 events used to compute the amplitude spectral ratio. Figure 5-11B shows the corresponding impulse response functions generated by using the average phase, and several of the single-event phases. The impulse response function using the average phase is more compressed in time than if single-event phases are used.

By construction, the amplitude spectral content of the impulse response functions exactly matches the observed spectral ratios; only the phase is variable. In choosing a specific relative phase spectra to develop impulse response functions, our goal is to produce qualitative agreement with the characteristics observed in the weak-motion data. For JLD2, the average phase provides a slight amplification and minimal prolonging of duration, which is observed in the weak-motion waveforms. Figure 5-12 shows the result of convolving the average and single-event impulse response functions with the Tabas E-W record (discussed in Section 6.6). For acceleration, each of the impulse functions reproduces the slight amplification observed in the weak-motion data,

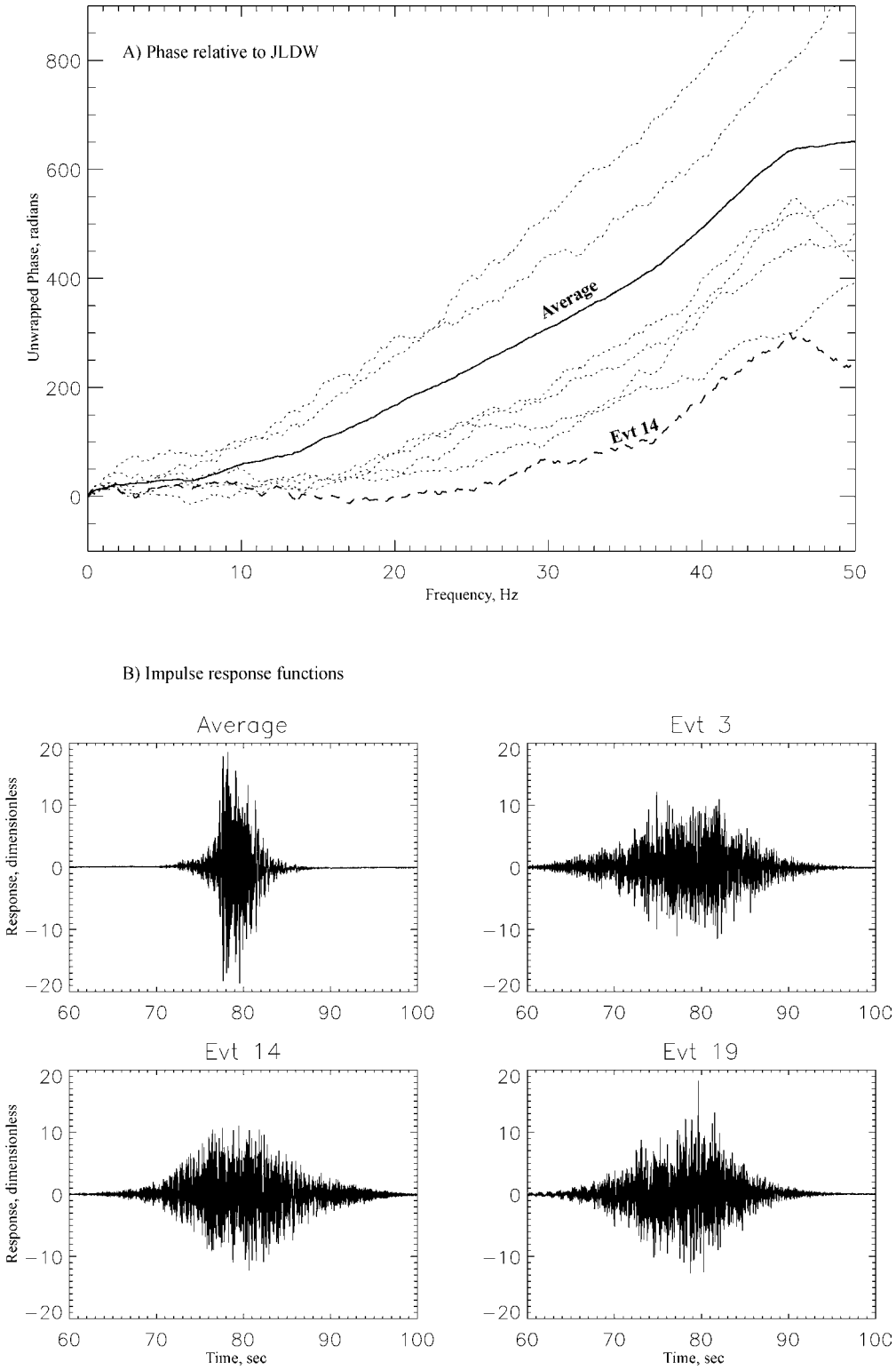

Figure 5-11: (A) Unwrapped phase at JLD2 relative to JLDW for 7 representative earthquakes. (B) Impulse response functions constructed from the average spectral ratio, and from individual or average relative phases. The non-causal part of the response is indicated by points prior to 81.92 seconds.

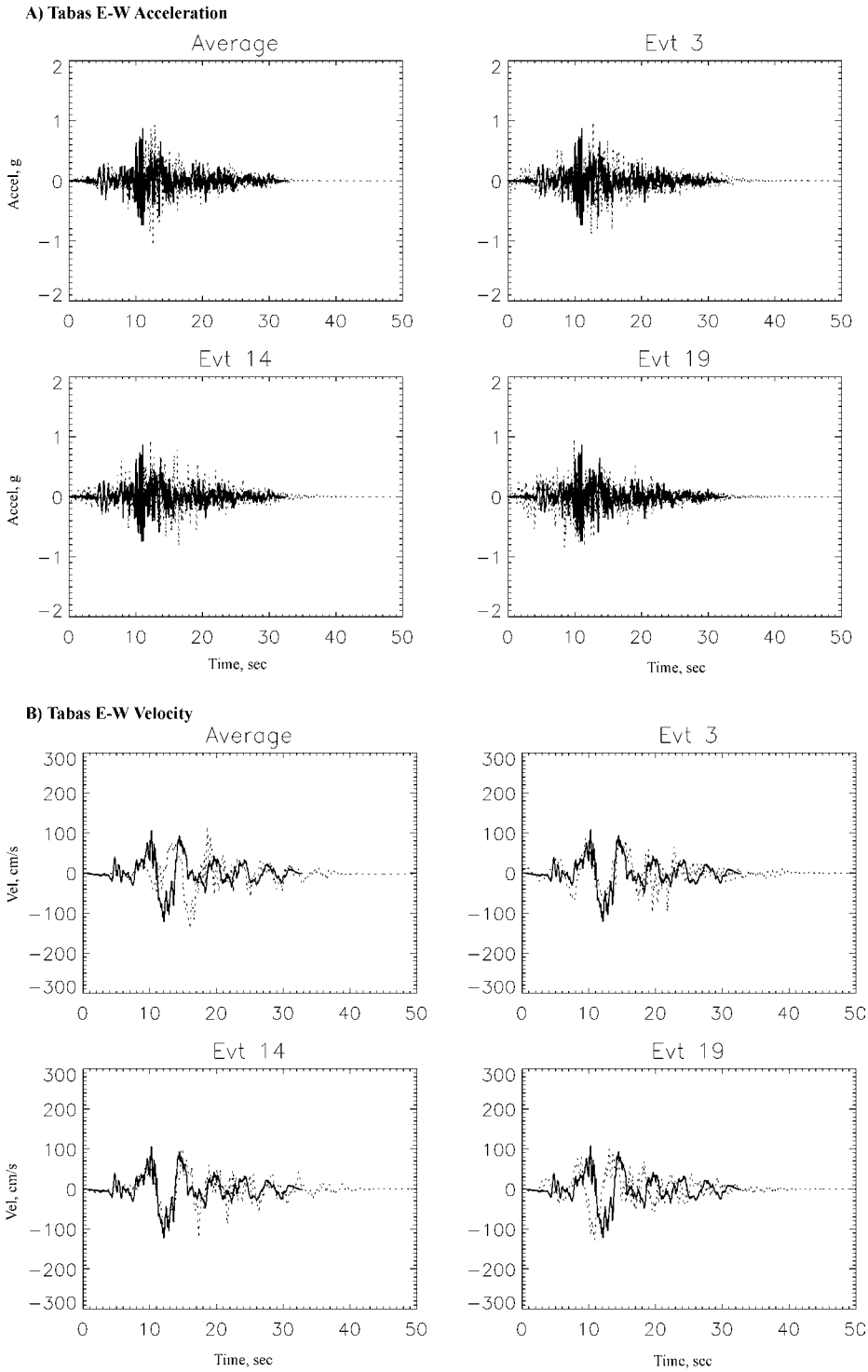

Figure 5-12: Tabas E-W acceleration and velocity waveforms (solid lines) convolved with several realizations of the JLD2 weak-motion impulse response functions (dashed lines). For acceleration, each of the impulse functions reproduces the slight amplification observed in the weak-motion data, with minimal prolonging of duration. In contrast, the single-event impulse-response functions tend to slightly increase the duration of the velocity waveform. The impulse response function based on the average phase is therefore selected for JLD2

with minimal prolonging of duration. In contrast, the single-event impulse-response functions tend to slightly increase the duration of the velocity waveform. We have therefore selected the impulse response function determined from the average relative phase spectra to best represent JLD2.

The main characteristics observed in the site response data for JLD3 are amplification and prolonging of durations for frequencies between 0.2 and 1 Hz. Figure 5-13A shows the unwrapped relative phase spectra for the same set of seven events, but recorded at JLD3. Figure 5-13B shows the corresponding impulse response functions generated by using the average phase and three single-event phases. Again, our goal is to select a phase that produces the best qualitative agreement with the observed weak motion data. For JLD3, the resulting impulse response function needs to amplify and extended the duration of the low-frequency components of the convolved input waveform. For JLD3, the average phase produces an impulse response function that is too compressed in time relative to those determined for the single-event phases, and relative to the observed data. The relative phase spectrum from the earthquake labeled "Evt 14" appears to provide better qualitative agreement with the observed weak motion data. Figure 5-14 shows the result of convolving the average and single-event impulse response functions determined for JLD3 with the Tabas E-W record. For acceleration, the average phase produces the strongest amplification but little prolonging of duration. In contrast, the single-event impulse-response function for Evt-14 produced the greatest increase in the duration of the velocity waveform. The relative phase spectrum for this event is labeled on Figure 5-13, and is seen to have the greatest delay of the phases considered. We have therefore selected the impulse response function determined from the relative phase spectra from Event 14 to best represent JLD3.

5.3.2 Bedrock Motions with Weak-Motion Site Response Included. Figure 5-15 shows the result of convolving selected design bedrock ground motions with the weak-motion impulse response function for JLD2. The three bedrock motions (described in Chapter 6) represent a range of realizations for the Teton Fault design ground motions. As with the observed weak-motion data, the ground motions convolved with the JLD2 site response have essentially the same duration as the input motions, and exhibit only minor high-frequency amplification.

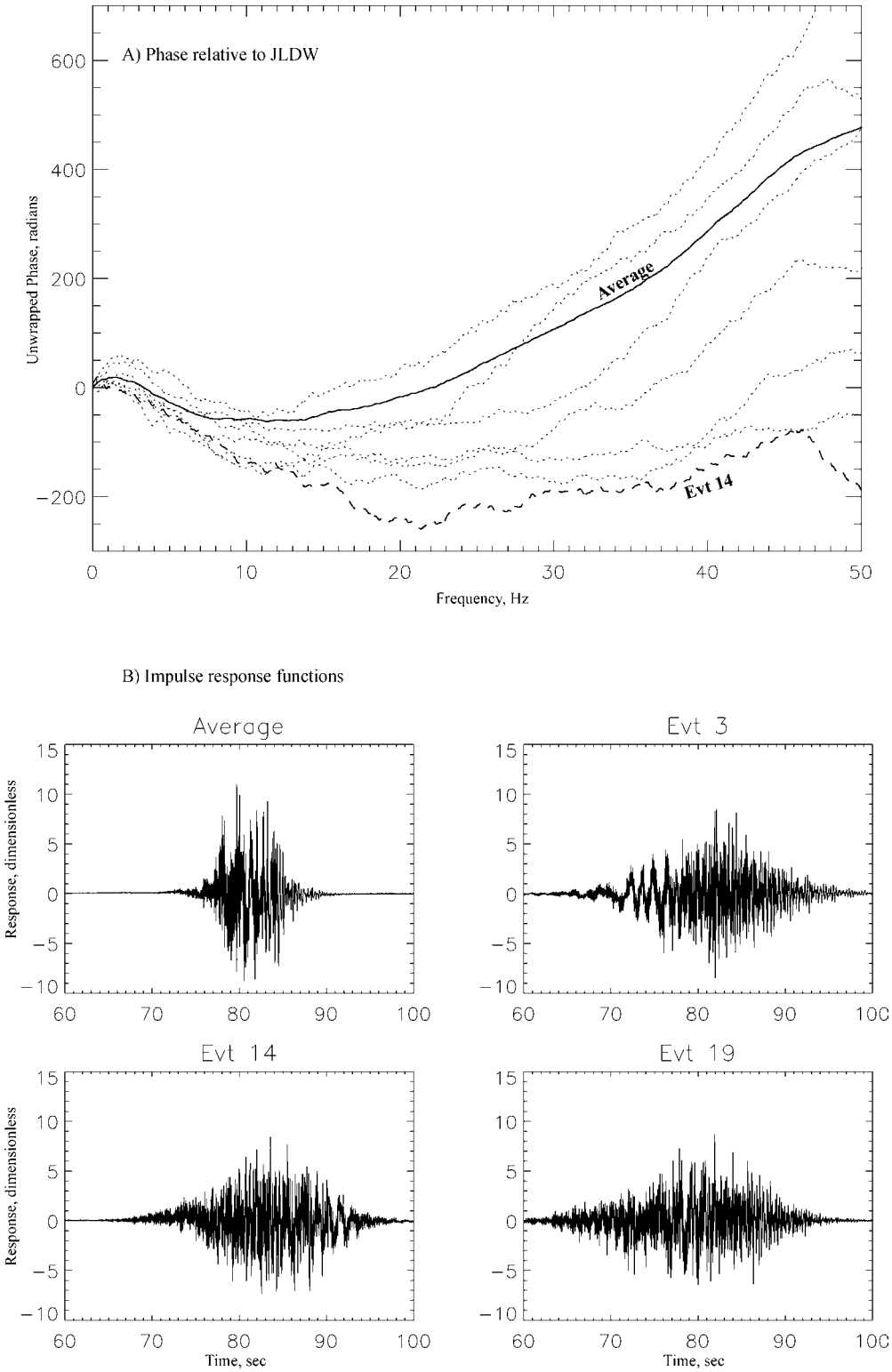

Figure 5-13: (A) Unwrapped phase at JLD3 relative to JLDW for 7 representative earthquakes. (B) Impulse response functions constructed from the average spectral ratio, and from individual or average relative phases. The non-causal part of the response is indicated by points prior to 81.92 seconds.

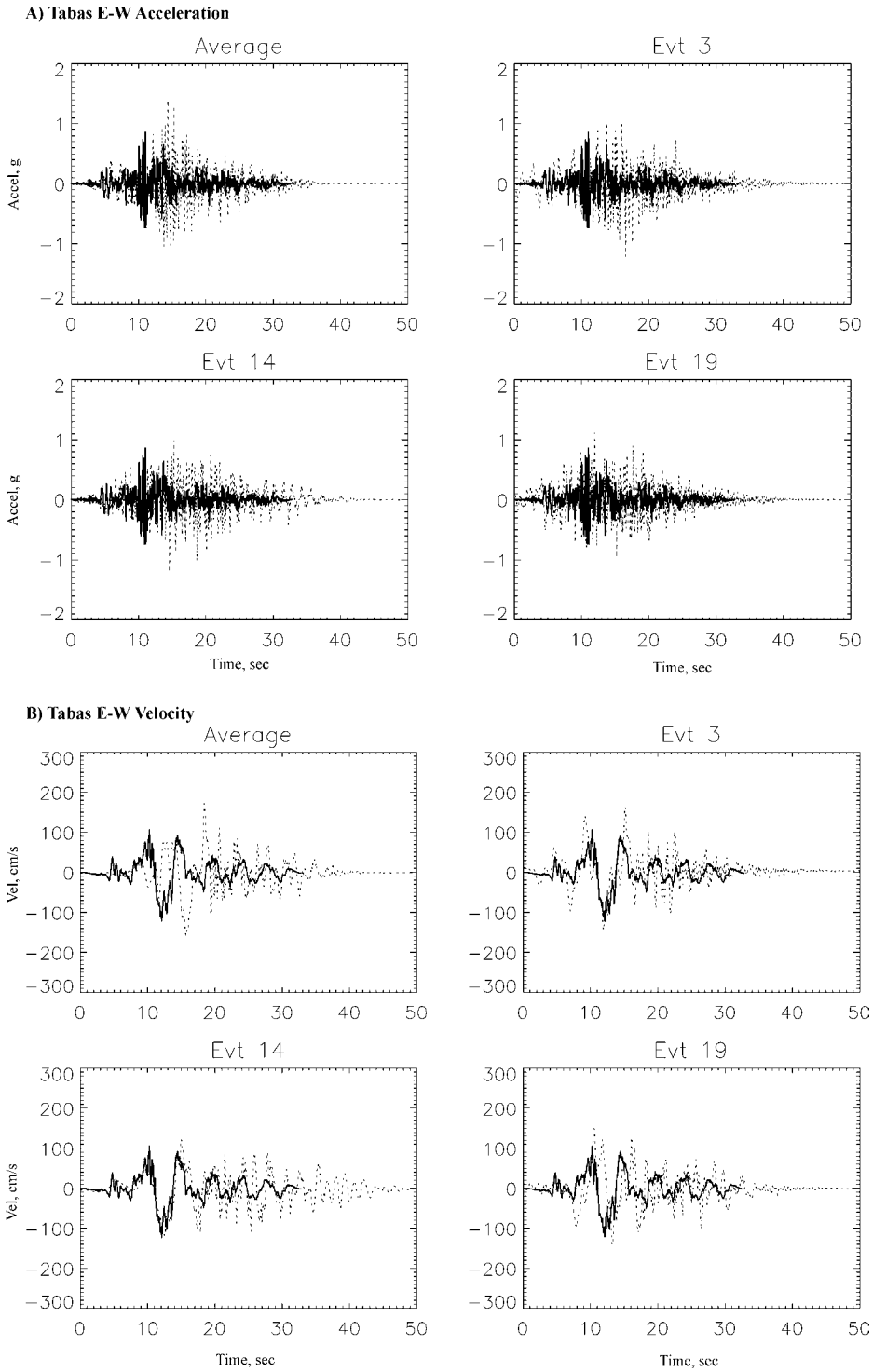

Figure 5-14: Tabas E-W acceleration and velocity waveforms (solid) convolved with several realizations of the JLD3 weak-motion impulse response functions (dashed). As discussed in the text, the impulse response constructed from the average of the relative phase spectra underpredicts duration and overpredicts amplification. The impulse response function obtained from the relative phase spectrum for Event 14 provides better agreement with the prolonged durations observed in the weak-motion data

The ground motion simulations for JLD2 shown in Figure 5-15 are intended to be used as design ground motions at stations 12+00 and less. Significant non-linear behavior of the soils at JLD2 is not expected. The underlying soil column consists of glacial drift, gravels, tuffs and ash which have much higher shear wave velocities than are seen in the fluviolacustrine sands and gravels further out on the north dike. The observed weak-motion response at JLD2 is very similar to the bedrock reference site JLDW. Thus the simulations presented in Figure 5-15 can be used for design loadings at stations 12+00 and less, including the concrete section and south dike.

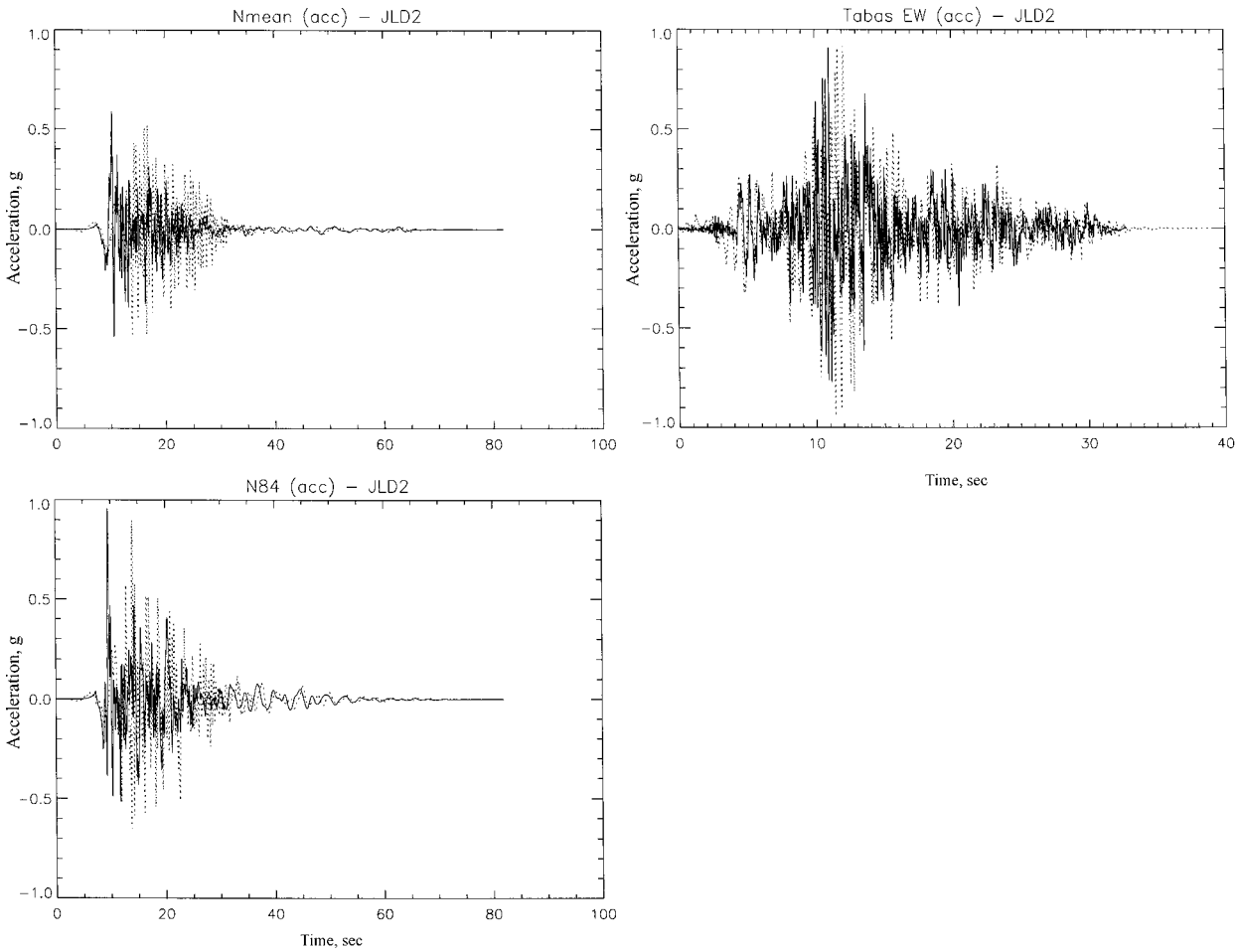

Figure 5-15: Bedrock input motions (solid lines), and bedrock motions convolved with JLD2 weak-motion response (dotted lines). Because the soil column underlying JLD2 appears to consist mostly of glacial drift and gravels, has reasonably high shear wave velocities, and has a low-frequency response that is not amplified relative to the bedrock reference site JLDW, a substantial nonlinear response to strong shaking is not expected. The bedrock motions convolved with the JLD2 site response should be used for design loadings at stations 13+00 and less.

Figure 5-16 shows the result of convolving the selected design bedrock motions with the JLD3 weak-motion site response. Velocity waveforms are shown. As expected, the convolved ground motions reproduce the longer durations observed in the weak motion data (though the amount depends on the input motion). By construction, the Fourier amplitude spectra of the convolved motions are simply the product of the input motion amplitude spectra and the average spectral ratio for JLD3 relative to JLDW. While the convolved waveforms shown on Figure 5-16 reproduce the observed effect of prolonged durations, the full non-linear site response needed for engineering analysis is not included.

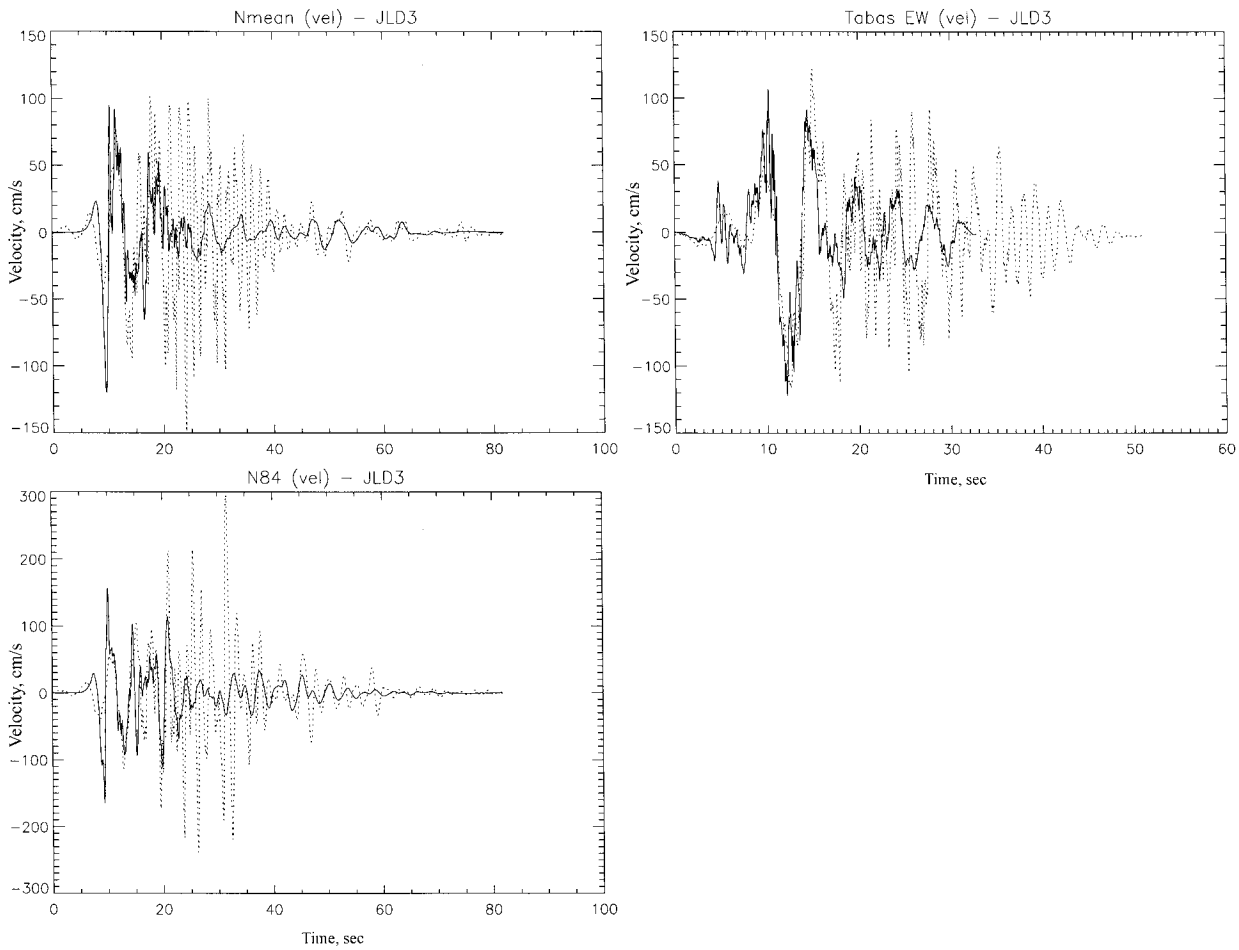

Figure 5-16: Bedrock input motions (solid lines), and bedrock motions convolved with JLD3 weak-motion response (dotted lines). The weak-motion response does not include the non-linear soil response expected during strong ground shaking

When subjected to strong ground motions, the soils at station 24+00 (JLD3) are expected to behave non-linearly. Poorly consolidated, potentially liquefiable fluviolacustrine sands and gravels with shear velocities as low as 300 ft/s (100 m/s) underlie much of the north dike. The bedrock motions convolved with the JLD3 weak-motion response do not account for non-linear soil behavior, which must be accounted for separately. The observed site response at JLD3 is consistent with the 2-D and 3-D response of a sedimentary basin, and likely results from the generation of surface waves, converted phases, and interface waves. These effects are not accounted for by 1-D models. However, available computer codes for estimating non-linear soil behavior are based on propagating an incident body wave (typically a horizontally polarized S wave) through a 1-D soil column. In order to permit use of 1-D non-linear soil response computer codes, while preserving the observed 2-D and 3-D effects of prolonged duration and long-period amplification, we will modify (in subsequent sections) the weak-motion impulse response for JLD3 to approximately account for the linear response of the soil column from a reference depth, and the free surface effect. The modified impulse response is then convolved with the simulated bedrock motions and input to the non-linear soil response codes at the selected reference depth. There is considerable uncertainty in this method because the reduction of the convolved surface motions to a reference depth cannot accurately account for the depth dependency of surface waves and converted phases.

As discussed in section 5.2, we don't know the precise location of the transition in site response observed between stations 13+00 (JLD2) and 24+00 (JLD3-5). Based on drilling and geophysical logging, we would expect the transition to be near 14+00, although this is not certain. Thus engineering analyses for stations at 14+00 or greater should use the JLD3 response, and stations less than 14+00 should use the JLD2 response.

We have constructed velocity and acceleration response spectra for each of the selected bedrock motions and for the motions convolved with the weak motion site response. These provide a further indication of the effects of the weak motion site response. Figure 5-17 shows the bedrock input motions convolved with the JLD2 site response. Absolute acceleration response spectra are provided. These response spectra for JLD2 may be used for engineering analyses at stations 13+00 or less, including the concrete interface structure, spillway and bridge.

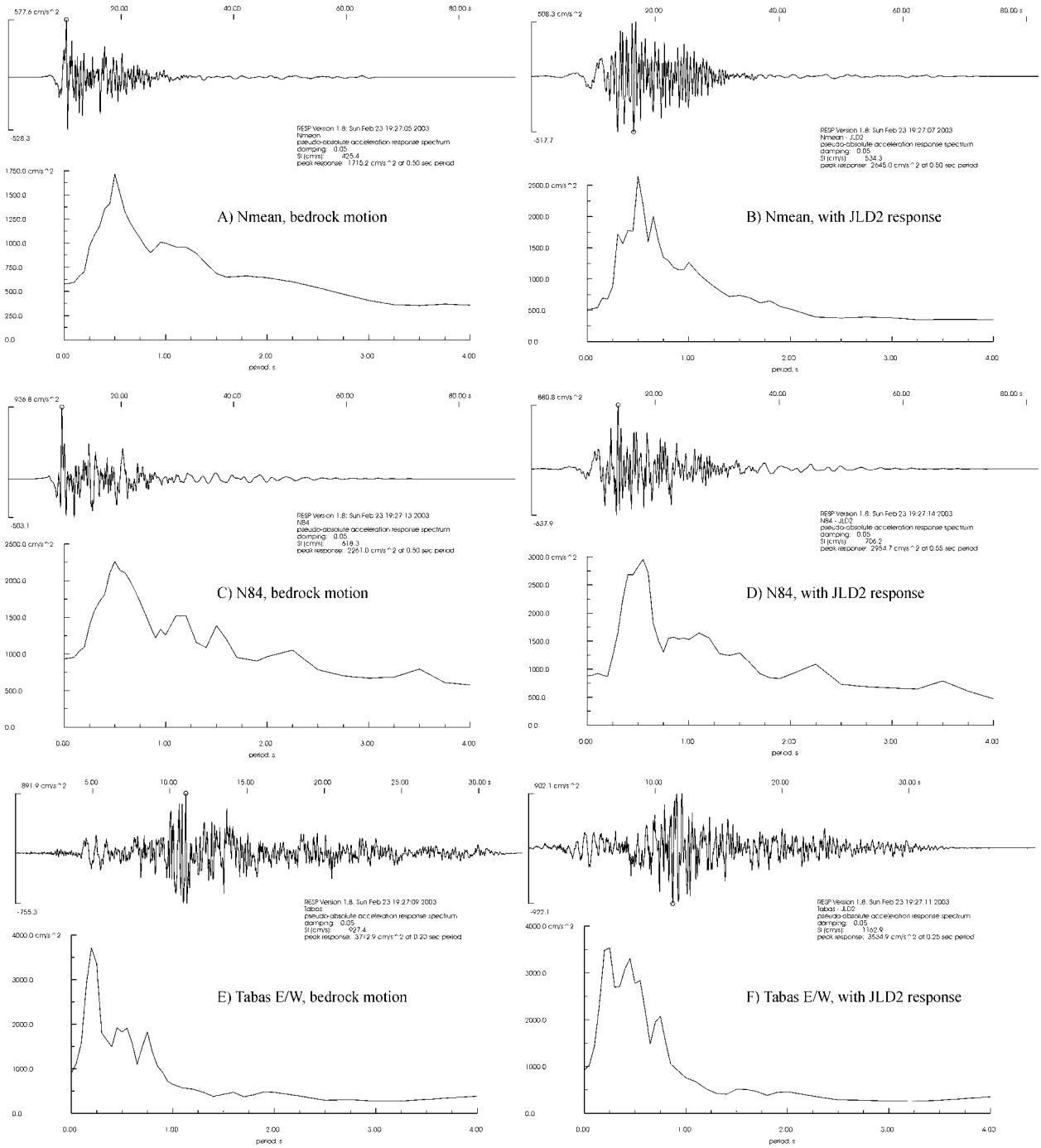

Figure 5-17: Bedrock input motions (left), and motions convolved with JLD2 weak-motion site response (right). Three bedrock motions (described in Chapter 6) representing a range of realizations for the Teton Fault design ground motions are shown: N-mean, N-84, and Tabas-E/W. Absolute acceleration response spectra for 5% damping are shown below each time history. The bedrock motions convolved with the weak motion JLD2 site response may be used for design loadings at stations 13+00 or less. A substantial non-linear response to strong shaking is not expected at these locations

Figure 5-18 shows pseudo-relative velocity response spectra for the bedrock motions convolved with the JLD3 site response. These response spectra are applicable at stations 14+00 and greater. However, because the convolved motions at JLD3 shown in Figure 5-18 do not include non-linear soil effects, these motions must be further modified to include non-linear soil behavior before they can be used in engineering analyses. This is done in the following sections.

5.4 2D Finite-Difference Site Response Modeling

Borehole recordings of ground motions in the soil section of Jackson Lake Dam are not available. Consequently, it is necessary to infer the properties of subsurface ground motions using theoretical methods with available geophysical information about the site conditions. The geological and geophysical data provide important information about the variation of materials and seismic velocities along the axis of the dam. However, very little information is available about the geometry and geophysical properties of soils upstream, downstream, and north of Jackson Lake Dam. Since information about the 3D geometry and velocity of the glacial scour basin is not available, 2D finite-difference methods are used to obtain a physical understanding of the likely composition of seismic waves that produce the amplification and prolonged durations observed at JLD3-7. The goal is to obtain sufficient understanding of wave propagation in the very-low-velocity soils to construct realistic input ground motion scenarios at sufficient depth to allow calculation of nonlinear soil responses using 1D approximations.

5.4.1 Previous Work. Lomnitz et al. (1999) provided theoretical evidence and ground motion recordings from Mexico City that showed that long duration monochromatic ground motions may be produced in basins that have low shear-wave velocities (0.1 to 0.2 km/s) and saturated sediments. However, Lomnitz et al. (1999) did not calculate synthetic seismograms to demonstrate the physical existence of their postulated PR mode. O'Connell and Ake (2003) performed 2D finite difference investigations of the existence of Lomnitz et al.'s (1999) PR mode and their results are reproduced here since the PR mode may be one way to explain the observed long duration soil ground motions described in Section 5.2 To test the ability of such a long duration mode to persist in a basin with strong intrinsic attenuation, a model of a small (0.3 km wide and 0.1 km deep), glacial scour is embedded in a 2D model with slightly higher shallow velocities outside the basin and higher velocities at depth (Figure 5-19a). Values of Q=10 were

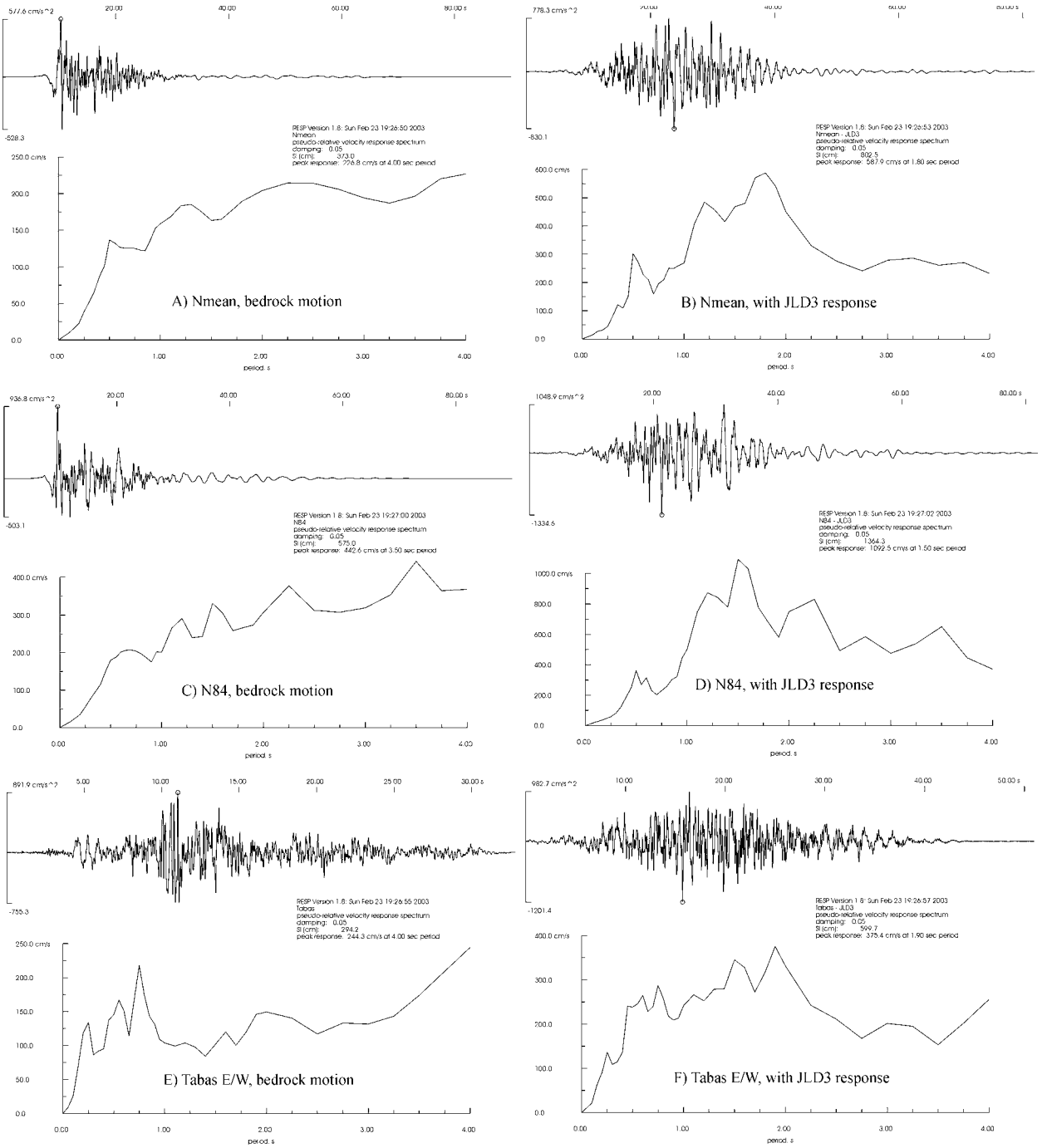

Figure 5-18: Bedrock input motions (left), and motions convolved with JLD3 weak-motion site response (right). Three bedrock motions (described in Chapter 6) representing a range of realizations for the Teton Fault design ground motions are shown: N-mean, N-84, and Tabas-E/W. Pseudo-relative velocity response spectra at 5% damping are shown below each time history. The bedrock motions convolved with the weak motion JLD3 site are intended to be used at stations 14+00 and greater with a suitable correction for non-linear soil response. A substantial non-linear response to strong shaking is expected at these locations, and the weak-motion surface response provided here must be corrected for input to the base of the soil column. That correction is provided in subsequent sections

used to simulate high-intrinsic attenuation in the near-surface, low-velocity materials. Compressional wave velocities were set to water velocities for the lowest velocity materials. The 2D version of the elastic finite-difference program E3D (Larsen and Grieger, 1998), which includes viscoelastic capabilities implemented using the approach of Robertsson et al. (1994), was used to calculate the seismic response of a *SV* plane-wave incident at 5° from vertical upon the basin with a total moment of 10^{20} dyne-cm. The numerical model was 8 km long and 5 km deep with attenuating boundaries to minimize spurious internal reflections. The source-time function was a differentiated 0.75 s-duration Gaussian pulse. The incident horizontal velocity response is shown at the bottom of Figure 5-19b.

Constructive interference at the center of the basin produces maximum amplitudes that persist for ~7 s and a slow amplitude decay lasting about 20 s (Figure 5-19b). Sites offset from the center of the basin experienced long-duration monochromatic horizontal motions with slowly decaying amplitudes that persisted to the maximum calculation time of 60 s. The long duration response are produced by the interface modes propagating horizontally back and forth across the basin as they reflect off the vertical boundaries at the basin edges (Figure 5-19c). Ground motion responses similar to the top time history in Figure 5-19b were observed for earthquakes recorded by stations JLD3, JLD4, JLD5, JLD6, and JLD7 (Figures 5-4 and 5-5). The simulation shows that this mode can persist for long durations with little effective attenuation of the mode, even though intrinsic S-wave attenuation is high. However, the schematic velocity model has limited applicability to Jackson Lake Dam. Consequently, a velocity model more consistent with the geophysical and geological data from Jackson Lake Dam is used in the next section to simulate responses in the low-velocity glacial scour.

5.4.2 Site-Specific Model. The available information about the variations of velocities in the glacial scour and the overall geometry of the glacial scour are limited. The southern extent of the glacial scour low-velocity basin is well constrained by geophysical and geological information. The drill logs provide good constraints on the depth to the ~1 km/s till from the south end of the glacial scour to the northern end of the embankment. In contrast the northern limit of the glacial scour low-velocity basin is unknown. The northernmost and deepest drill log indicates that the glacial scour basin is still deepening at the northern end of the embankment. A velocity

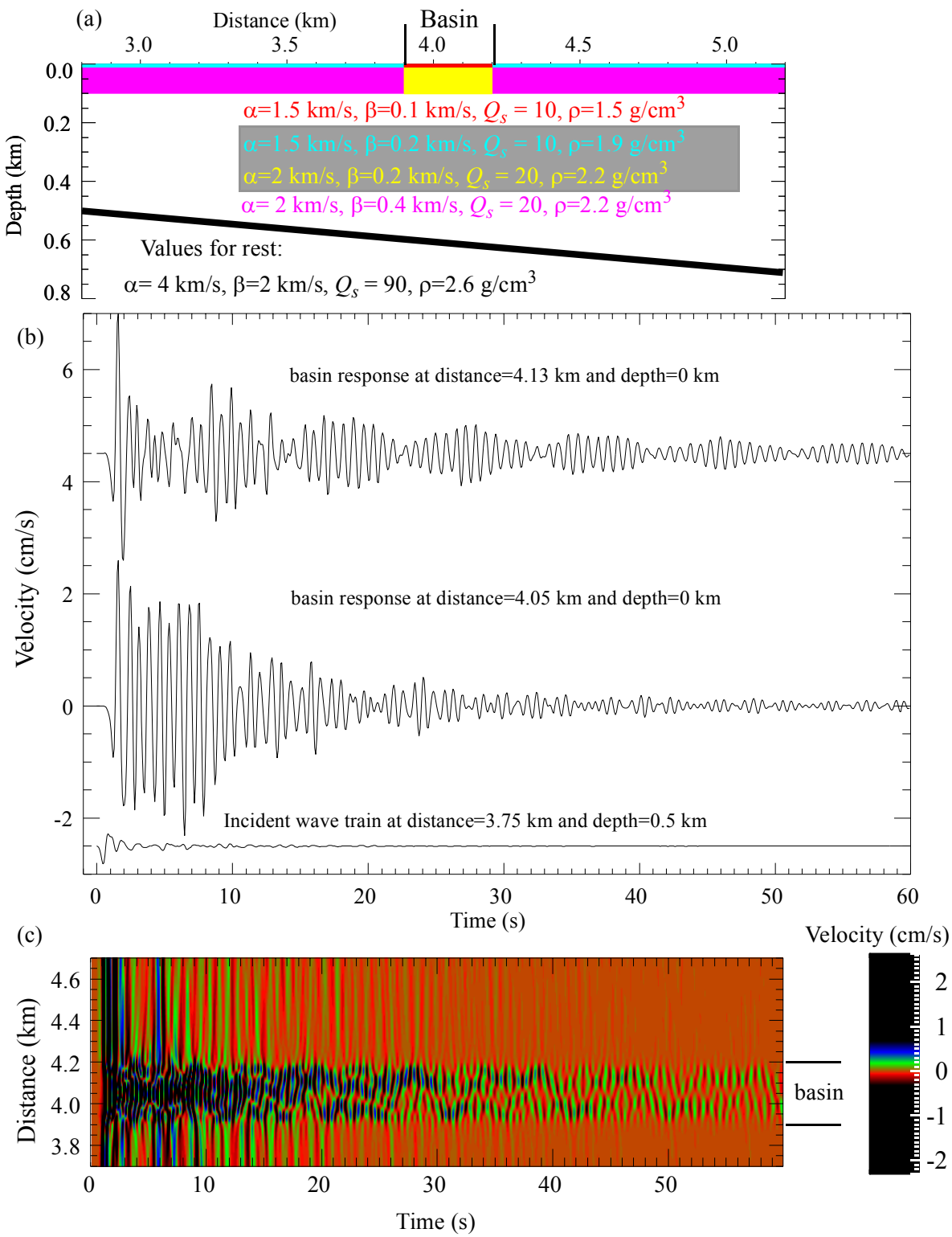

Figure 5-19: Simulation of Lomnitz et al.'s (1999) soil response. (a) Color-coded 2D material model. Thick line shows the incident SV plane wave. (b) Incident waveform at a depth of 0.5 km modified by internal reverberations is shown at the bottom, with two surface waveforms from sites located within the basin as labeled shown above. (c) Color-coded horizontal velocity time histories for surface sites located at distances from 3.7 km to 4.7 km.

model was constructed to produce a glacial scour basin at least as wide as permitted by the available observations (Figure 5-20); the actual glacial scour low-velocity basin may be significantly wider.

The lateral continuity of velocity discontinuities within the soils of the glacial scour are unknown. The approach used here was to minimize strong velocity discontinuities in depth to the two sharpest first-order velocity discontinuities (~27 m depth) and the interface with the underlying ~1 km/s S-wave-velocity till, and to use smooth velocity gradients for all other velocity changes (Figure 5-21). The premise is that if even this overly smooth velocity model produces long durations, it would be straightforward to identify the origins and characteristics of long duration waves. Since weak-motion attenuation of the soils may be very large, Qs was set to 5 at the surface and increased with S-wave velocity as show in Figure 5-22. The same 2D finite-difference approach used in Section 5.4.1 was used to model glacial scour responses at the surface and at depths of 0.1, 0.2, 0.3, 0.4, and 0.5 km as shown in Figure 5-20. A plane SV-wave inclined 5° from vertical incidence was input into the 2D finite-difference calculation as shown in Figure 5-20. The model was 8 km long and 5 km deep to minimize boundary reflections, the only significant boundary reflection is the primary reflection off the bottom of the model that produces a small S-wave arrival about 6 s following the first S-wave arrival. Since LVB-edge S-waves from the large-scale LVB are nearly ubiquitous at the dam, this reflected S-wave provides a somewhat more realistic input scenario than a single plane SV wave. The grid interval of 5 m and minimum S-wave velocity of 0.1 km/s limit the maximum frequency in the analysis to 4 Hz. The same time-differentiated Gaussian pulse used in Section 5.4.1 was used here.

The horizontal acceleration surface responses in Figure 5-23 show extended durations and amplification for sites located in the low-velocity glacial scour. The edge of the basin at 3 km produce the largest basin-edge wave amplitudes because the SV plane wave is incident toward the basin at 3 km. The dashed blue line shows that the early portion of the basin-edge waves are composed of S-waves with apparent velocities of ~0.2 km/s refracted below 25 m depth, followed by Rayleigh waves that end with a large-amplitude, broadband Airy phase (red dashed line is located at the end of the Airy phase at an apparent velocity of ~0.09 km/s, the minimum Rayleigh velocity for a surface velocity of 0.1 km/s). Within about 1 km of the basin-edge at 3 km, the

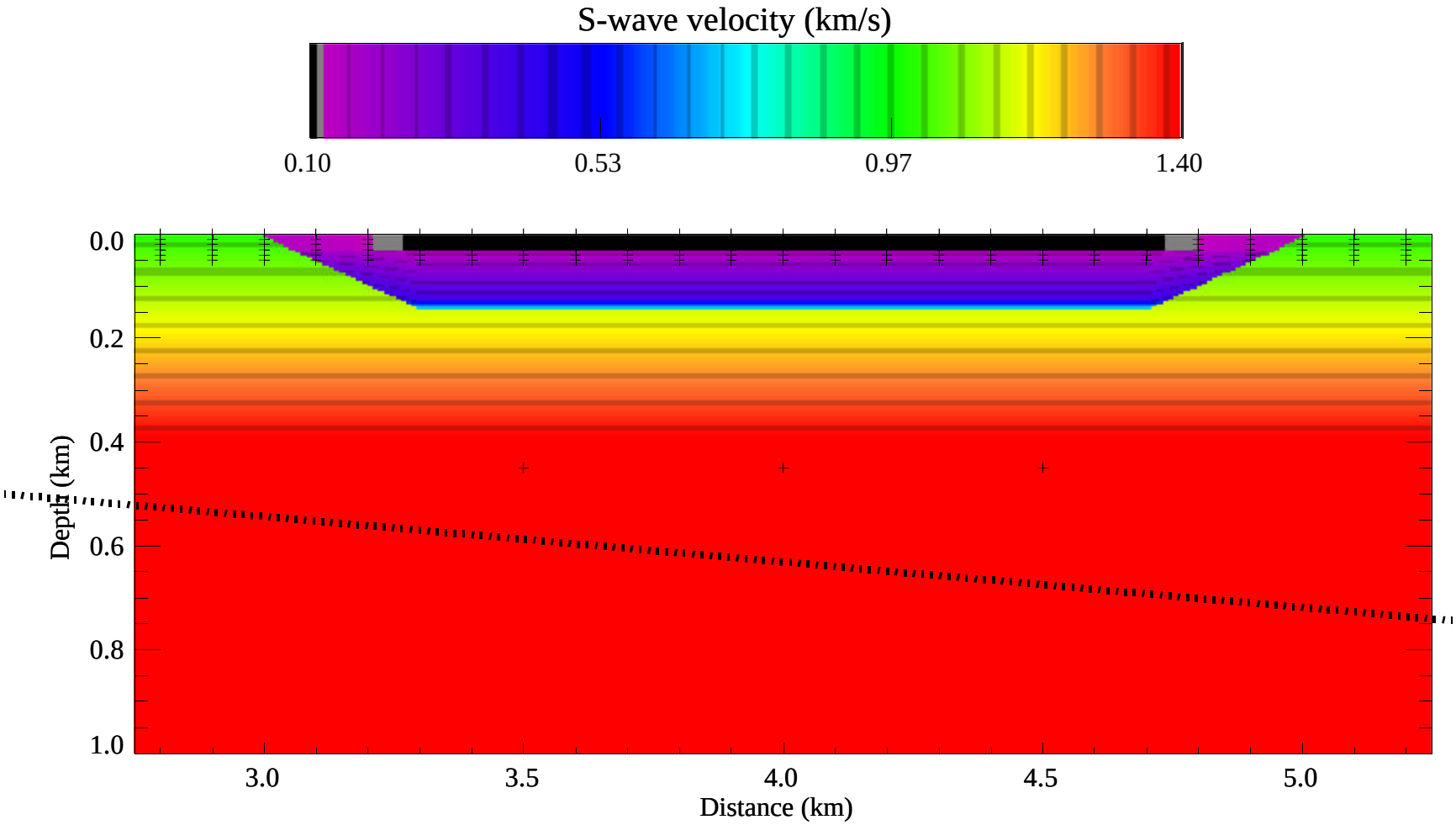

Figure 5-20: Simple 2D S-wave velocity model of the glacial scour basin beneath the dam.The dashed line represents the SV plane wave incident 5° from vertical. The plus symbols show where ground motion information was extracted from the model. The boundaries have 22.5° dips and horizontal velocity gradients which take the uniform 1D velocity variations in the flat-bottom portion of the very-low-velocity basin and linearly increase the velocities laterally toward the basin edges

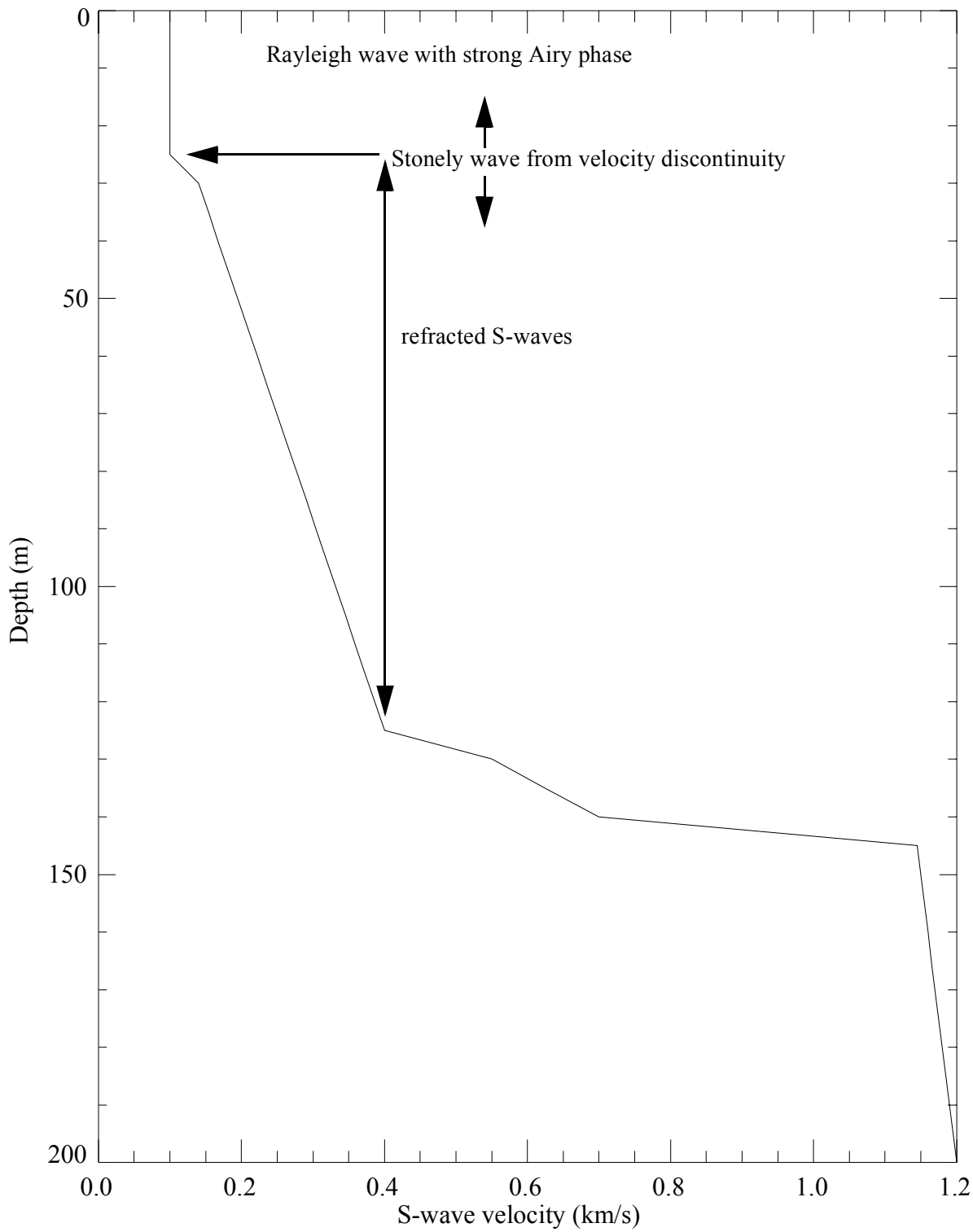

Figure 5-21: 1D S-wave velocity profile from the middle of the 2D glacial scour basin.The origin of different wave types is indicated schematically with depth; Fundamental Rayleigh waves in the top 25 m with associated large-amplitude Airy phase, Stonely waves radiated up and down from the velocity discontinuity at 25 m, and S-wave refracted by the velocity gradients below 25 m.

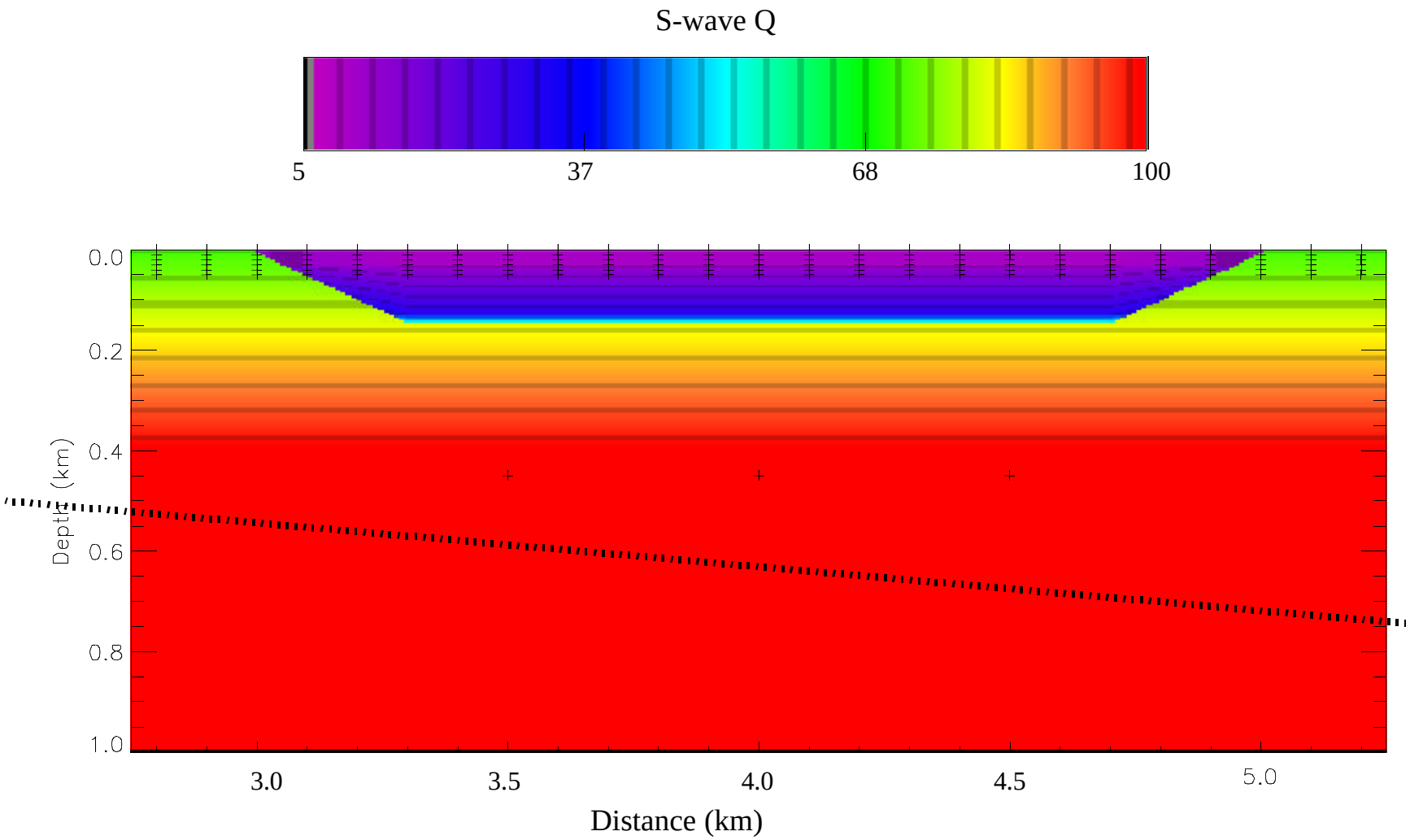

Figure 5-22: Simple 2D S-wave Qs model of the glacial scour basin beneath the dam.The dashed line represents the SV plane wave incident 5° from vertical. The plus symbols show where ground motion information was extracted from the model. The boundaries have 22.5° dips and horizontal Qs gradients which take the uniform 1D Q variations in the flat-bottom portion of the very-low-velocity basin and linearly increase Qs laterally toward the basin edges.

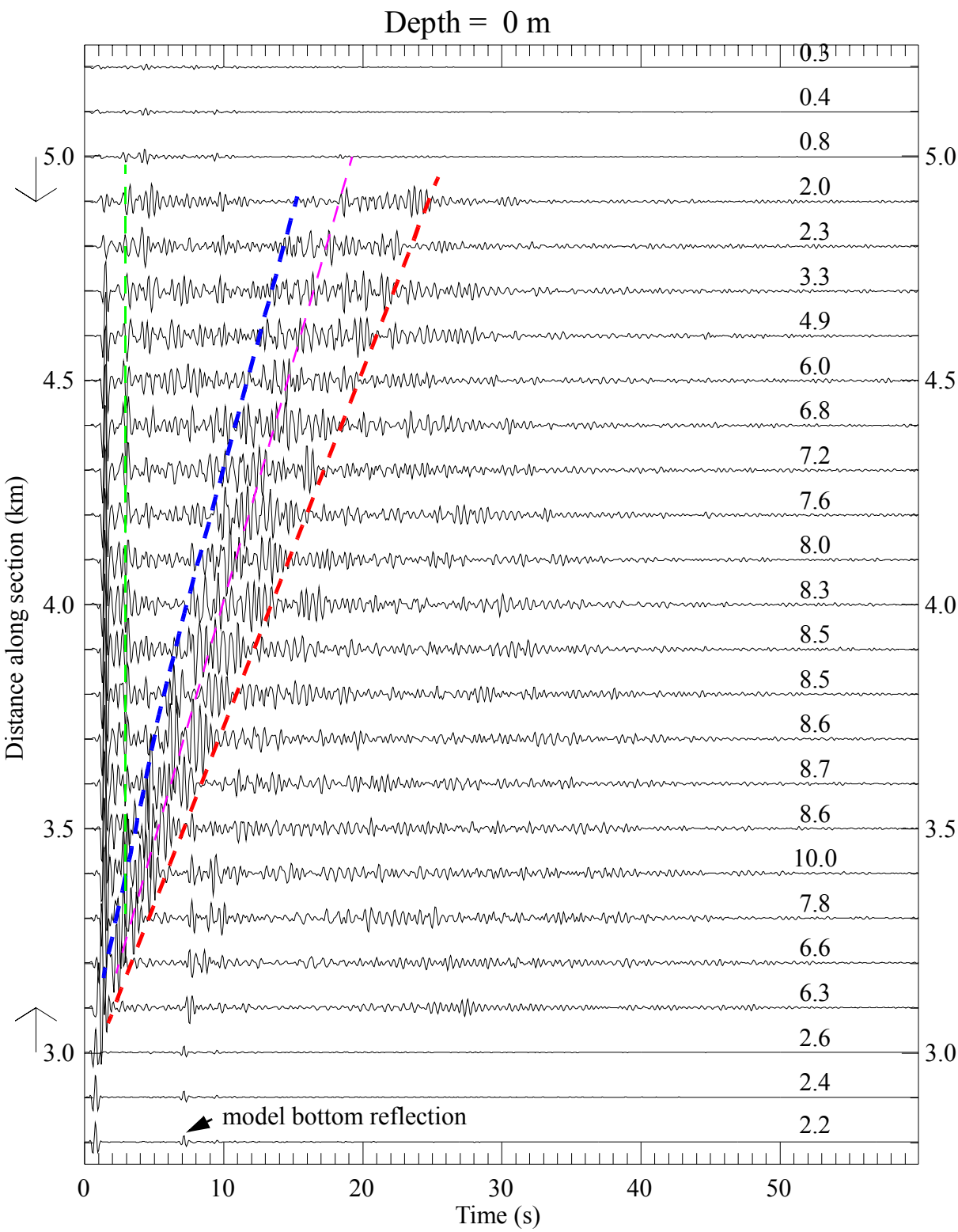

Figure 5-23: Horizontal 2D finite-difference acceleration record section z = 0 m. Distances are as shown in Figure 5-22. Peak amplitudes are labels on the right normalized to a maximum value of 10 for all sites in the model. Low-velocity glacial scour sites are between the arrows on the left. Dashed red line shows the end of the basin-edge Airy phase. Dashed blue line is the basin-edge refracted S-wave. Dashed magenta line is the Stonely wave. Primary S-wave multiple is the dashed green line.

refracted S-wave has the largest amplitude. For distances > 4.4 km the low near-surface Qs properties and amplitude reduction past the S-wave triplication, leave the surface waves with the largest accelerations for the basin positions > 4.4 km (Figure 5-23). The fundamental mode Rayleigh Airy phase has the largest amplitudes at the far side of the basin, as surface wave amplitudes decay more slowly with distance. The basin edge waves contain substantial acceleration responses in the 1-4 Hz frequency range, as is expected for the S-waves, but the Rayleigh waves also have strong amplitudes in this frequency range. Figure 5-23 indicates that the portions of the southern glacial scour boundaries within several km of the dam are likely to produce substantial short-period acceleration responses along the embankment portion of the dam.

Figure 5-24 shows that horizontal acceleration durations decrease only slightly at 10 m depth and accelerations mostly decrease by about a factor of two, consistent with removing the free-surface effect. The refracted basin-edge S-waves are less attenuated since they don't have to propagate through as much shallow low Qs material. Also, as depth increases the multiple reflections from high-velocity basal till become less attenuated (compare Figures 5-23 to 5-24) because Qs increases with depth in the model. The Stonely wave arrival is the dominant later arrival after the multiple S-wave reflections for depths of 20 m (Figure 5-25) and 30 m (Figure 5-26) because these depths are closest to the velocity discontinuity at 25 m where the Stonely waves propagate with velocities of ~0.9 * Vs of the lowest velocity side of the interface. At depths of 40 m (Figure 5-27) and 50 m (Figure 5-28), the refracted S-waves and Stonely waves have comparable amplitudes (Figures 5-27 and 5-28), but the S-waves tend to retain higher frequencies, particularly closer to the basin margins, which are the secondary sources of these extended duration phases. It is clear that down to a depth of 50 m, the horizontal acceleration durations are not significantly less than the surface durations. In fact basin-edge refracted S-waves retain higher frequency acceleration responses relative to surface sites because deeper refracted S-waves are not subjected to the lowest Qs regions near the surface. Figures 5-23 to 5-28 demonstrate that it is necessary to use the observed durations at the surface stations, like JLD3, at depth to provide realistic duration input motions for nonlinear analyses of the soil responses. This is necessary because the 1D SH-propagator nonlinear codes SHAKE and NOAH will not generate the strong-amplitude S-waves or Stonely waves produced at the basin margins. Since the Stonely waves are

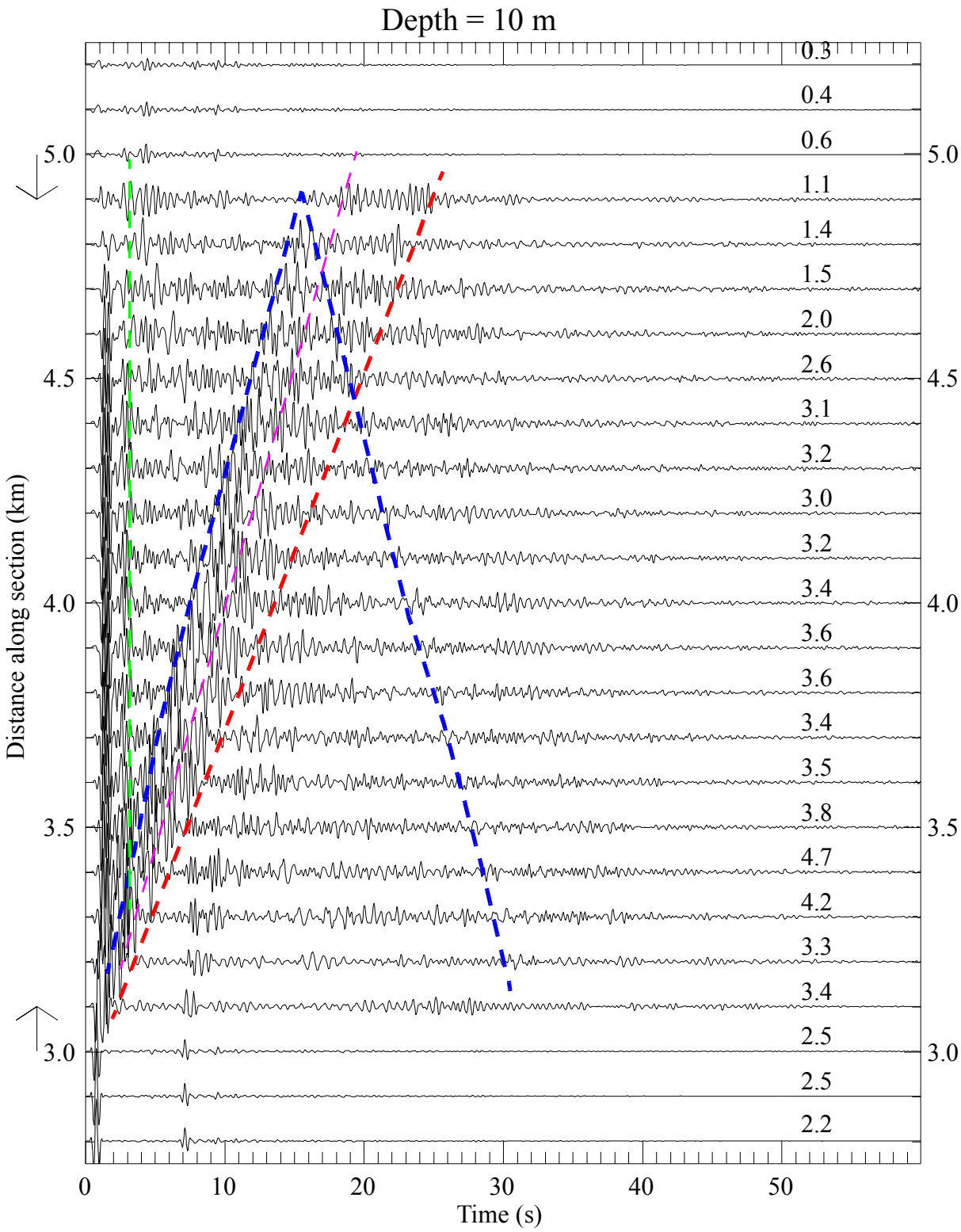

Figure 5-24: Horizontal 2D finite-difference acceleration record section z = 10 m. See Figure 5-22 for distance reference. Dashed red line shows the end of the basin-edge Airy phase. Dashed blue lines show the refracted basin-edge S-waves and surface waves, and their reflection back across the basin from the far edge. Primary S-wave multiple reflection from the ~1 km/s till is the dashed green line. The dashed magenta line shows the Stonely wave from the velocity discontinuity at 25 m depth.

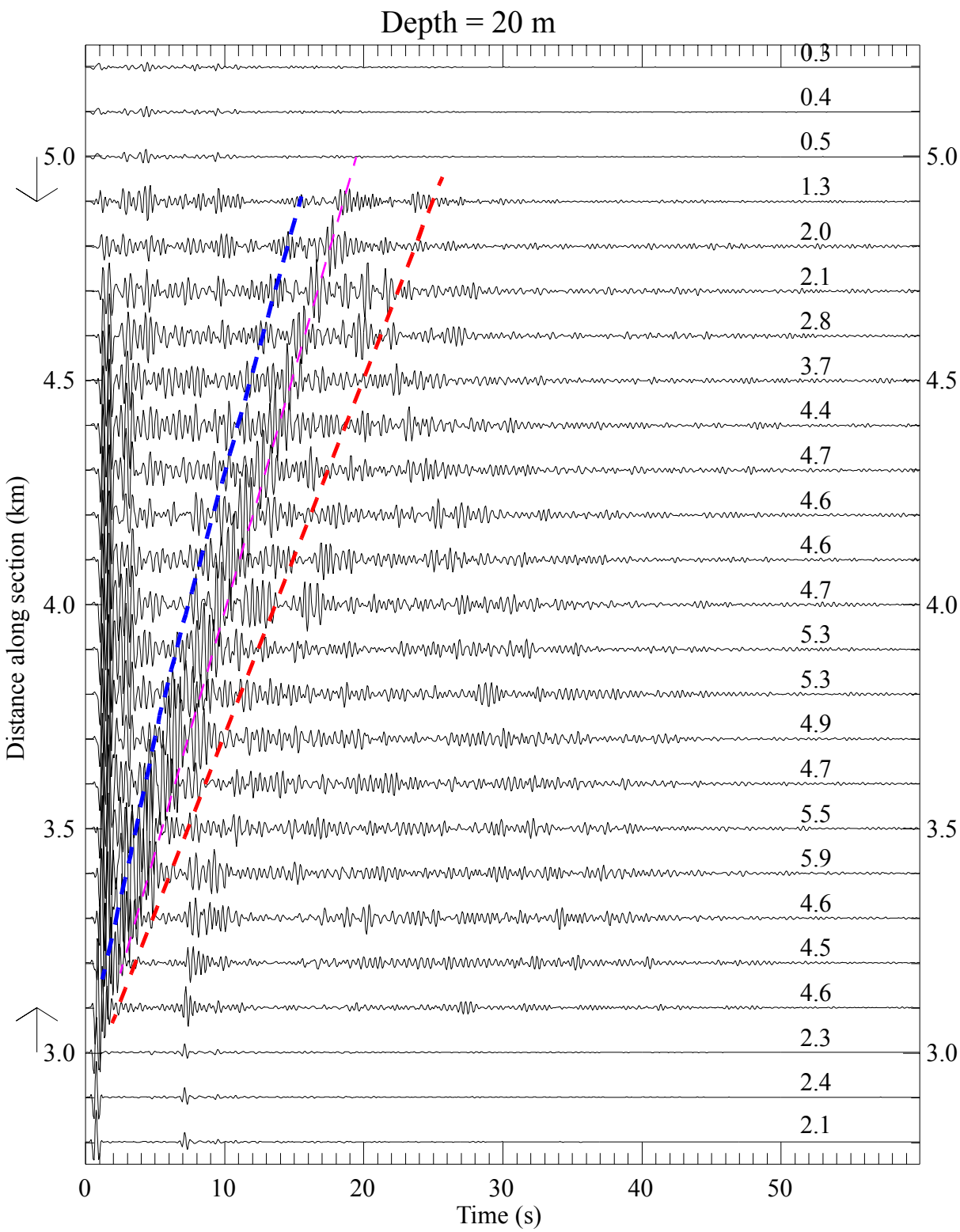

Figure 5-25: Horizontal 2D finite-difference acceleration record section z = 20 m. See Figure 5-22 for distance reference. Dashed red line shows the end of the basin-edge Airy phase. Dashed blue lines show the refracted basin-edge S-waves and surface waves, and their reflection back across the basin from the far edge. The dashed magenta line shows the Stonely wave from the velocity discontinuity at 25 m depth.

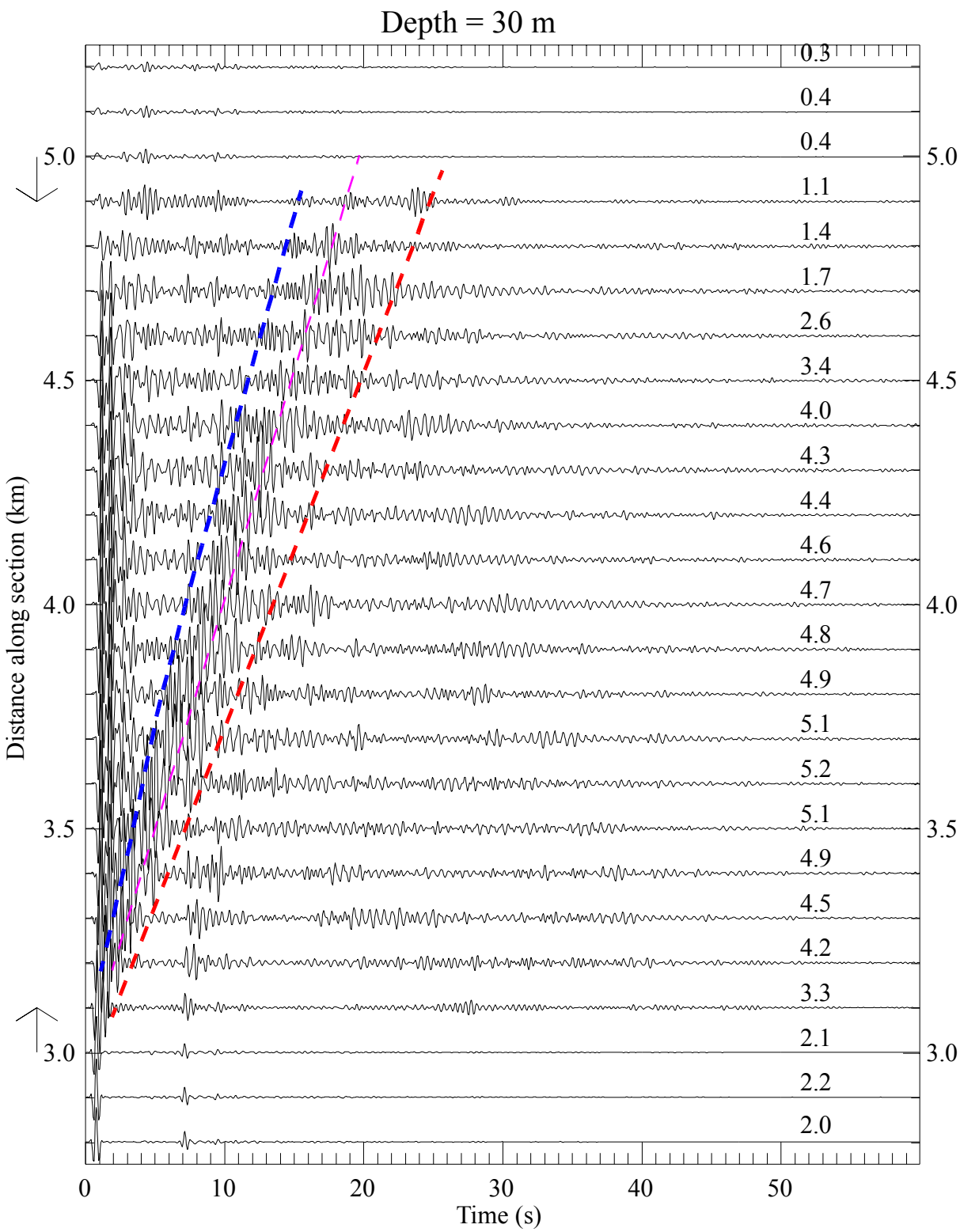

Figure 5-26: Horizontal 2D finite-difference acceleration record section z = 30 m. See Figure 5-22 for distance reference. Dashed red line shows the end of the basin-edge Airy phase. Dashed blue lines show the refracted basin-edge S-waves and surface waves, and their reflection back across the basin from the far edge. The dashed magenta line shows the Stonely wave from the velocity discontinuity at 25 m depth.

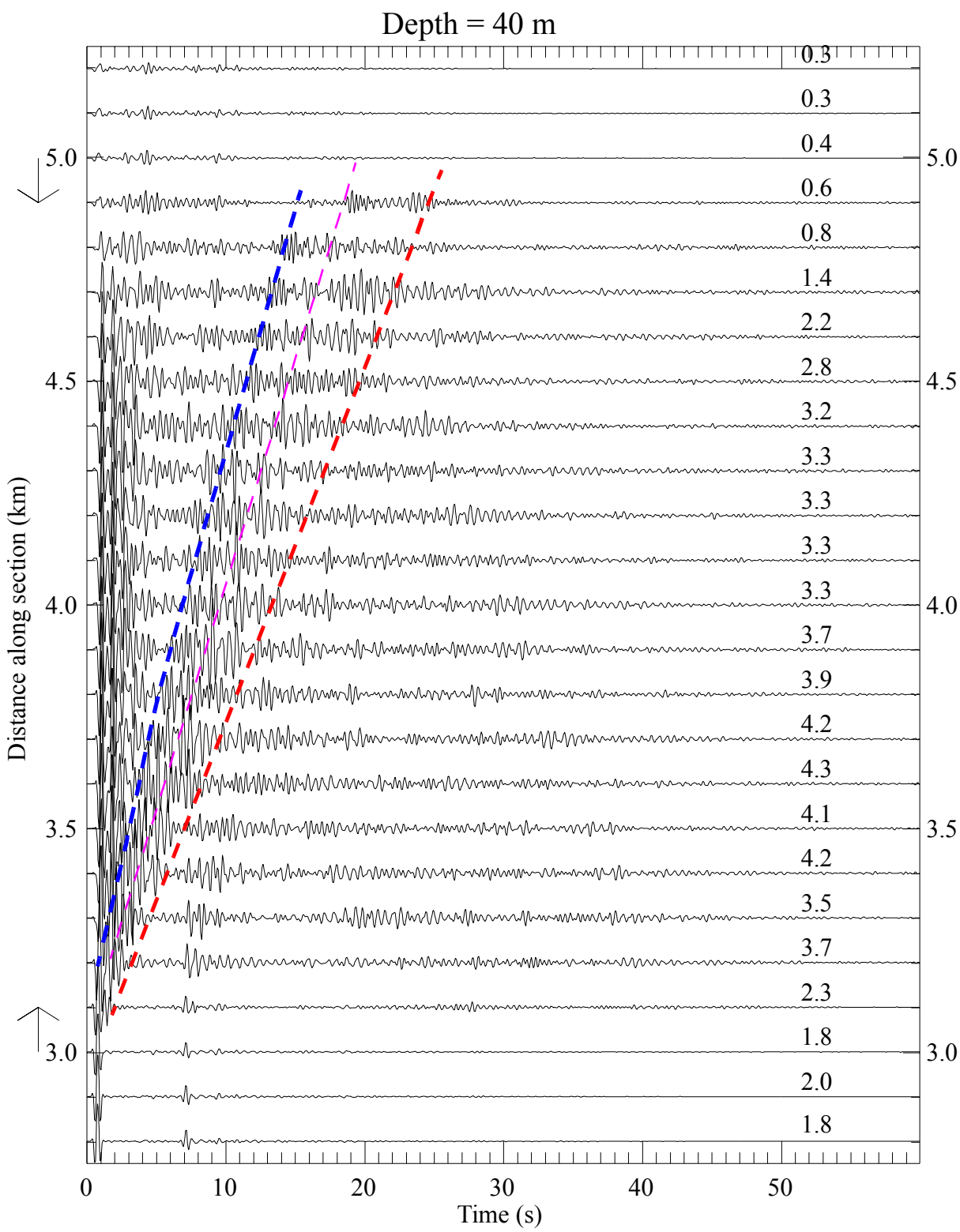

Figure 5-27: Horizontal 2D finite-difference acceleration record section z = 40 m. See Figure 5-22 for distance reference. Dashed red line shows the end of the basin-edge Airy phase. Dashed blue lines show the refracted basin-edge S-waves and surface waves, and their reflection back across the basin from the far edge. The dashed magenta line shows the Stonely wave from the velocity discontinuity at 25 m depth.

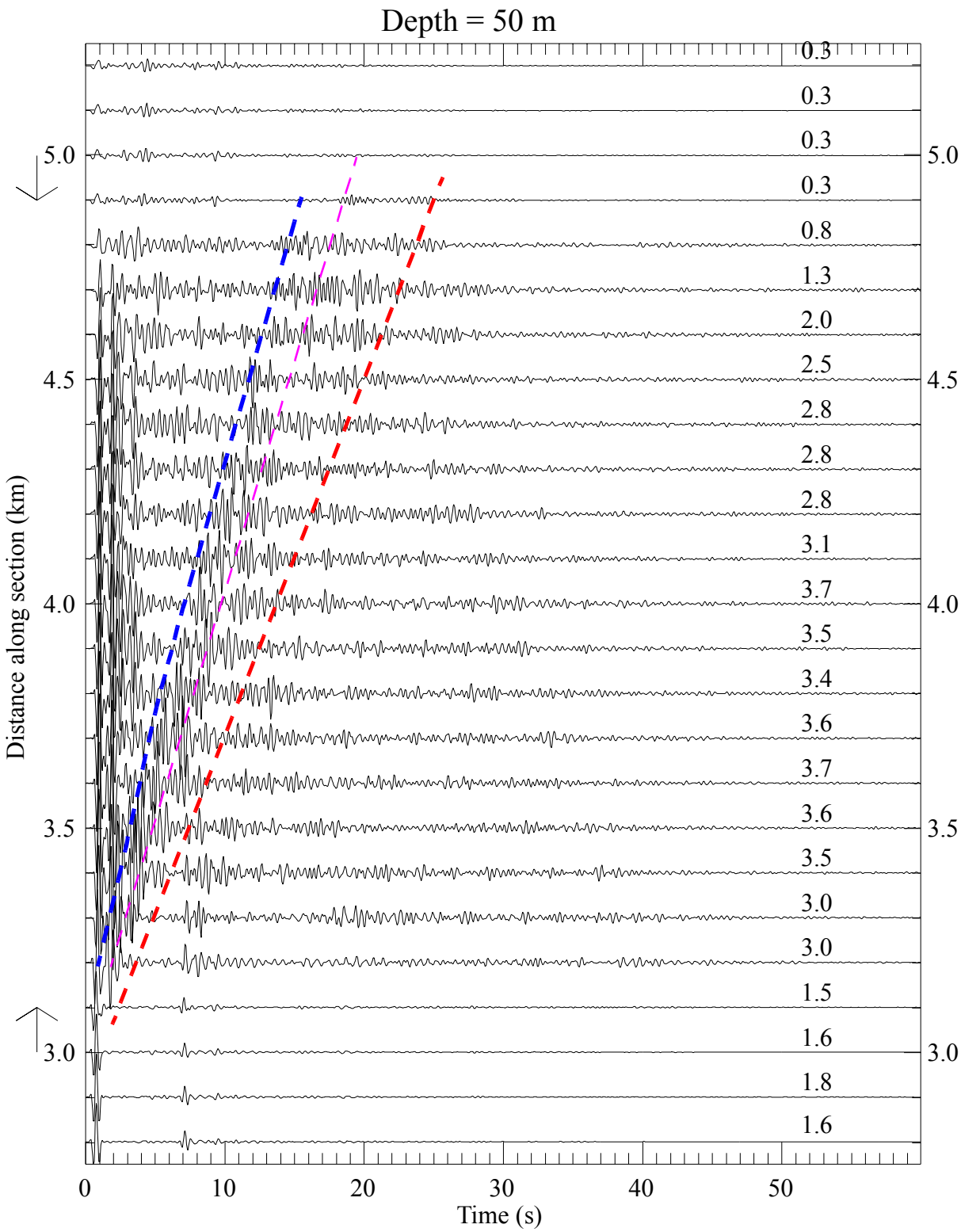

Figure 5-28: Horizontal 2D finite-difference acceleration record section z = 50 m. See Figure 5-22 for distance reference. Dashed red line shows the end of the basin-edge Airy phase. Dashed blue lines show the refracted basin-edge S-waves and surface waves, and their reflection back across the basin from the far edge. The dashed magenta line shows the Stonely wave from the velocity discontinuity at 25 m depth.

elliptically polarized, horizontal propagating, they are least compatible with the SH body wave assumptions of SHAKE and NOAH.

Vertical component synthetic acceleration record sections compliment the horizontal component record sections in Figures 5-23 to 5-28 because the vertical motions show predominantly interface waves. Thus, the vertical component synthetic data provide a natural visual means to distinguish the S-wave arrivals from the interface waves. The largest vertical accelerations observed at any position in the model are normalized to a value of 10; the absolute vertical accelerations are much smaller than the horizontal accelerations given the steep incidence angle of the SV plane wave. Figure 5-29 shows that the arrivals following the refracted SV-waves (which are very weak on the vertical component) are associated with the Stonely wave produced at ~25 m depth and strong Airy phases associated with the fundamental model Rayleigh waves produced at the basin margins. The Airy phase associated with the Rayleigh wave is also the strongest arrival at depths of 10 m (Figure 5-30) and 20 m (Figure 5-31), but the Stonely wave becomes the strongest arrival at a depth of 30 m (Figure 5-32). The Stonely wave train produces the largest vertical accelerations at depths of 40 m (Figure 5-33) and 50 m (Figure 5-34). The largest vertical accelerations occur at 10 m and 20 m depth (Figures 5-30 and 5-31) and are associated with the Rayleigh Airy phase. Vertical accelerations at all depths extending to 50 m are larger than surface vertical accelerations, indicating the dominance of the horizontal propagating interface modes on vertical accelerations.

The 2D synthetic seismograms show that the extended durations observed at the surface are likely associated with a mixture of refracted S-waves, and horizontally propagating surface and interface waves. For shallow depths of 0 m to 20 m the largest accelerations after the near-vertical incidence S-wave directed and reflected arrivals consist of a mixture of refracted S-waves and broadband Rayleigh wave Airy phases. For depths of 30 m and larger, the largest accelerations after the near-vertical incidence S-wave directed and reflected arrivals are associated with refracted S-waves for the portion of the dam located within 1.5 km of the southern glacial scour. At distances > 1.5 km from the glacial scour boundary the Stonely wave produces the largest accelerations for depths of 30 m and larger. The influence of soil nonlinearity on the amplitudes of these interface waves is unknown, although the continued existence of the free surface and

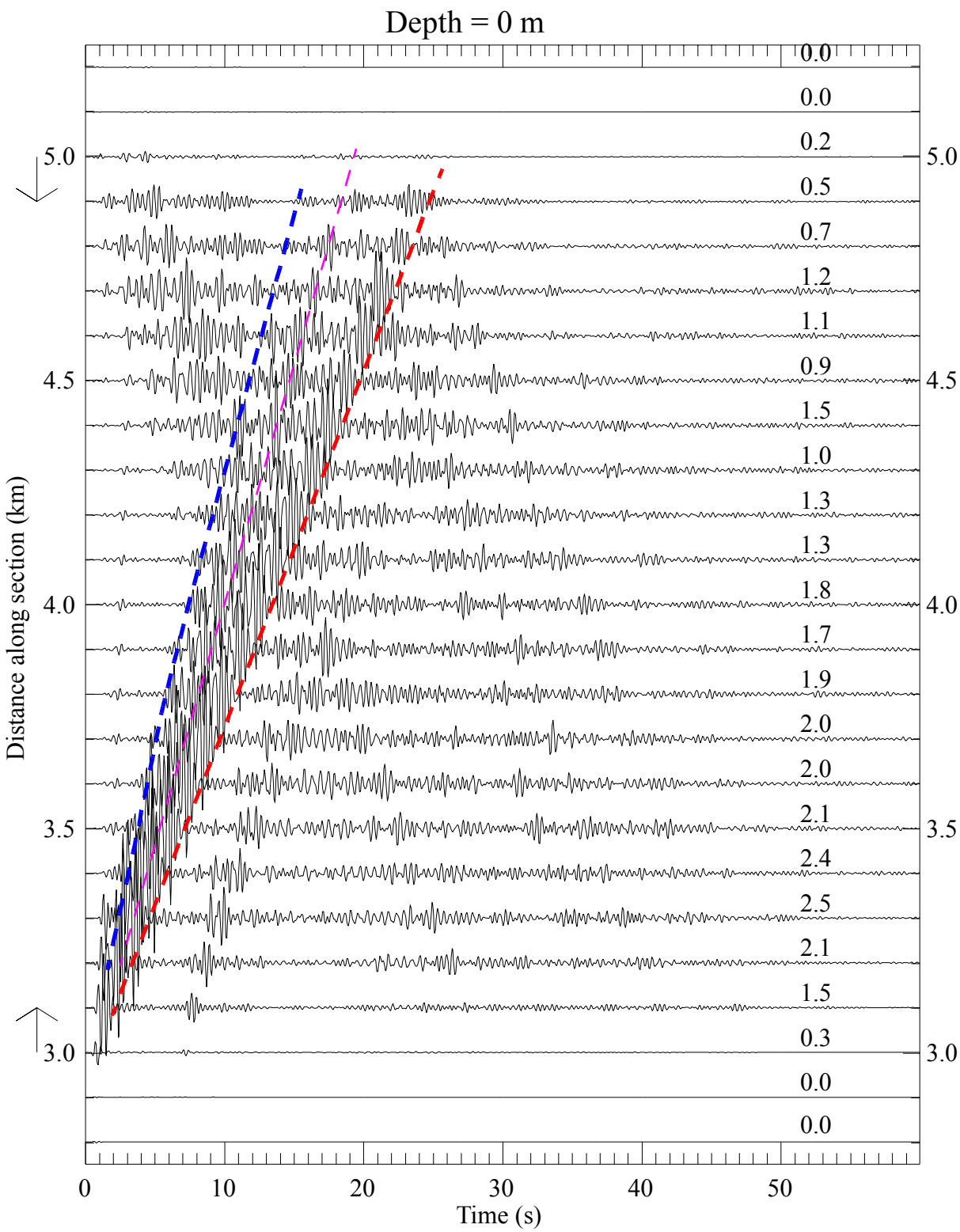

Figure 5-29: Vertical 2D finite-difference acceleration record section z = 0 m.Distances are as shown in Figure 5-22. Peak amplitudes are labels on the right normalized to a maximum value of 10 for all sites in the model. Low-velocity glacial scour sites are between the arrows on the left. Dashed red line shows the end of the basin-edge Airy phase. Dashed blue line is the basin-edge refracted S-wave. Dashed magenta line is the Stonely wave.

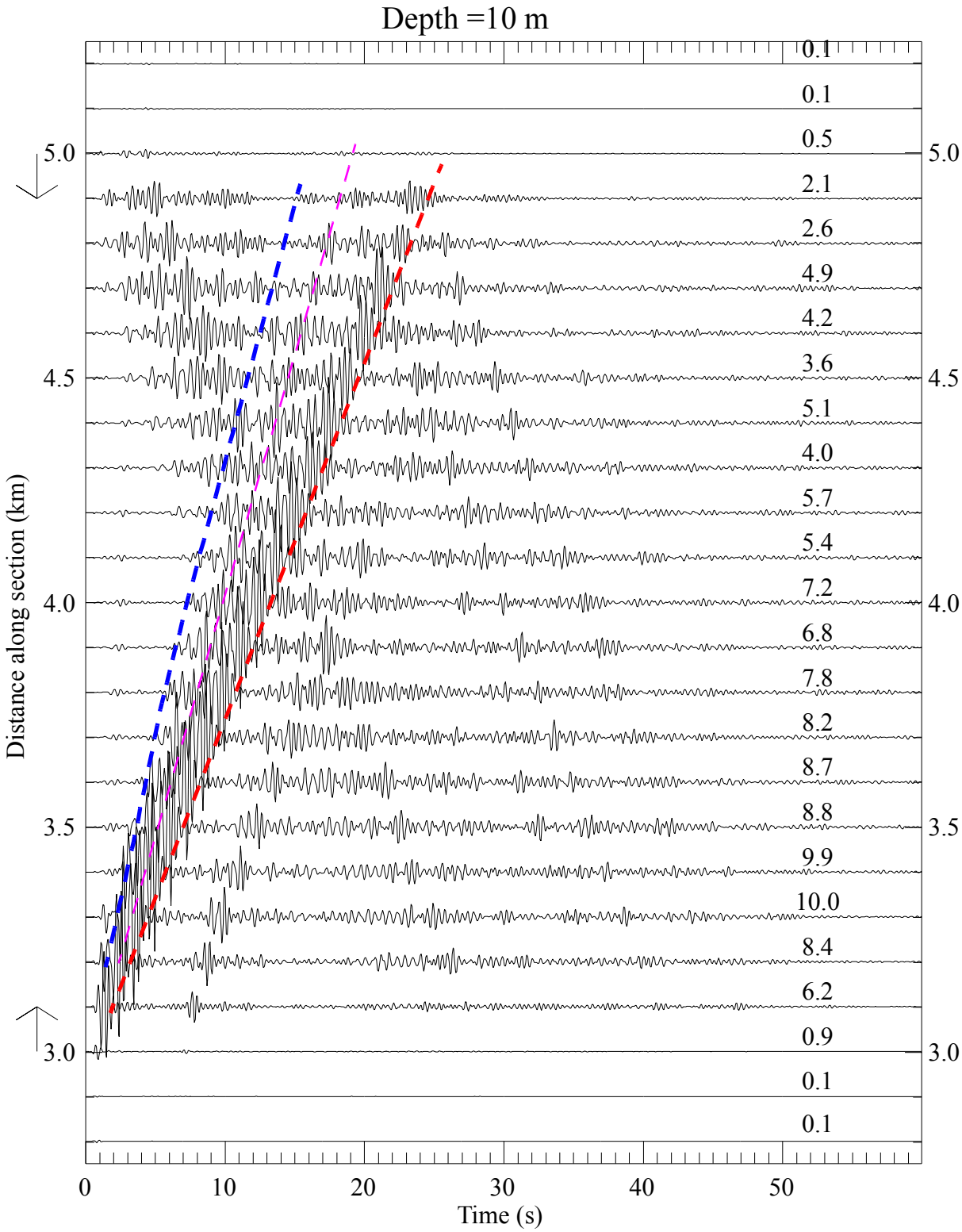

Figure 5-30: Vertical 2D finite-difference acceleration record section z = 10 m.Distances are as shown in Figure 5-22. Peak amplitudes are labels on the right normalized to a maximum value of 10 for all sites in the model. Low-velocity glacial scour sites are between the arrows on the left. Dashed red line shows the end of the basin-edge Airy phase. Dashed blue line is the basin-edge refracted S-wave. Dashed magenta line is the Stonely wave.

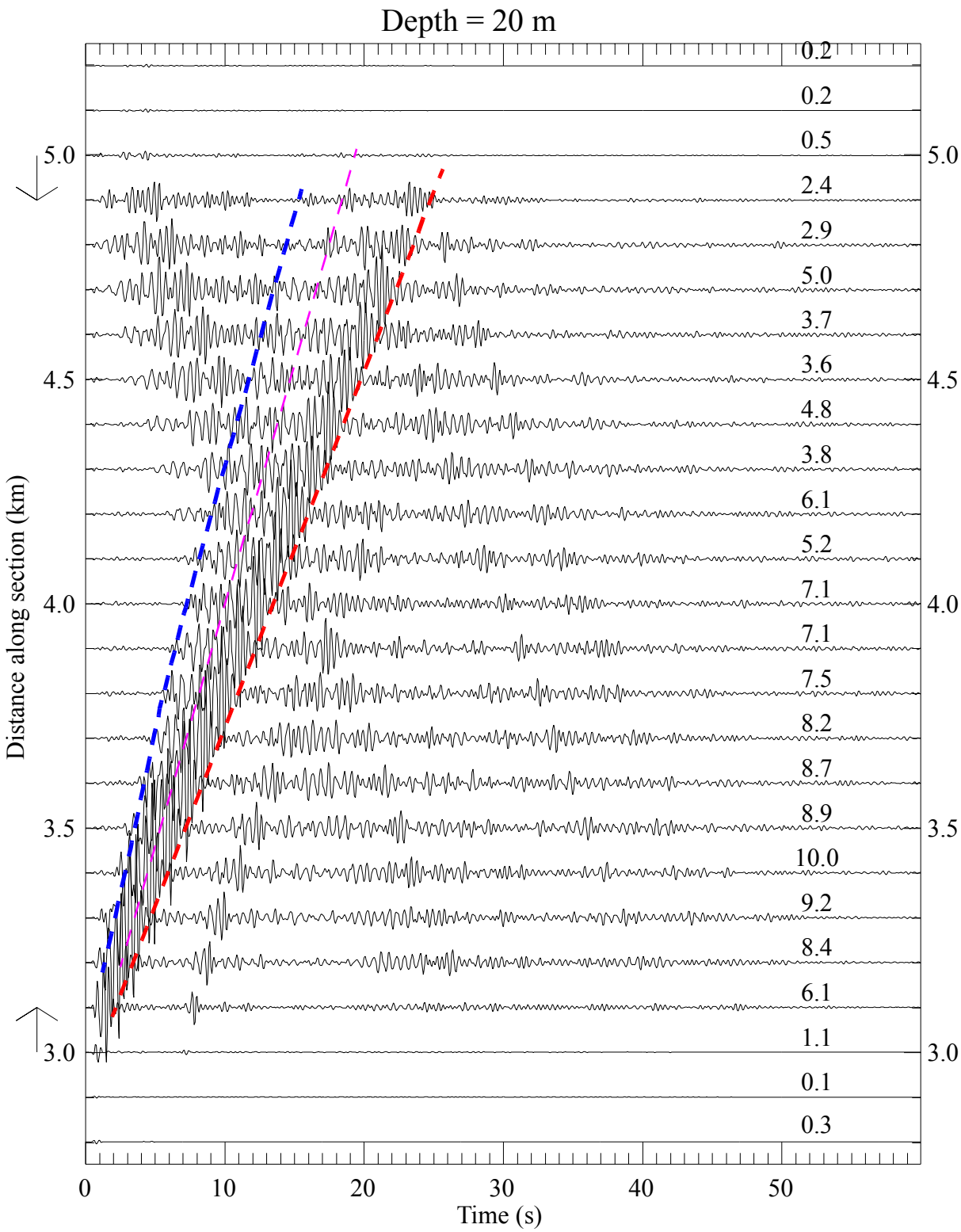

Figure 5-31: Vertical 2D finite-difference acceleration record section z = 20 m.Distances are as shown in Figure 5-22. Peak amplitudes are labels on the right normalized to a maximum value of 10 for all sites in the model. Low-velocity glacial scour sites are between the arrows on the left. Dashed red line shows the end of the basin-edge Airy phase. Dashed blue line is the basin-edge refracted S-wave. Dashed magenta line is the Stonely wave.

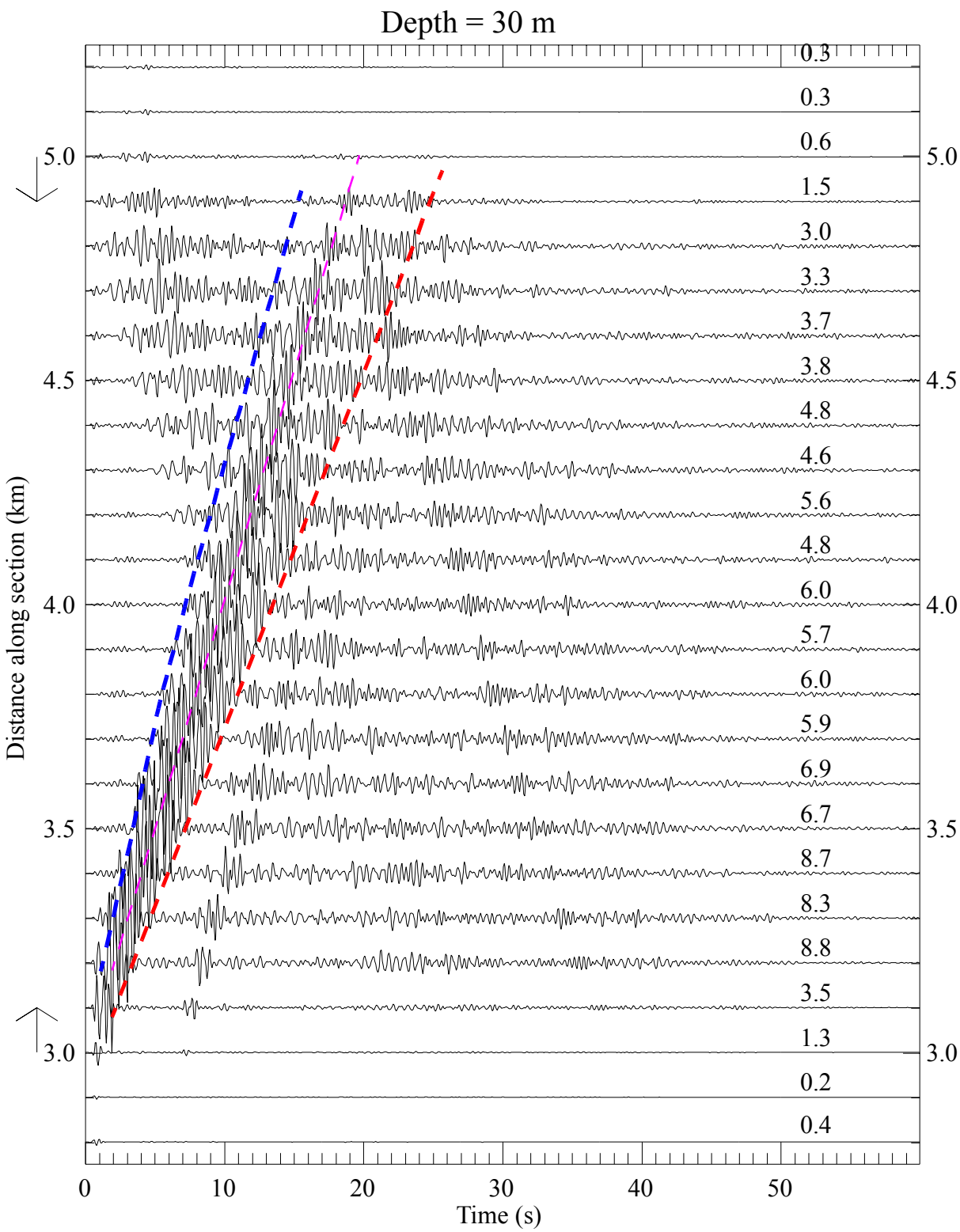

Figure 5-32: Vertical 2D finite-difference acceleration record section z = 30 m.Distances are as shown in Figure 5-22. Peak amplitudes are labels on the right normalized to a maximum value of 10 for all sites in the model. Low-velocity glacial scour sites are between the arrows on the left. Dashed red line shows the end of the basin-edge Airy phase. Dashed blue line is the basin-edge refracted S-wave. Dashed magenta line is the Stonely wave.

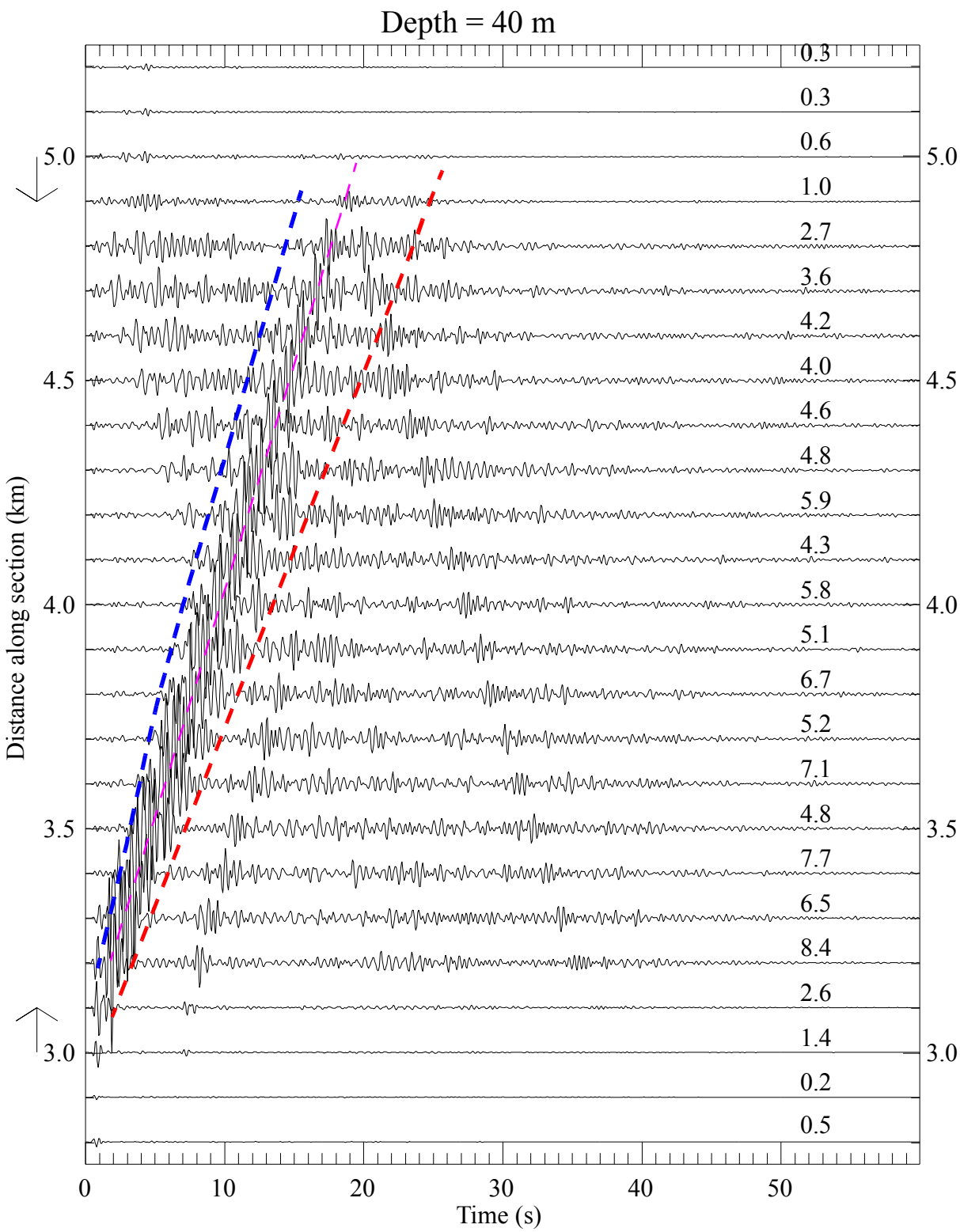

Figure 5-33: Vertical 2D finite-difference acceleration record section z = 40 m.Distances are as shown in Figure 5-22. Peak amplitudes are labels on the right normalized to a maximum value of 10 for all sites in the model. Low-velocity glacial scour sites are between the arrows on the left. Dashed red line shows the end of the basin-edge Airy phase. Dashed blue line is the basin-edge refracted S-wave. Dashed magenta line is the Stonely wave.

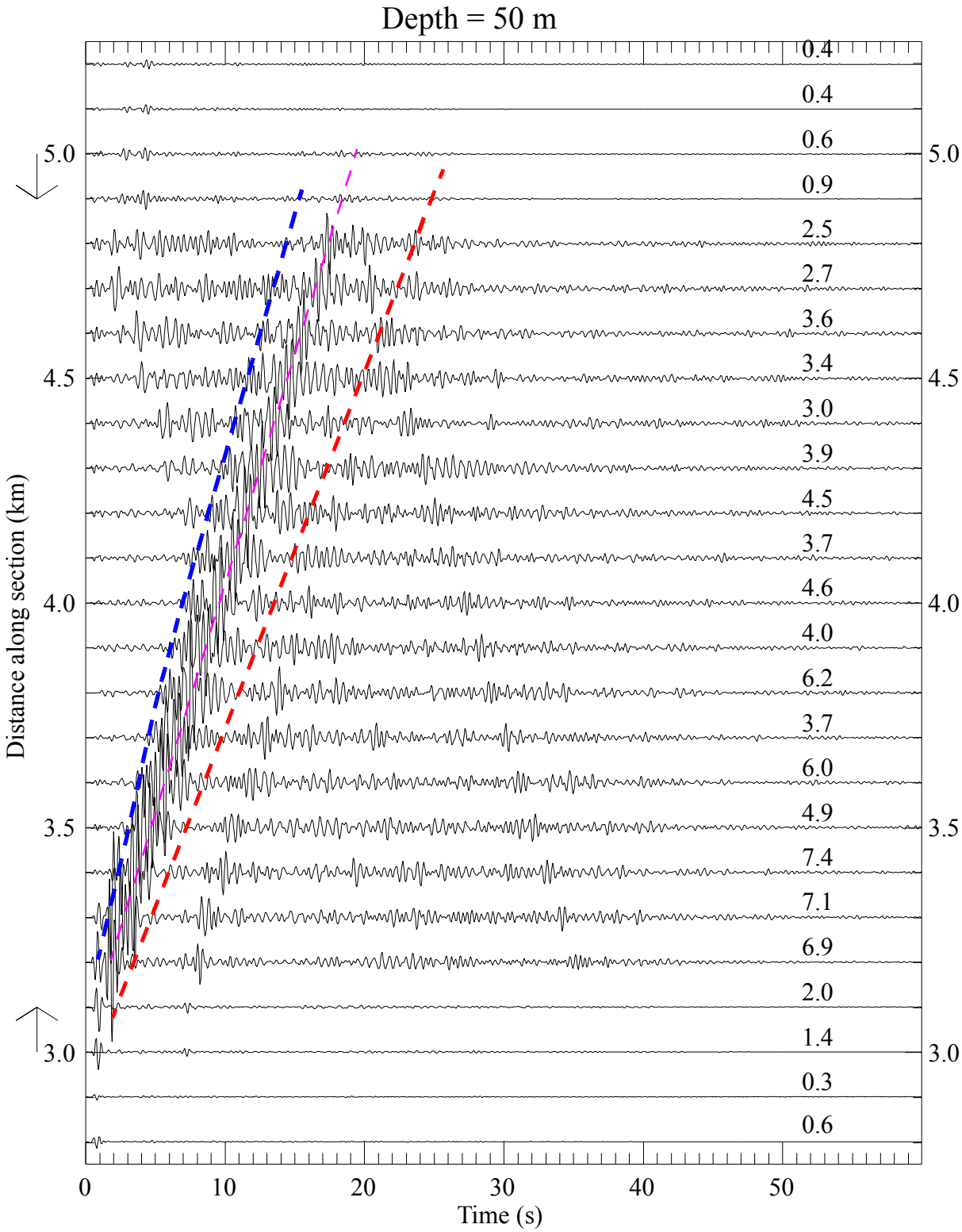

Figure 5-34: Vertical 2D finite-difference acceleration record section z = 50 m.Distances are as shown in Figure 5-22. Peak amplitudes are labels on the right normalized to a maximum value of 10 for all sites in the model. Low-velocity glacial scour sites are between the arrows on the left. Dashed red line shows the end of the basin-edge Airy phase. Dashed blue line is the basin-edge refracted S-wave. Dashed magenta line is the Stonely wave.

internal velocity discontinuities during modulus degradation suggests that these phases will persist as soils respond nonlinearly. Since a significant amount of energy is propagating horizontally at depths of up to 50 m (Figures 5-23 To 5-28), it is necessary to account for this significant seismic energy in 1D vertical-incident SH nonlinear simulations of nonlinear soil effects, since these codes will not simulate the production of these observed phases. Consequently, it is necessary to include the extended durations in the 1D nonlinear inputs to account for observed, broadband, strong-amplitude extended soil response durations, as discussed in Section 6.

The 2D synthetic seismograms show that there is a critical distance range from the southern margin of the glacial scour where peak horizontal acceleration responses are likely to be amplified relative to most of the embankment section of the dam. This amplification is associated with the constructive interference of the scour basin-edge interface waves, particularly the broadband Airy phases, but also the Stonely wave, with the direct, reflected, and basin-edge refracted S-waves. The critical distance of maximum amplification is a function of the sediment velocities, which limited geophysical measurements (Sirles, 1986) show vary vertically and laterally from near the southern glacial scour margin and the borehole located between stations JLD3 and JLD6. There are no geophysical velocity measurements or ground motion recordings between stations JLD2 (modest amplification) and station JLD3 (strong amplification). Although the 2D velocity model does not contain all the complex features of the glacial scour geometry inferred in Section 2, the 2D finite-difference synthetic results indicate that it is likely that amplifications stronger than those measured at stations JLD3 and JL6 probably occur somewhere between stations JLD2 and JLD3 (along the tallest portion of the embankment section of the dam). Due to the lack of sediment velocity information between stations JLD2 and JLD3, it is not possible to indicate the position or magnitude of the additional amplification relative to station JLD3. It is important to understand that the amplification responses at JLD3 are unlikely to represent the maximum amplification along the embankment portion of the dam between stations JLD2 and JLD3.

The glacial scour S-wave velocity structure at the dam is very similar to the Valley of Mexico in Mexico City (Bodin et al., 1997), except that low-velocities extend ~20 m deeper at Jackson Lake Dam. In the Valley of Mexico, monochromatic, large-amplitude ground motions have durations of

~250 s for M > 6.5 seismic sources located > 200 km from the site (Lomnitz et al., 1999). In contrast, the closest portion of the Teton fault is located ~10 km from Jackson Lake Dam. However, the Valley of Mexico is probably significantly longer and wider than the glacial scour basin at Jackson Lake Dam, although the total extent of the glacial scour basin north of the dam is unknown. Consequently, it is likely that the durations in the central portion of the Valley of Mexico would be somewhat longer than at Jackson Lake Dam because the propagation times from the edges of the very-low-velocity basin to the basin interior would be longer.

While the shallowest ~20 m of sediments at Jackson Lake Dam have S-wave velocities very similar to the Valley of Mexico of 80-100 m/s, the compositions of the shallowest sediments differ. The shallowest sediments in the Valley of Mexico consist almost entirely of lacustrine mud (Lomnitz et al., 1999), but the shallowest sediments at Jackson Lake Dam consist of predominantly fluvial units near the surface grading toward dominantly lacustrine sediments at > 20 m depth (Section 2). Consequently, the shallow sediments at Jackson Lake Dam may respond somewhat differently than the shallow sediments in the Valley of Mexico, particularly at large strains. Bodin et al. (1997) noted that the dominance of clays in the Valley of Mexico surficial deposits probably reduced nonlinear ground motion effects from the 1985 M 8.5 Michocaon earthquake because peak strains were about 0.1%, insufficient to cause significant modulus degradation in clay-dominated soils. Nonlinear soil responses in the surficial fluvial deposits at Jackson Lake Dam are expected to more strongly influence S-wave responses than in the Valley of Mexico because expected strains of > 1% from the nearby M ~7 earthquake (Section 6) are likely to cause modulus degradation. While the impact of nonlinear soil responses on the amplitudes of large-amplitude, broadband Airy phases is unknown, it is likely that nonlinear soil responses will increase the duration of ground motions at the dam, relative to linear soil responses. This is a consequence of dynamic modulus degradation, which reduces shallow S-wave velocities during the earthquake, thereby increasing the travel times of Airy phases propagating in the vicinity of the free surface. For example, for a portion of Jackson Lake Dam located 2 km from a glacial scour lateral terminus, it takes about 20 s for the first basin-edge Airy phase to arrive at the site. If the shallow sediment shear modulus is reduced by a factor of four due to nonlinear response, the S-wave velocity is halved and it will take 40 s for the first basin-edge Airy phase to arrive at the site. Thus, if the shallow sediment section is expected to have a

consistent nonlinear shear modulus reduction, the total duration of ground motions at the dam associated with shallow Airy phases is expected to substantially increase if the shallow sediments respond nonlinearly. With respect to the weak-motion Airy phase responses recorded at the dam, a M 7 earthquake is very likely to produced substantially longer duration Airy phase responses along the embankment portion of the dam (even for linear soil responses) because all edges of the glacial scour will be excited by incident S-waves from all possible azimuths (the dam is located near the middle of the fault) for about 20-30 s (duration of rupture plus delays associated with propagation of basin-edge S-waves from the edge of the low-velocity basin near the fault to the dam). Thus, all the edges of the glacial scour will be strongly excited because substantial S-wave arrivals are almost always certain to be incident at angles to maximize basin-edge Airy phase amplitudes (incident at non vertical angles toward the interior of the scour basin). Rupture of the entire length of the Teton fault will increase Airy phase durations and amplitudes at the dam because about 2/3 of the fault is located south of the dam, and all the S-wave arrivals from the southern 2/3 of the fault are likely to produce strong Airy phase amplitudes along the southern portion of the embankment section (e.g., all these S-waves are incident at non vertical angles pointing into the northern interior of the scour basin). It is important to note that Bodin et al. (1997) emphasize an unusual aspect of very-low velocity basins is the large strains that result from the very short wavelengths and horizontally propagating large-amplitude phases, like Airy phases.

5.5 Summary and Conclusions.

Bedrock ground motions propagating from the Teton fault will be modified by the soil column underlying much of Jackson Lake Dam. Recordings of strong ground shaking at the dam that would be needed to directly estimate this effect do not exist. Instead, ground motions from moderate-magnitude local earthquakes were recorded by three-component broadband velocity seismometers at six locations on the dam, and one location on the right abutment. These recordings were compared to reference sites using the method of spectral ratios.

Ground motions on the north dike at stations 24+00, 30+95, and 52+00 are amplified in the frequency range of 0.2 to 1.5 Hz, in comparison to the right abutment. The duration of ground shaking in this frequency band is substantially prolonged. Ground motions at station 13+00 are

not similarly amplified over this frequency range, nor are the durations appreciably prolonged. Shallow sedimentary basins can generate surface waves and converted body waves which result in this type of site response, as shown in Section 5.4. Low-velocity fluviolacustrine sands, gravels and a northward thickening wedge of fines overly higher-velocity glacial drift and gravels below the north dike (for stations greater than 14+00), which effectively produces a sedimentary basin structure.

High-frequency (>1.0 Hz) ground motions recorded directly above the treated embankment foundation at station 24+00 are observed to be lower in amplitude than outside of the treated zone, consistent with the higher shear-wave velocities obtained from the dynamic compaction and Soil Mix Wall (SMW) treatments. However, for frequencies below 1.0 Hz, substantial amplification and prolonging of duration are observed both inside and outside of the treated zone.

Poorly consolidated, potentially liquefiable fluviolacustrine sands and gravels with shear velocities as low as <300 ft/s (<100 m/s) underlie much of the north dike at stations 13+00 and greater. The site response to strong shaking is expected to be non-linear, in contrast to the observed weak motion response. However, both the weak and strong motion responses are influenced by the same shallow depositional basin structure underlying the dam. While the observed weak motion site response (amplification and prolonging of duration) is consistent with that of a shallow closed basin (2-D and 3-D response), it is not easily explained by a vertically-propagating shear-wave in a horizontally stratified soil column (1-D response). The response of a one-dimensional soil column is difficult to reconcile with the observed response on the dam, which appears to be characterized by surface and interface waves and converted body-waves.

Available computer codes for estimating non-linear site response are based on propagating an incident body wave through a 1-D soil column. These codes will tend to underestimate the observed duration of shaking at Jackson Lake Dam because they do not fully account for the 2-D and 3-D response of the local sedimentary basin (converted phases, surface waves, etc.). In order to better account for the 2-D or 3-D character of the observed weak-motion site response, yet employ available one-dimensional codes for estimating non-linear site response, a hybrid approach is used. This approach incorporates the longer durations observed in the weak motion data to modify the bedrock input motions for use in one-dimensional computer codes.

At stations 12+00 and less, the response to strong ground shaking is not expected to have a substantial non-linear component. The observed weak motion response may therefore be applied to bedrock design ground motions without further modifiation.

This section provided vital information necessary to estimate site-specific rock and soil ground motion responses at Jackson Lake Dam associated with **M** ~7 earthquakes on the Teton fault, the topic of the next section.

6.0 GROUND MOTION MODELING

The influences of large-scale crustal velocity structure and source radiation on rock and soil ground motions at Jackson Lake Dam are the focus of this section. Ground motions are synthesized for the rock site station JLDW for a variety of magnitudes and source geometries to quantify peak ground motions scaling and variability associated with earthquake rupture scenarios postulated for earthquakes on nearby Teton fault segments. The uncertainties in fault dip are accounted for by considering three values of dip for each fault segment, yielding a total of six fault segments to consider when simulating ground motions. The northern segment is assigned a strike length of 42 km and the southern segment is assigned a strike length of 18 km. The depth to the bottom of the Teton fault is assumed to be 16 km for all rupture segments and fault dip scenarios (Figures 6-1 and 6-3). Rupture of the northern Teton fault segment is likely to produce a **M** 6.9 earthquake for a dip of 60° and **M** 7.0 for a dip of 45° (**M** 7.0 is also used for a dip of 35°) based on moment fault area relations of Wells and Coppersmith (1994). Rupture of the northern and southern Teton fault segments in a single fault rupture increases **M** by ~0.2 based on moment fault area relations of Wells and Coppersmith (1994) applied to the entire length of the Teton fault. Rupture of the northern segment for dips of 35° and 45° involves fault rupture directly beneath the dam (Figures 6-1 and 6-3). It is necessary to determine how strongly rupture directivity may influence peak ground motions and ground motion variability at the dam for all of these near-source earthquake scenarios. Impacts of 3D crustal velocity structure are substantial and much of the modeling effort is devoted to accounting for the influences of 3D velocity heterogeneity on ground motion amplitudes and durations, and evaluating the influence of fault dip uncertainties on ground motion characteristics.

6.1 Overall Approach

The basic approach follows Spudich and Archuleta (1987). We use the representation theorem, with a kinematic approximation for seismic radiation from a propagating fault rupture, to estimate linear ground motions for south abutment “rock” site conditions. Synthetic reciprocity Green’s functions (RGF) are calculated using 3D viscoelastic finite-differences using the approach of Graves and Wald (2001) and the 3D velocity-density-attenuation model from Section 4. These 3D

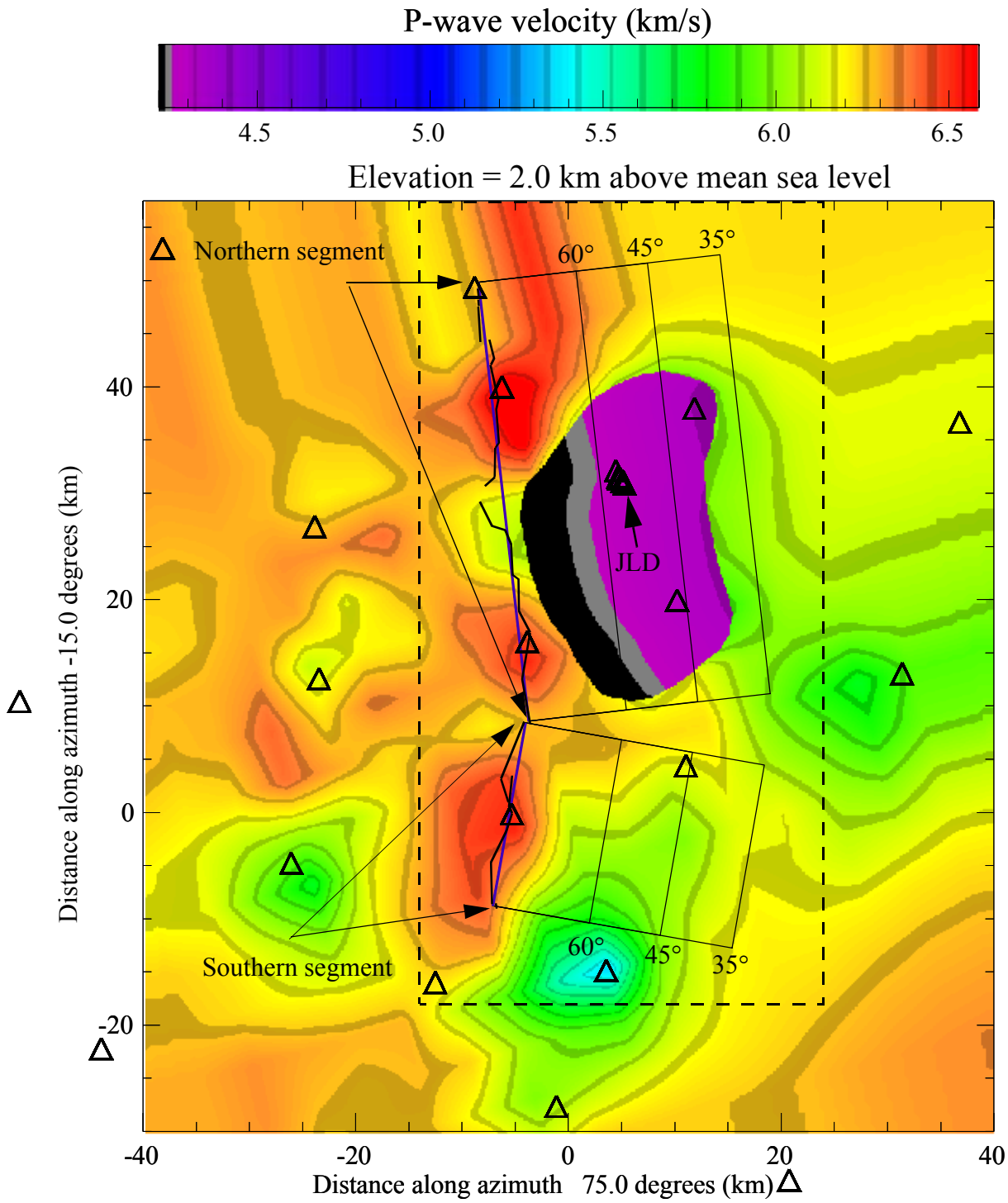

Figure 6-1: Plan view of the ground motion P-wave 3D velocity model at elevation 2 km. Seismographic stations are triangles with the cluster of stations at Jackson Lake Dam as indicated by JLD. Solid rectangles show plan projections of the Teton fault segments for dips as labeled for total fault depths of 16 km. The blue line segments show the approximation to the surface traces of the Teton fault indicated by the irregular solid line segments. Large dashed rectangle shows the limits of the 3D elastic finite-difference grids. Arrows show the limits of the two fault segments considered in ground motion simulations as labeled.

RGFs are mostly used for frequencies < 1 Hz. Empirical Green's functions (EGF) are extracted from site-response recordings of local earthquakes to provide responses > 1 Hz. Point source summation with Kostrov-like slip-velocity time functions is used to compute synthetic ground motion time histories in an approach similar to O'Connell et al. (2001). The nonlinear approach of Bonilla (2001) is used to calculate soil ground motions, including nonlinear soil responses, in low-velocity soils beneath the embankment portion of the dam. Response spectral quantiles are used to associated simulated ground motions with specific probabilities of occurrence and several simulated and observed ground motions time histories are recommended for dynamic analyses of the dam.

6.1.1 Green's Function For Linear Ground Motions. The 3D elastic finite-difference approach of Graves (1996), modified to included viscoelastic responses (Graves and Day, 2003), is applied invoking reciprocity to calculate the primarily < 1 Hz Green's functions on all six fault segments, using a nominal 0.2 km point-source spacing on the faults. This requires specifying a great deal of information about the 3D variations of seismic velocities, density, and attenuation; derivation of these quantities is summarized in Section 4. Site-response recordings of eight local earthquakes are used to construct a suite of empirical Green's functions, primarily for the purposes of synthesizing ground motion responses for frequencies > 1 Hz. The 3D Green's function were used to establish EGF amplitudes for integration points on all fault segments. The details of the preparation of the Green's functions are presented in Section 6.3.

6.1.2 Nonlinear Soil Ground Motions. The seismic responses of near-surface soils often exhibit nonlinear stress-strain relationships. Long-duration ground motions were observed on the embankment section site-response stations located on low (~100 m/s) S-wave velocity soils (Section 5). It is necessary to estimate ground motions at sufficient depth to provide linear input ground motions for nonlinear ground motion calculations necessary for engineering analyses of the dam. One option was to input rock motions at the base of the low-velocity soils at ~140 m, but the rock motions do not contain the long-durations ground motion responses characteristic of the very-low-velocity (VLV) glacial scour portion of the dam. In Section 5, it was demonstrated that the long-duration soil motions at the surface are likely to originate at > ~25 m depth due to strong vertical velocity gradients and velocity discontinuities within the low-velocity materials within

the glacial scour. A difficult problem is to accurately represent the seismic responses within the low-velocity soils to include the 3D duration influences of the glacial scour low-velocity structure as inputs into nonlinear soil response calculations, in part, because it is not clear *a priori* at what depth the soil responses behavior becomes significantly nonlinear. A convolution operator developed in Chapter 5 with weak-motion site-response data is used to develop subsurface ground motions for input into nonlinear soil response calculations. Details are presented in Section 6.6.

A second problem is to find a way to propagate the long-duration responses at > ~25 m depth to the surface that includes likely nonlinear soil responses. The one-dimensional (1D) equivalent-linear method represented by SHAKE (Schnabel et al., 1972) is the most common method for engineering analysis of earthquake ground motions for soil site conditions. However, it is an approximate method that does not have the ability to reproduce some observed classes of nonlinear soil response associated with saturated, low-velocity soils (typical of the soils in portions of the foundation of the embankment portions of Jackson Lake Dam), particularly the sometimes large-amplitude cusped, one-sided accelerograms that arrive behind the first S-waves (Porcella, 1980; Holzer et al., 1989; Zeghal and Elgamal, 1994; Iai et al., 1995; Archuleta, 1998; Bonilla *et al.*, 1998, Frankel et al., 2002). Holzer et al. (1989) reported large-amplitude cusped, one-sided accelerograms in surface seismograms of the 1987 Superstition Hills earthquake recorded on an array of surface and borehole accelerometers and downhole pore-pressure transducers. This site underwent liquefaction during the shaking. Holzer et al. (1989) found that these pulses occurred during drops in the pore pressure and suggested that they were related to episodic lateral spreading. Zeghal and Elgamal (1994) analyzed the same array data and proposed that at large strains after initial liquefaction, the soil became dilatant, pore pressure dropped, and the soil increased in strength, thus producing the cusped pulses. Strain hardening from soil dilatancy has also been observed in laboratory studies (Ishihara, 1985; Kramer and Arduino, 1999). Frankel et al. (2002) note that the cusped arrivals observed from the **M** 6.8 2001 Nisqually earthquake that arrived after the S-waves sometimes actually increased the peak accelerations relative to the peak accelerations associated with the S waves. In some cases, the nonlinear response increases the peak accelerations compared with the linear response, an observation contrary to conventional wisdom on nonlinear response.

To date no one has published results using SHAKE that reproduce the nonlinear behavior discussed above. In view of the inability of SHAKE (Schnabel et al., 1972) to reproduce observed nonlinear soil responses associated with site conditions similar to site conditions at Jackson Lake Dam (Archuleta, 1998), the NOAH nonlinear code (Bonilla et al., 1998; Bonilla, 2000) is also used to estimate ground motions as a function of depth below the portion of the embankment with ~140 m total thickness of soil deposits above the overcompacted till. NOAH is a NOnlinear Anelastic Hysteretic finite difference code, which computes the nonlinear wave propagation in water saturated soil deposits subjected to vertically incident SH ground motion. The constitutive equation implemented in this code corresponds to the strain space multishear mechanism model developed by Towhata and Ishihara (1985) and Iai et al. (1990). The code is able to perform total and effective stress analyses. The current rheology works particularly well to model the cyclic mobility of sands under undrained conditions. Results of these investigations are summarized in Section 6.6 and Appendices E and F.

6.2 Source Parameterization

A kinematic rupture model is used that mimics the spontaneous dynamic rupture behavior of a self-similar stress distribution model of Andrews and Boatwright (1998). The kinematic rupture model is also similar to the rupture model of Herrero and Benard (1994). Self-similar effective stresses (and slip velocities) are generated over the fault with rise times that are inversely proportional to effective stress. Peak rupture slip velocities evolve from ratios of one relative to the sliding (or healing peak) slip velocity at the hypocenter to a maximum ratio of 4:1 consistent with the dynamic rupture results of Andrews and Boatwright (1998) that shows a subdued Kostrov-like growth of peak slip velocities as rupture grows over a fault. The kinematic model used here produces slip models with $1/k^2$ (k is wavenumber) distributions consistent with estimates of earthquake slip distributions (Somerville *et al.*, 1999) and ω^2 (ω is angular frequency) displacement spectra in the far-field. Oglesby and Day (2002) used numerical simulations of dynamic fault rupture to show that rupture velocity, rise time, and slip are associated with fault strength and stress drop, as well as each other. The kinematic rupture model used here enforces correlations between these parameters by using a common fractal seed to specify relationships between all these fault rupture parameters, as discussed in more detail in Section 7.2 in relation to modeling of near-source ground motions from the 1994 M 6.7

Northridge, California, earthquake and in O'Connell et al. (2001). Oglesby and Day (2002) and Guatteri et al. (2003) used dynamic rupture simulations to demonstrate that rupture parameter correlation, as implemented in the stochastic kinematic rupture model outlined here, is necessary to produce realistic source parameters for ground motion estimation.

To calculate peak slip velocities, healing slip velocities, and displacements for moment calculations, we used the approximation of the Kostrov slip-velocity function of O'Connell and Ake (1995)

$$\dot{s}(\underline{r}, t) \approx C(\upsilon_r, \alpha, \beta)\frac{\sigma_E}{\mu}\beta A(H(t - T_{initial}) - H(t - T_{heal}))$$
$$\left(0.7exp\left(-\frac{t}{(0.9a)}\right) + 0.15exp\left(-\frac{t}{(0.4b)}\right) + 0.15exp\left(-\frac{t}{(0.8b)}\right)\right. \tag{6-1}$$
$$\left.\frac{-(t - T_{stop})}{h}[H(t - T_{stop}) - H(t - (T_{heal}))] + H(t - T_{initial}) - H(t - T_{heal})\right)$$

in the kinematic rupture code, where $\underline{r}$ is the distance on the fault from the hypocenter, α is the compressional velocity, β is the shear velocity, μ is the rigidity, σ_E is the effective stress, $C(\upsilon_r, \alpha, \beta)$ is a number determined from υ_r, the rupture velocity, and α/β (Dahlen, 1974; Richards; 1976), H is the Heaviside step function, t is time of rupture, $T_{initial}$ is the time of rupture initiation, T_{heal} is the time the rupture begins to stop, and T_{stop} is the time rupture ceases. A is an amplitude factor calculated from the Kostrov slip-velocity function of Archuleta and Hartzell (1981) at dt after $T_{initial}$ that allows (6-1) to replicate the Kostrov slip-velocity function, and a, b, and c, are times from the onset of rupture until the slip velocity reaches, 0.5, 0.1, and 0.05 of the difference between peak slip-velocity amplitudes and steady slip-velocity amplitudes, respectively. Equation (6-1) was normalized over the entire fault to produce a maximum ratio of peak rupture slip velocity to peak healing slip velocity of 3:1. The approximation to $C(\upsilon_r, \alpha, \beta)$ of O'Connell and Ake (1995)

$$C(\upsilon_r, \alpha, \beta) = 0.446437 + 0.707423\upsilon_r - 0.151251\frac{\alpha}{\beta} \tag{6-2}$$

was used in (6-1). It has a maximum error of less than 2% relative to the results of Dahlen (1974) and Richards (1976). Guatteri et al. (2003) showed with dynamic rupture simulations that

Kostrov-like slip-velocity functions provide the most-realistic slip-velocity functions for ground motion estimation.

The time domain Kostrov slip velocity function of Archuleta and Hartzell (1981)

$$\dot{s}(\underline{r}, t) = C(\upsilon_r, \alpha, \beta)\frac{\sigma_E}{\mu}\beta t\frac{H\left(t - \frac{r}{v}\right)}{\sqrt{t^2 - r^2/v_r^2}} \tag{6-3}$$

was convolved with the 3D Green's functions to produce the < 1 Hz synthetic ground motions. The EGF summations required 16 times more integration points than the RGF summations to ensure integral convergence, resulting in > 400,000 point source integrations to calculate for each single ground motion. To eliminate the slip-velocity convolutions from inside the point source summation integral, an approximate "Kostrov" function was convolved after the EGF point-source summation to approximate the amplitude and phase effects of the a Kostrov slip velocity functions. The high-frequency approximation to the Kostrov function was constructed by extracting the portion of the Kostrov function that produces the deviation of the Kostrov function from a boxcar function (Figure 6-2a), and convolving that "residual function" (Figure 6-2b) with the EGF synthetic ground motions. This produces a high-frequency decay similar to using the exact Kostrov function (Figure 6-2c), but does not to account for variation in Kostrov slip velocity behavior as a function of rupture time. This approach is more accurate than other methods of high-frequency summation methods, like stochastic subevent summation used by Silva and Lee (1987), Schneider et al. (1993), Zeng et al. (1994), and Beresnev and Atkinson (1997), because it employs a rigorous point-source integration accuracy of 6 points-per-shortest-wavelength (Spudich and Archuleta, 1987), but is less accurate than retaining the slip-velocity function convolution at each integration point.

Effective stress correlation lengths were increased by 33% relative to the **M** 6.7 Northridge rupture simulations of O'Connell (2001) to be consistent with the empirical relations of Somerville et al. (1999), that indicate that asperity size increases with magnitude. Rupture velocities were allowed to vary over a wide range (between 0.6*β to 1.05*β) in each rupture simulation to allow rupture directivity caustics to develop, and to produce variable rupture times.

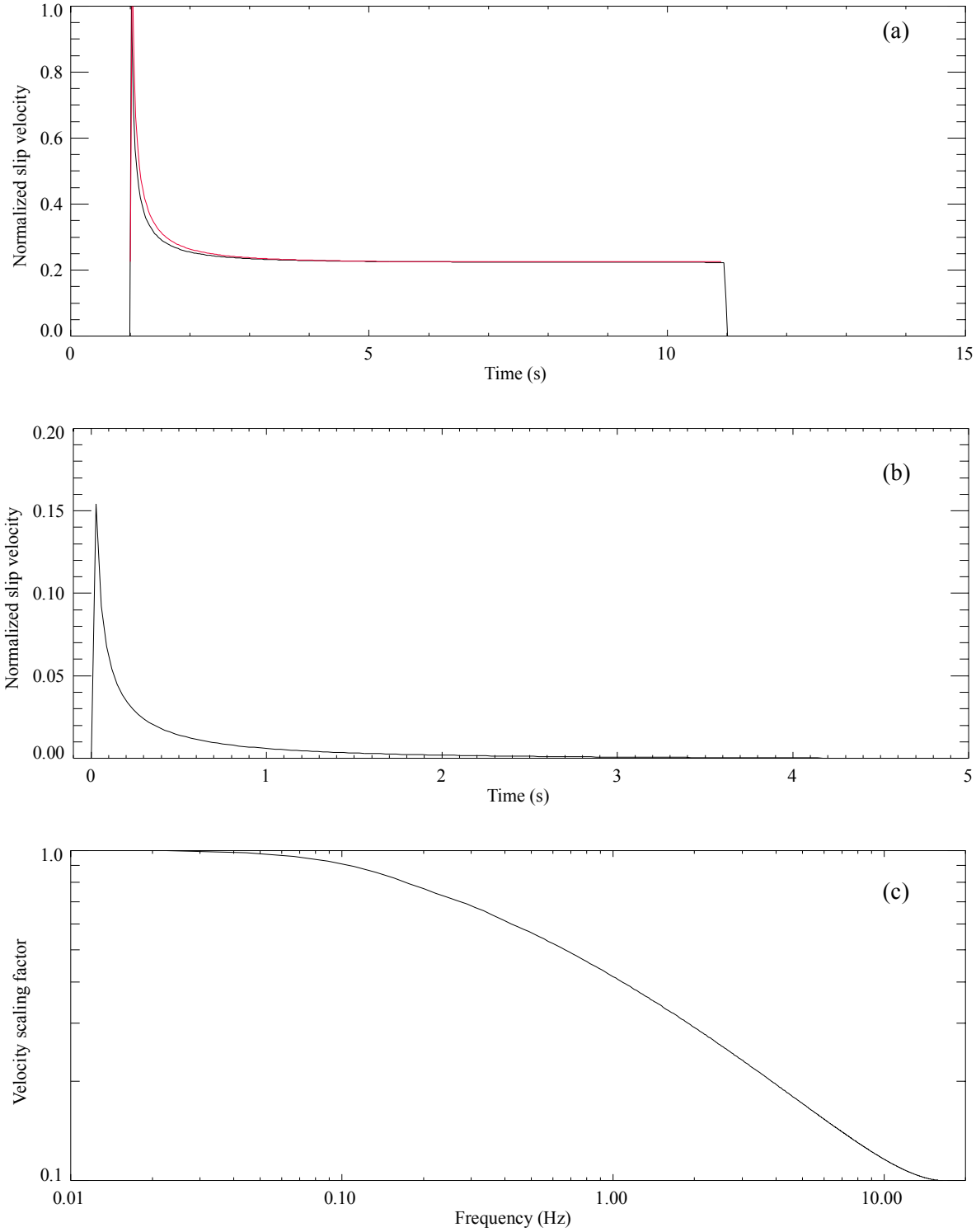

Figure 6-2: High-frequency approximation to the Kostrov slip-velocity function. (a) Exact Kostrov slip-velocity function for a rupture time of 1 s and duration of 10 s is the black curve and the red curve is the portion of the slip-velocity function extracted and rescaled to unit amplitude at a frequency of 0.022 Hz and plotted in (b). (c) Ground velocity scaling factor as a function of frequency obtained from (b).

Effective stresses averaged 30-40 bars, consistent with stress drops typically associated with normal-faulting earthquakes (McGarr, 1984; Mendoza and Hartzell, 1988; Anderson et al., 2001).

A large number of assumptions and choices must be made to specify earthquake rupture models. This discussion focuses on significant assumptions made in this study:

1. The radiation pattern is applied at all frequencies. As discussed in O'Connell and Ake (2002), the high frequency limits of coherent seismic radiation are not well established. There are theoretical reasons to expect seismic radiation to become incoherent at sufficiently high frequencies as a result of dynamic rupture processes (Madariaga, 1977; Boatwright, 1982). The scattering properties of crustal velocity heterogeneity also contribute to reducing high-frequency coherence (O'Connell, 1999a). The crustal wave propagation filter is sufficiently strong to make it impossible to determine the source limits of coherent seismic radiation from surface ground motion observations. Abercrombie (1995) showed that the top several km of the crust severely attenuate high-frequencies and that downhole earthquake recordings show that earthquake source processes are self-similar. Since coherence at the site persists to at least 4 Hz, and possible to 6 Hz (Section 4), it is prudent to apply the radiation pattern for all frequencies.

2. A total of eight EGF's are used in the simulations (Appendix D). In this study phase is not spatially interpolated between EGF's, as suggested by Hutchings (1994). Since phase is not randomized beyond phase variability contained in the eight distinct EGF's, phase is less coherent than the approach of Hutchings (1994). The random selection of one of the eight EGF's at each point-source positions and the considerably variable initial phases of the direct S-waves in the EGF's suggests that phase may be overly randomized in the EGF ground motion simulations for low frequencies. Conversely, the random selection of EGF's at each point-source position is effectively a proxy for randomizing the phase of high-frequencies, e.g., reducing the coherence of the effective radiation pattern for all frequencies.

3. Rupture velocity is assumed to not exceed 1.105*β. As discussed in O'Connell and Ake (2003), there are a number of earthquakes where rupture velocity may have reached ~1.4*β. and there are theoretical reasons to expect high rupture velocities in some situations (Ben-

Zion, 2001). A significant caveat is that there are no dynamic investigations of rupture velocities and systematic velocity contrasts across faults for dipping faults have been performed (Ben-Zion, 2001; O'Connell and Ake, 2003). So the arguments presented below w.r.t. high rupture velocities on the Teton fault are by analogy to strike-slip simulations (summarized in Ben-Zion, 2001) and observations (Bouchon et al., 2001).

Rupture velocities ~1.4*β. on the Teton fault are not likely to occur for the following reasons:

1. Rupture is likely to propagate from near the bottom of the fault to the surface, in the opposite direction to the normal-slip direction of the hanging wall. The 3D velocity inversion shows a slight decrease of P-wave velocity from the footwall to the hanging wall below 5 km depth (admittedly, the resolution of this velocity change is marginal, at best). Thus, slip direction and rupture direction are the same for the stiffer side of the fault and supershear rupture velocities of ~1.4*β are unlikely for depths > 5 km (by appealing to strike-slip results summarized in Ben-Zion, 2001).

2. Oglesby et al. (1998) present dynamic rupture simulations that show that slip may jump to the free surface and propagate downdip to intersect the primary updip rupture front. This results was reproduced using the approach of Andrews (1999). In this case, rupture is coincident with the slip direction of the hanging wall. However, the gravity modeling summarized in Byrd et al. (1994 and references therein) and velocity structure modeling in Section 4 suggest that a high-density body is located in the hanging wall between the fault and the LVB. Consequently, the compliant material is on the footwall and is not moving in the direction of rupture for downdip rupture; supershear rupture velocities of ~1.4*Vs are unlikely for this configuration (Ben-Zion, 2001).

There is a possible exception that would allow for rupture velocities of ~1.4*β on a portion of the Teton fault. Updip rupture and footwall slip direction are parallel for the top several km of the fault, so supershear rupture velocities of ~1.4*β are not precluded in this region (Ben-Zion, 2001). However, the velocity contrast across the fault in the top 5 km may be insufficient to allow supershear rupture velocities of ~1.4*Vs. Without dynamic rupture simulations using the fault geometries of the Teton fault in a realistic 3D modulii structure, it is unclear what various rupture

velocity scenarios are likely or unlikely. This is an issue that could significantly influence ground motions at Jackson Lake Dam and may merit further investigation.

6.3 Linear Wave Propagation Methods

This section provides details of the application of the viscoelastic 3D finite difference methods of Graves and Day (2003) and P.C. Liu (pers. comm.) to calculate ground motions for frequencies < 1 Hz, and construction of empirical Green's functions for simulated ground motions for frequencies > 1 Hz.

6.3.1 Low-Frequency 3D Green's Functions. In Section 4, a finite 3D grid of velocities, densities, and attenuation coefficients that contains the Teton fault segments, the dam, and sufficient distance from the grid boundaries to minimize artificial boundary effects was constructed using available geophysical data. In Figure 6-3 representative cross-sections show the positions of the Teton fault for the three discrete dips used in ground motions simulations. As discussed in Section 4, there are significant caveats concerning the velocity model, particularly the LVB that contains the dam. First, while the strong velocity contrast between the LVB and the surrounding medium reproduce overall amplitude and duration characteristics of MEQ ground motions recorded at the dam, the eastern extent of the LVB is artificially truncated, based on the refraction travel-time data. The overall shape and roughness of the bottom of the LVB are not well constrained by the data analyzed to date. The 2D finite-difference modeling suggested that strong correlated-random velocity variations may exist in the LVB, but the velocity model used here (Figures 6-1 and 6-3, Appendix C) has no randomization of LVB velocities. The only velocity randomization was applied to the medium outside the LVB in the form of vertical velocity oscillations with wavelengths of ~1 km that are strongest in the highest velocity gradient portions of the model (Figure 6-3). More sophisticated randomizations (O'Connell, 1999a) could significantly change predicted ground motions, but would entail a significantly expanded scope of investigation. Since as is shown in Section 6.4, the LVB strongly influences peak ground motion scaling and durations at the dam, the uncertainty in the 3D velocity-model may be an important source of ground motion estimation uncertainty at the dam. To better characterize ground motion estimation uncertainties, several alternative ground motion estimation approaches that use purely empirical Green's functions are presented and used in Section 7.

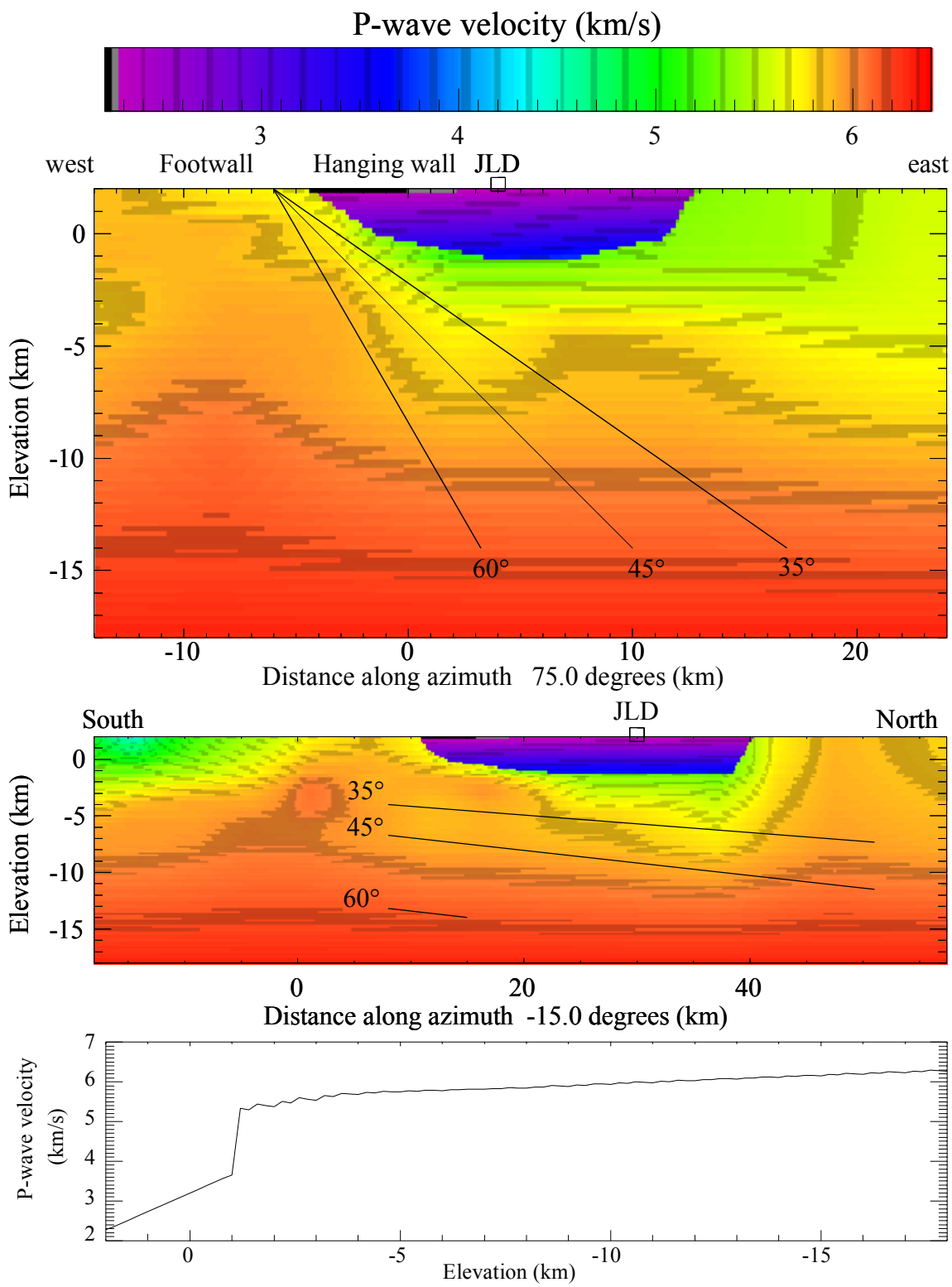

Figure 6-3: Two cross sections of the ground motion P-wave 3D velocity model with orientations as labeled. Approximate position of the south abutment of the dam is the box labeled JLD. Line segments are the intersections of the northern Teton fault segments for dips as labeled (top figure shows depth limits for ground motion simulations). The P-wave velocity-elevation profile beneath JLD is shown in at the bottom.

6.3.1.1 Viscoelastic 3D Finite-Difference Calculations. Viscoelastic 3D finite difference methods are used for forward-modeling ground simulations of single and multiple segment finite-fault rupture of the Teton fault using the method of P.C. Liu (pers. comm). The approach of Graves and Wald (2001), updated as per Graves and Day (2003) to provide a more realistic approximation for damping, was used to calculate reciprocity Green's functions for grids of point sources distributed on the six fault segments used to evaluate ground motions associated with earthquakes on the Teton fault.

Reciprocity Green's function were obtained for the south abutment of Jackson Lake Dam by calculating the moment tensor responses at 93,485 point-source positions distributed across the six Teton fault segment scenarios for each ground motion component, yielding 280,455 Green's function files. The nominal point-source spacing along strike and downdip was 0.2 km, but deviates slightly from 0.2 km, because point-source positions coordinates are rounded to the nearest integer node position in the reciprocity calculations. The forward-modeling code interpolates precisely between nodes to enforce a 0.2 km point-source spacing along strike and down dip. The maximum frequency before velocity dispersion begins to influence calculated responses is 0.8-1.0 Hz using these node spacings. Consequently, the 3D finite-difference results were low-pass filtered using a two-pole Butterworth filter with a corner frequency of 0.8 Hz to smoothly attenuate high-frequency responses prior to blending with EGF ground motions, as described below. This filter reduced 1.0 Hz amplitudes by half, making 1.0 Hz the cross-over frequency for blending high- and low-frequency synthetic ground motions. A time step of 0.0015 s was used to meet explicit stability requirements. After anti-alias filtering, computed responses were saved every 0.015 s. The anti-alias filter was applied to the source time function, a Gaussian velocity pulse, to improve computational efficiency. The anti-alias filter and Gaussian source-time function responses were deconvolved from the reciprocity Green's function in preparation for the imposition of Kostrov-like source time functions for ground motion synthesis.

6.3.2 High-Frequency Empirical Green's Functions. In theory there is no reason the **M** < 3 EGF's could not be used to produce broadband ground motions. In practice, ambient background noise precludes using the EGF's for frequencies substantially < 1 Hz. A total of eight MEQ three-component seismograms obtained from site-response stations in the vicinity of

Jackson Lake Dam were used to produce EGF's for ground motion simulations corresponding to earthquake ruptures on the northern Teton fault segment (Figure 6-4, Table 6-1). Seven

Table 6-1: Empirical Green's Function Earthquake Information

Date.	Time.	Latitude.	Longitude.	Elevation.	Magnitude.
1996/09/29	00:35:59.471	43.91073	-110.64070	-3.720	1.6
1996/10/15	22:03:12.602	43.89276	-110.67271	-8.050	2.0
1996/11/28	09:56:56.902	44.00331	-110.54839	-7.230	2.2
1997/02/06	18:56: 7.464	43.70396	-110.43253	-4.830	2.2
1997/09/11	04:11:18.022	43.93142	-110.56208	-6.550	2.0
2001/04/19	03:28:19.000	43.82266	-110.69444	-1.870	1.4
2001/11/15	02:16:10.000	43.68424	-110.49812	-2.870	2.9
2001/12/06	14:15:14.000	43.82436	-110.82595	-7.890	2.2

seismograms were obtained from station JLDW, located on the south abutment of the dam. One seismogram was obtained from station JLD7 located on the northern end of the dam because the seismograms from stations JLDW and JLD2 were dominated by noise. These earthquakes were selected because of their proximity to the northern segment of the Teton fault. Several of the earthquakes conceivably are located on the Teton fault; the uncertainties in fault dip and hypocenter locations precludes definitive assignment of these earthquakes to the Teton fault.

The mean spectral velocity responses of the 3D reciprocity Green's functions in the ~0.8 Hz to 1.5 Hz frequency band were used to establish EGF scaling for integration points on all fault segments. Although the strict grid dispersion limit for the 3D RGFs was about 1 Hz (Moczo et al., 2000), the realities of EGFs signal-to-noise as a function of frequency required calculating mean amplitudes in the ~0.8 Hz to 1.5 Hz frequency band. Rigorously extending the 3D RGF calculations to 2 Hz would have required 8 times more memory and storage, and 16 times more computer time (about 2 months), and was not feasible within the project schedule. The approach used was probably the most accurate approximation available; alternative 1D wave methods including reflectivity approaches were considered, but would have produce larger errors. Further calibrations of estimated ground motion amplitudes using purely empirical Green's functions are presented in

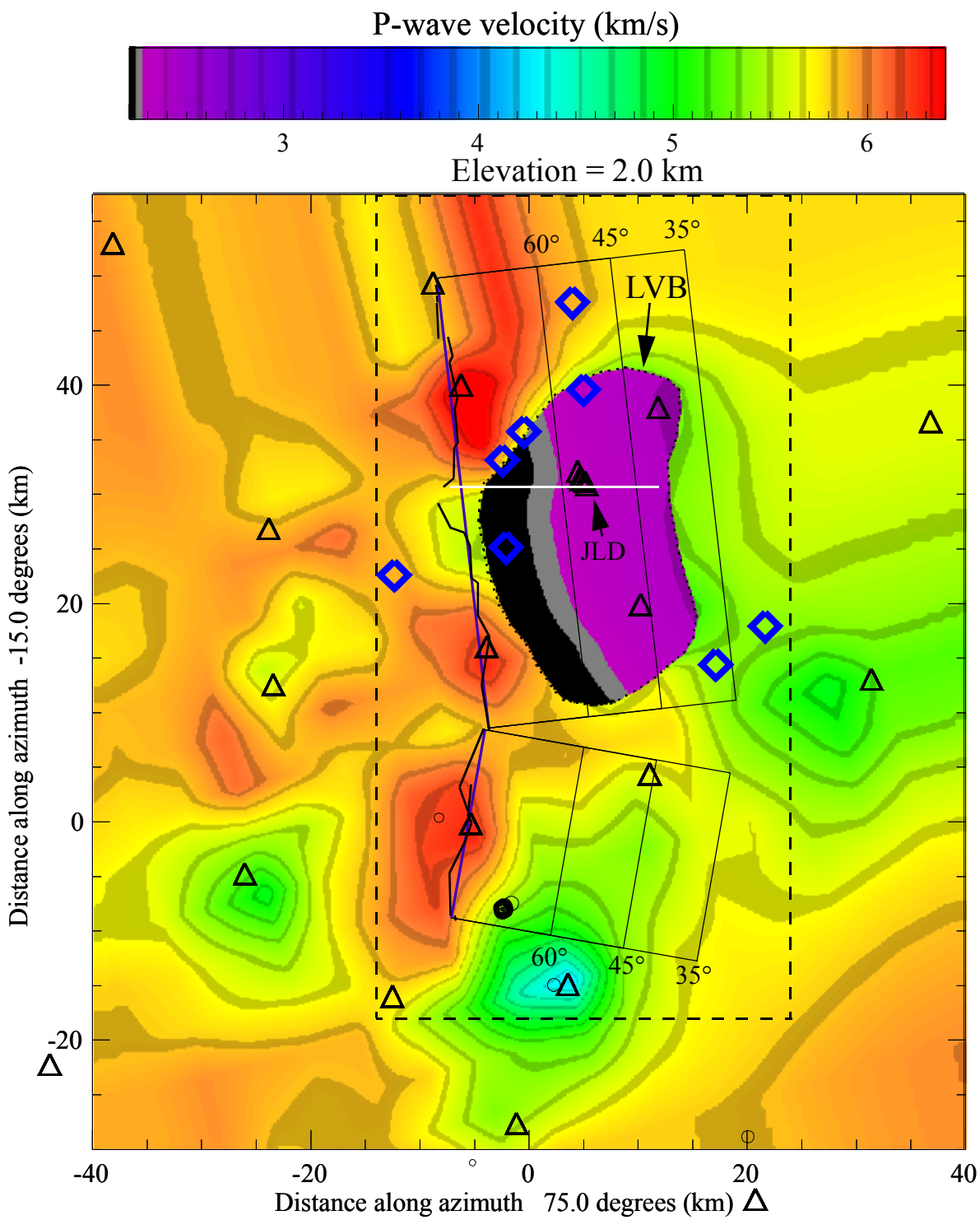

Figure 6-4: Epicenters of the EGFs with P-wave 3D velocity model at elevation 2 km. Blue diamonds are EGF epicenters. Seismographic stations are triangles with the cluster of site-response stations at Jackson Lake Dam indicated as JLD. Solid rectangles are plan projections of the Teton fault segments for dips as labeled. Blue line segments show approximations to the surface traces of the Teton fault (irregular solid line segments). Large dashed rectangle shows the limits of the 3D elastic finite-difference grids. Closed dotted curve labeled LVB denotes the limits of the LVB and circles are event epicenters. The white line shows ground motion profiles in Figs. 6-8 to 6-15.

Section 7 to better ascertain ground motion the significance of theorectical Green's function assumptions on ground motion uncertainties.

The amplitude and polarity plots in Figures 6-5 to 6-7 provide insights into the factors that most strongly influence ground motion amplitudes at the dam. For E15S horizontal motions, large slip-velocities on the upper half of the fault within a ~15 km strike distance region centered on the dam produce ground velocities at the dam 3 to 6 times stronger than slip-velocities on the rest of the upper half of the fault (Figure 6-5). The polarities of the largest contributors to ground velocity at the dam have mixed S-wave polarities, which generally reduces amplitudes associated with directivity, although the dam is located too far east of the fault to experience the strongest directivity effects (see Section 6.4). The polarity variability is a product of a simple radiation pattern effect where the polarity changes at ~15 km downdip distance. S-wave propagation complexity accounts for the varying polarities at downdip distance < 10 km; S-wave interacts with the 3D LVB make polarity identification ambiguous and may produce phases shifts sufficient to switch first S-wave arrival polarities. Slip-velocities in the ~20 km strike distance region centered on the lower half of the fault produce ground velocities at the dam ~2 times stronger than slip-velocities on the rest of the lower half of the fault (Figure 6-5). For the dam to experience decreased E15S ground motion velocities, would require that no high slip-velocity asperties occur in the central half of the northern rupture segment. Somerville et al. (1999) obtained relations between seismic moment and asperities radius. Using there relation for a **M** 7.0 earthquake on the northern Teton fault segments, indicates that the largest asperity would have diameters of ~11-15 km. Somerville et al. (1999) found that the location of the centers of asperities for dip slip faults were located within the central 80% of fault strike about 86% of the time. Asperities centered 20% or 80% of the strike distance would have nearly half of their asperity areas intersecting the regions of elevated amplitude contribution in Figure 6-5. Thus, it is likely (> 86%) that at least half or more of the area of the largest asperity on the northern Teton fault segment will occur on the portions of the fault that produce the strongest E15S ground shaking.

The situation is more complex for the N15E horizontal component (Figure 6-6); the polarities switch along strike centered on the strike position of JLDW and the radiation pattern produces a

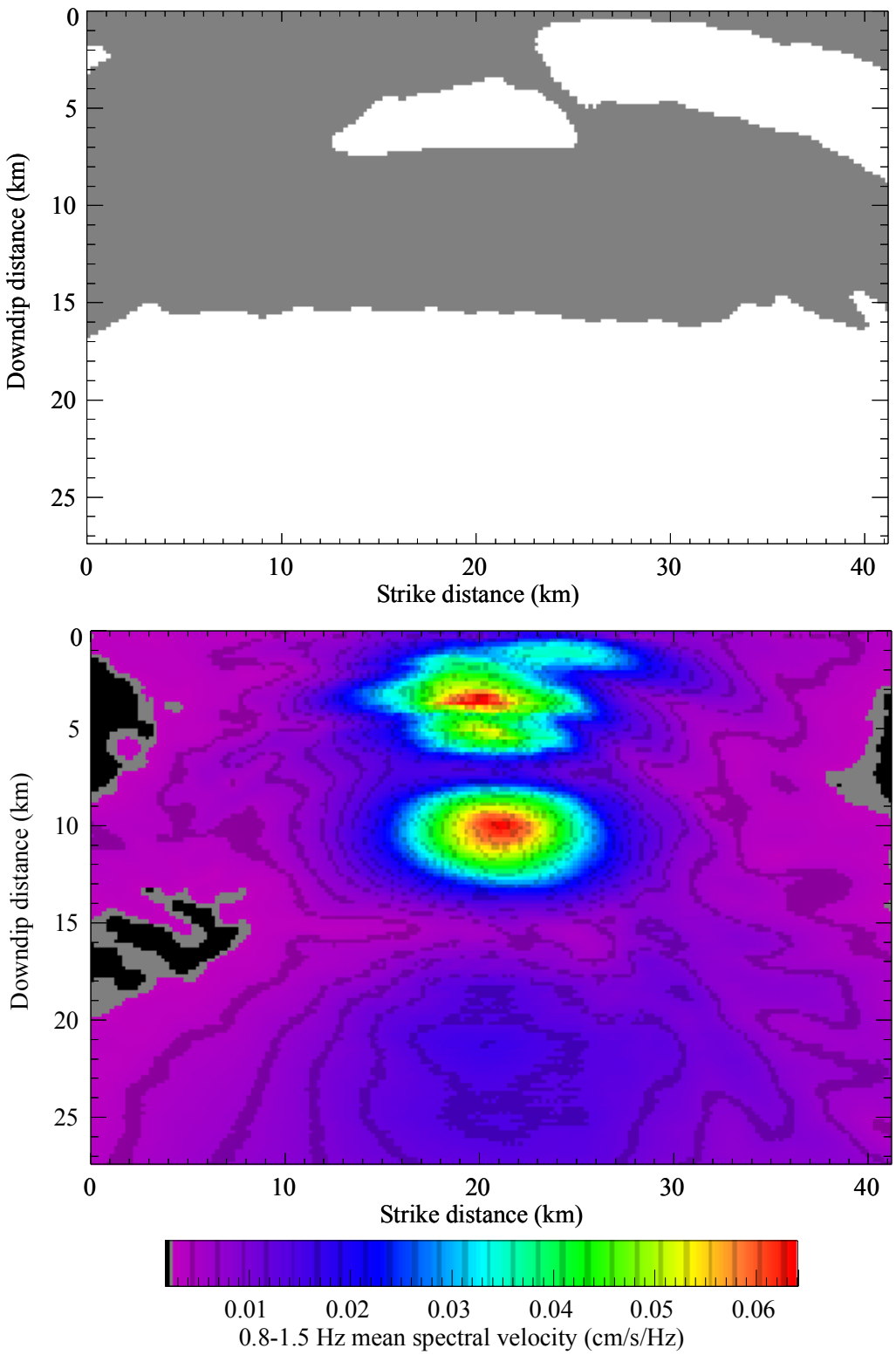

Figure 6-5: E15S-component S-wave normal-dip-slip polarities and 0.8-1.5 Hz amplitudes at JLDW for a 35° fault dip. Perspective is normal to the fault surface. Polarity is shown at the top with grey positive and white negative. RGF mean spectral amplitudes are color contoured with the color bar showing the amplitude range. Point source spacing is 0.2 km. JLDW's strike position is ~21 km.

nearly quadrapole amplitude variation about the position of the normal on the fault to JLDW. It appears that the LVB substantially amplifies N15E ground motions associated with seismic radiation from the shallow portion of the fault located in the ~10 km portion of the fault south of the JLDW. Again the central half of the fault produces the largest ground motion amplification at the dam, similar to the E15S component (Figure 6-5), except there are near nulls associated with the quadrapole radiation pattern in the center of the fault (Figure 6-6). Thus, the N15E motions are also likely (>86%) to be amplified by the largest rupture asperity, in a manner similar to the E15S component. The polarities for the vertical S-wave contributions are complex and the strongest contributions to vertical motions are confined to the upper half of the fault (Figure 6-7). Consequently, if most of the largest asperity were located on the lower half of the fault, vertical ground velocities at JLDW would be lower than for either of the horizontal components.

The polarity complexities in Figures 6-5 to 6-7 ensure that realistic radiation patterns are used when summing the EGF. Vidale (1989) showed that the standard double-couple radiation pattern is observable to 6 Hz based on analysis of the mainshock and an aftershock from the Whittier Narrows, California, thrust-faulting earthquake sequence. In contrast, Liu and Helmberger (1985) found that a double-couple radiation pattern was only discernible for frequencies extending to 1 Hz based on analysis the 1979 Imperial Valley earthquake and an aftershock. Since it was possible to model MEQ S-waves to at least 4 Hz in Section 4, it is more appropriate to include the radiation pattern explicitly in the EGF summations, than to assume random polarities at frequencies > 1 Hz. Consequently, polarity-corrected EGFs are likely more realistic for frequencies extend to 4-6 Hz than assuming random polarities EGFs (e.g., stochastic subevent summation as used by Silva and Lee, 1987; Schneider et al., 1993; Zeng et al., 1994; Beresnev and Atkinson; 1997).

Several processing steps were required to convert the seismograms to EGF's. First, the S-wave arrival times were picked to provide a time reference for the finite-fault summations. Also, the polarities of the initial S-wave arrivals were picked and the seismograms normalized to have positive initial polarities on all components prior to application of the radiation pattern polarities. The radiation pattern polarities and overall amplitude scaling were obtained by using the mean ~0.8 Hz to 1.5 Hz spectral amplitudes from the 3D Green's functions distributed over the fault surfaces (remember we have three fault dips to consider for the northern segment) to scale the

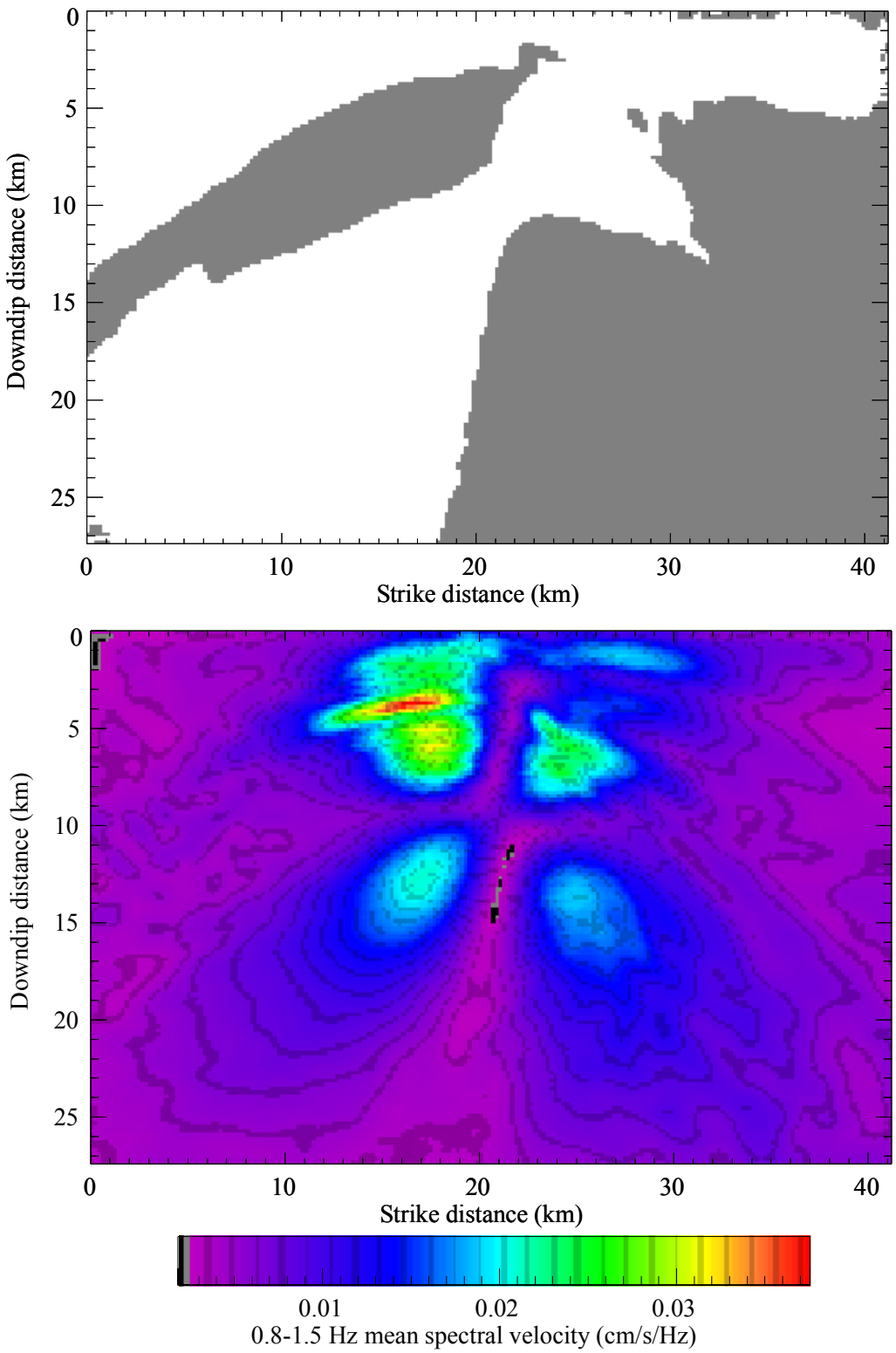

Figure 6-6: N15E-component S-wave normal-dip-slip polarities and 0.8-1.5 Hz amplitudes at JLDW for a 35° fault dip. Perspective is normal to the fault surface. Polarity is shown at the top with grey positive and white negative. RGF mean spectral amplitudes are color contoured with the color bar showing the amplitude range. Point source spacing is 0.2 km. JLDW's strike position is ~21 km.

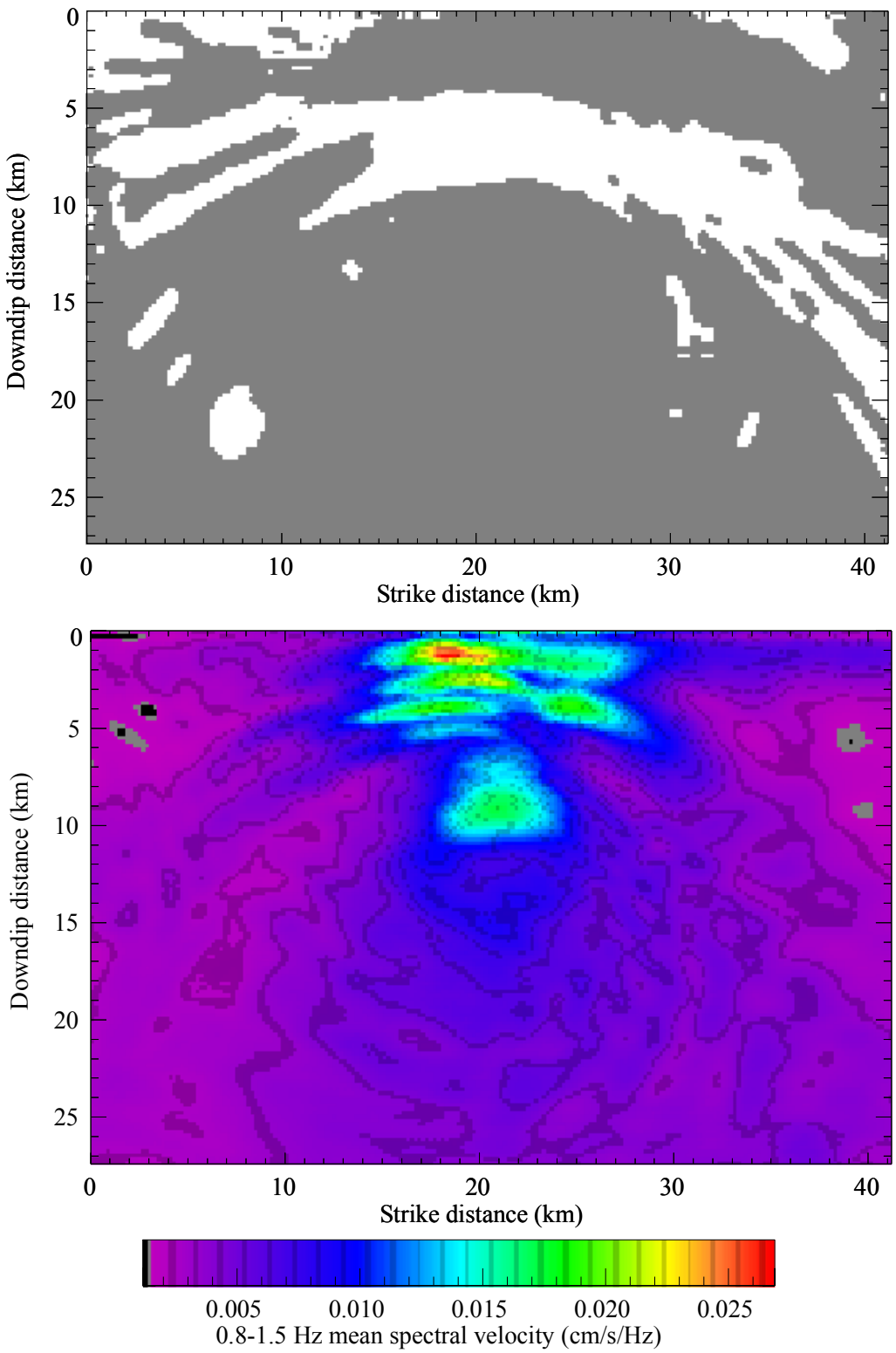

Figure 6-7: Vertical-component S-wave normal-dip-slip polarities and 0.8-1.5 Hz amplitudes at JLDW for a 35° fault dip. Perspective is normal to the fault surface. Polarity is shown at the top with grey positive and white negative. RGF mean spectral amplitudes are color contoured with the color bar showing the amplitude range. Point source spacing is 0.2 km. JLDW's strike position is ~21 km.

EGF's. The 3D eikonal equation solver of Hole and Zelt (1995) was used to calculate first S-wave arrival times and the polarities of the 3D Green's function were estimated by extracting the signs of the integrals over 0.4 s of each component of the 3D Green's function starting at the computed S-wave arrival time. A median smoother was applied to the polarities obtained over fault surface to obtain the polarities used in the EGF calculations. EGFs were constructed of total lengths of 15 s to ensure ground motion calculations could be accomplished on a reasonable project schedule. The 15 s EGFs, consisted of about 1.5 s of pre-S-wave and ~13.5 s of post S-wave ground motions. The ~1.5 s of ground motion preceding the first S-wave was included to capture any significant converted phases that had apparent velocities similar to the first S-wave arrival. All EGF's are presented in Appendix D.

A point-source integration interval of 0.05 km was used in the EGF ground motion simulations to ensure a sampling of at least 6 points per wavelength for frequencies < 10 Hz and rupture velocities of ~3 km/s. To achieve this, the polarity and amplitude factors from the 3D Green's functions were bilinearly interpolated onto the integration grid.

To approximate the influence of a Kostrov-like slip velocity function while avoiding the computational demands of performing slip-velocity function convolutions at every integration point, a modification of the isochrone approach of O'Connell and Ake (2003) was used. The "residual" Kostrov-like slip-velocity function that represented the most "typical" Kostrov slip-velocity function in terms of rise-time documented in Section 6.2 was convolved with the ground motions after point-source summation. This produces an appropriate ground motion scaling (e.g., ω^2 displacement spectral rolloff), but is not as accurate as convolving the Kostrov slip-velocity functions at each integrating point on the fault. However, it reduces the computational burden by factors of ~10^3 and makes simulations of many ground motion scenarios possible. Uncertainties in the application of the Kostrov slip-velocity functions introduce uncertainties, more accurately potential biases, in the high-frequency acceleration amplitudes of 10% to 30%. This is less than the uncertainty in ground motion synthesis when specifying the distribution of subevent sizes using Brune sources to achieve an ω^2 displacement spectral rolloff (Bereznev and Atkinson, 1997).

6.4 Linear Ground Motion Simulations

The 3D ground motion velocity model presented in Section 4 and shown in Figures 6-1 and 6-3 is used to synthesize all ground motions. The 3D reciprocity Green's functions and empirical Green's functions were used to synthesize ground motions at site JLDW located ~200 m east of the southern end of Jackson Lake Dam to provide reference rock motions. The 3D ground motion S-wave velocity model is also used to calculate S-wave travel times for empirical Green's function ground motions. These synthesized ground motions provide the basis for all rock and soil ground motions recommended for dynamic analyses of the dam.

6.4.1 Idealized Fault Rupture Geometries. The Teton fault consists of numerous, sometimes discontinuous, fault traces (Section 2). For the purposes of ground motion simulations, the Teton fault has been idealized using two planar fault rupture segments. The ~42-km-long northern rupture segment consists of the central and northern sections of the Teton fault as defined in Section 2, approximated by a single planar fault striking N8E with dips of 35°, 45°, or 60°, as shown in Figure 6-1. The ~18-km-long southern rupture segment consists of the southern section of the Teton fault as defined in Section 2, approximated by a single planar fault striking N21E with dips of 35°, 45°, or 60°, as shown in Figure 6-1. Maximum fault depth is 16 km for all dip scenarios and both fault segments as indicated in Figure 6-3. Low-frequency 3D ground motion simulations were used to determine the impact of rupturing both rupture segments in a single earthquake on peak ground motions and durations at the dam (Section 6.4.2.2).

6.4.2 Forward Calculations of Low-Frequency 3D Ground Motions. It is important to calculate ground motions over a significant region in plan view to understand how ground ground motions vary in space in relation to distance from the Teton fault, and in relation to the 3D crustal velocity structure. Several 3D finite-difference simulations of Teton fault rupture scenarios provided ground motion profiles for sites extending from the footwall of the Teton fault through site JLDW to points just west of the eastern limit of the LVB in Figure 6-4. These calculations were also used to compare ground motions produced by rupture of the entire Teton fault with ground motions produced by rupture of the northern ~42 km of the Teton Fault. These calculations were performed for dips of 35° and 60° to bracket the range of ground motion responses associated with plausible ranges of fault dip. These are by necessity, low-frequency (<

1 Hz) ground motion simulations, so peak velocities, peak accelerations, and Arias intensities are all smaller than would be associated with broadband ground motions.

Ground motions for rupture of the entire Teton fault were constructed by using ground motions produced by rupture from the southern end of the southern segment added to ground motions produce by rupture of the northern segment from its southern edge, with a 1 s rupture delay between the time rupture arrived at the northern end of the southern segment, and when rupture was initiated at the southern end of the northern rupture segment. The horizontal component orientations of the simulated ground motion are 7° from being perfectly aligned parallel (N15E) and normal (E15S), respectively, to the idealized strike of the northern Teton fault rupture segment. For the purposes of discussion the 7° deviation is ignored. Jackson Lake Dam strikes generally north along the northern ~40% of its crest length, but generally has a NNW strike for most of the rest of the dam. For the southern half of the embankment section the N15E horizontal component is more representative of downstream motions than the E15S component, whereas those roles are reversed for the northern embankment section and concrete section.

For a Teton fault dip of 35° the largest peak horizontal velocities (PHV) occur on the fault normal horizontal component for sites about 4.5 km east of the fault (Figure 6-8). The largest PHV does not occur above the deepest portions of the LVB, but occur along the western portion of the LVB, indicating a complex interaction between rupture directivity and LVB structure. The PHVs within the LVB, and at the dam, are larger than PHVs at two of the three rock motions located < 2 km from the Teton fault (Figures 6-8 and 6.9). In contrast, the largest vertical velocities occur adjacent to the Teton fault on the rock portion of the hanging wall (Figure 6-10). The dam experiences larger PHAs and PHVs than rock sites located within 2 km of the Teton fault, but PHAs and PHVs are about 2/3 of the maximum PHAs and PHVs that occur the western portion of the LVB (Figure 6-11). The dam is located at the edge of a region of elevated Arias Intensity (Figure 6-11) associated with LVB amplification, and the interactions of prolonged ground motions associated with LVB-edge waves and resonant LVB responses with direct S-waves from later portions of the fault rupture. Strong ground velocity pulses nearly comparable in amplitude to the PHVs associated with direct S-waves occur about 8 s after the first S-wave arrival at the dam (dashed lines in Figures 6-8 and 6-9). These arrivals have apparent velocities indicating that

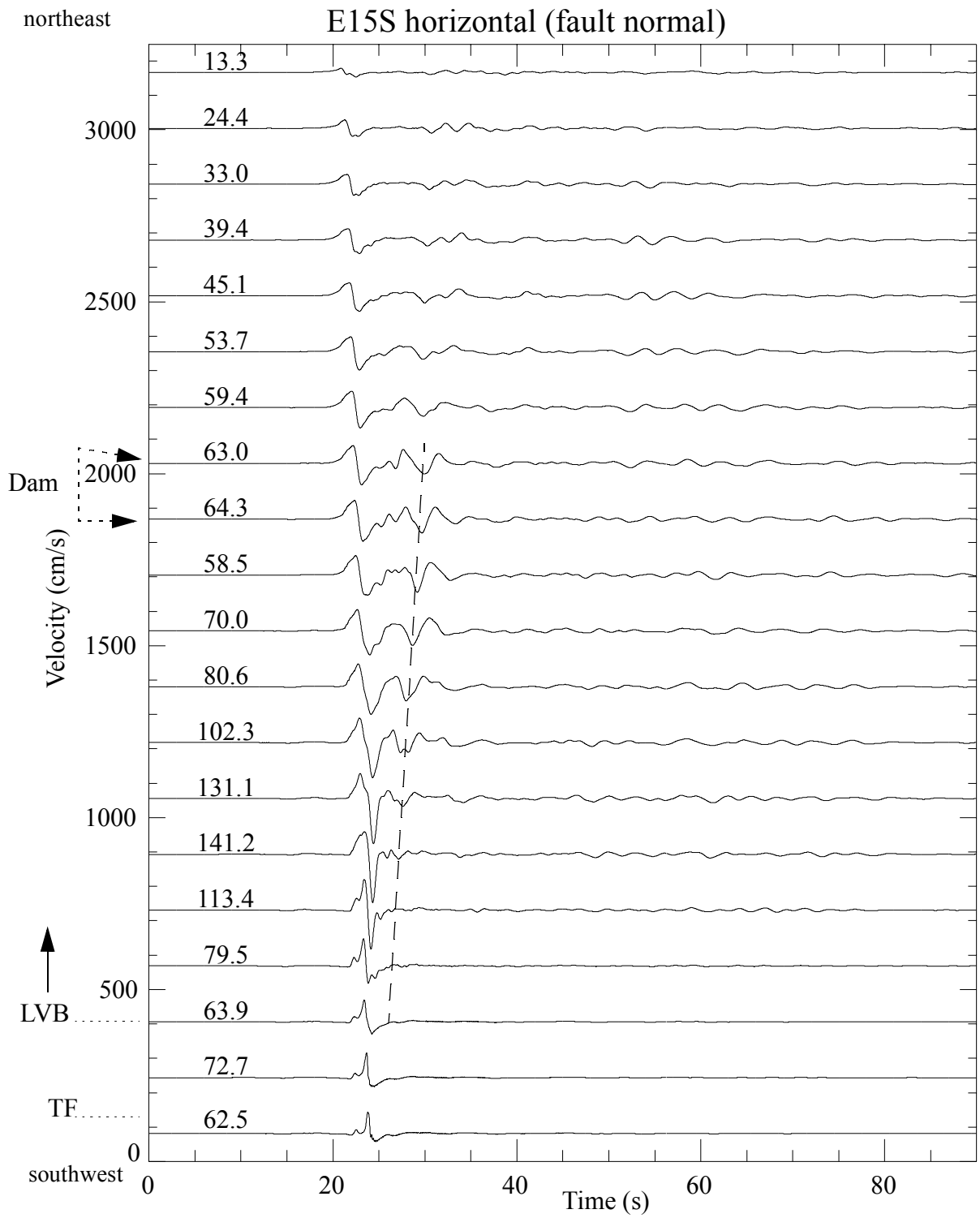

Figure 6-8: Low-frequency (< 1 Hz) E15S-component velocity waveforms for a full Teton fault rupture with a 35° fault dip. The seismograms span a 19-km profile (as shown in Figure 6-4) extending from 330 m west of the Teton fault (bottom waveform) through site JLDW with a 1 km seismogram spacing. TF is the Teton fault, western LVB-edge is dotted line labeled LVB, and dotted arrows show the two seismograms representative of the range of positions represented by the dam. Above each seismogram is its peak velocity in cm/s. Dashed line shows strong LVB-edge S-wave arrivals.

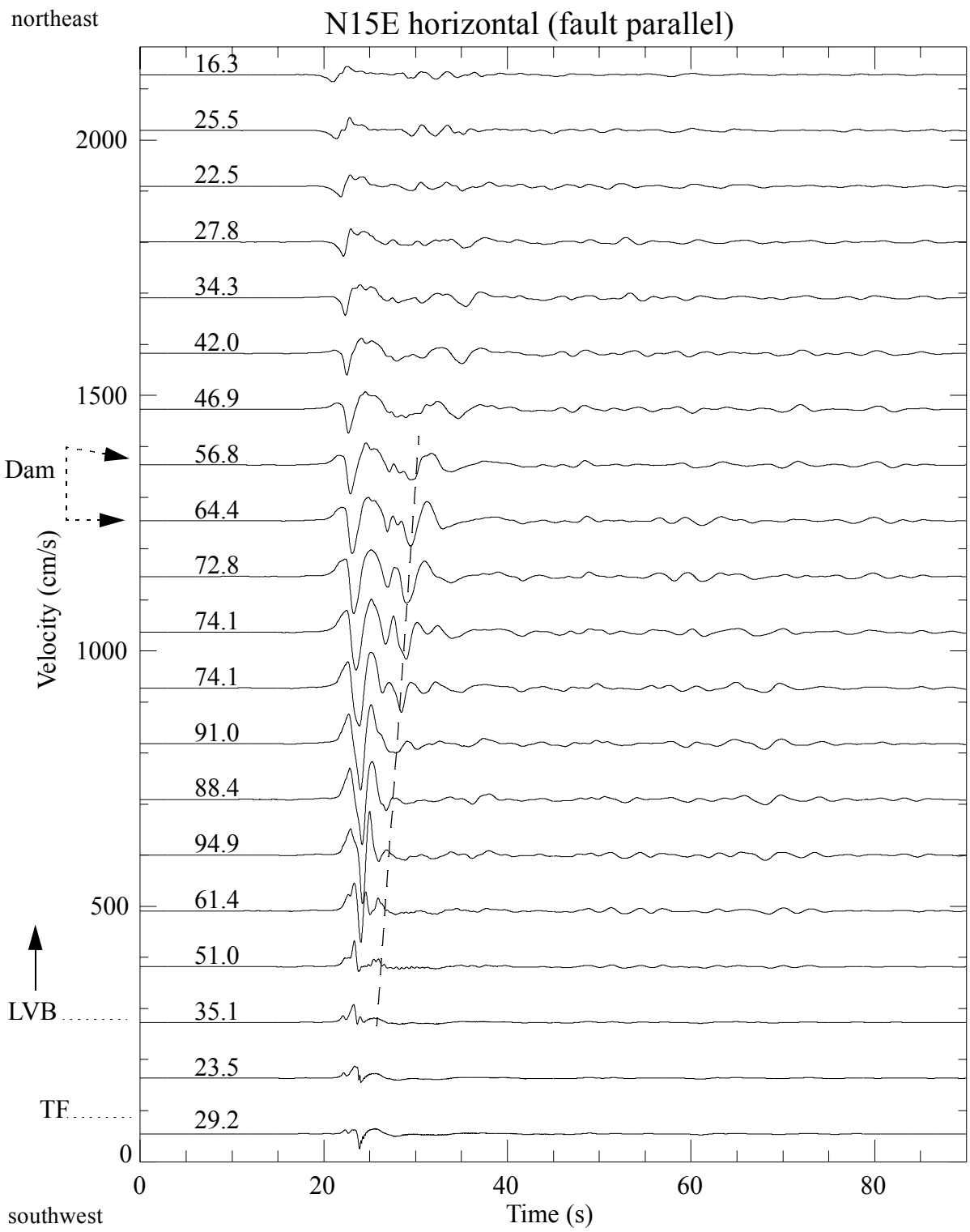

Figure 6-9: Low-frequency (< 1 Hz) N15E-component velocity waveforms for a full Teton fault rupture with a 35° fault dip. See Figure 6-8 for plot details.

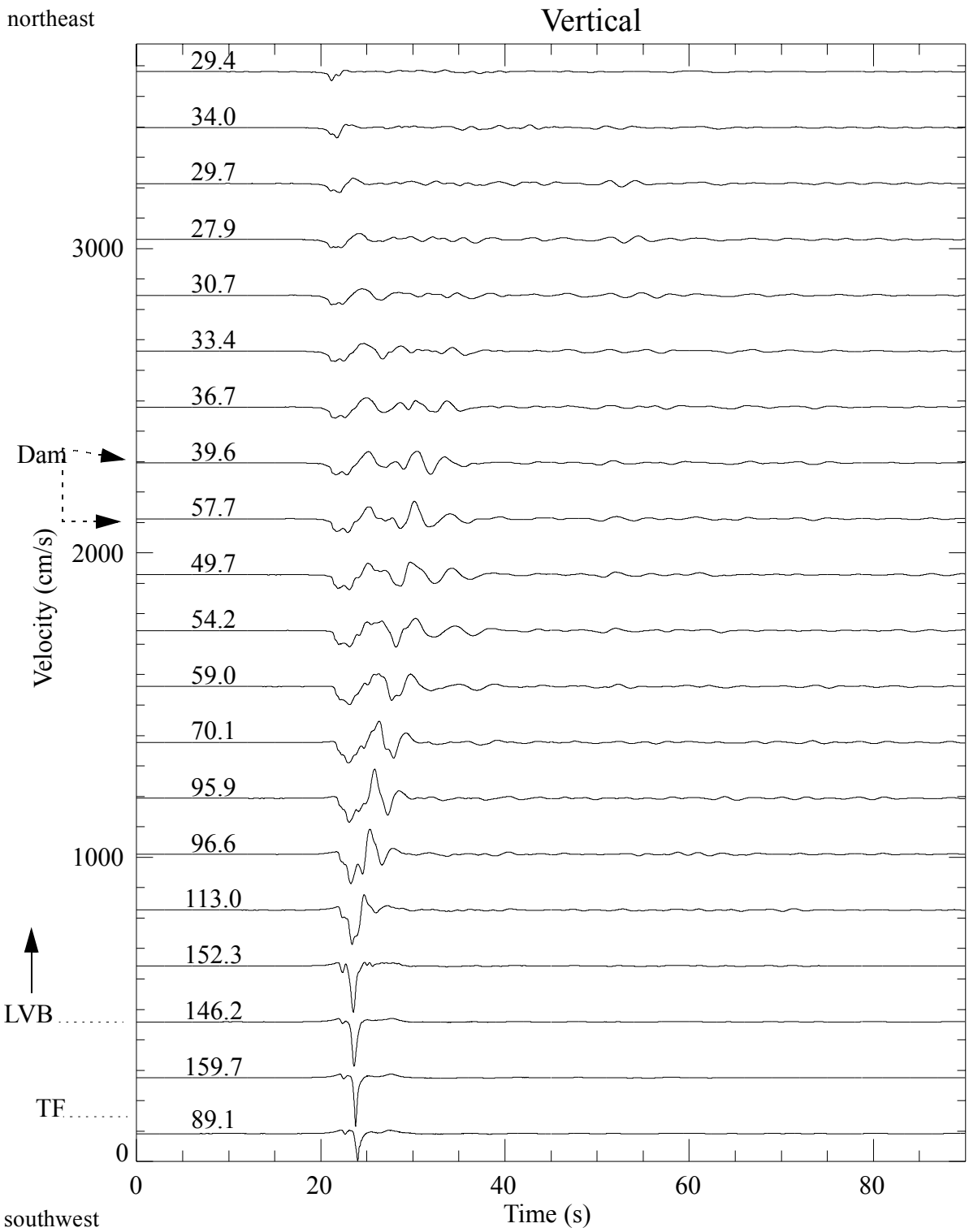

Figure 6-10: Low-frequency (< 1 Hz) vertical-component velocity waveforms for a full Teton fault rupture with a 35° fault dip. See Figure 6-8 for plot details.

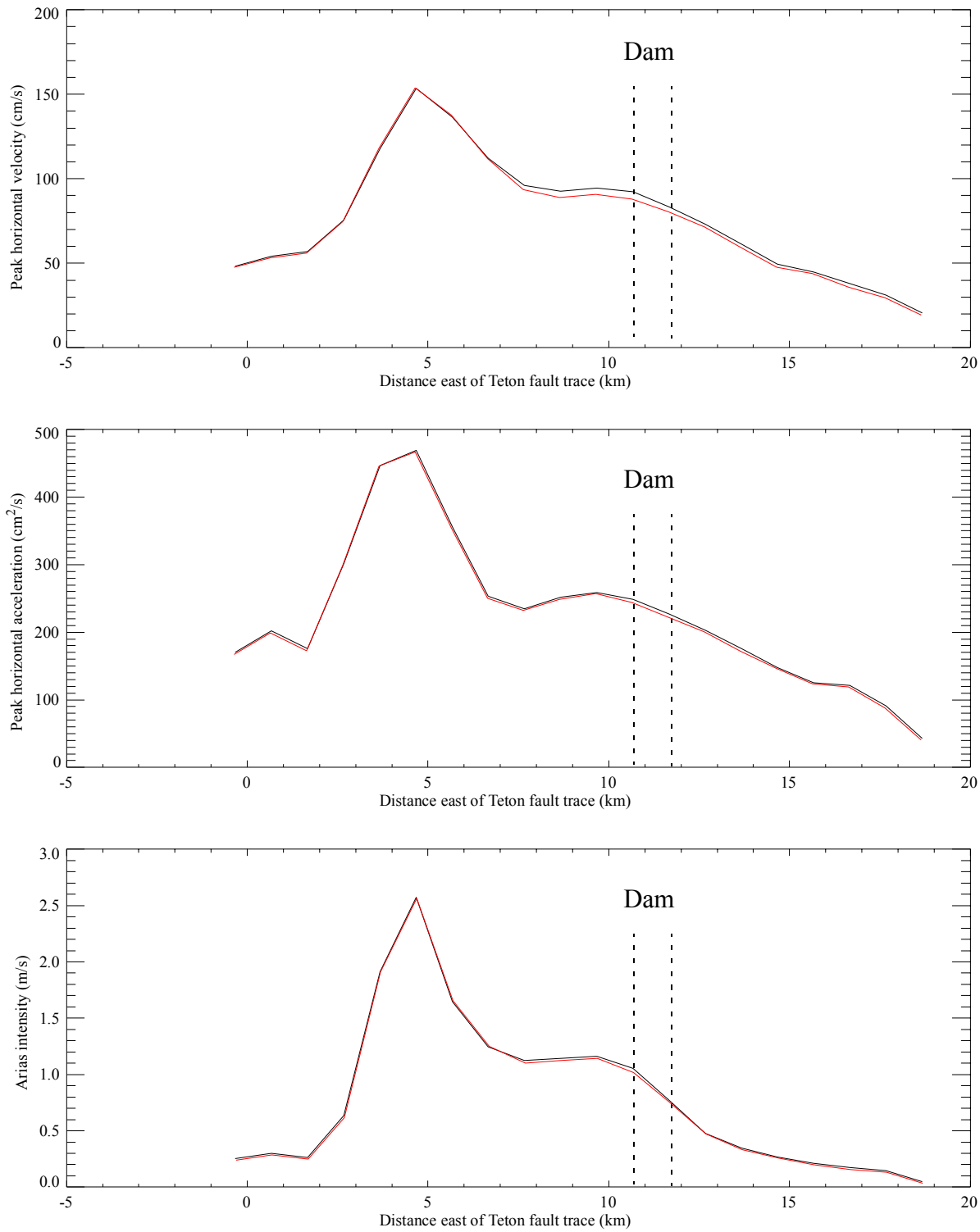

Figure 6-11: Low-frequency (< 1 Hz) horizontal peak velocity, acceleration, and Arias intensity profiles for a full Teton fault rupture with a 35° dip (black curves). The ground motion profiles span a 19-km profile extending from 330 m west of the Teton fault through site JLDW as shown in Figure 6-4. Red curves are results when only the 42-km-long northern rupture segment is used instead of the entire length of the Teton fault. Note, minimum near-surface S-wave velocities of ~1 km/s in the 3D model represent rock site conditions. These results do not account for soil responses.

they originate as S-waves at the western edge of the LVB and contribute to the increased Arias Intensities at the dam. They diminish rapidly in amplitude east of the dam (Figures 6-8 and 6-9), producing the sharp reduction in Arias Intensity east of the dam (Figure 6-11).

Figure 6-11 shows that peak ground motions and Arias Intensities at the latitude of the dam are relatively insensitive to the inclusion of seismic energy associated with rupture of the ~18-km-long southern Teton fault rupture segment. Likewise, the addition of the southern ~18-km-long rupture segment does not appreciably increase ground motion durations at the dam. For instance, PHVs > 15 cm/s occur ~40 s after the beginning of strong shaking on the E15S component associated with the first S-wave arrivals even when the seismic energy from the southern Teton fault rupture segment is not included in the simulated ground motions. The closest point of the southern Teton fault rupture segment is > 22 km from the south end of the dam and is located beyond the southern limits of the LVB. Essentially the same conclusions were reached in 3D finite-difference simulations of ground motions using two other asperity models of earthquake rupture. Rupture toward the dam (from the southern edge of the southern rupture segment) was used in all three asperity model ground motion simulations, but inclusion of the southern rupture segment in the ground motion calculations produced little change in PHA, PHA, or Areas Intensity relative to omitting the seismic energy from the southern rupture segment from the simulated ground motions Consequently, it was concluded that the southern Teton fault rupture segment does not strongly influence peak ground motions or durations at site JLDW for fault dips of 35°.

For a Teton fault dip of 60°, the PHVs on the fault normal component (Figure 6-12) are not always larger than on the fault parallel component (Figure 6-13). In fact, the largest PHV occurs on the fault parallel component, providing clear evidence of strong 3D LVB influences on the strong ground motions. As was the case with a fault dip of 35°, the strongest vertical ground motions occur adjacent to the fault on the rock portion of the hanging wall (Figure 6-14). PHVs > 15 cm/s occur ~40 s after the first S-wave arrival (Figures 6-12 and 6-13), as also occurred for a fault of 35°; the LVB duration effects is not a strong function of fault dip. Strong velocity pulses nearly comparable in amplitude to the PHVs associated with direct S-waves occur about 8 s after the first S-wave arrival at the dam (dashed lines in Figures 6-12 and 6-13). These arrivals have

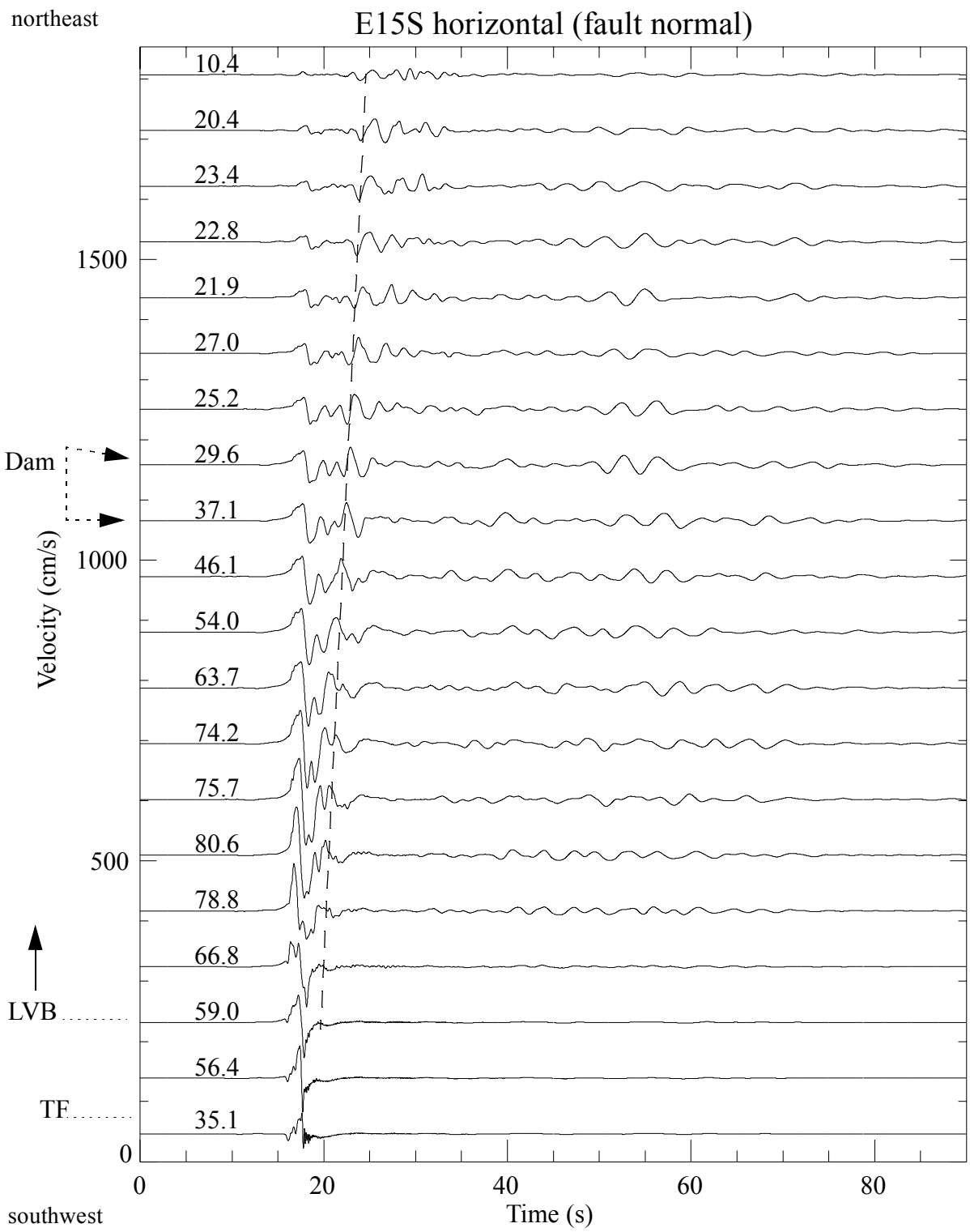

Figure 6-12: Low-frequency (< 1 Hz) E15S-component velocity waveforms for a full Teton fault rupture with a 60° fault dip. See Figure 6-8 for plot details.

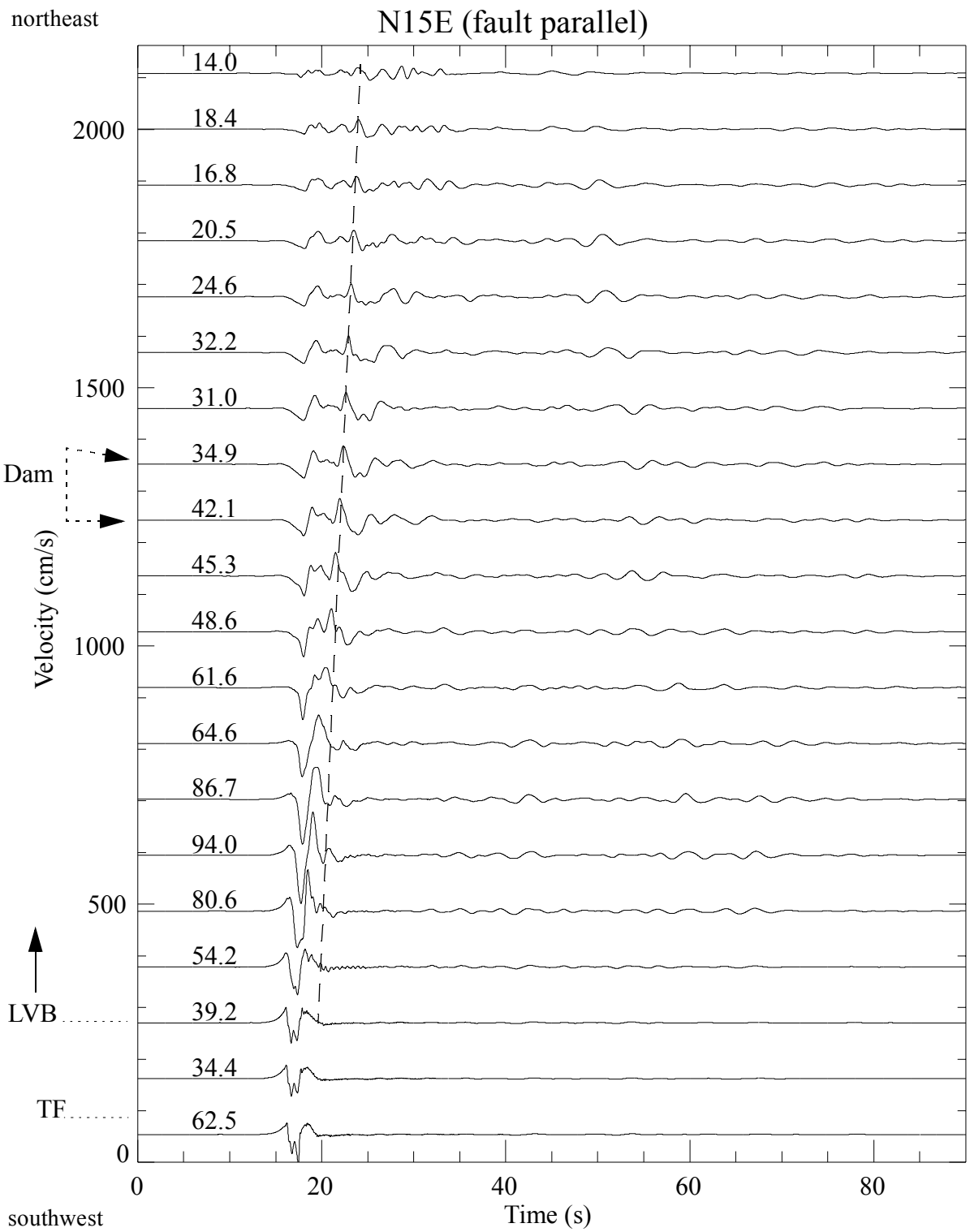

Figure 6-13: Low-frequency (< 1 Hz) N15E-component velocity waveforms for a full Teton fault rupture with a 60° fault dip. See Figure 6-8 for plot details.

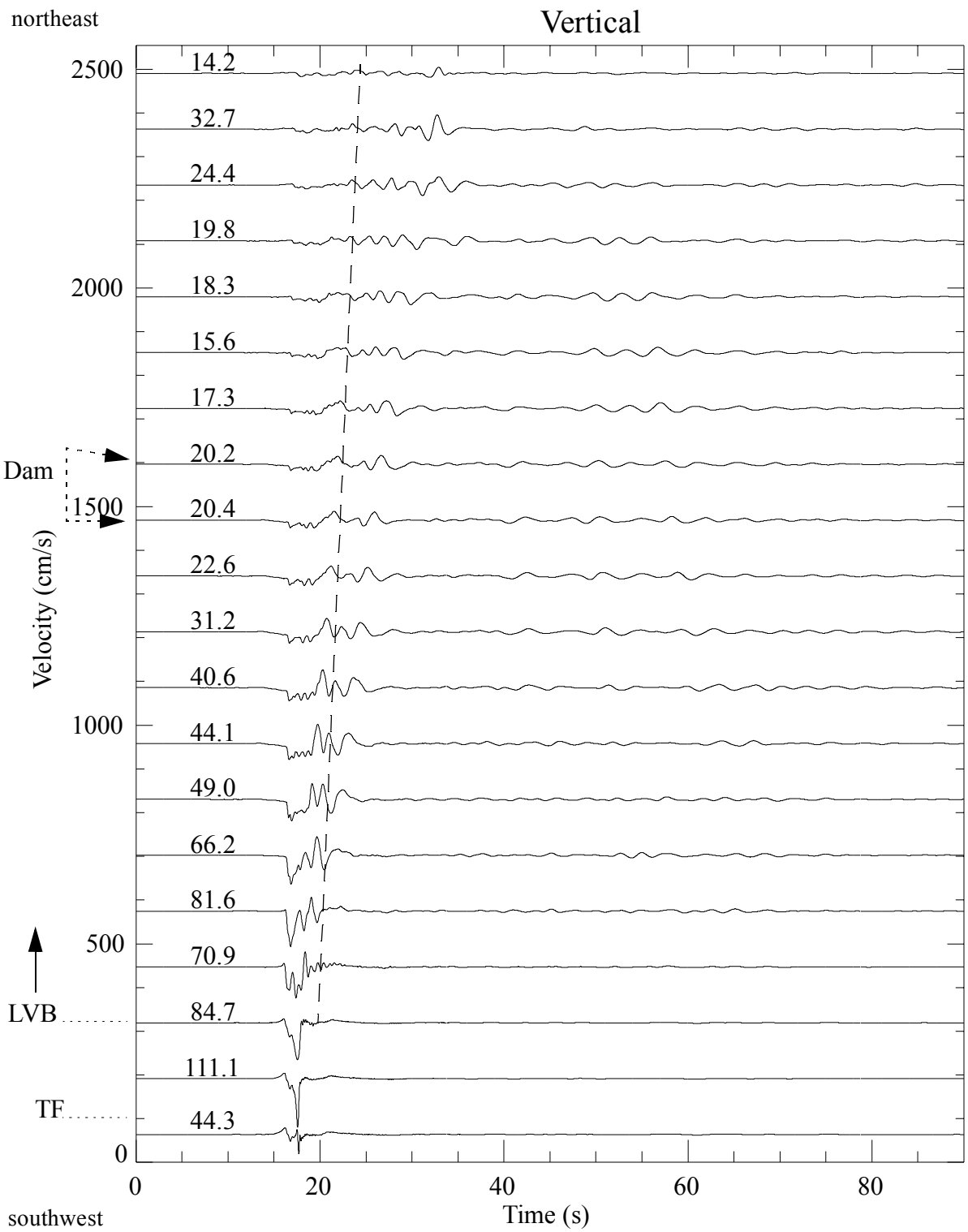

Figure 6-14: Low-frequency (< 1 Hz) vertical-component velocity waveforms for a full Teton fault rupture with a 60° fault dip. See Figure 6-8 for plot details.

apparent velocities indicating that they originate as S-waves at the western edge of the LVB and contribute to the increased Arias Intensities at the dam. They diminish slowly in amplitude west of the dam (Figures 6-12 and 6-13), producing a more gradual reduction in Arias Intensity east of the dam (Figure 6-15), compared to the case of a 35° fault dip (Figure 6-11). These results indicate that large-amplitude LVB-edge S-waves will occur at the dam, independent of fault dip. However, PHVs and PHAs are reduced for a fault dip of 60°, and PHVs and PHAs at the dam are lower than PHVs and PHAs near the fault (Figure 6-15) Arias Intensities for a fault dip of 60° are reduced by 50% relative to a fault dip of 35° (compare Figures 6-15 with 6-11). As was the case of a fault dip of 35°, for a fault dip of 60° PHVs, PHAs, and Arias Intensities at the latitude of the dam are little affected by rupture of the southern Teton fault rupture segment (Figure 6-15). Consequently, further investigations of the influence of the southern Teton fault rupture segment on ground motions at site JLDW were not pursued.

6.4.3 Broadband Hybrid Ground Motions. Only the combined broadband RGF and EGF ground motion results are reported for brevity. Based on the results of Section 6.4.2 we only simulate ground motions for rupture on the 42-km-long northern segment of the Teton fault. A total of 3300 rupture scenarios and resultant ground motions were calculated using 33 hypocenter positions and 100 rupture model fractal randomizations. Eleven strike positions at distances (in km) of 0.8, 4.8, 8.8, 12.8, 16.8, 20.8, 24.8, 28.8, 32.8, 36.8, and 40.8 from the south end of the fault were used to ensure a even span of hypocenter strike positions, since there is no prior information as to where along strike rupture is likely to start. Conversely, most normal-faulting earthquake rupture from near the base of seismicity towards the surface, so hypocenters were placed at depths of 13.8, 14.8, and 15.8 km, consistent with the findings of Doser and Smith (1989). They found that in the extensional region of the western United States that all **M** ≥ 7.0 earthquakes occurred at depths of ≥ 12 km. Since each hypocenter position interacts differently with the 100 fractal randomizations of rupture and healing velocities, and effective stress, the 33 hypocenter positions produce a total of 3300 discrete rupture scenarios and independent ground motions; this number of ground motions simulations is sufficient to calculate various ground motion quantiles and to investigate the dependence of ground motions on hypocenter position.

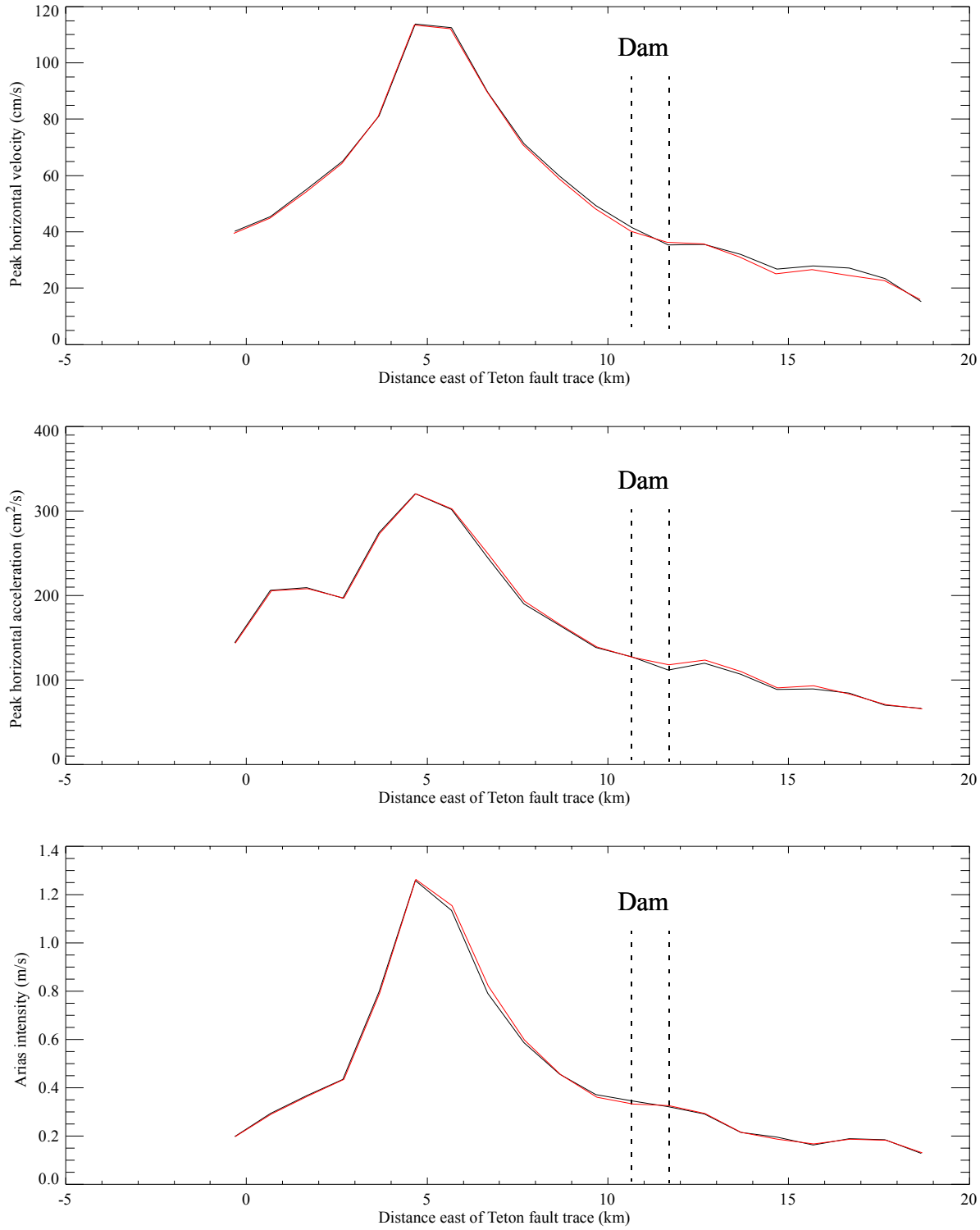

Figure 6-15: Low-frequency (< 1 Hz) horizontal peak velocity, acceleration, and Arias intensity profiles for a full Teton fault rupture with a 60° dip (black curves). The ground motion profiles span a 19-km profile extending from 330 m west of the Teton fault through site JLDW as shown in Figure 6-4. Red curves are results when only the 42-km-long northern rupture segment is used, instead of the entire length of the Teton fault. Note, minimum near-surface S-wave velocities of ~1 km/s in the 3D model represent rock site conditions. These results do not account for soil responses.

6.4.3.2 Northern Teton Fault Segment - 35° Dip. Table 6-2 summarizes the characteristics of broadband ground motions synthesized for station JLDW. Arias duration and energy duration are defined as the time between the 5% and 95% of total Arias Intensity and cumulative kinetic energy, respectively. Since the EGFs were limited to ~13.5 s durations, all duration-related quantities (Arias Intensity and duration, and energy duration) are lower bounds.

Table 6-2: JLDW Rock Ground Motion Parameters: 35°-Dipping Northern Teton Fault Segment.

Component	Peak velocity	Arias Intensity	Cumulative energy	Arias duration	Energy duration
	(cm/s)	(m/s)	(J)	(s)	(s)
E15S mean	146	6.2	10,928	15.1	21.2
E15S 84%	201	9.3	15,343	17.7	27.9
N15E mean	102	3.5	9,111	18.5	21.2
N15E 84%	135	5.1	14,154	21.4	26.3
Vertical mean	125	2.4	11,233	16.5	14.3
Vertical 84%	147	3.4	15,709	20.1	16.9

The strongest shaking occurs on the fault-normal (E15S) horizontal component, indicating a substantial influence from rupture directivity. However, ground motions on the fault-parallel (N15E) horizontal component are also substantial. Peak velocities are very large, exceeding the largest median and 84% peak velocities estimated previously for a Reclamation dam by > 50% (Casitas Dam, O'Connell, 1999b). Maximum Arias Intensities are similar to empirical attenuation relation predictions of Kayen and Mitchell (1997) for rock sites. The energy durations exceed the Arias durations by about 10 s because the LVB and relatively high site kappa of ~0.08 produce stronger long duration velocity responses than high-frequency acceleration responses.

The mean (Figure 6-16) and 84% (Figure 6-17) E15S acceleration response spectra (PSA) exhibit responses more similar to soil responses from the Spudich et al. (1999) extensional acceleration attenuation relations than rock responses. At periods > ~1.2 s the 35° PSA response become much larger than predicted by Spudich et al. (1999), reflecting the strong influence of the LVB at rock site JLDW, and the unusually large peak velocities in Table 6-2. Conversely, E15S acceleration

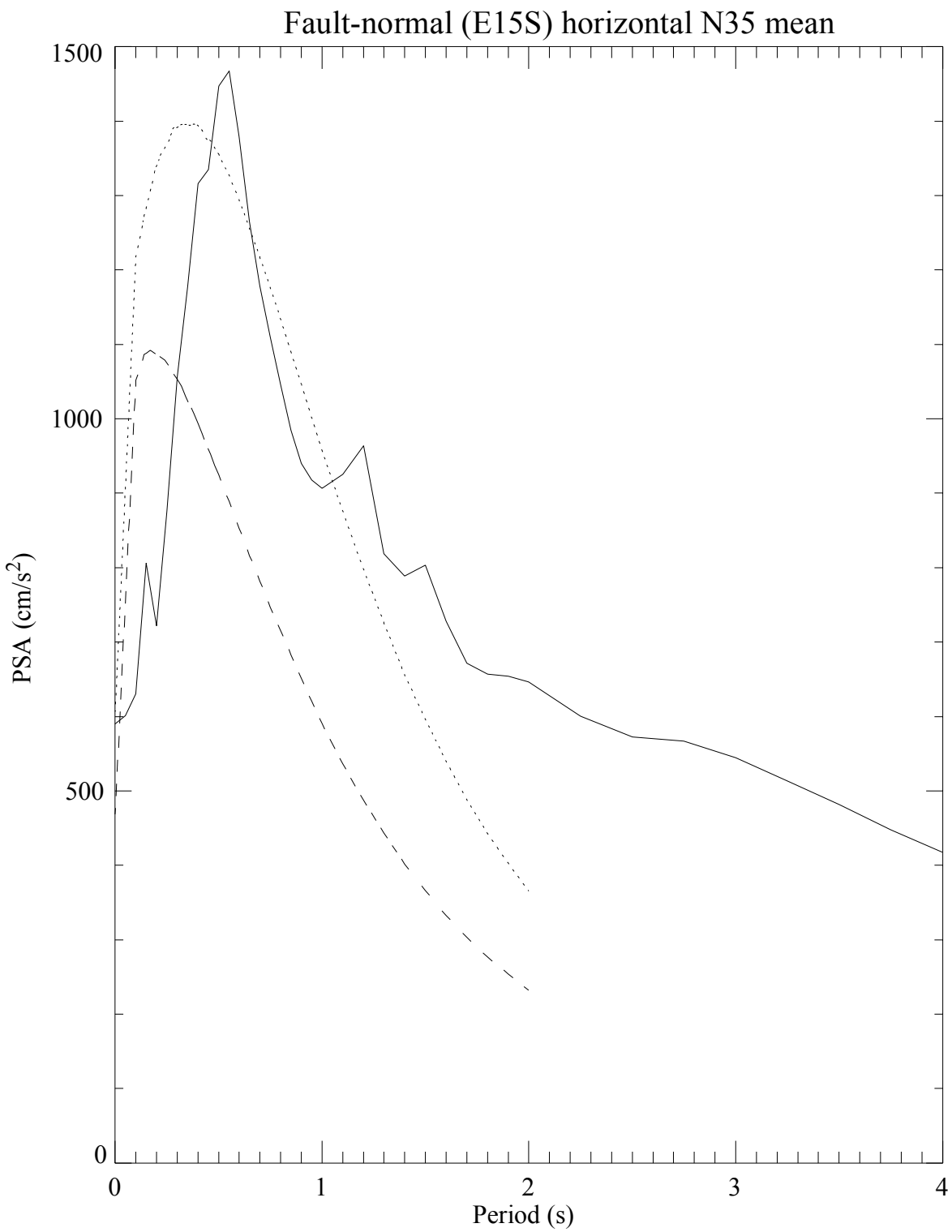

Figure 6-16: JLDW rock site mean downstream horizontal PSA response spectra for a 35°-dipping northern Teton fault segment (solid). SEA99 average horizontal component estimates for a **M** 7.0 normal-faulting earthquake are shown for soil (dotted) and rock (dashed) site conditions.

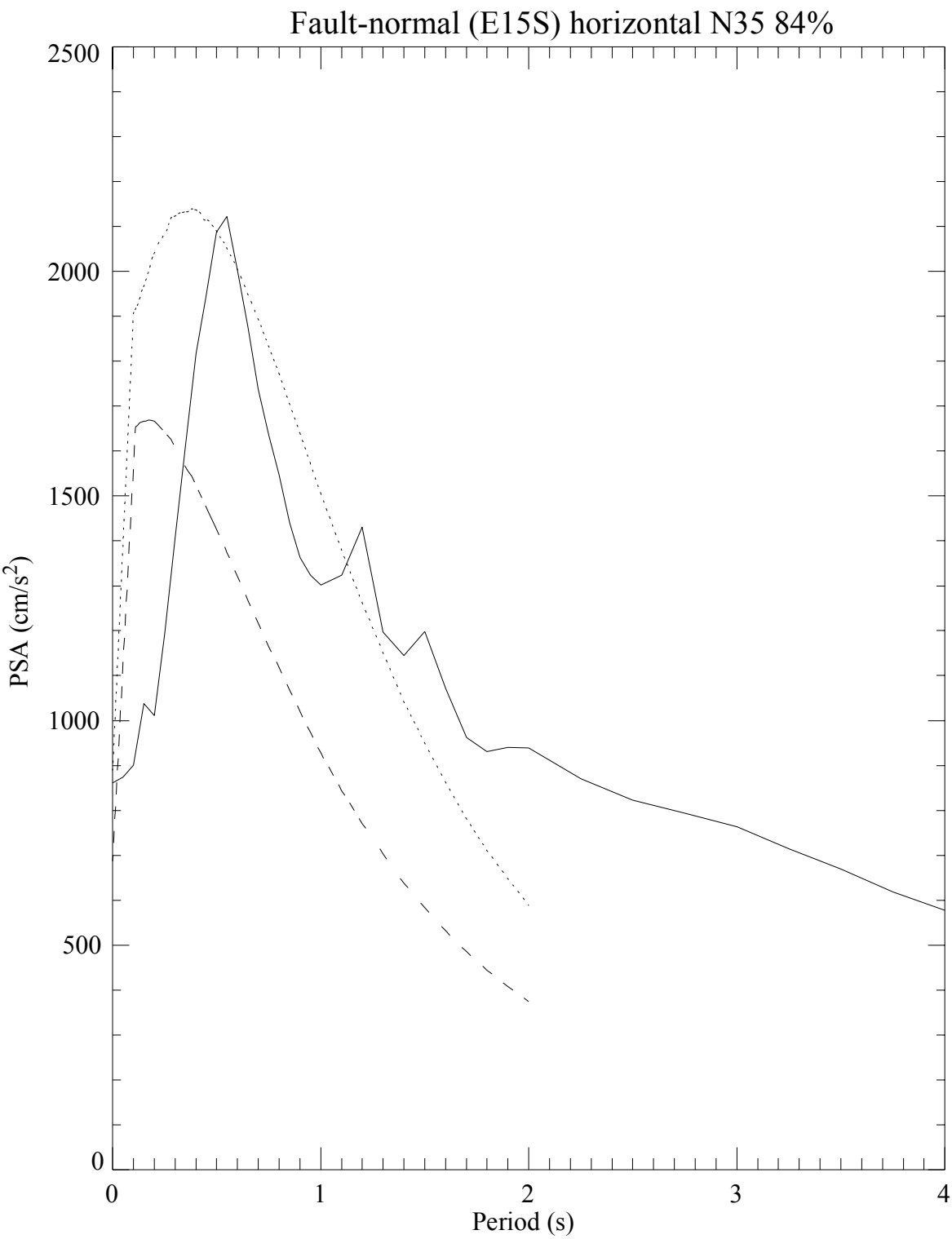

Figure 6-17: JLDW rock site 84% quantile downstream horizontal PSA response spectra for a 35°-dipping northern Teton fault segment (solid). SEA99 average horizontal component estimates for a **M** 7.0 normal-faulting earthquake are shown for soil (dotted) and rock (dashed) site conditions.

responses decrease more rapidly for periods < 0.5 s than Spudich et al. (1999), reflecting the relatively large kappa of ~0.08 at site JLDW, relative to rock kappa values of ~0.04 more typically associated with rock sites. However, peak accelerations in Figures 6-16 and 6-17 are very similar to the Spudich et al. (1999) estimates for a **M** 7.0 normal-faulting earthquake.

The fault-parallel (N15E) PSAs are about 60% of the fault-normal (E15S) PSAs for periods < 1 s indicating a significant influence from directivity (Figure 6-18), as expected for a dip slip fault (O'Connell and Ake, 2003), but the horizontal PSAs become nearly equal at periods > 3 s; the long-period responses are dominated by the influences of the 3D LVB and nearly independent of horizontal component orientation. The vertical PSA have a secondary maximum between 2 s and 3 s associated with some aspect of the 3D LVB response.

PSA responses are sensitive to hypocenter position. Hypocenters near the center of the fault along strike produce typical vertical and fault-normal (E15S) responses, but produce substantially lower fault-parallel (N15E) responses (Figure 6-18), with 84% fault-parallel PSAs being barely larger than mean PSAs for all hypocenter positions. Conversely, fault-parallel and fault-normal PSAs are significantly larger for northern hypocenters (Figure 6-19). For fault-normal PSAs, PSAs increase primarily for periods < 1s, indicating that the interaction between northern 3D LVB structure and north hypocenter rupture times increases rupture directivity. For fault-parallel PSAs, PSAs increase nearly uniformly for nearly all periods, indicating a strong contribution of some aspect of the 3D LVB structure to fault-parallel ground motions. Southern hypocenters (Figures 6-20) produce substantially lower fault-normal responses and only slightly larger fault-parallel PSA responses. The combination of a steep LVB boundary dip, a deeper basin at the north end of the 3D LVB, and hypocenters near the northern LVB boundary, produce the strongest ground motions at the dam and indicate that this type of velocity structure would likely produce peak acceleration responses at the dam about 50% larger than indicated in Figures 6-16 and 6-17. Thus, the assumptions about details of LVB margin structure strongly influence estimated ground motions at the dam. As indicated in Section 4, there are significant uncertainties about structure of the northern, eastern, and southwestern margins of the LVB. If the southwestern margin of the LVB has a steeper dip and a thicker section of low-velocity sediments, peak ground motion responses at the dam may be under predicted. Conversely, if the northeastern margins of the LVB have

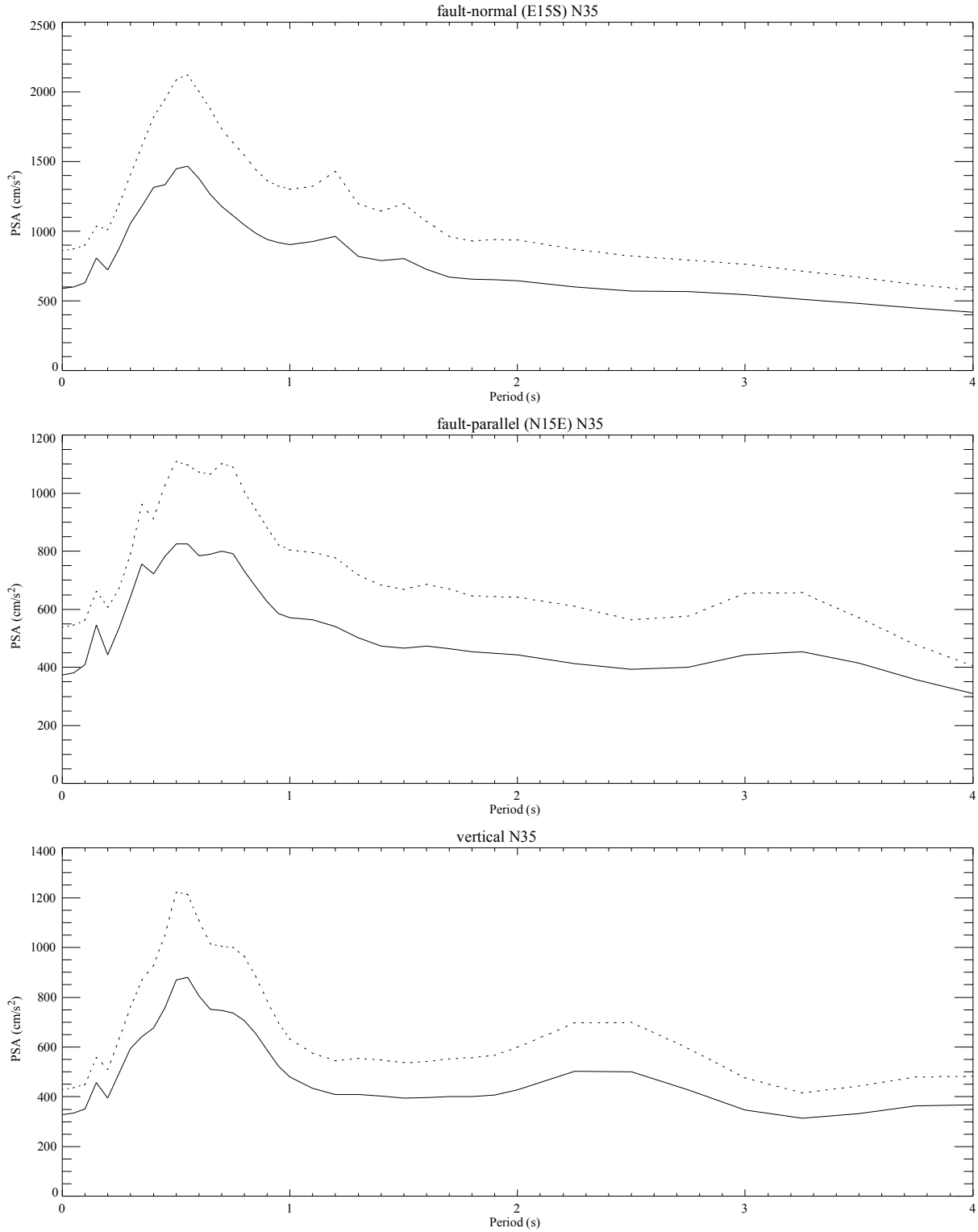

Figure 6-18: JLDW rock site PSA response spectra for a 35°-dipping northern Teton fault segment for all hypocenters. Mean curves are solid and 84% quantile curves are dotted. Components are as labeled.

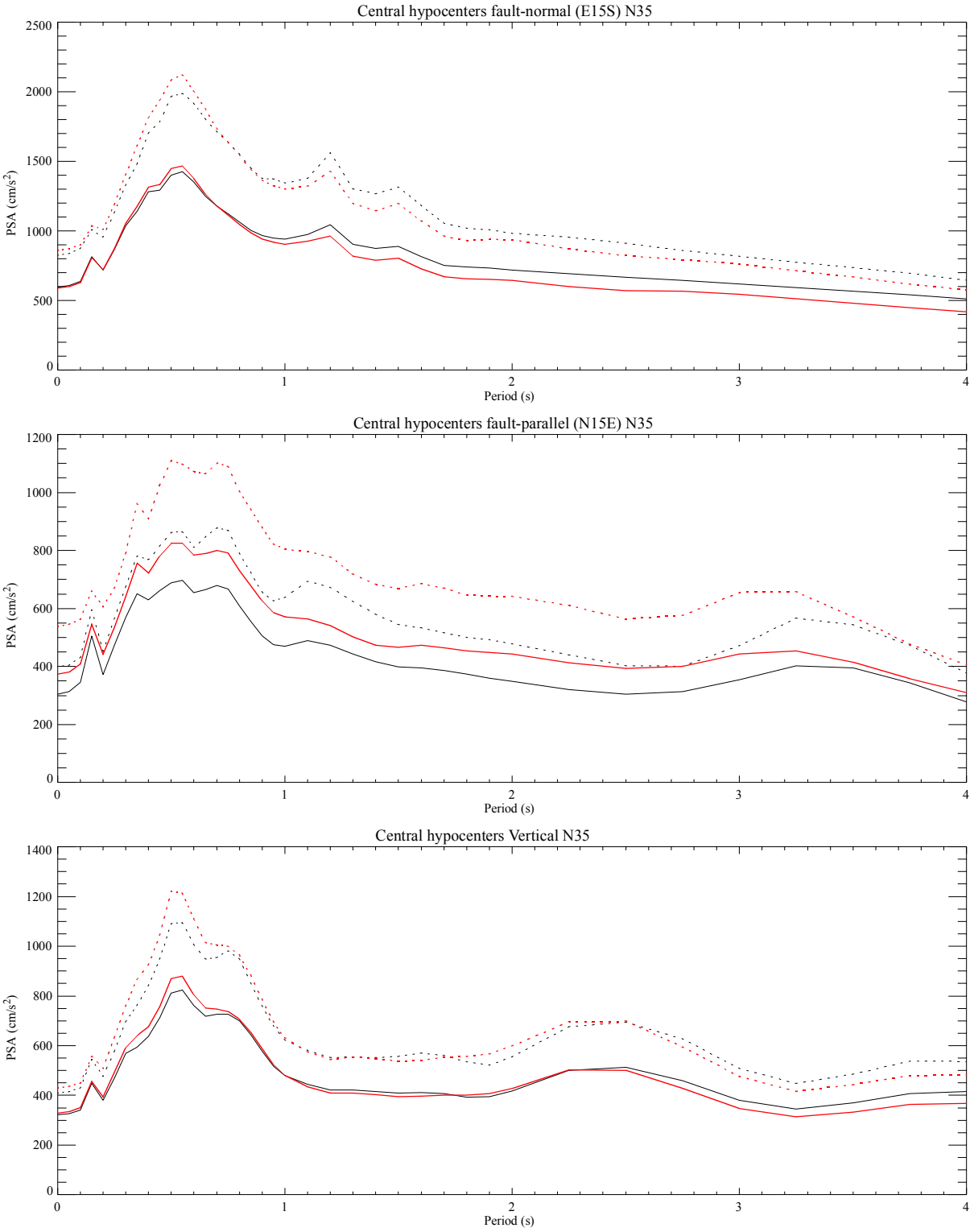

Figure 6-19: JLDW rock site central hypocenter PSA response spectra for a 35°-dipping northern Teton fault segment (black). Red curves are reference mean (solid) and 84% quantile (dotted) results using all hypocenters (from Figure 6-18). Components are as labeled.

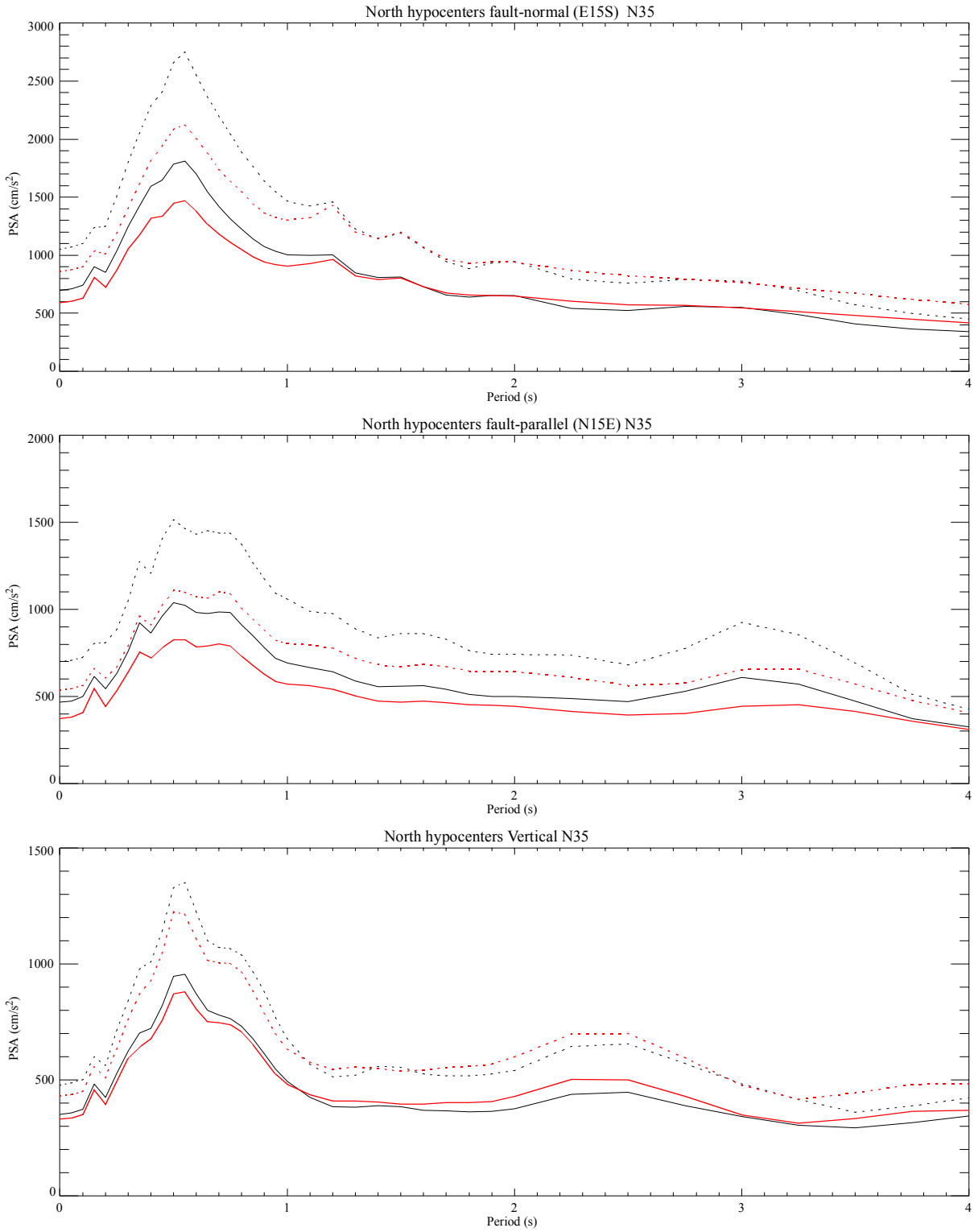

Figure 6-20: JLDW rock site northern hypocenter PSA response spectra for a 35°-dipping northern Teton fault segment (black). Red curves are reference mean (solid) and 84% quantile (dotted) results using all hypocenters (from Figure 6-18). Components are as labeled.

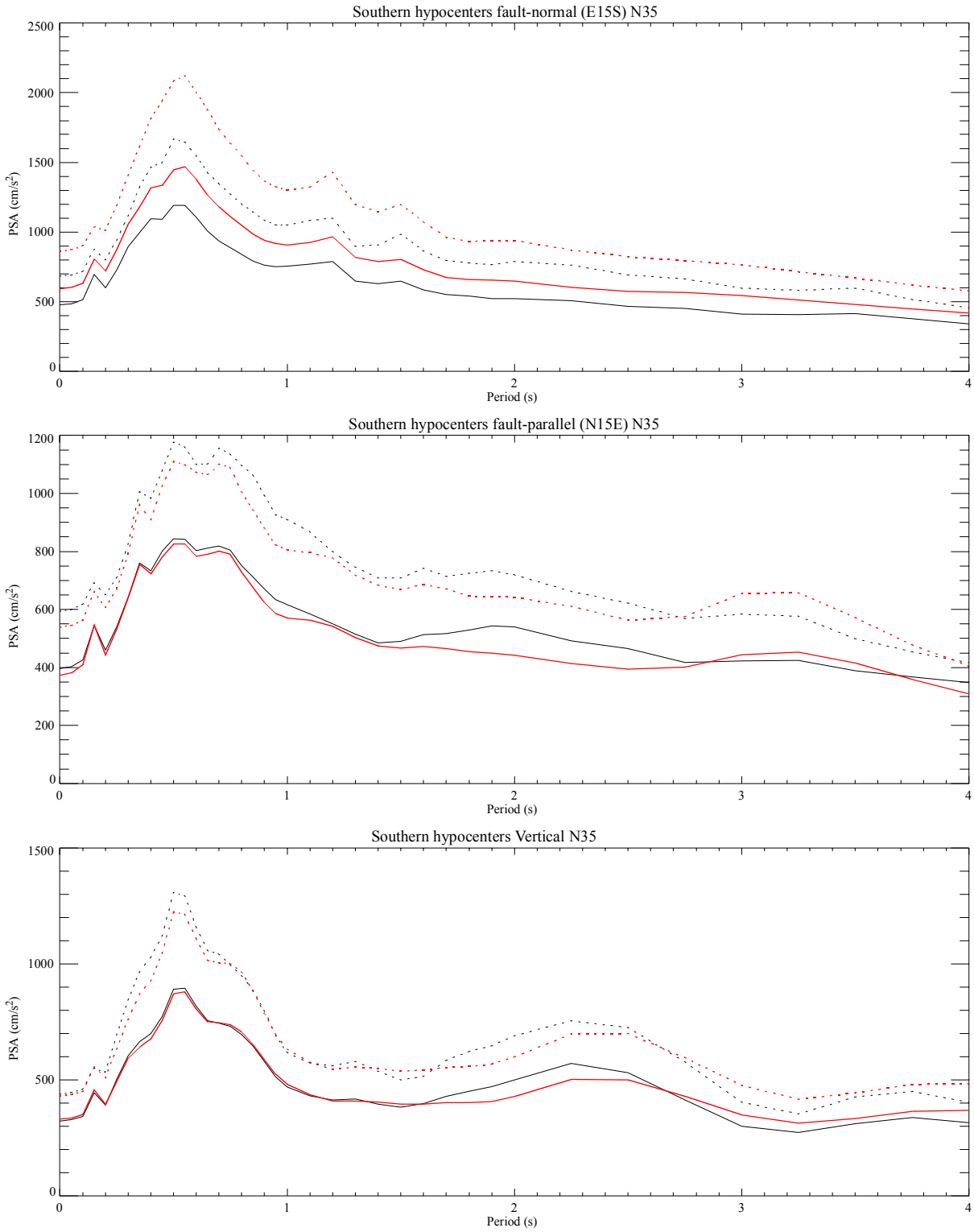

Figure 6-21: JLDW rock site southern hypocenter PSA response spectra for a 35°-dipping northern Teton fault segment (black). Red curves are reference mean (solid) and 84% quantile (dotted) results using all hypocenters (from Figure 6-18). Components are as labeled.

shallower dips and a smaller thickness of low-velocity sediments, peak ground responses at the dam may be overpredicted. These issues are evaluated in detail in Section 7 using earthquakes recorded at the dam from a variety of azimuths and distances.

6.4.3.3 Northern Teton Fault Segment - 45° Dip. While fault-normal peak velocities and Arias Intensities decrease relative to the 35°-fault-dip results, fault-parallel Arias Intensities are larger than the 35°-fault-dip results (compare Table 6-3 to 6-2). Vertical peak velocities decrease, but Arias Intensities are the same, compared to the 35°-fault-dip results.

Table 6-3: JLDW Rock Ground Motion Parameters: 45°-Dipping Northern Teton Fault Segment.

Component	Peak velocity	Arias Intensity	Cumulative energy	Arias duration	Energy duration
	(cm/s)	(m/s)	(J)	(s)	(s)
E15S mean	133	4.8	11,767	16.1	23.4
E15S 84%	171	7.1	16,956	18.1	33.1
N15E mean	111	4.0	10,063	18.5	21.8
N15E 84%	155	6.1	16,010	21.1	27.4
Vertical mean	105	2.4	9,605	16.3	16.7
Vertical 84%	130	3.6	14,111	19.1	20.1

Fault-normal PSA responses are about 50% larger than fault-parallel PSA responses (Figure 6-22), indicating that rupture directivity still dominates the short-period responses at the dam. Mean (Figure 6-23) and 84% (Figure 6-24) fault-normal PSA are lower than Spudich et al. (1999) soil responses, but greater than corresponding rock responses for periods < 1.5 s. For periods > 2 s, simulated PSA substantially exceed Spudich et al. (1999) soil responses, consistent with the strong influence of the 3D LVB on long-period responses; these are large acceleration loads for long-periods.

As was the case for a fault dip of 35°, N15E PSA responses for central hypocenters (Figure 6-25) are substantially lower than for southern hypocenters (Figure 6-26) or northern hypocenters (Figure 6-27). The phasing of fault rupture times, direct S-wave travel times, and LVB-edge S-

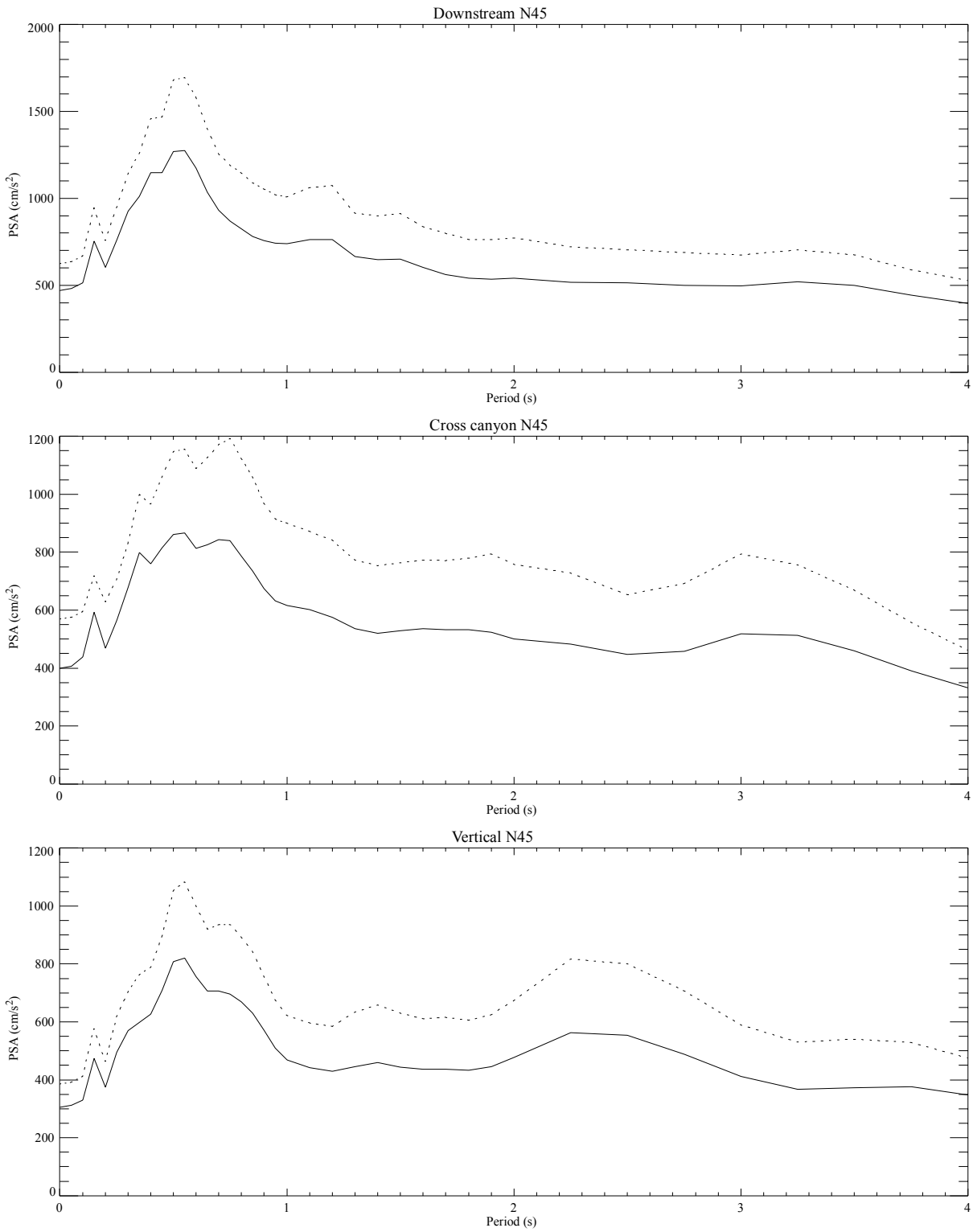

Figure 6-22: JLDW rock site PSA response spectra for a 45°-dipping northern Teton fault segment using all hypocenter positions. Mean curves are solid and 84% quantile curves are dotted. Components are as labeled.

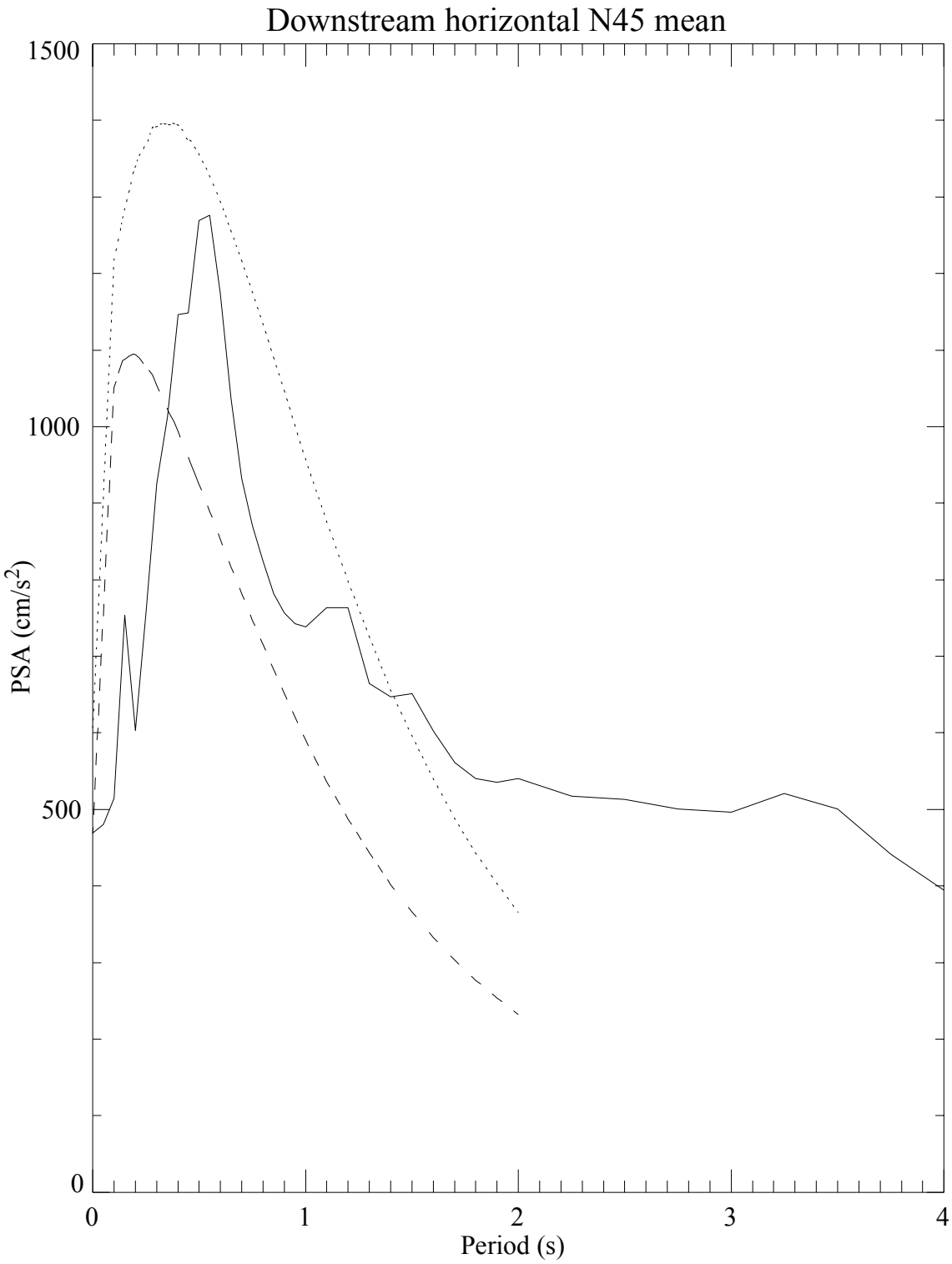

Figure 6-23: JLDW rock site mean downstream horizontal PSA response spectra for a 45°-dipping northern Teton fault segment (solid). SEA99 average horizontal component estimates for a **M** 7.0 normal-faulting earthquake are shown for soil (dotted) and rock (dashed) site conditions.

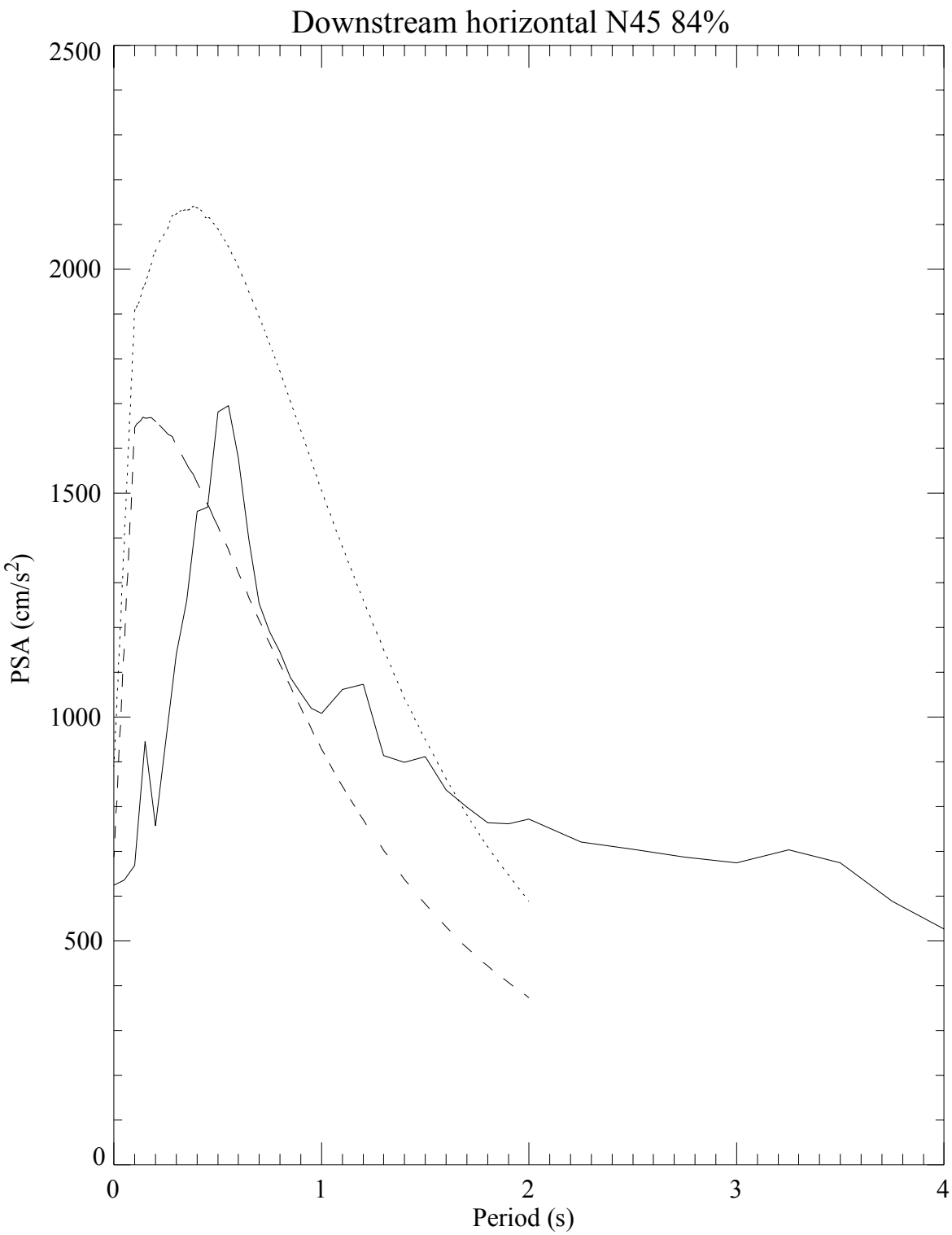

Figure 6-24: JLDW rock site 84% quantile downstream horizontal PSA response spectra for a 45°-dipping northern Teton fault segment (solid). SEA99 average horizontal component estimates for a **M** 7.0 normal-faulting earthquake are shown for soil (dotted) and rock (dashed) site conditions.

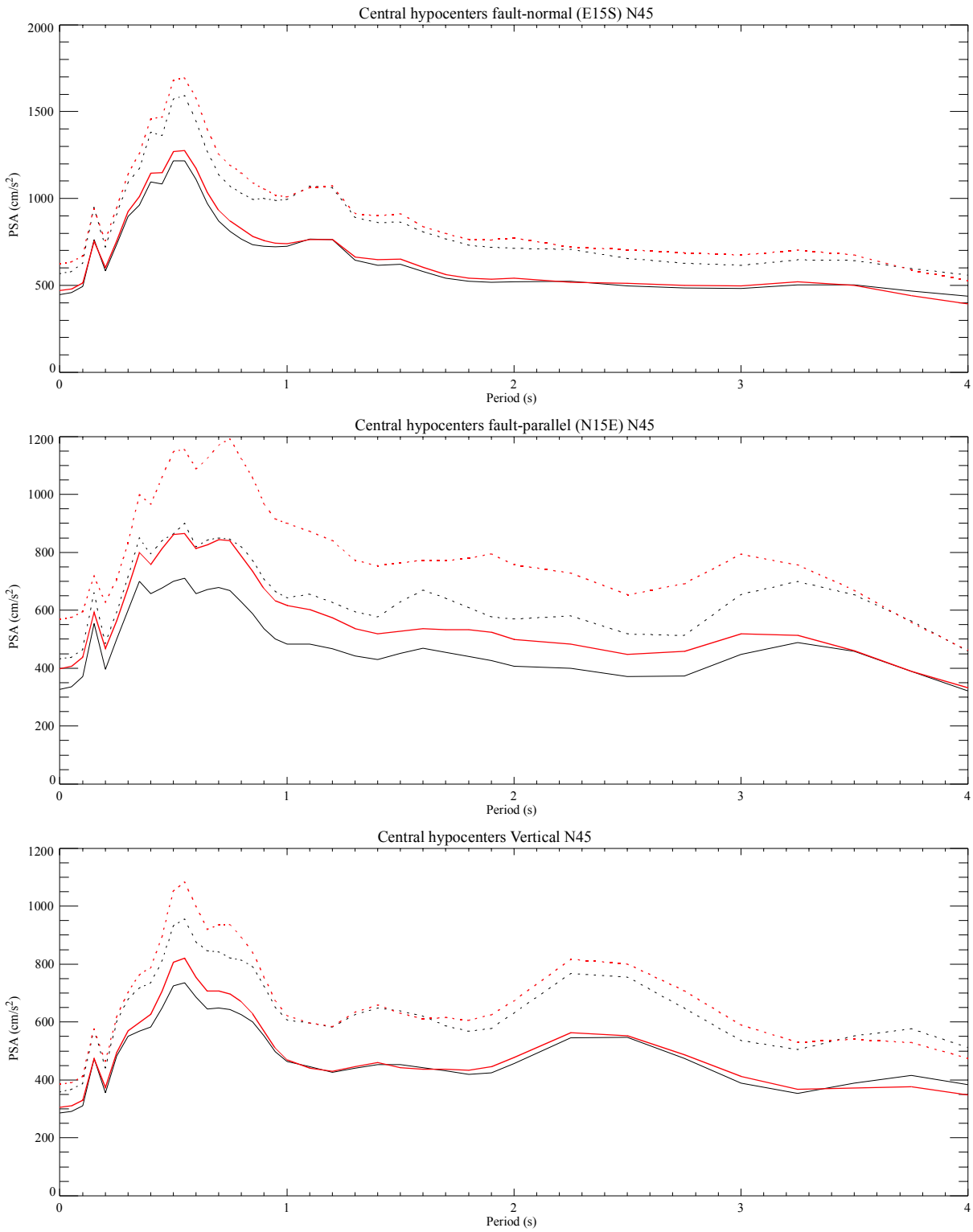

Figure 6-25: JLDW rock site central hypocenter PSA response spectra for a 45°-dipping northern Teton fault segment (black). Red curves are reference mean (solid) and 84% quantile (dotted) results using all hypocenters (from Figure 6-22). Components are as labeled.

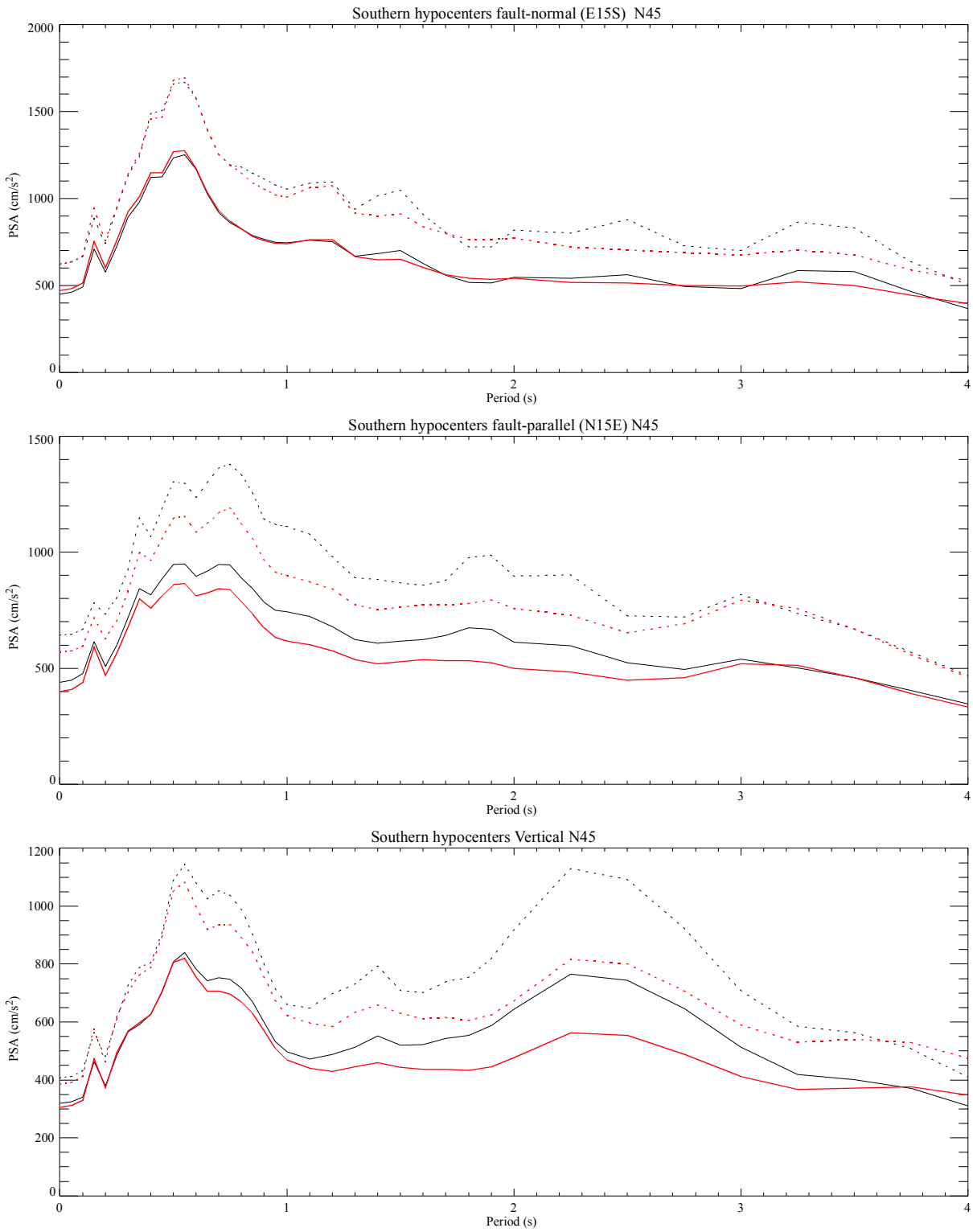

Figure 6-26: JLDW rock site southern hypocenter PSA response spectra for a 45°-dipping northern Teton fault segment (black). Red curves are reference mean (solid) and 84% quantile (dotted) results using all hypocenters (from Figure 6-22). Components are as labeled.

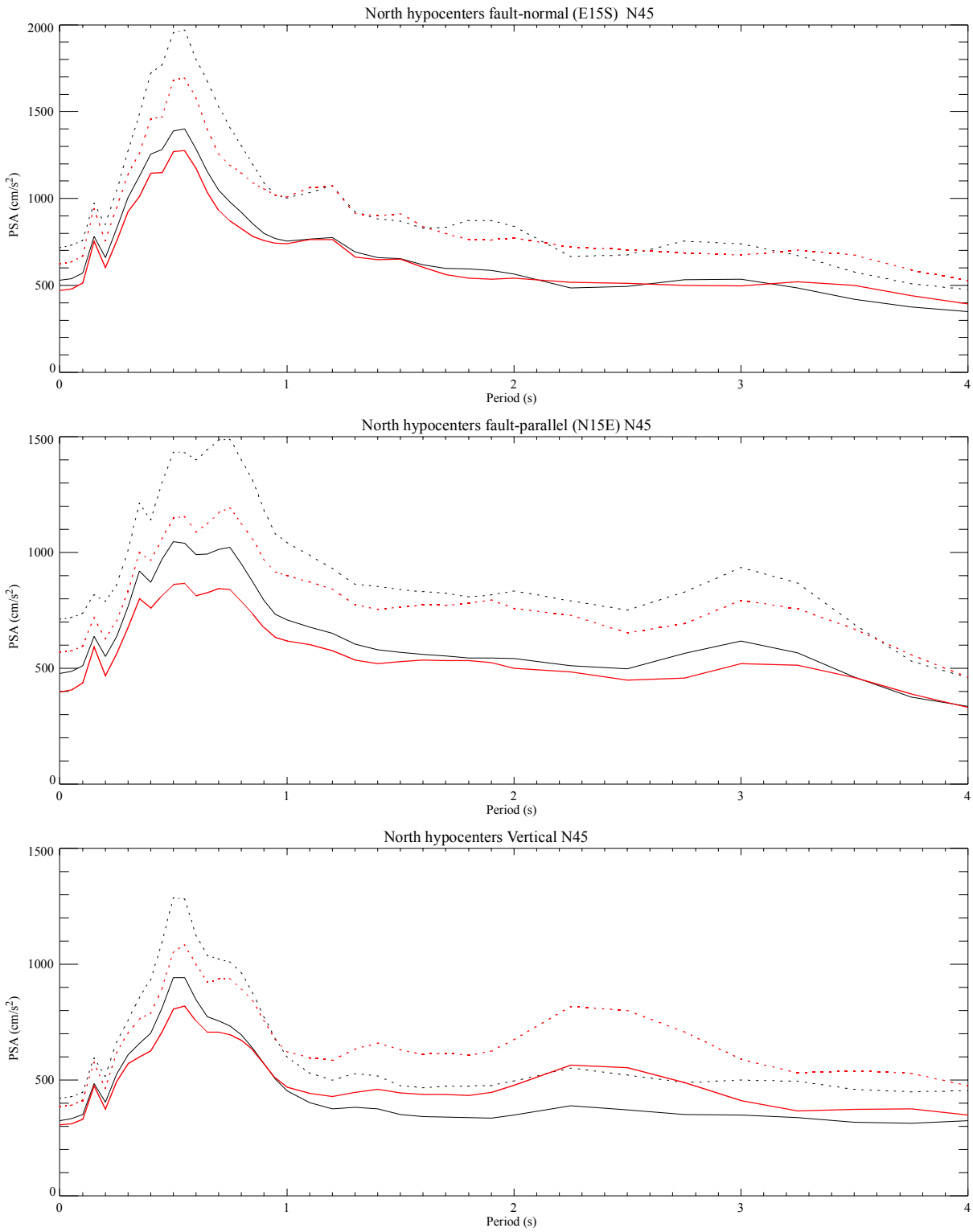

Figure 6-27: JLDW rock site northern hypocenter PSA response spectra for a 45°-dipping northern Teton fault segment (black). Red curves are reference mean (solid) and 84% quantile (dotted) results using all hypocenters (from Figure 6-22). Components are as labeled.

wave and surface wave travel times provide a qualitative explanation of these results. When hypocenters are located near the ends of the LVB, a coherent wavetrain of LVB-edge waves is preferentially generated at the hypocenter end of the LVB early in the rupture process that proceed to propagate coherently across the LVB and constructively add to direct S-wave energy produced later in the rupture process. For central hypocenters, LVB edge waves are generated much later in the rupture process and have less opportunity to add to direct S-wave energy associated with rupture of the fault, since most direct S-waves will have arrived at the JLDW prior to the arrival of the LVB edge-waves. The differences in the onset times of rupture for different hypocenter positions also explains the amplified short-period fault-normal PSA responses for northern hypocenters (Figure 6-27). Since the northern edge of the LVB is located closer to the dam than the southern end of the LVB (Figure 6-4), the LVB-edge S-waves generated at the north end of the LVB for early portions of the fault rupture can add energy to direct S-waves from later rupture beneath the dam, increasing the influence of directivity on the short period fault-normal, fault-parallel, and vertical PSA (Figure 6-27). Since the EGFs were used to construct the > 1 Hz responses and contain a wide variety of LVB-edge S-wave amplitudes and time moveouts relative to the direct S-wave arrival, the < 1 s PSA responses may be significantly underestimated because LVB-edge S-waves would likely have more systematic move-outs, amplitudes, and phasing that represented by the random summing of eight EGF responses.

The southern hypocenters produce very large (> 1 g at 84%) 2-2.5 s period vertical PSA responses, relative to other hypocenter positions (Figure 6-26). The southern end of the LVB is about twice as far from the dam as the northern end of the LVB (Figure 6-4). As noted in Section 4, LVB-edge Rayleigh waves develop only large amplitudes at the dam for the microearthquake source near the southeast edge of the LVB. It is likely that the very large 2-2.5 s period vertical PSA responses for southern hypocenter are a product of LVB-edge Rayleigh wave response generated at the southern end of the LVB. These vertical responses have PSA comparable to peak short period (< 1 s) vertical responses. Amplification of 2-2.5 s period vertical PSA responses is more subtle for a fault dip of 35° (Figure 6-21), indicating a very strong dependence of vertical LVB response to Teton fault dip, when rupture of the northern Teton fault segment initiates in the southern portion of the fault segment.

6.4.3.4 Northern Teton Fault Segment - 60° Dip. Peak ground motions are smaller for a Teton fault dip of 60° than for fault dips of 35° or 45° (Table 6-4). Peak velocities and Arias

Table 6-4: JLDW Rock Ground Motion Parameters: 60°-Dipping Northern Teton Fault Segment.

Component	Peak velocity	Arias Intensity	Cumulative energy	Arias duration	Energy duration
	(cm/s)	(m/s)	(J)	(s)	(s)
E15S mean	96	2.7	9,366	18.3	24.8
E15S 84%	122	3.9	14,100	23.0	33.8
N15E mean	84	2.6	5,616	19.5	26.0
N15E 84%	116	3.9	8,510	22.4	36.0
Vertical mean	76	1.8	4,819	15.9	20.0
Vertical 84%	98	2.6	,7220	18.7	28.2

Intensities are nearly identical on the two horizontal components of ground motion. Only cumulative kinetic energy is substantially larger on the fault-normal (E15S) component relative to the fault-parallel (N15E) component, indicating a smaller influence of rupture directivity and a proportionally larger influence of the 3D LVB on ground motion responses. Fault-normal (E15S) PSA responses are peaked at ~0.5 s (Figure 6-28), indicating that directivity does mildly amplify short period responses. Fault-parallel (N15E) PSA responses increase slightly at short periods (< 1 s), but have remarkably constant PSA responses between 1 s and 3 s period, indicating significant amplification of > 1 s responses by the 3D LVB. As seen with the 35° and 45° Teton fault dip cases, fault-parallel responses for central hypocenters (Figure 6-29) are substantially less than PSA responses for hypocenters near the ends of the fault segment, particularly hypocenters near the southern end of the fault (Figure 6-30). In the case of a fault dip of 45° both southern and northern hypocenters produced amplified fault-parallel PSA responses (Figures 6-26 and 6-27). In contrast to the case of a 60° fault dip, for a fault dip of 35° hypocenters at the northern end of the fault produced the largest fault-parallel responses (Figure 6-20). Thus, there is a very strong dependence of fault-normal motions on fault dip and hypocenter position. For a fault dip of 60°, hypocenters at the northern end of the rupture segment produce PSA closest to the simulated

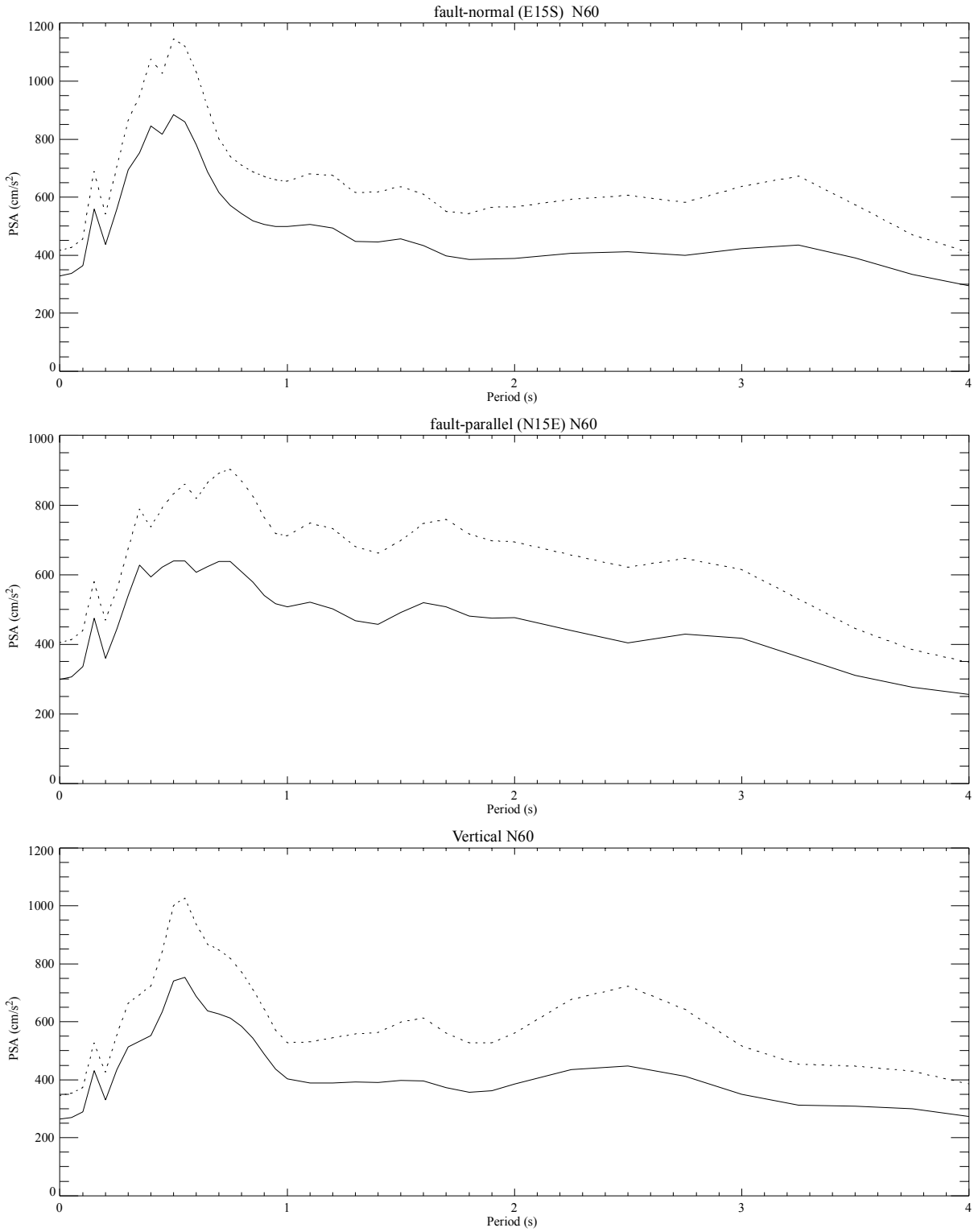

Figure 6-28: JLDW rock site PSA response spectra for a 60°-dipping northern Teton fault segment using all hypocenter positions. Mean curves are solid and 84% quantile curves are dotted. Components are as labeled.

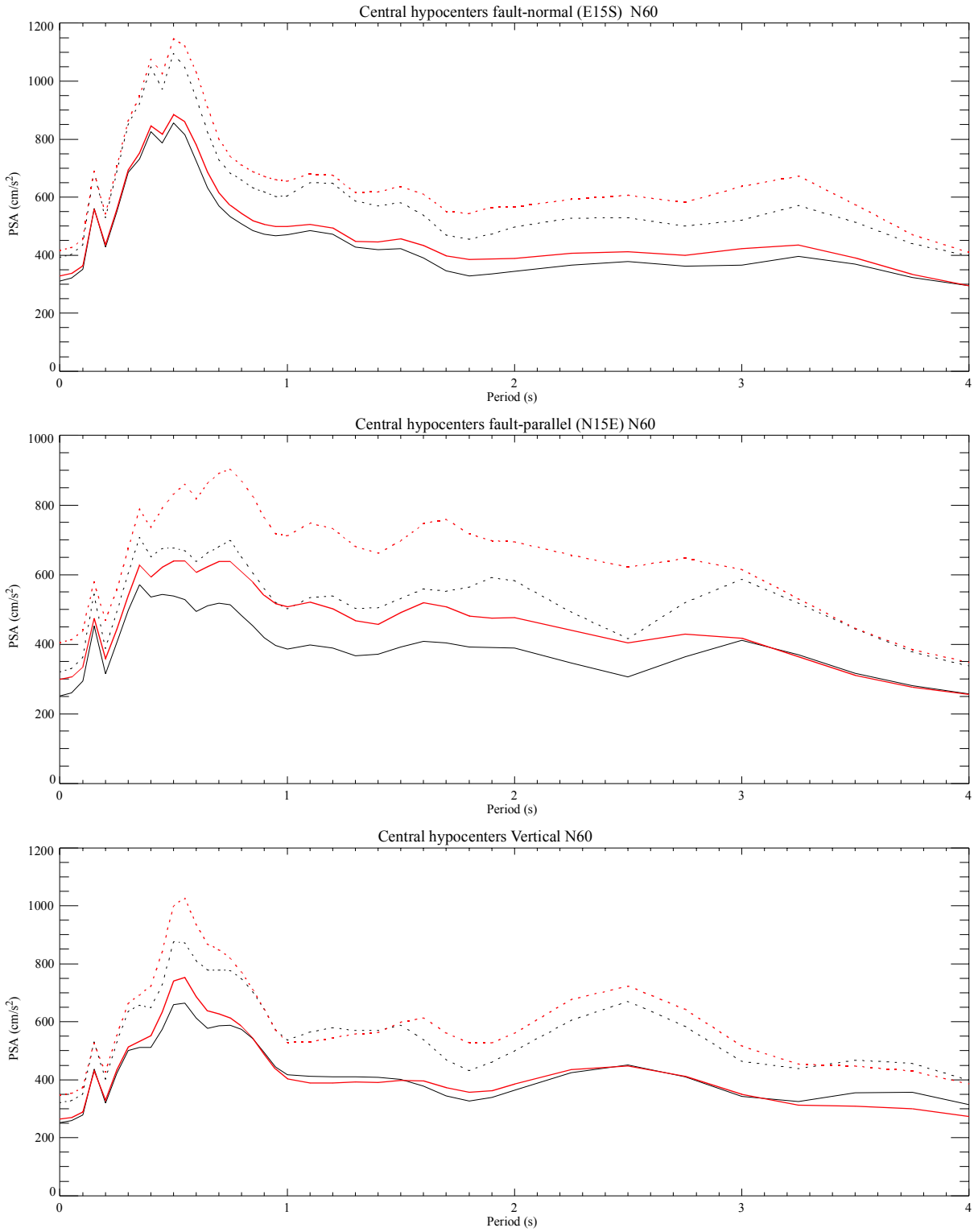

Figure 6-29: JLDW rock site central hypocenter PSA response spectra for a 60°-dipping northern Teton fault segment (black). Red curves are reference mean (solid) and 84% quantile (dotted) results using all hypocenters (from Figure 6-28). Components are as labeled.

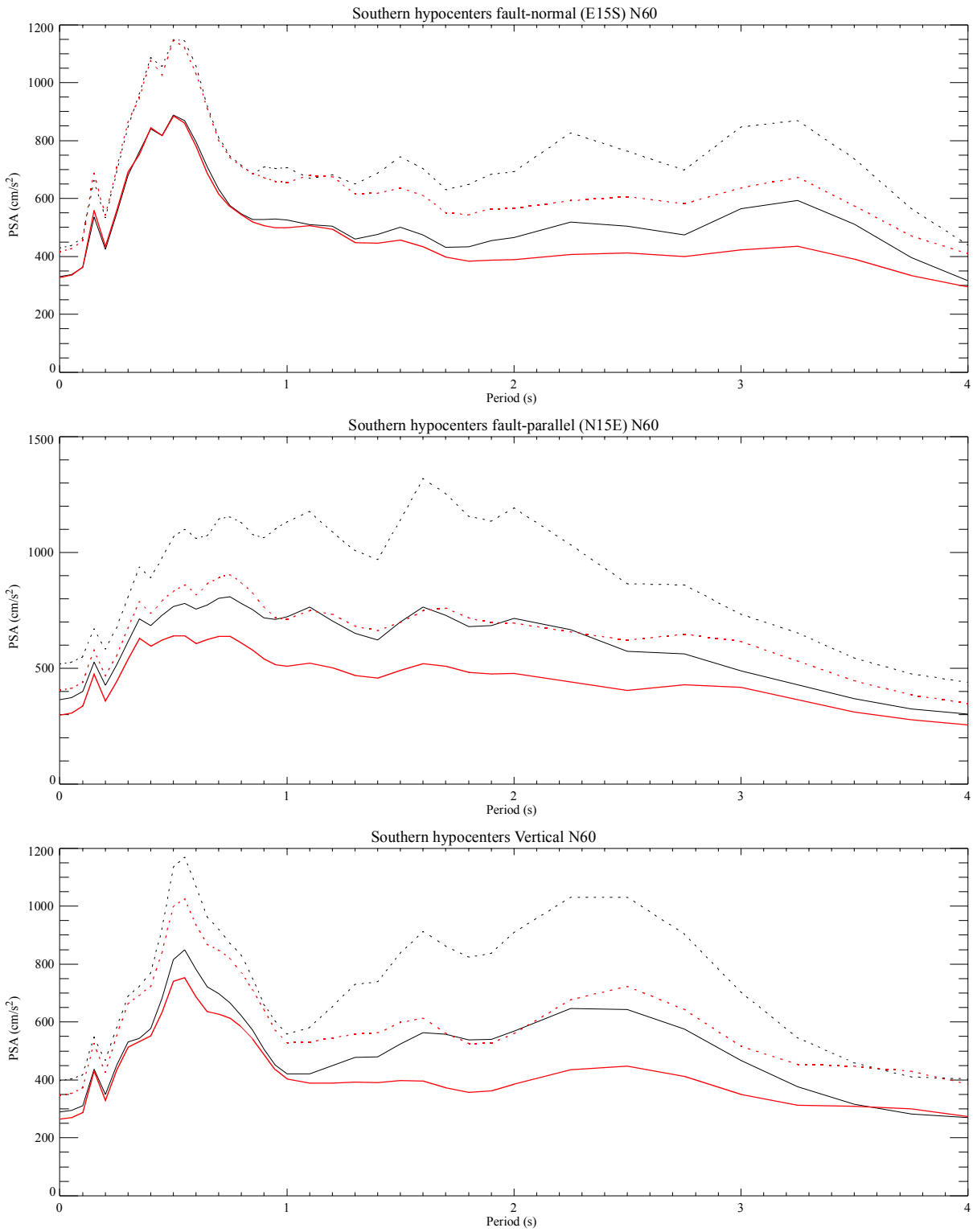

Figure 6-30: JLDW rock site southern hypocenter PSA response spectra for a 60°-dipping northern Teton fault segment (black). Red curves are reference mean (solid) and 84% quantile (dotted) results using all hypocenters (from Figure 6-28). Components are as labeled.

mean and 84% PSA responses for all hypocenter positions (Figure 6-31). Vertical PSA responses to southern hypocenters are strongly amplified between 1.5 s and 3 s period for a fault dip of 60° (Figure 6-30), similar to the southern hypocenter vertical PSA results for a fault dip of 45° (Figure 6-26), but extending over a broader period range.

The rupture area for the 60°-dipping fault is nearly half the rupture area of the 35°-dipping fault, and for a 60° dip none of the fault projects beneath the dam (Figure 6-4). Consequently, mean (Figure 6-32) and 84% (Figure 6-33) horizontal response spectra are general lower than Spudich et al. (1999) rock responses. The site to source distance definition for Spudich et al. (1999) only changes to 2 km for a 60° fault dip from 0 km for 35° and 45° fault dips. Consequently, the Spudich et al. (1999) relations do not predict the reduced short period directivity indicated by the simulated ground motions because the distances, defined using the criteria of Joyner et al. (1994), hardly change. Joyner et al. (1994) intended distance to act as a proxy for directivity (W. Joyner, pers. comm.), as opposed to concocting a hanging wall definition of directivity, such as Abrahamson and Silva (1997). Consequently, the Spudich et al. (1999) relations probably overpredict the influences of directivity for a fault dip of 60° and may underpredict directivity effects for a fault dip of 35°. Both mean and 84% PSA responses on both horizontal components substantially exceed Spudich et al. (1999) PSA responses for periods > 2 s.

6.4.4 Comparison of Linear Ground Motions for Varying Fault Dips. The assumed dip of the northern Teton fault segment strongly influences peak ground motion responses. Fault-normal component peak ground motion responses for a dip of 35° are 50% to 100% larger than corresponding responses for a dip of 60° in the 0.5 s to 2.0 s period range (Figure 6-34) ; fault-parallel responses are about 30% larger for periods < 1 s and > 3 s and vertical responses are about 20% larger. The net effect of systematically increasing both horizontal peak responses for a dip of 35° relative to a dip of 60° is that peak horizontal acceleration responses are about twice as large for a fault dip of 35°. PSA responses for a fault dip of 45° are also systematically higher than 60° responses (Figure 6-35); peak horizontal PSA responses for a fault dip of 45° are systematically about 50% larger than 60° fault dip responses for periods < 2 s. The smallest changes in PSA responses occurs between dips of 35° and 45° (Figure 6-36). Fault-normal PSA responses generally increased only about 20%-30% for periods < 2 s when dip was reduced from 45° to 35°,

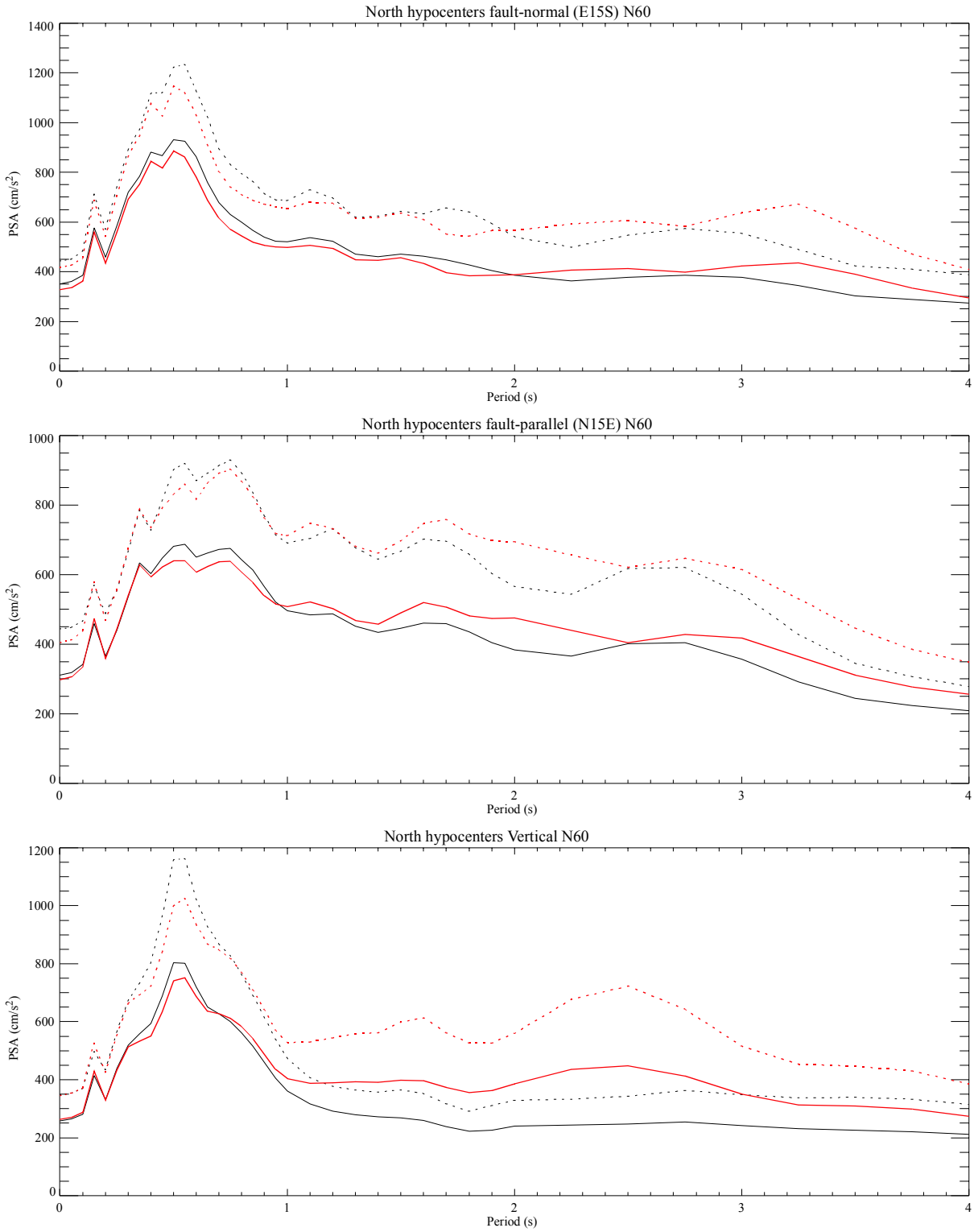

Figure 6-31: JLDW rock site northern hypocenter PSA response spectra for a 60°-dipping northern Teton fault segment (black). Red curves are reference mean (solid) and 84% quantile (dotted) results using all hypocenters (from Figure 6-28). Components are as labeled.

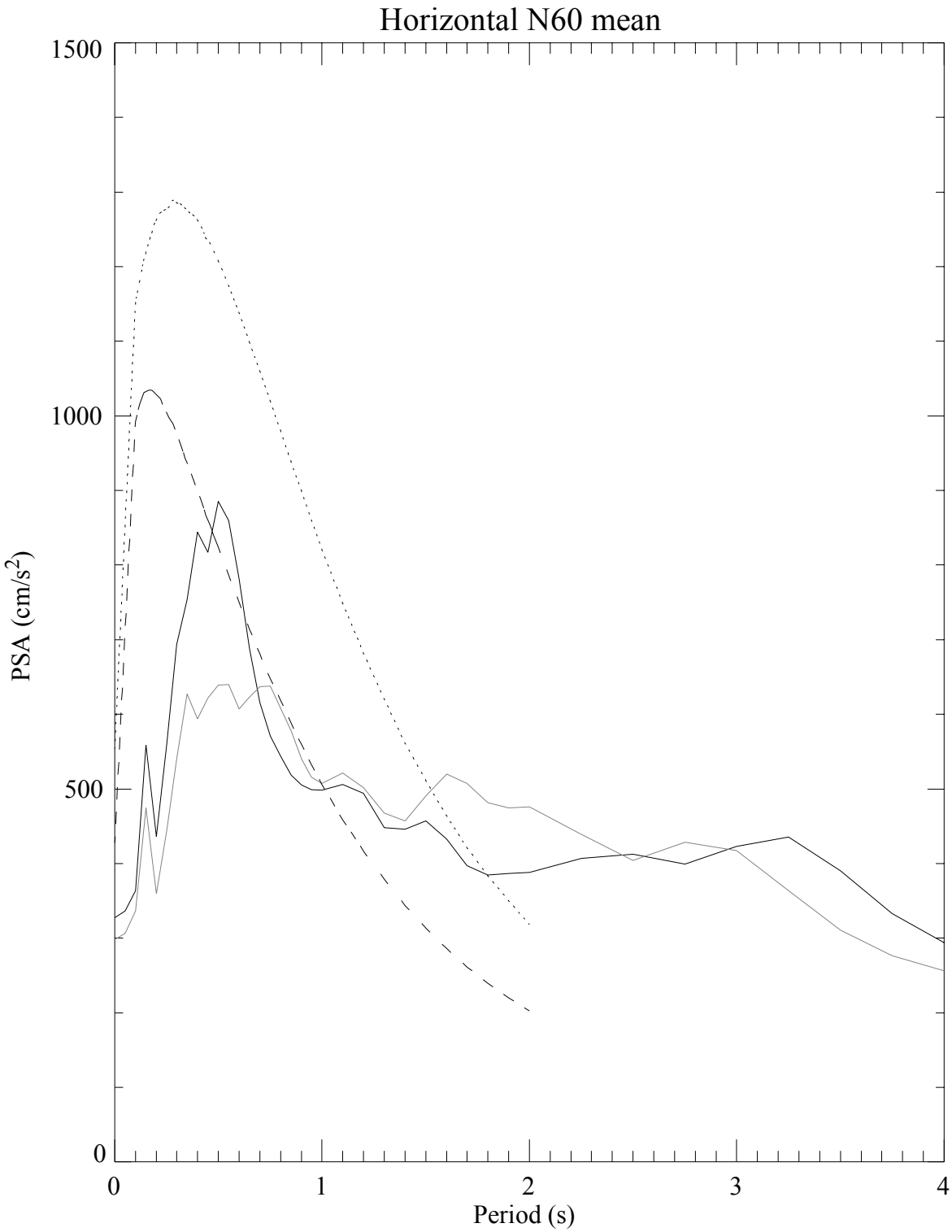

Figure 6-32: JLDW rock site mean PSA horizontal response spectra for a 60°-dipping northern Teton fault segment. The E15S component is solid and the N15E component is gray. SEA99 average horizontal component estimates for a **M** 6.9 normal-faulting earthquake are shown for soil (dotted) and rock (dashed) site conditions.

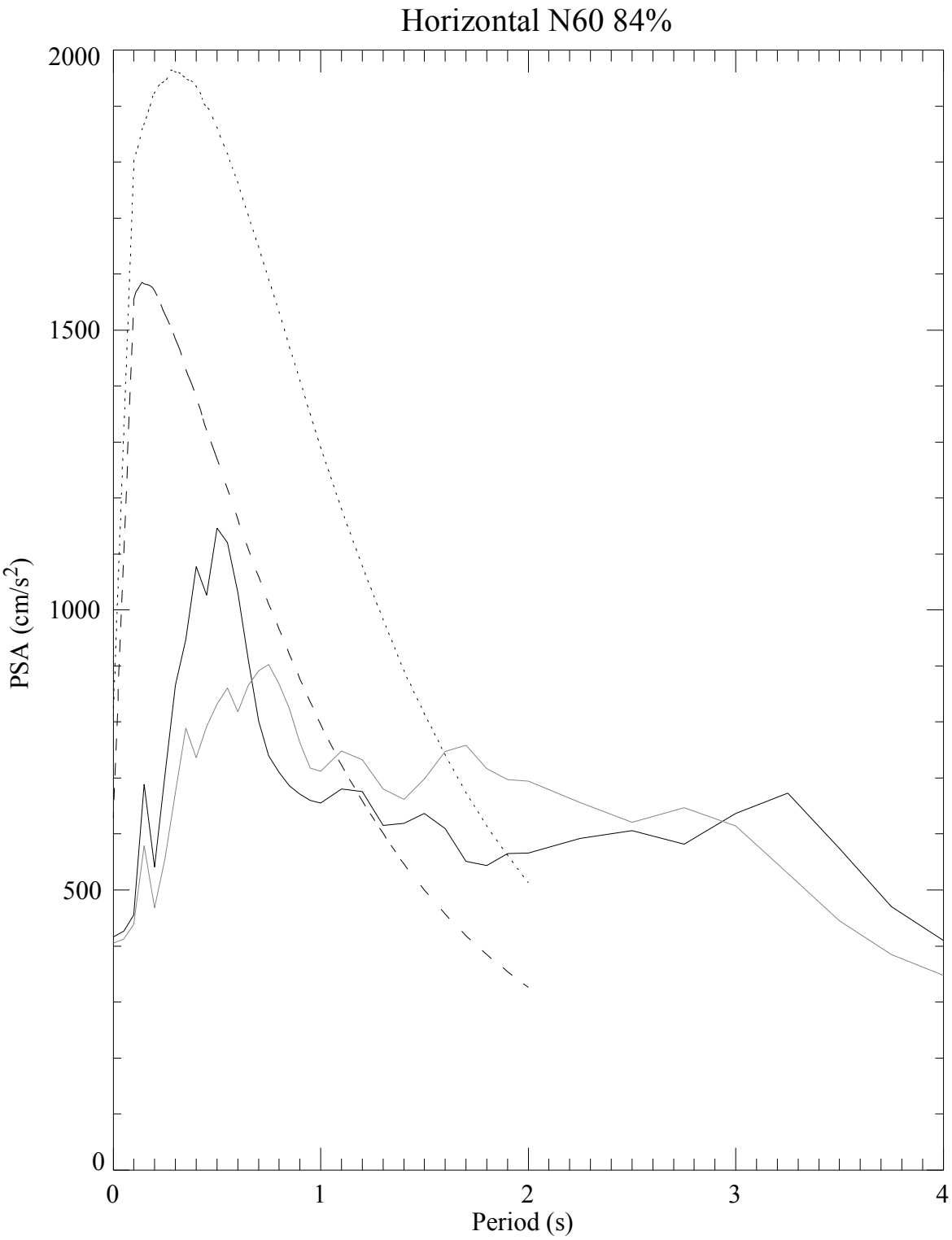

Figure 6-33: JLDW rock site 84% quantile PSA horizontal response spectra for a 60°-dipping northern Teton fault segment. The E15S component is solid and the N15E component is gray. SEA99 average horizontal component estimates for a **M** 6.9 normal-faulting earthquake are shown for soil (dotted) and rock (dashed) site conditions.

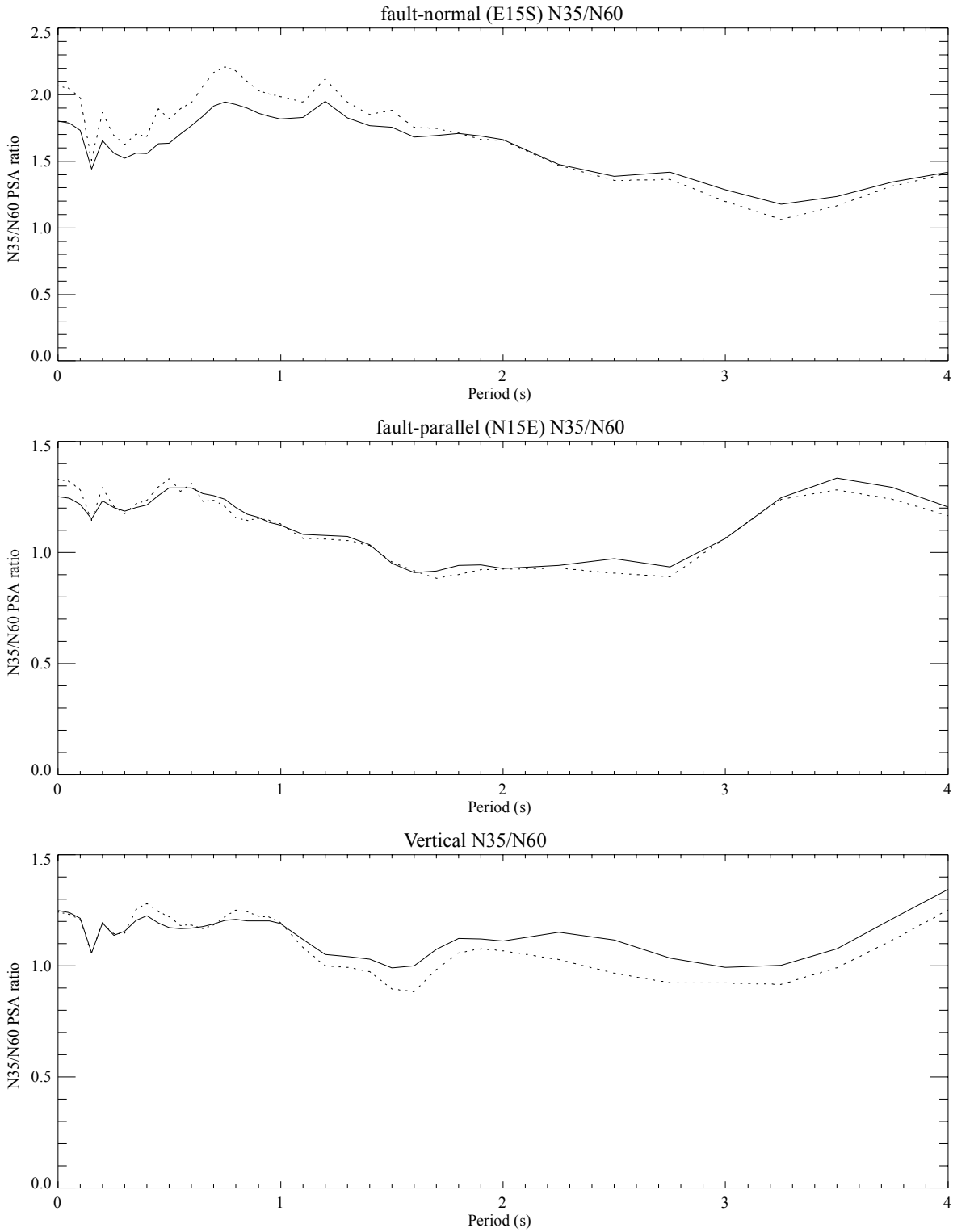

Figure 6-34: JLDW rock site ratios of 35°-to-60°-dipping northern Teton fault segment PSA response spectra. Mean curves are solid and 84% quantile curves are dotted for components as labeled.

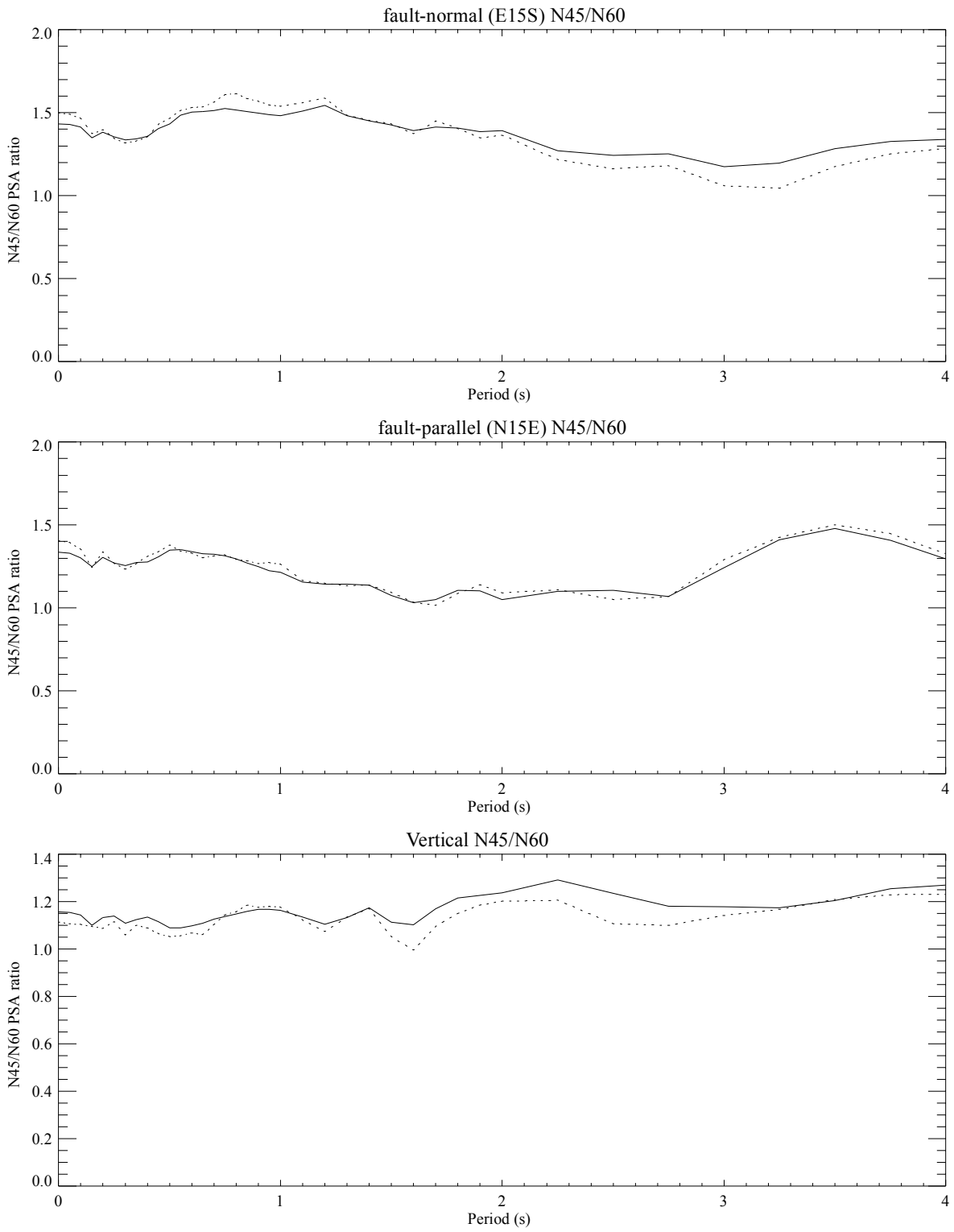

Figure 6-35: JLDW rock site ratios of 45°-to-60°-dipping northern Teton fault segment PSA response spectra. Mean curves are solid and 84% quantile curves are dotted for components as labeled.

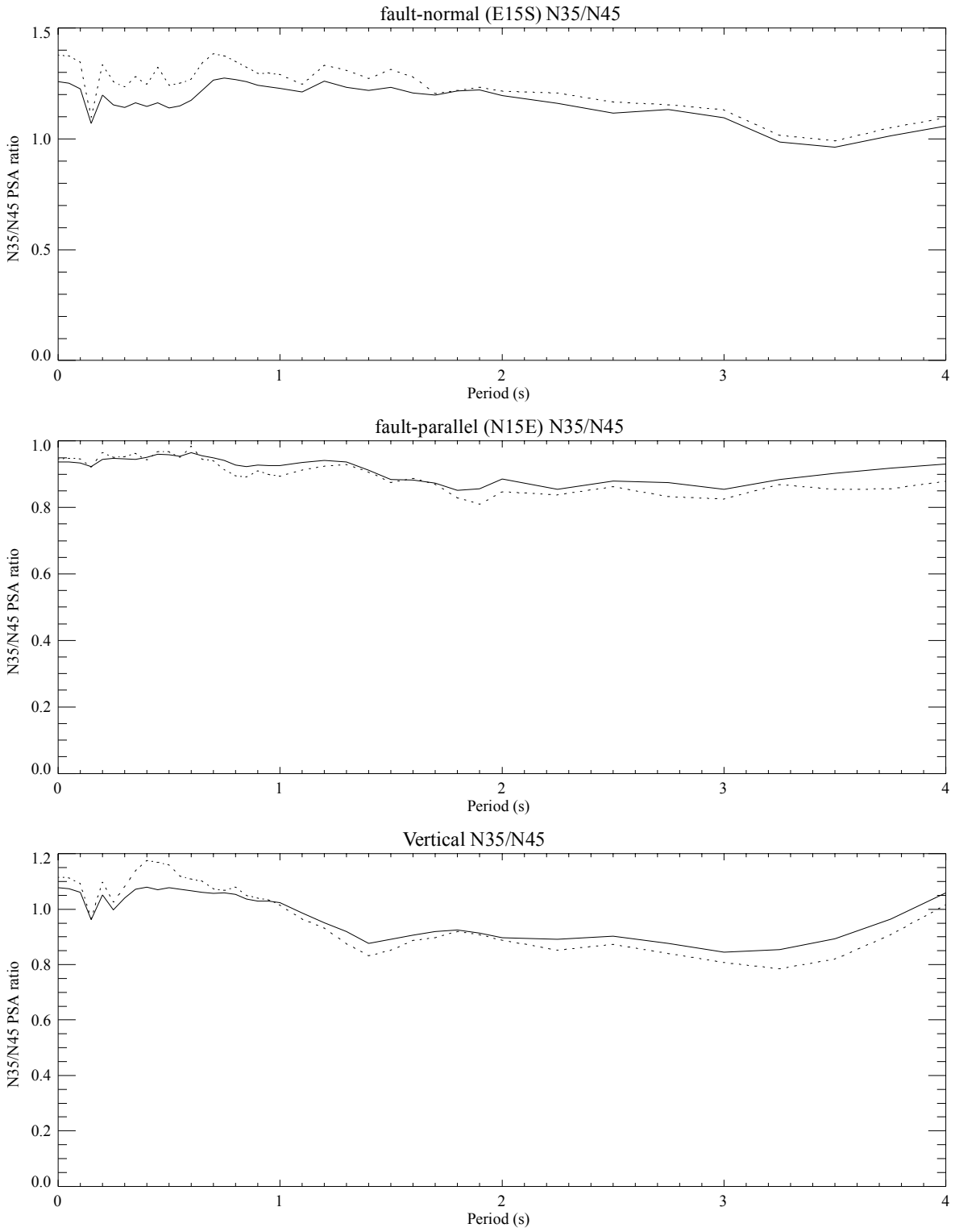

Figure 6-36: JLDW rock site ratios of 35°-to-45°-dipping northern Teton fault segment PSA response spectra. Mean curves are solid and 84% quantile curves are dotted for components as labeled.

fault-parallel motions actually decreased 10%-20%, and vertical motions showed modest changes. Thus, the largest change in peak ground motion acceleration responses is between fault dips of 60° (smallest peak response) to 45°. The 60° fault dip peak responses do show potentially very large long-period vertical responses that are larger over a broader range of periods than for a fault dip of 45°, but otherwise, both the 45° and 35° fault dip PSA responses are much larger than the 60° fault dip PSA responses. If definitive constraints on fault dip become available, particularly if the fault dip is found to be about 60°, then seismic loads at Jackson Lake Dam are likely to be significantly smaller than those recommened for dynamic analyses of the dam in the next section.

6.5 Ground Motions for Dynamic Analyses of the Concrete Portion of Jackson Lake Dam.

Jackson Lake Dam is a complex dam consisting of concrete and embankment sections founded on rock and soil. The concrete section of the dam is primarily founded on overcompacted glacial till and tuff with ~1 km/s near-surface shear wave velocities similar to site JLDW (Sirles, 1986). Ground motions for use in engineering analyses of the embankment section are provided in the Section 6.6. Ground motion developed using the responses calculated at site JLDW are presented here for use in engineering analyses of the concrete section of the dam.

The northern section of the concrete section of the dam is located adjacent to site JLD2, which shows some amplification relative to site JLDW (Section 5). While this report provides ground motions with JLDW site characteristics for engineering analyses of the concrete section of the dam, it may also be valuable to use these JLDW ground motions convolved with JLD2 responses for dynamic engineering analyses. While ground motions modified to contain the amplification observed at station JLD2 are not provided in this report, they can be produced if needed.

There are no **M** ~7 normal-faulting ground motion recordings from hanging wall sites located in low-velocity basins (Spudich et al., 1999). Consequently, other ground motion sources must be used to supply three-component acceleration time histories suitable for dynamic analyses of the concrete portion of the dam founded on “rock”. Two broadband synthetic ground motions produced in Section 6.4 are selected for dynamic analyses of the concrete portion of the dam and

one strong motion recording is recommended to provide extended high-frequency durations absent from the synthetic ground motions.

Since the peak ground motions strongly dependent on the assumed dip of the Teton fault, it is necessary to decide which dip scenario is most representative of expected ground motions at the dam. As discussed in Section 2, worldwide **M** > 5.5 earthquake data for normal-faulting earthquakes indicate that normal-fault dips of ≤ 50° comprise 76% of the normal-faulting earthquakes (Collettini and Sibson, 2001). The focal mechanism data in Section 3 allow for a Teton fault dip of 25° to 60°, but do not place strong constraints on fault dip. As discussed in Section 4, detailed waveform modeling of two earthquakes suggest that the northern Teton fault segment dips < 50°. Normal fault dips vary widely in the western United States. Abbott et al. (2001) suggest that the 16 Dec. 1954 **M** 6.8 Dixie Valley earthquake, Nevada, occurred on a 30°-dip normal fault. However, Doser (1986) found that the nearby 16 Dec. 1954 **M** 7.1 Fairview peak earthquake occurred on an oblique-slip normal fault dipping 60° and the largest magnitude Rainbow Mountain earthquake, **M** 6.8 24. Aug. 1954, occurred on an oblique-slip normal faulting dipping 50°. The primary difference between these three normal faults is that purely normal slip was inferred for the 30°-dip Dixie Valley fault and oblique normal-slip was inferred for the more steeply-dipping normal faults. Doser and Smith (1989) studied source parameters for 50 **M** ≥ 5.5 earthquakes in the cordillera of the western United States and found that fault dips were ≥ 38° and found no evidence for listric low angle planer faulting (very low dips). The largest ISB crustal normal-faulting earthquake with a well constrained focal mechanism is the 1983 **M** 7.3 Borah Peak, Idaho, earthquake with a inferred dip of 45° (see Doser and Smith, 1989, for complete references). The local and region evidence for normal-faulting dip suggests that the 35° and 45° fault dip ground motion scenarios represent the most likely dip scenarios for the Teton fault. In view of the lack of any definitive information indicating that the northern Teton fault rupture segment dips > 50°, the 60° fault dip ground motion scenarios are not discounted for the purposes of recommending ground motions for dynamic analyses of Jackson Lake Dam. Although a fault dip of 45° is plausible, the ground motions producing using a fault dip of 35° are recommended for dynamic analyses of Jackson Lake Dam for the following reasons:

1. Doser and Smith (1989) found that unilateral rupture dominated **M** ≥ 5 earthquake ruptures in the extensional region of the western United States. The ground motion simulations in Section 6.4 showed larger acceleration responses for unilateral rupture scenarios, because LVB-edge S-waves and surface waves coincide with direct S-wave arrivals from fault rupture in most of the central portion of the fault, amplifying acceleration ground motion responses. Using global earthquake data, McGuire et al. (2002) conclude that about 80% of the ruptures of **M** ≥ 7 earthquakes since 1994 where unilateral. Thus, the larger peak motions produced by a 35° fault dip serve as approximations to the amplified 45° fault dip motions associated with unilateral fault rupture.

2. Experimentation with correlated-random velocity randomization of the LVB in the 2D finite-difference ground motion simulations in Section 4 showed that fractal velocity randomizations with standard deviations of about 9% could reproduce the long coda durations observed in microearthquake recordings at station JLDW. It would be necessary to run a suite of velocity randomizations of the 3D crustal velocity model to investigate the influence of random velocity variations on peak ground motion amplitudes and ground motion durations. Since each 3D Green's function calculation required several days to compute and more time to setup and process, it was not feasible to conduct such an investigation and maintain the project schedule. Synthetic ground motion durations are likely underestimated because most the 3D crustal velocity model is relatively smooth, and because it was necessary to limit the total duration of the EGFs to accomplish the ground motion simulations in a timely fashion. Consequently, the synthetic ground motion durations for a fault dip of 35° are likely more representative of expected ground motion durations for a fault dip of 45°, and synthetic ground motion durations for a fault dip of 45° are more likely to represent expected ground motion durations for a fault dip of 60°. Consequently, the 35°-dipping Teton fault results are most likely to contain durations adequate for dynamic analyses of Jackson Lake Dam.

3. Normal fault ruptures are likely to be more complex than the kinematic rupture models used to simulation ground motions in Section 6.4. Oglesby et al. (1998; 2000) considered the consequences of the free surface on the dynamic rupture characteristics of dipping faults

using 2D and 3D finite-element models. One consequence of the free-surface boundary condition on stress is that for normal faults with dip angles between about 30° and 75°, fault rupture proceeding from the bottom of the fault toward the free surface brings the fault near the free surface closer to failure than it would have been in a whole space. This effect is predominantly due to the decrease in normal stress on the fault with a resultant decrease in the yield frictional stress. In some circumstances, this effect can lead to the rupture front jumping ahead (a secondary nucleation) near the free surface of a normal fault. After rupture proceeds downdip from the free-surface, normal stresses increase behind the rupture (Oglesby et al., 1998), which may cause the downdip rupture region to heal near the surface prior to the onset of updip rupture, in effect producing two distinct slip events along the shallow portions of the fault. This dynamic rupture behavior may explain the tendency for some normal faults to produce surface slips that appear out of proportion relative to the surface scarp lengths (Wells and Coppersmith, 1994). The implications for ground motions at Jackson Lake Dam is that excitation of LVB-edge S-waves near the Teton fault could occur twice during an earthquake, once when rupture jumps to the free surface and proceeds down dip, and once when rupture preceding updip and intersects the free surface. As shown in Section 4, S-waves produced along the shallow portion of the Teton fault produce large-amplitude LVB-edge S-waves at the dam, due to the focusing effects of the LVB structure. The dynamic rupture simulations results for normal faults of Oblesby et al., (1998;), specifically the tendency for rupture to discontinuously jump to the free surface and produce enhanced slip and multiple slip velocity pulse in the shallow region of the normal fault, were reproduced using the 3D finite-difference approach of Andrews (1999). The results are unlikely to change for different constitutive laws for fault slip (Bizzarri et al., 2001). Since these normal-faulting dynamic slip velocity effects are not included in the kinematic rupture model used to synthesize ground motions at the dam, a reasonable conclusion is that the simulated peak ground motions provide lower bounds on ground motion amplitudes at the dam, and may underestimate peak velocities and accelerations at the dam. In view of these factors, it appears that the peak amplitudes associated with the 35°-dipping Teton fault are likely to be more representative of ground motion associated with a 45°-dipping fault, and peak amplitudes associated with the 45°-dipping Teton fault are likely to be more representative of ground motions associated with a 60°-dipping Teton

fault. Consequently, the 35°-dipping Teton fault results are most likely to contain adequate durations to use for dynamic analyses of Jackson Lake Dam.

4. The rock motions were simulated for the rock reference site JLDW, which is located ~200 m east of the easternmost section of Jackson Lake Dam. As shown in Section 6.4, peak ground motion amplitudes decrease east of the dam. Consequently, rock motions at Jackson Lake Dam will probably be moderately larger than ground motions computed at site JLDW. This is another factor that supports substituting lower-dip ground motion estimates for the next larger dip to provide more representative seismic loads at the dam.

5. The summation of the EGF's LVB-edge S-waves is probably less constructive than would occur in practice since the EGF's are aligned on the first S-wave arrival, and the LVB-edge S-waves have travel-time moveouts that varying systematically between ~3 s and ~6 s, depending on the position of the fault source relative to the site. In contrast the EGF's have a wide variety of LVB-edge S-wave moveouts and are selected at random at each point-source integration point. Consequently, the EGF ground motions are likely to underestimate peak amplitudes somewhat, particularly in the 1 Hz to 6 Hz frequency band where coherent LVB-edge S-waves where observed and modeled in Section 4 using 2D finite-difference methods.

6. The EGF's were low-pass filtered at 6 Hz to ensure convergence of the point-source summations at high frequencies. Consequently, peak acceleration are likely lower bounds because there will be a nonzero contribution of frequencies > 6 Hz to ground motions that was not included in the simulated ground motions. This should not be a large effect because the site kappa estimated from the site responses at the JLDW rock site are large, on the order of 0.08, so seismic energy for frequencies > 6 Hz is naturally attenuated, although not as strongly as in the simulated ground motions.

In light of these seismic source and wave propagation complications, and the practical realities of simulating ground motions, the simulated 45°-fault-dip and 60°-fault-dip ground motions are discounted for the purposes of providing ground motions suitable for dynamic analyses of the dam. Our judgement is that the 35°-dipping ground motions are probably most representative of

expected ground motions for faults dips < 50°, the most likely range of dips for the Teton fault, based on world-wide distributions of normal fault dips (Section 2) and the limited inferences that can be made about Teton fault dip from microearthquake data (Sections 3 and 4).

Response spectra from the 3300 simulated ground motions with a fault dip of 35° where compared to the mean and 84% response spectra to find the ground motion simulations that produced horizontal response spectra that most closely resembled mean and 84% PSA responses. Since the E15S horizontal component consistently had the largest PSA responses, it was used to as the basis for comparison. A simulated ground motion was found that closely reproduced the mean E15S PSA response from the 3300 simulations (Figure 6-37). The PHA (Figure 6-38) and PHV (Figure 6-39) responses are close to mean responses for a dip of 35° (PHA are the zero period PSA values). The acceleration time histories in Figure 6-38 were high-pass filtered to eliminate permanent displacement so these ground motions were compatible with typical requirements of dynamic engineering analyses programs. Consequently, the displacement seismograms (Figure 6-40) do not contain the significant permanent displacements associated with translation of the hanging wall during faulting. Significant accelerations, velocities, and displacements persist for > 60 s. These synthetic ground motions become artificially depleted of high-frequency responses after about 30 s because of the ~13.5 s limit on the EGF durations used in the ground motion simulations. However, it is expected that the predominant period of the ground motions will progressively shift toward longer periods with increasing time as large-scale LVB responses dominant the responses after ~35 s, just not as abruptly as indicated in Figures 6-38 and 6-39.

A simulated ground motion was found that closely reproduced the 84% E15S PSA response from the 3300 simulations (Figure 6-41). The durations of high-frequency accelerations (Figure 6-42) are shorter (~50 s of significant acceleration response) than for the mean scenario (Figure 6-38), consistent with amplification associated with rupture directivity producing the stronger 84% peak responses. Peak velocities are on the N15E component, although velocities > 100 cm/s persist longer on the E15S component (Figure 6-43). Strong velocities (> 20 cm/s) persist for ~40 s on the E15S and vertical components, indicating a strong response from the LVB (Figure 6-43), as is also evident in the horizontal displacements (Figure 6-44).

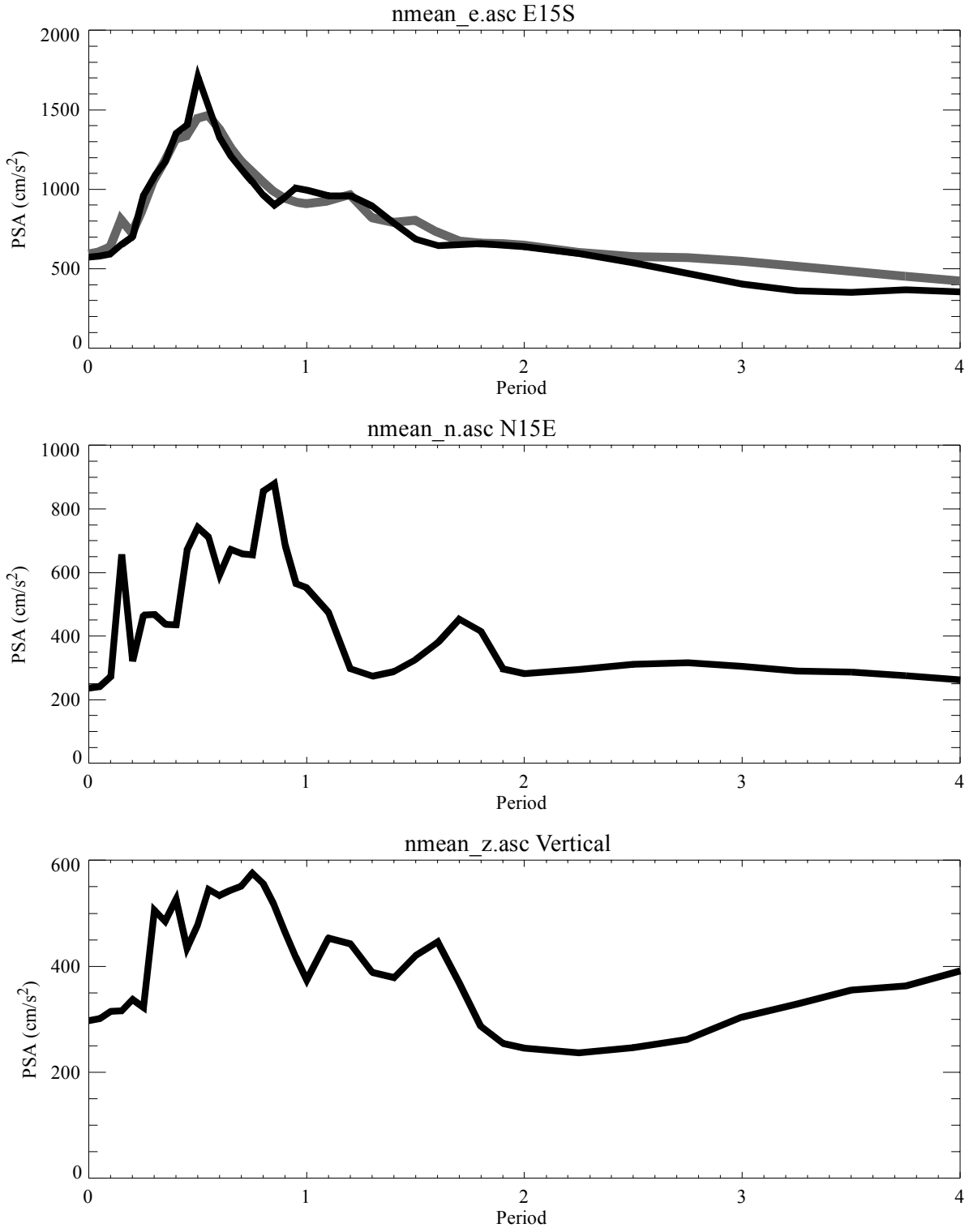

Figure 6-37: JLDW rock site PSA response spectra corresponding to the mean acceleration seismograms.Components are labeled with time history filename and component orientation. The arithmetic mean of the 3300 simulated response spectra for the upstream component for a fault dip of 35° are plotted as the grey curve for comparison at the top.

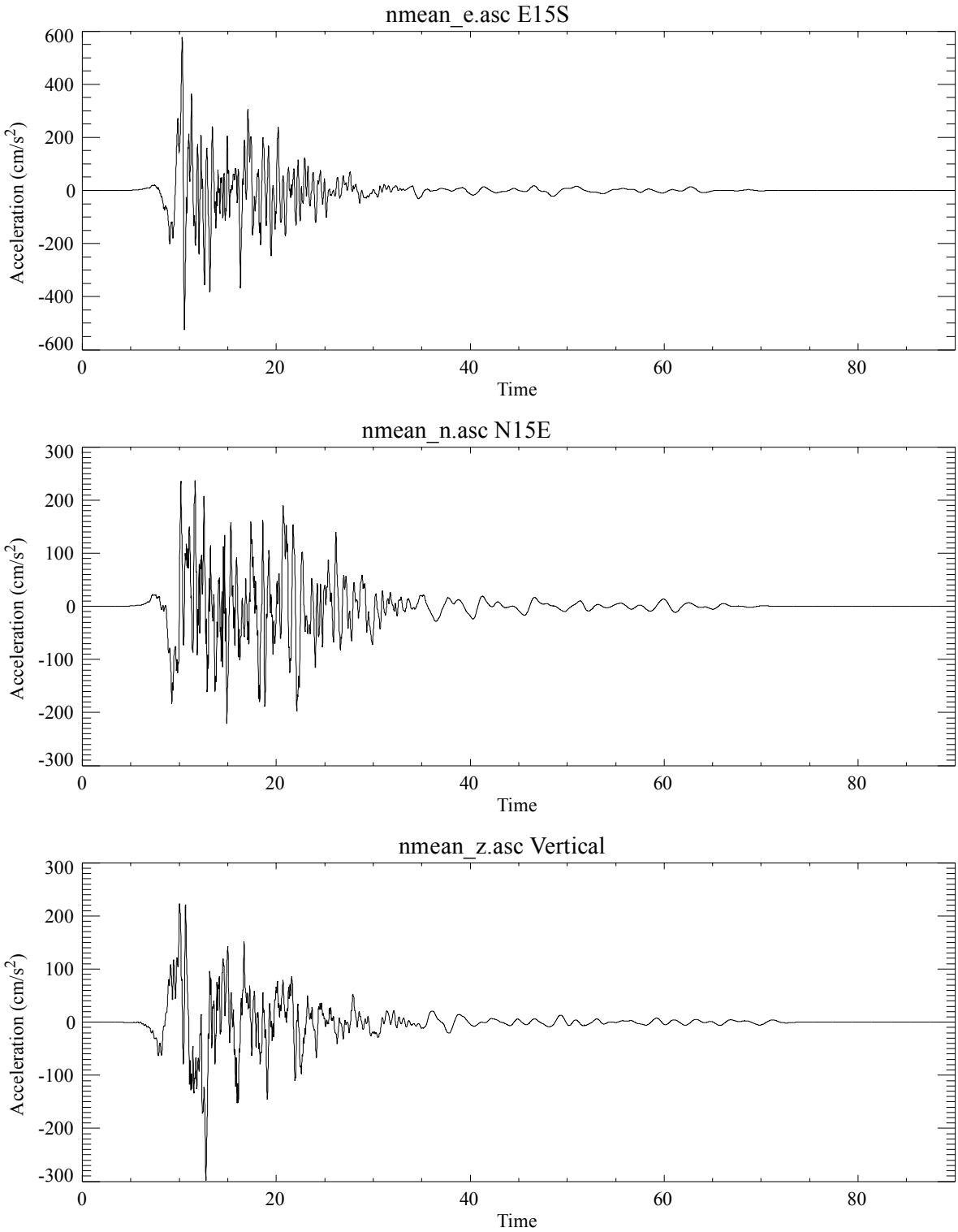

Figure 6-38: JLDW rock site mean acceleration seismograms for dynamic analyses of Jackson Lake Dam. Components are labeled with time history filename and component orientation, with horizontal components orientated upstream and cross canyon (along the dam axis). These seismograms correspond to the best-fitting acceleration response spectra to the mean of 3300 response spectra for a fault dip of 35°.

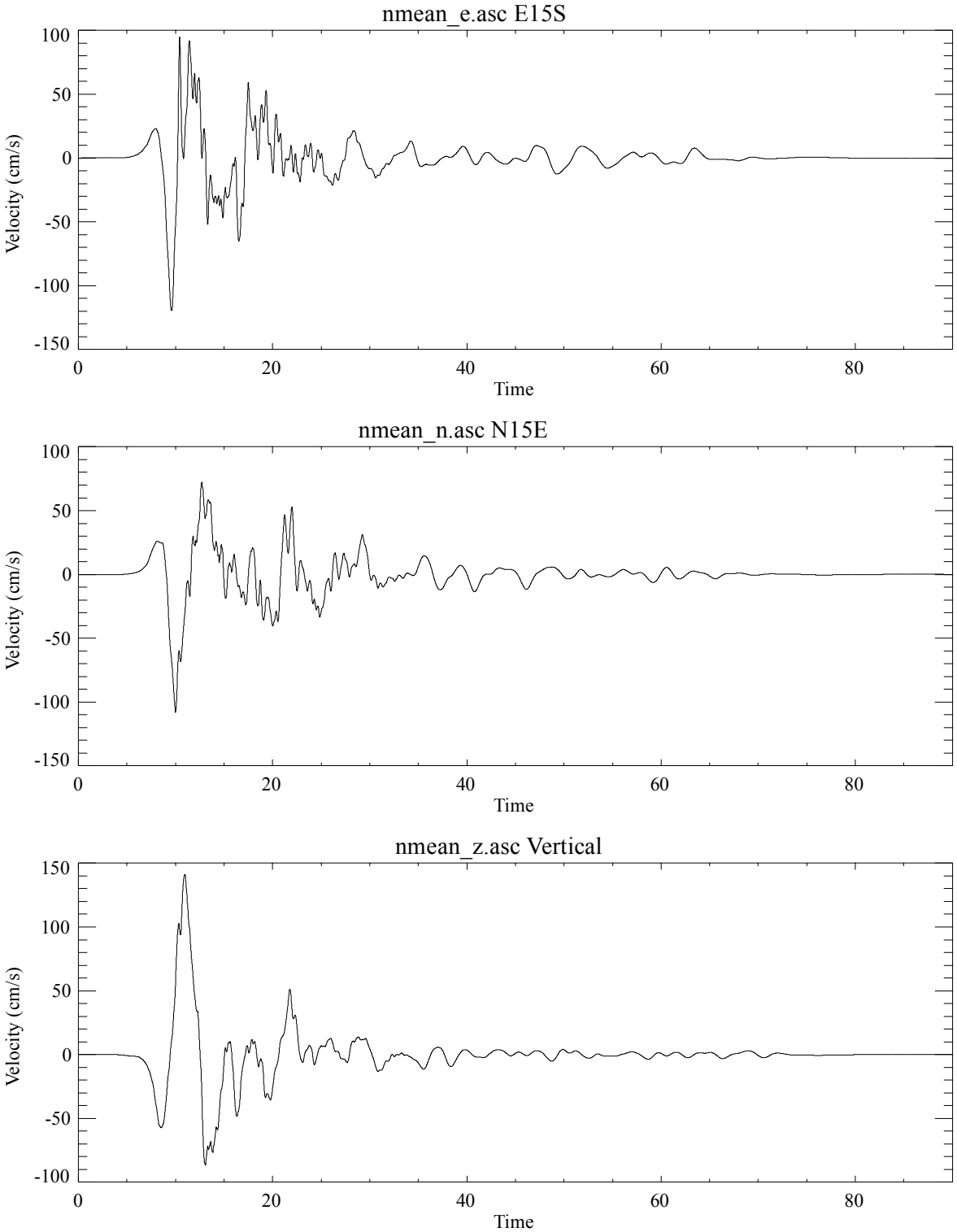

Figure 6-39: JLDW rock site mean velocity seismograms for dynamic analyses of Jackson Lake Dam. Components are labeled with time history filename and component orientation, with horizontal components orientated upstream and cross canyon (along the dam axis). These seismograms correspond to the best-fitting response spectra to the mean of 3300 acceleration response spectra for a fault dip of 35°.

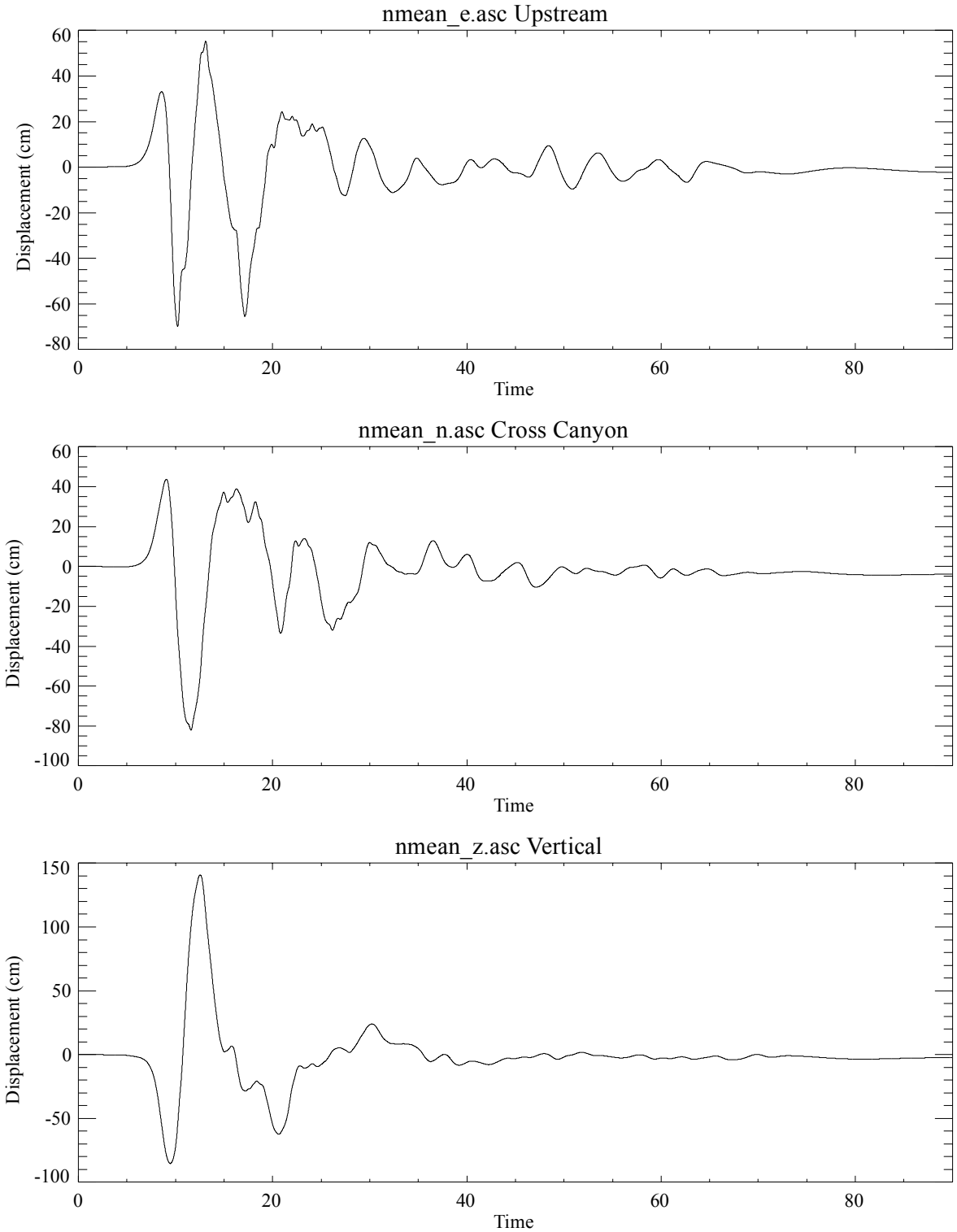

Figure 6-40: JLDW rock site mean displacement seismograms for dynamic analyses of Jackson Lake Dam. Components are labeled with time history filename and component orientation. These seismograms correspond to the best-fitting response spectra to the mean acceleration response spectra for a fault dip of 35°.

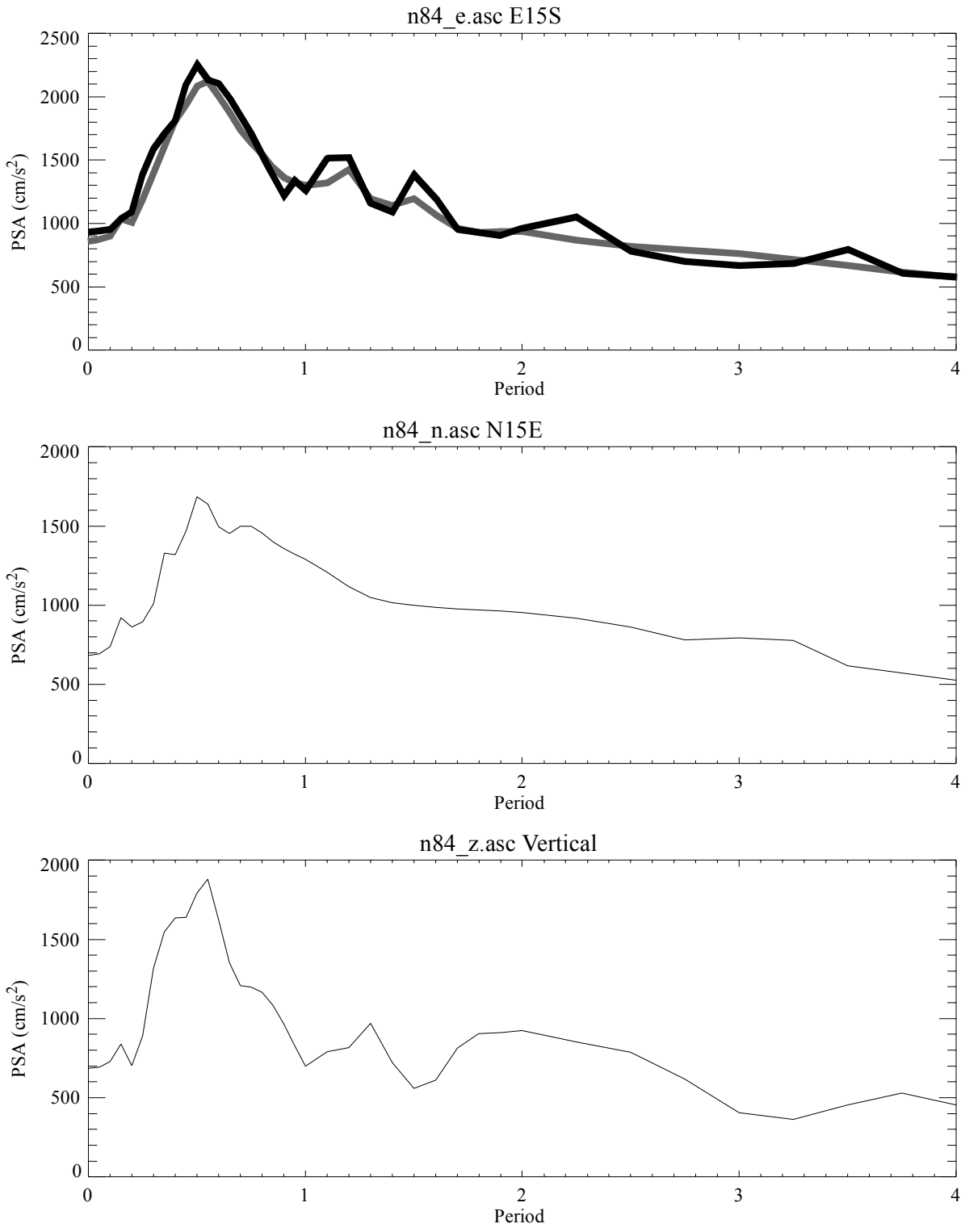

Figure 6-41: JLDW rock site PSA response spectra corresponding to the 84 percentile acceleration seismograms.Components are labeled with time history filename and component orientation. The 84% quantile from 3300 response spectra for the upstream component for a fault dip of 35° are plotted as the grey curve for comparison at the top.

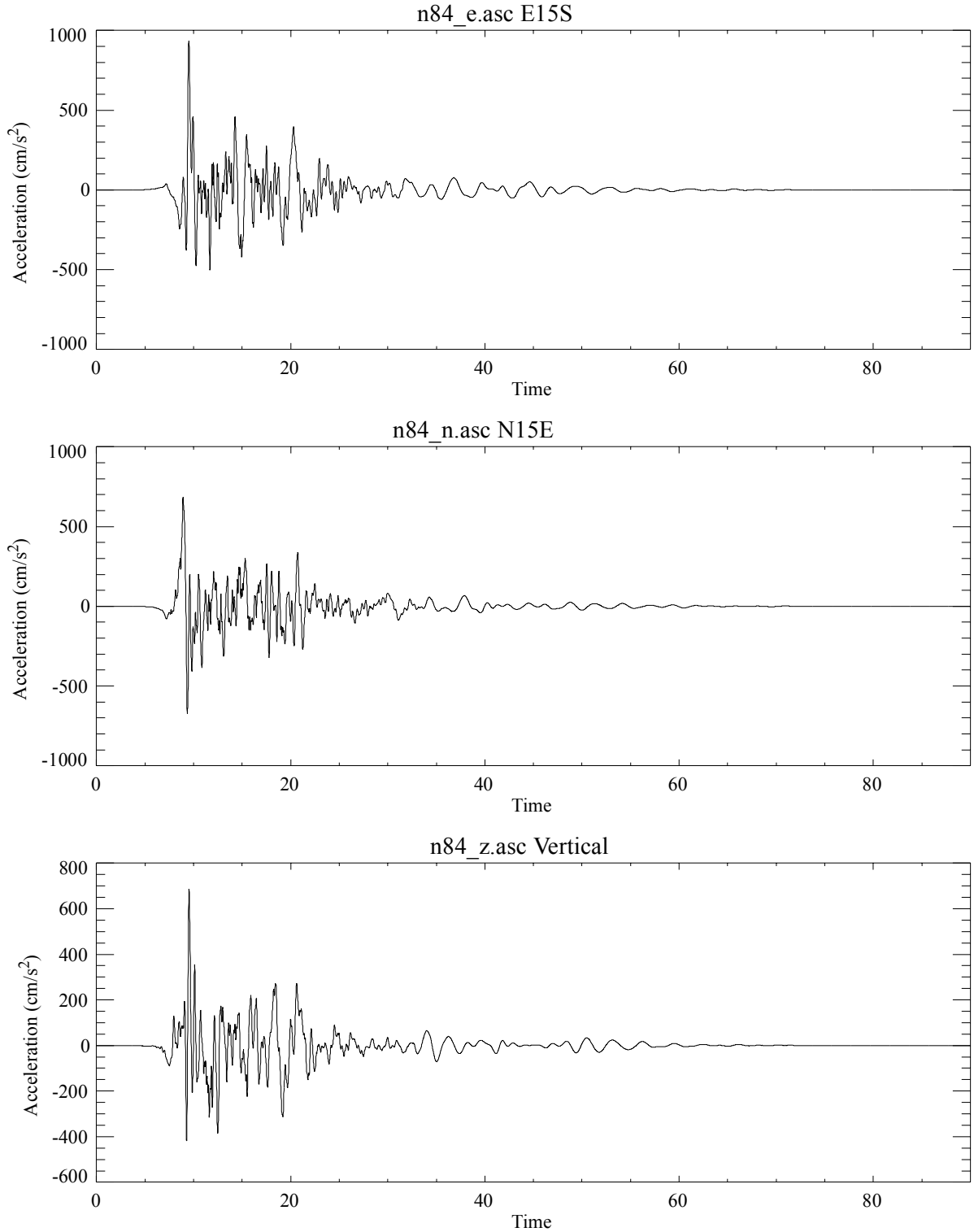

Figure 6-42: JLDW rock site 84 percentile acceleration seismograms for dynamic analyses of Jackson Lake Dam. Components are labeled with time history filename and component orientation, with horizontal components orientated upstream and cross canyon (along the dam axis). These seismograms correspond to the best-fitting acceleration response spectra to the 84 percentile response spectra from 3300 ground motion simulations for a fault dip of 35°.

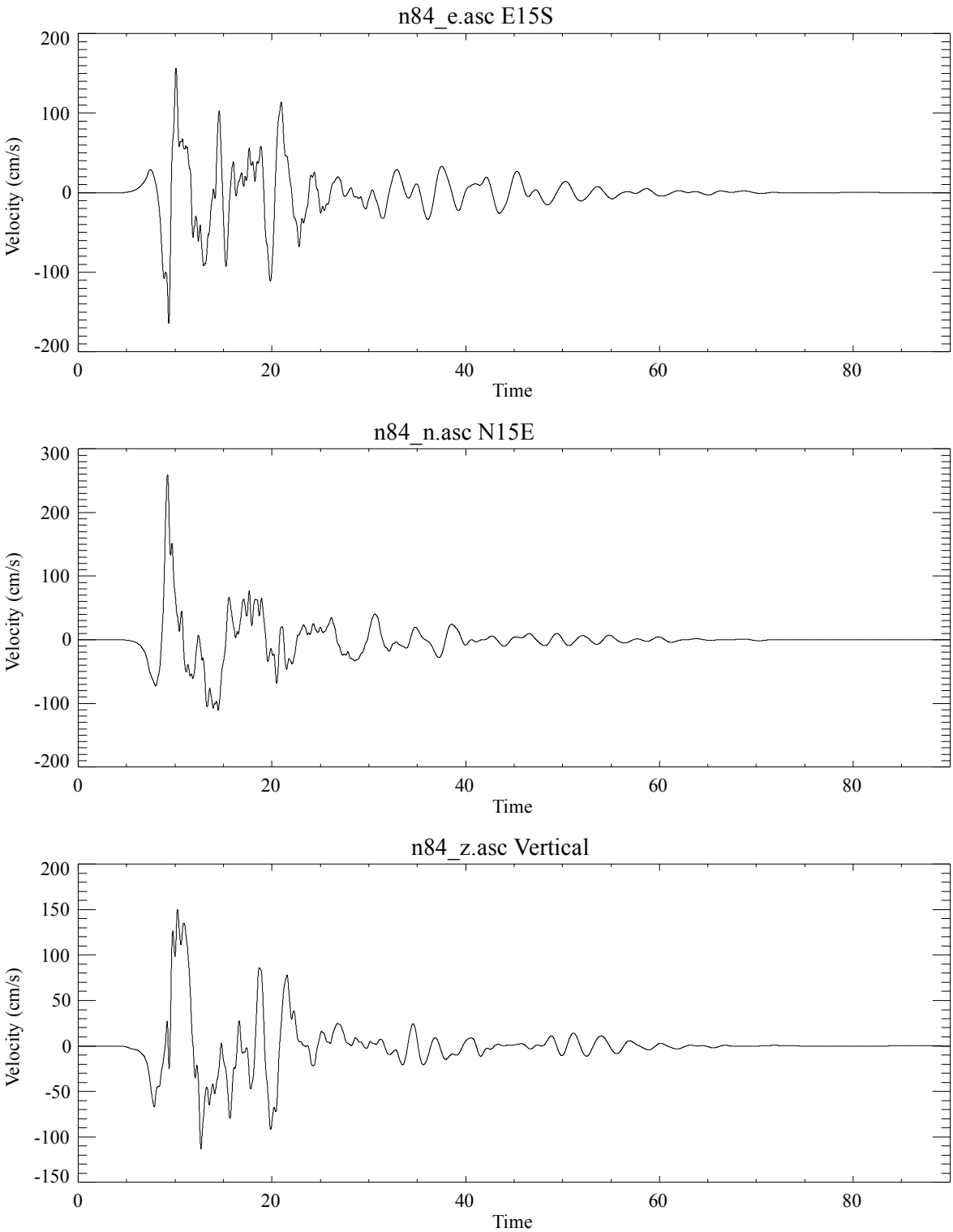

Figure 6-43: JLDW rock site 84 percentile velocity seismograms for dynamic analyses of Jackson Lake Dam. Components are labeled with time history filename and component orientation, with horizontal components orientated upstream and cross canyon (along the dam axis). These seismograms correspond to the best-fitting acceleration response spectra to the 84 percentile response spectra from 3300 ground motion simulations for a fault dip of 35°.

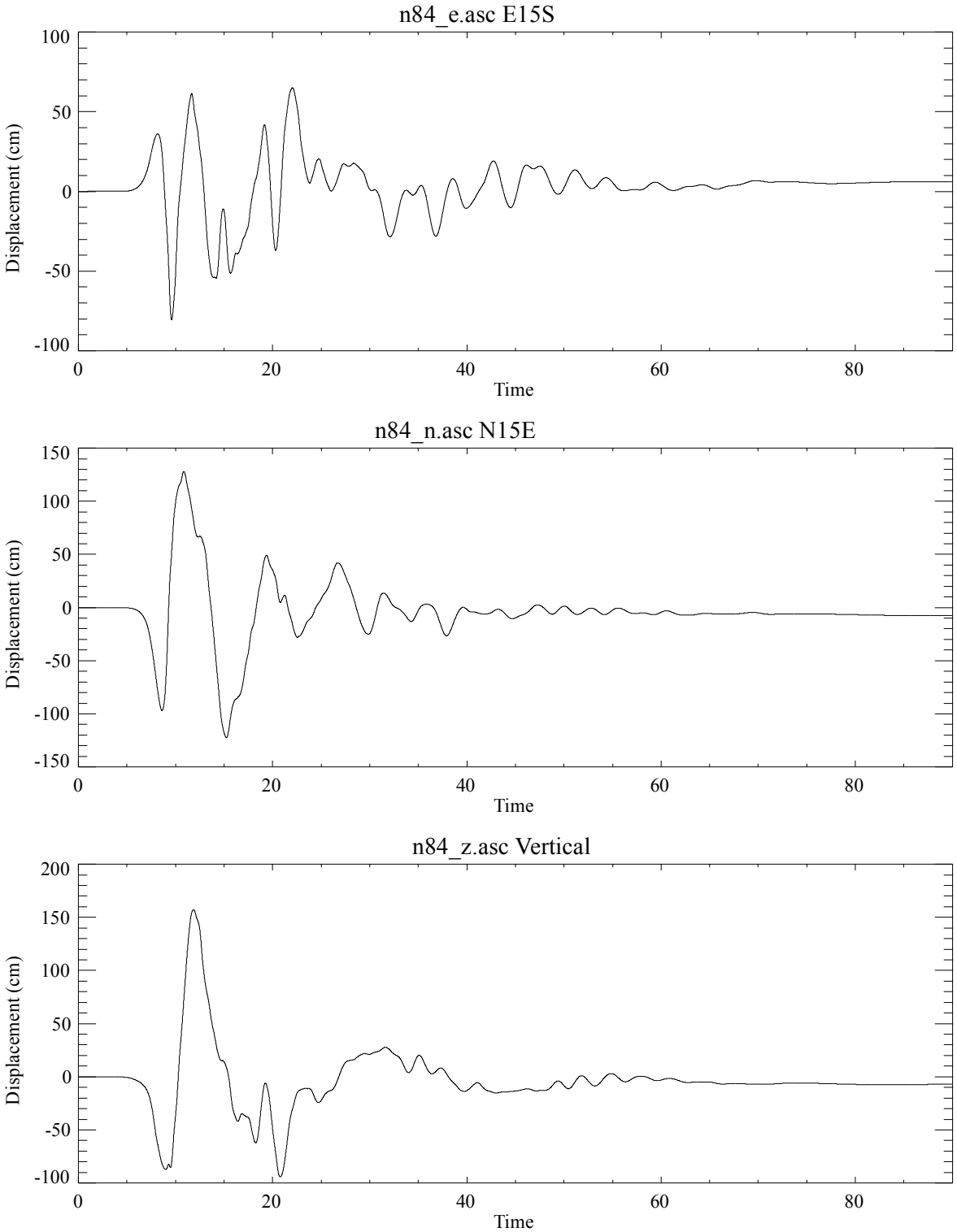

Figure 6-44: JLDW rock site 84 percentile displacement seismograms for dynamic analyses of Jackson Lake Dam. Components are labeled with time history filename and component orientation, with horizontal components orientated upstream and cross canyon (along the dam axis). These seismograms correspond to the best-fitting acceleration response spectra to the 84 percentile response spectra from 3300 ground motion simulations for a fault dip of 35°.

These synthesized mean and 84% ground motions are solely intended for use in dynamic analyses of the concrete portion of the dam, particularly the southern half of the concrete section. The northern end of the concrete section experiences amplified and prolonged ground motion responses associated with the close proximity of the very-low-velocity glacial scour to the northern end of the concrete section. There are likely to be significant soil-structure interactions at the northern end of the concrete section of the dam (Wolf and Song, 1996). One way to account for the foundation complications on ground motion inputs into the northern concrete section of the dam would be to convolve three-component JLD2 site responses with the mean and 84% ground motions in Figures 6-37 to 6-44.

A significant concern with the synthesized ground motions is that the high-frequency durations are probably too short. To address this concern a ground motion recording is also recommended exclusively for use in the dynamic analyses of the concrete portion of the dam that contains significant high frequency duration. The Llolleo station recordings of the 1985 **M** 8 Chilean subduction earthquake is one of the few such long-duration acceleration strong motion records available (Figure 6-45). It provides a long duration consistent with LVB responses and has been recommended for dynamic analyses in Seattle (SAC Steel Project, 1997). However, it lacks the significant peak velocity (Figure 6-46) and displacement (Figure 6-47) responses expected at the dam, and is intended primarily to tests the sensitivity of the concrete section of the dam to prolonged short-period shaking. The Llolleo record should not be used for dynamic analyses beyond the stage of initiation of cracking, particularly to estimate total displacements, since it clearly lacks the substantial velocities and displacements characteristic of ground motions at Jackson Lake Dam. Inadequate peak velocities and displacements are reflected in the relatively low Llolleo PSA responses for periods > 0.8 s (Figure 6-48). The orientation of the horizontal components was selected to assign the peak responses to the E15S component for dynamic analyses. The short period (< 0.4 s) acceleration responses on the E15S component exceed target mean and 84% PSA responses (Figure 6-48), but peak N15E responses are less than peak 84% PSA response.

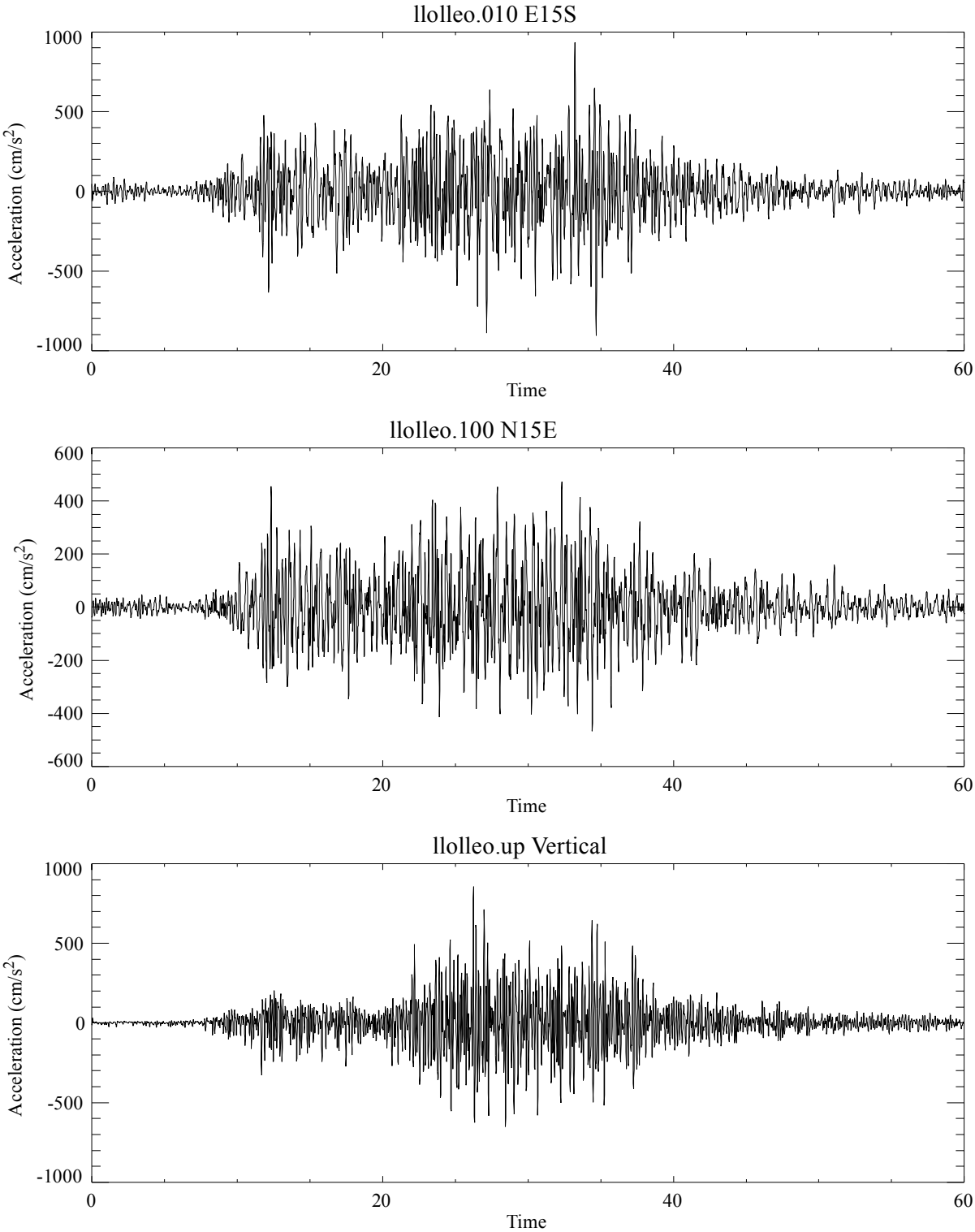

Figure 6-45: Llolleo, Chile, acceleration seismograms for dynamic analyses of the concrete section of Jackson Lake Dam. Components are labeled with time history filename and component orientation.

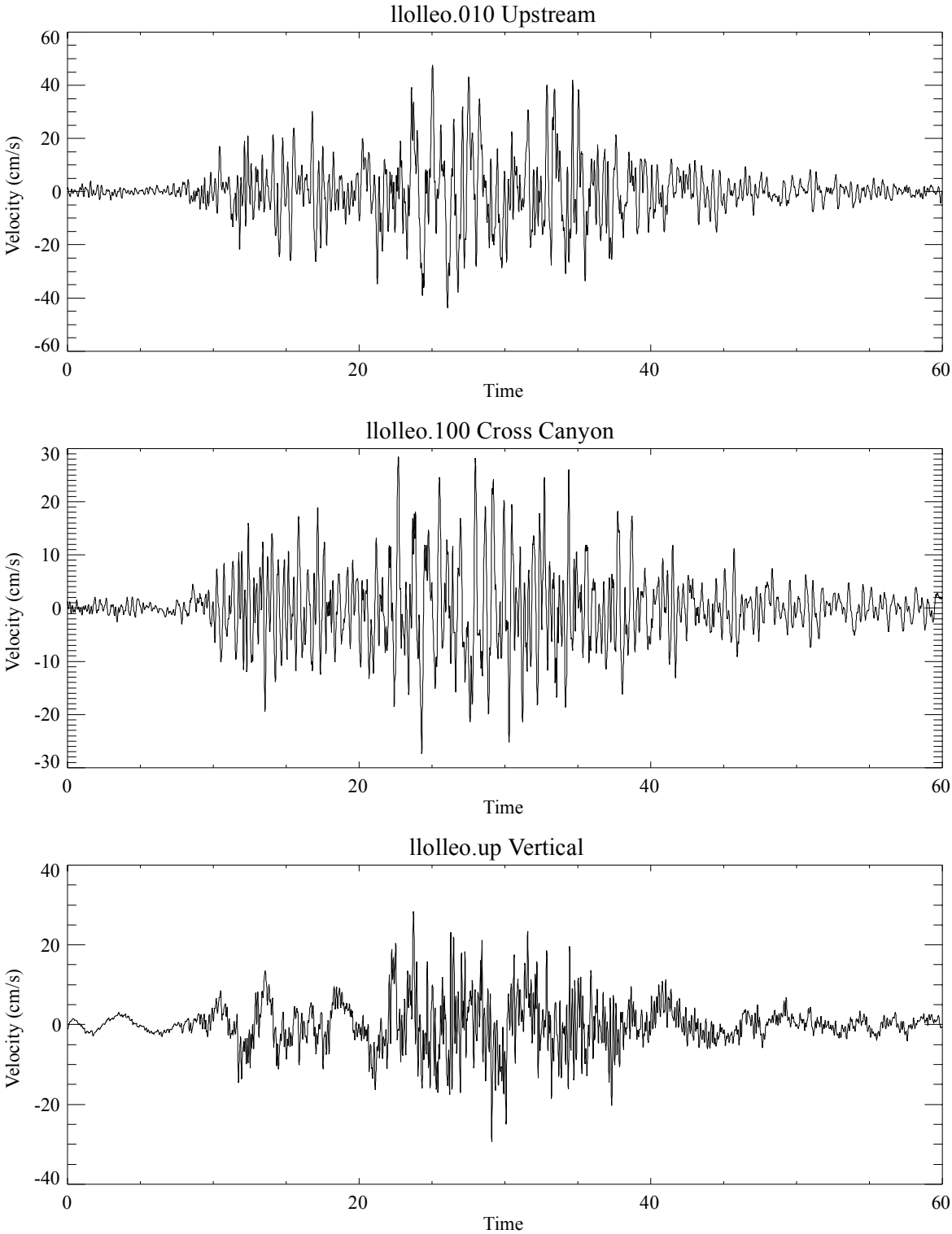

Figure 6-46: Llolleo, Chile, velocity seismograms for dynamic analyses of Jackson Lake Dam. Components are labeled with time history filename and component orientation, with horizontal components orientated upstream and cross canyon (along the dam axis).

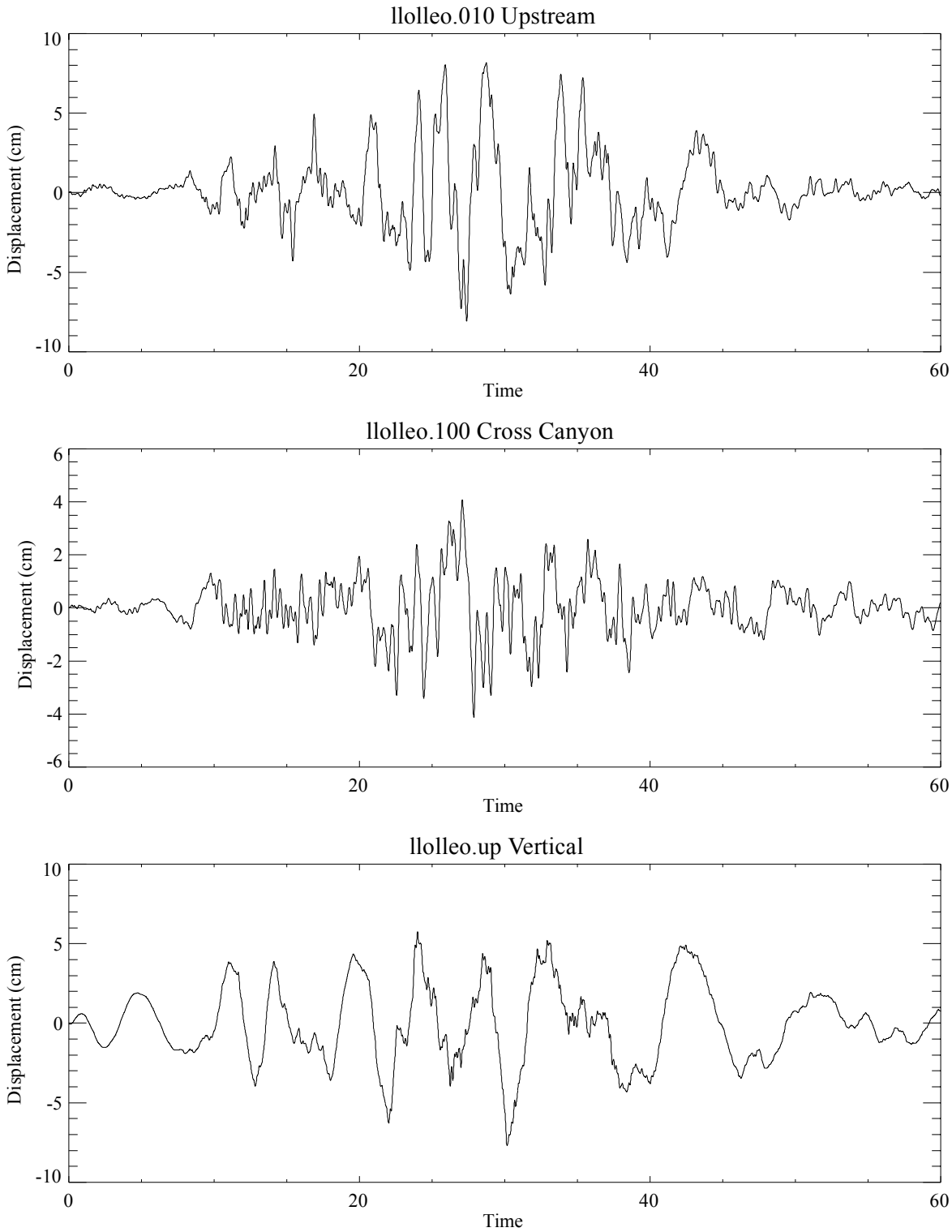

Figure 6-47: Llolleo, Chile, displacement seismograms for dynamic analyses of Jackson Lake Dam. Components are labeled with time history filename and component orientation, with horizontal components orientated upstream and cross canyon (along the dam axis).

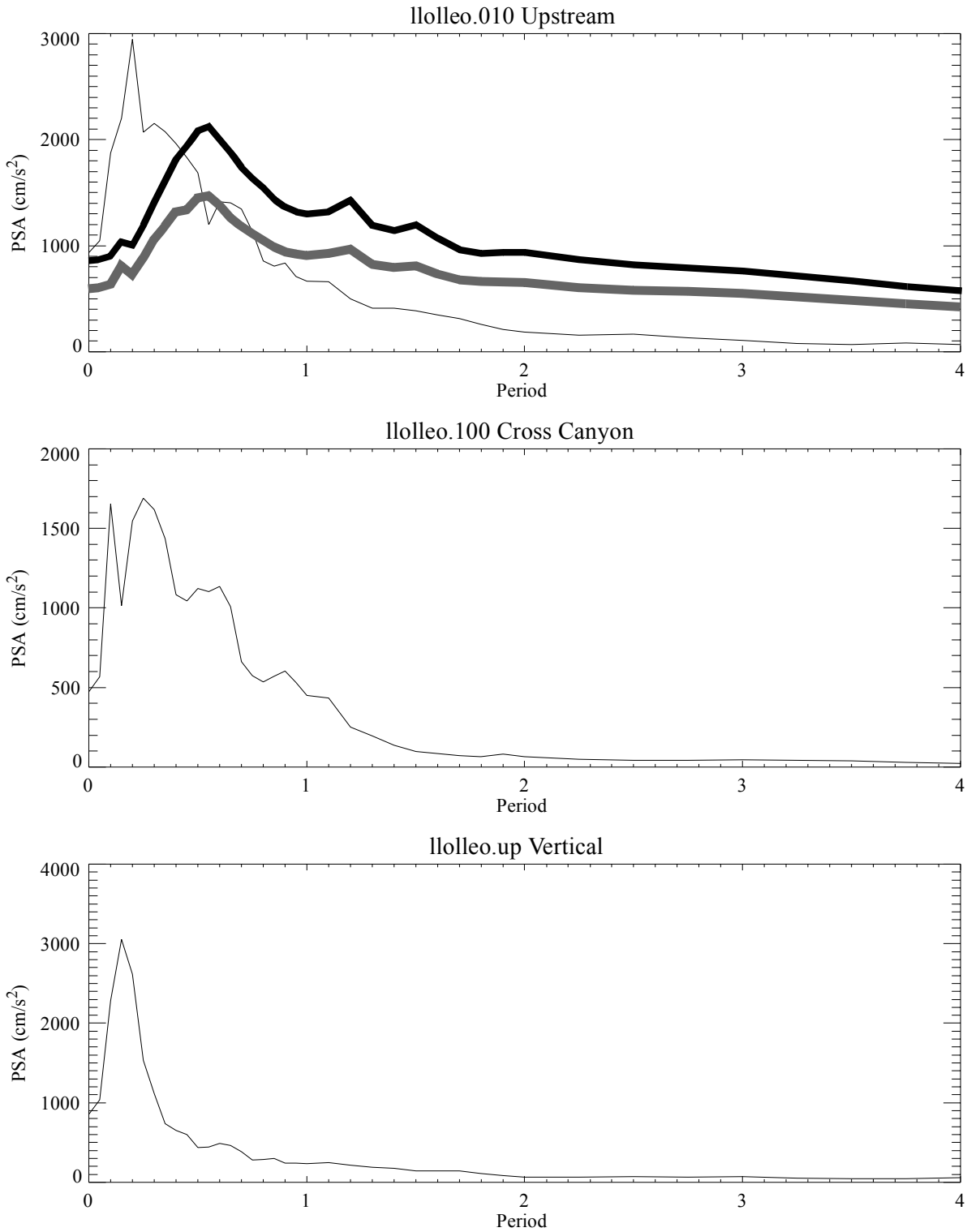

Figure 6-48: Response spectra corresponding to the Lloleo acceleration seismograms.Components are labeled with time history filename and component orientation. The synthetic 84% quantile and mean response spectra for the upstream component for a fault dip of 35° are plotted as the black and grey curves, respectively, for comparison at the top (Llolleo responses are the thin black curves).

6.6 Inputs for Nonlinear Ground Motion Calculations

As discussed in Sectoin 6.1, the finite-difference code NOAH is used to approximate nonlinear soil responses. The site response investigations in Section 5 showed that low-velocity fluvial-lacustrine deposits beneath the embankment portion of the dam amplify ground motions and significantly increase durations, relative to the JLDW rock site (Figure 6-49). Synthetic modeling of the observed long duration ground motions near the embankment section in Section 5 showed that the durations are probably produced by glacial-scour-edge S-waves and horizontally-propagating interface waves, including Stonely waves that radiate energy to the surface from first-order velocity discontinuities and vertical velocity gradients located at depths > ~25 m. The glacial-scour-edge Rayleigh waves produce large amplitude, broadband Airy phases. Stonely waves are freely propagating interface waves with evanescent decay away from the interface into the media on either side; they are not body waves. The Stonely waves attenuate very slowly, even for Q's of 5, and may not be significantly influenced by soil nonlinearity. Stonely waves cannot be modeled with SHAKE or NOAH. Consequently, the prolonged soil durations associated with Stonely wave energy must be included in the input ground motion to 1D programs like SHAKE and NOAH. The glacial-scour-basin-edge S-waves propagate primarily below 25 m depth and produce strong high-frequency amplitudes for portions of the embankment dam located with 1 km of the southern margin of the glacial scour. Consequently, the most probable scenario is that ground motions impinging on the low-velocity shallow nonlinear soils will have durations comparable to those observed in the weak motion surface recordings presented in Section 5. Time-frequency plots calculated using 1.6 s time windows centered on each time point, illustrate significant differences in the amplitudes and durations between the JLDW rock site (Figures 6-49 and 6-50) and the JLD3 soil site (Figures 6-40 and 6-51). The durations of frequencies > 3 Hz is ~2.5 times longer for JLD3 than JLDW. The duration of 1 Hz responses at JLD3 is 3 times longer than at station JLDW. JLD3 spectral amplitudes that are about half of the peak 0.5-to-1 Hz spectral amplitude in the JLD3 seismogram persist for about 60 s.

Three scenarios were used to construct ground motions for use in nonlinear soil calculations to bracket the ranges of possible ground motion inputs into nonlinear soils (Table 6-5). In scenarios 1 and 3, halving the surface motion amplitudes removes the nominal free surface amplification.

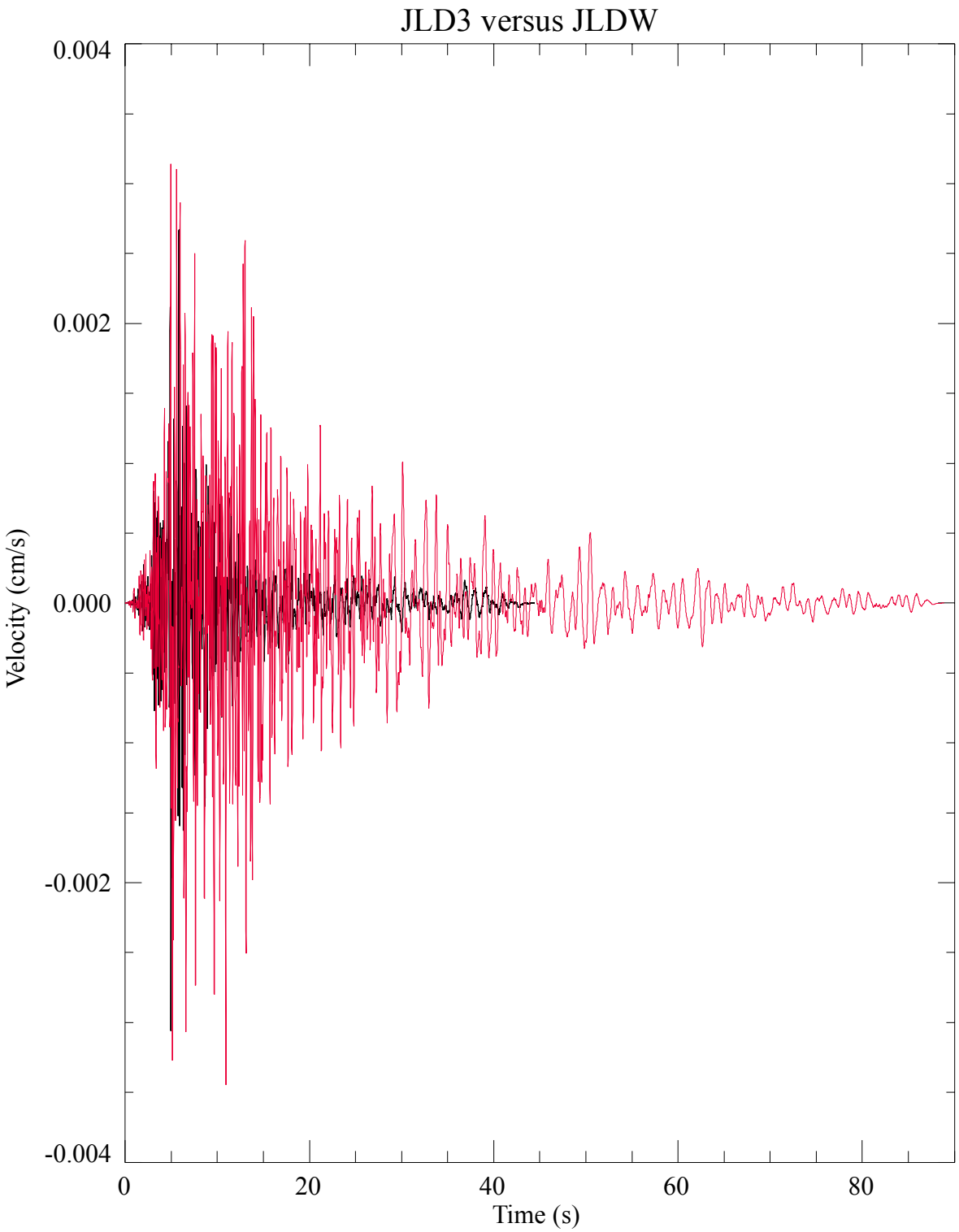

Figure 6-49: East horizontal component microearthquake velocity seismograms for JLDW and JLD3. JLDW is black and JLD3 is red.

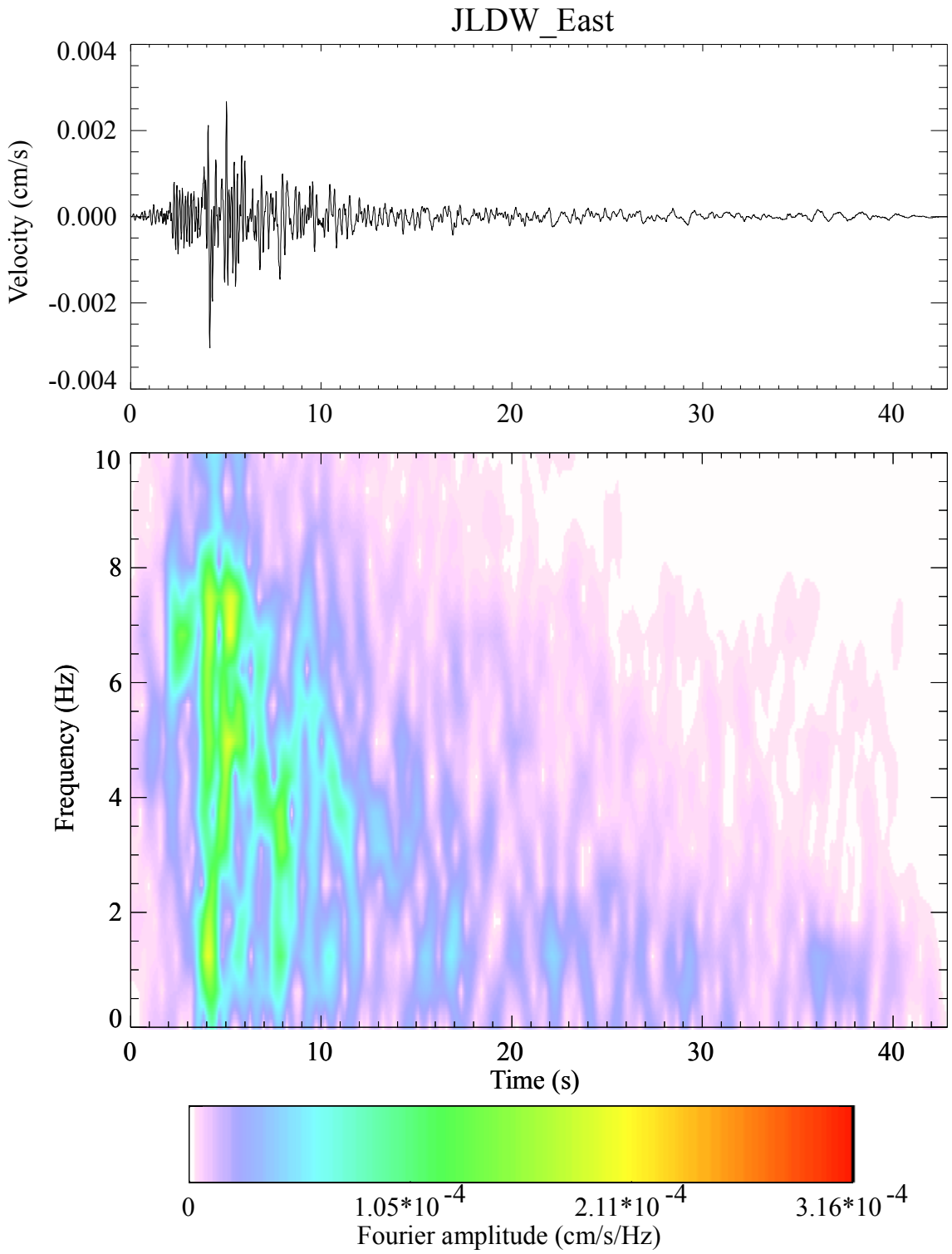

Figure 6-50: Time-frequency for the JLDW east-component seismogram from Figure 6-49. The amplitude scales are the same as in Figure 6-51 for the corresponding JLD3 seismogram.

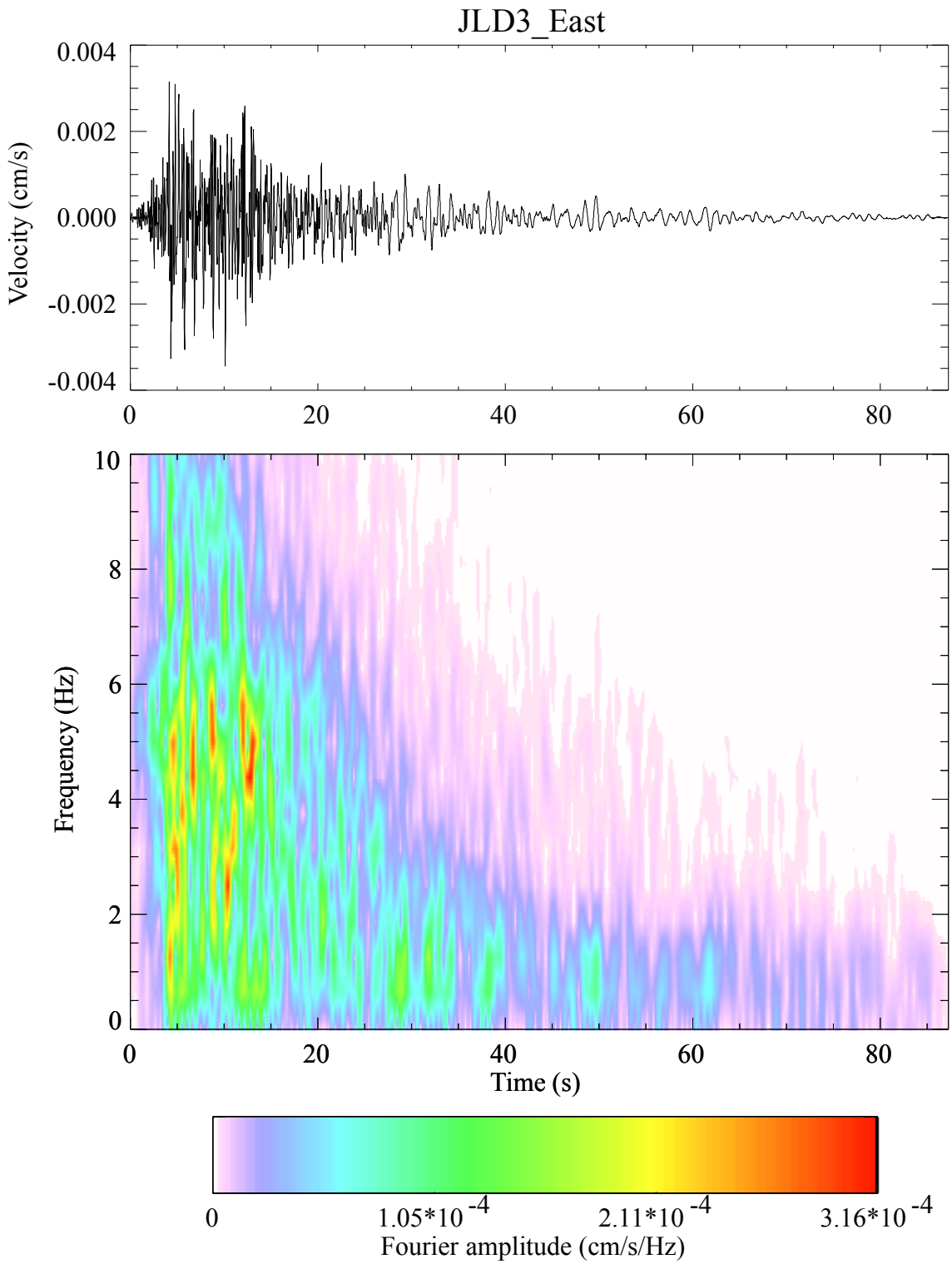

Figure 6-51: Time-frequency for the JLD3 east-component seismogram from Figure 6-49. The amplitude scales are the same as in Figure 6-50 for the corresponding JLDW seismogram, but the duration is about twice as long as in Figure 6-50.

Since the JLDW responses are at the free surface on the same type of material (glacial till) as the material at 140 m depth below the soil, halving the rock responses is reasonable. However, since the incident ground motions are predominantly composed of P-SV waves, and not SH waves, halving can overcorrect for the free-surface amplification, and always over corrects at long periods; halving is appropriate for high frequencies for input motions at 140 m depth. For

Table 6-5: Ground Motion Input Scenarios for Nonlinear Soil Calculations

Scenario number.	Characteristics.
1	Half amplitude, rock duration
2	2/3 * Half amplitude, soil duration
3	Half amplitude, soil duration

scenarios 2 and 3, the rock responses were convolved with JLD3 responses to obtain reasonable soil durations and scaled as 2/3 of half of the surface responses or half of the surface responses. Scaling by 2/3 in scenario 2 was done to compensate for the ~50% amplification of the input peak velocities at the surface by 1D SH propagation (obtained by running weak motion responses through NOAH with the soil compaction velocity profile). Scenario 3 provides a larger input scaling (only removing the free-surface amplification) that accounts for the failure of a 1D SH propagation approach to fully reproduce observed soil amplifications. The rock durations in scenario 1 are very likely to be too short, but combined with the soil durations in scenarios 2 and 3 provide a means to crudely bracket possible durations. Scenarios 2 and 3 are probably most representative of expected soil responses. To account for elastic boundary conditions at the bottom of the NOAH models, all the input motions were scaled by an additional 0.65 to reproduce the intended subsurface rock peak amplitudes immediately above 140 m depth.

Two velocity models were used to approximate the conditions in the compacted soil beneath the embankment (Figure 6-52) and the soil mix walls (Figure 6-53). Obviously, the simplest realistic configuration would require a 2D calculation method to account for the mass and shape of the dam and for the lateral variations in the upstream-downstream direction. Laterally from upstream to downstream, conditions vary from untreated soils upstream of the dam, with near-surface S-wave velocities of ~80-100 m/s (Sirles, 1988), a ~16 m-wide upstream soil mix wall, with S-wave

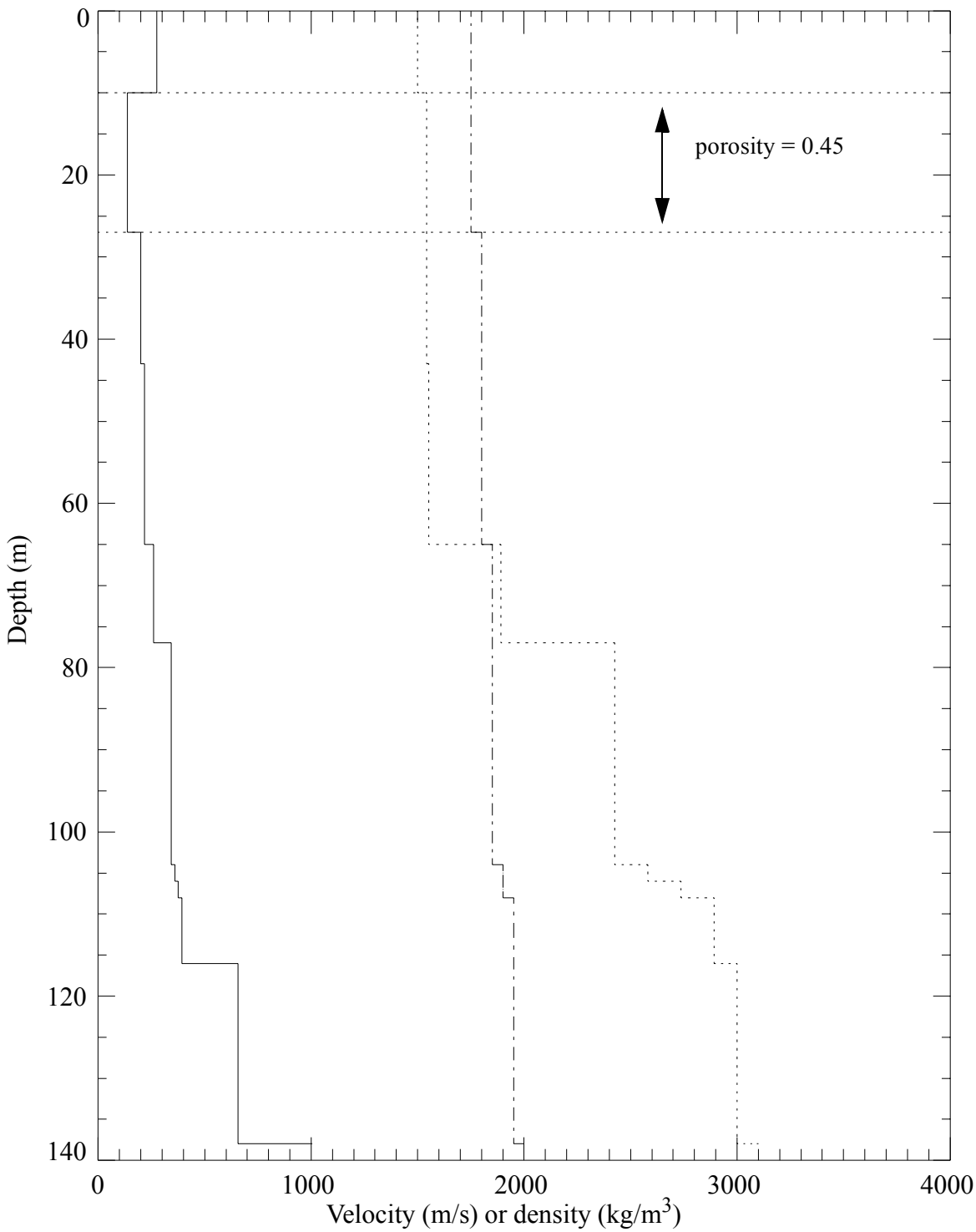

Figure 6-52: NOAH velocity-density depth model for the compaction region. The model extends from the free surface to the high-velocity till at 138 m depth. S-wave velocity is the solid curve, P-wave velocity is the dotted curve, and density is the dash-dot curve. Dotted horizontal lines show the upper and lower limits of the low-velocity region with nonzero porosity.

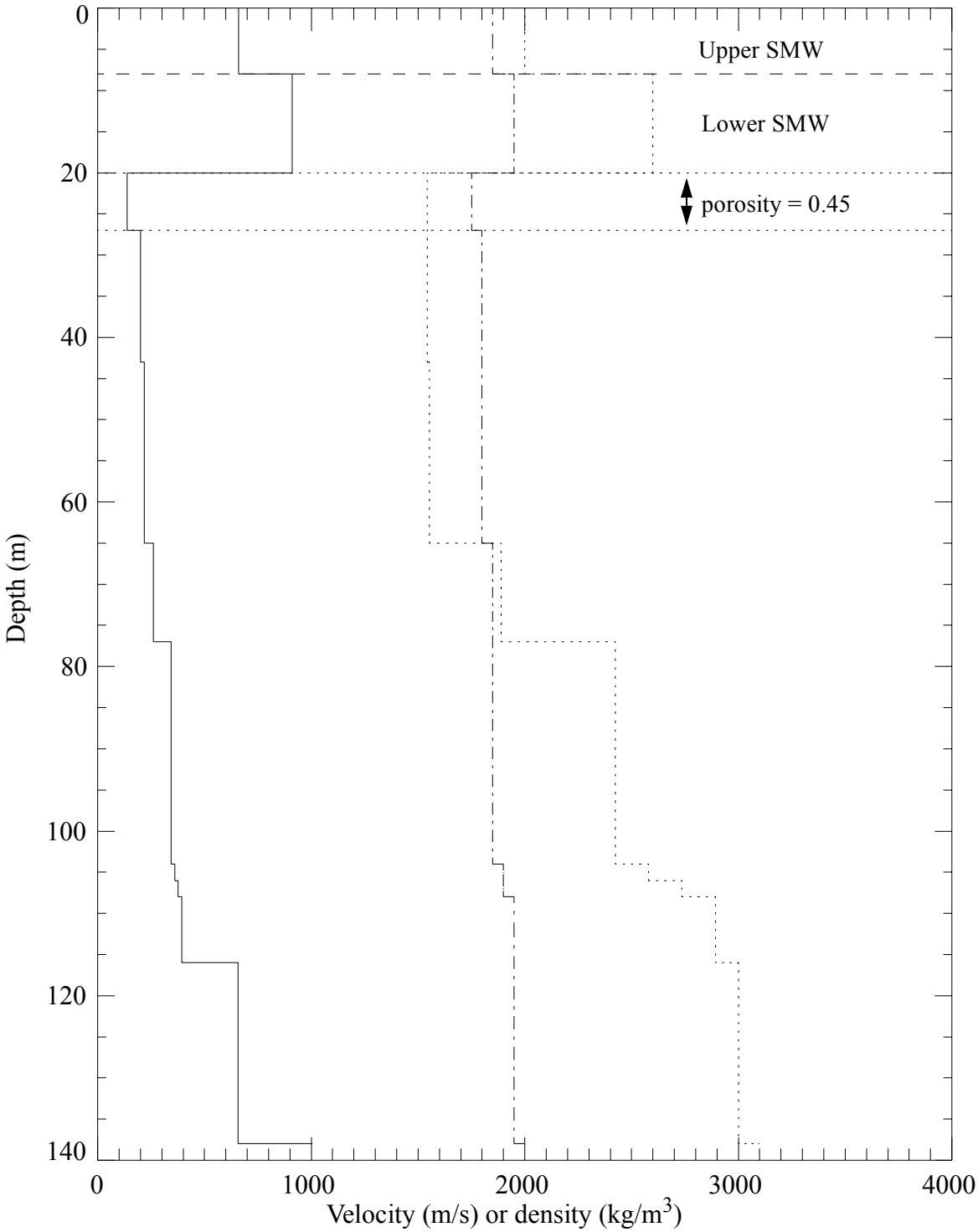

Figure 6-53: NOAH velocity-density depth model for the soil mix wall region. The model extends from the free surface to the high-velocity till at 138 m depth. S-wave velocity is the solid curve, P-wave velocity is the dotted curve, and density is the dash-dot curve. Dotted horizontal lines show the upper and lower limits of the low-velocity region with nonzero porosity. The upper horizontal dotted line shows the bottom of the soil mix wall (SMW) and the horizontal dashed line shows the bottom of the upper, low-velocity portion of the SMW.

velocities of ~660 m/s to a depth of ~8 m and S-wave velocities of ~910 m/s to a depth of ~20 m (Wright, 1990), a ~30 m-wide compacted soil zone beneath the central embankment section with S-wave velocities of ~275 m/s to a depth of ~10 m and S-wave velocities of ~138 m/s to a depth of ~27 m (Dave Gillette, personal communication), a 16 m-wide downstream soil mix wall with the same properties as the upstream soil-mix wall, and untreated downstream materials with near-surface S-wave velocities of ~80-100 m/s (Sirles, 1988). Soil-structure interactions between the soil mix walls and adjoining compacted and untreated soils are likely to complicate responses in all materials relative to the 1D approximations used in SHAKE and NOAH. For instance, ground motions at station JLD4 located on a soil mix wall was deamplified for frequencies > 1 Hz relative to motions at station JLD3, located ~28 m downstream of JLD4 on untreated soil (Section 5). Consequently, peak motions near the center of the soil mix walls may be lower than calculated in the 1D approximation, but compacted soil responses are likely to be underestimated (the soil mix walls will likely focus energy into the compacted soils beneath the dam, particularly for frequencies > 1 Hz). The water table is placed at a depth of 2 m, but the soil mix walls and compacted soil are assumed to be always dry (zero porosity). Only the low-velocity layer below the soil mix walls and compacted soil are assign a nonzero porosity of 0.45 (Figures 6-52 and 6-53).

The synthetic rock reference site ground motions and the recording of the 1978 **M** 7.4 Tabas, Iran, earthquake were combined with the empirical site response information from Section 5 to develop ground motion time histories for input into nonlinear soil responses calculations using NOAH and SHAKE. Only NOAH effective stress results, which account for pore pressure (Bonilla et al., 1998; Bonilla, 2000), are presented in this report. The approximated impulse response function obtained by deconvolving the station JLDW east horizontal component from the soil station JLD3 described in Section 5 was convolved with the three rock site ground motions, and rescaled to produce scenarios 2 and 3 inputs for nonlinear calculations at 140 m depth (Figures 6-54 to 6-56 show scenario 3 seismograms). NOAH results were also produced using the three rock motions divided by two as inputs at 140 m depth. The nonlinear rock motion inputs are solely used to provide a lower bound on soil responses. The rock motions lack the soil amplification and duration responses characteristic of the soil responses at JLD3 and the 1D SH approximations used in NOAH and SHAKE are not sufficient to convert rock durations to realistic soil durations.

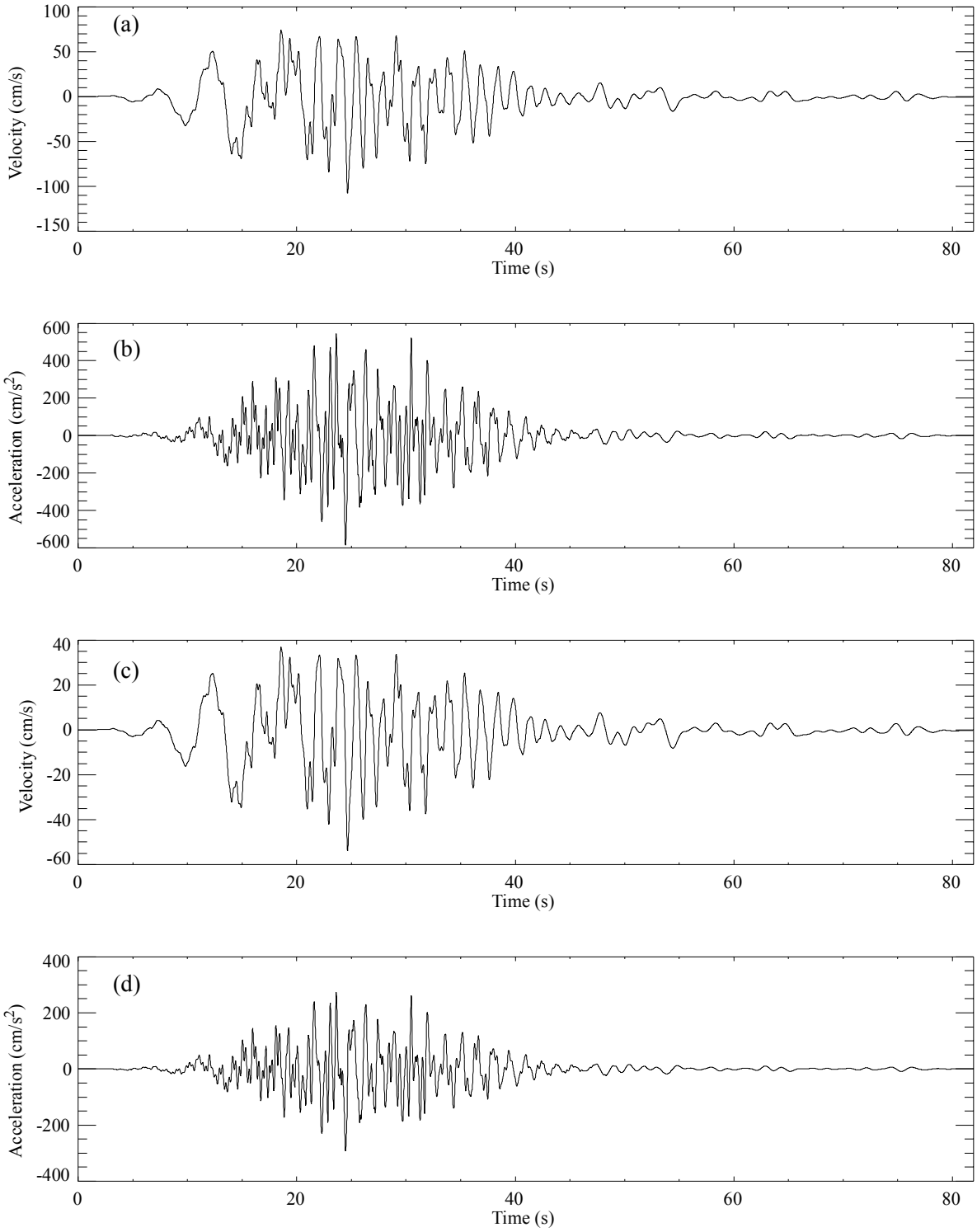

Figure 6-54: Mean JLDW E15S rock motion velocity (a) and acceleration (b) convolved with the JLD3 soil response transfer function. The resulting motion was rescaled by half for input into NOAH (c-d).

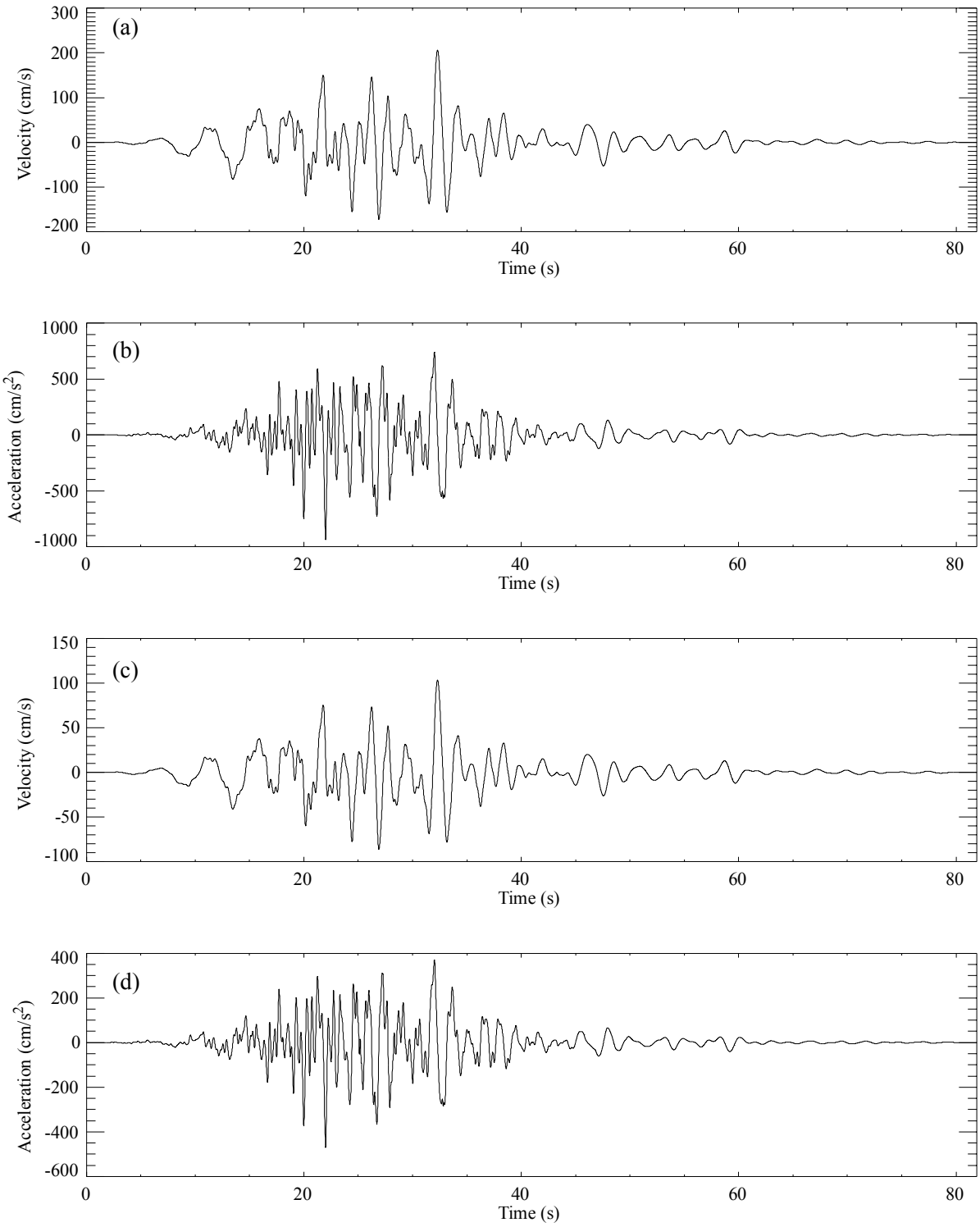

Figure 6-55: 84% JLDW E15S rock motion velocity (a) and acceleration (b) convolved with the JLD3 soil response transfer function. The resulting motion was rescaled by half for input into NOAH (c-d).

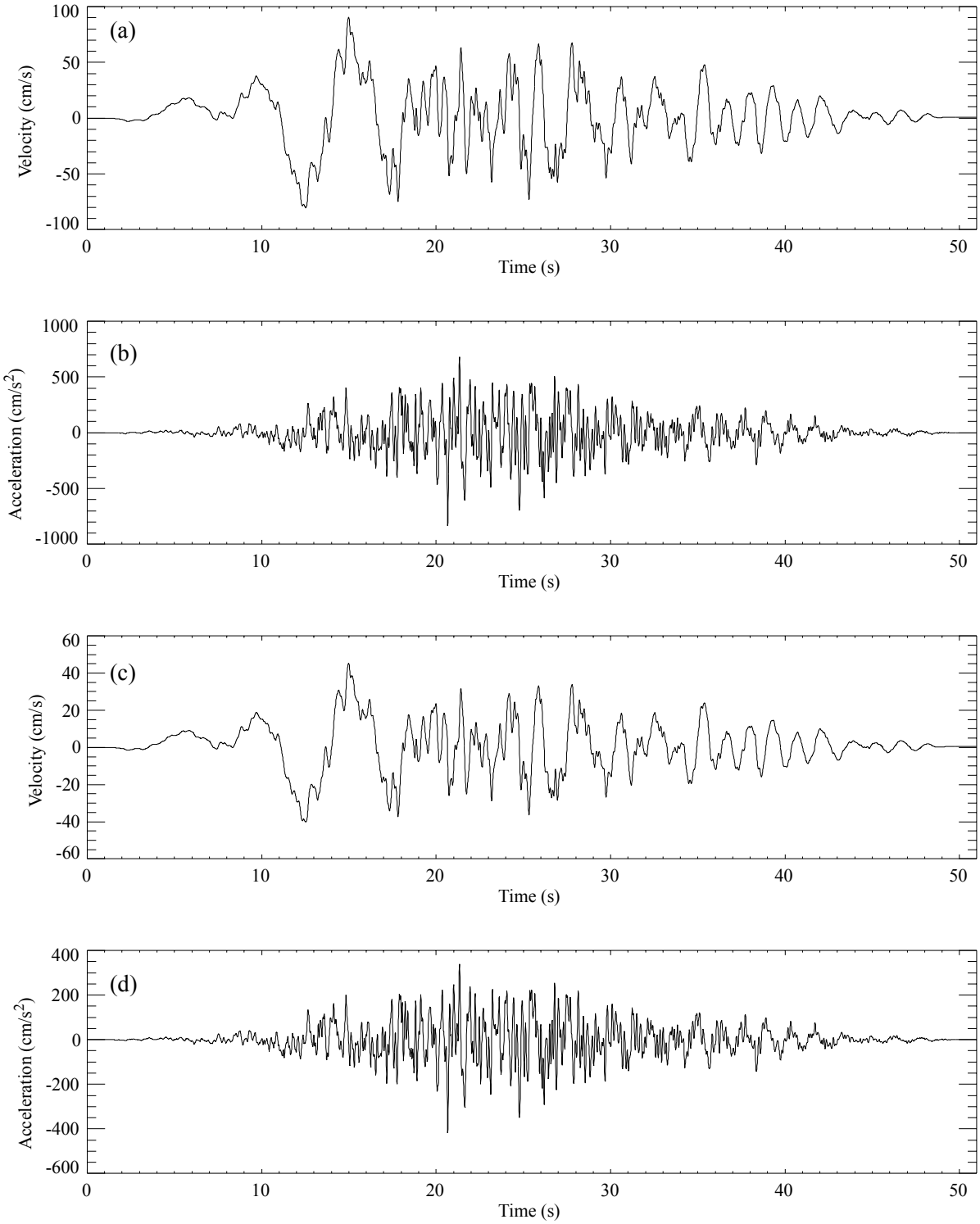

Figure 6-56: Tabas E15S rock motion velocity (a) and acceleration (b) convolved with the JLD3 soil response transfer function. The resulting motion was rescaled by half for input into NOAH (c-d).

Only summary results are presented in this section. The NOAH inputs and outputs for scenarios 1-3 are presented in Appendix E and UCSB nonlinear soil analyses are presented in Appendix F.

6.6.1 Nonlinear Compacted Soil Zone Results. Nonlinear NOAH JLD3 site-response input results for the compacted soil zone velocity model (Figure 5-52) are summarized in Figure 6-57. The minimum peak acceleration in the lower portion of the compaction layer is > 0.4 g (Figure 6-57). Arias Intensities and durations in portions of the compaction layer are always larger than corresponding rock motions (Tables 6-2 to 6-4) and approach values associated with **M** ~8 earthquakes based on the relations of Kayen and Mitchell (1997) and Bommer and Martinez-Pereira (1999). Since peak accelerations are often dominated by frequencies > 10 Hz, response spectra for periods of 0.2 s, 0.5 s, 1 s, and 2 s are presented in Figure 6-58 to provide relevant acceleration loads for the dam. For periods of 1 s and longer, the PSA exceed 0.4 g for all JLD3 response inputs. Comparison of the nonlinear NOAH rock site-response input results for the compacted soil zone velocity model in Figure 6-59 with the JLD3 response input results in Figure 6-57 show the influence of input ground motion duration on calculated soil responses. For rock motion inputs, Arias Intensities and durations are generally a two-thirds to half of the JLD3 response inputs. Minimum peak accelerations are only slightly smaller in the compaction layer, but maximum peak shear strains are strongly reduced using rock input motion durations (Figure 6-59). Duration also strongly influences PSA responses. Figure 6-60 shows that the shorter rock input durations produced reduced PSA responses. The rock input results likely underestimate soil responses because they lack the long soil durations that are result of horizontally-propagating trapped waves propagating at various depths within the ~140 m deep low-velocity glacial scour. Consequently, the JLD3 response input results (Figures 6-57 and 6-58) are more likely to represent expected responses at the dam.

6.6.2 Nonlinear Soil Mix Wall Results. Nonlinear NOAH JLD3 site-response input results for the soil mix wall velocity model (Figure 5-53) are summarized in Figure 6-61. Minimum Arias durations are somewhat longer than rock motions, but minimum Arias Intensities are larger than for rock motions. Minimum peak accelerations exceed 0.2 g. The PSA response in Figure 6-62 provide more robust acceleration load estimates than peak accelerations, which are dominated by > 10 Hz responses. The nonlinear soil responses decrease PSA response for 0.2 s

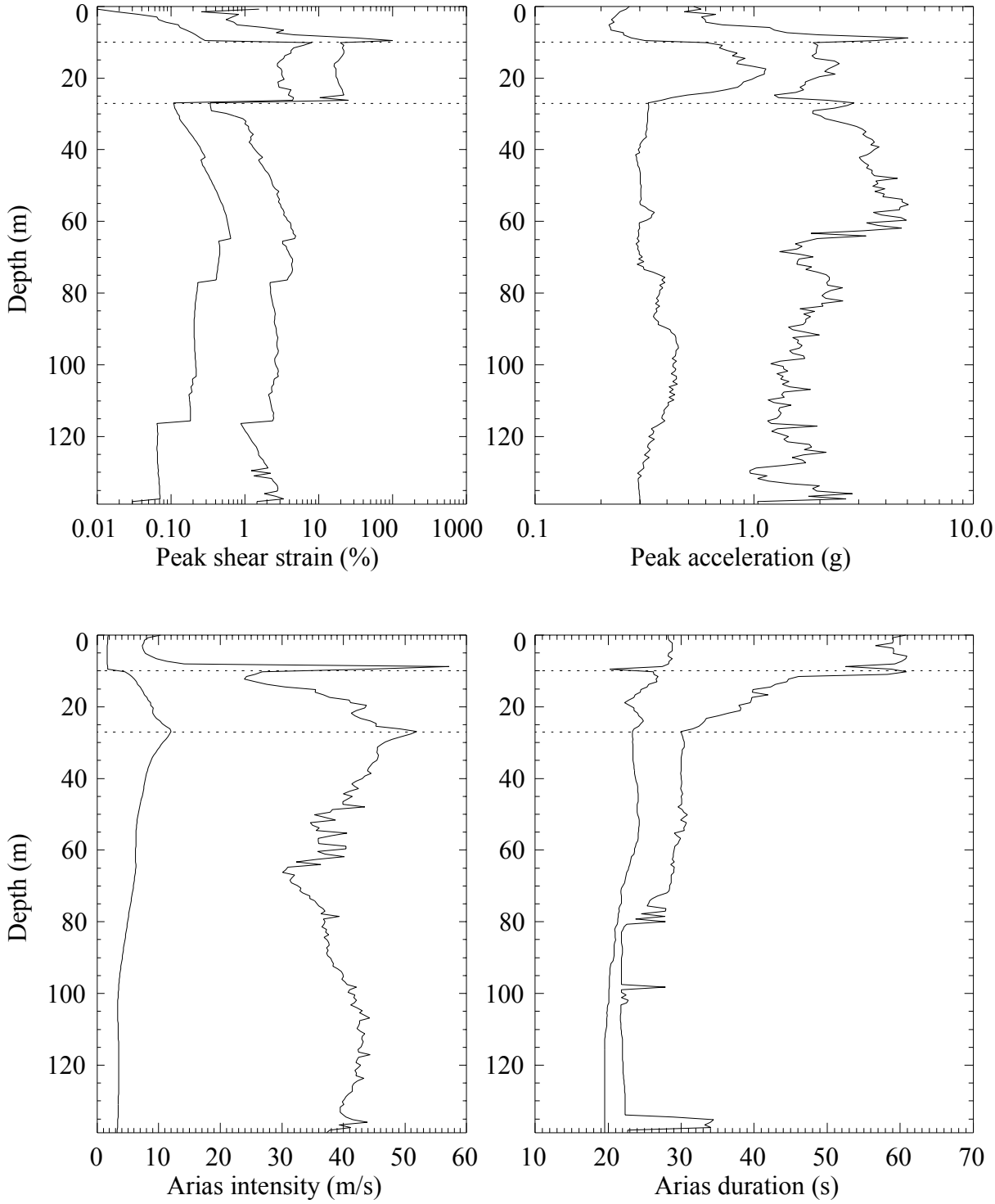

Figure 6-57: Time-domain compacted soil responses for JLD3 response input motions. In each figure the solid lines indicate minimum and maximum responses at each depth from the six input ground motions. The horizontal dotted lines show the depth range of the low-velocity layer with nonzero porosity. The compaction zone is the region above the top dotted line.

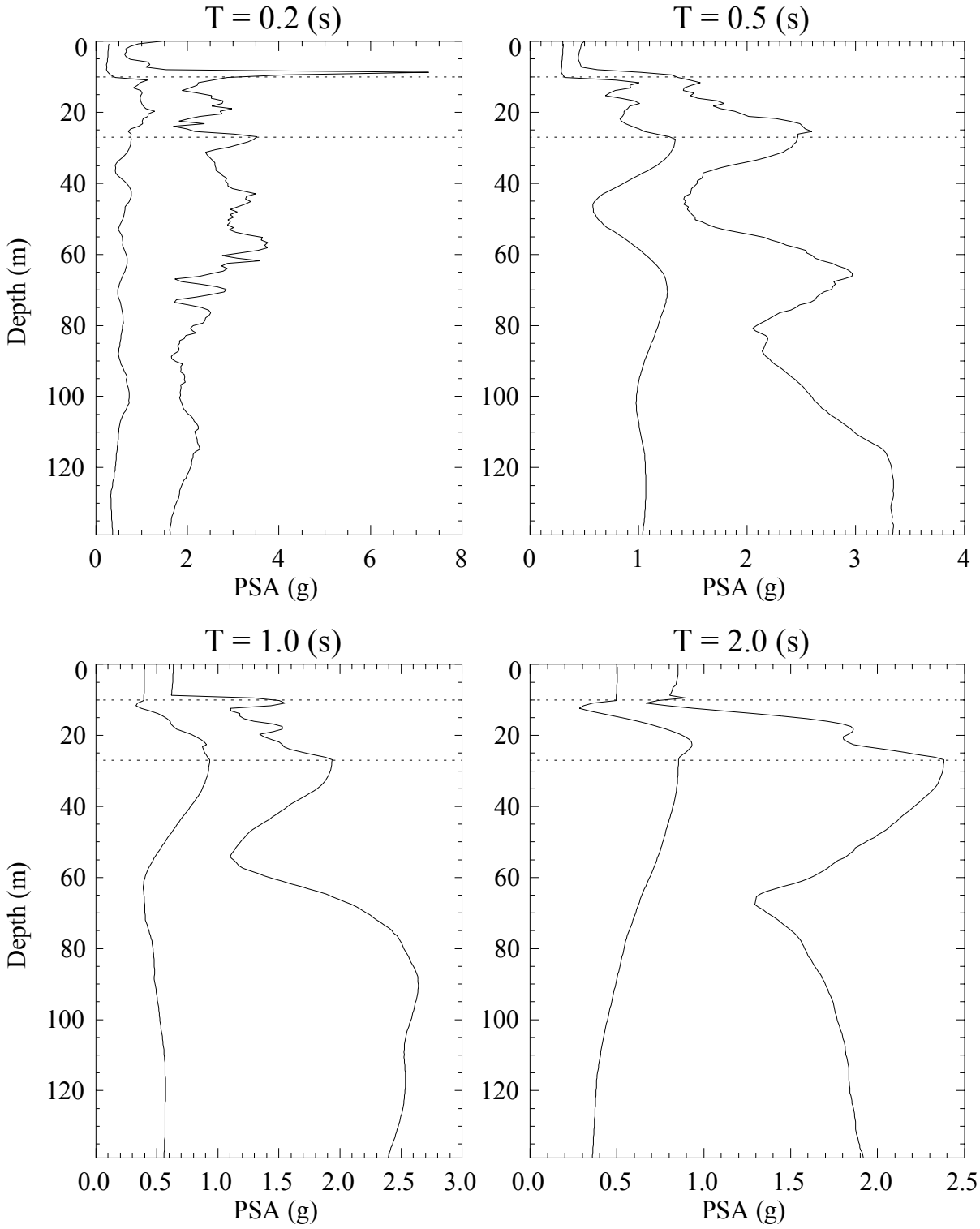

Figure 6-58: Compacted soil acceleration response spectra for JLD3 response input motions. Title of each figure is the period and the solid lines indicate minimum and maximum responses at each depth from the six input ground motions. The horizontal dotted lines show the depth range of the low-velocity layer with nonzero porosity. The compaction zone is the region above the top dotted line.

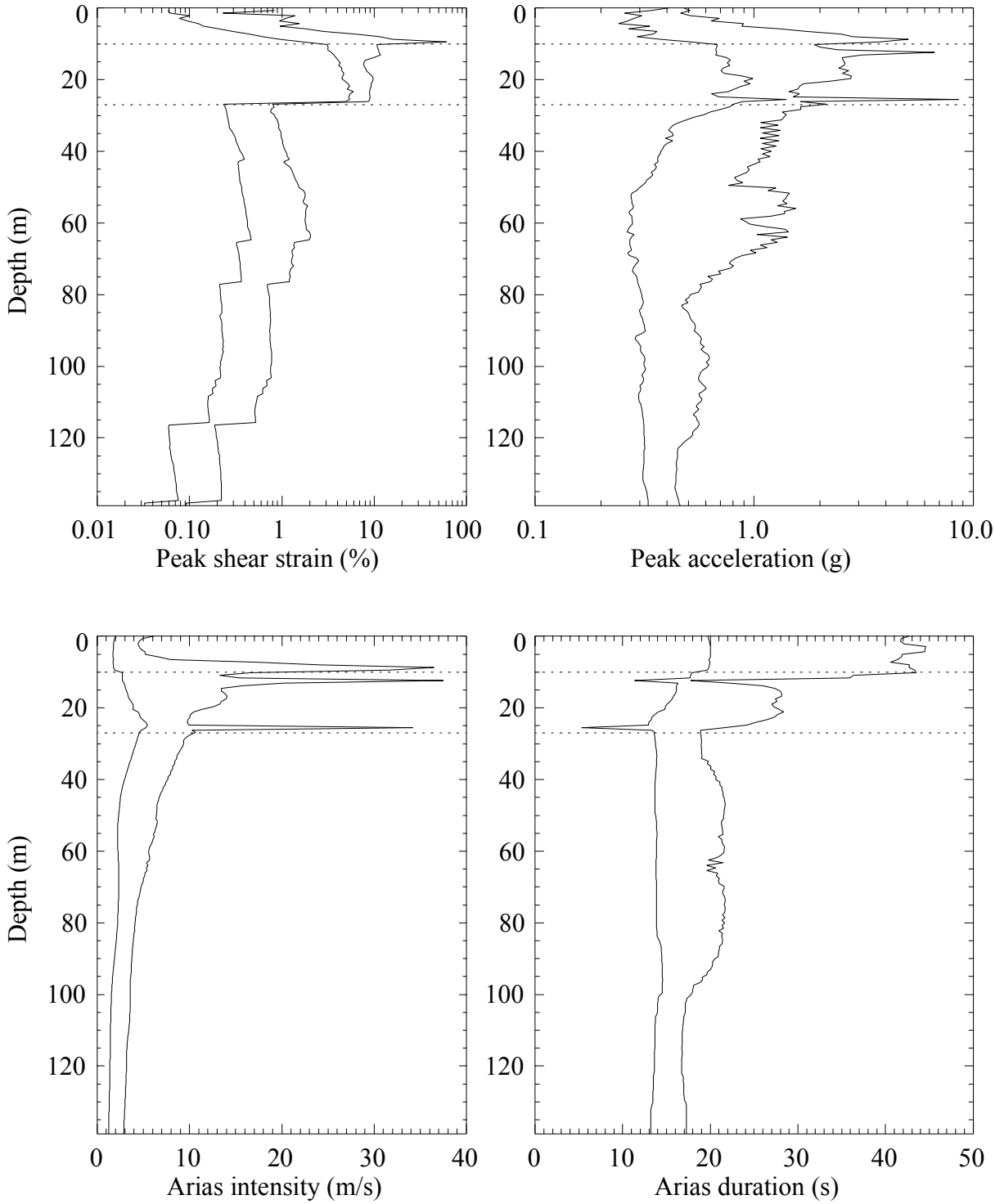

Figure 6-59: Time-domain compacted soil responses for rock response input motions. In each figure the solid lines indicate minimum and maximum responses at each depth from the six input ground motions. The horizontal dotted lines show the depth range of the low-velocity layer with nonzero porosity. The compaction zone is the region above the top dotted line.

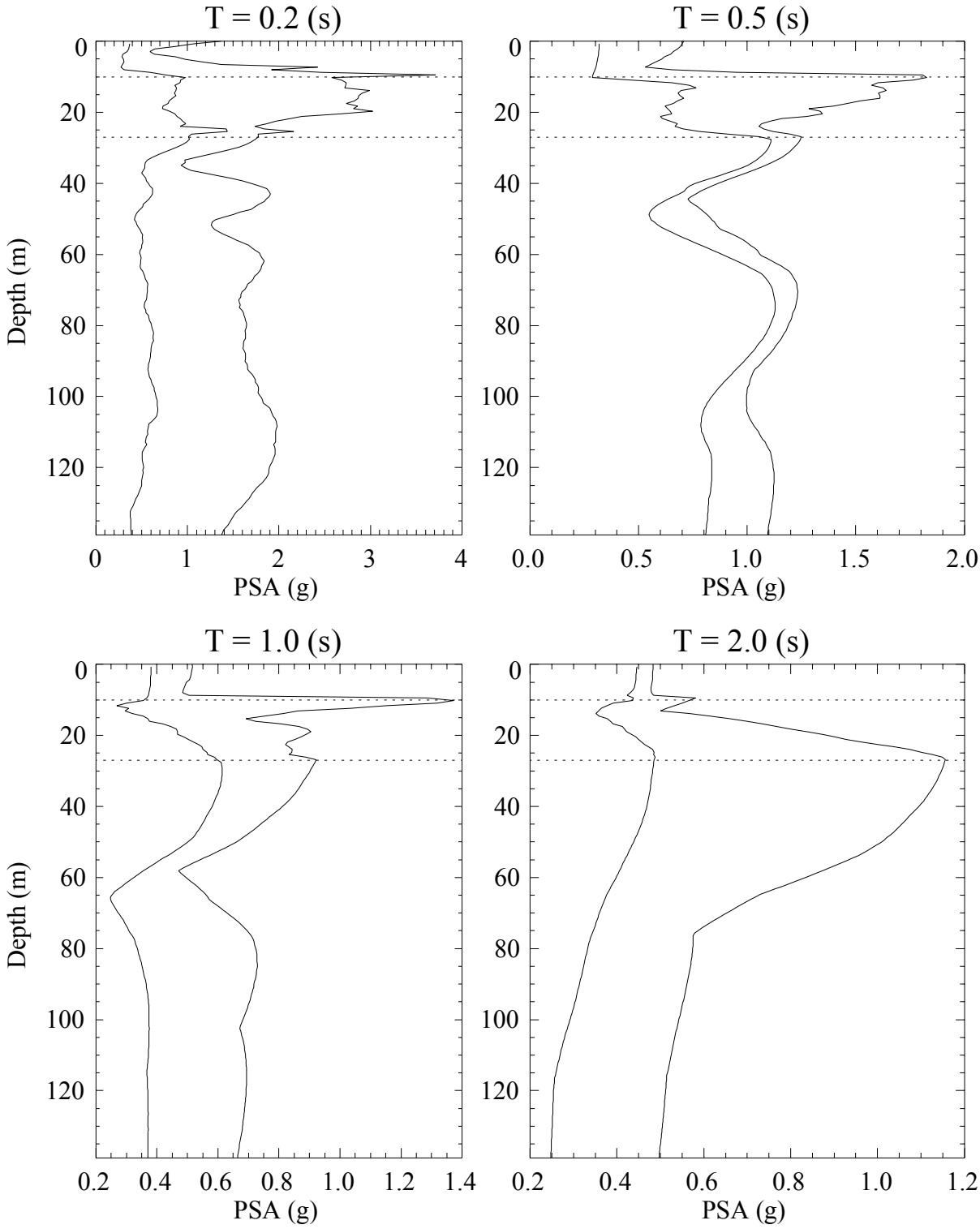

Figure 6-60: Compacted soil acceleration response spectra for rock response input motions. Title of each figure is the period and the solid lines indicate minimum and maximum responses at each depth from the six input ground motions. The horizontal dotted lines show the depth range of the low-velocity layer with nonzero porosity. The compaction zone is the region above the top dotted line.

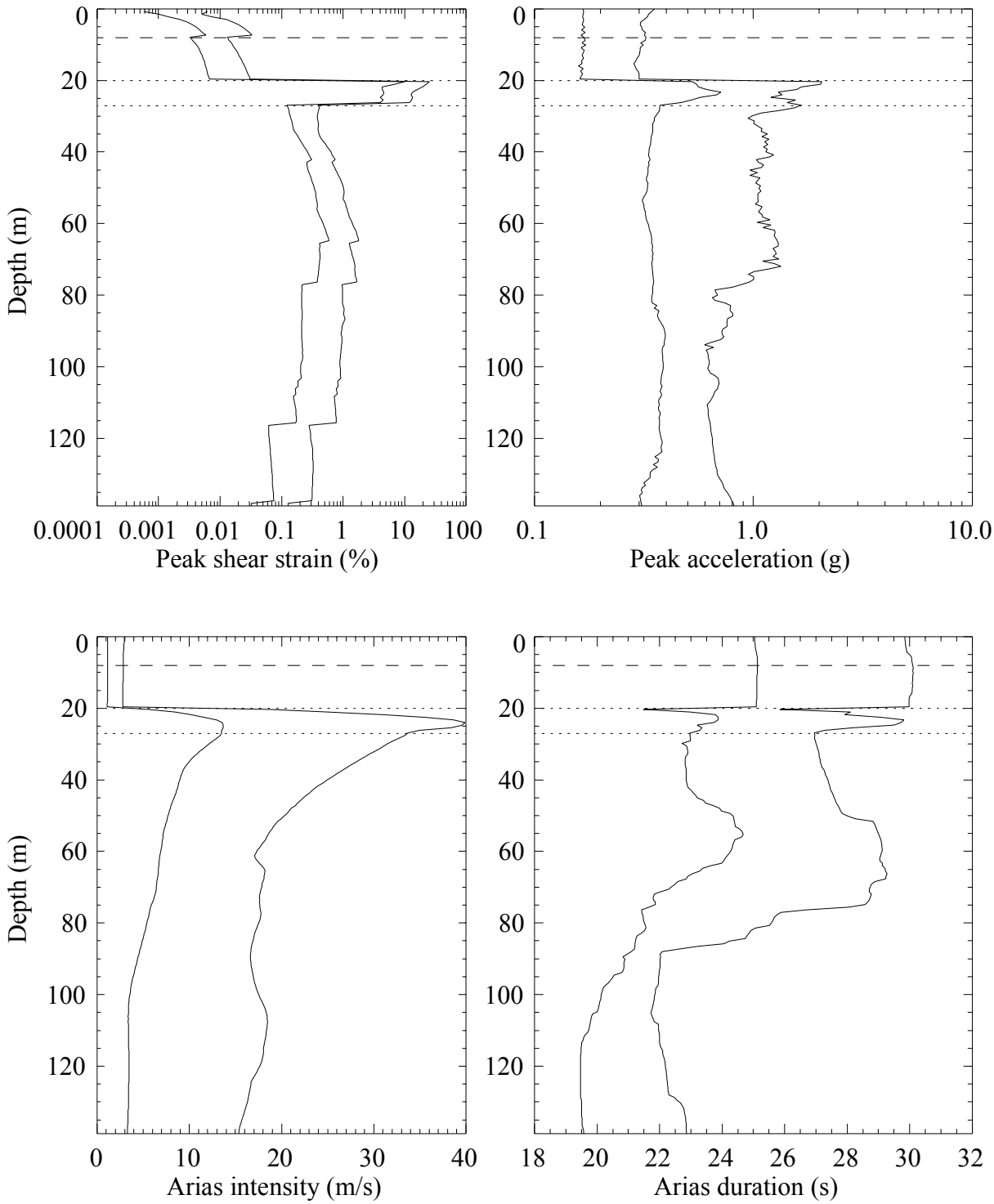

Figure 6-61: Time-domain soil mix wall responses for JLD3 response input motions. In each figure the solid lines indicate minimum and maximum responses at each depth from the six input ground motions. The horizontal dotted lines show the depth range of the low-velocity layer with nonzero porosity. The high-velocity SMW layer is located between the horizontal dashed line and the top dotted line. The lower-velocity SMW layer is located above the horizontal dashed line.

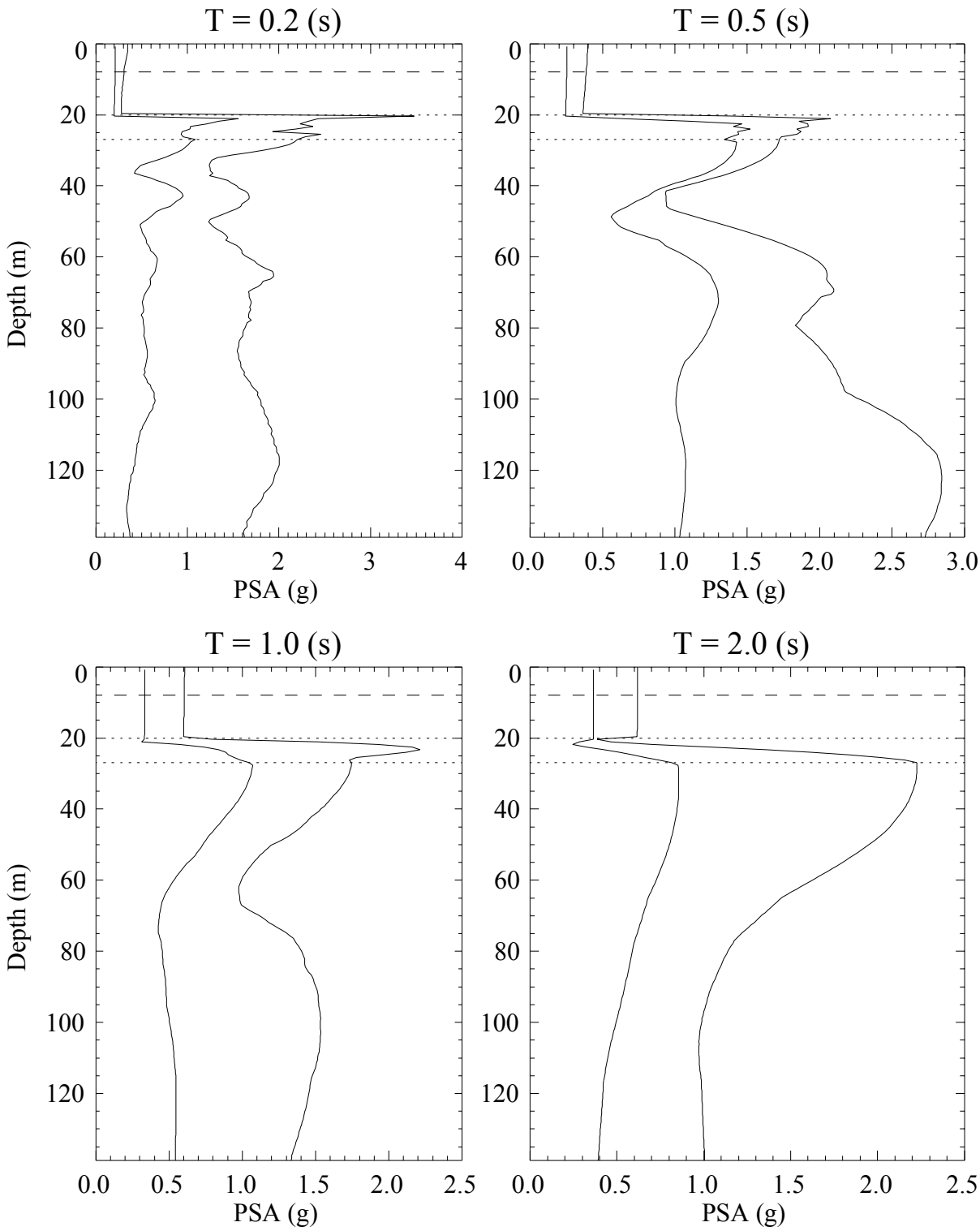

Figure 6-62: SMW soil acceleration response spectra for JLD3 response input motions. Title of each figure is the period. The solid lines indicate minimum and maximum responses at each depth from the six input ground motions. Horizontal dotted lines show the depth range of the low-velocity layer with nonzero porosity. The high-velocity SMW layer is located between the horizontal dashed line and the top dotted line. The lower-velocity SMW layer is located above the horizontal dashed line.

period. However, for periods of 0.5 s or larger, minimum PSA responses in the SMW are > 0.3 g (Figure 6-62). Comparison of the JLD3 response nonlinear results with nonlinear responses with rock input motions (Figure 6-63) shows a different dependence of peak motions and duration on input motion duration compared to Section 6.6.1. Peak accelerations and Arias Intensities are only slightly smaller for shorter duration rock input motions (Figure 6-63) than for long duration soil motions (Figure 6-61), but rock motion Arias durations are substantially smaller. PSA responses are only slightly lower for rock input motions (Figure 6-64), showing a weak influence of duration on SMW peak acceleration responses over a wide range of periods.The rock input results likely underestimate soil responses because they lack the long soil durations that are result of horizontally-propagating trapped waves propagating at various depths by significant velocity discontinuities and vertical velocity gradients within the ~140 m deep low-velocity glacial scour. Consequently, the JLD3 response input results (Figures 6-61 and 6-62) are more likely to represent expected SMW responses at the dam.

6.6.3 Discussion of Nonlinear Results. While nine different ground motion load scenarios were considered used in the nonlinear ground motion calculations, an important fact to consider is that both SHAKE and NOAH simplify seismic motions to vertically-propagating SH waves. At Jackson Lake Dam the seismic phases that produce the largest peak accelerations and velocities are likely to be SV waves in a coupled P-SV wavefield. Thus, neither SHAKE nor NOAH represent the physical quantities that will produce the strong ground motions at the dam. Consequently, the nonlinear ground motion calculations that use rock input motions are only provided to indicate lower bounds on soil motion responses. The nonlinear input motions produced using the JLD3 responses provide more realistic soil response scenarios than the rock input motions. A 2D (plane-wave) P-SV nonlinear calculation is necessary to determine if SHAKE or NOAH adequately represent nonlinear ground motion responses likely to occur at the dam. NOAH only predicts large-amplitude cusped, one-sided accelerograms for certain combinations of soil properties. It is not clear how well NOAH (or any other nonlinear approach) will predict nonlinear soil behavior at the dam, because estimates of important nonlinear soil parameters were not available from the dam site and must be inferred. A common assumption is that peak accelerations will generally decrease with depth in soils. Yoshida et al. (2002) showed that peak accelerations at the Kobe Port Island (a site that experienced liquefaction during the

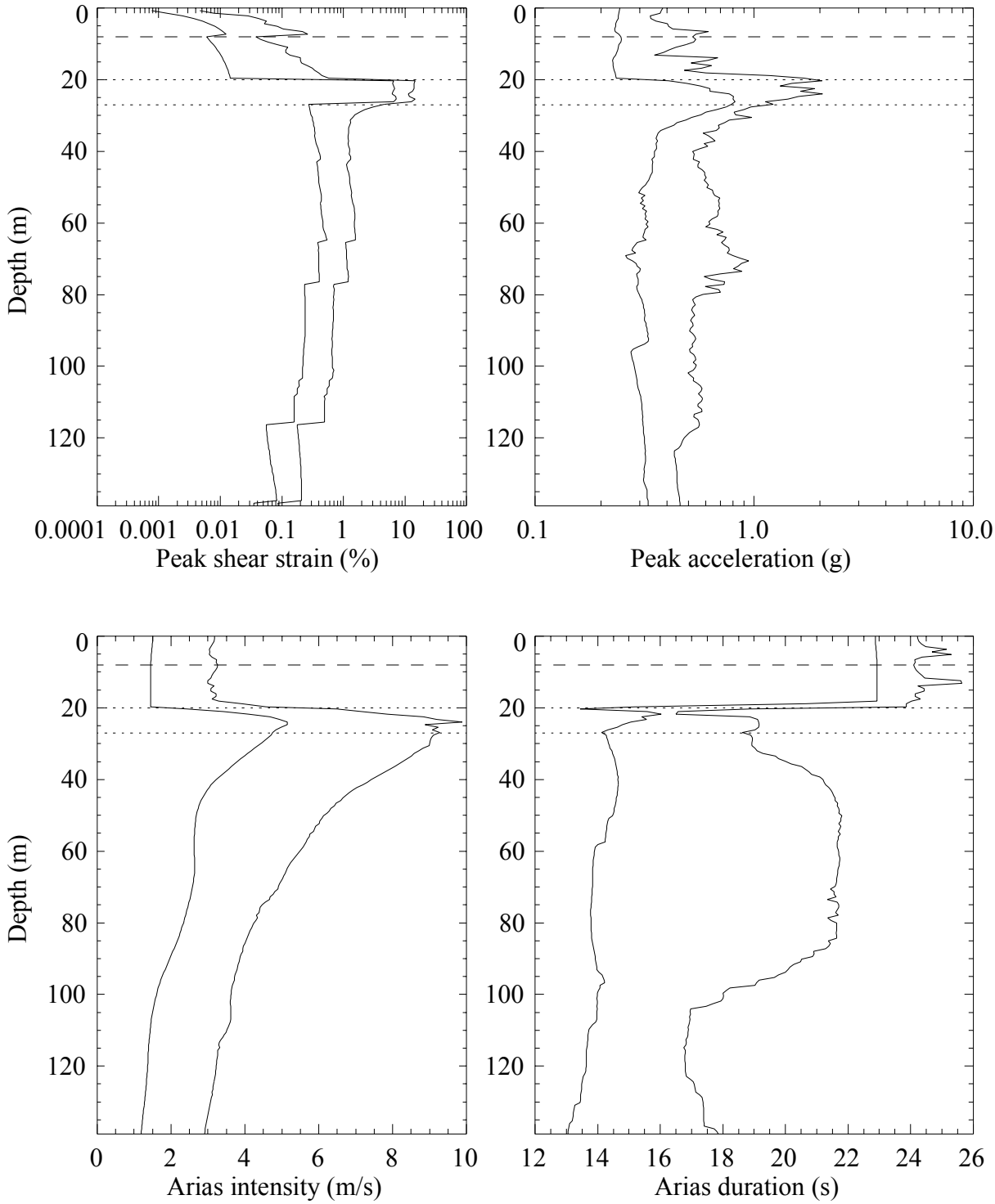

Figure 6-63: Time-domain soil mix wall responses for rock response input motions. In each figure the solid lines indicate minimum and maximum responses at each depth from the six input ground motions. The horizontal dotted lines show the depth range of the low-velocity layer with nonzero porosity. The high-velocity SMW layer is located between the horizontal dashed line and the top dotted line. The lower-velocity SMW layer is located above the horizontal dashed line.

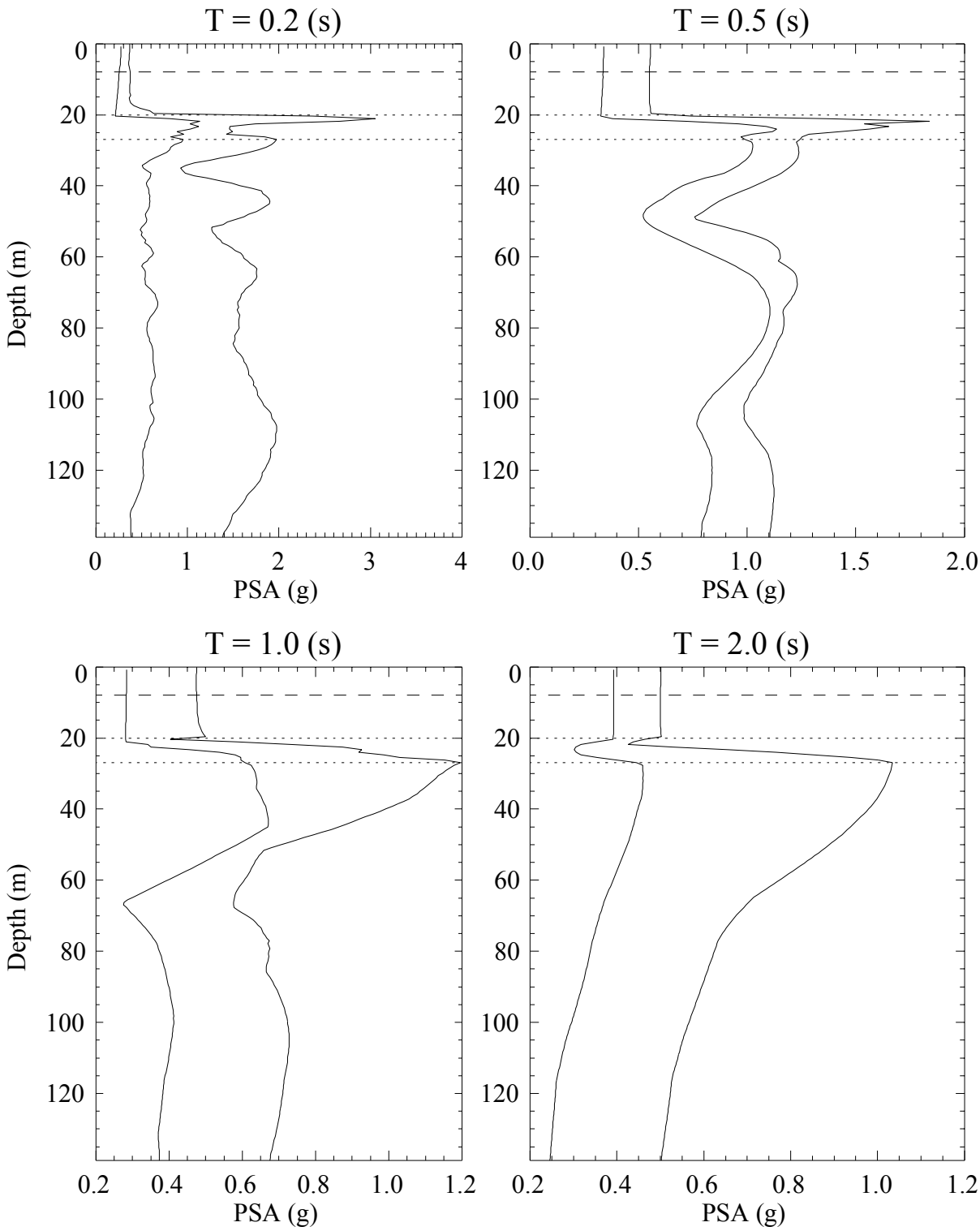

Figure 6-64: SMW soil acceleration response spectra for rock response input motions. Title of each figure is the period. The solid lines indicate minimum and maximum responses at each depth from the six input ground motions. Horizontal dotted lines show the depth range of the low-velocity layer with nonzero porosity. The high-velocity SMW layer is located between the horizontal dashed line and the top dotted line. The lower-velocity SMW layer is located above the horizontal dashed line.

1995 **M** 6.9 Kobe earthquake) increased from ~0.3 g at the surface, to ~0.6 g at 16.4 m depth, and ~0.55 g at 32.4 m depth. Similarly, NOAH sometimes predicted large peak accelerations at depths that depended on the assumed depth of potentially liquefiable materials (see Appendices E and F). Information on the nonlinear soil properties as a function of depth below the dam is necessary to reliably predict peak accelerations, stresses, and strains at depth and at the surface. Due to the presence of the soil-mix columns with low velocities to 10-30 foot depths, underlain by higher velocity soil-mix (Wright, 1990) and the compacted soils beneath the dam, the material properties vary strongly in the upstream-downstream direction; both NOAH and SHAKE assume lateral homogeneity. The presence of the higher-velocity soil-mix columns than the surrounding soil, will result in amplification of seismic waves in the soil beneath the dam and in the untreated soil adjacent to the soil-mix columns.

6.7 Ground Motion Summary

The location of Jackson Lake Dam in the LVB located above the Teton fault results in substantial seismic loads at the dam associated with **M** ~7 earthquakes on the Teton fault. The hybrid ground motion simulations of **M** ~7 earthquakes on the northern Teton fault segment predict larger rock peak velocities, and comparable peak accelerations to those estimated at Casitas Dam (O'Connell, 1999b), previously the strongest seismic loads estimated for a Reclamation structure. Casitas Dam is located on the hanging wall of the Red Mountain reverse fault, placing it on the highest velocity rocks in the vicinity of the Red Mountain fault. Casitas Dam was subjected to maximum rupture directivity because it was located closer to the Red Mountain fault than Jackson Lake Dam is relative to the Teton fault. While much of the concrete portion of Jackson Lake Dam is located on ~1 km/s S-wave velocity material that would be considered rock sites in California, their are large velocity contrasts between the LVB containing the dam and the basement rocks. Thus, Jackson Lake Dam is located in the lowest velocity rocks in its crustal neighborhood and it experiences ground motion amplification as a result. Since the EGFs were used to construct the > 1 Hz responses and contain a wide variety of LVB-edge S-wave amplitudes and time moveouts relative to the direct S-wave arrival, the < 1 s PSA responses may be underestimated because LVB-edge S-waves would likely have more systematic move-outs, amplitudes, and phasing that represented by the random summing of eight EGF responses. In spite of potential underestimation of < 1 s period responses, the hybrid ground motion simulations for Teton fault dips of 35° and

45°, the mean and 84% PSAs for periods > 0.35 s exceed Spudich et al.'s (1999) empirical predictions for rock for site JLDW; the combined influences of rupture directivity and the LVB amplify rock motions at the dam to produce PSA rock responses more like a soil site than a ~1 km/s S-wave velocity rock site. For a fault dip of 35°, the mean and 84% PSA exceed Spudich et al.'s (1999) empirical prediction for soil at rock site JLDW for periods > 1 s. For a fault dip of 45°, the mean and 84% PSA exceed Spudich et al.'s (1999) empirical prediction for soil at rock site JLDW for periods > ~1.5 s. Unfortunately, hanging wall LVB amplification produces ground motions at Jackson Lake Dam that mimic extreme ground motion characteristics of rupture directivity while producing extended durations of strong ground shaking, not typically associated with rupture directivity. The ground motions recommended for dynamic analyses of the concrete section of Jackson Lake Dam in Section 6.5 reflect these realities.

Ground motions are also provided for nonlinear analyses of the embankment section of the dam that reflect the extended durations and amplification associated with the ~140-m-deep very-low-velocity glacial scour that is the foundation for most of the embankment section of the dam. To provide realistic inputs for nonlinear soil responses calculations at depth, these soil ground motions were constructed with a JLD3 site response to account for the wide variety of S-wave and interface wave phases that likely exist at depths > 25 m in the VLV glacial scour sediments. Nonlinear effective-stress soil response calculations with NOAH show that near-surface Arias Intensities and peak acceleration responses, and their associated durations are very sensitive to input motion peak amplitudes and durations. Certain combinations of input motions produced nonlinear soil Arias Intensity and Arias duration responses that exceeded corresponding rock responses by a factor of six. Nonlinear soil response (modulus reduction) may increase ground motions durations because interface phase velocities will be reduced, increasing the time required for Airy phases to propagate from the boundaries of the glacial scour to the dam.

Jackson Lake Dam is > 1.5 km long and spans a wide variety of foundation materials with widely varying S-wave velocities and straddles a region with > 10:1 S-wave velocity contrasts. These large velocity contrasts occur between the overcompacted till (Vs ~ 1 km/s) and the soils in the glacial scour (Vs ~ 0.1 km/s). S-wave velocities also vary both laterally and vertically within the glacial scour region that is composed of fluvial-lacustrine deposits with Vs varying from to 0.09

km/s to 0.2 km/s (Sirles, 1986). Ground motions are likely to vary substantially, both along the dam's axis and in the upstream-downstream direction, because the low soil S-wave velocities result in wavelengths nearly equal to the dam's width at 1 Hz. Chen and Harichandran (2001) showed that spatially varying ground motions are likely to substantially increase shear stresses in foundation materials at the toes of an embankment dam, particularly when spatial coherence is significantly < 1 for low frequencies. Santa-Cruz et al. (1999) showed that for low-velocity basins, the absolute value of coherency can be substantially less than 1 for frequencies as low as 0.3 Hz, for separation distances as low as 800 m, and for frequencies as low as 1 Hz, for separation distances as lows as 100 m. Given the results of Santa-Cruz et al. (1999), and the substantial and variable thickness of low S-wave velocity materials in the glacial scour that comprises the foundation for the embankment section of the dam, and the strongly varying site responses noted in Chapter 5 from the Jackson Lake Dam site response stations, it is likely that ground motions coherency will be substantially < 1 for frequencies as low as 0.3 Hz along the embankment portion of the dam.

The southern portion of the dam, consisting primarily of the concrete section, is founded on ~1 km/s S-wave velocity till and tuff. The rest of the dam is founded on ~0.1 km/s S-wave fluvial-lacustrine deposits that increase in thickness towards the northern end of the dam. The southern portion of the dam will shake less strongly and for shorter durations than the rest of the dam. Consequently, the largest strains resulting from differential motions along the axis of the dam are likely to be located in the embankment section extending from the concrete section to station 32, where Sirles (1986) found a ~140 m thick section of fluvial-lacustrine deposits below the ground surface. The distances between stations JLD2 near the northern end of the concrete section and station JLD3 near station 24+00 is 356 m. For a vertically-incident shear wave, the propagation delay at station JLD3 relative to JLD2 due to ~140 m of fluvial-lacustrine fill with an average S-wave velocity of ~140 m/s is 0.87 s (1 s travel-time through the last 140 m for JLD3 and 0.13 s travel time through the last 140 m for JLD2). This yields a S-wave apparent velocity of 0.41 km/s, which will likely reduce S-wave coherency at low frequencies, based on the results of Santa-Cruz et al. (1999). This is an apparent velocity 10 times *smaller* than considered by Chen and Harichandran (2001) in their analyses of the influence of coherency on the dynamic analysis of embankment dams. Since the peak velocity loads at Jackson Lake Dam are substantially larger

than considered by Chen and Harichandran (2001), and apparent velocities are much lower, differential displacements, and correspond strains and stresses are likely to be larger at Jackson Lake Dam than those considered in Chen and Harichandran (2001). S-wave apparent velocities will decrease for S-waves arriving from the south (about half of the northern Teton rupture segment, and the entire southern Teton rupture segment). S-wave apparent velocities will be increased slightly for S-wave arrivals from north of station JLD3, but the increases in apparent velocity will be modest.

Consistent with past approaches to reduce ground motion estimation biases and uncertainties (Anderson and O'Connell, 1998; Anderson and O'Connell, 1993; O'Connell and Unruh, 2000; Ake et al., 2002) microearthquake data from the Jackson Lake Seismic Network provided the crucial information about the subsurface fault geometries, particularly dip of faults at depth, and seismotectonic constraints on state-of-stress and fault kinematics, information necessary to estimation ground motions at Jackson Lake Dam. The combination of broadband site response stations at Jackson Lake Dam and the short-period JLSN provided empirical Green's functions and the ability to estimate site responses in the same manner as the site response stations in previous studies (O'Connell and Ake, 1995; O'Connell, 1999b; O'Connell and Unruh, 2000; O'Connell, 2001), where local seismographic networks such as the short-period Southern California Seismic Network and the Northern California Seismic Network provided crucial information necessary to convert site response recordings into empirical Green's functions. The development of site-specific ground motions using empirical Green's functions substantially reduced ground motion biases in several previous studies (O'Connell, 1999a, 1999b; O'Connell and Unruh, 2000; O'Connell, 2001). For instance, site-response recordings used in conjunction with short-period data from the Southern California Seismic Network showed that convention approaches to estimating near-source ground motions at stiff-soil sites in southern California were likely to strongly overpredict peak ground motions (O'Connell, 1999a). At a high-velocity hard-rock site, broadband site-response data in conjunction with short-period data from the Northern California Seismic Network showed that source characterization of blind thrust faults in the western Sacramento Valley were incorrect (O'Connell and Unruh, 2000; O'Connell et al., 2001) and that peak acceleration loads would likely be about 2/3 empirical predictions, resulting in substantially lower final peak ground motion estimates (LaForge, 1999). Estimation of the 3D

velocity structure of the crust and discovery of the significant impacts of 3D velocity structure on peak ground motions and ground motion durations were made possible by the earthquake data from the JLSN and the broadband site response seismographs at Jackson Lake Dam. The earthquake data provided by the JLSN were necessary to fully exploit the site response earthquake recordings to develop empirical Green's functions and site response information for nonlinear soil analyses. At Jackson Lake Dam, development of site-specific ground motions increases confidence that estimated ground motions are not likely to be significantly biased.

There are several factors that produce significant ground motion uncertainties. The uncertainty in Teton fault dip produces at least a factor of two uncertainty in peak seismic loads at the dam. Since it appears the Teton fault is entirely located within basement rocks, a significant velocity contrast across the fault is unlikely; seismic reflection/refraction methods are unlikely to be able to image the fault at depth. Several earthquake recorded by the JLSN suggest the Teton fault dips ~45°. As is typically the case at other Reclamation dams (Casitas, B.F. Sisk, Hoover, Monticello, O'Neill, and Ridgway Dams), earthquake locations and focal mechanisms are probably the only feasible way to constrain the dip of the Teton fault at depth, in the absence of a strong geodetic signal produced by a **M** ~7 earthquake on the Teton fault. Uncertainties in the spatial extent and velocities in the LVB produce, as yet, unknown uncertainties in peak ground motions and durations.

Uncertainties about the velocity structure and spatial extent of the glacial scour produce uncertainties of about a factor of two in peak soil ground motions, and factor of four uncertainties in soil ground motion durations. It is necessary to determine the wave-types that comprise the long duration soil ground motions to determine the appropriate methods to calculate nonlinear soil responses. Synthetic calculations in Section 5 indicate that a significant fraction of the long-duration high-amplitude soil motions at the dam may be produced by S-waves and horizontally propagating interface waves occurring at depth in the glacial scour basin.

The 20-station short-period seismographic network provided many critical pieces of data necessary to estimate ground motions at the dam. However, its configuration was not well-suited to obtain the seismic data necessary to substantially reduce remaining ground motion uncertainties. In particular, the vertical-component short-period JLSN did not provide S-wave

velocity constraints. Earthquake depth estimation capabilities in the vicinity of the Teton fault were limited by the large area spanned by the JLSN, the 10-20 km JLSN station spacing, and the absence of three-component seismographs. A smaller broadband three-component network located within and on the periphery of the LVB, combined with one or more soil borehole three-component packages at the dam, with three-component sensors at the surface and at several depths extending to ~50 m depth, would provide much more valuable and relevant information for Jackson Lake Dam than the 20-station short-period JLSN.

Earthquake magnitude is sometimes used as a proxy for ground motion duration in engineering analyses of soils. The earthquake magnitudes used to simulate ground motions at Jackson Lake Dam from earthquakes on the Teton fault should *not* be used for this purpose. Due to the proximity of the Teton fault to the LVB and glacial scour very-low-velocity basin, and the resulting peak ground motion amplifications, extended durations, and increased Arias intensities of ground motions at the dam, effective magnitudes for geotechnical analyses of the seismic loads are 7 1/2 for the rock ground motions, and are 8 for the soil ground motions. These recommended magnitudes for soil analyses are 1/4 to 1/2 magnitude units larger than the moment magnitudes of all-segment and northern segment rupture scenarios of the Teton fault, specifically to account for the extended durations and amplifications of ground motions observed at the dam (Section 5). The most likely scenarios for soil response based on section 5 and nonlinear soil calculations using NOAH indicate ground motion durations of at least 60 seconds and possibly as long as 120 s for the embankment portion of the dam.

Because this section only considers the Teton fault as a seismic source and background seismicity clearly increases the seismic loading rates (Section 3), it is necessary to increase annual exceedence probabilities relative to activity rates of the Teton fault to provide representative probabilistic seismic loads for dynamic analyses of the dam. These analyses are presented in the next section.

7.0 ANALYSIS OF ESTIMATED GROUND MOTIONS

The simulated ground motions for the "rock" (~1 km/s surface shear-velocity) portion of Jackson Lake Dam (site JLDW) are larger than predicted by the empirical ground motion model developed for transtensional faulting environments by Spudich et al. (1999). The most unusual characteristic of the simulated "rock" ground motions is that they substantially exceed predicted soil accelerations from Spudich et al. (1999) at periods longer than 2 s. Somerville (2003) suggested two potential causes, near-fault rupture directivity and basin effects. One concern is that the simulation procedure, specifically the kinematic rupture model used in Section 6, may systematically overpredict near-fault ground motions, especially at long periods. While validation of any simulation procedure is not possible (Oreskes et al., 1994) a necessary credible condition is that a model reproduce past experience. Modeling of near-fault strong ground motions from the 1994 **M** 6.7 Northridge earthquake is used in Section 7.1 to evaluate the performance and credibility of the kinematic source model. The Northridge data represent the densest near-fault recordings of a dip-slip earthquake and are the best data available in the absence of a well-recorded normal-faulting earthquake. Ground motions are also synthesized in Section 7.4 using a simplified source model to provide an alternative approach to test the sensitivity of estimated ground motions to source model specification.

There are several possible tacts to evaluate the influence of the 3D basin velocity model on estimated ground motions. These could include performing ground motion simulations with alternative velocity models or completely removing the low-velocity-basin from the velocity model to provide a frame of reference for comparison with other strong motion data. Such approaches require considerable effort. There are recent recordings of larger magnitude (**M** > 4.5) earthquakes within 150 km of Jackson Lake Dam. These ground motion recording have sufficient signal-to-noise (S/N) to evaluate ground motion characteristics for periods extending to 5-10 s, much longer periods than was possible with the high-frequency empirical Green's functions in Section 6 and Appendix D (see Table 6-1). These larger magnitude earthquake recordings directly incorporating propagation effects associated with 3D low-velocity-basin structure. There are also two **M** ~3 earthquakes located in the vicinity of the northern Teton fault segment that provide empirical Green's functions that allow simulation of ground motions to periods of ~3 s, although the long-period signal-to-noise is lower than the recordings of the **M** > 4.5 regional earthquakes.

The availability of broadband empirical Green's functions affords an opportunity to construct a second test of the kinematic source model and the ground motion simulation approach used in Section 6 by using an entirely different simulation method to estimate ground motions at Jackson Lake Dam using the previously tested approach of Frankel (1995). Frankel's (1995) approach is appealing because it uses very simple assumptions that only require specifying a small number of parameters, it produces source properties and ground motions consistent with known constraints (Andrews, 1980; Frankel, 1991), and it reproduced near-fault acceleration responses from the 1989 **M** 7.0 Loma Prieta earthquake (Frankel, 1995).

Before moving on to kinematic source model and ground motion simulation presentations, it is reasonable to ask: Is there a precedent for the large long-period ground motions estimated in Section 6 in strong motion observations? The 1979 **M** 6.5 Imperial Valley earthquake was recorded by an array of strong motion instruments located in the vicinity of the fault rupture. The Imperial fault and several near-fault strong motion stations are located in a sedimentary basin (Fuis et al., 1982). In the next section, the three strong motion records from this earthquake closest to the Imperial fault which contain large > 2 s acceleration responses are compared to predicted ground motions at Jackson Lake Dam.

7.1 Strong Ground Motions From the 1979 M 6.5 Imperial Valley Earthquake

On 15 October 1979 a **M** 6.5 earthquake occurred on the Imperial fault near the United States-Mexico border. The epicenter was located in northern Mexico and rupture proceeded north along the Imperial and Brawley faults producing particularly strong ground shaking in the El Centro array of accelerometers located along the northern portion of the Imperial fault (Figure 7-1). Since the Imperial fault is located in a sedimentary trough (Fuis et al., 1982) with a low-velocity basin structure similar to the low-velocity basin adjacent to the Teton fault, the strong motion recordings from sites close to the Imperial fault provide a qualitative indication of near-fault ground motion characteristics in a basin.

Fuis et al. (1982) showed that the Imperial fault is embedded in a 4-5 km deep low-velocity sedimentary basin with P-wave velocities and velocity gradients vary similar to velocity structure inferred for the low-velocity basin adjacent to the Teton fault in Section 4. Specifically, P-wave

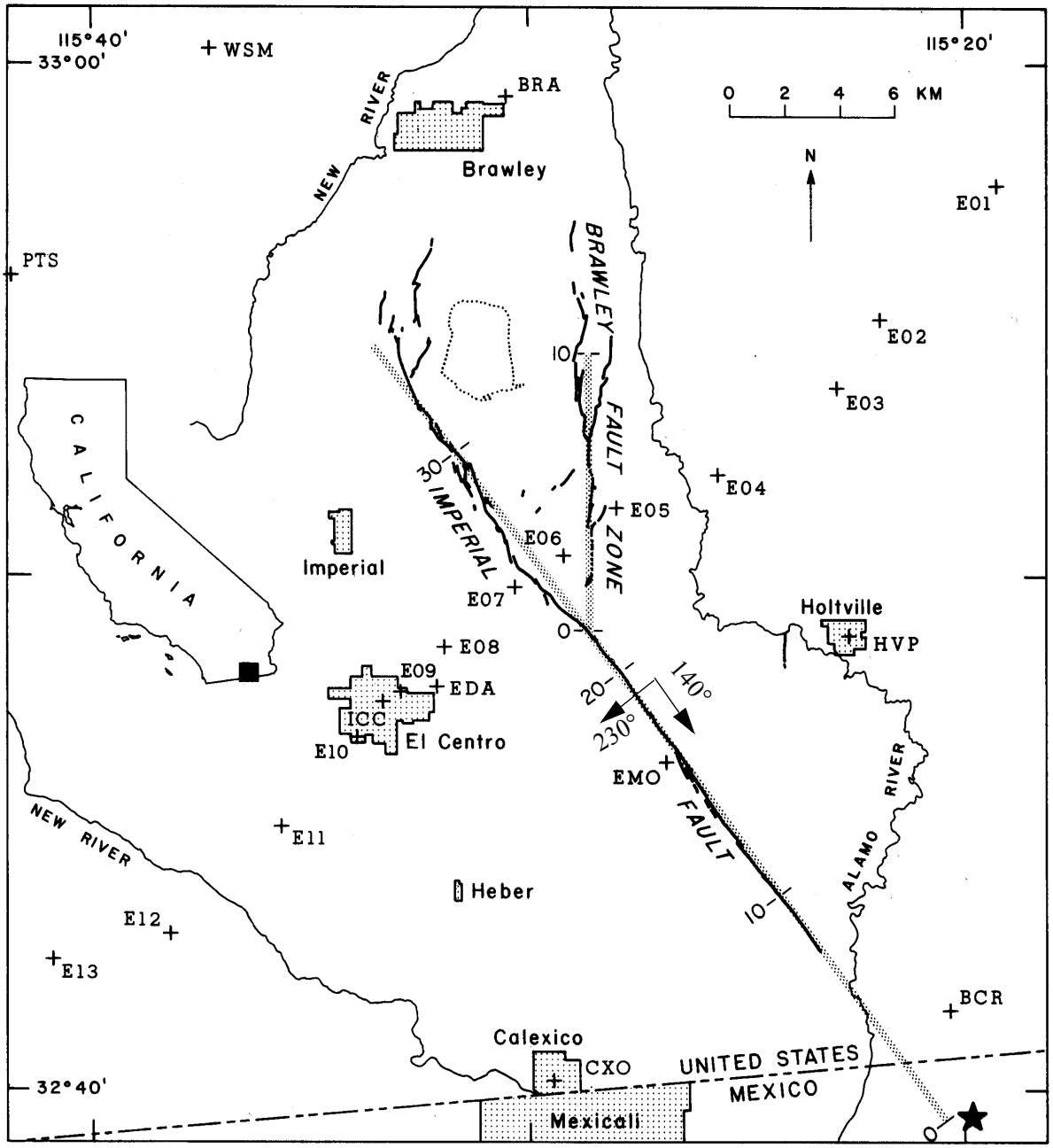

Figure 7-1: Map view of the Imperial Valley area from Archuleta (1984). Strong motion stations are labeled plus symbols. The portions of the Imperial and Brawly faults with measured surface offsets are shown by the dark line segments. Linear stippled regions show the idealized fault geometries used in Archuleta (1984) to model strong motions. The inset of California shows the approximate location of this map. Stations E06, E07, and EMO show strong long period responses as indicated in Figure 7-2 to 7-10. The labeled arrows indicate the orientation of the horizontal components in strike parallel (140°) and strike normal (230°) directions.

velocities in Imperial Valley near the surface along the refraction profile closest to the Imperial fault (SP-6 to SP-13) are ~2 km/s and are ~4.5 km/s at the bottom of the basin (Fuis et al., 1982). Basement P-wave velocities are > 5.5 km/s at both Jackson Lake and Imperial Valley. The biggest difference in the velocity structures are near the bottoms of the basins where P-wave velocities in the low-velocity-basin adjacent to the Teton fault are about 1 km/s slower at the bottom of the basin relative to Imperial Valley. In Imperial Valley the refraction data suggest a ~0.5-km-thick transition zone below the sediments that increase P-wave velocities to ~5.5 km/s at the contact with the ~6 km/s basement. The refraction data and waveform modeling of velocity structure at Jackson Lake Dam suggest a very-large velocity discontinuity between the deepest sediments (~3.5-4 km/s) and basement (~5.5 km/s) (see Figure 4-13). This results in a much stronger impedance contrast at the bottom of the low-velocity basin near the Teton fault relative to Imperial Valley. The larger impedance contrast at the base of the low-velocity basin beneath Jackson Lake Dam suggest that > 1 s period acceleration responses are likely to be larger than those observed from 1979 Imperial Valley earthquake due to stronger amplification and more efficient trapping of body and surface waves. Also, long-period responses at Jackson Lake Dam will likely have much longer durations. These differences in basin structure suggest that the strong motion records from Imperial Valley provide a rough lower bound on expected long-period accelerations at Jackson Lake Dam.

Stations E06, E07, and EMO are located within 2 km of the Imperial fault (Figure 7-1) and exhibit influences of directivity in the form of peak fault-normal velocities on the order of 100 cm/s. These sites are also located near the axis of the deepest portion of low-velocity sedimentary basin. While peak horizontal accelerations are not remarkable at station E06 (Figure 7-2), the peak vertical acceleration exceeds 1.6 g. The vertical peak accelerations's high-frequency content and arrival time suggest that it is an *S-P* conversion from inside the low-velocity basin. Strong S-P conversions are not a typical characteristic of Jackson Lake Dam JLDW ground motions. This suggests there may be stronger interval velocity discontinuities within the Imperial Valley low-velocity basin relative to the low-velocity basin at Jackson Lake Dam. Strong interval velocity discontinuities in trial velocity models of the Jackson Lake Dam low-velocity basin strongly reduced ground motion durations relative to smooth vertical-velocity-gradient models of basin structure, as discussed in Section 4. This may explain the relatively short-duration of station E06

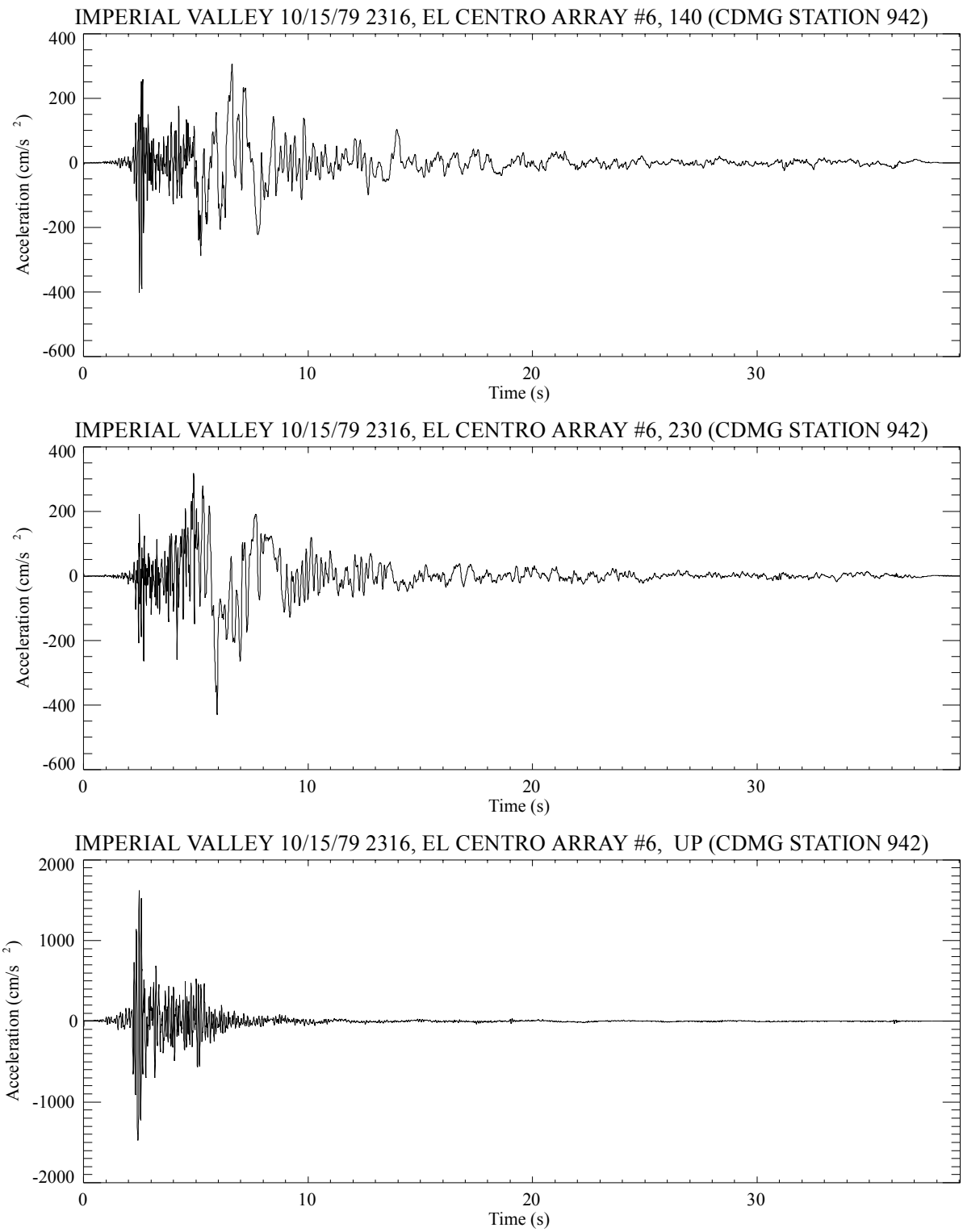

Figure 7-2: El Centro Array station E06 acceleration seismograms. Vertical is labeled UP. Horizontal components are labeled by their orientation in degrees east of north (e.g., 140° and 230°). See Figure 7-1 for station position relative to fault rupture.

motions (Figures 7-2 to 7-3) relative to ground motions observed at Jackson Lake Dam. Acceleration responses for periods larger than 2 s are remarkably large (> ~0.4 g) for the fault-normal component of station E06 (Figure 7-4) and are also quite large for periods of 2 s to 3 s for the fault-parallel component. In contrast, the vertical acceleration responses much lower at periods larger than 2 s.

Peak horizontal accelerations at Station E07 (Figure 7-5) are somewhat lower than for Station E06 (Figure 7-2), but broadband frequency content of the peak fault-normal accelerations and velocities (Figure 7-6) associated with rupture directivity are clearly evident in the 0-1 s period band in the spectral accelerations (Figure 7-7). However, strong accelerations> 0.4 g persist between periods of 2 s and 3s and > 0.3 g for periods > 3 s on the fault-normal component (Figure 7-7). In contrast, the > 2 s period responses on the vertical and fault-parallel horizontal components are much lower (Figure 7-7).

Station EMO is located at about the halfway point along the rupture of the Imperial fault. Consequently, rupture directivity was not as strong as at station E06 and E07 and peak accelerations are lower (Figure 7-8) and peak velocities are also lower (< 100 cm/s) (Figure 7-9). However, fault-normal accelerations for periods between 2 s and 3 s are > 0.4 g (Figure 7-10), exceeding comparable accelerations at station E07 (Figure 7-7) even though rupture directivity is weaker at station EMO. While peak accelerations and velocities vary considerably between stations E06, E07, and EMO because of the variability of fault slip and station positions (Archuleta, 1984), the consistently elevated > 2 s acceleration fault-normal responses at all these stations is consistent with elevated long-period responses expected for low-velocity basins (Somerville et al., 2003).

Strike-slip faulting is likely to produce less complex ground motions in a basin because *P-SV* excitation is minimal compared to dip-slip faulting. Consequently, the Imperial Valley ground motions do not provide a direct analog for motions in the low-velocity basin adjacent to the Teton fault. However, the > 0.4 g > 2 s period acceleration responses observed in Imperial Valley indicate that the large (> 0.5 g) > 2 s period acceleration responses predicted for Jackson Lake Dam are not without precedent. Considering the more extreme impedance contrast between the

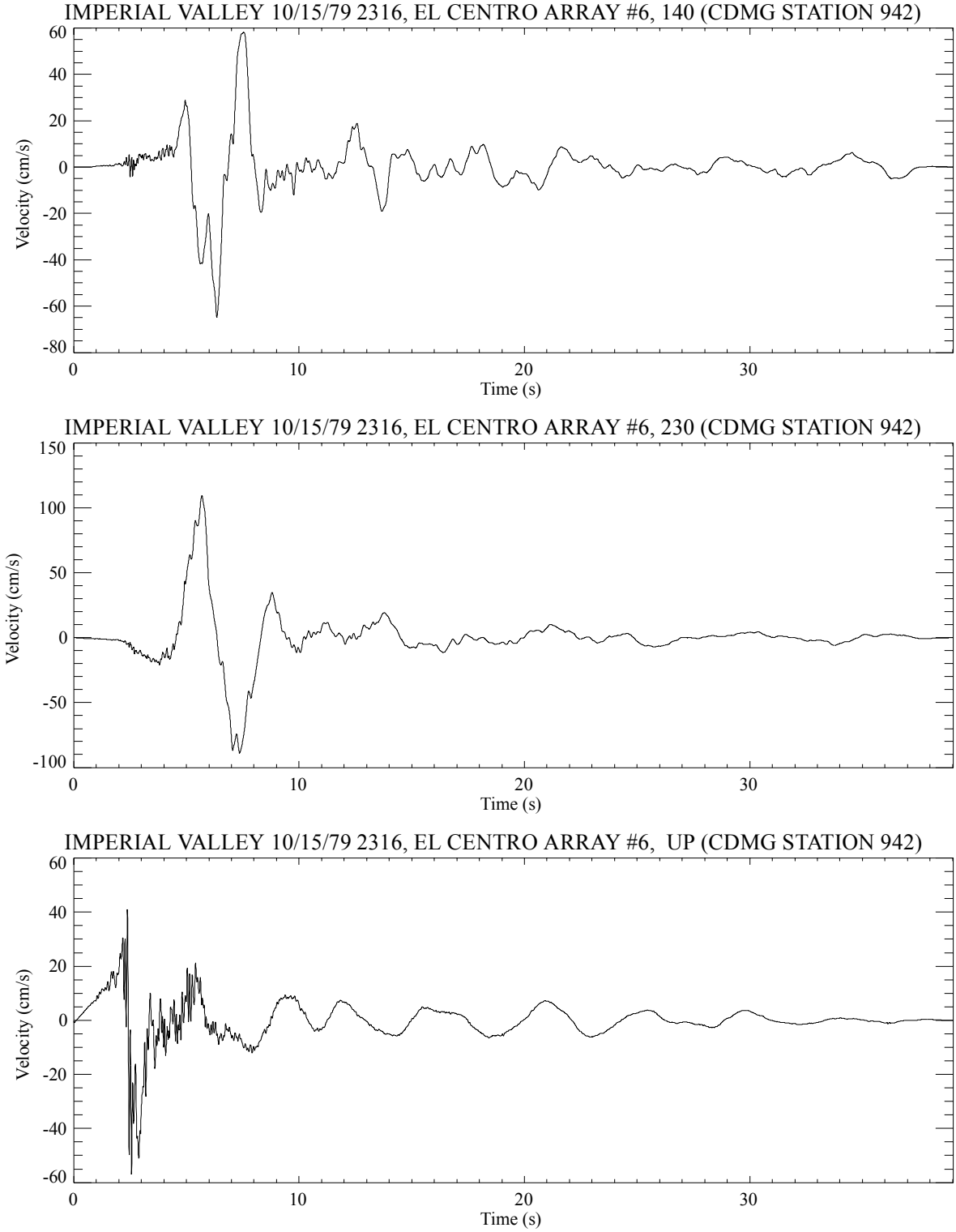

Figure 7-3: El Centro Array station E06 velocity seismograms. Vertical is labeled UP. Horizontal components are labeled by their orientation in degrees east of north (e.g., 140° and 230°). See Figure 7-1 for station position relative to fault rupture. The horizontal components are oriented in approximately strike-normal (230°) and strike-parallel (140°) directions relative to the strike of the Imperial fault.

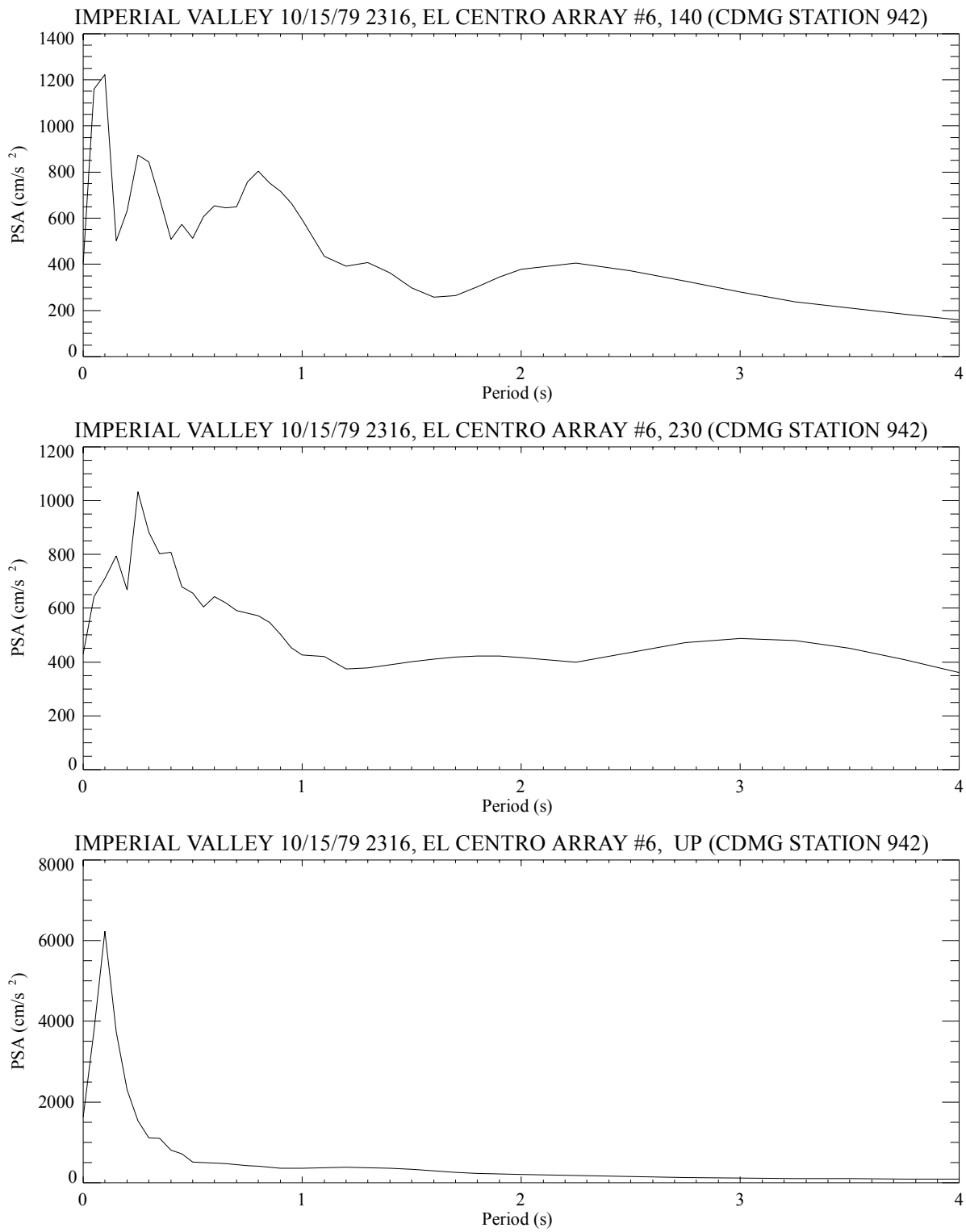

Figure 7-4: El Centro Array station E06 pseudo-acceleration response spectra. Vertical is labeled UP. Horizontal components are labeled by their orientation in degrees east of north (e.g., 140° and 230°). See Figure 7-1 for station position relative to fault rupture. The horizontal components are oriented in approximately strike-normal (230°) and strike-parallel (140°) directions relative to the strike of the Imperial fault.

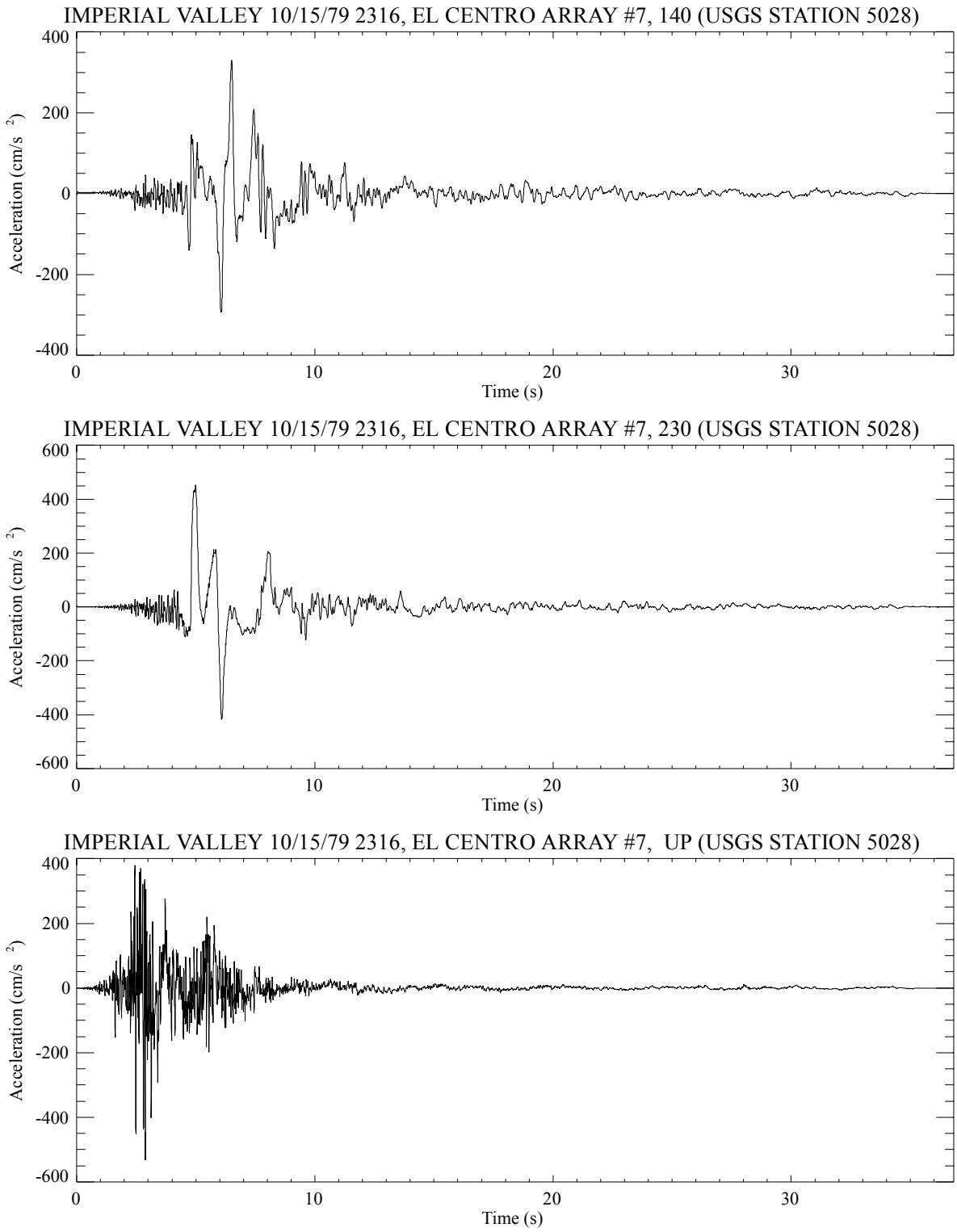

Figure 7-5: El Centro Array station E07 acceleration seismograms. Vertical is labeled UP. Horizontal components are labeled by their orientation in degrees east of north (e.g., 140° and 230°). See Figure 7-1 for station position relative to fault rupture. The horizontal components are oriented in approximately strike-normal (230°) and strike-parallel (140°) directions relative to the strike of the Imperial fault.

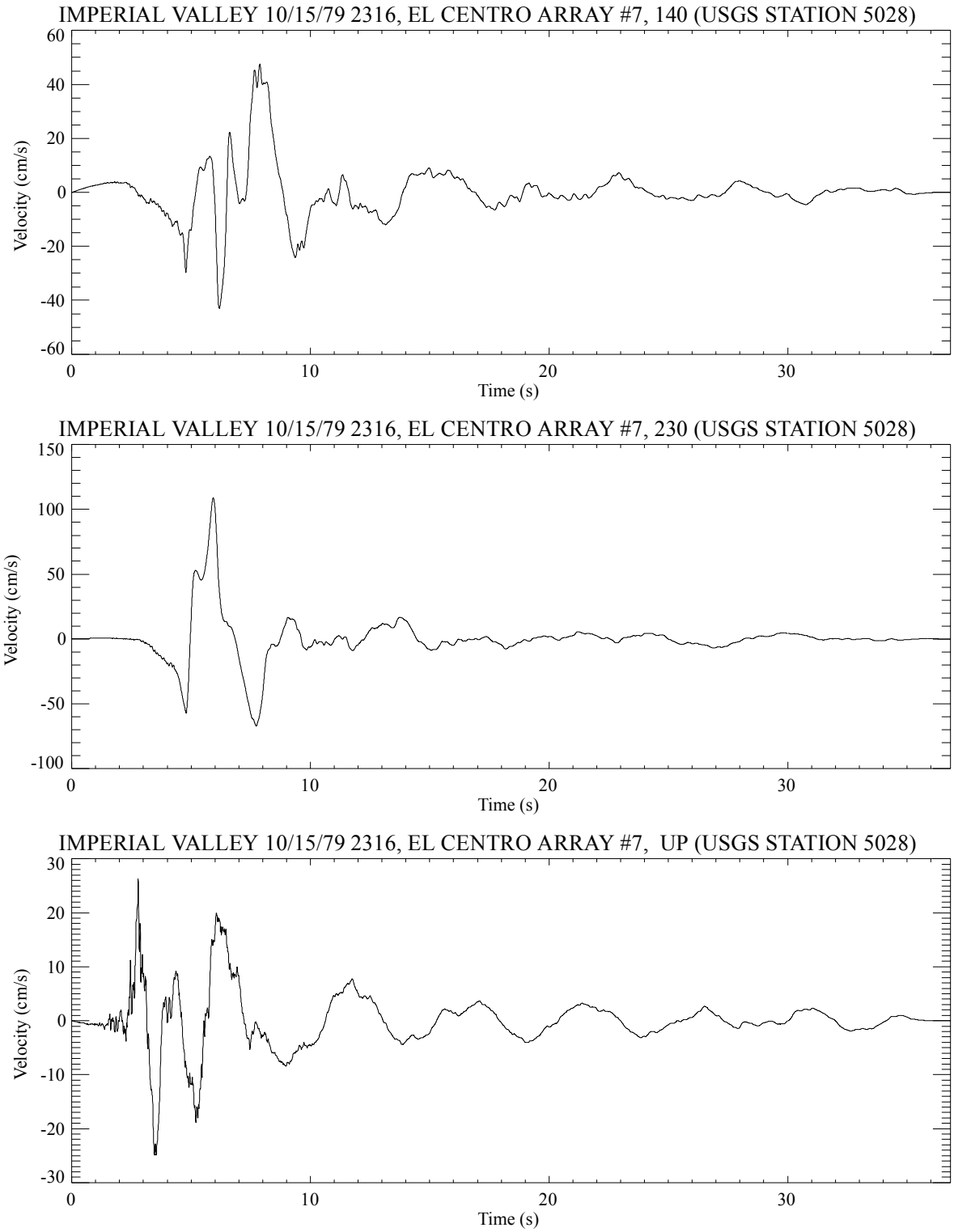

Figure 7-6: El Centro Array station E07 velocity seismograms. Vertical is labeled UP. Horizontal components are labeled by their orientation in degrees east of north (e.g., 140° and 230°). See Figure 7-1 for station position relative to fault rupture. The horizontal components are oriented in approximately strike-normal (230°) and strike-parallel (140°) directions relative to the strike of the Imperial fault.

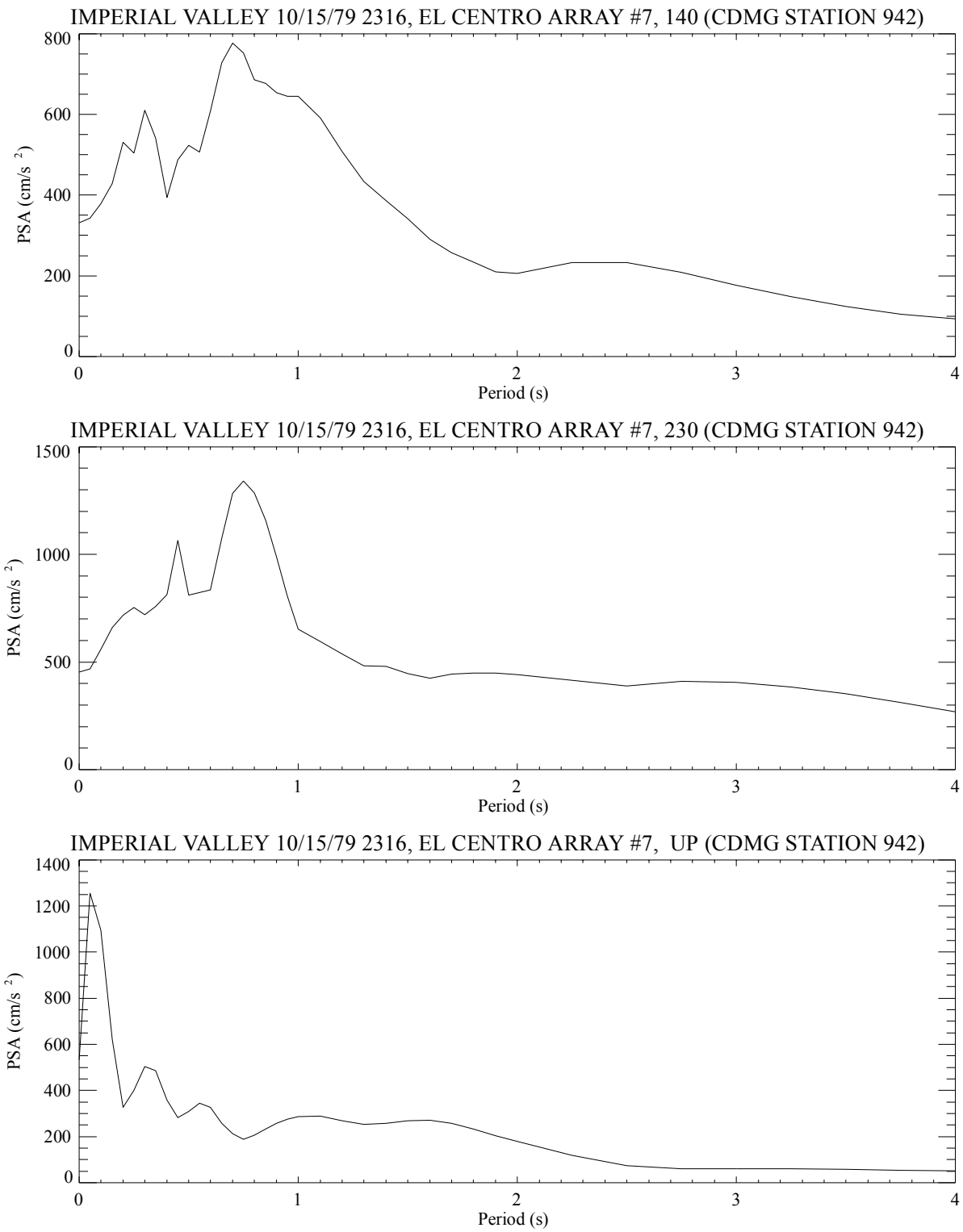

Figure 7-7: El Centro Array station E07 pseudo-acceleration response spectra. Vertical is labeled UP. Horizontal components are labeled by their orientation in degrees east of north (e.g., 140° and 230°). See Figure 7-1 for station position relative to fault rupture. The horizontal components are oriented in approximately strike-normal (230°) and strike-parallel (140°) directions relative to the strike of the Imperial fault.

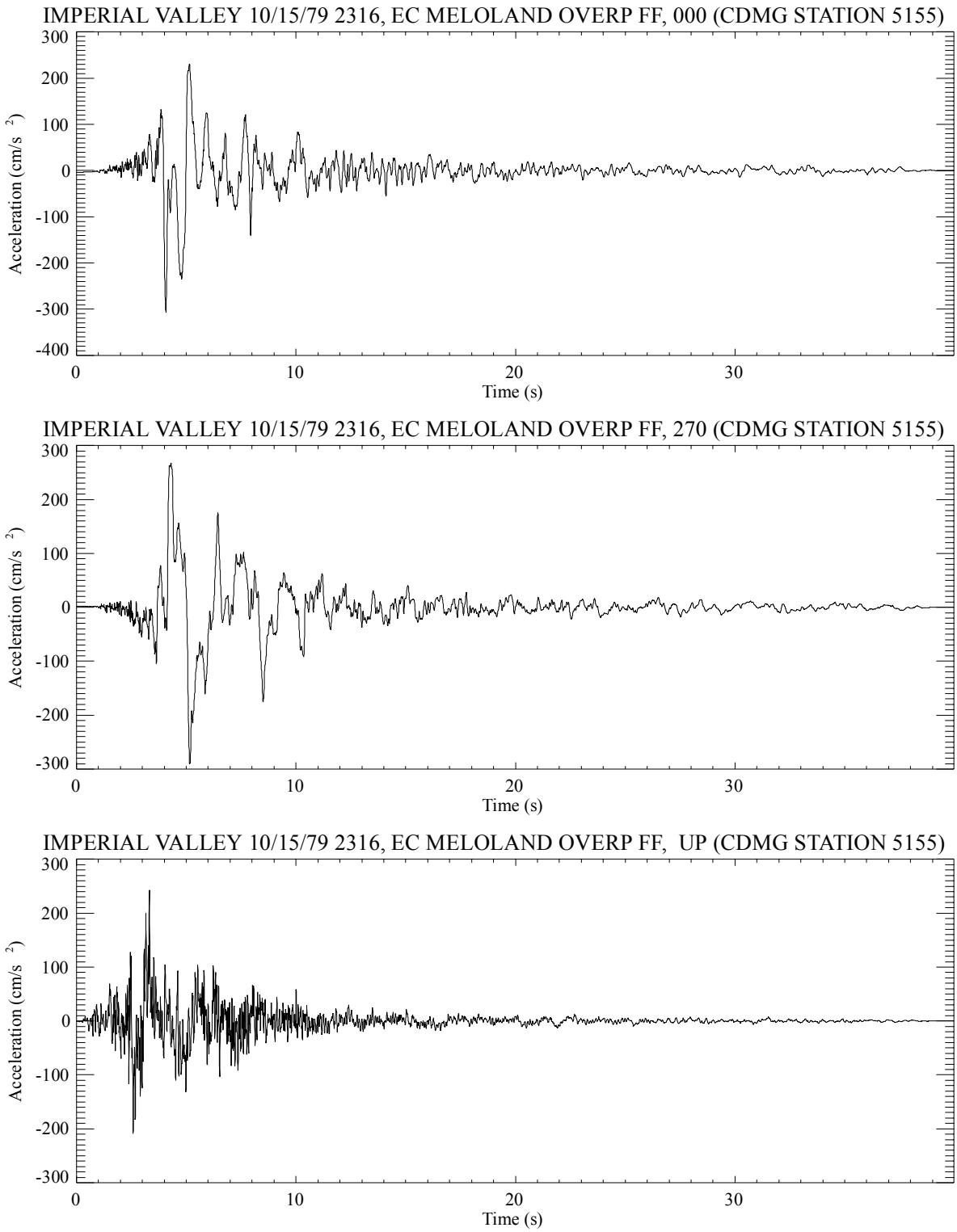

Figure 7-8: El Centro Array station EMO acceleration seismograms. Vertical is labeled UP. Horizontal components are labeled by their orientation in degrees east of north (e.g., 0° and 270°). See Figure 7-1 for station position relative to fault rupture.

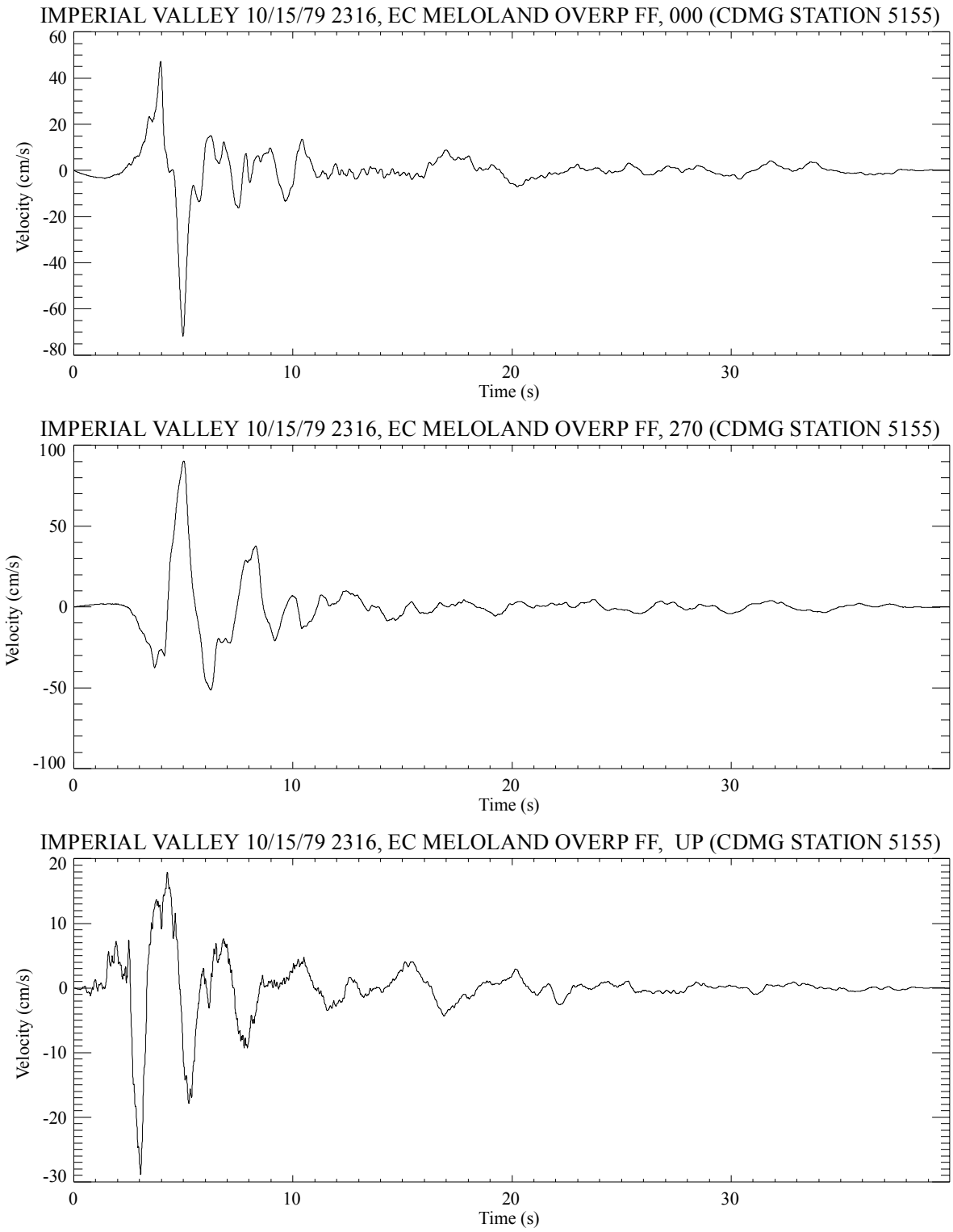

Figure 7-9: El Centro Array station EMO velocity seismograms. Vertical is labeled UP. Horizontal components are labeled by their orientation in degrees east of north (e.g., 0° and 270°). See Figure 7-1 for station position relative to fault rupture.

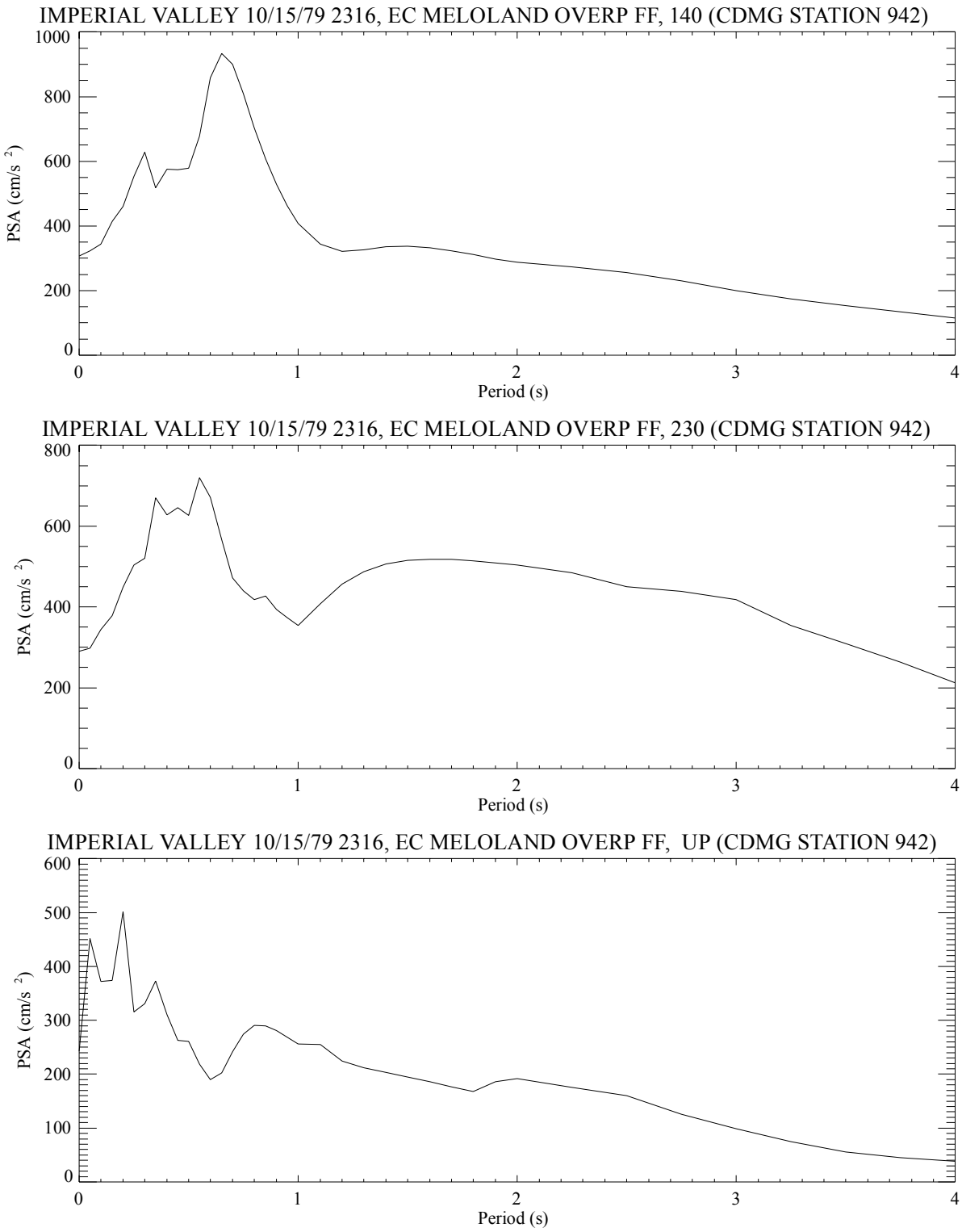

Figure 7-10: El Centro Array station EMO pseudo-acceleration response spectra. Vertical is labeled UP. Horizontal components are labeled by their orientation in degrees east of north (e.g., 0° and 270°). See Figure 7-1 for station position relative to fault rupture.

low-velocity sediments and the basement at Jackson Lake Dam, the large (> 0.5 g) > 2-s-period acceleration responses make physical sense, particularly with respect to the incidence angle criteria of Somerville et al. (2003) for predicting the amplification of long-period motions in low-velocity basin. Sections 7.4 and 7.5 use broadband site recordings of earthquakes at Jackson Lake Dam to evaluate the likelihood of unusually large > 2-s-period acceleration responses at the dam. To reduce ground motion uncertainties associated with ground motion synthesis approaches, the next two sections present and evaluate two source models and ground motion simulation approaches. First, in Section 7.2, the kinematic rupture model of Section 6 is used to simulate near-source ground motions from the 1994 **M** 6.7 Northridge earthquake. A simplified ground motion synthesis technique developed in Frankel (1995) is summarized in Section 7.3 in preparation for its application withe broadband earthquake records to simulation ground motions at Jackson Lake Dam from **M** 7. 1 earthquakes on the northern Teton fault segment in Sections 7.4 and 7.5.

7.2 Performance of the Kinematic Rupture Model

The primary purpose of the synthetic ground motion modeling in this report is to determine peak ground motion responses, ground motion variability, and durations as a function of site position relative to the Teton fault. To establish that the synthetic ground motion modeling approach outlined in Section 6 (in particular, the stochastic kinematic rupture model) provides a reasonable basis to estimate peak ground motions, synthetic Green's function are used to calculate ground motions at near-source sites that recorded strong ground motions from the 1994 **M** 6.7 Northridge, California, blind thrust earthquake using the same ground motion simulation methods used in Section 6.

The peak ground motions at a site near a fault are strongly dependent on the orientation of the fault relative to the site and details of the fault rupture. These differences in peak ground motions are well illustrated using peak velocity and acceleration data from the Northridge blind thrust earthquake (Figure 7-11). Sites located within about 5 km of the fault tip were subjected to updip rupture directivity and typically experienced peak velocities in the 80-160 cm/s range and peak accelerations between 500 cm/s^2 and 1000 cm/s^2. Sites outside this zone experienced peak velocities of less than about 50 cm/s and accelerations generally less than 500 cm/s^2.

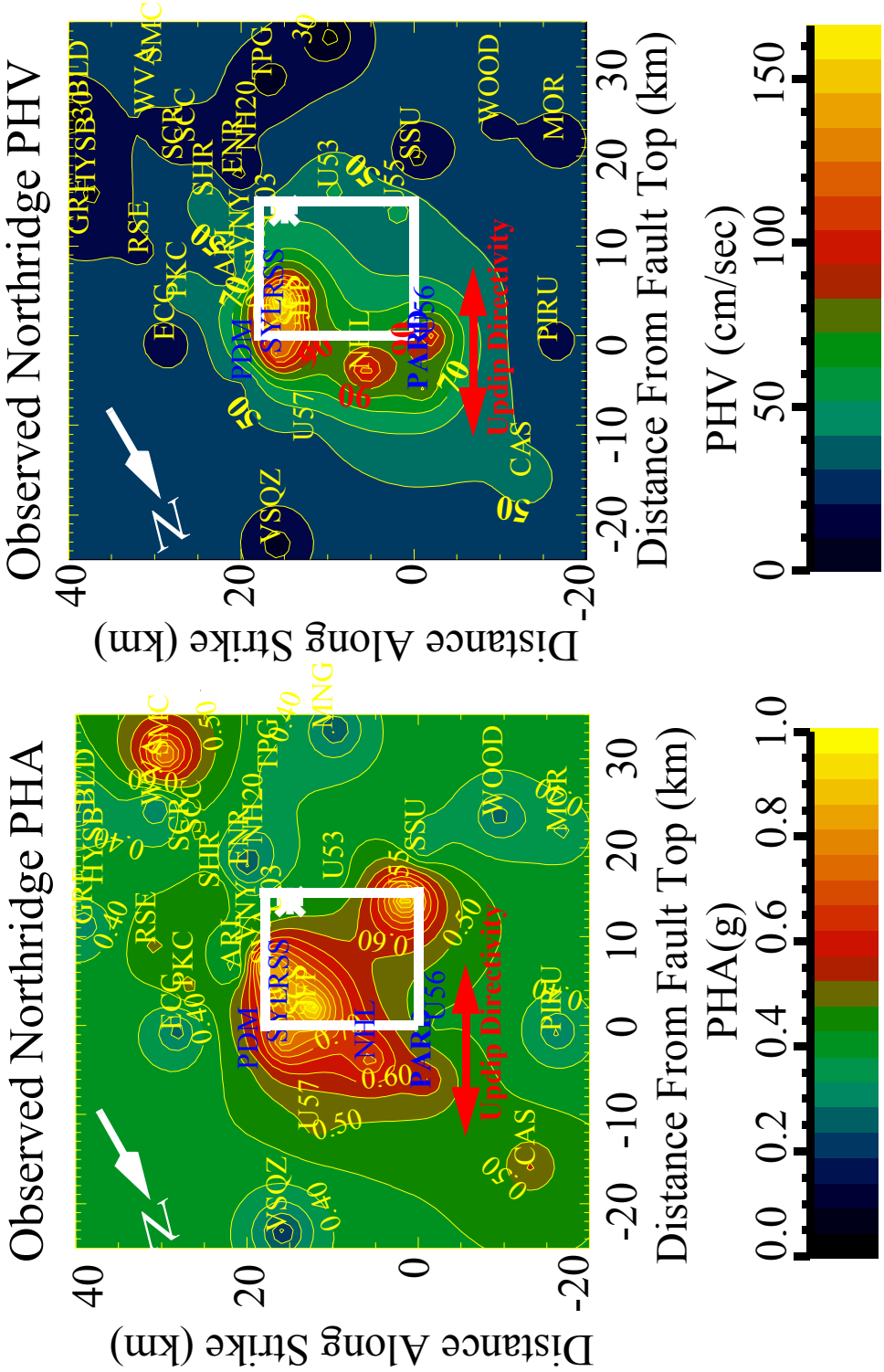

Figure 7-11: Plan view of observed peak velocities and accelerations from the **M** 6.7 1994 Northridge earthquake. The stations used in ground motion model are labeled in blue. The extent of pronounced rupture directivity around the fault tip is shown in red. The white box outlines the surface projection of the fault plane. The top of the fault is to the left at 5 km depth and the fault extends to 20 km depth at a dip of 45 degrees.

While the Northridge earthquake provides a nice illustration of directivity, it is important to realize that there are significant differences between conditions at Northridge and Jackson Lake Dam. However, for the purposes of evaluating the performance of the kinematic rupture model, these differences are probably not important.

7.2.1 Validation Ground Motion Modeling Approach: Green's Functions. Site-specific ground motion recordings were used in Section 6 to simulated strong ground motions. Here, purely theoretical Green's functions appropriate for crustal and site conditions in the near-fault region of the Northridge earthquake are used and it is necessary to discuss them in detail. Bernard and Madariaga (1984) and Spudich and Frazer (1984; 1987) developed the isochrone integration method to compute near-field seismograms for finite-fault rupture models. Isochrones are all the positions on a fault that contribute seismic energy that arrives at a specific receiver at the same time. The simplest way to employ the isochrone method in the near-field is to assume that all significant seismic radiation from the fault consists of direct shear-wave arrivals. This assumption is reasonable in the near-field, particularly for a deeply buried, blind-thrust fault that produces dominantly near-vertical source-receiver paths. A further simplification is to use a simple trapezoidal slip-velocity pulse. Let $f(t)$ be the slip function, For simplicity we assumed $\ddot{f}(t) = \delta(t - t_r) - \delta(t - t_h)$, where t_r is rupture time, and t_h is healing time. Then, all seismic radiation from a fault can be described with rupture and healing isochrones. Surface ground motions velocities, v, and accelerations, a, from rupture or healing can be calculated from (Spudich and Frazer, 1984)

$$v(\boldsymbol{x}, t) = \ddot{f}(t) \otimes \int_{y(t,\boldsymbol{x})} (\boldsymbol{s} \cdot \boldsymbol{G}) c\, dl \tag{7-1}$$

$$a(\boldsymbol{x}, t) = \ddot{f}(t) \otimes \int_{y(t,\boldsymbol{x})} \left[c^2 \left(\frac{d\boldsymbol{s}}{dq} \cdot G \right) + c^2 \left(\frac{dG}{dq} \cdot \boldsymbol{s} \right) + \frac{dc}{dt} \cdot (\boldsymbol{s} \cdot G) \right] dl \tag{7-2}$$

where c is isochrone velocity, $\boldsymbol{s}$ is slip velocity (either rupture or healing), $d\mathbf{q}$ is the spatial derivative, y(t, **x**) defines the isochrone, and **G** is a hybrid ray theory Green's function combined with synthetic 3D scattering functions or microearthquake ground motions recorded at the dam as described below.

Spudich and Frazer (1984) showed that c can be eliminated from (7-1) by integrating along an isochrone over a finite time window defined by the isochrones t - dt and t + dt. By limiting the integration to frequencies lower than 10 Hz (dt = 0.05 s) band-limited ground motions are obtained making the isochrone method useful for qualitatively evaluating accelerations. This approach was used here with a first-order approximation, where (7-1) was reduced to a point-source summation of over the isochrone strip corresponding to the finite time window:

$$v\ (\boldsymbol{x}, t) = \ddot{f}(t) \cdot \int_A \int \boldsymbol{s}_r \cdot \boldsymbol{G}^S \frac{1}{dt} B\left[\frac{(t - t^S)}{dt}\right] dA \tag{7-3}$$

We used this approach to efficiently calculate seismograms for a large number of receiver positions relative to a fault. For the point source integrations, the ray theory portion of $\boldsymbol{G}$ was approximated as

$$G^S(x, \xi) \ = \ \frac{F(x, \xi) \cdot \tilde{W}(x, \xi)}{4\pi\sqrt{\rho(x)\rho(\xi)\beta(x)}\beta(\xi)^{5/2}\sqrt{(x-\xi)^2}} \tag{7-4}$$

where x is the receiver position, ξ is position on the fault, $F(x, \xi)$ is the source radiation term, $\tilde{W}(x, \xi)$ is the free surface amplification factor, ρ is density, and β is the shear-wave velocity. In this approximation, only first shear arrivals are included in the calculation. Although ray spreading factors are simply approximated by the inverse source-receiver distance, a 1D approximation consistent with crustal shear-wave velocities in southern California, was used to calculate, $\beta(\xi)$, takeoff angles for $F(x, \xi)$, and incidence angles for $\tilde{W}(x, \xi)$ to incorporate first-order geometric effects of vertically heterogeneous velocity structure which varied from β=1.7 at the surface to β=3.5 km/s at 9 km depth (details in O'Connell, 1999a). This produced realistic partitioning of S_V velocities between vertical and horizontal components of ground motion.

The amplitude effects of S_V transmission were approximated by computing the median vertical-incidence amplification of a band-limited (0.5-5 Hz) S_V plane wave propagated through a 3D heterogeneous media. A self-similar, fractal correlation model of random spatial variations of crustal seismic velocities with an autocorrelation function, P, of the form

$$P(k_r) \approx \frac{a^n}{1 + (k_r a)^n} \tag{7-5}$$

where a is the correlation distance, k_r is the radial wavenumber, and $n = 3$ was used in a 3D elastic finite-difference calculation to compute S_V transmission amplification through the top 9 km of the crust. The free-surface was omitted since (7-4) was used to calculate free-surface amplification. The 3D randomization of the 1D velocity model was normalized to produce a standard deviation of 5% of β for $ak_r \gg 1$ with $a = 2.5$ km.

O'Connell (1999a) showed that 3D scattering in the upper crust can have a significant influence on the scaling of near-field peak ground motions. Scattering of direct S_V waves by correlated-random crustal velocity variations tends to reduce peak horizontal velocities associated with near-field rupture directivity by increasing the time and phase dispersion of direct S_V waves. Scattering is included here using the 3D finite-difference approach of Graves (1996) to produce synthetic three-component S_V scattering functions. S_V plane waves were propagated at incidence angles of 80° and azimuths of 45° and 135° relative to the strike of the steeply-dipping sedimentary rocks through the upper 2 km of the crust using a velocity structure typical of fold-and-thrust belts (Figure 7-12). Three-component S_V scattering functions were obtained for receiver positions within the high-velocity portion of the velocity model as shown in Figure 7-12. The depth limit of 4 km in the 3D velocity model was dictated by the need to produce scattering functions to a maximum frequency of 10 Hz, the horizontal dimensions necessary to sample a 2.5 km correlation distance adequately (12 km), and the limitations of fitting a 3D elastic finite-difference calculation into computer memory.

The 3D scattering functions were normalized so that the median peak velocity for each component matched the median S_V transmission amplifications derived above. Geometric spreading and free-surface amplification were applied using (7-4). A 3D scattering function was chosen at random at each integration position in the point source summation from a total of 5200 scattering functions used in the ground motion simulations.

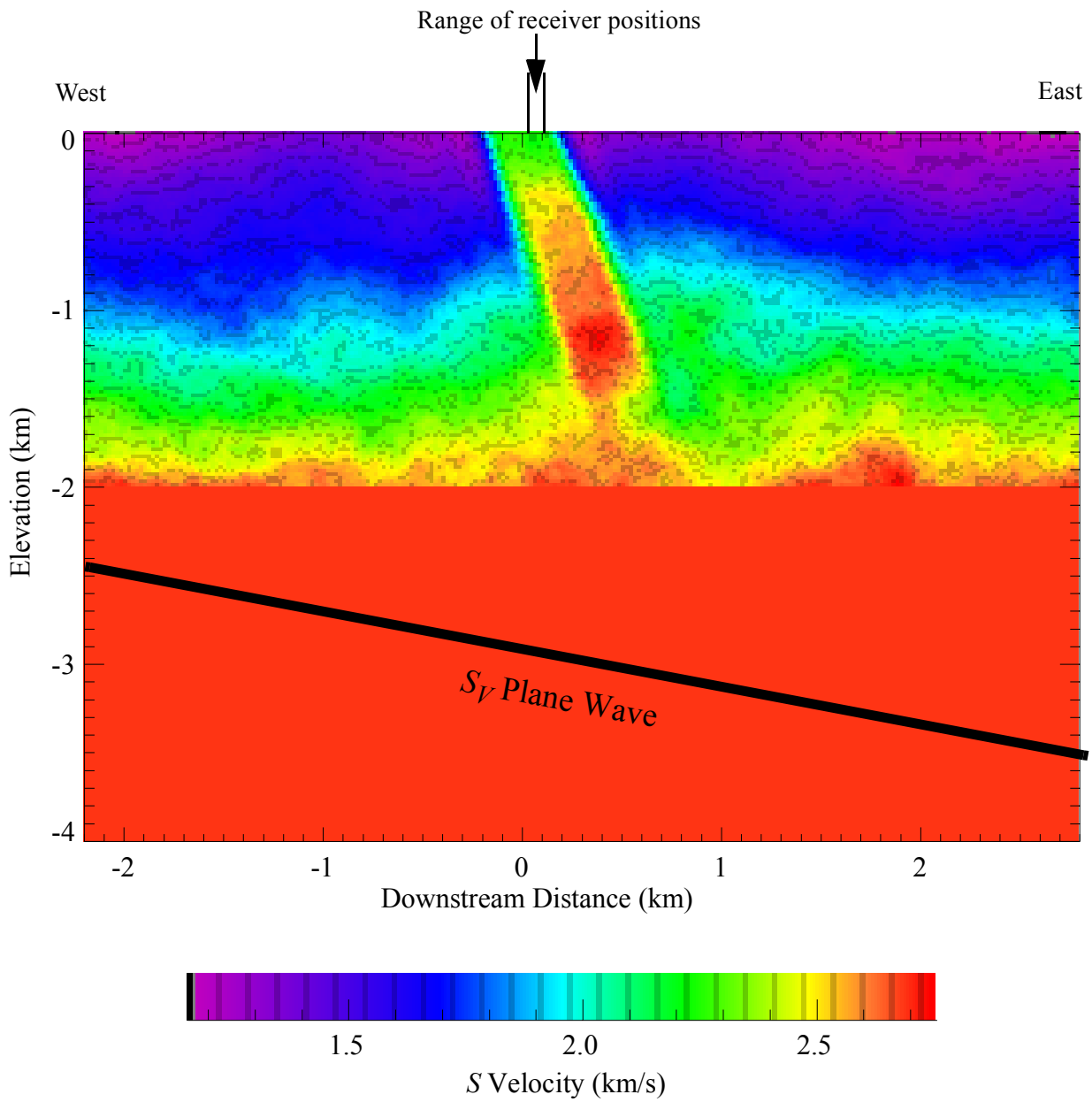

Figure 7-12: *S*-wave velocity profile from a 3D randomization of a 2D velocity model for the top 2 km of the crust. For (7-5) n=2 and a=1 km. A 2 km thick homogeneous region is inserted at the bottom to introduce a uniform amplitude S_V plane wave. The scattering functions for the ground motion simulations were derived using n=3 and a=2.5 km to produce the 3D randomization of the 2D velocity model. The standard deviation of the velocity randomization was set to 5% for all cases. The extent of the region used to extract scattering functions is shown at the top.

The scattering functions possess fairly simple waveforms (see Figures 7-13 and 7-14). The scattering function responses are consistent with the rather simple site responses; coda durations are relatively short, and direct *S* waveforms are fairly simple. Shear-wave splitting is often observed associated with folded sedimentary rocks Consequently, kinematic time-shifting of horizontal components was used to delay east-west polarized, direct *S* waves relative to north-south components using the method described in O'Connell (1999c).

7.2.2 Kinematic Rupture Model Test: Northridge Ground Motions. The synthetic Green's function from Section 7.2.1 are used to provide rock-site synthetic ground motions. A total of 200 random rupture models were generated using the approach in Section 6.2 to simulate strong ground motions at the six stations shown in blue in Figure 7-11. The station naming convention follows Wald et al. (1996). The **M** 6.7 Northridge hypocenter was fixed at a depth of 19 km and 1.5 km from the eastern edge of the fault. Figures 7-15 to 7-20 show the rupture model that produced the best fit to six near-fault strong motion recordings and illustrate detailed aspects of the kinematic rupture model used in Section 6.

A large number of parameters must be specified in the kinematic rupture model. Velocity ground motions are the direct outputs of the simulations, from which, all other quantities, such as accelerations and response spectra, are obtained. Fractal parameterizations of effective stress (Figure 7-15) produce slip velocity models (Figure 7-16) consistent with the dynamic rupture modeling results of Boatwright and Andrews (1998). The rise times (Figure 7-17) are specified using an approach similar to Herrero and Bernard (1994) which makes rise time inversely proportional to effective stress (Figure 7-15). Let k be spectral wavenumber and ω be angular frequency. Resulting fault slip models (Figure 7-18) are consistent with the k^{-2} decay slip behavior proposed by Somerville et al. (1999), based on analyses of slip inversions for recent earthquakes. The synthetic slip models also have displacement spectra with a ω^{-2} spectral decay consistent with Andrews (1980) and Frankel (1991). For the Jackson Lake Dam ground motion simulations, effective stress correlation lengths were increased by 33% relative to the **M** 6.7 Northridge rupture simulations of this section to be consistent with the empirical relations of Somerville et al. (1999), that indicate that asperity size increases with magnitude. Rupture

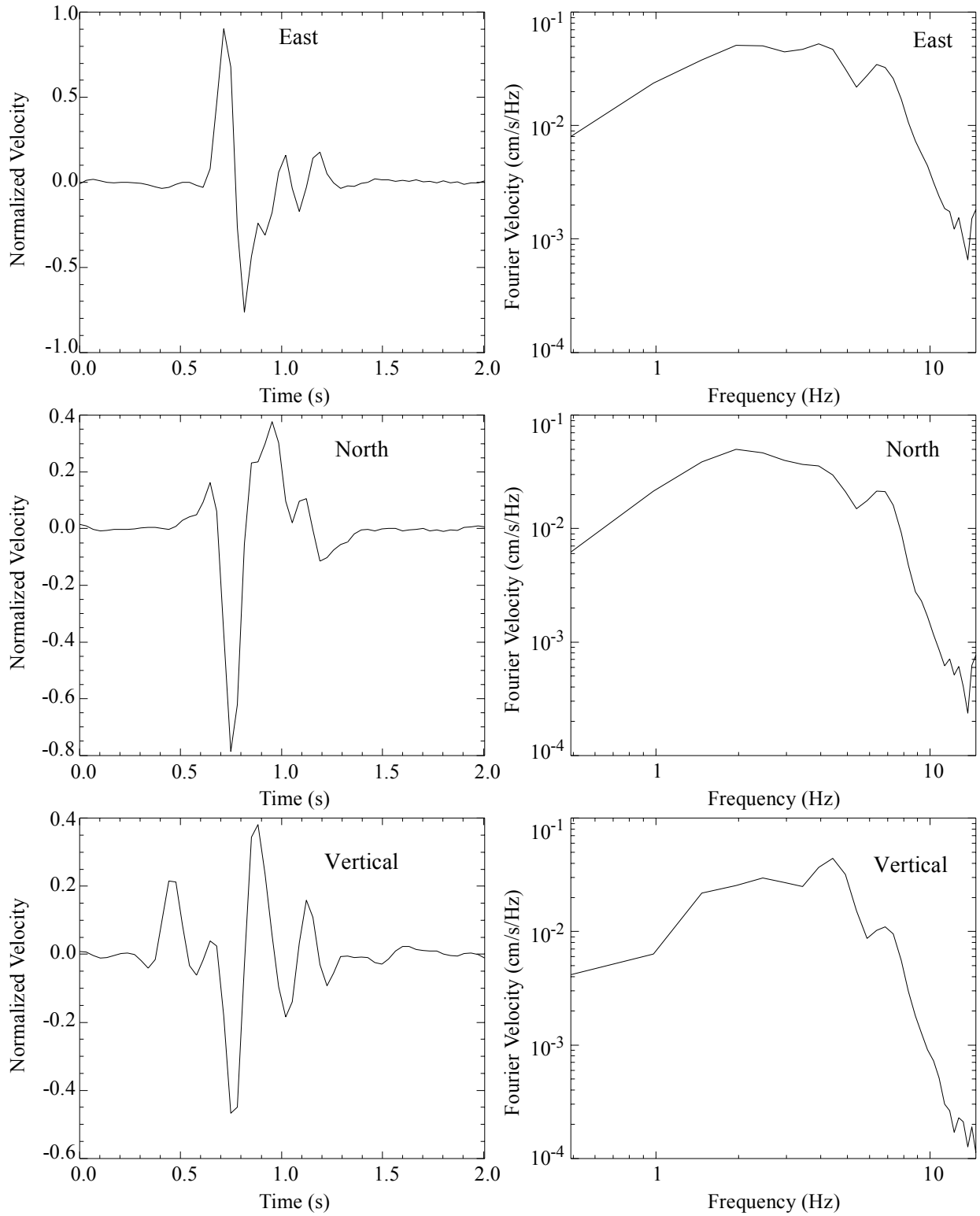

Figure 7-13: First example of a synthetic three-component S_V scattering function.Normalized velocity waveforms on the left and Fourier velocity spectra on the right for the components as labeled.

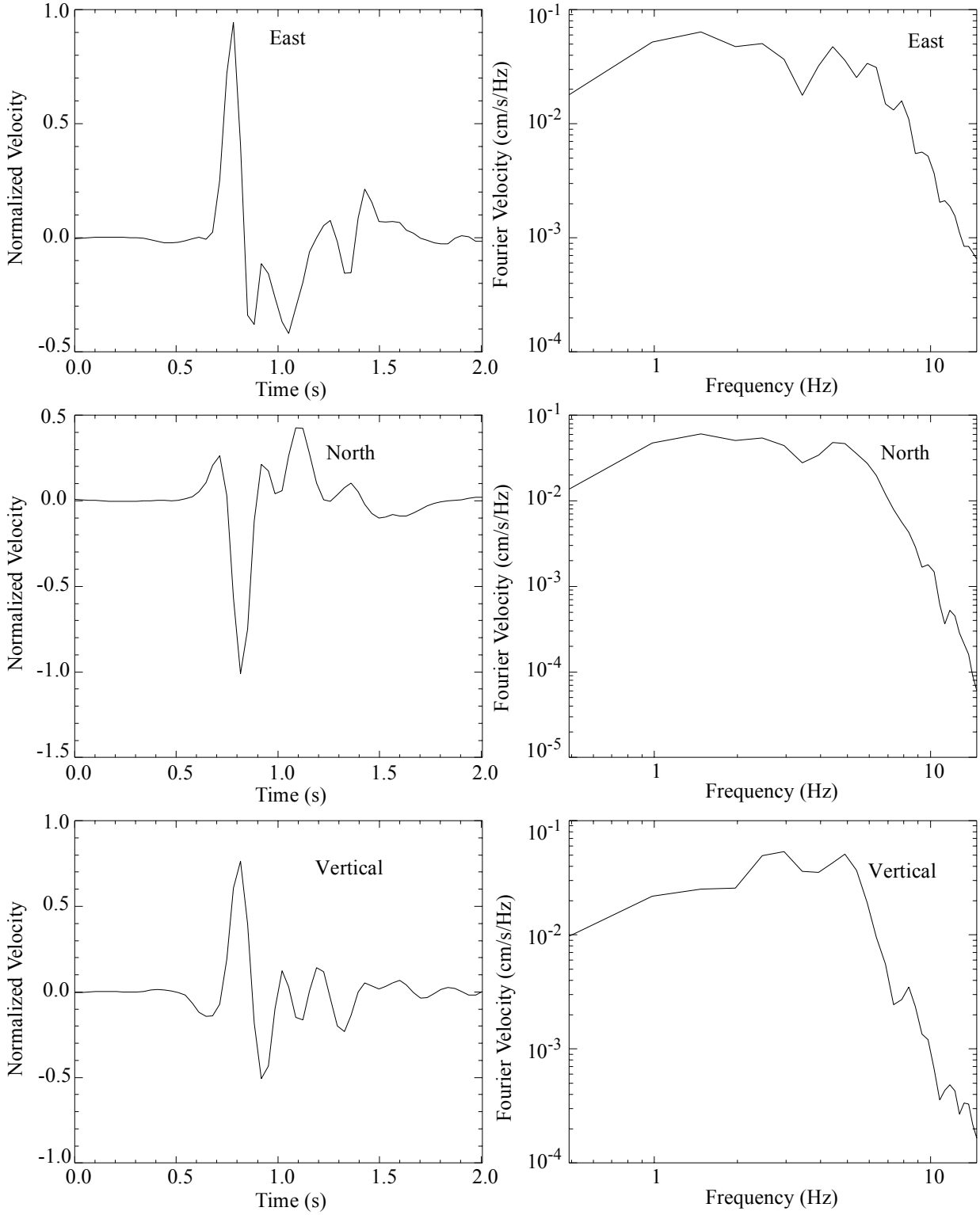

Figure 7-14: Another example of a synthetic three-component S_V scattering function. Normalized velocity waveforms on the left and Fourier velocity spectra on the right for the components as labeled.

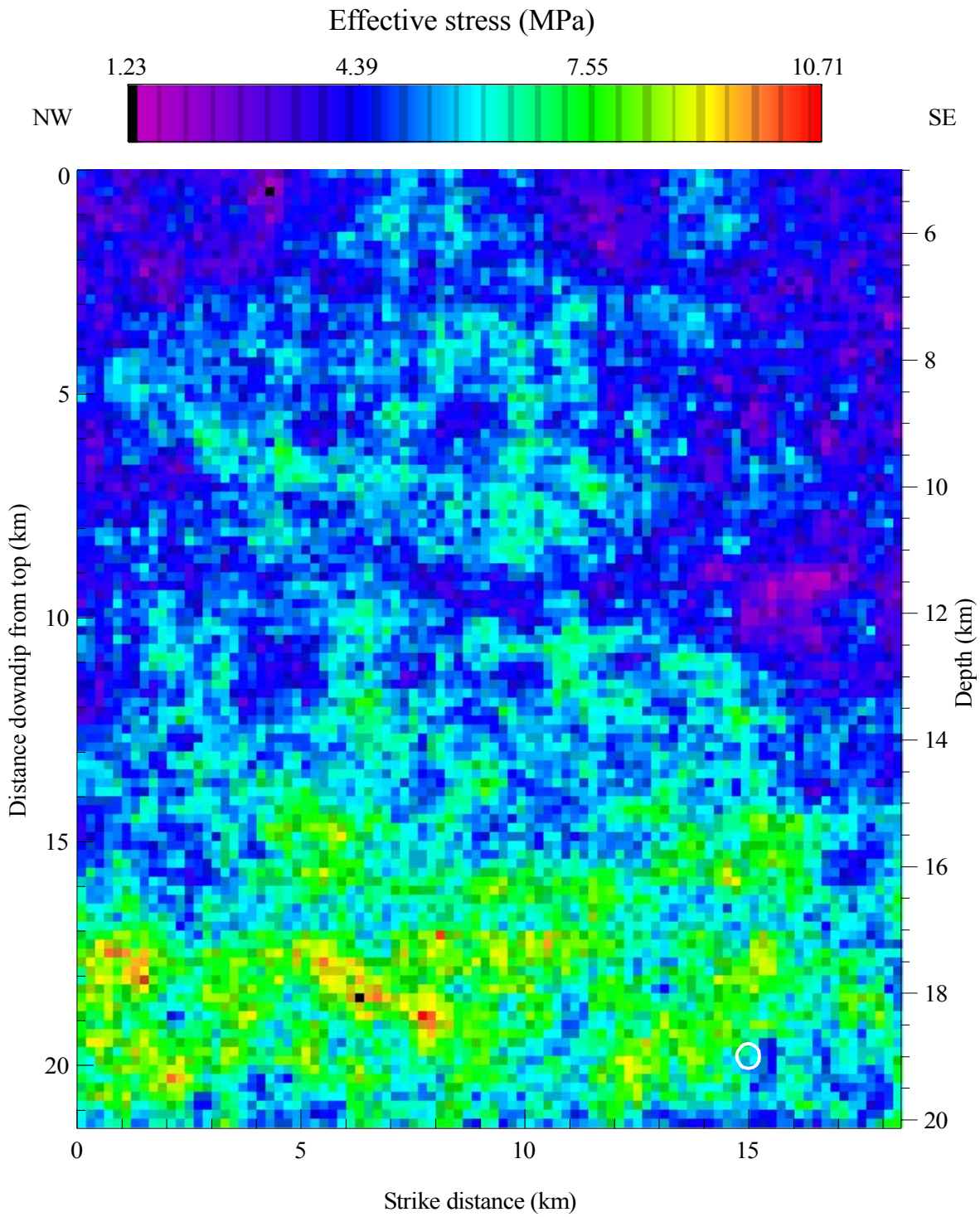

Figure 7-15: Effective stress distribution that produced the best-fitting Northridge ground motions. The effective stress correlation length is 15 km. The perspective is looking down, normal to the fault plane. The hypocenter is the white circle. The fault is discretized using a 0.2 km spacing.

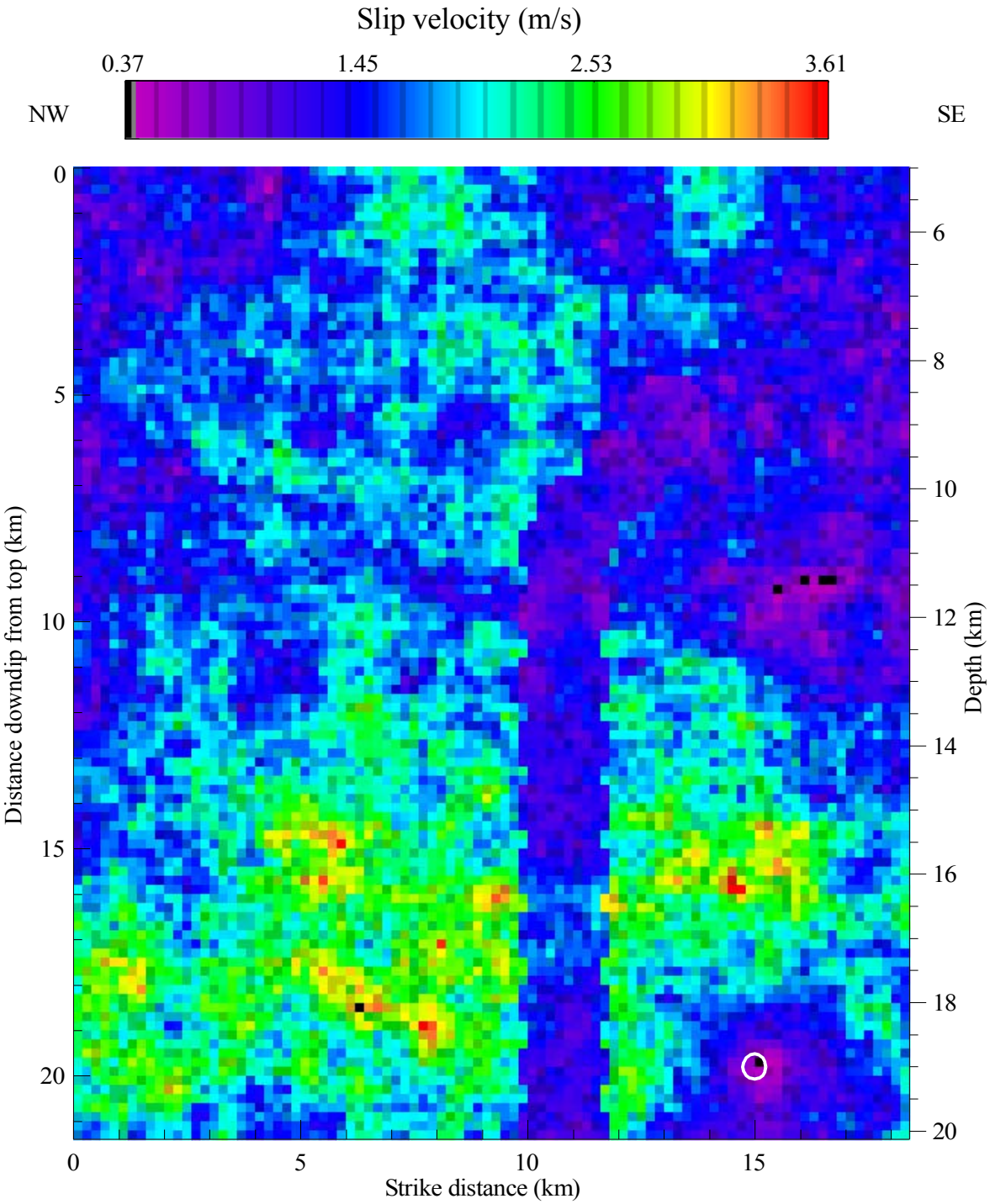

Figure 7-16: Slip-velocity distribution that produced the best-fitting Northridge ground motions. Produced using a effective stress correlation length of 15 km. The perspective is looking down, normal to the fault plane. The hypocenter is the white circle. The fault is discretized using a 0.2 km spacing. The slip velocity increases away from the hypocenter under the influence of a modified Kostrov time function, that is limited to a slip velocity-to-initial-slip-velocity ratio of 4. Slip velocity also depends on rupture velocity (Figure 7-19) and rupture time (Figure 7-20).

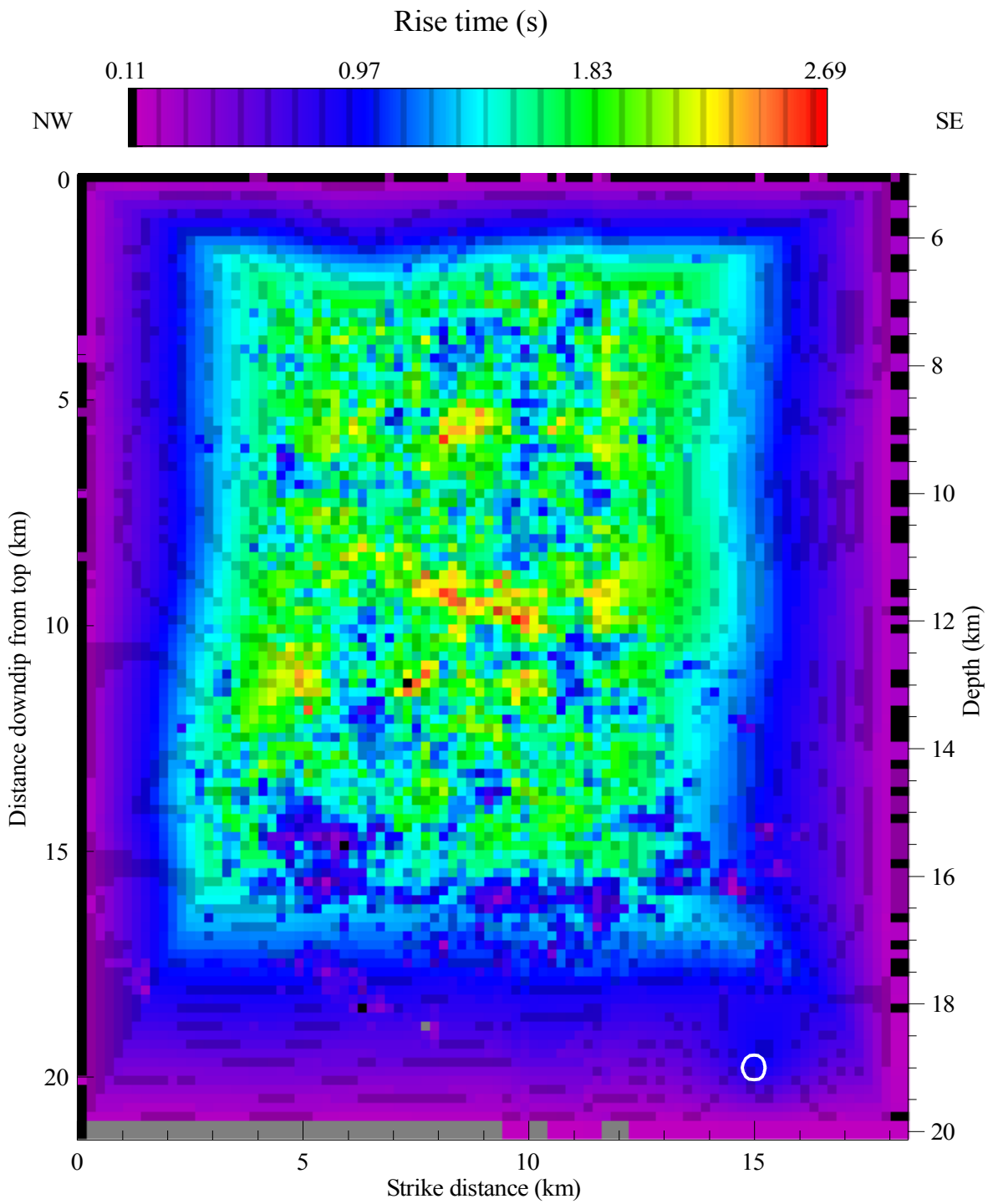

Figure 7-17: Rise-time distribution that produced the best-fitting Northridge ground motion . Since rise time is inversely proportional to slip velocity (Figure 7-16), it is dependent on effective stress (Figure 7-15) and rupture time (Figure 7-20). The perspective is looking down, normal to the fault plane. The hypocenter is the white circle. The fault is discretized using a 0.2 km spacing. The healing of the fault boundaries tapers rise times toward zero at the boundaries, resulting in a tapering of slip toward the boundaries as well (Figure 7-18). In the interior of the fault, rise time strongly inversely correlates with slip velocity (Figure 7-16).

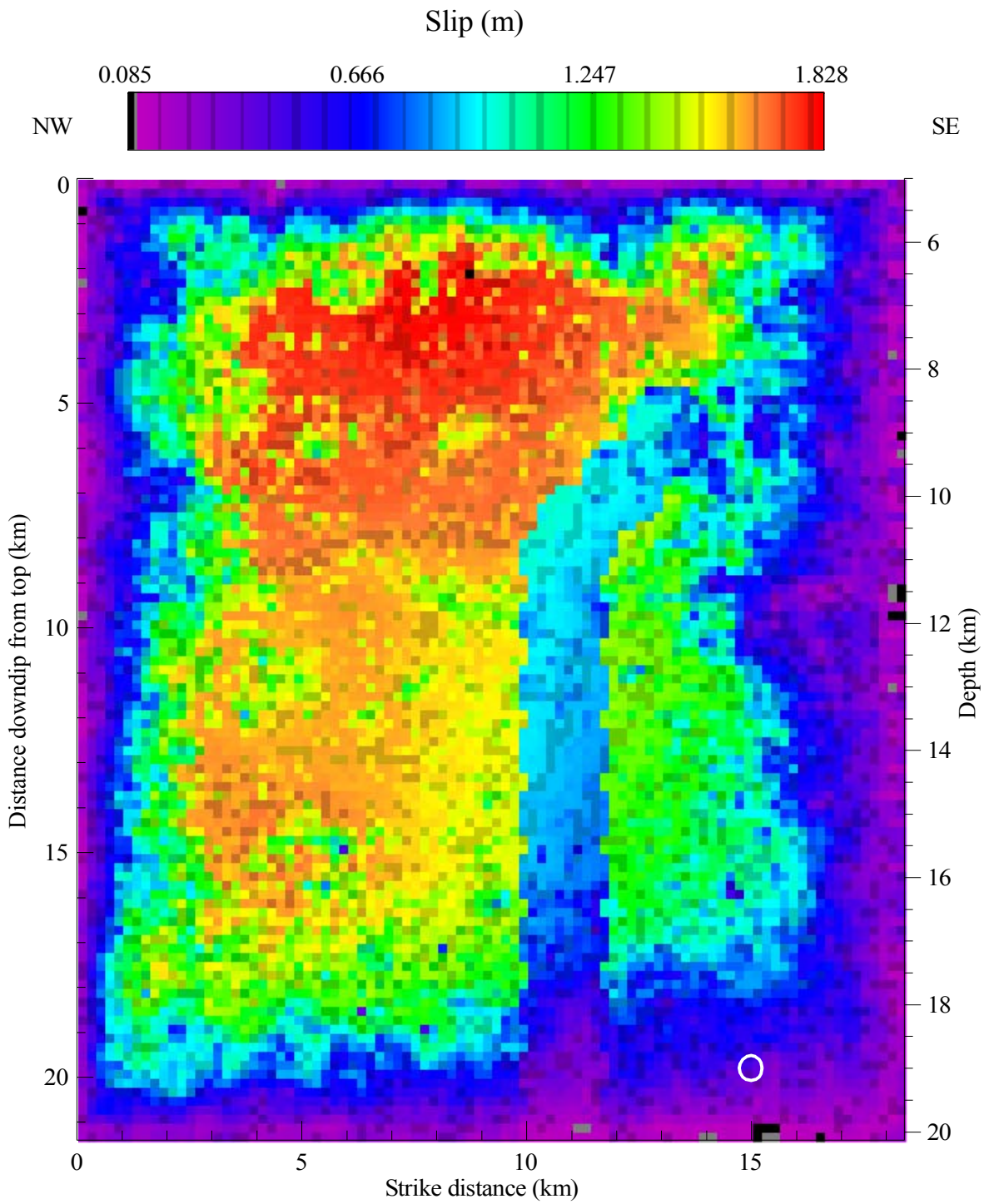

Figure 7-18: Slip distribution that produced the best-fitting Northridge ground motion. Slip is proportional to slip velocity (figure 7-16) and rise time (Figure 7-17), which produces a dependence on effective stress (Figure 7-15), rupture velocity (Figure 7-19), and rupture time (Figure 7-20). The healing of the fault boundaries tapers rise times toward zero at the boundaries (Figure 7-17) resulting in a tapering of slip toward the boundaries as well. In the interior of the fault, rise time strongly inversely correlates with slip velocity (Figure 7-16). Thus, long rise times combined with low slip velocities, or short rise times with high slip velocities, produce relatively uniform slip in the fault's interior.

velocities were allowed to vary over a wide range (between 0.6*β to 1.05*β, see Figure 7-19) to allow rupture directivity caustics to develop, and to produce variable rupture times (Figure 7-20). A large number of assumptions and choices must be made to specify an earthquake rupture models. Some of the interdependencies between different rupture parameters are discussed in the captions of Figures 7-15 to 7-20.

A scale factor of 1.5 was used for the five stiff soil sites since hard-rock site-specific stochastic 3D Green's functions were used at all sites, consistent with the results of Field et al. (1997). The scale factor for the Paicoma Dam (PDM) record was set to one since it's foundation shear-wave velocities of ~2 km/s correspond to a hard rock site. The rupture model that produced the best-fitting synthetic peak azimuth oriented velocity and acceleration horizontal ground motions (Figures 7-21 to 7-26) and response spectra (Figure 7-27) fit the observed data about as well as O'Connell (1999a; 1999c). The stochastic kinematic rupture model and synthetic Green's function reproduce the Northridge near-source strong motion data as well as the deterministic kinematic rupture model of O'Connell (1999a; 1999c).

The region of low rupture velocity west of the hypocenter in Figure 7-19 is required to reproduce the observed delays between the initial shear waves from the hypocentral region and the largest amplitude shear waves that generally occur several seconds later (Figure 7-23 to 7-25). Hartzell et al. (1996) also find a region of relatively low rupture velocity west of the hypocenter in their inversion for slip, rupture velocity, and rake associated with the Northridge earthquake. This region of low rupture velocities is the only deterministic aspect of the Northridge rupture model. All other portions of the model where generated using stochastic methods intrinsic to the kinematic rupture model of Section 6.

The slip model (Figure 7-18) is similar estimated slip from Wald et al. (1996). Hartzell et al. (1996) estimate a greater proportion of slip near the hypocenter. The stochastic rupture slip-velocity model has largest slip-velocities below 14 km depth (Figure 7-16), but the longest rise times are at shallower depths (Figure 7-17) which results in the largest slips occurring at in the top portion of the rupture (Figure 7-18). It may be possible to reconcile the contrasting slip estimates of Wald et al. (1996) and Hartzell et al. (1996), if the Wald et al. (1996) results are more sensitive

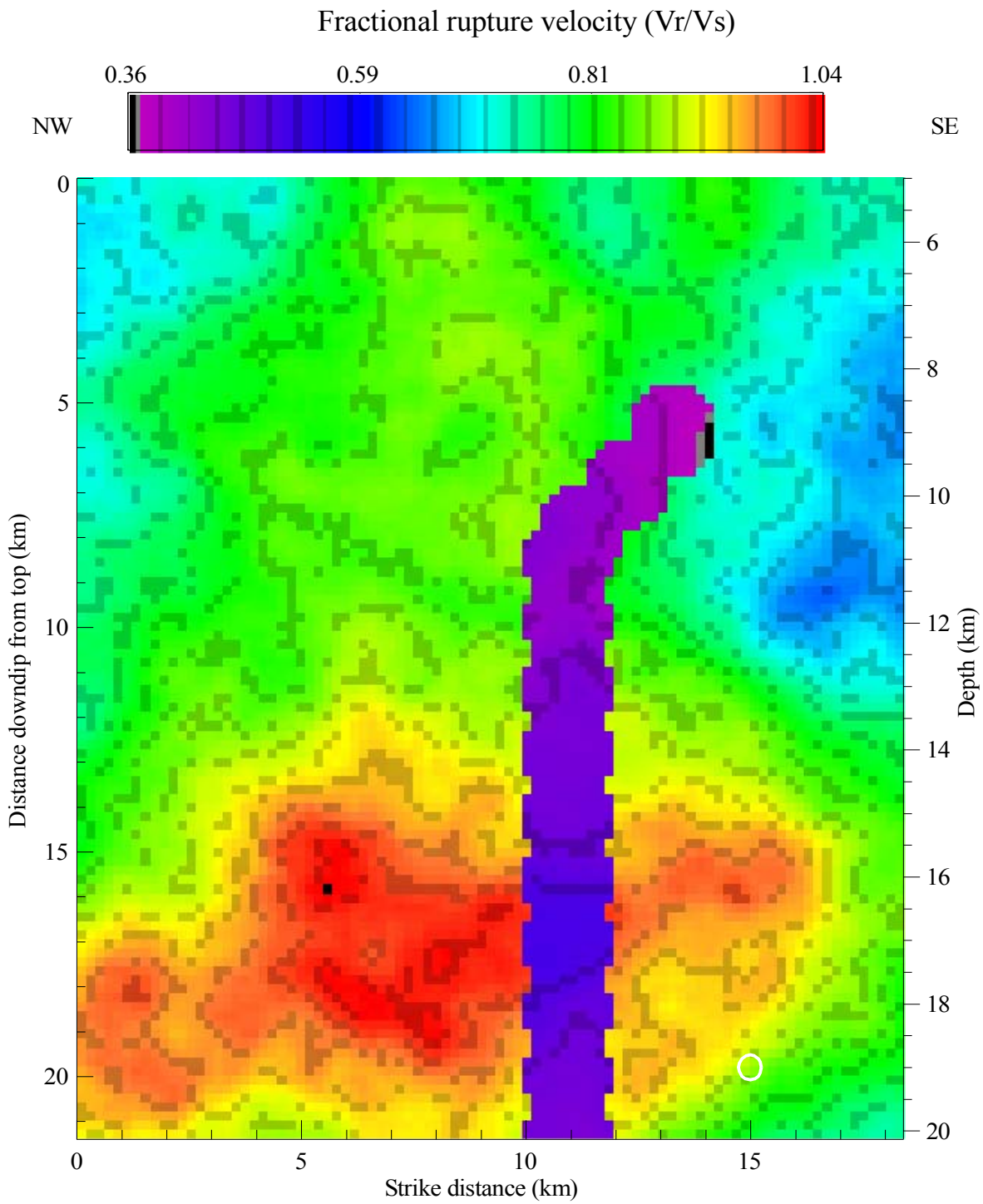

Figure 7-19: Fractional-rupture-velocity distribution that produced the best-fitting Northridge ground motion. Slip velocity (Figure 7-16) is dependent on (V_r/V_s). The perspective is looking down, normal to the fault plane. The hypocenter is the white circle. The fault is discretized using a 0.2 km spacing. A correlation length of 5 km is used to generate the fractal rupture velocity variations. The slip-velocity distribution is produced by effective stresses with 15 km correlation lengths combined with (V_r/V_s) variations produced using 5 km correlation lengths. Thus, the correlation length of slip velocity is intermediate between these two values.

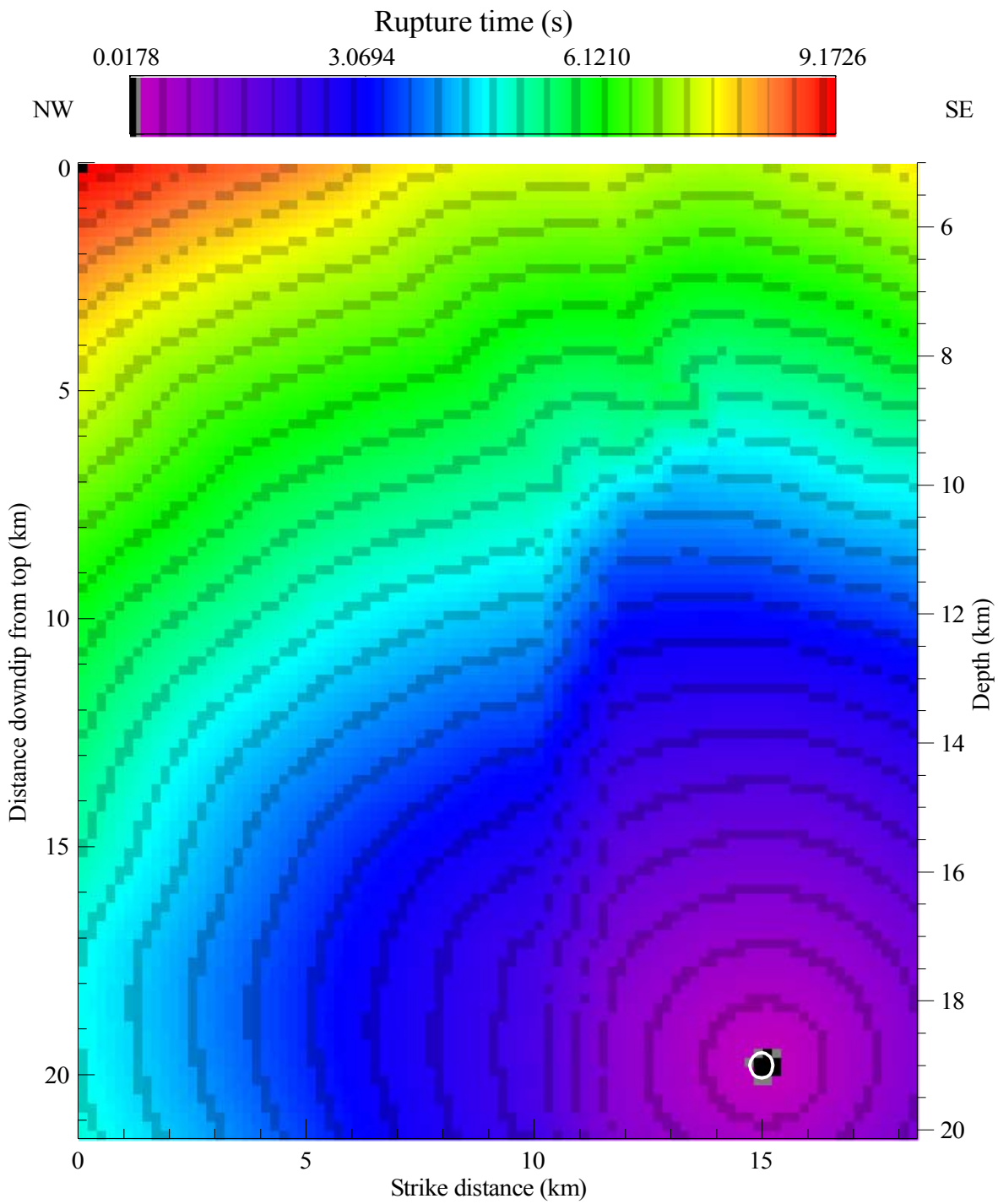

Figure 7-20: Rupture time distribution that produced the best-fitting Northridge ground motion. The 2D eikonal travel-time approach of O'Connell (1999c) is used with V_r/V_s from Figure 7-19 to estimate rupture time. The perspective is looking down, normal to the fault plane. The hypocenter is the white circle. The fault is discretized using a 0.2 km spacing. Without manually inserting regions of systematic rupture as was done for the Northridge simulations here, this approach does not allow for discontinuous rupture velocities that have been inferred for several earthquakes, including the 1984 **M** 6.2 Morgan Hill earthquake (Beroza and Spudich, 1988) and the 1992 **M** 7.1 Petrolia earthquake (Oglesby and Archuleta, 1997).

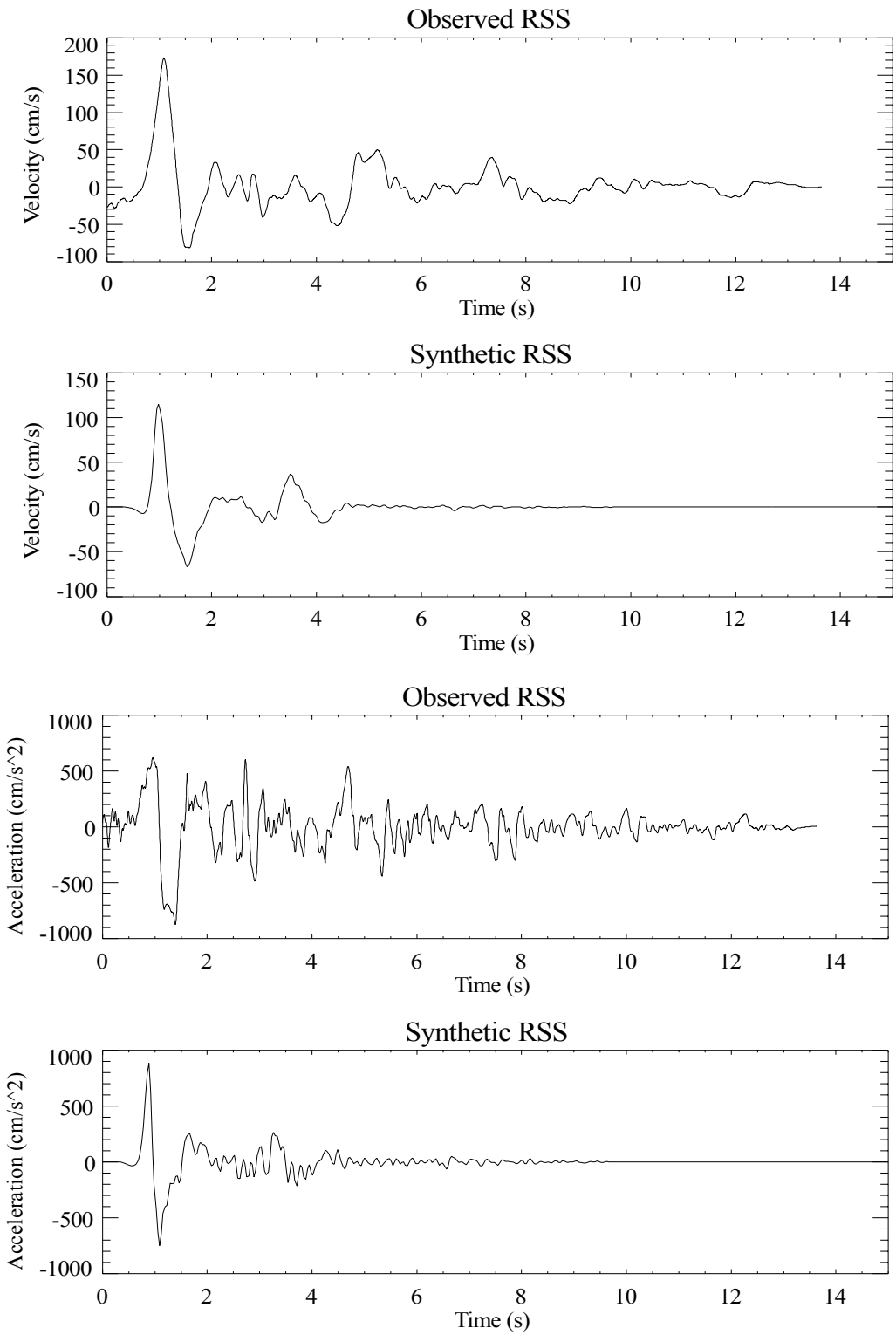

Figure 7-21: Observed and simulated peak horizontal component velocities and accelerations as labeled for station RSS (Rinaldi). Figure 7-11 provides station position.

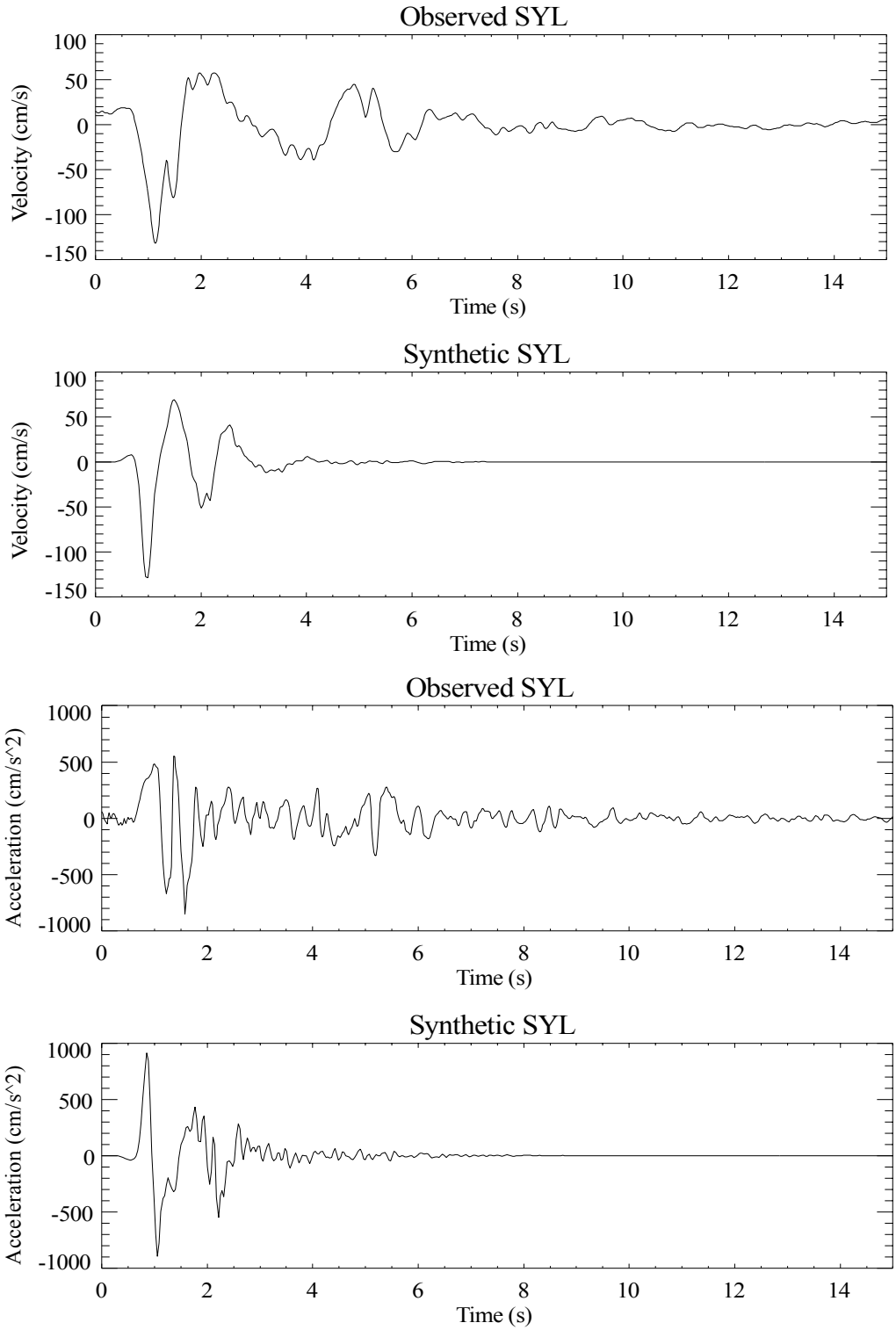

Figure 7-22: Observed and simulated peak horizontal component velocities and accelerations as labeled for station SYL (Sylmar). Figure 7-11 provides station position.

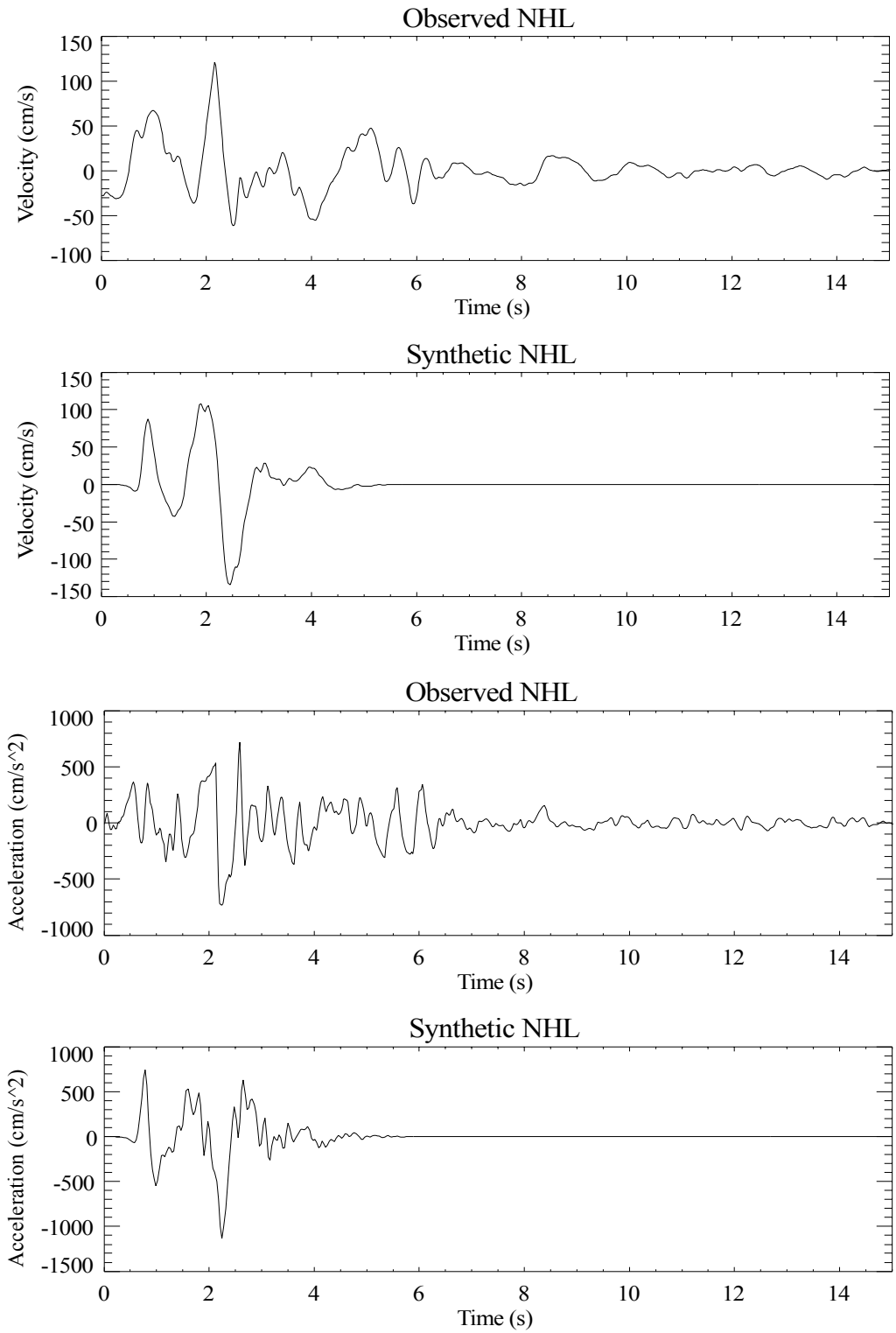

Figure 7-23: Observed and simulated peak horizontal component velocities and accelerations as labeled for station NHL (Newhall). Figure 7-11 provides station position.

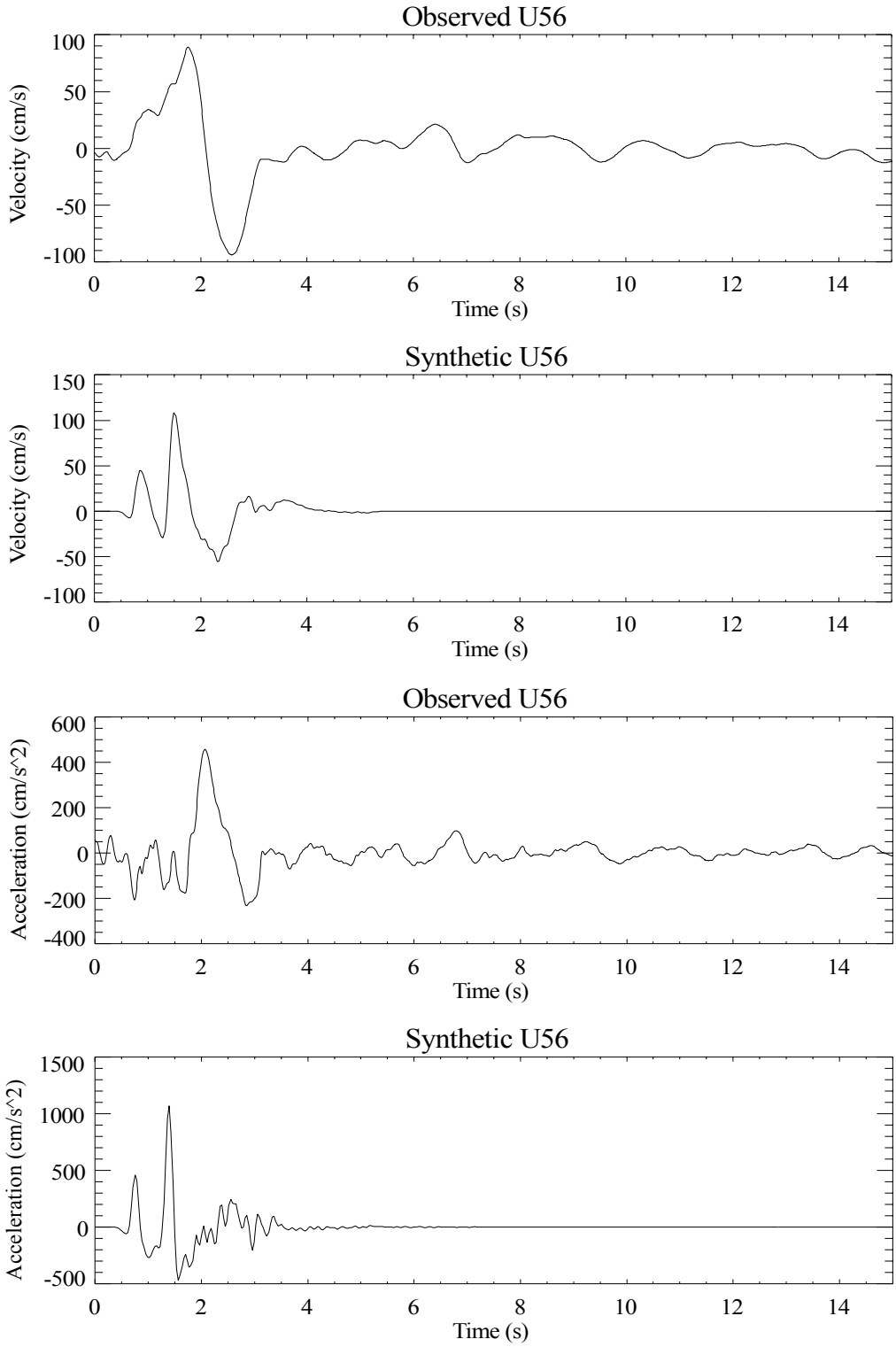

Figure 7-24: Observed and simulated peak horizontal component velocities and accelerations as labeled for station U56. Figure 7-11 provides station position.

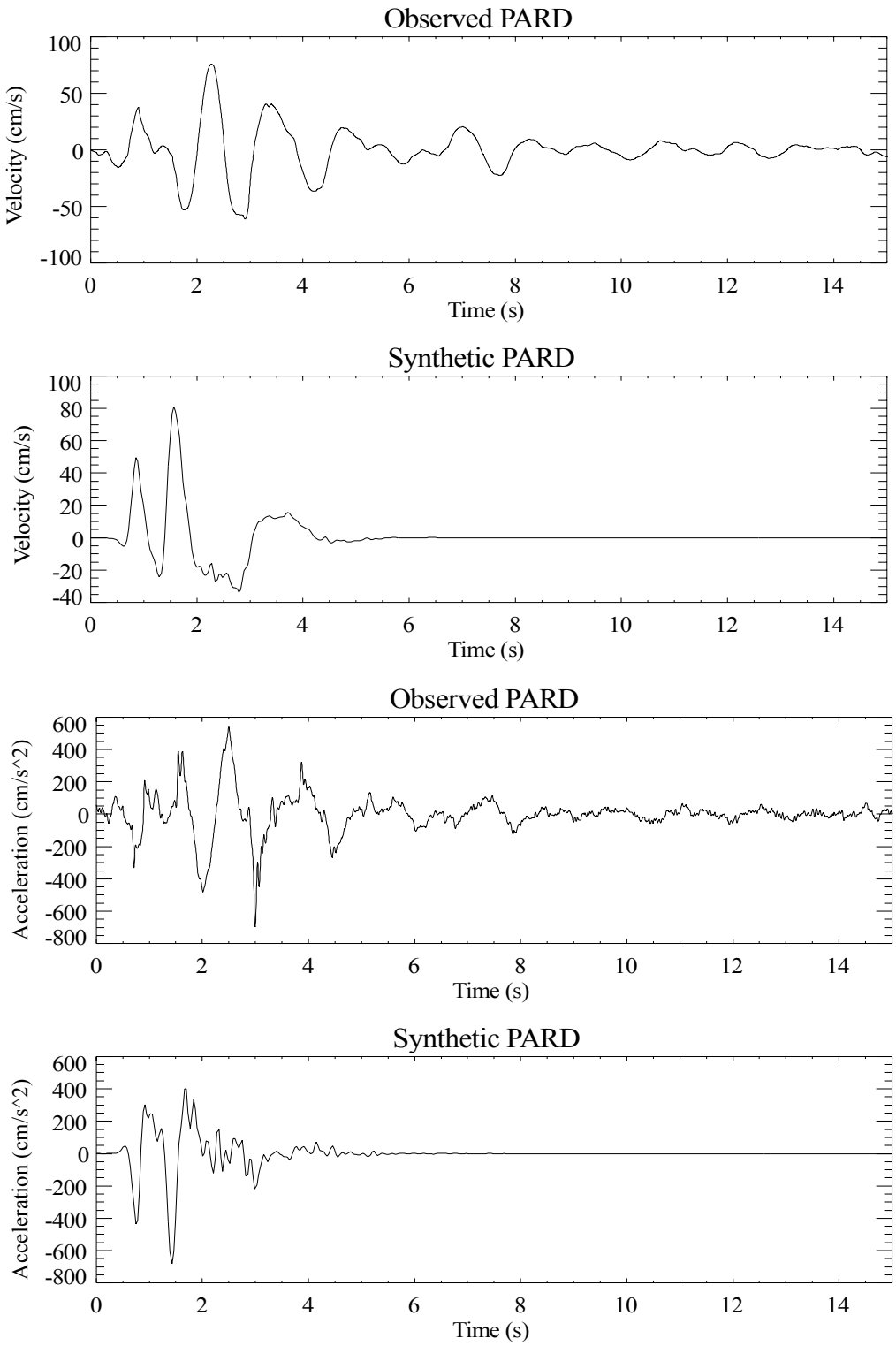

Figure 7-25: Observed and simulated peak horizontal component velocities and accelerations as labeled for station PARD. Figure 7-11 provides station position.

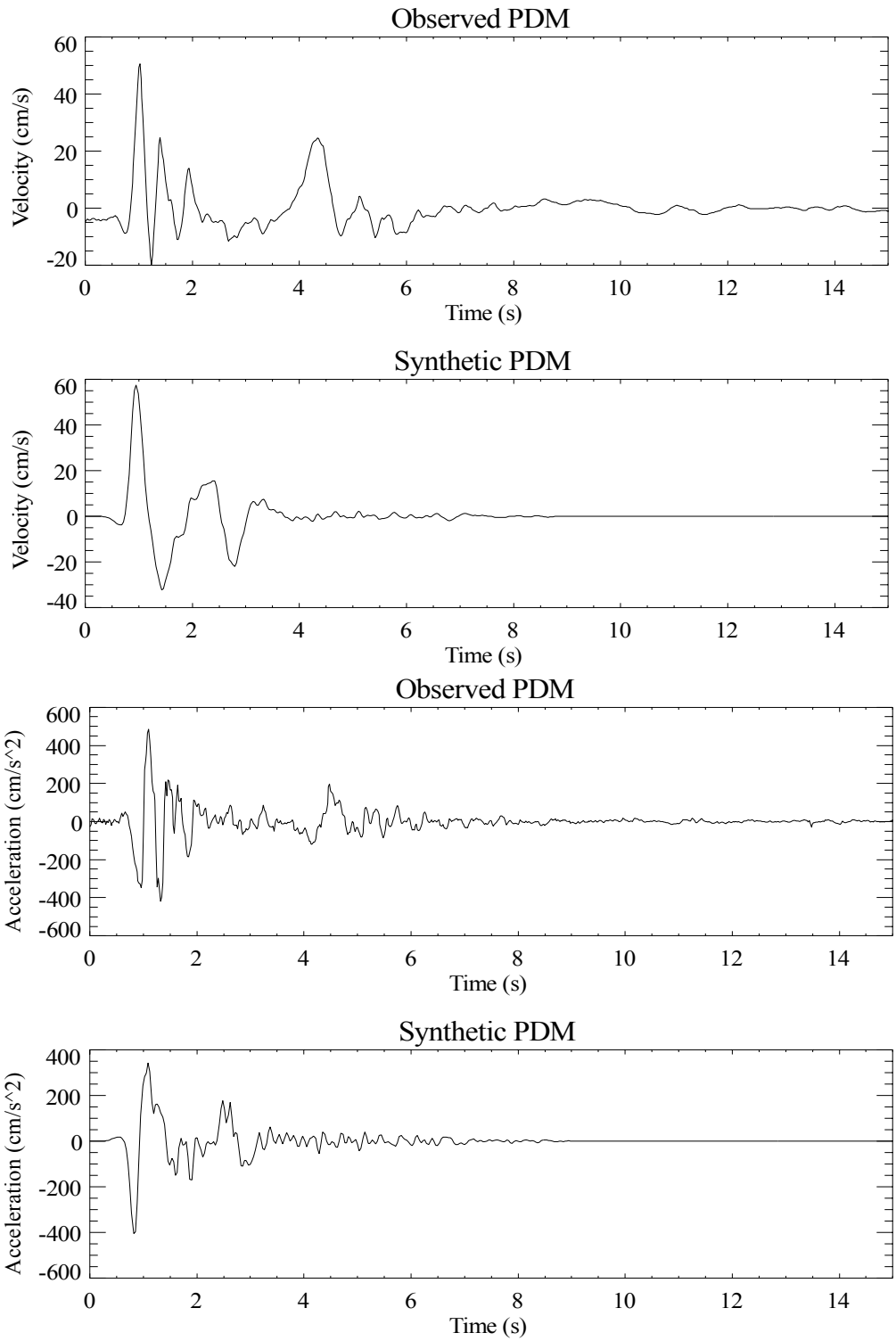

Figure 7-26: Observed and simulated peak horizontal component velocities and accelerations as labeled for station PDM (Pacoima Dam downstream station). Figure 7-11provides station position.

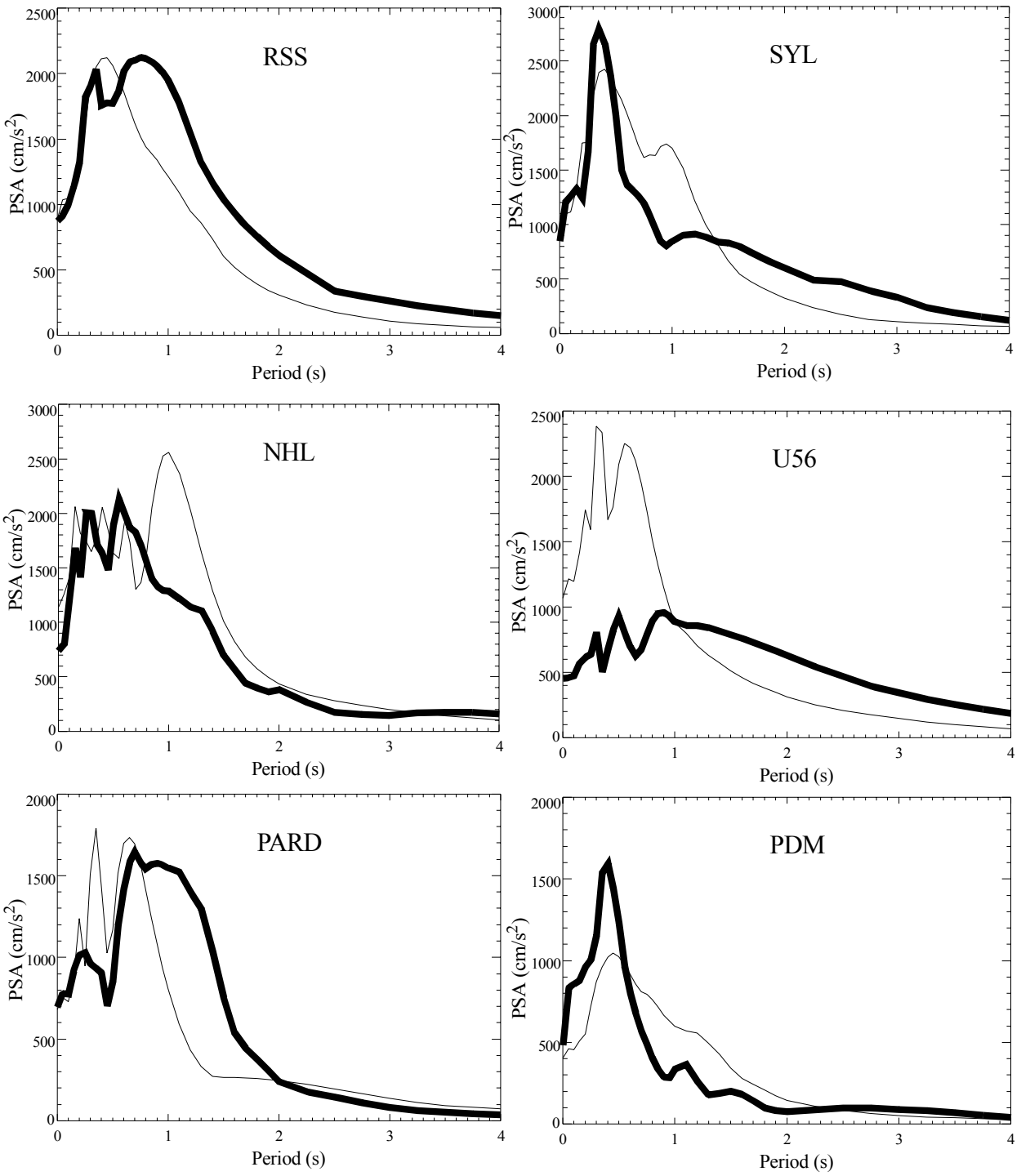

Figure 7-27: Observed and best-fitting Northridge horizontal PSA response spectra. Observed spectra are thick curves and best-fitting synthetic spectra are thin curves. Stations are as labeled.

to total slip, because they include geodetic data, and Hartzell et al. (1996) are more sensitive to slip velocity because they only use strong motion data. Since Hartzell et al. (1996) used an L2 norm their inversion may only weakly constrain rise times because the inversion strongly emphasizes fitting the largest amplitudes. Interestingly, Hartzell et al.'s (1996) inversions for high-frequency radiation intensity are very similar to the slip-velocity patterns in Figure 7-16, with the highest intensities confined to depths > 14 km. Thus, it may be possible that the stochastic Northridge rupture model is compatible with both Wald et al. (1996) and Hartzell et al. (1996). Resolution of these issues would require extensive resolution-trade-off analyses of the various rupture inversion approaches.

The fractional rupture velocities suggest that supershear rupture velocities occurred below 15 km depth over a significant portion of the fault (Figure 7-19). However, a 1D velocity model was used to specify crustal shear-wave velocities in the source model. The 3D shear-wave velocity model of Hauckssson and Haase (1997) shows a strong velocity change between the footwall and hangingwall of the Northridge fault between 15 and 20 km depth, with footwall velocities ~20% higher than hangingwall velocities. Fault rupture propagating at about 85% of the local footwall shear-wave velocities below 15 km depth would appear as slightly supershear rupture relative to the 1D reference shear-wave velocity model. Consequently, the apparently large fractional rupture velocities in Figure 7-19 most likely represent rupture velocities of 80-90% of local 3D shear-wave velocities from Hauckssson and Haase (1997). Using a hybrid global search inversion Hartzell et al. (1996) obtain a similar pattern of rupture velocities as Figure 7-19.

The kinematic rupture model produces a broad range of ground motions as illustrated by the quantile plots for the acceleration response spectra at the six stations (Figure 7-28). The rupture model is clearly capable of produce ground motions larger and smaller than observed during the Northridge earthquake. The Northridge simulations produced PSA natural logarithm variability of ~0.6, consistent with existing ground motion relations (Abrahamson and Silva, 1997; Sadigh et al., 1997; Spudich et al., 1999). For instance, the synthetic model suggests that the Rinaldi (RSS) ground motions correspond to 84% quantiles for the Northridge rupture geometry and that most of the observed near-fault ground motions represent near-median expectations based on the simulations. Thus, the stochastic kinematic rupture model produce ground motions consistent

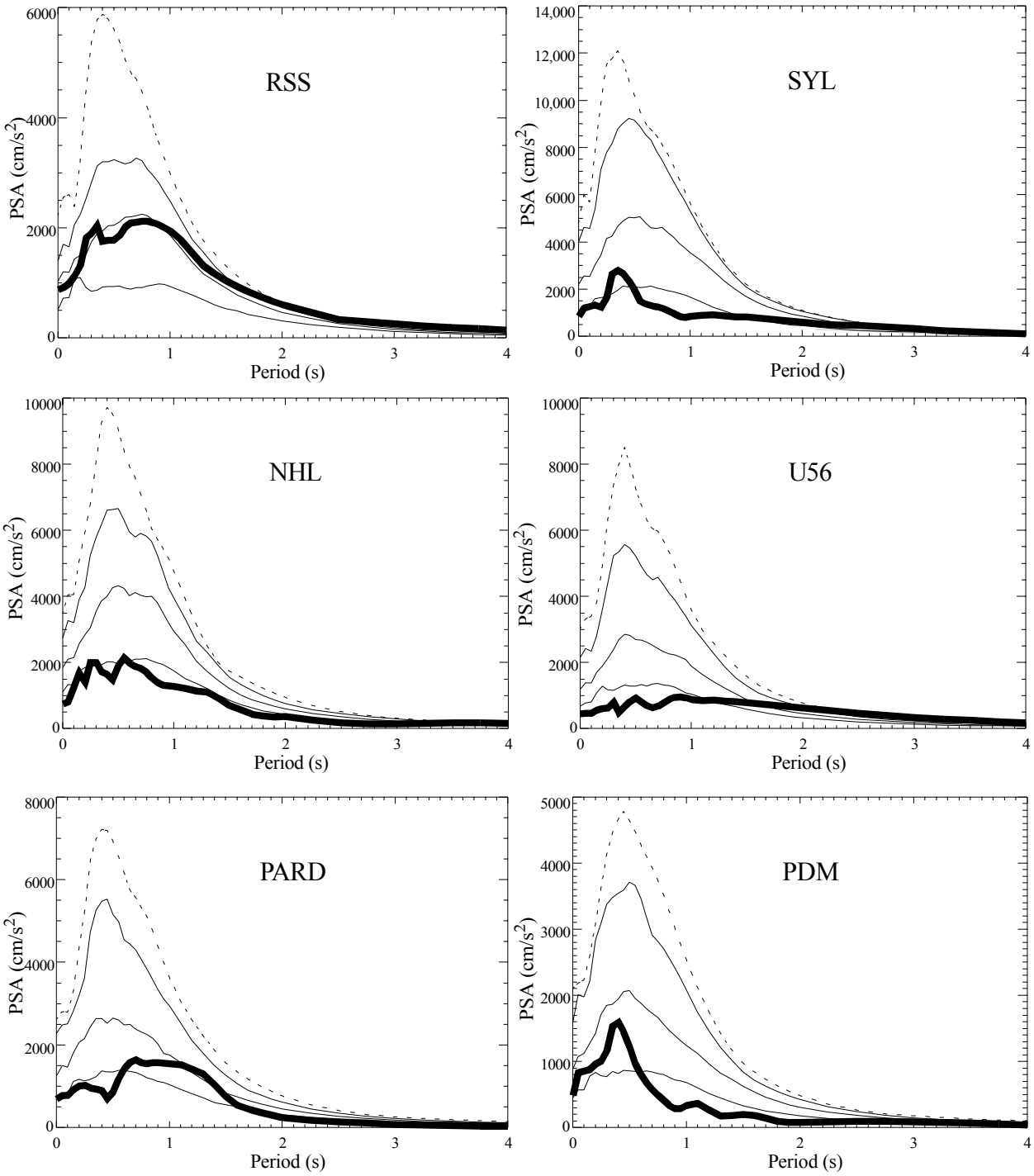

Figure 7-28: Statistical synthetic PSA results. Observed Northridge horizontal PSA response spectra are thick curves, synthetic PSA response spectra quantiles are thin curves, and the envelopes of the maximum amplitudes are dashed curves for stations as labeled. The quantiles from lowest to highest are 0.5, 0.84, and 0.975.

with statistical expectations. Some stochastically-generated kinematic rupture models may be physically unrealizable (see Oglesby and Day, 2002) but this is a problem common to all kinematic rupture models. The waveform-fitting and PSA spectral performance tests indicate that the stochastic kinematic rupture model used to estimate ground motions in Section 6 performs as well or better than other published kinematic rupture models (Silva and Lee, 1987; Somerville et al., 1991; Schneider et al., 1993; Heaton et al., 1995; Jarpe and Kasameyer, 1996; Zeng et al., 1994; Beresnev and Atkinson, 1997; Zeng and Anderson, 2000) for predicting realistic near-source ground motions. The only differences between the Northridge rupture models and the Teton fault rupture models, besides obvious differences in fault geometry, were that no regions of very low rupture velocity (< 0.6*Vs) where used for the Teton fault rupture simulations and correlation lengths for effective stresses and other fault parameters where increased 33% to account for the differences in magnitude between Northridge (**M** 6.7) and the northern Teton fault segment (**M** 7.1), an approach consistent with the findings of Somerville et al. (1999). Confirmation that the synthetic ground modeling approach used in Section 6 can reproduce near-source ground motions from Northridge provides a justification to use the approach to consider other dip-slip earthquake rupture geometries, including modeling ground motions associated with normal-slip earthquakes on the Teton fault.

7.3 Alternative Ground Motion Synthesis Approach of Frankel (1995)

Frankel (1995) developed a ground motion synthesis approach that is relatively simple, consistent with fundamental constraints on earthquake source properties, and reproduced near-fault ground motions from the 1989 **M** 7.0 Loma Prieta earthquake using aftershocks as empirical Green's functions (EGF), an approach pioneered by Hartzell (1978). The information necessary to synthesize ground motions are the moments of the mainshock and the EGF earthquake, the focal mechanism and corner frequency of the EGF earthquake, the distance of the EGF earthquake from the site, the geometry of the mainshock fault surface, fault rupture times, shear-wave travel times from the fault to the site, and a model for the spatial variability of stress drop on the mainshock fault surface. Compared to the source model presented in Section 7.2, Frankel's (1995) approach is much simpler; it does not require explicit specification of parameters such as slip, slip velocity, or rise time.

Let M_{0main} be the moment of the mainshock, M_{0small} be the moment of the EGF earthquake, and A_{main} be the fault area of the mainshock. Frankel's (1995) ground motion synthesis approach consists of the following steps:

1. Calculate the empirical Green's function fault area using the ratio of the EGF moment to the target mainshock moment in a manner to preserve constant stress-drop scaling. This is done by dividing the mainshock fault area into square cells (subfaults) with dimensions h by h, where h^2 is the area of the smaller EGF earthquake. The estimate of h is derived from

$$h^2 = \left(\frac{M_{0small}}{M_{0main}}\right)^{2/3} A_{main} \tag{7-6}$$

2. Sum the EGF of subfault patches distributed over the mainshock fault surface with appropriate delays for rupture times and shear-wave propagation times and scaling at each fault EGF patch by the ratio of the local stress drop to the mean EGF stress drop to obtain ground velocity as

$$\dot{u}(\mathbf{X}, t) = \sum_{i=1}^{N} \left(\frac{R_0}{R_i}\right)\left(\frac{\Delta\sigma_i}{\Delta\sigma_{small}}\right) g(t - t_{si} - t_{ri}) \tag{7-7}$$

where $g(t)$ is the EGF velocity seismogram at the receiver site, $\mathbf{X}$, N is the number of square cells on the mainshock fault, $\Delta\sigma_i$ is the cell stress drop, $\Delta\sigma_{small}$ is the stress drop of the EGF earthquake, t_{si} is the travel-time from the center of the subfault cell to the receiver, calculated using the 3D shear-wave velocity model from Section 4, and t_{ri} is the rupture time calculated using the kinematic rupture model outlined in Sections 6 and 7.2, R_0 is the distance of the EGF recording site from the EGF hypocenter, and R_i is the distance from the EGF recording site from the subfault cell on the mainshock fault.

3. Apply a minimum phase convolution operator to $\dot{u}(t)$ from (7-7) to scale frequencies less than the EGF corner frequency to produce the correct proportion mainshock longer-period energy relative to the EGF earthquake a relative slip-velocity with the spectrum

$$S(f) = C\frac{1 + (f/f_{0small})^2}{1 + (f/f_{0main})^2} \tag{7-8}$$

where f is frequency, f_{0small} is the corner frequency of the EGF earthquake, and f_{0main} is the corner frequency of the mainshock. The term C is chosen so that the total moment of the summed subevents is the same as the mainshock moment using

$$C = \frac{M_{0main}}{\sum_{i=1}^{N} \frac{\Delta\sigma_i}{\Delta\sigma_{small}} M_{0small}} \tag{7-9}$$

where f_{0main} is determined to produce a unity spectrum for frequencies greater than the small earthquake f_{0small} using

$$f_{0main} = \frac{f_{0small}}{\sqrt{C}} \tag{7-10}$$

Frankel (1995) notes that f_{0main} is proportional to $(M_{0small})^{-1/6}$. While this is an undesirable feature of Frankel's approach, since the corner frequency of the mainshock will depend on the moment of the EGF earthquake, it is not a practical concern for Jackson Lake ground motions for periods < 6 s.

The spectral factorization method of Claerbout (1976) is used to find the minimum phase operator with the spectrum from (7-8). This produces a relative slip-velocity function that starts with a delta function (Figure 7-29) to preserve high-frequency response followed by a long-period pulse to increases energy at frequencies less than the EGF corner frequency. The function in Figure 7-29 is not the slip-velocity function of the mainshock, but is essentially the mainshock slip-velocity function deconvolved using the source-time function of the EGF earthquake (Frankel, 1995). The final step is to high-pass filter the estimated ground motions using corner frequencies dictated by the signal-to-noise characteristics of the EGF earthquake recordings. Specific filter corner frequencies are listed in subsequent sections for each EGF earthquake considered.

Andrews (1980) and Frankel (1991) showed that correlated-random spatial stress drop variations on faults are necessary to reproduce ground motion characteristics, particularly the squared

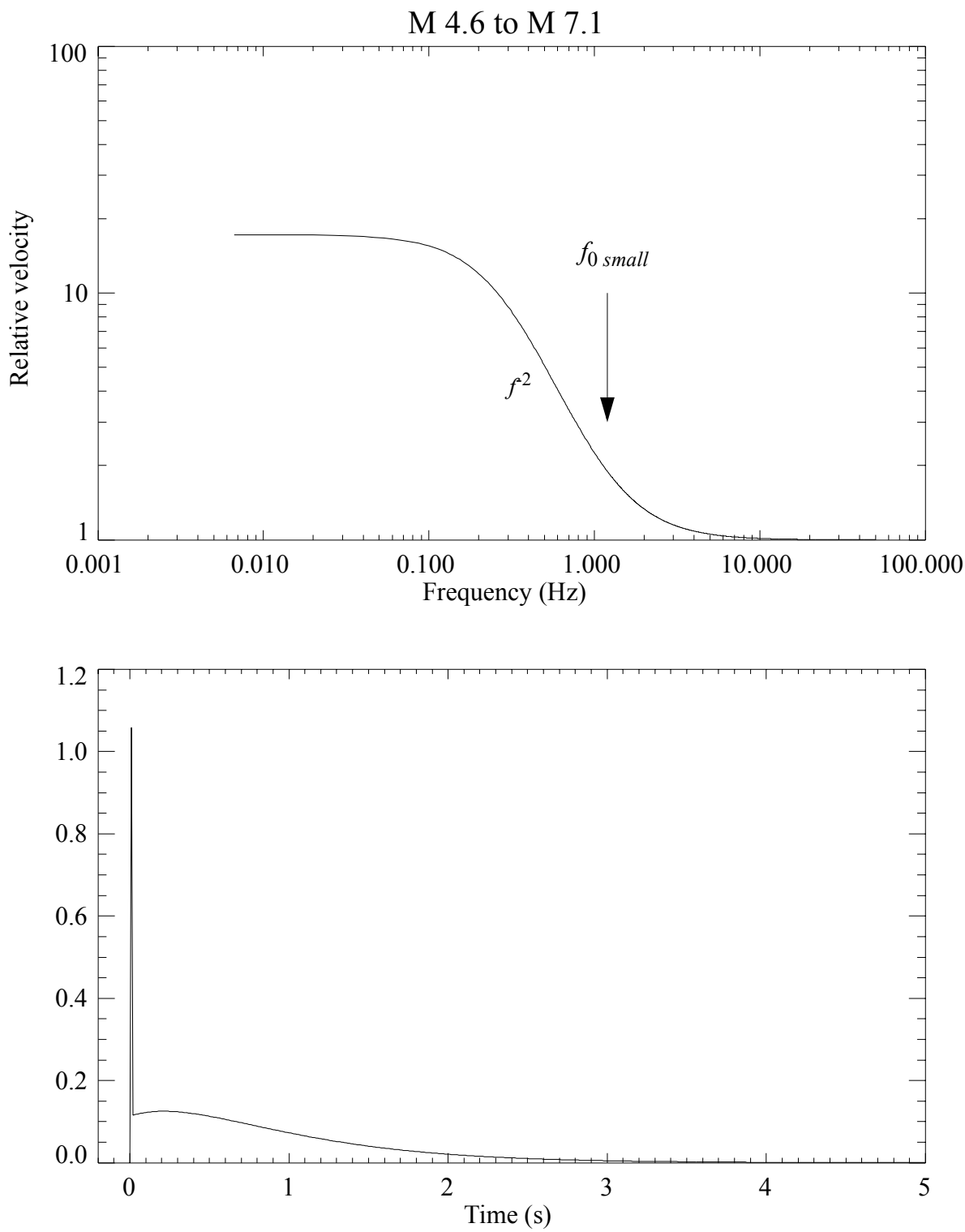

Figure 7-29: Example of relative slip-velocity function. (a) is the Fourier spectrum of the relative slip-velocity function for converting a **M** 4.6 EGF to a **M** 7.1 mainshock. The corner frequency ($f_{0\ small}$) of the M 4.6 EGF is denoted by the arrow. (b) Minimum phase relative slip-velocity function corresponding to the spectrum in (a).

frequency spectral decay of ground displacement amplitudes with increasing frequency for frequencies greater than a corner frequency which is inversely proportional to fault rupture dimensions. Estimated ground motions implicitly include EGF effective stresses. If EGF effective stresses are considered representative of mean effective stresses for a region, there is no need to explicitly specify effective stresses. Instead, spatial variability of effective stresses on the fault about the EGF effective stress are specified as indicated in Andrews (1980) and Frankel (1991) using correlation distances that produce dominant asperity dimensions consistent with the asperity size-magnitude relations of Somerville et al. (1999). As shown in Frankel (1995) synthesized ground motions are only modestly dependent on stress drop characteristics. A range of possible rupture velocities (e.g., subshear to supershear as discussed in Ben-Zion, 2002, and O'Connell and Ake, in press) is easily incorporated into rupture time estimates. In all Jackson Lake Dam ground motion simulations in this report, correlated-random Gaussian variations of rupture velocities are constrained to values between 0.6*Vs(z) and 1.1*Vs(z) with a mean value of 0.85*Vs(z), where Vs(z) represents variations in shear-wave velocity with depth. This wide range of rupture velocities provides a rough way to account for modest three-dimensional velocity variations in the crust relative to the 1D shear-velocity model used to calculate rupture times and stopping times on the fault. For instance, a rupture velocity of 1.0*Vs(z) would correspond to a rupture velocity of 0.91*Vs(x,y,z) at a point in the 3D velocity model where Vs(x,y,z) is 10% faster than Vs(z). This is one way to incorporate Gaussian variations of crustal shear-wave velocities in the kinematic component of the finite-fault source model.

Another appeal of Frankel's (1995) approach is that it requires relatively few parameters that are generally well constrained to specify the influence of wave propagation between the source and the site. For instance, use of empirical Green's functions reduces wave propagation assumptions to the point that the only parameters are the distance of the empirical Green's function from the site and the distances of the discrete fault sub-elements from the site. For this study, broadband recordings at site JLDW of several larger (**M** ~5) regional earthquakes and of two **M** ~3 earthquakes in the vicinity of the northern Teton fault segment provide empirical Green's functions necessary to estimate ground motions in the 0.2 Hz to 10 Hz frequency band.

Frankel (1995) does not apply a radiation pattern correction to synthesize ground motions. The approach used here is similar. The only portion of the radiation pattern that is accounted for in applications of Frankel's method is the application of shear-wave polarities at each EGF patch on the fault as calculated from the 3D RGF's in Section 6. There was no attempt to calculate the amplitude variation of shear-wave radiation with azimuth and take-off angle. In contrast, in Section 6, the RGF estimates of shear-wave amplitudes in the 0.5-1.5 Hz frequency band for dip-slip faulting where used to scale the EGF amplitudes at each point-source integration point. As summarized in Frankel (1995), a philosophical difficulty of fully employing the shear-wave radiation pattern to the EGF is that scaling of phases following the initial shear-wave may be inappropriate, and at some frequency between 1-10 Hz, the radiation pattern is likely to become statistically insignificant. Since most existing ground motion synthesis methods do not incorporate radiation patterns (Silva and Lee, 1987; Somerville et al., 1991; Schneider et al., 1993; Zeng et al., 1994; Beresnev and Atkinson, 1997; Zeng and Anderson, 2000) using Frankel's approach provides a nice basis for comparison and contrast with the results from Section 6.

7.4 Ground Motions From Larger Regional Earthquakes

Broadband site recordings of **M** ~4-5 EGF earthquakes on the Teton fault would represent ideal EGF's for the purposes of synthesizing ground motions at Jackson Lake Dam because large S/N ratios would be available in the 0.1 to 10 Hz frequency band of engineering interest. Such data does not exist. However, several regional earthquakes within 150 km of Jackson Lake Dam were recorded at sites JLDW and JLD3 which have adequate signal-to-noise (S/N) ratios to serve as EGF's for synthesizing ground motions in the 0.1-0.2 Hz to 5-10 Hz frequency band. The two best regional earthquakes are a **M** 5.2 earthquake in Idaho about 120 km from site JLDW and a **M** 4.6 earthquake near Yellowstone about 100 km from site JLDW (Table 7-1).

Table 7-1: Regional EGF Earthquake Locations

Date/Time (day mon yr hr:min:s)	Latitude (degrees)	Longitude (degrees)	Stress drop (MPa)	Depth (km)	**M**	Moment (dyne-cm)
21 Apr. 2001 17:18:57	42.925	-111.395	2.7	16.0	5.2	$6.4*10^{23}$
24 Nov. 2000 04:20:06	44.750	-111.690	3.1	4.6	4.6	$8.9*10^{22}$

The best S/N ratios are obtained for the **M** 5.2 earthquake that occurred on 21 April 2001 in southeastern Idaho, about 120 km from site JLDW (Figure 7-30). The 211° azimuth from JLDW to the epicenter makes this earthquake a rough analog for seismic energy emitted from the southwestern corner of the northern segment of the Teton fault. The advantages of this earthquake are that surface wave responses are minimized by the position of the Teton Range between the site and the epicenter and the horst and graben structure along the western portion of the travel path to the dam site, the relatively low attenuation of the lower-crusted refracted initial shear-wave arrival, the incidence of the shear-wave through the Teton fault surface toward the site, the normal-faulting mechanism and moment estimate (USGS, PDE, Harvard CMT), the > 15 s delay between the arrival of the initial shear-wave energy and the likely arrival of surface waves, and the site and basin scaling and duration affects are implicitly contained in the site recordings. The obvious disadvantages are that the earthquake is located more than 8 times distant from the site relative to the mean distance of JLDW from the northern segment of the Teton fault (122 km epicentral distance versus ~15 km mean distance from the northern segment of the Teton fault) and surface waves attenuate more slowly than shear waves, so simple distance scaling will over emphasize whole-path surface-wave amplitudes. Conversely, basin-edge waves including basin-edge surface waves will be appropriately scaled as they are directly produced by incidence shear-waves that are appropriately scaled by distance ratios. Since no broadband stations were installed outside the low-velocity basin, clear identification of whole-path surface waves is not possible. Table 7-1 provides PDE location information and Table 7-2 shows the focal mechanism estimated from organization sources as indicated. The PDE source estimate were used because they where

Table 7-2: 21 April 2001 EGF Focal Mechanism Nodal Plane Estimates

Solution	strike	dip	rake
PDE fault plane1:	345	43	-106
PDE fault plane2:	186	49	-76
Harvard fault plane1:	11	43	-77
Harvard fault plane2:	173	48	-102
FAST NEIC fault plane1:	32	41	-75
FAST NEIC fault plane2:	193	50	-103

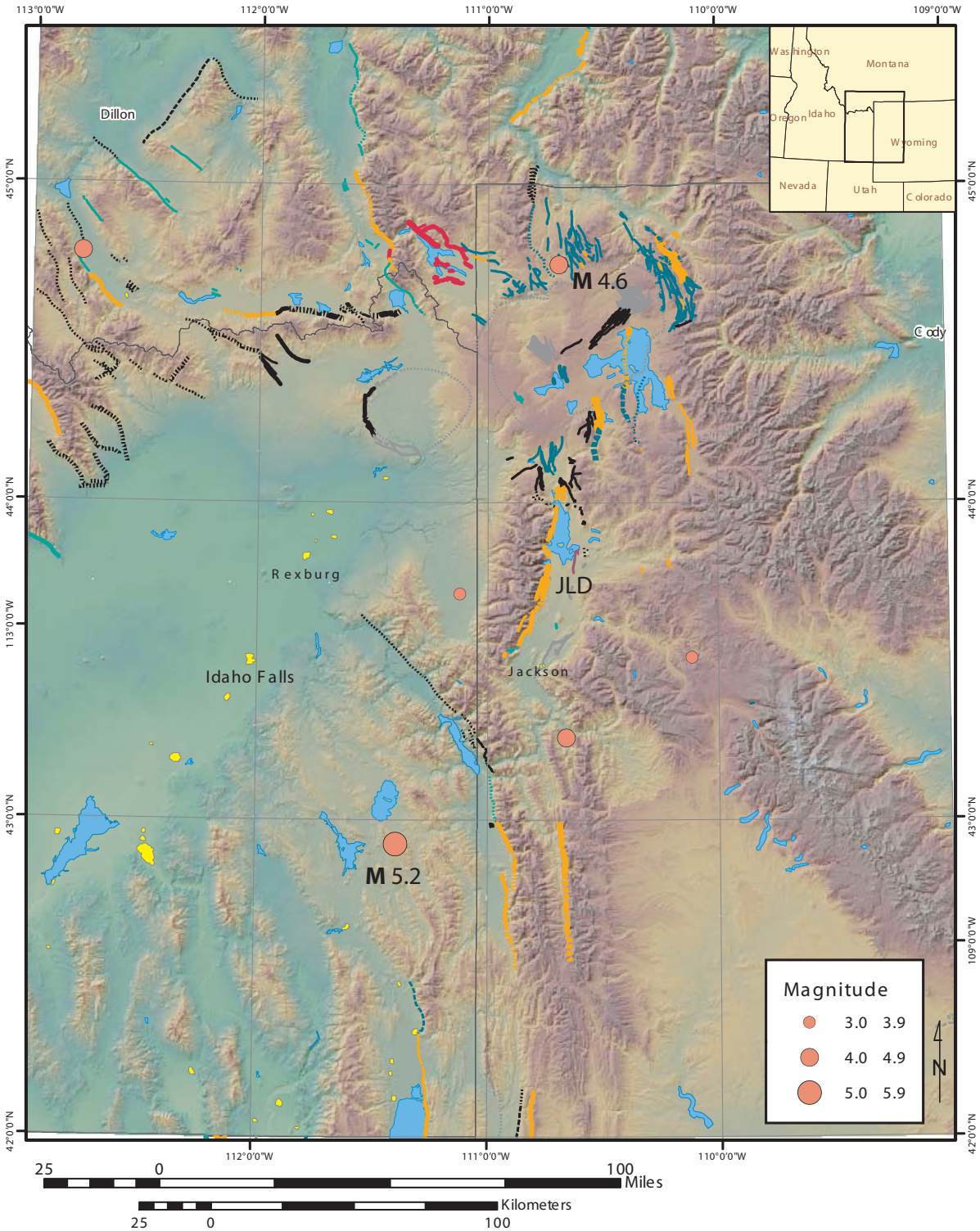

Figure 7-30: Map showing the location of the regional EGF earthquakes relative to the dam. The Idaho earthquake is the red circle labeled **M** 5.2 and the Yellowstone earthquake is the red circle labeled **M** 4.6. The Idaho and Teton Ranges are located between the **M** 5.2 epicenter and the dam (JLD). Map is colored in relation to topography. Black lines are Quaternary faults, orange lines are late Pleistocene faults, and red lines are faults associated with historical large earthquakes.

the only estimates available for both earthquakes. Harvard moment tensor estimates were also available for the 21 April 2001 earthquake which had moment estimates about 60% larger than the PDE estimates. Since the PDE estimates used more regional stations than Harvard, the PDE estimates were given preference. Although the PDE indicated the availability of a focal mechanism for the **M** 4.6 24 Nov. 2000 Yellowstone earthquake in the monthly listings, no focal mechanism information was found in the monthly listings.

For the **M** 5.2 21 April 2001 earthquake, the average S_V radiation pattern for the azimuth and take-off angle to station JLDW of 0.2 was found by searching over the range of possible strikes, dips, and rakes indicated in Table 7-2 and take-off angle uncertainties of 10°. The average S_V radiation coefficient at site JLDW for a northern segment Teton fault normal-slip earthquake on a 35-45°-dipping normal fault is 0.44. Consequently, the EGF's for the M 5.2 21 April 2001 were scaled by a factor of 2.2 to roughly correspond to expected S_V radiation of the northern Teton fault at site JLDW. The EGF's were corrected for crustal shear-wave attenuation since the EGF earthquakes were located at significantly larger distances than distances of sites JLDW and JLD3 from then northern Teton fault segment. A shear-wave quality factor (q) of 200 and average crustal shear-wave velocity (c) of 3.5 km/s were used to produce the frequency-domain attenuation amplitude correction

$$A(f) = \frac{e^{(-r_{egf}\pi f^{0.5}/(cq))}}{e^{(-r_{main}\pi f^{0.5}/(cq))}} \tag{7-11}$$

where f is frequency, r_{egf} is the distance of the EGF earthquake from the site, and r_{main} is the average distance of the simulated mainshock fault from the site. The frequency-dependence in (7-11) ensures that attenuation is not overestimated for large frequencies, although this is not a serious concern, since the principal objective is to evaluate > 1 s responses at sites JLDW and JLD3 using these regional earthquake EGF's.

The second regional EGF earthquake (**M** 4.6) occurred in the Yellowstone region on 24 November 2000 about 100 km from site JLDW. The advantage of this earthquake is that its nearly due north azimuth demonstrates the strong > 1 s period excitation of the low-velocity basin for seismic energy incident from the north. However, there are several significant caveats concerning

using EGF's from this earthquake. The source depth is relatively shallow (~4.4 km) and the refracted low-crustal shear wave likely traversed one or more partial-melt zones associated with the Yellowstone caldera (Nelson and Smith, 1999). Consequently, shear-waves appear severely attenuated at short periods. No moment tensor inversion estimates are available for this event, so event focal mechanism is not known and event moment uncertainties are probably > a factor of two (+- 0.2 moment magnitude). The USGS PDE body-wave magnitude is 4.6 and the Yellowstone seismic network local magnitude (M_L) estimate is 4.3. The USGS PDE magnitude was used to provide a consistent magnitude reference relative to the **M** 5.2 Idaho earthquake. The delay of whole-path surface waves relative to the initial shear-wave arrival are probably ~10 s. It's not possible to distinguish between whole-path and basin-edge surface waves owing to the lack of broadband recordings at stations outside the low-velocity basin. The simple distance correction will overestimate whole-path surface wave amplitudes, but basin-edge surface amplitudes induced by shear-wave arrivals will be appropriated scaled. Thus, the inability to identify and distinguish the various surface waves due to the lack of a broadband seismographic station adjacent to the low-velocity basin severely limits the quantitative interpretation of estimated ground motions within the low-velocity basin produced using these regional EGF's. Attenuation corrections were applied using (7-11). although these corrections are not adequate to account for the severe shear-wave attenuation likely associated with potential partial-melt zones in the Yellowstone area.

The specification of the source parameters in the Frankel (1995) method was made as simple as possible. For the northern Teton fault segment, a hypocenter between the end of the fault segment and station JLDW, and a receiver at site JLDW, isochrones (sum of rupture and shear-wave travel times) have a hyperbolic distribution with a maximum isochrones time of 15 s. Uniform random numbers totaling the number of subfault cells were generated, squared, and scaled to a maximum of 15 s to produce approximate isochrone estimates for each subfault cell. Stress drop variations were constructed using uniform random variations scaled to ratios < a factor of two about the mean while making the mean stress drop of the mainshock the same as the EGF earthquake. This implicitly sets the stress drop correlation length to the subcell dimensions of the EGF earthquakes (see Table 7-3). This provides a source model specification completely independent of the approach used in Sections 6 and 7.2 to test the sensitivity of estimated ground motions to

kinematic source model specifications. EGF parameters used in the ground motion simulations are shown in Table 7-3. The minimum frequencies were determined by inspection of S/N ratios in

Table 7-3: Regional EGF Earthquake Simulation Parameters

Date/Time (day mon yr hr:min:s)	Min f (Hz)	f_{0small} (Hz)	Stress drop (MPa)	**M**	Moment (dyne-cm)	Scaling
21 Apr. 2001 17:18:57	0.05	0.6	2.7	5.2	$6.4*10^{23}$	2.26
24 Nov. 2000 04:20:06	0.1	1.2	3.1	4.6	$8.9*10^{22}$	1.0

the site recordings. Corner frequencies were difficult to impossible to reliably selected from the low-velocity basin recordings, given uncertainties due to various propagation effects including attenuation, amplification, etc. Consequently, while the data provide some support for picking the corner frequency of the **M** 5.2 21 April 2001 EGF earthquake, the corner frequency **M** 4.6 for 24 November 2000 EGF earthquake was assigned to produce a stress drop consistent with mean stress drops for the Basin and Range (see discussion in Ichinose et al, 1997) because the severe attenuation of shear-waves precluded estimating the corner frequency from the JLDW site recordings. Ground motions were simulated using the recordings of both regional EGF earthquakes at rock site JLDW and soil site JLD3.

7.4.1 Rock Site JLDW. Site JLDW velocity seismograms from the **M** 5.2 Idaho, earthquake (Figure 7-31) have remarkably long short-period durations for a rock site. Large peak horizontal velocities (PHV) > 50% of initial shear-wave PHV's persist for > 40 s. Peak vertical velocities are about half the PHV's (Figure 7-31). Since there are no broadband seismographic stations outside the low-velocity basin, it is not possible to clearly identify whole-path surface waves or to ascertain if they are significant contributors to the observed ground motions at site JLDW. The S/N for all three components is adequate to model ground motions to periods extending to 10-20 s and for frequencies < 10 Hz (Figure 7-32). The acceleration response spectra are shown in (Figure 7-33).

The synthetic JLDW vertical response prior to application of (7-8) in Figure 7-34 have the spectral responses for typical soil sites with acceleration response spectra amplitudes nearly

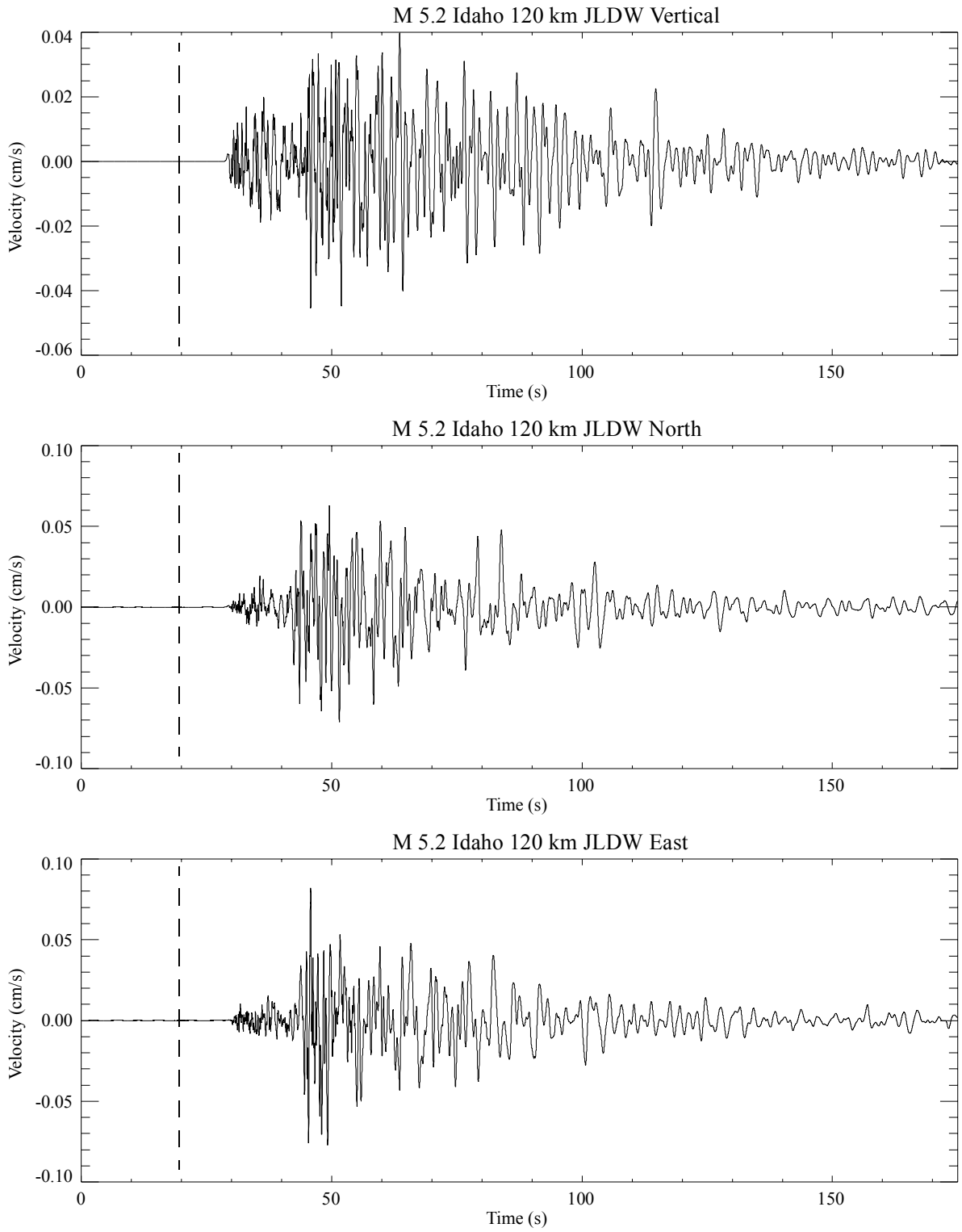

Figure 7-31: Site JLDW velocity seismograms from the 21 Apr. 2001 **M** 5.2 Idaho earthquake. Components are as labeled. Vertical dashed lines divided the seismograms into pre-event noise and signal portions for spectra shown in Figure 7-32.

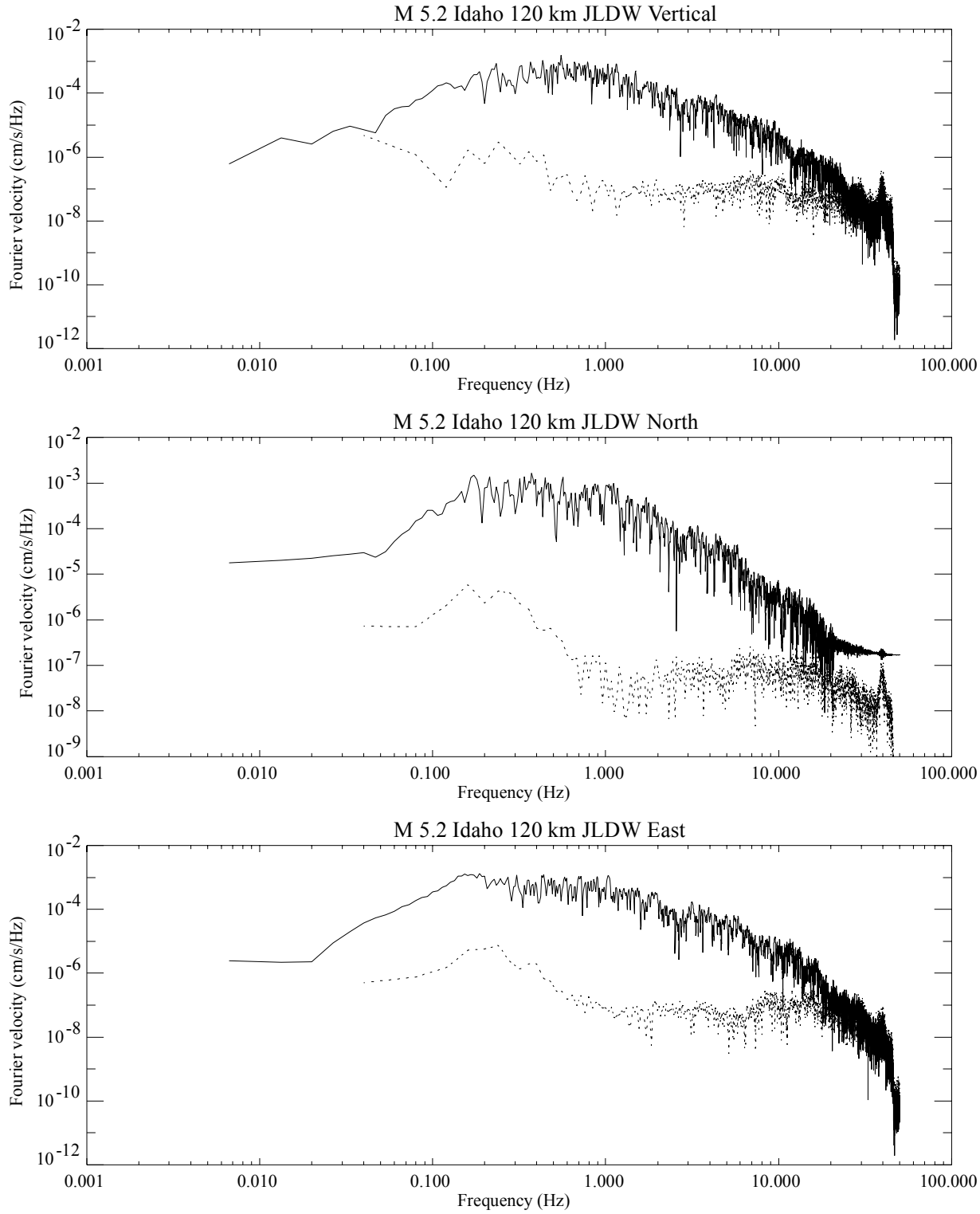

Figure 7-32: Site JLDW Fourier velocity spectra from the 21 Apr. 2001 **M** 5.2 Idaho earthquake. Components are as labeled. Solid curves are signal spectra and dotted curves are noise spectra using the time windows indicated in Figure 7-31.

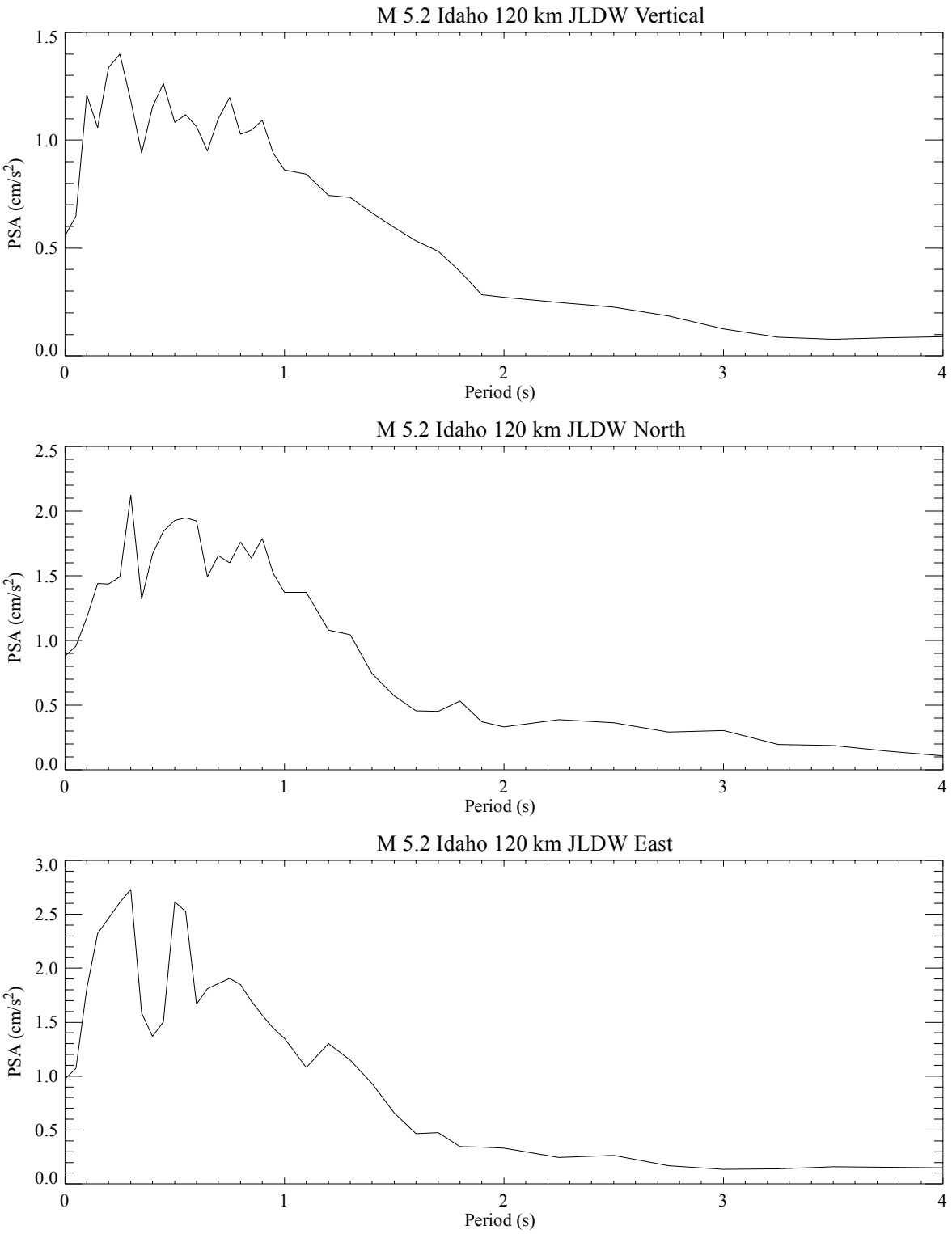

Figure 7-33: Site JLDW acceleration response spectra from the 21 Apr. 2001 **M** 5.2 Idaho earthquake. Components are as labeled.

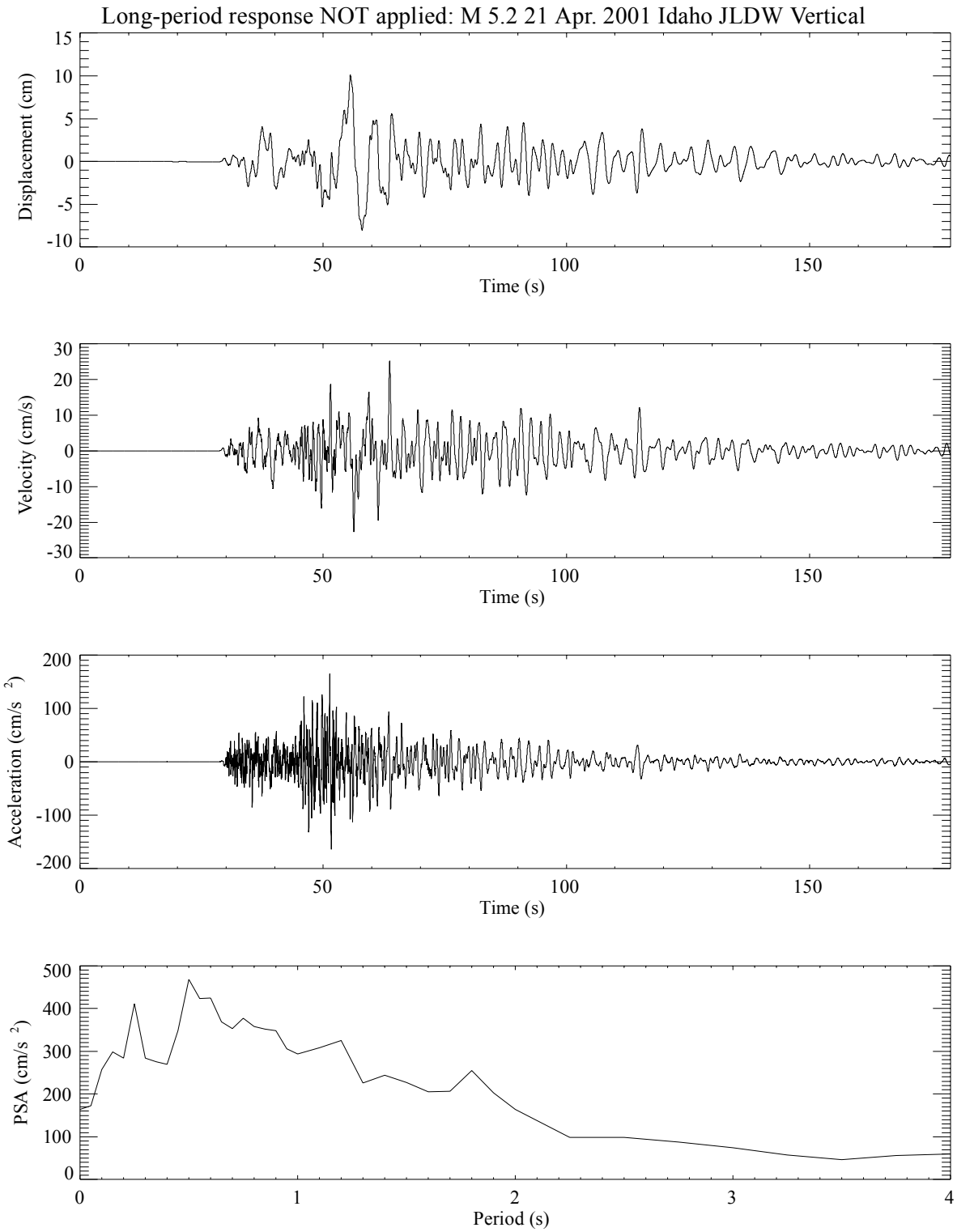

Figure 7-34: Subevent sum **M** 7.1 northern Teton fault earthquake simulation JLDW vertical response before long-period correction. The **M** 5.2 JLDW seismograms from Figure 7-31 were the EGF's used in (7-7). Corresponding complete synthetic vertical responses incorporating (7-8) are shown in Figure 7-35.

monotonically decreasing with increasing period from a peak amplitude at 0.5 s. However, when (7-8) is applied to produce vertical ground motions corresponding to a **M** 7.1 northern Teton fault segment earthquake (Figure 7-35), acceleration response spectral amplitudes begin to increase with period for periods > 3.5 s. This is consistent with the 5-10 s period of the dominant displacement pulse in Figure 7-35, which is also present in Figure 7-34. The timing of the large-displacement pulse within 10 s of the earliest arriving shear-wave is **inconsistent** with the large-displacement pulse being associated with a whole-path surface wave arrival, which should arrive at least 15 s after the initial shear wave, e.g., at times > 60 s. Thus, the large > 3 s synthetic vertical acceleration response at site JLDW in Section 6 appear reasonable because they are produced using purely empirical body-wave site responses (e.g., EGF's) with excellent S/N (Figure 7-32).

The shear-wave attenuation correction over-amplifies the P-wave arrivals at the beginning of the north component (Figure 7-36), particularly when the total amplitude and phases corrections from (7-8) are applied (Figure 7-37). The shear-wave attenuation reverses dispersion which results in overly compressed high-frequency P-wave arrivals. Since the focus here is on responses for periods > 1 s this is not a serious issue. The most remarkable aspect of the north component at rock site JLDW is that peak velocities > 100 cm/s persist for about 40 s and that peak velocities > 50 cm/s span a 60 s time window (Figure 7-37). Peak velocities > 10 cm/s persist for more than 2 minutes. These are long durations for a **M** ~7 earthquake close to a rock site. Spectral accelerations remain > 0.5 g for periods extending to 4 s. The north component's long durations and strong long-period acceleration responses are consistent with hypothesis that the low-velocity basin in the hangingwall of the Teton fault efficiently traps energy, amplifying long-period motions, and substantially increasing strong motion durations at even rock sites within the low-velocity basin. The east component exhibits a nearly monochromatic strong ~4-5 s response with peak velocities > 100 cm/s starting with a few seconds of the initial shear-wave arrival at ~47 s, even before application of (7-8) (Figure 7-38), The 4-5 s responses are even more pronounced in the complete east synthetic motions (Figure 7-39). The strong excitation of the 4-5 s responses clearly visible in the velocity and displacement seismogram begins within 5 s of the initial shear-wave arrival, which is too early to correspond to whole-path surface wave arrivals in the EGF's. Thus, the increase in acceleration responses for periods > 3 s in Figure 7-39 is associated with real

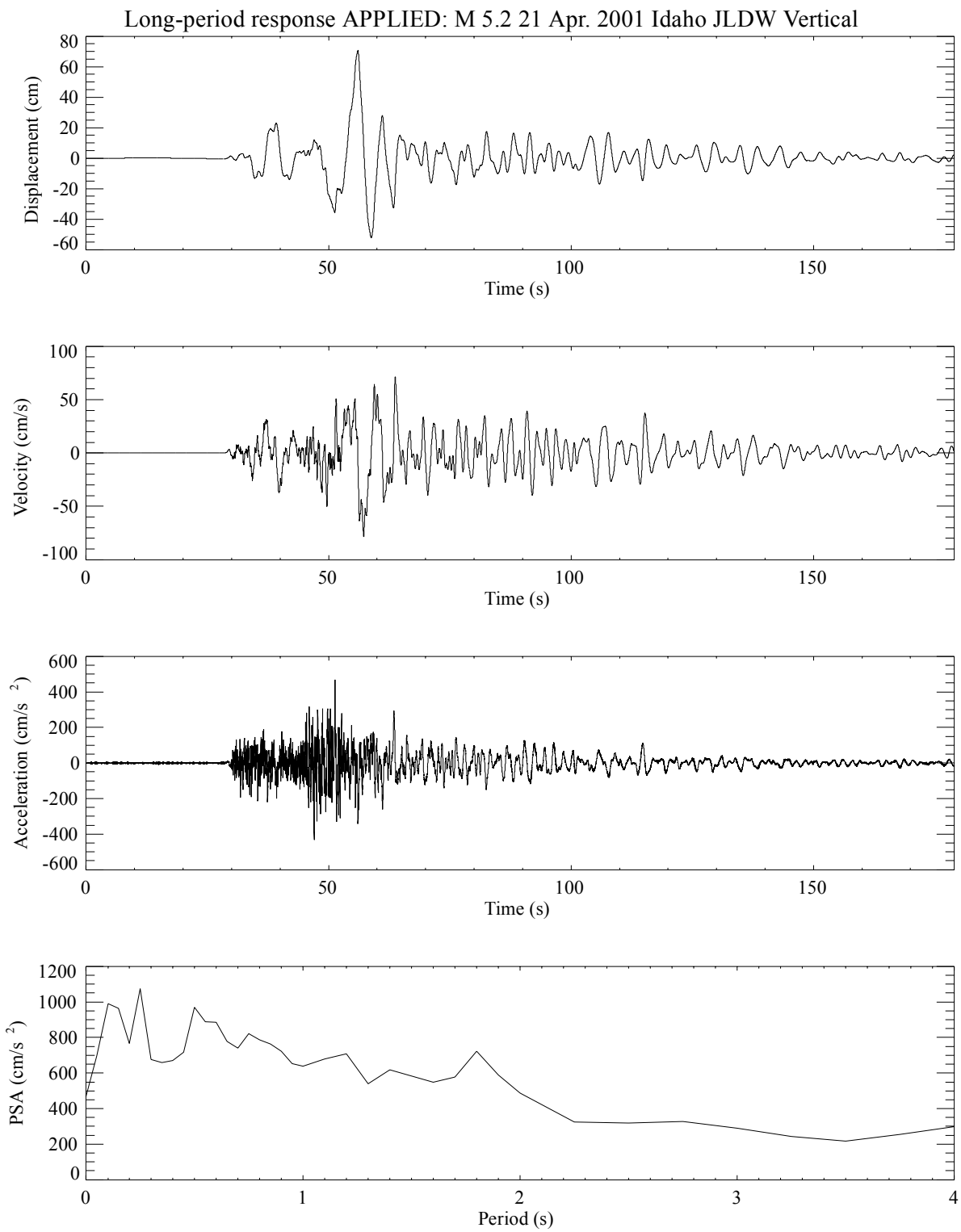

Figure 7-35: **M** 7.1 northern Teton fault earthquake simulation JLDW vertical response. This is the total response obtained by combining the velocity seismograms from Figure 7-34 with (7-8).

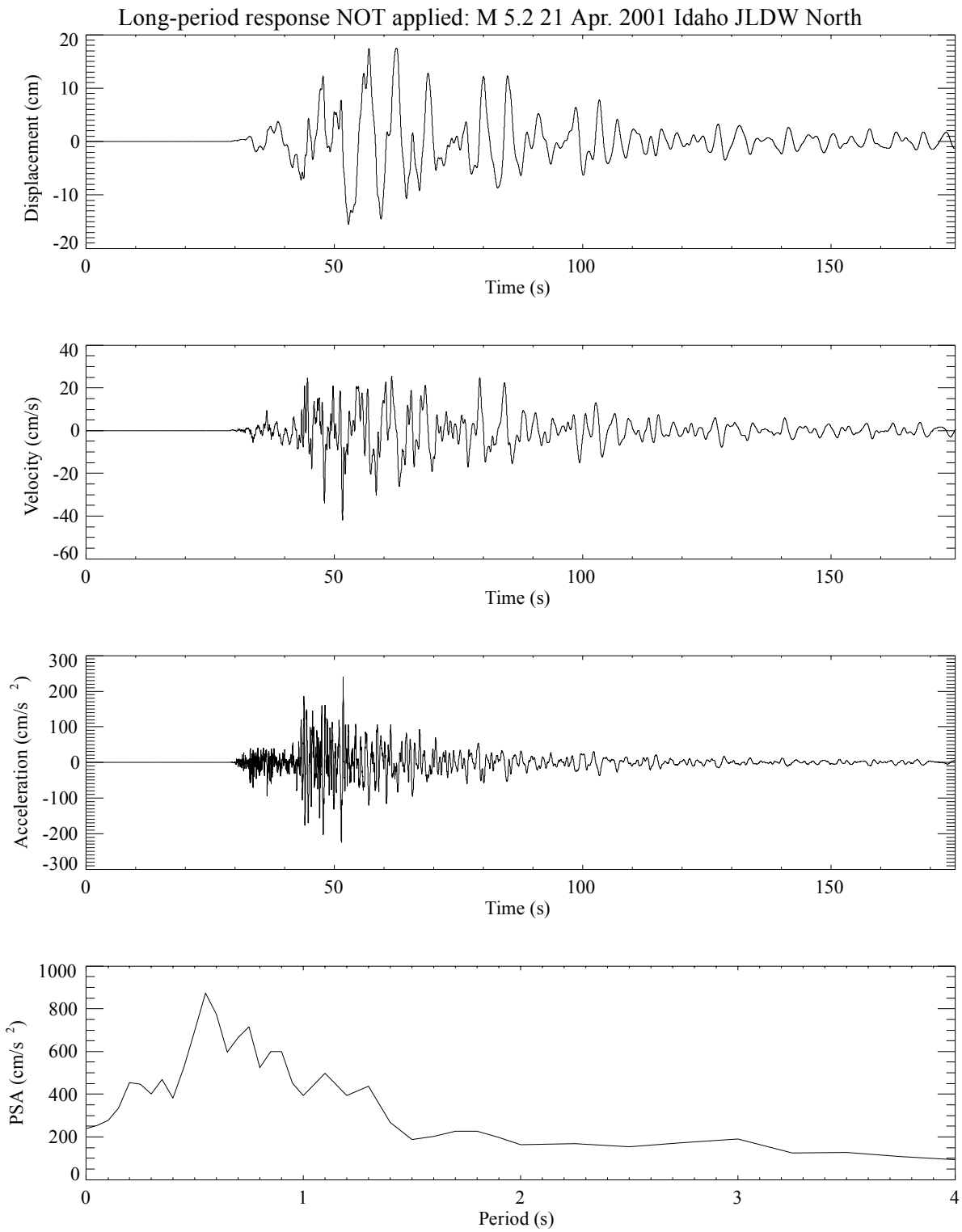

Figure 7-36: Subevent sum **M** 7.1 northern Teton fault earthquake simulation JLDW north response before long-period correction. The **M** 5.2 JLDW seismograms from Figure 7-31 were the EGF's used in (7-7). Corresponding complete synthetic vertical responses incorporating (7-8) are shown in Figure 7-37.

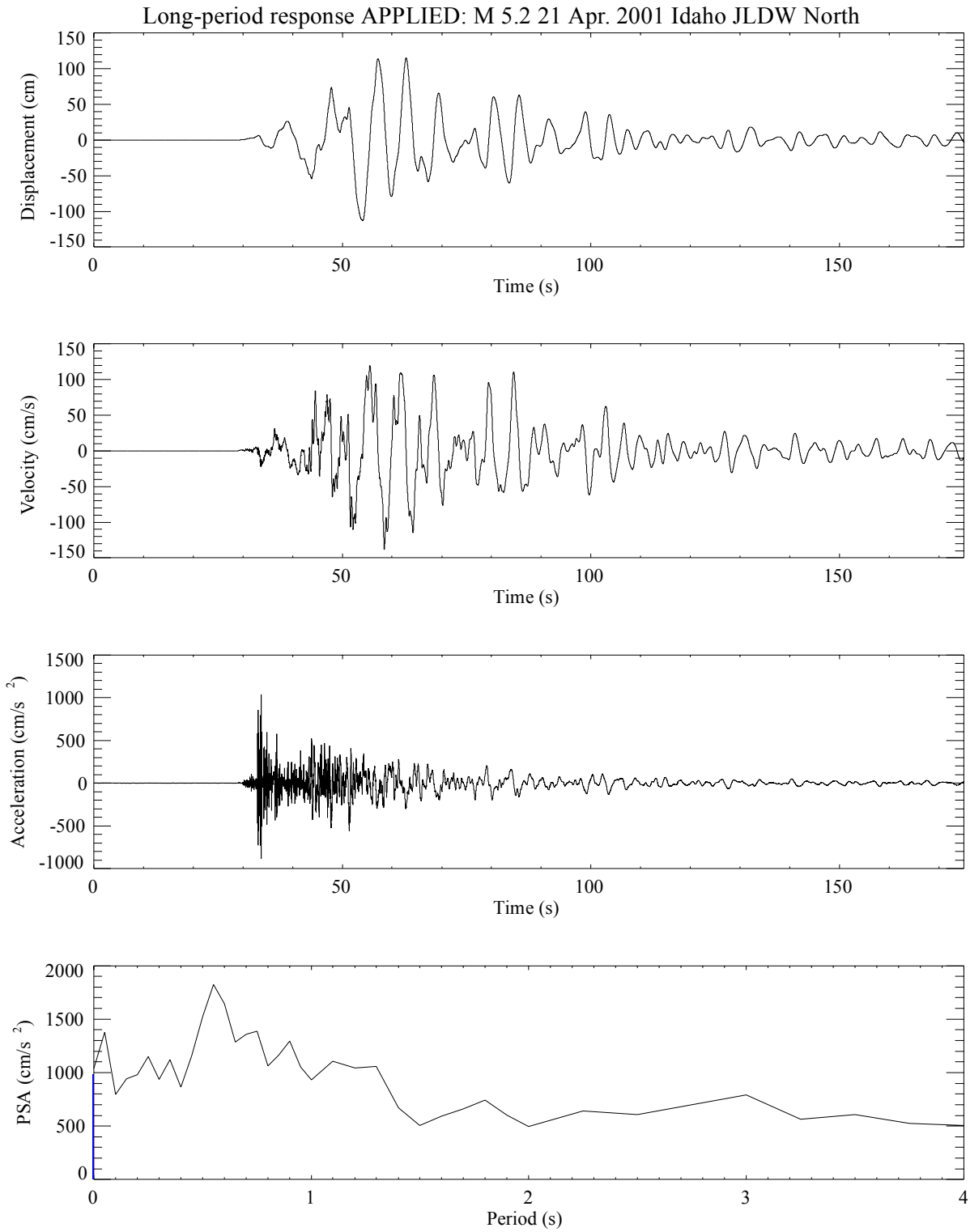

Figure 7-37: **M** 7.1 northern Teton fault earthquake simulation JLDW north response. This is the total response obtained by combining the velocity seismograms from Figure 7-36 with (7-8). Note the largest accelerations are associated with P-wave energy near the beginning of the shaking that reflects overcorrection of the pre-shear-wave energy for whole-path crustal shear-wave attenuation.

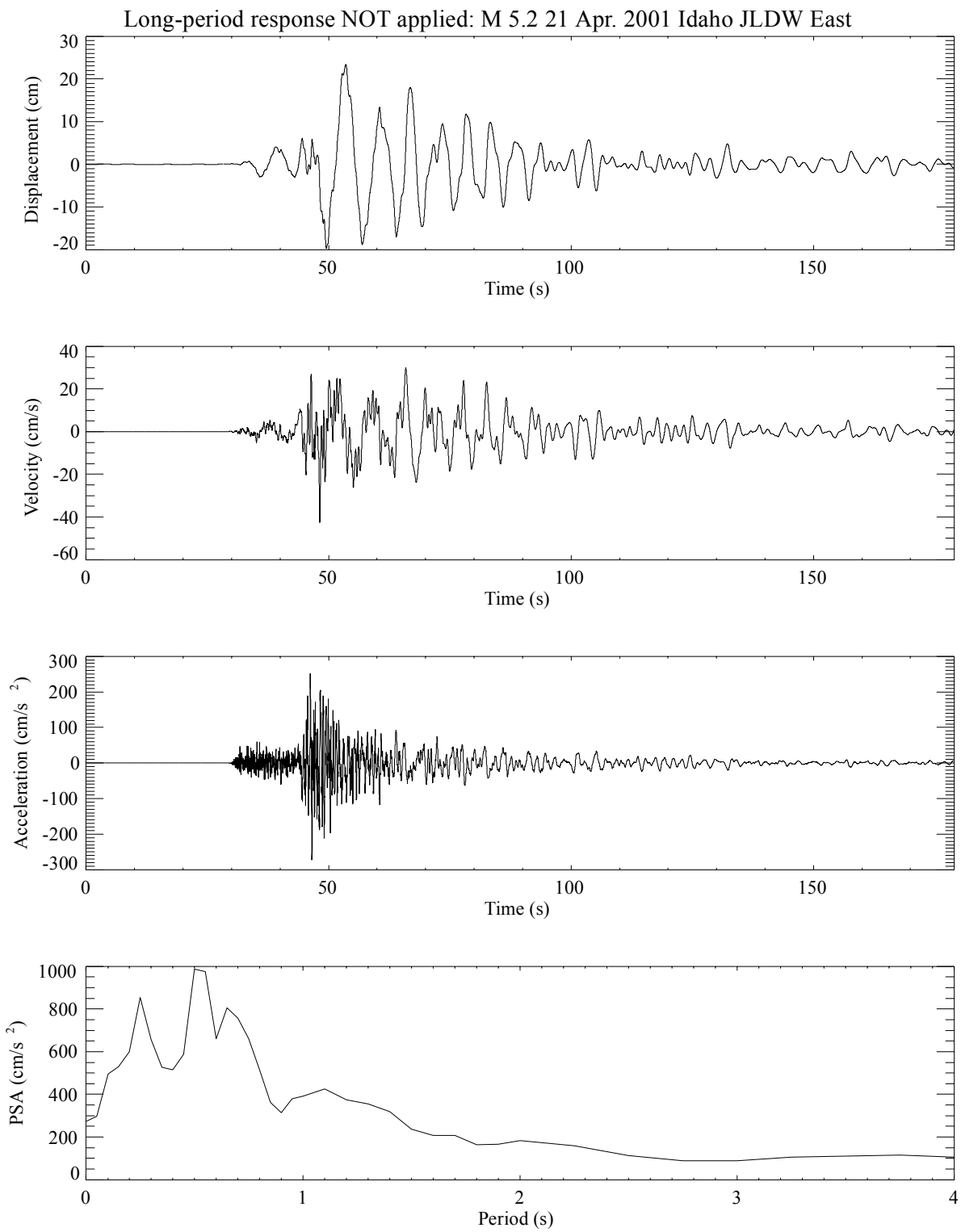

Figure 7-38: Subevent sum **M** 7.1 northern Teton fault earthquake simulation JLDW east response before long-period correction. The **M** 5.2 JLDW seismograms from Figure 7-31 were the EGF's used in (7-7). Corresponding complete synthetic vertical responses incorporating (7-8) are shown in Figure 7-39.

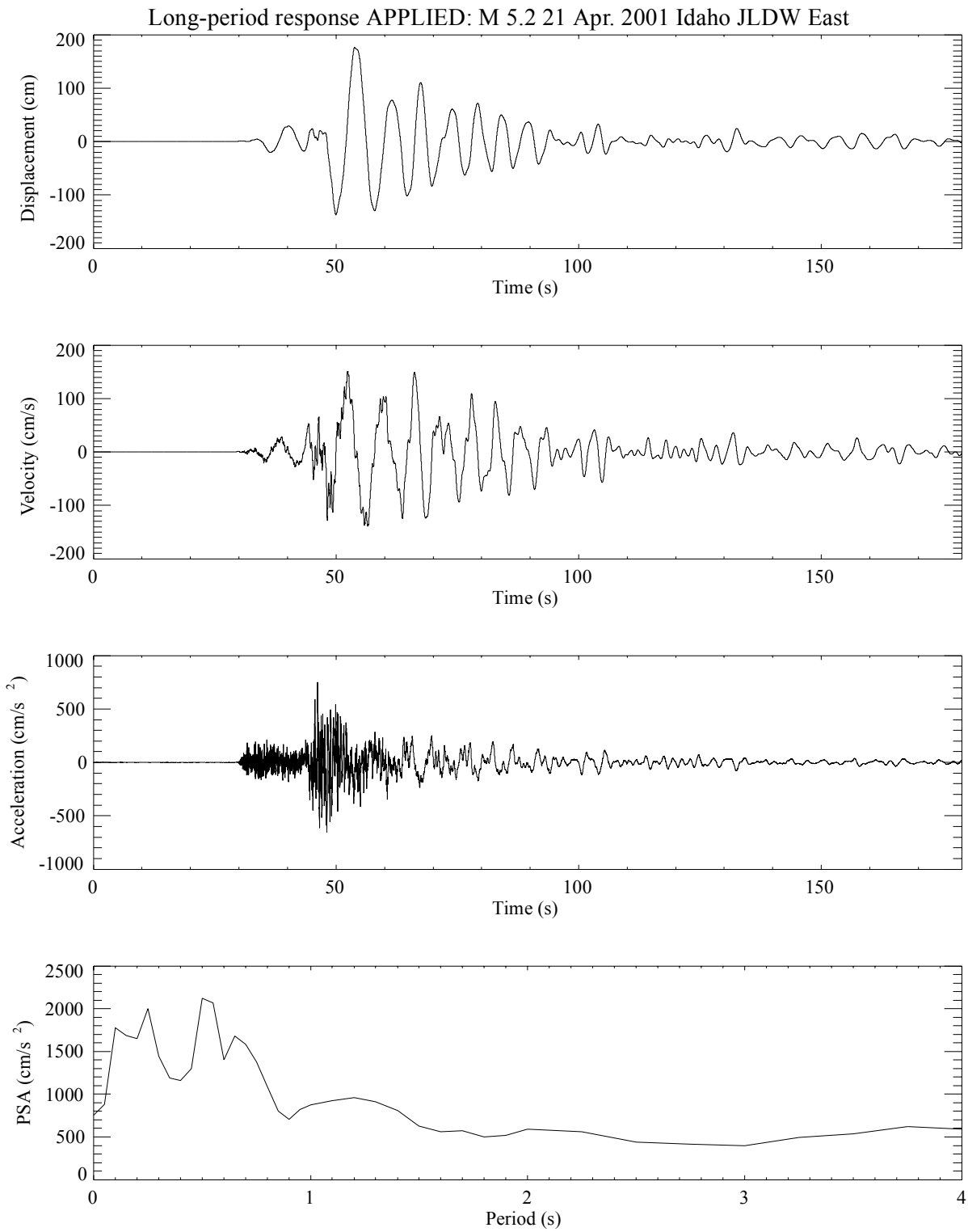

Figure 7-39: **M** 7.1 northern Teton fault earthquake simulation JLDW east response. This is the total response obtained by combining the velocity seismograms from Figure 7-38 with (7-8).

signal because S/N is > 10 for periods < 10 s (Figure 7-32) and suggests that the strong > 3 s synthetic acceleration responses in Section 6 are probably realistic. Conversely, the greater than two-minute-long > 10 cm/s velocity responses in Figures 7-35, 7-37, and 7-39 indicate that the synthetic durations in Section 6 are probably less than half of realistic durations for site JLDW. However, the lack of reference broadband stations adjacent to the low-velocity basin preclude definitive conclusions concerning the basin responses because whole-path surface responses (that could significantly bias impressions of responses within the low-velocity basin) cannot be determined from the basin recordings. To put these rock durations in some perspective, assuming a "normal" duration of about 40 s of coda for a rock site close to a **M** ~7 earthquake, a 140 s total duration from results in Figures 3-34 to 3-39, and a rupture velocity of 3 km/s, a duration of 100 s would correspond to a 300-km-long unilateral rupture. The rupture-length relations of Wells and Coppersmith (1994) estimate a magnitude 8 for a rupture length of 300 km. Thus, the effective magnitude at rock site JLDW is about one magnitude higher than the actual earthquake.

The rock site JLDW seismograms from the **M** 4.6 Yellowstone earthquake are virtually devoid of high-frequency shear-waves (Figure 7-40) in stark contrast to the corresponding seismograms from the **M** 5.2 Idaho earthquake (Figure 7-31). As discussed earlier, this is consistent with strong shear-wave attenuation associated with partial-melt in the Yellowstone region (Miller and Smith, 1999). Only the east component has adequate S/N to model ground motions to periods extending to 10 s (Figure 7-41), although adequate S/N is available on the vertical and north components to model ground motions to periods extending to 5 s. The minimum periods of adequate S/N are limited to periods > 0.5 s for the horizontal components and periods > 1 s for the vertical component (Figure 7-41). These represent minimally adequate S/N to evaluate long-period ground motions at the site JLDW. The most striking aspect of the seismograms and their acceleration response spectra is the increase of acceleration responses for periods > 2.5 s (Figure 7-42) and the associated long-durations of these long-period motions (> 100 s) at this rock site. It is likely that some of the large-amplitude arrivals in the 50-60 s time window are whole-path surface waves, based on expected surface-wave travel times. However, the persistent reverberations for times substantially later than 60 s are likely the result of waves trapped in the low-velocity basin. This indicates that the basin is more strongly excited by seismic energy approaching from the NNW. Lacking reference broadband stations outside the low-velocity basin

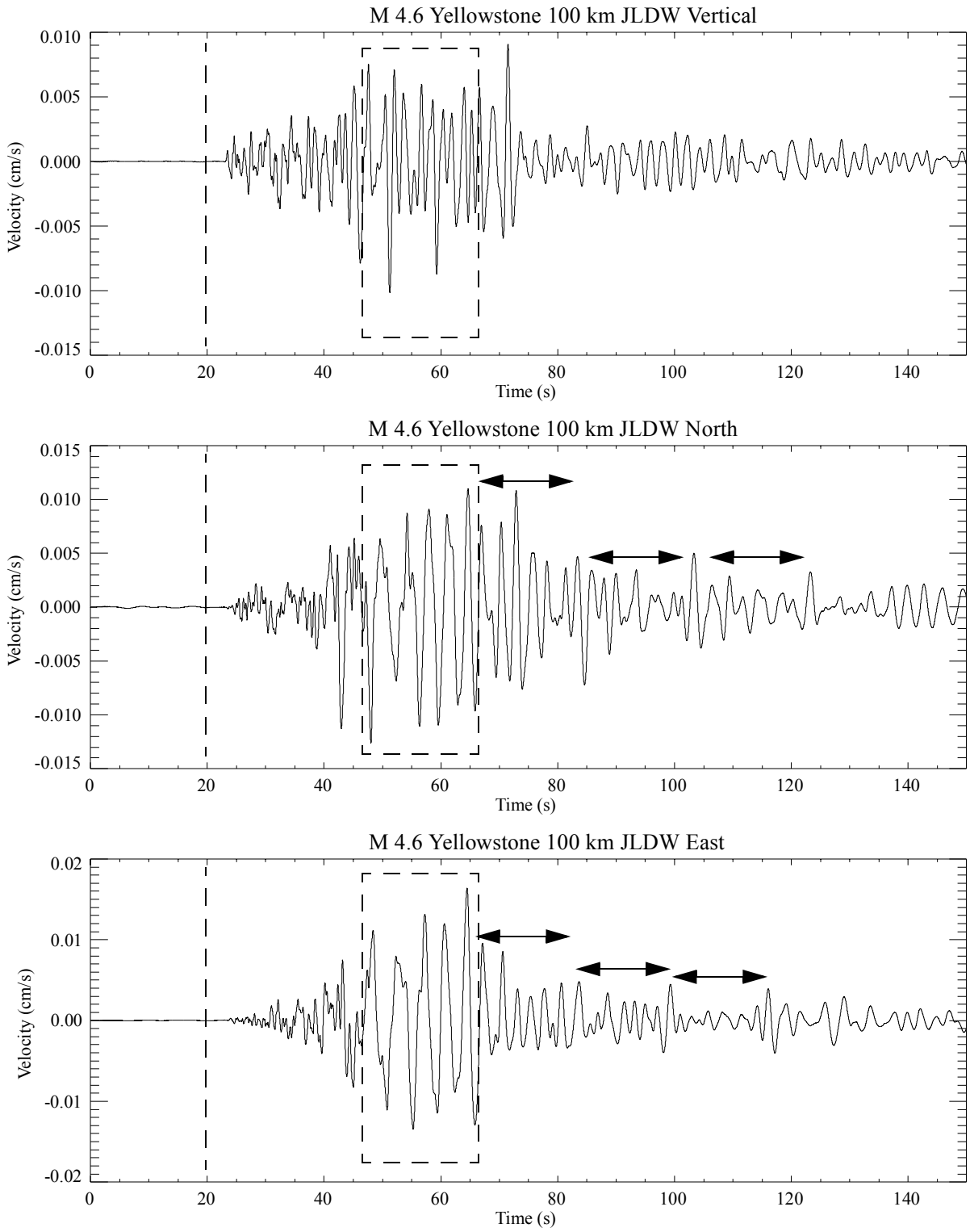

Figure 7-40: Site JLDW velocity seismograms from the 24 Nov. 2000 **M** 4.6 Yellowstone earthquake. Components are as labeled. Vertical dashed lines divide the seismograms into pre-event noise and signal portions for spectra shown in Figure 7-41. Note significant amplitudes persist to the end of the record. The double arrows show ~20 s time intervals between local peak velocities in the coda following the time interval of likely whole-path surface waves, denoted by the dashed-rectangles.

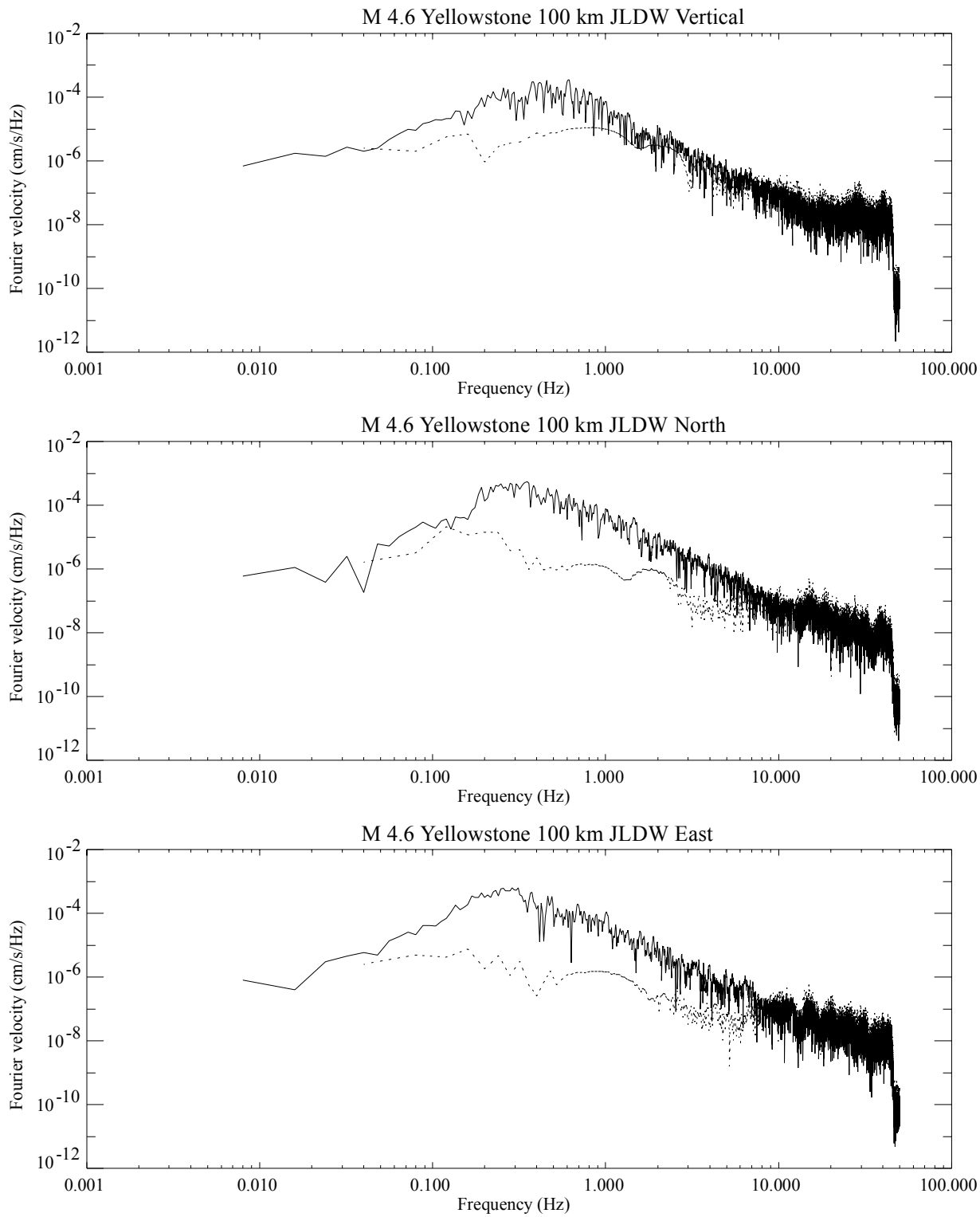

Figure 7-41: Site JLDW Fourier velocity spectra from the 24 Nov. 2000 **M** 4.6 Yellowstone earthquake. Components are as labeled. Solid curves are signal spectra and dotted curves are noise spectra using the time windows indicated in Figure 7-40.

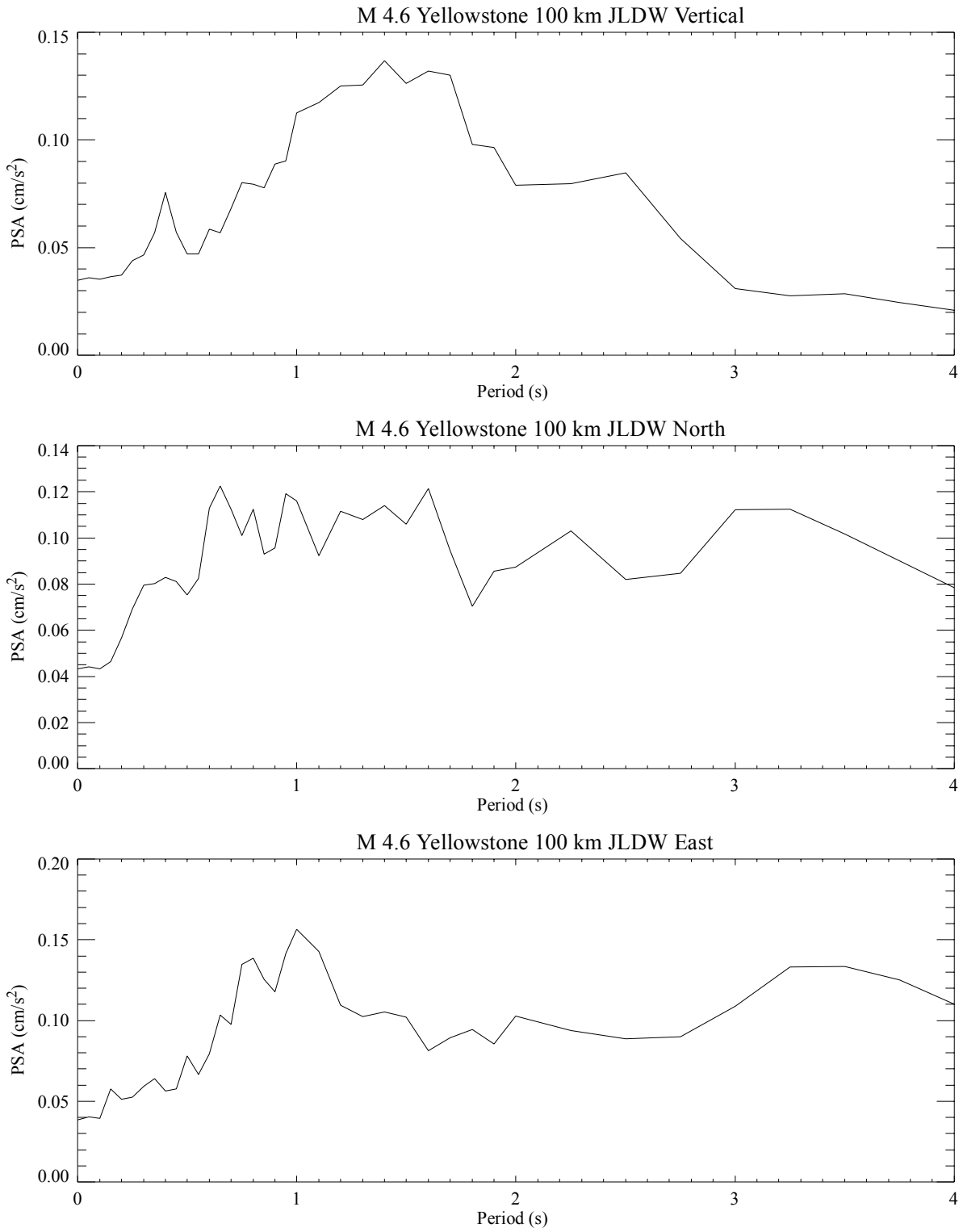

Figure 7-42: Site JLDW acceleration response spectra from the 24 Nov. 2000 **M** 4.6 Yellowstone earthquake. Components are as labeled.

it is not possible to draw definitive conclusions as to the relative proportions of whole-path and basin-edge induced responses from the JLDW seismograms. There is weak evidence in the horizontal seismograms, particularly the north component, of a ~20 s repeating of local peaks in ground velocity (Figure 7-40) which would be consistent with ~1-km/s phase velocities of trapped waves reverberating in the ~20-km-long (north-south extent) low-velocity basin in the 3D velocity model of Sections 4 and 6. The time interval is slightly longer than 20 s for the north component and slightly less than 20 s for the east component which would be consistent with basin-edge-induced Love waves on the east component and basin-edge-induced Rayleight waves on the north and vertical components and expected surface wave polarizations for energy incident from the NNW. The strong > 2 s horizontal acceleration responses (Figure 7-42) are probably whole-path fundamental-mode surface waves and likely produce the maximum horizontal velocities in Figure 7-40. Thus, long-period acceleration spectra produced using the Yellowstone earthquake as EGF's should be interpreted with caution since body-wave distance-amplitude corrections will overcorrect whole-path surface wave amplitudes for the **M** 4.6 Yellowstone earthquake by as much as a factor of 2.5.

Simulated vertical motions using the Yellowstone earthquake EGF decrease very slowly with increasing time (Figures 7-43 and 7-44). It is likely that some of the largest amplitudes in the 40-60 s time window are associated with exaggerated-amplitude whole-path surface waves. However, it is remarkable that peak amplitudes at 120 s are comparable to peak amplitudes prior to 40 s; neither of these time windows is likely to contain whole-path surface wave energy. The north component has the strongest long-duration responses (Figure 7-45 and 7-46) with a local peak velocity at about 85 s of ~50 cm/s that appears to repeat three more times in the record with about 20 s delays between peaks (105 s, 125 s, and 145 s). The peak velocity of each successive peak decreases slowly and is only halved in the third peak at ~145 s relative to the peak at ~85 s. The acceleration responses for periods > 2 s are probably exaggerated by whole-path surface waves in the 40-60 s time window, but probably not by more than a factor of two since the longer-period basin-edge induced arrivals later than 60 s have amplitudes more than half of the initial shear-waves. The east component (Figures 7-47 and 7-48) shows a weaker pattern of repeated local coda peak amplitudes that have a slightly reduced time separation relative to the north component (Figure 7-48), consistent with the coda of the east component being dominantly

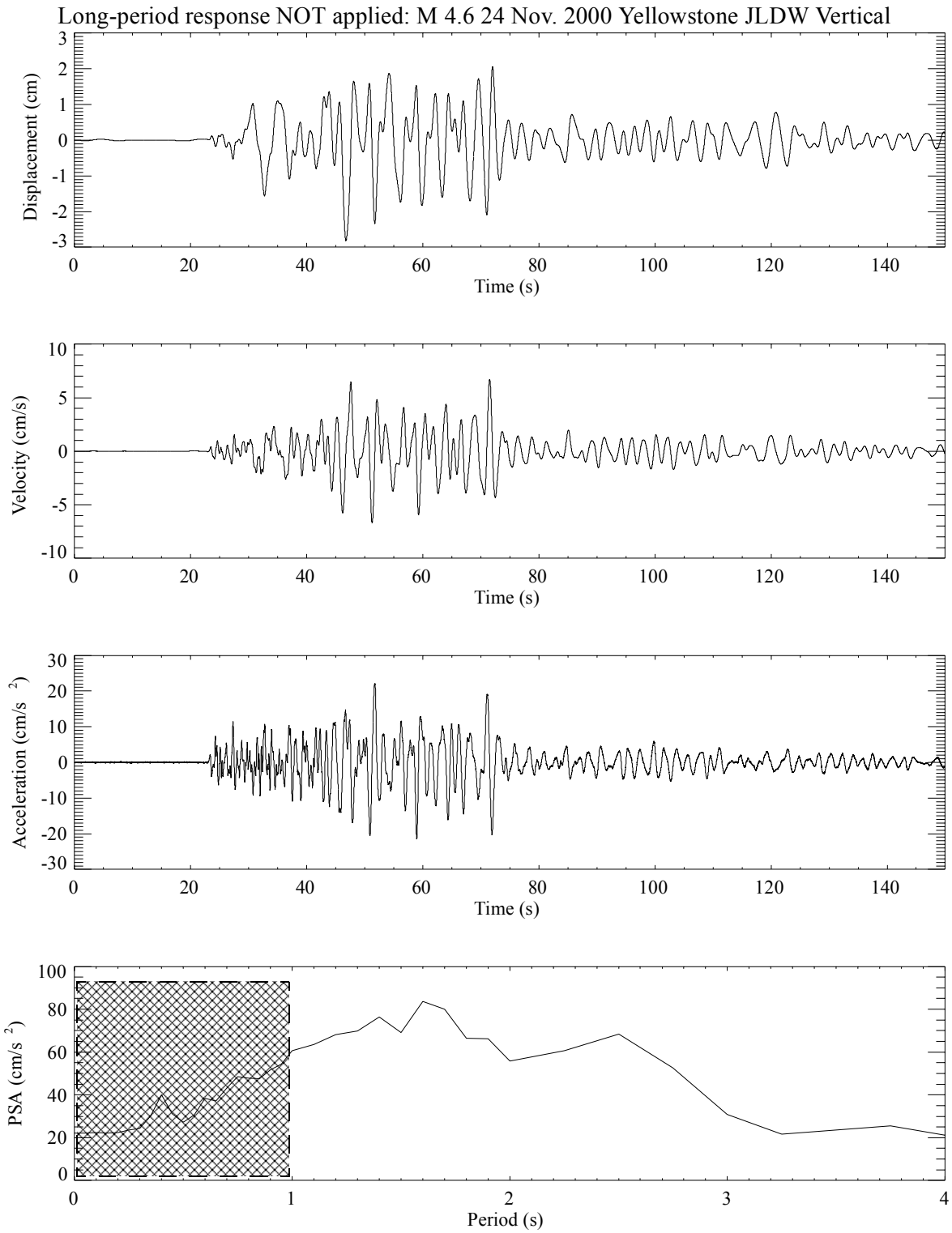

Figure 7-43: Subevent sum **M** 7.1 northern Teton fault earthquake simulation JLDW vertical response before long-period correction. The **M** 4.6 JLDW seismograms from Figure 7-40 were the EGF's used in (7-7). Corresponding complete synthetic vertical responses incorporating (7-8) are shown in Figure 7-44. Periods with inadequate S/N are hatchered.

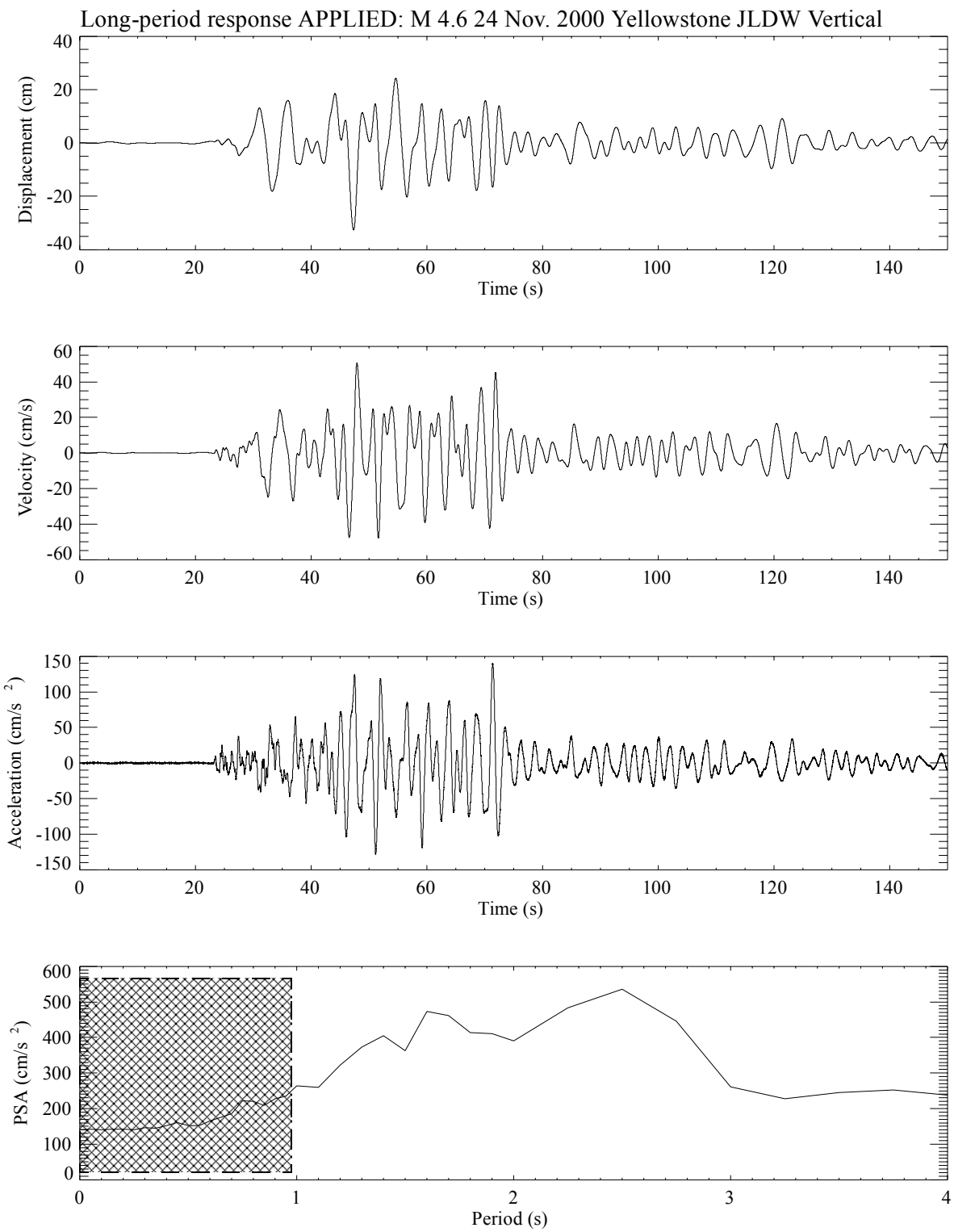

Figure 7-44: **M** 7.1 northern Teton fault earthquake simulation JLDW vertical response. This is the total response obtained by combining the velocity seismograms from Figure 7-43 with (7-8). Periods with inadequate S/N are hatchered.

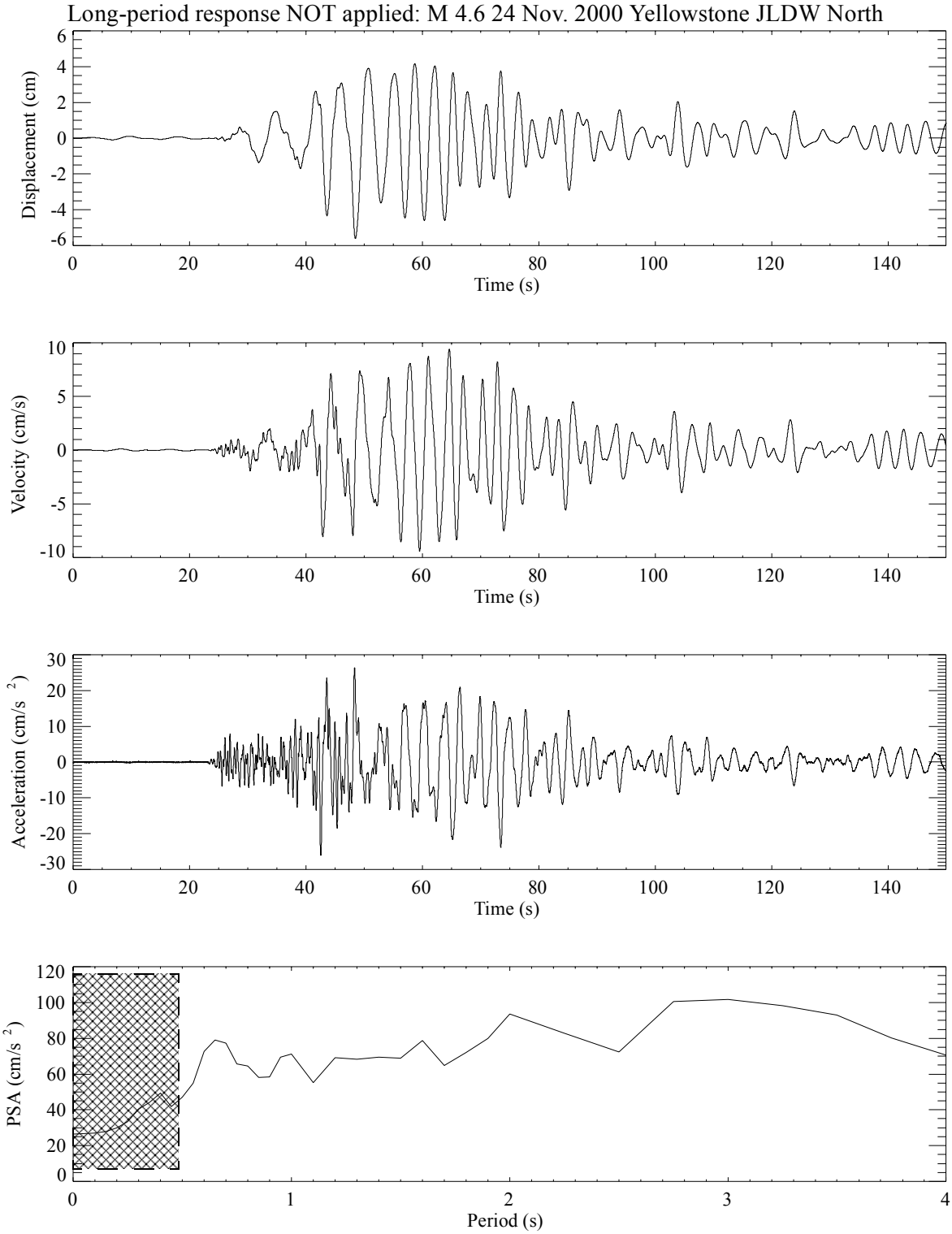

Figure 7-45: Subevent sum **M** 7.1 northern Teton fault earthquake simulation JLDW north response before long-period correction. The **M** 4.6 JLDW seismograms from Figure 7-44 were the EGF's used in (7-7). Corresponding complete synthetic vertical responses incorporating (7-8) are shown in Figure 7-46. Periods with inadequate S/N are hatchered.

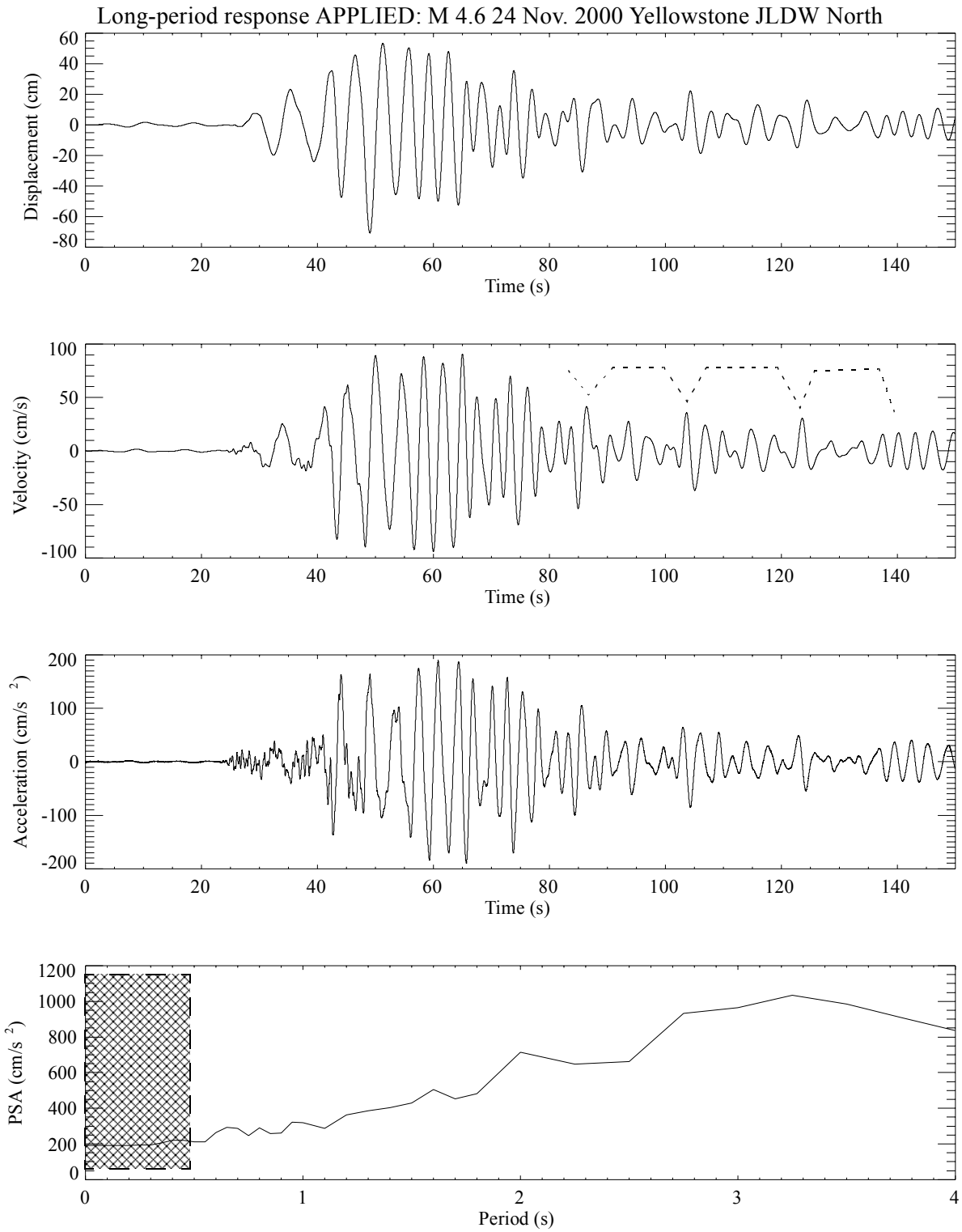

Figure 7-46: **M** 7.1 northern Teton fault earthquake simulation JLDW north response. This is the total response obtained by combining the velocity seismograms from Figure 7-45 with (7-8). Periods with inadequate S/N are hatchered. Dotted line outlines local peak amplitudes in the coda separated by ~20 s intervals.

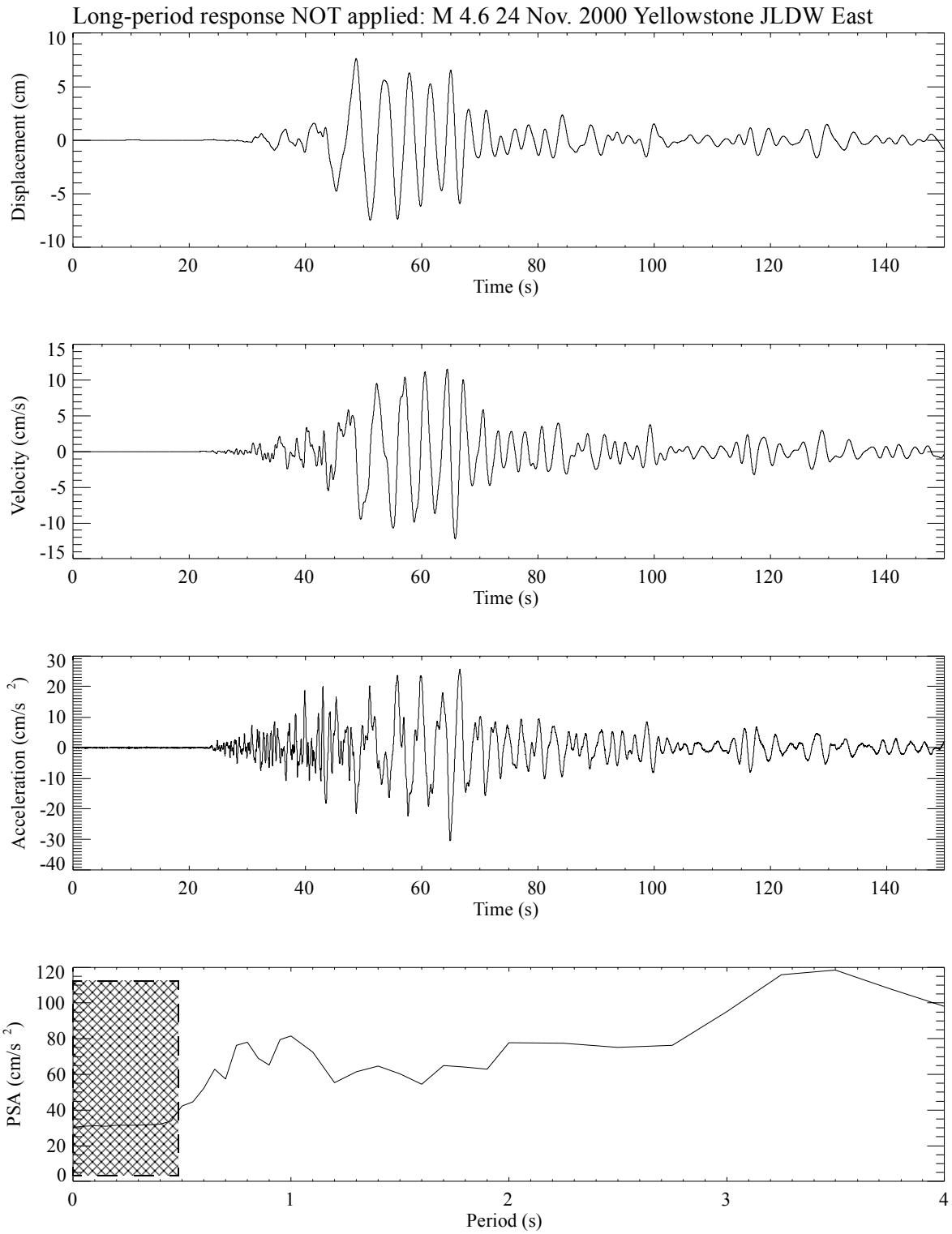

Figure 7-47: Subevent sum **M** 7.1 northern Teton fault earthquake simulation JLDW east response before long-period correction. The **M** 4.6 JLDW seismograms from Figure 7-44 were the EGF's used in (7-7). Corresponding complete synthetic vertical responses incorporating (7-8) are shown in Figure 7-48. Periods with inadequate S/N are hatchered.

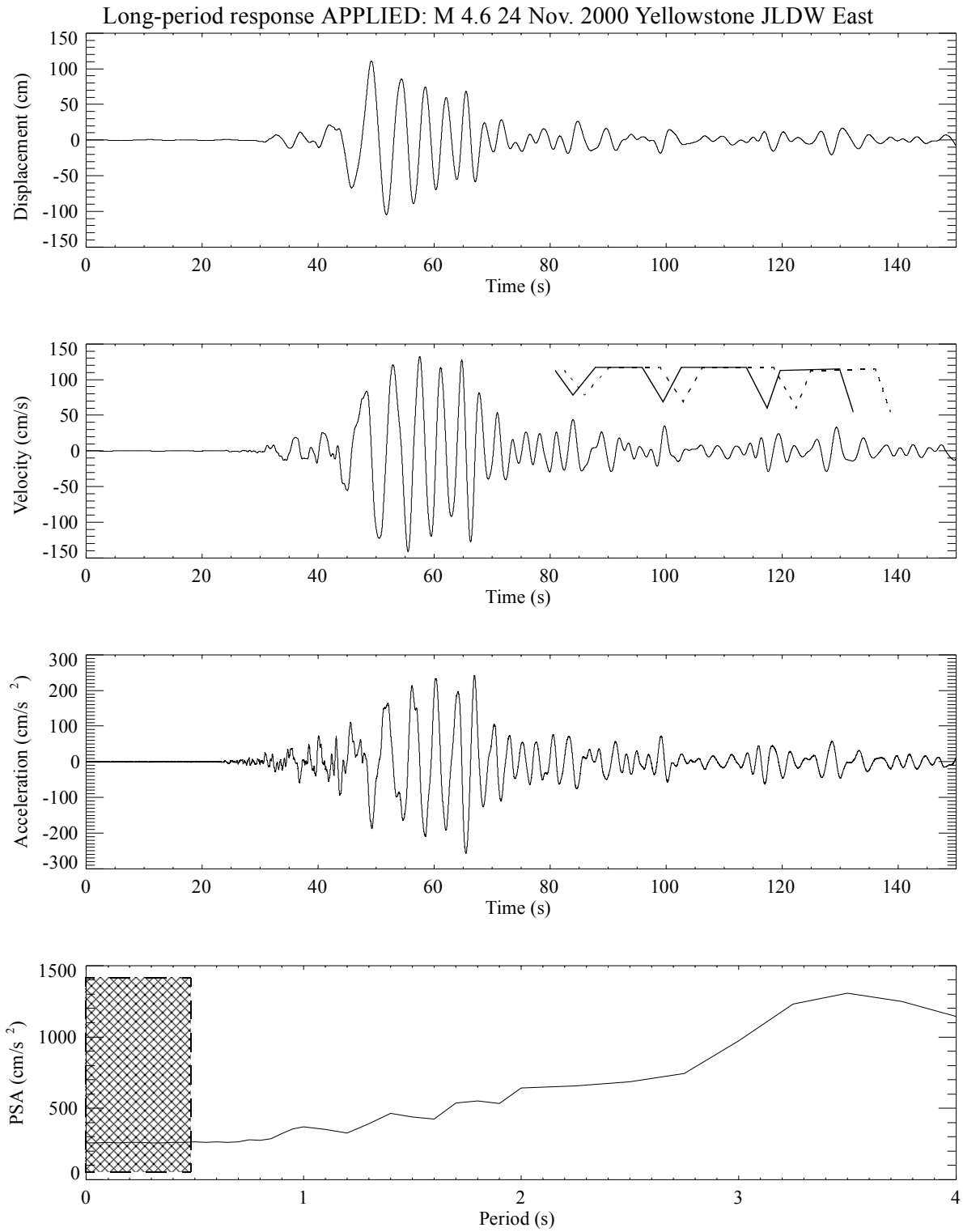

Figure 7-48: **M** 7.1 northern Teton fault earthquake simulation JLDW north response. This is the total response obtained by combining the velocity seismograms from Figure 7-47 with (7-8). Periods with inadequate S/N are hatchered. Dotted line outlines local peak amplitudes in the coda separated by ~20 s intervals in the north component (Figure 7-46) and the solid line shows weaker local amplitude peaks with < 20 s intervals that may be associated with basin-edge-induced Love waves.

comprised of basin-edge-induced Love waves (~10% faster phase velocities relative to Rayleigh waves on the north component). Probably a significant portion of the 45-60 s time window on the east component is dominated by whole-path surface waves, so peak acceleration responses at periods > 2 s in Figure 7-48 are probably overestimated. Without reference broadband recordings outside the low-velocity basin it is not appropriate to make quantitative interpretations of the long-period acceleration responses in Figures 7-44, 7-46, and 7-48. What is clear from these simulations is that energy from the shallow portion of the northern Teton fault segment north of the low-velocity basin is likely to substantially increase strong motion durations at rock site JLDW, with peak velocities possibly exceeding 20 cm/s after two minutes of shaking. This strong basin excitation for energy arriving from a NNW azimuth may be associated with the abrupt, steeply dipping geometry of the northwest portion of the low-velocity basin margin as is discussed in more detail in Section 7.6.

7.4.2 Soil Site JLD3. Soil site JLD3's peak velocities from the **M** 5.2 Idaho earthquake (Figure 7-49) are amplified by a factors of 2-3 relative to the rock abutment reference site JLDW (Figure 7-31) which results in longer durations of stronger ground shaking with east peak velocities at a time of 170 s on Figure 7-49 that are four times larger than corresponding peak velocities at site JLDW. Figure 7-50 shows that there is adequate S/N to synthesize ground motions in the 0.1-10 Hz frequency band. The acceleration response spectra (Figure 7-51) have several strong resonances peak that are absent from the rock site JLD3 (Figure 7-33). The 5 Hz (0.2 s) resonance peak on all components in Figure 7-51 is probably associated with fundamental-mode resonance of the embankment. Assuming a 15 m structural height, an average embankment shear-wave velocity of 300 m/s, and a quarter-wavelength approximation, yields a resonance frequency of 5 Hz. Observation of embankment resonance response at site JLD3 is not surprising, since site JLD3 is located within ~15 m of the downstream toe of the embankment. Because site JLD3 is contaminated with structural resonance responses for frequencies of ~ 5 Hz are greater, interpretation of the JLD3 synthesized motions must be limited to periods > 0.2-0.3 s. The horizontal component resonance at 2 Hz correlates reasonably well with an impedance contrast at a depth of ~10 m in Figure 5-3 and average shear-wave velocities of 80-100 m/s. There is a strong local horizontal acceleration response peak at a period of ~1.2 s (Figure 7-51), consistent with a fundamental quarter-wavelength soil resonance for a 30 m deep soil with an average shear-wave

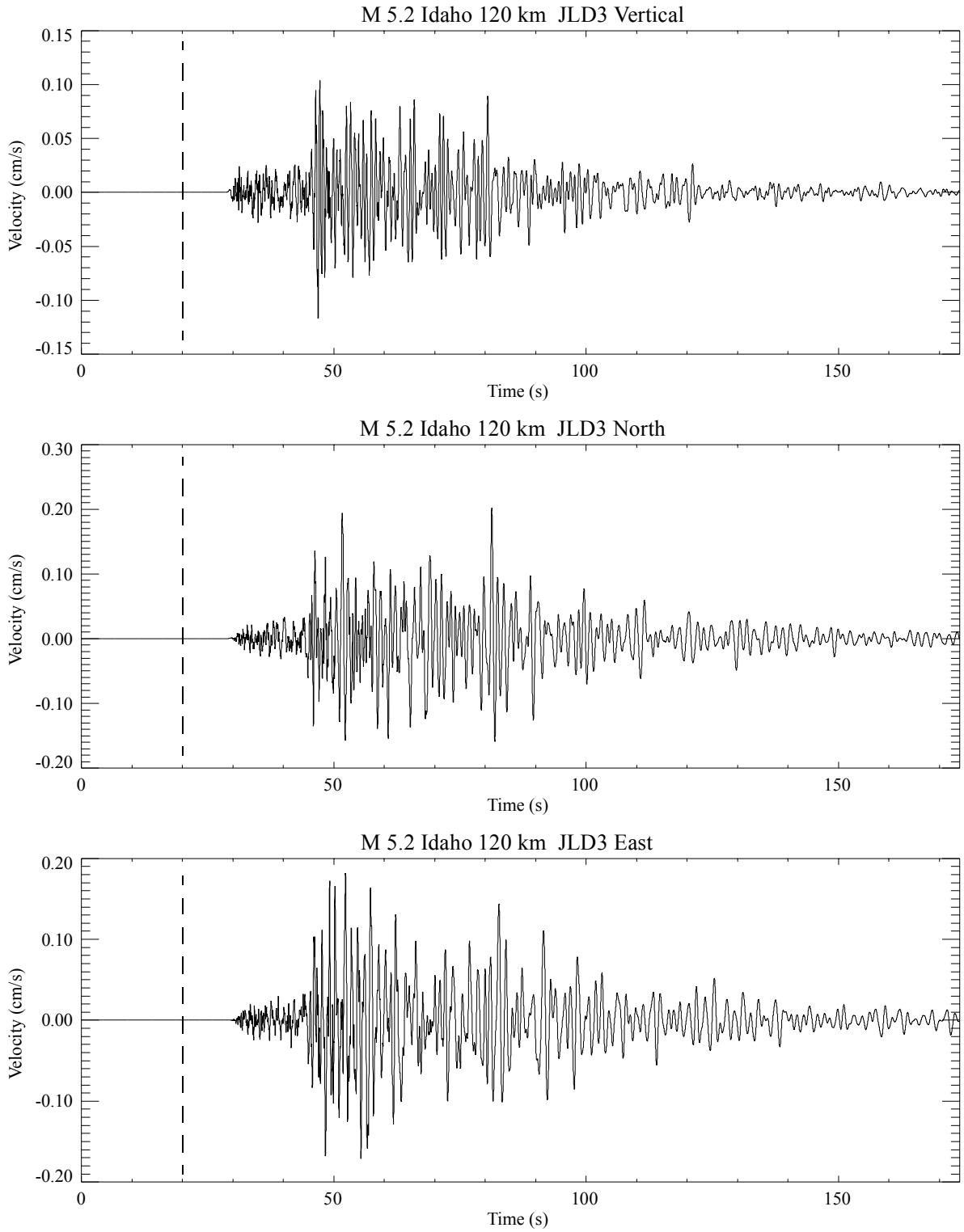

Figure 7-49: Site JLD3 velocity seismograms from the 21 Apr. 2001 **M** 5.2 Idaho earthquake. Components are as labeled. Vertical dashed lines divided the seismograms into pre-event noise and signal portions for spectra shown in Figure 7-50.

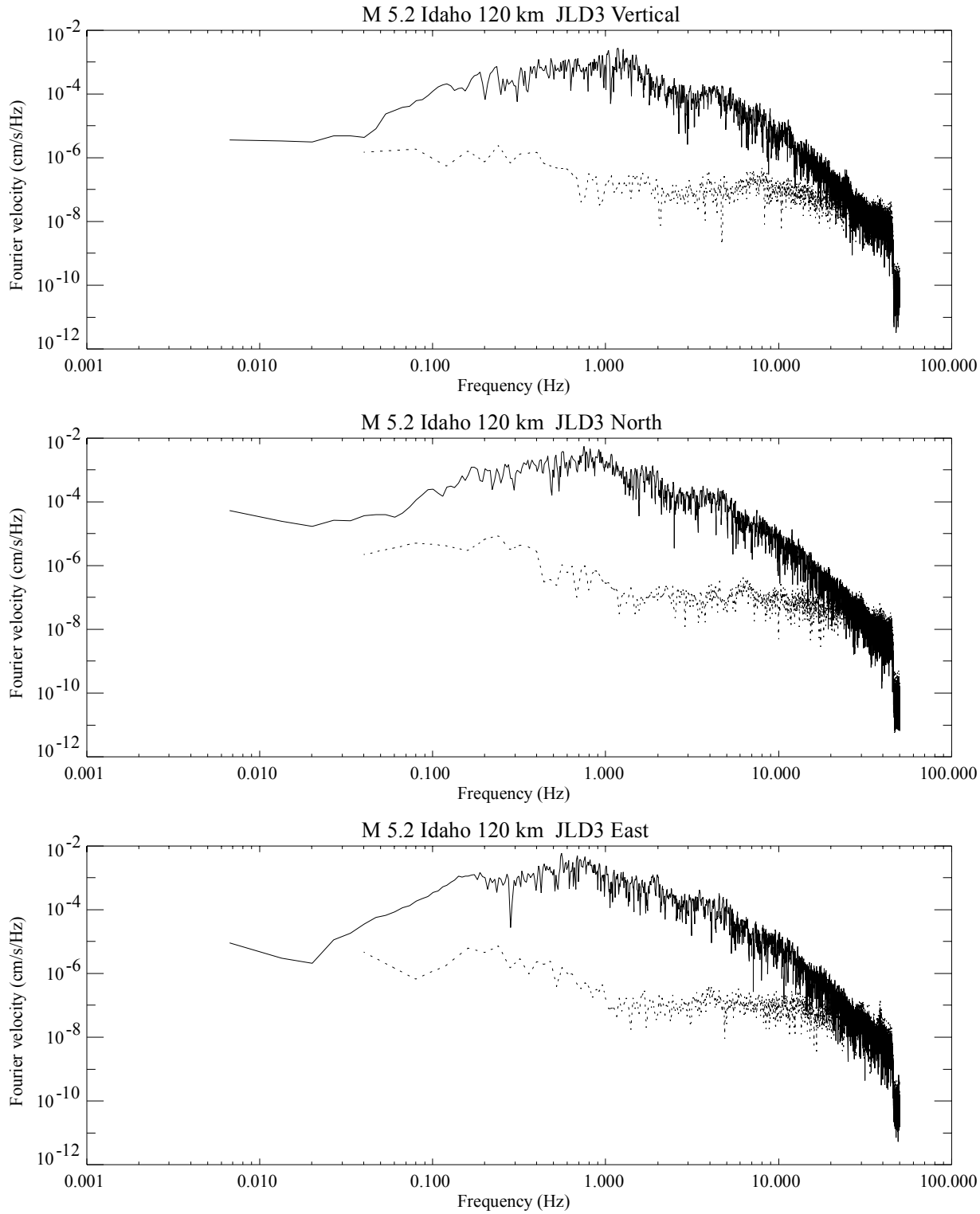

Figure 7-50: Site JLD3 Fourier velocity spectra from the 21 Apr. 2001 **M** 5.2 Idaho earthquake. Components are as labeled. Solid curves are signal spectra and dotted curves are noise spectra using the time windows indicated in Figure 7-49.

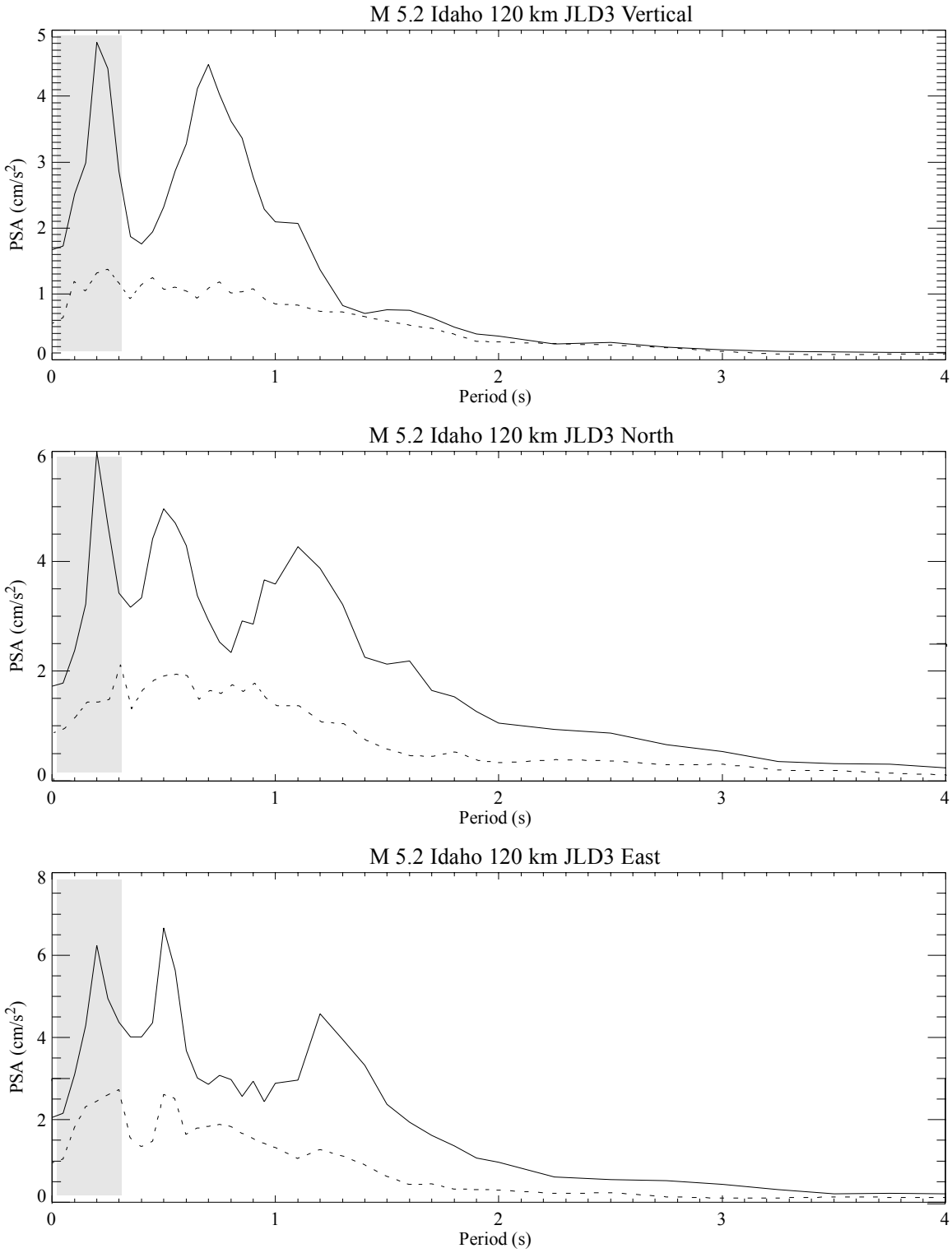

Figure 7-51: Site JLD3 acceleration response spectra from the 21 Apr. 2001 **M** 5.2 Idaho earthquake. Components are as labeled. The large 1-1.5 s horizontal responses are consistent with ~30 m thickness of low-velocity (~100 m/s shear-wave velocity) sediments. Dashed lines show corresponding rock site JLDW responses from Figure 7-33. Gray regions denote periods where the embankments resonant responses preclude interpreting the results in terms of ground response.

velocity of 100 m/s (From Figure 5-3). This represents a spectral acceleration amplification at 1.2 s of about a factor of 3-4 larger than rock site JLDW. Strong spectral acceleration amplification extends to periods of 3-4 s, consistent with an average soil basin shear-velocity of 140 m/s and an average soil thickness of 140 m beneath site JLD3 (and most of the embankment section of the dam). There is a 0.7 s resonant peak on the vertical component (Figure 7-51) that correlates with a persistent package of large amplitude arrivals in the 45-80 s time window in Figure 7-49 which is not easily explained using P-wave or shear-wave velocities indicated for the site in Figure 5-3.

For the vertical component synthetic motions, the largest differences in response between soil site JLD3 and rock site JLDW are at periods < 1 s (Figure 7-52 and 7-53). This is somewhat inexplicable because soil responses are generally assumed to not strongly influence vertical ground motions (shear-waves at near-vertical-incidence should only weakly influence vertical motions). It's difficult to invoke *S*-to-*P* converted phases as a suspect since the maximum vertical acceleration responses coincide with the arrival of the first shear-waves and large acceleration phases on the horizontal components (Figures 7-54 to 7-57). If nearly-vertical shear-waves are not responsible for the large < 1 s vertical accelerations, it is not clear how to account for the influence of soil nonlinearity on the vertical soil ground motions.

JLD3 north component soil acceleration responses are nearly uniformly amplified (Figures 7-54 and 7-55) relative to rock site JLDW responses for periods < 2 s with soil amplification nearly monotonically decreasing with increasing period for periods > 2 s (Figure 7-55). Peak velocities exceeding 70 cm/s span an 85 s time window and peak velocities exceeding 100 cm/s span a 45 s time window. While soil nonlinearly is expected to sharply attenuate acceleration responses for periods < 1 s, recent investigations (Archuleta et al., 2000; Bonilla, 2000) have showed that soil nonlinearity is likely to *increase* accelerations responses for periods > 1 s. Thus, while north component soil acceleration responses at site JLD3 for periods in the 1-2 s range exceed 2 g (Figure 7-55) soil nonlinearity may actually further amplify > 1 s acceleration responses. Comparable results are obtained for the east component (Figure 7-56 and 7-57) except that peak accelerations, velocities, and displacements are larger than the north component.

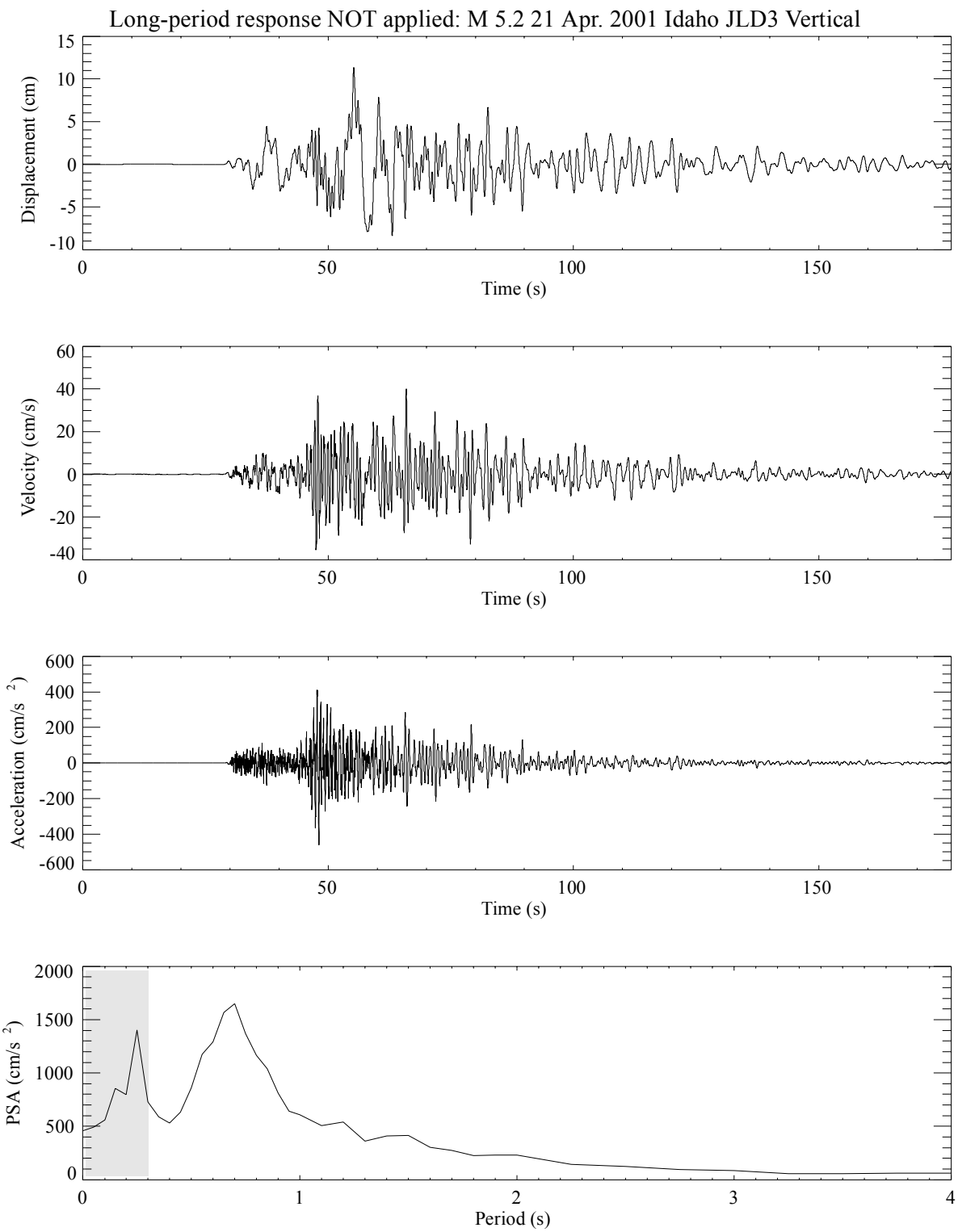

Figure 7-52: Subevent sum **M** 7.1 northern Teton fault earthquake simulation JLD3 vertical response before long-period correction. The **M** 5.2 JLDW seismograms from Figure 7-49 were the EGF's used in (7-7). Corresponding complete synthetic vertical responses incorporating (7-8) are shown in Figure 7-53. Gray region is contaminated with embankment resonant responses.

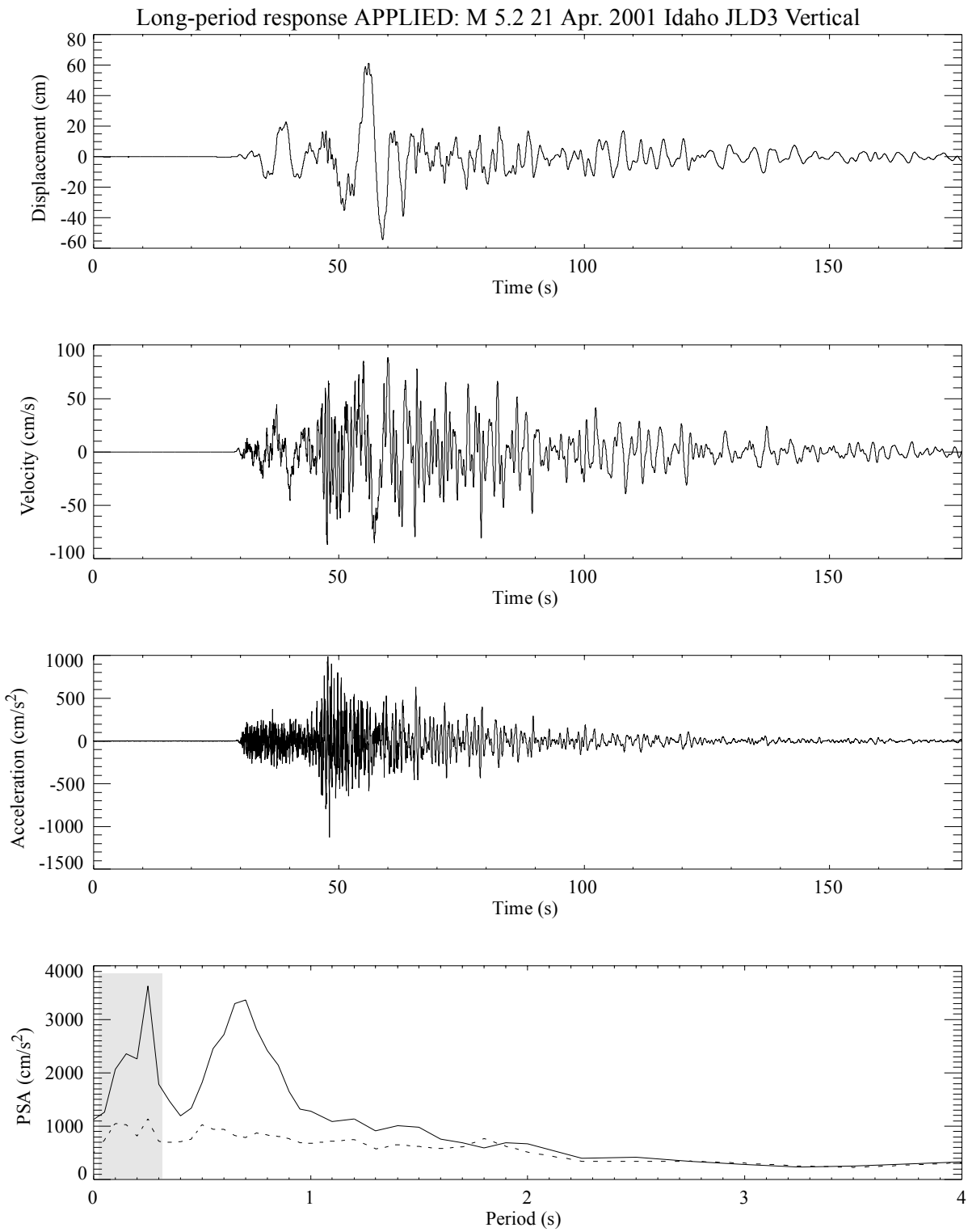

Figure 7-53: **M** 7.1 northern Teton fault earthquake simulation JLD3 vertical response. This is the total response obtained by combining the velocity seismograms from Figure 7-52 with (7-8). Dashed line shows the corresponding JLDW rock site PSA response. Gray region is contaminated with embankment resonant responses.

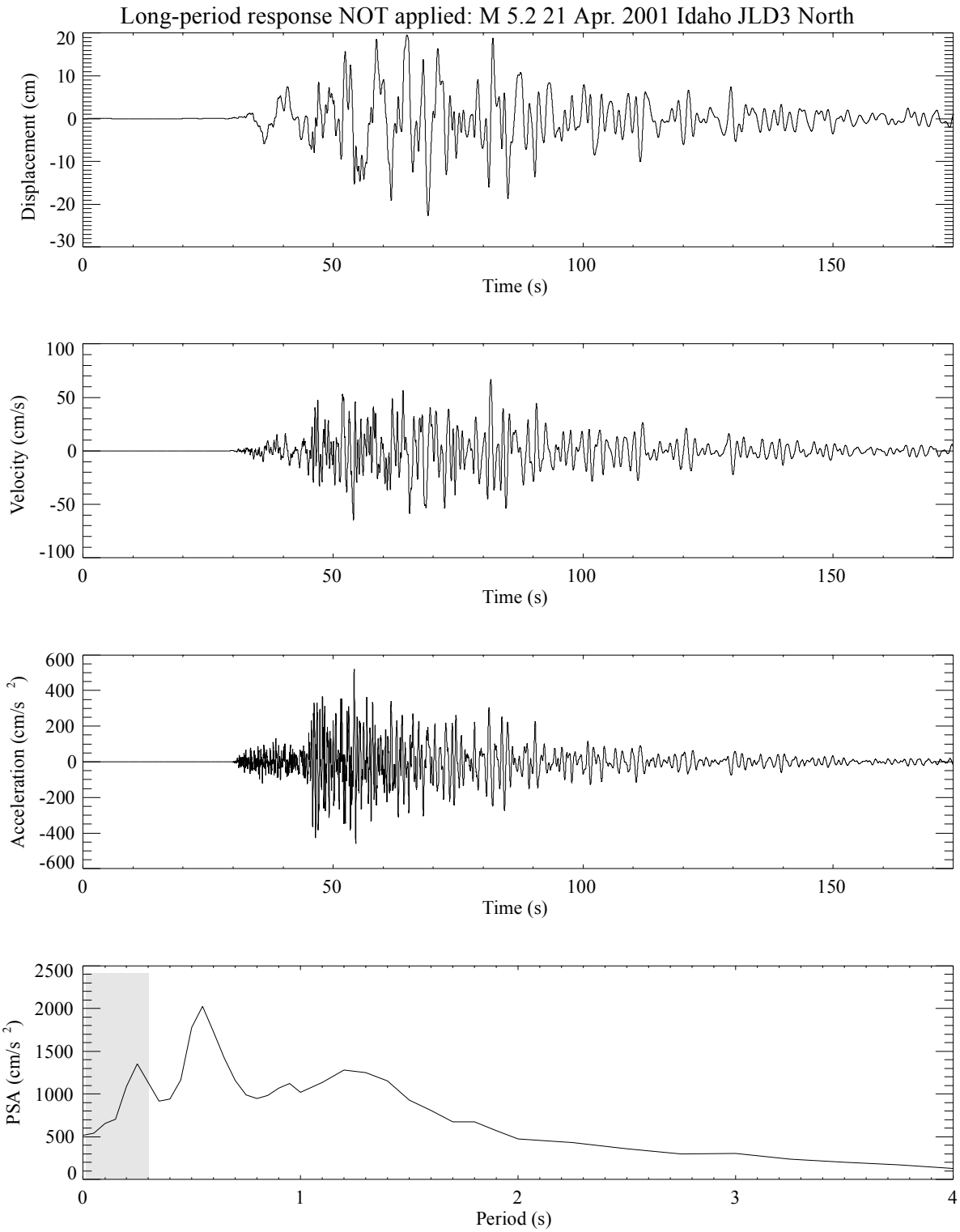

Figure 7-54: Subevent sum **M** 7.1 northern Teton fault earthquake simulation JLD3 north response before long-period correction. The **M** 5.2 JLDW seismograms from Figure 7-49 were the EGF's used in (7-7). Corresponding complete synthetic vertical responses incorporating (7-8) are shown in Figure 7-55. Gray region is contaminated with embankment resonant responses.

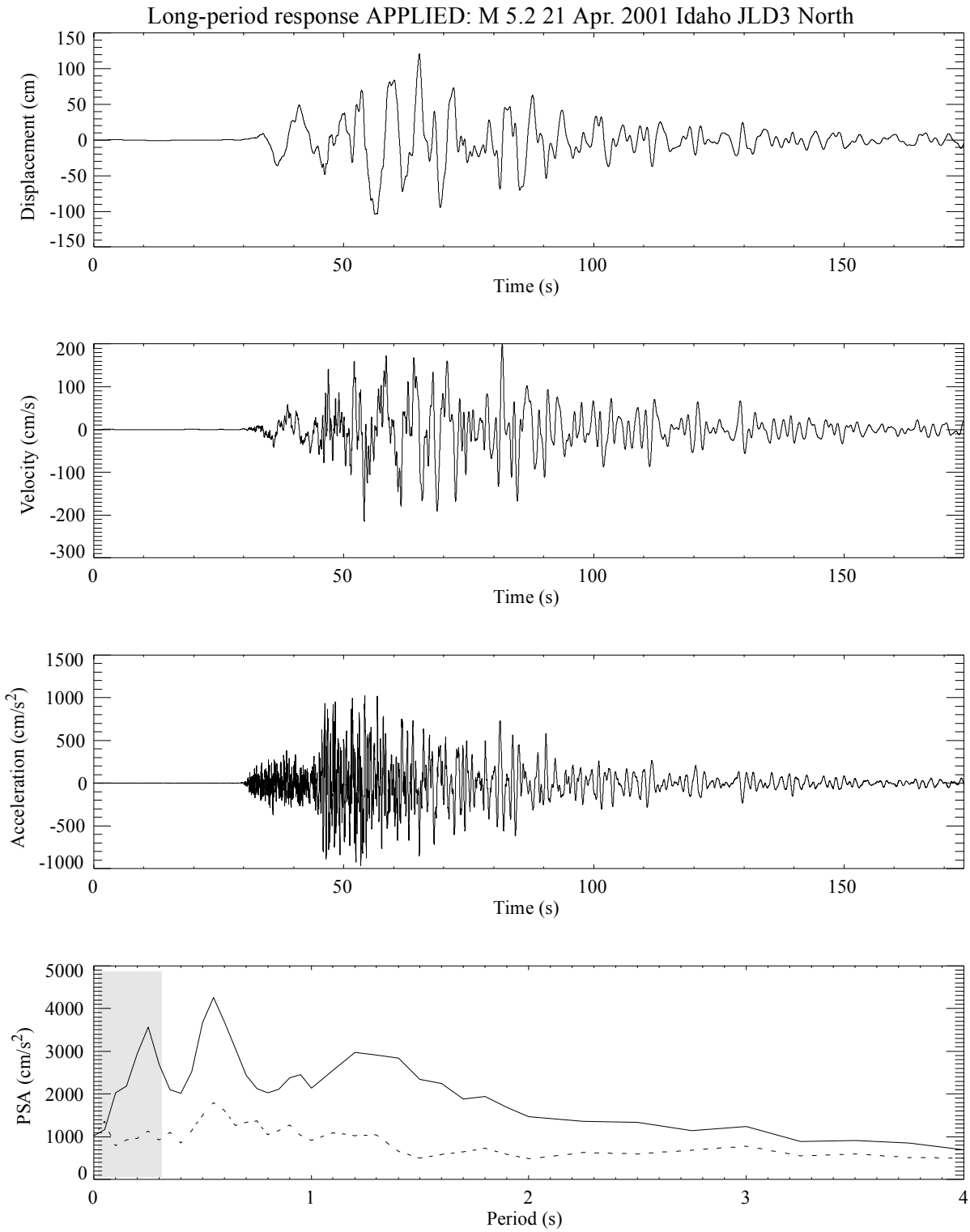

Figure 7-55: **M** 7.1 northern Teton fault earthquake simulation JLD3 north response. This is the total response obtained by combining the velocity seismograms from Figure 7-54 with (7-8). Dashed line shows the corresponding JLDW rock site PSA response. Gray region is contaminated with embankment resonant responses.

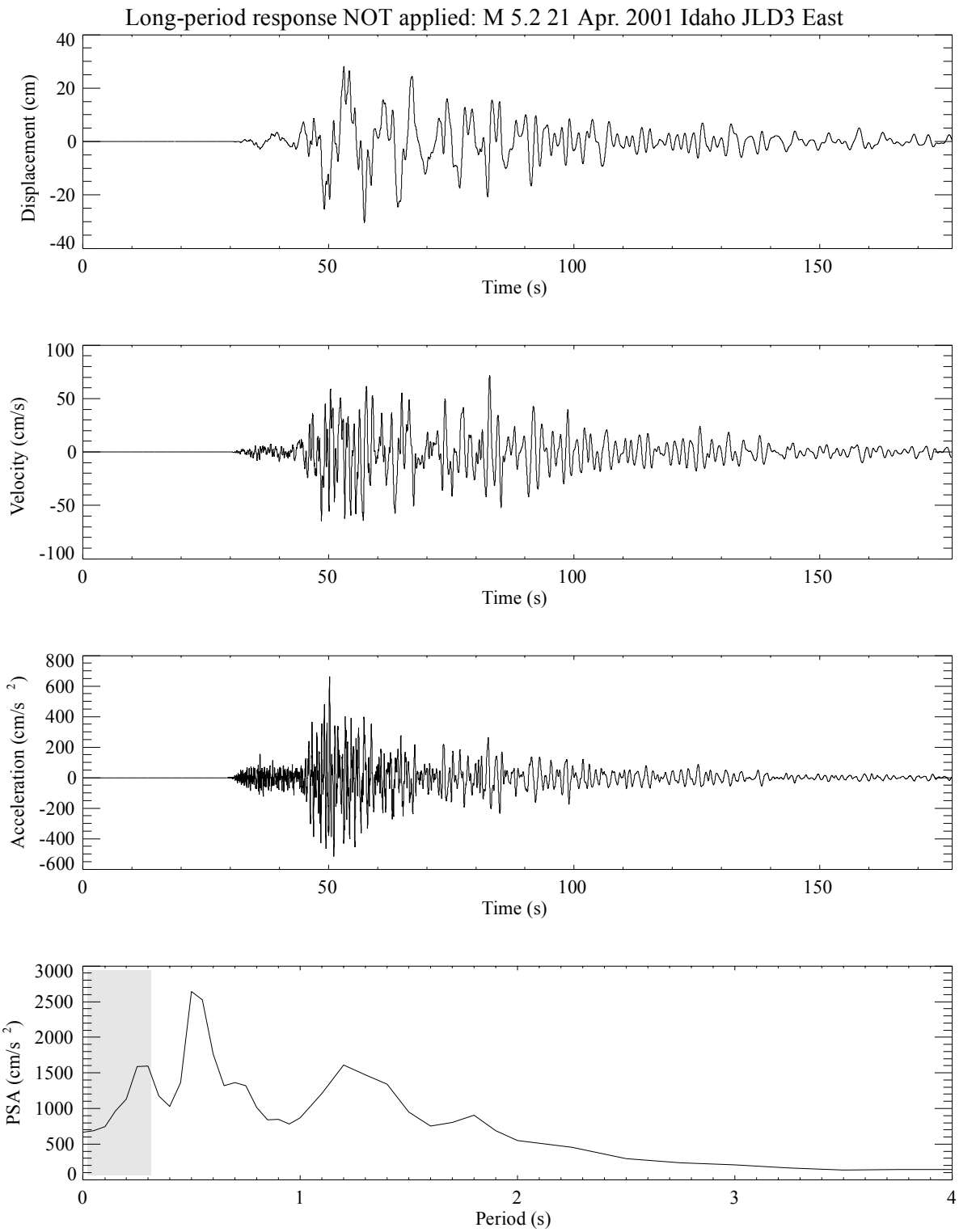

Figure 7-56: Subevent sum **M** 7.1 northern Teton fault earthquake simulation JLD3 east response before long-period correction. The **M** 5.2 JLDW seismograms from Figure 7-49 were the EGF's used in (7-7). Corresponding complete synthetic vertical responses incorporating (7-8) are shown in Figure 7-57. Gray region is contaminated with embankment resonant responses.

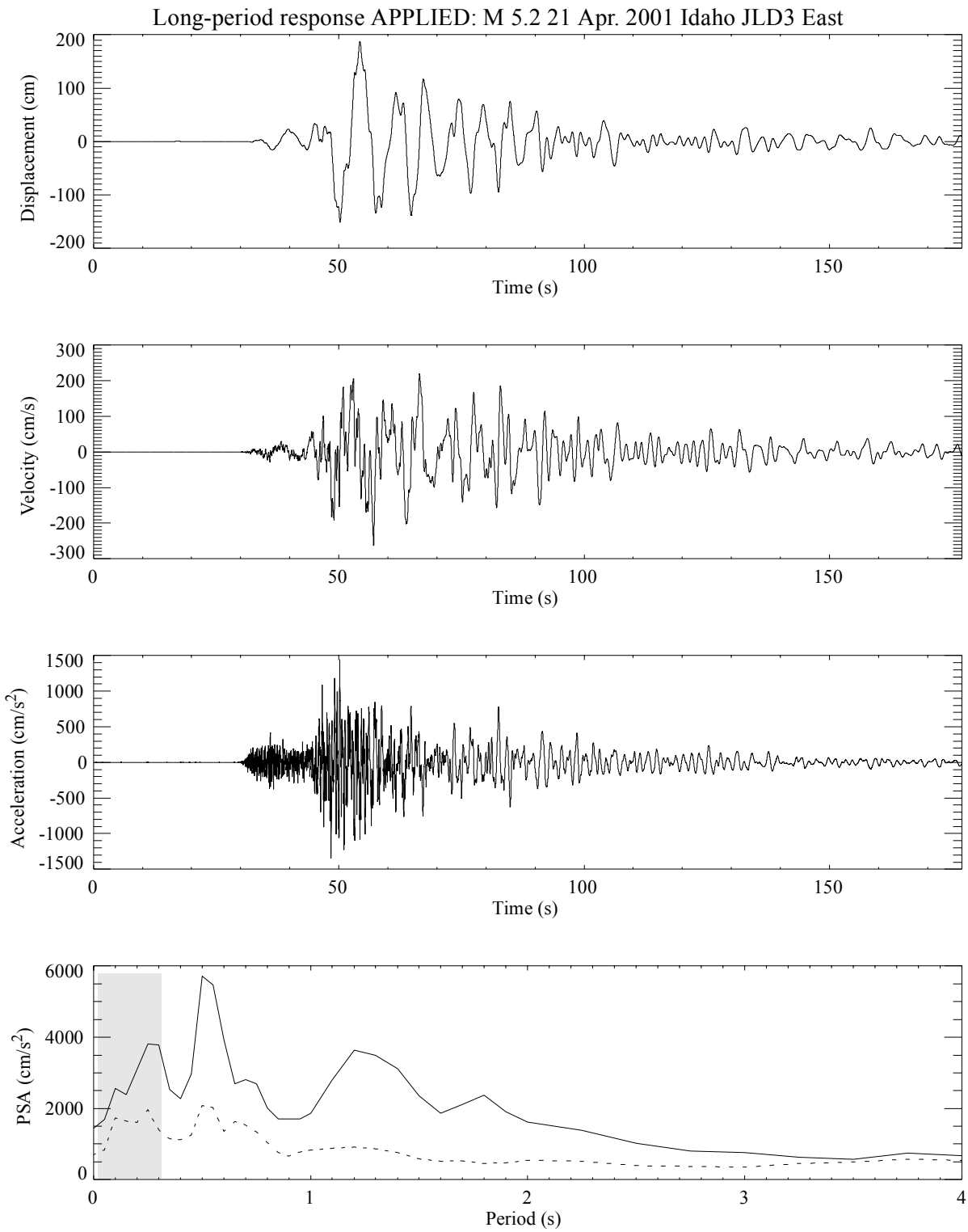

Figure 7-57: **M** 7.1 northern Teton fault earthquake simulation JLD3 east response. This is the total response obtained by combining the velocity seismograms from Figure 7-56 with (7-8). Dashed line shows the corresponding JLDW rock site PSA response. Gray region is contaminated with embankment resonant responses.

Soil site JLD3 seismograms from the **M** 4.6 Yellowstone earthquake are virtually devoid of high-frequency shear-waves (Figure 7-58) as were the rock site seismograms (Figure 7-40). The usable periods band with adequate S/N extends from about 0.5 s to 5 s (Figure 7-59). The amplified 1-2 s period soil site responses are clearly apparent in the acceleration response spectra (Figure 7-60). Synthesized vertical responses are only modestly amplified, except for periods < 1 s (Figures 7-61 and 7-62), similar to the vertical responses obtained using the **M** 5.2 Idaho JLD3 vertical EGF. North component acceleration responses are nearly uniformly amplified independent of period (Figure 7-63 and 7-64) relative to rock site JLDW responses. In contrast, east component acceleration amplification modestly decreases with increase period for periods > 2.5 s (Figures 7-65 and 7-66). The very-low-velocity soil basin deepens in the northerly direction and the increased acceleration amplifications at soil site JLD3 at periods > 2 s relative to the rock site JLDW for the Yellowstone earthquake probably reflect an effectively deeper soil basin for energy incident from the NNW relative to energy arriving from the SSW (Idaho earthquake). The Yellowstone EGF results suggest that energy arriving from the northern end of the northern Teton fault segment will more strongly amplify long-period accelerations along the embankment section of the dam than energy incident from the southern end of the northern Teton fault segment or the southern Teton fault segment. This is discussed in more detail using local earthquakes in Section 7.5 below.

7.5 Ground Motion Synthesis with Local Broadband Empirical Green's Functions

The database of site response earthquake recordings yielded two local earthquakes located near the northern Teton fault segment with sufficient S/N to use as EGF's for simulating ground motions for periods extending to 2-3 s (Table 7-4). A third local **M** 3.7 earthquake located near

Table 7-4: Local Broadband Empirical Green's Function Earthquake Information

Date (yr/mon/day)	Time (hr,min,sec)	Latitude (degrees N)	Longitude (degrees E)	Elevation (km wrt msl)	Magnitude
1998/07/11	16:10:3.152	43.91073	-110.64070	-3.72	2.9
2002/11/20	02:14:2.000	43.68424	-110.49812	-2.87	3.2

the southern Teton fault segment provides some information about the likely response

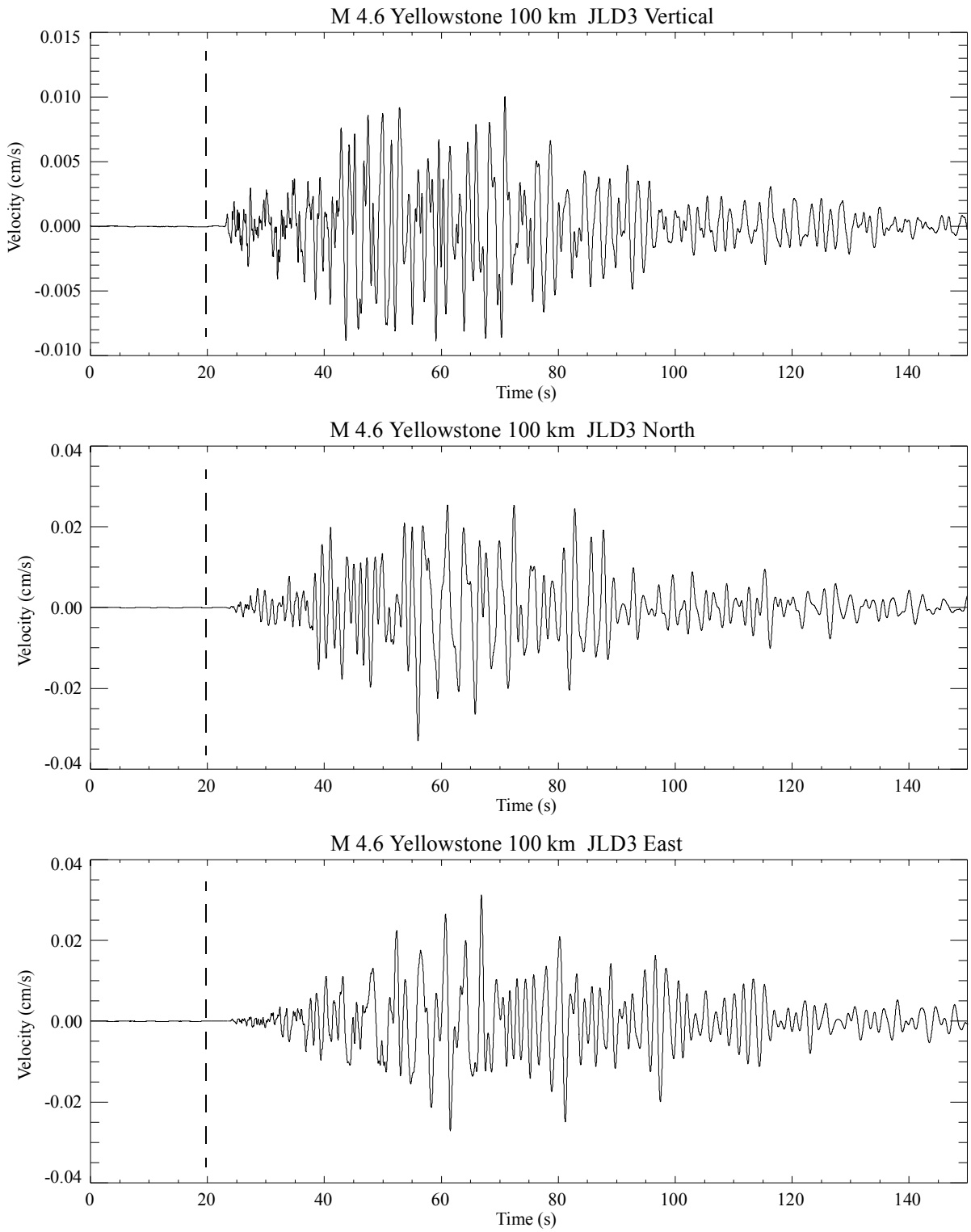

Figure 7-58: Site JLD3 velocity seismograms from the 24 Nov. 2000 **M** 4.6 Yellowstone earthquake. Components are as labeled. Vertical dashed lines divided the seismograms into pre-event noise and signal portions for spectra shown in Figure 7-59. Note significant amplitudes persist to the end of the record.

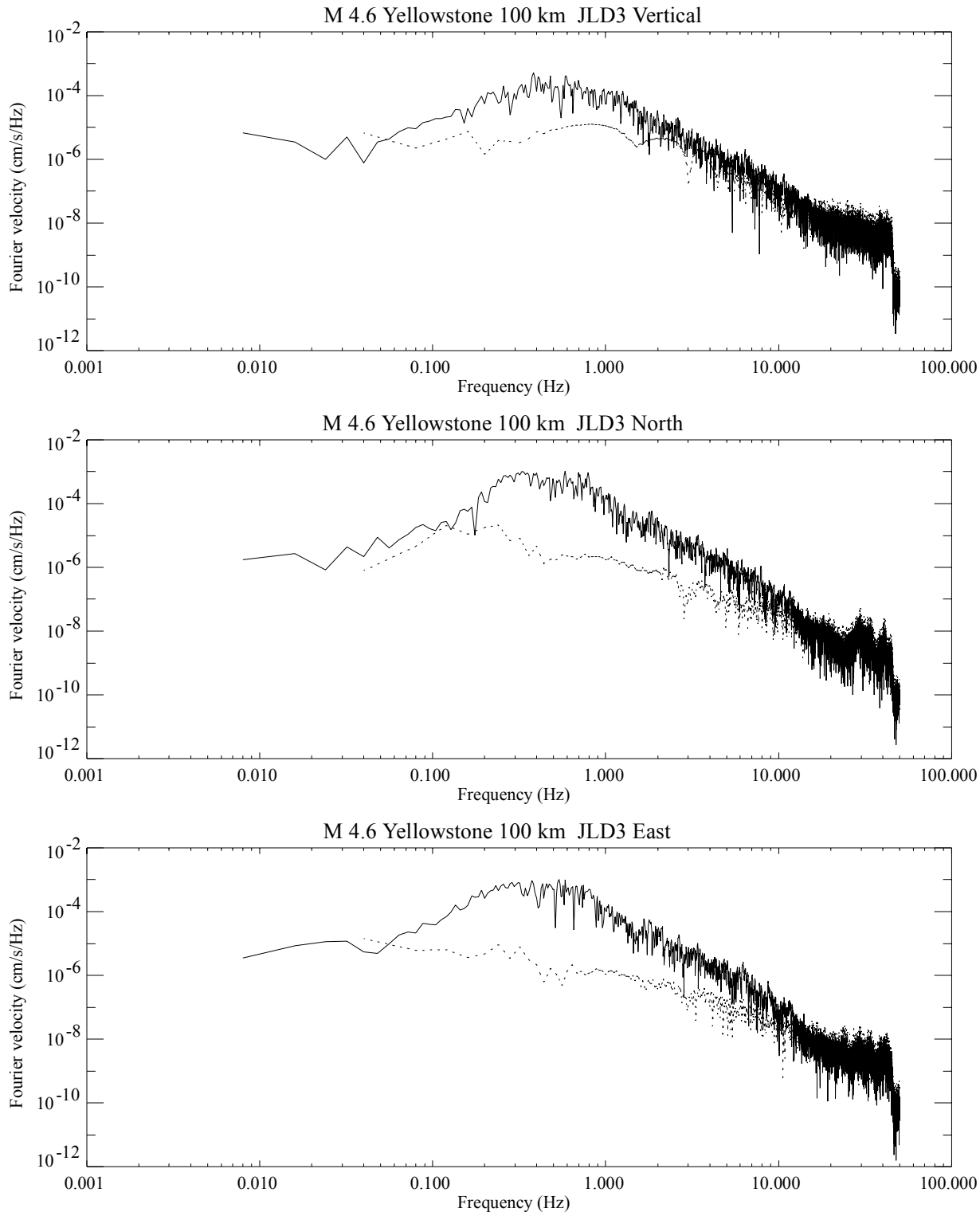

Figure 7-59: Site JLD3 Fourier velocity spectra from the 24 Nov. 2000 **M** 4.6 Yellowstone earthquake. Components are as labeled. Solid curves are signal spectra and dotted curves are noise spectra using the time windows indicated in Figure 7-58.

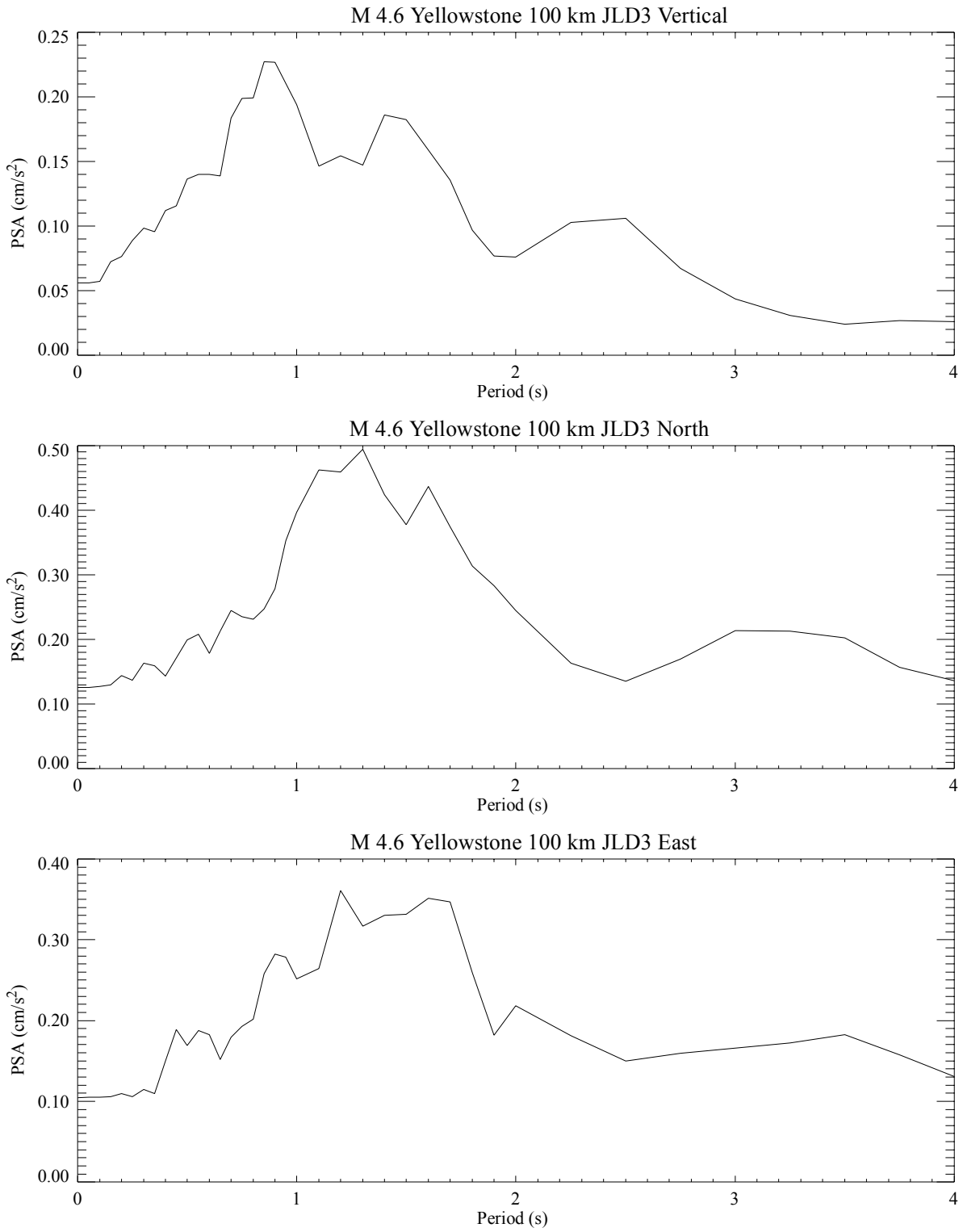

Figure 7-60: Site JLD3 acceleration response spectra from the 24 Nov. 2000 **M** 4.6 Yellowstone earthquake. Components are as labeled. Note the largest horizontal responses are between 1 s and 2 s.

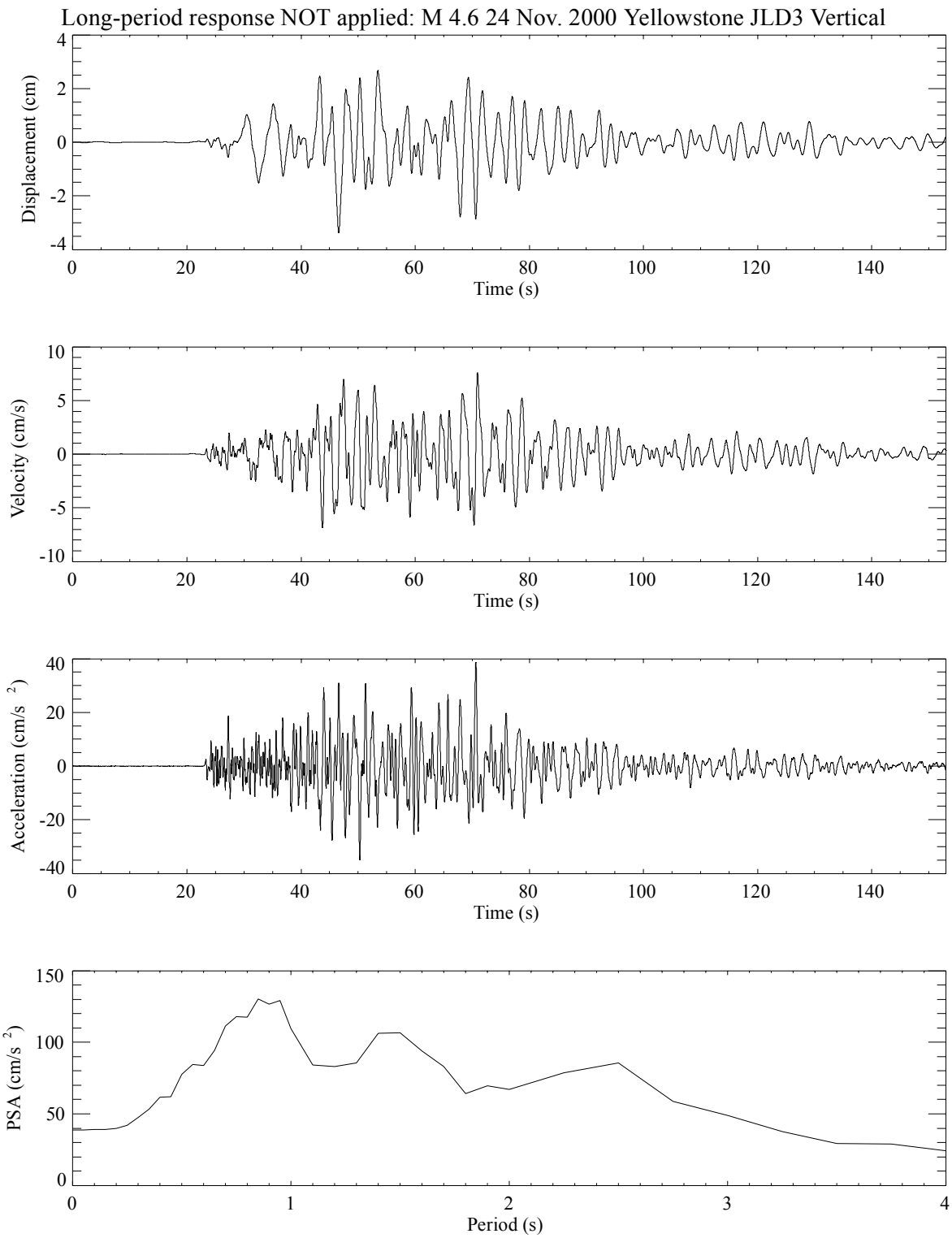

Figure 7-61: Subevent sum **M** 7.1 northern Teton fault earthquake simulation JLD3 vertical response before long-period correction. The **M** 4.6 JLDW seismograms from Figure 7-58 were the EGF's used in (7-7). Corresponding complete synthetic vertical responses incorporating (7-8) are shown in Figure 7-62.

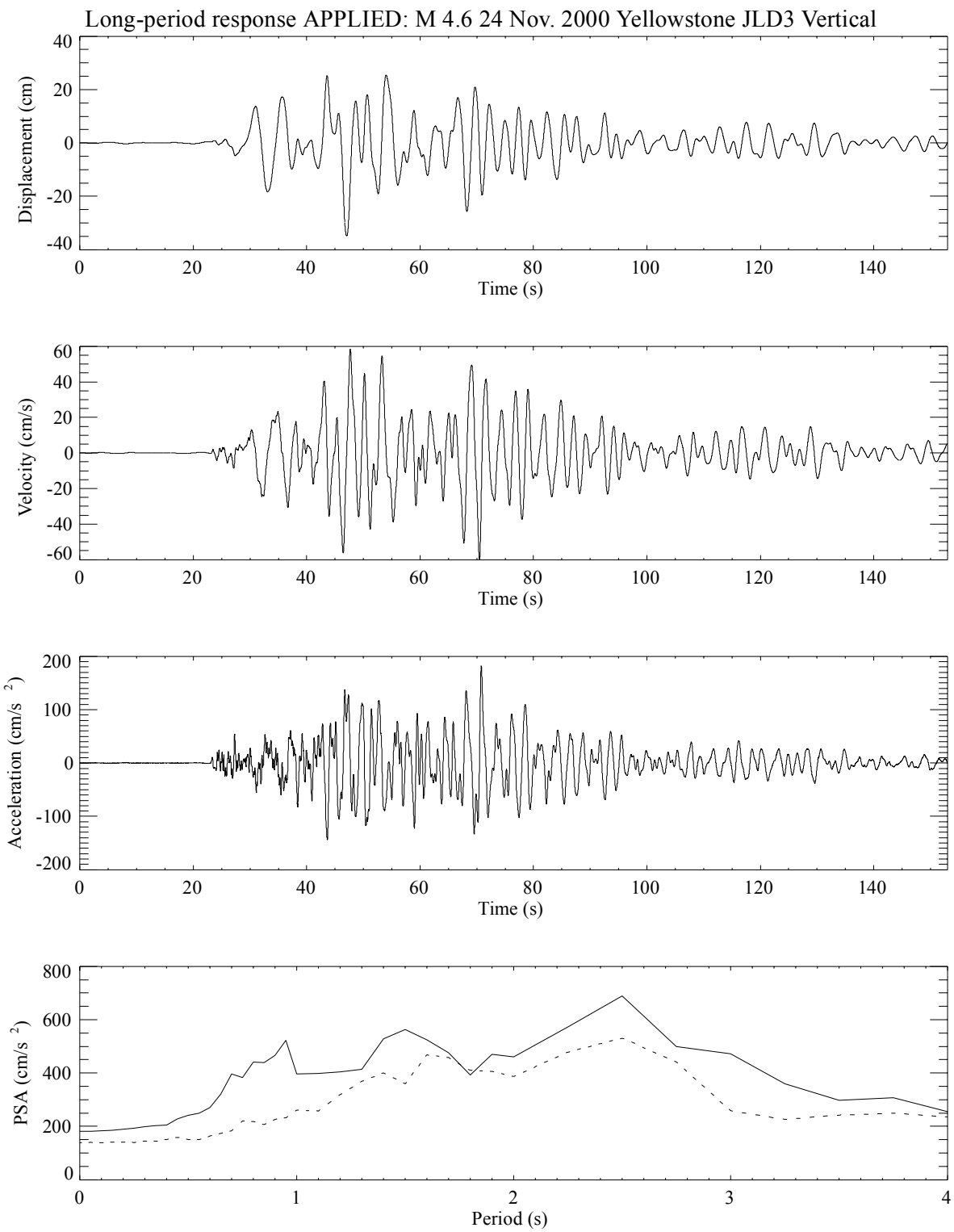

Figure 7-62: **M** 7.1 northern Teton fault earthquake simulation JLD3 vertical response. This is the total response obtained by combining the velocity seismograms from Figure 7-61 with (7-8).

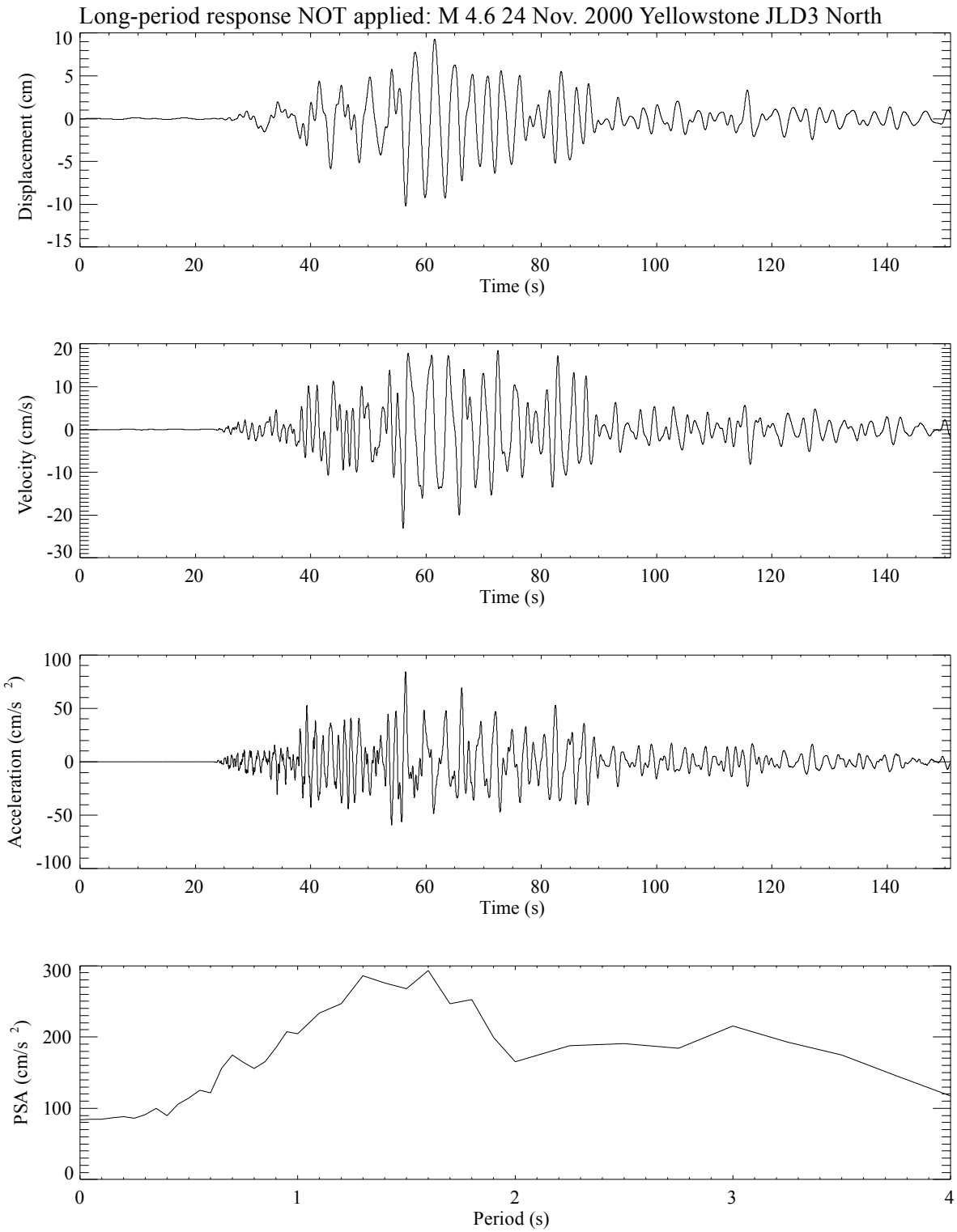

Figure 7-63: Subevent sum **M** 7.1 northern Teton fault earthquake simulation JLD3 north response before long-period correction. The **M** 4.6 JLDW seismograms from Figure 7-58 were the EGF's used in (7-7). Corresponding complete synthetic vertical responses incorporating (7-8) are shown in Figure 7-64.

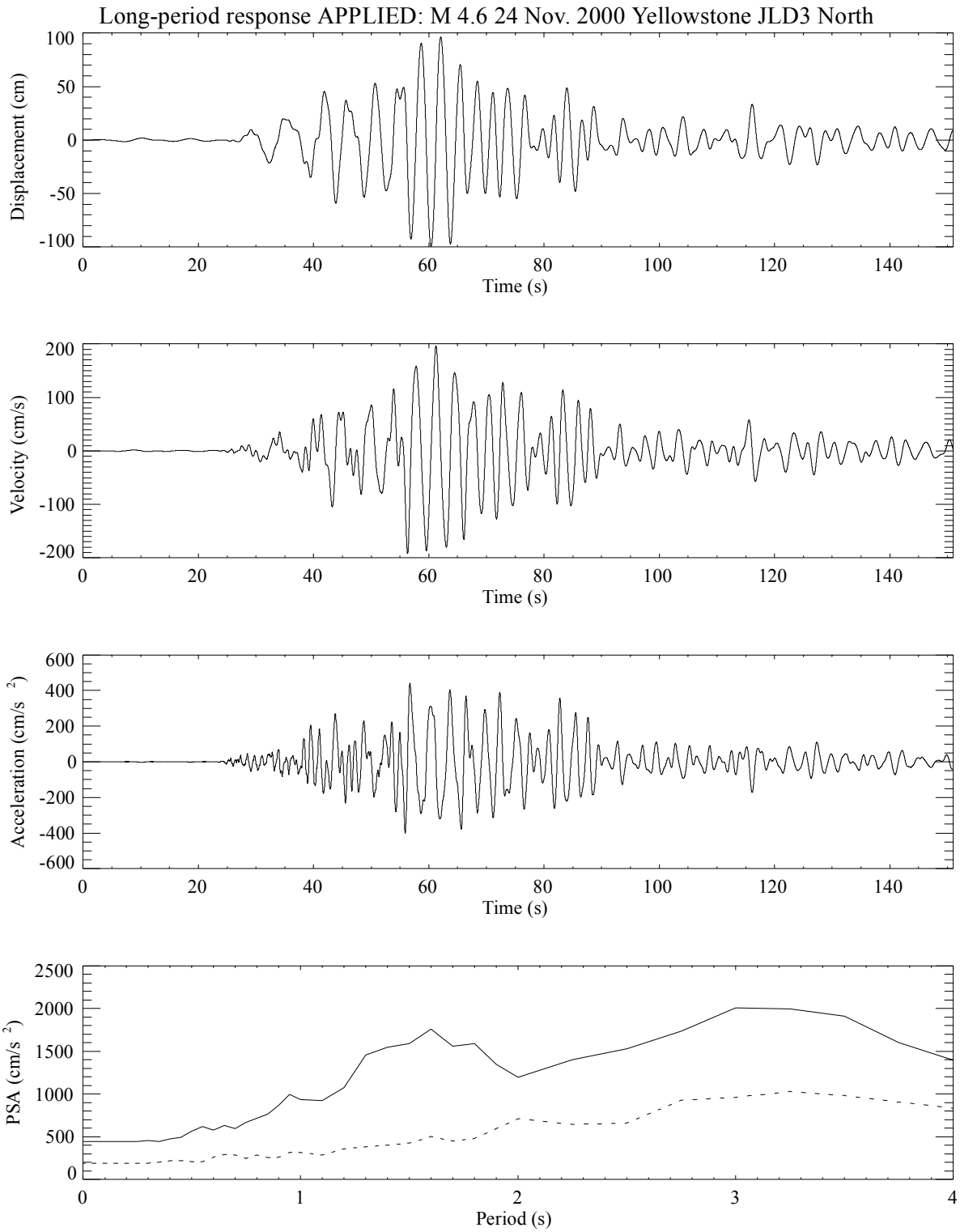

Figure 7-64: **M** 7.1 northern Teton fault earthquake simulation JLD3 north response. This is the total response obtained by combining the velocity seismograms from Figure 7-45 with (7-8).

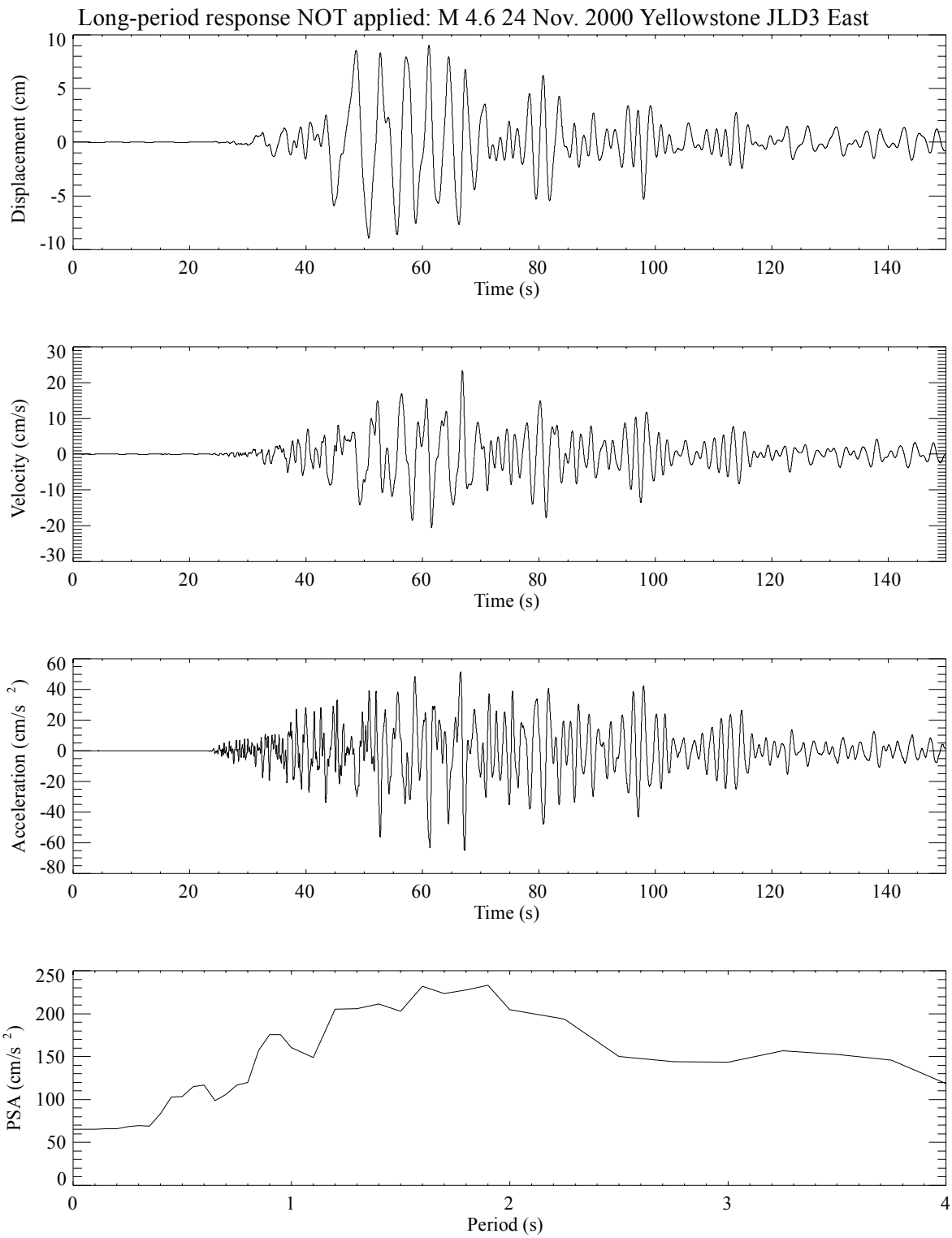

Figure 7-65: Subevent sum **M** 7.1 northern Teton fault earthquake simulation JLD3 east response before long-period correction. The **M** 4.6 JLDW seismograms from Figure 7-58 were the EGF's used in (7-7). Corresponding complete synthetic vertical responses incorporating (7-8) are shown in Figure 7-66.

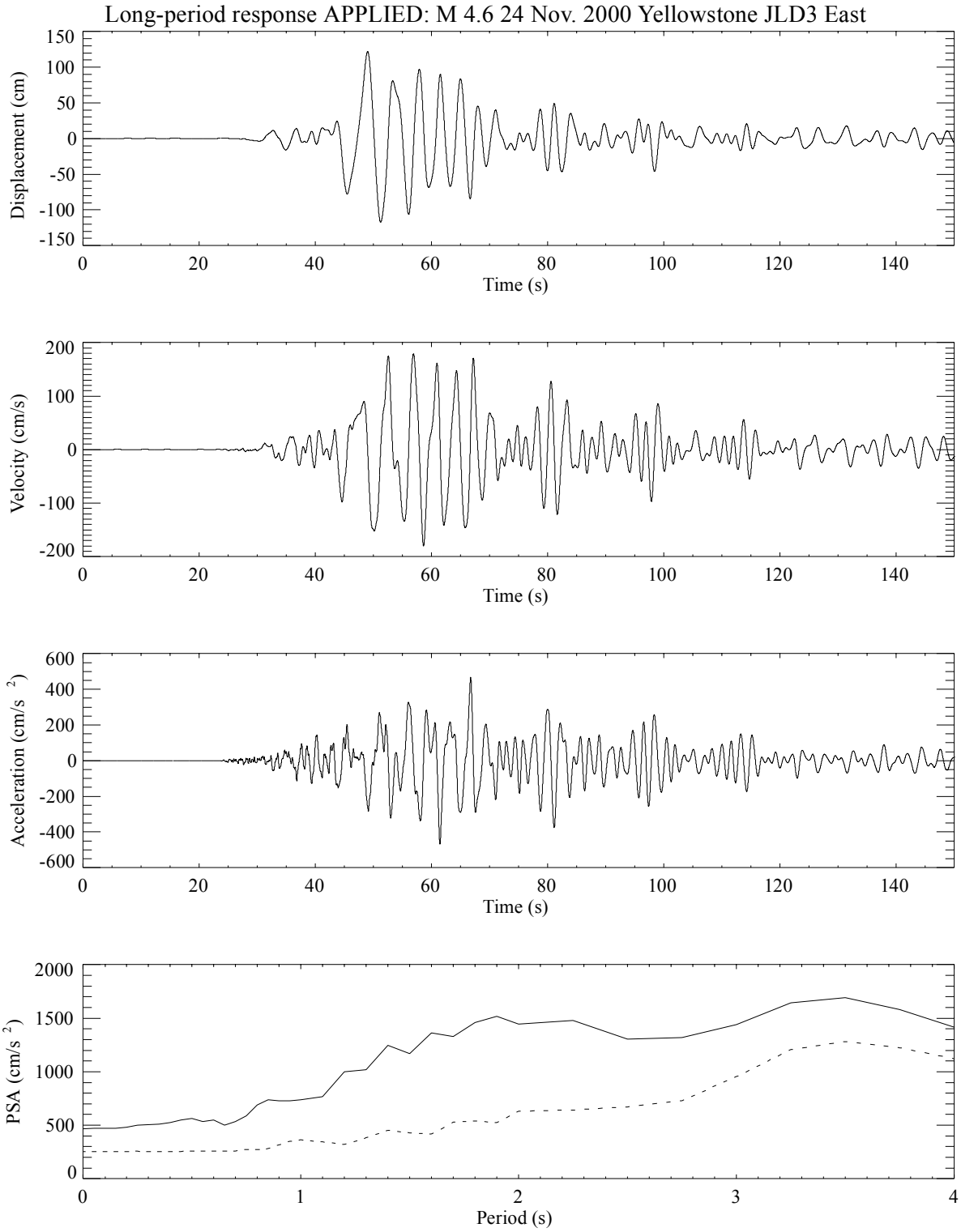

Figure 7-66: **M** 7.1 northern Teton fault earthquake simulation JLD3 north response. This is the total response obtained by combining the velocity seismograms from Figure 7-58 with (7-8).

characteristics for periods > 1 s to seismic waves incident from the southern Teton fault segment. The epicenters of these three earthquakes are shown in Figure 7-67. The vertical components of the EGF earthquakes in Table 7-4 have lower S/N relative to the horizontal components (Figure 7-68 and 7-69), limiting the usable period range to 0.5 s to 2 s for the vertical components, and 0.2 s to 3 s for the horizontal components. The **M** 3.7 earthquake of 29 January 2002 has higher S/N on all components (Figure 7-70), but is solely used to illustrate differential long-period responses with respect to the **M** 2.9 EGF, whose S/N limits the period band of comparison. The same rupture models used in Section 6 where used with the local earthquake EGF's to ascertain the influence of the Green's functions on estimated ground motions at site JLDW. A total of 3300 ground motion simulations were produced using each of the two local EGF's by varying hypocenter locations, asperity models, etc. in precisely the same manner as in Section 6. The EGF's for the **M** 2.9 11 July 1998 earthquake are limited in duration because the older digital recording system limited the total recording duration allowed for a single event (Figure 7-68). More complete (longer duration) recordings were obtained using the newer digital recording systems for the other two EGF earthquakes (Figures 7-69 and 7-70); record lengths for both these earthquakes exceed two minutes.

7.5.1 Simulated Ground Motions Using the 11 July 1998 M2.9 EGF's. The July 11, 1998 EGF event had an oblique normal-slip focal mechanism (Figure 7-71) and was located ~8 km south of site JLDW. The focal mechanism constraints on rake required including > 30° of strike-slip motion in the rake. This focal mechanism, azimuth, and takeoff angle produced an average *SV* radiation coefficient (0.21) at site JLDW about half of the average *SV* radiation coefficient for a northern segment Teton fault normal-slip earthquake on a 35-45°-dipping normal fault (0.44). Consequently, the EGF was scaled by a factor of two to produce an effective *SV* scaling consistent with the average radiation pattern on the northern segment of the Teton fault for site JLDW.

For the purposes of illustration, the simulated ground motion with acceleration response spectra closest to 84% quantile acceleration responses spectra (Figure 7-72) are shown in Figures 7-73 to 7-75. An L1 norm was used to find the synthetic ground motions with the smallest departure from the 84% quantile PSA in the period range of 0.5 s to 3 s. As expected the fault-normal component

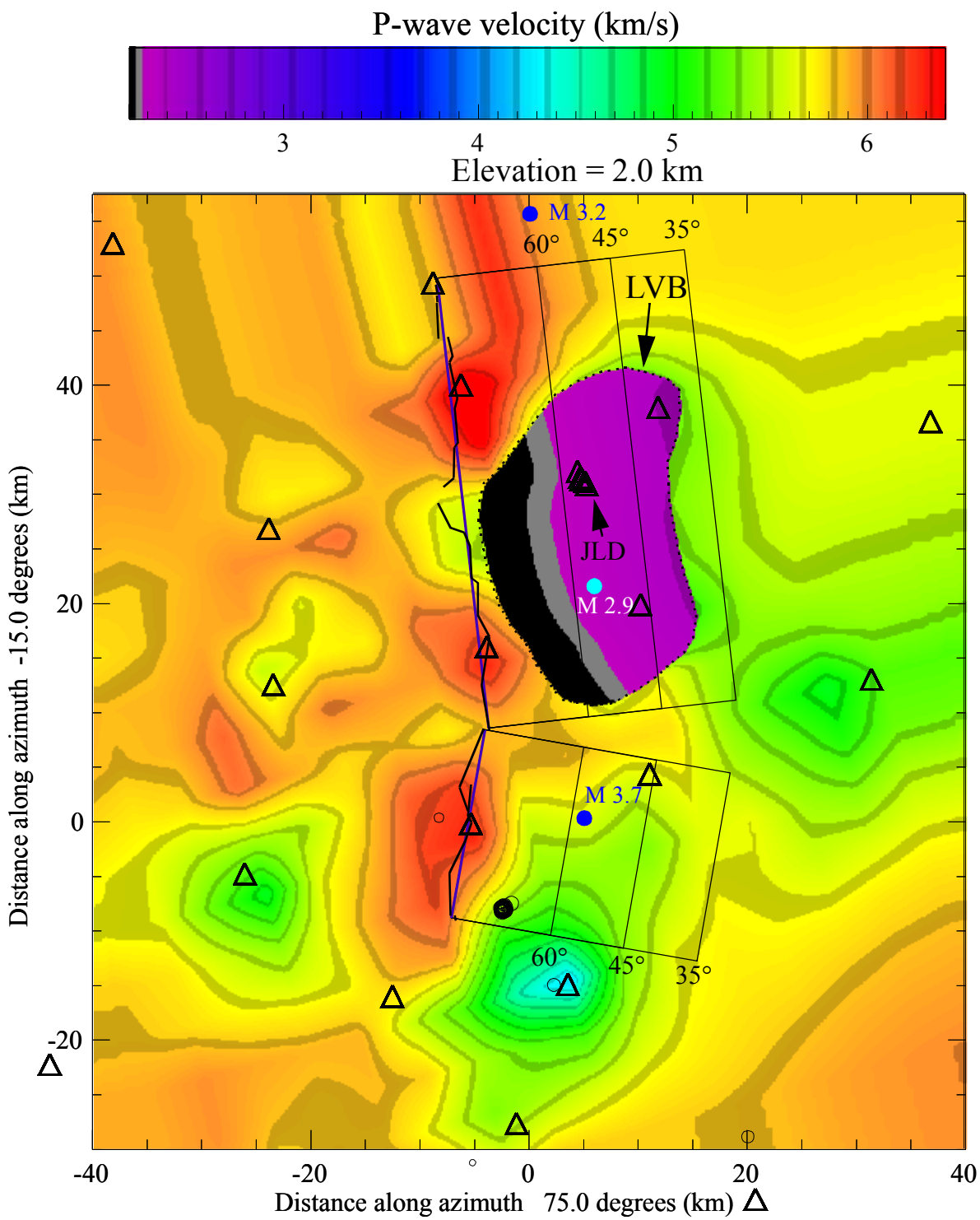

Figure 7-67: Epicenters of the three "broadband" EGF local earthquakes with P-wave 3D velocity model at elevation 2 km. Filled blue circles labeled with magnitudes are the EGF epicenters. Seismographic stations are triangles with the cluster of site-response stations at Jackson Lake Dam indicated as JLD. Solid rectangles are plan projections of the Teton fault segments for dips as labeled. Blue line segments show approximations to the surface traces of the Teton fault (irregular solid line segments). Closed dotted curve labeled LVB denotes the limits of the LVB.

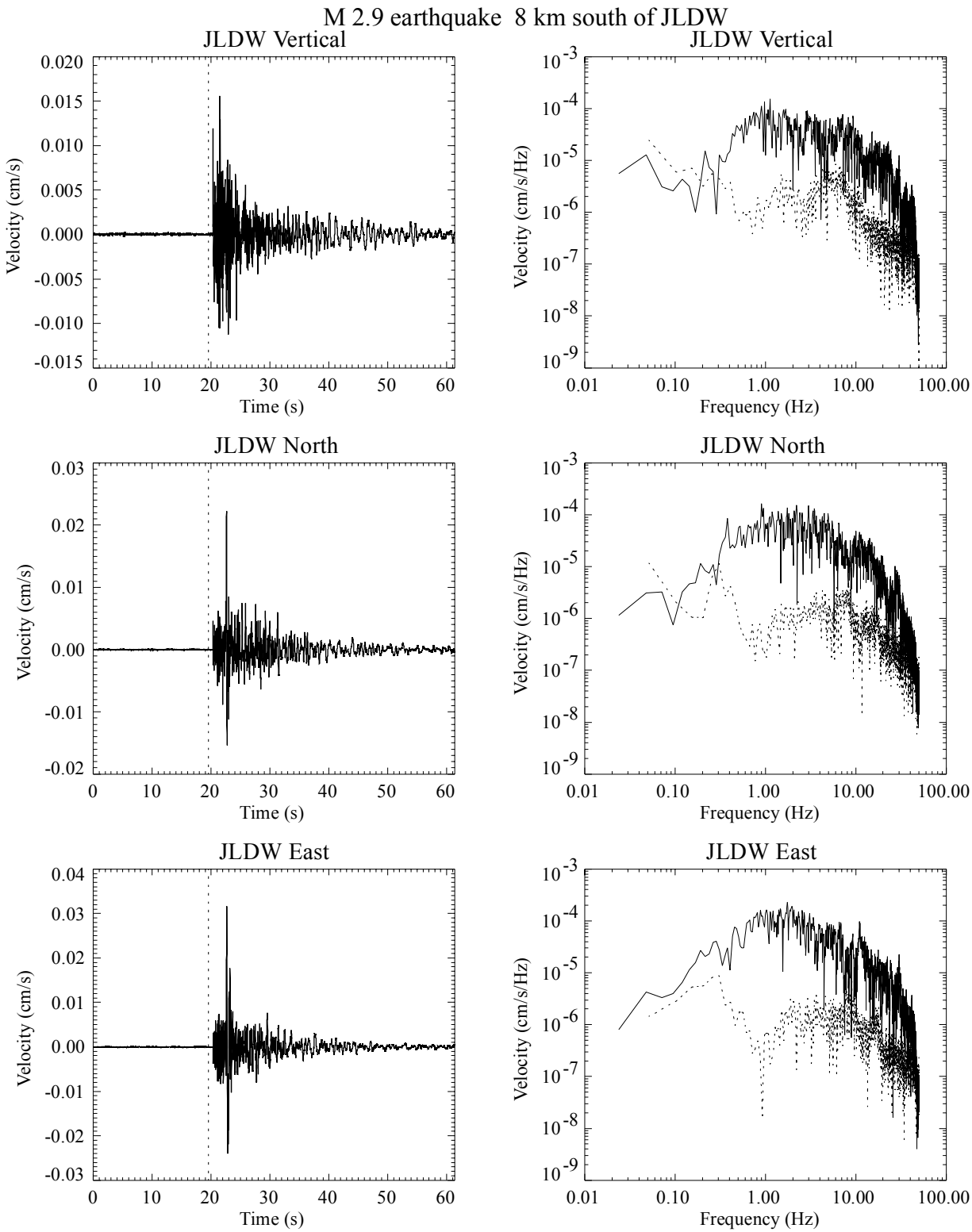

Figure 7-68: Site JLDW velocity seismograms and Fourier spectra from the **M** 2.9 11 July 1998 earthquake. The vertical dashed lines on the seismograms indicate the end time of the noise time windows (dashed curves in the Fourier spectra) and the signal windows (solid curves in the Fourier spectra). Epicenter is shown on Figure 7-67 and event information is in Table 7-4.

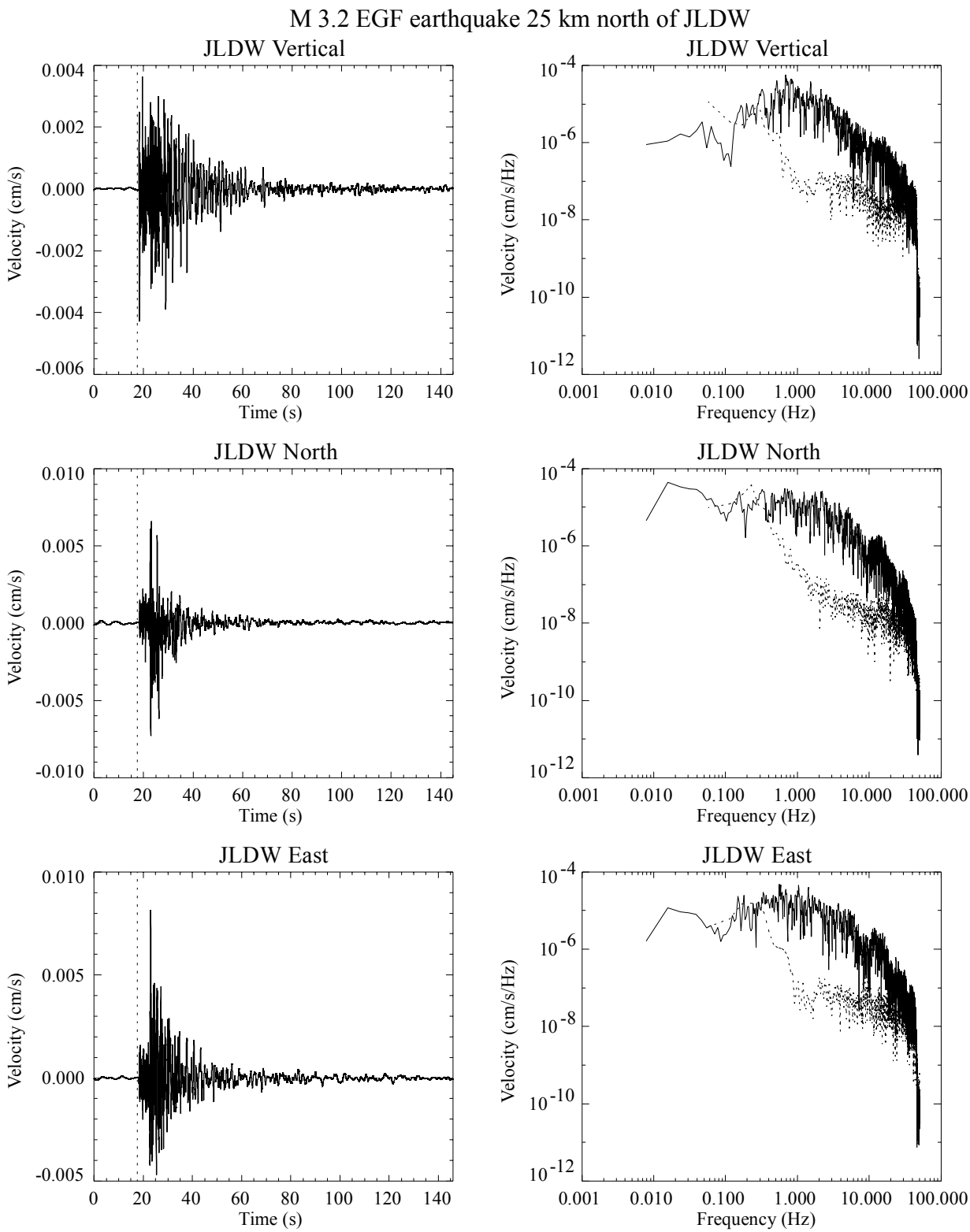

Figure 7-69: Site JLDW velocity seismograms and Fourier spectra from the **M** 3.2 20 November 2002 earthquake. The vertical dashed lines on the seismograms indicate the end time of the noise time windows (dashed curves in the Fourier spectra) and the signal windows (solid curves in the Fourier spectra). Epicenter is shown on Figure 7-67 and event information is in Table 7-4.

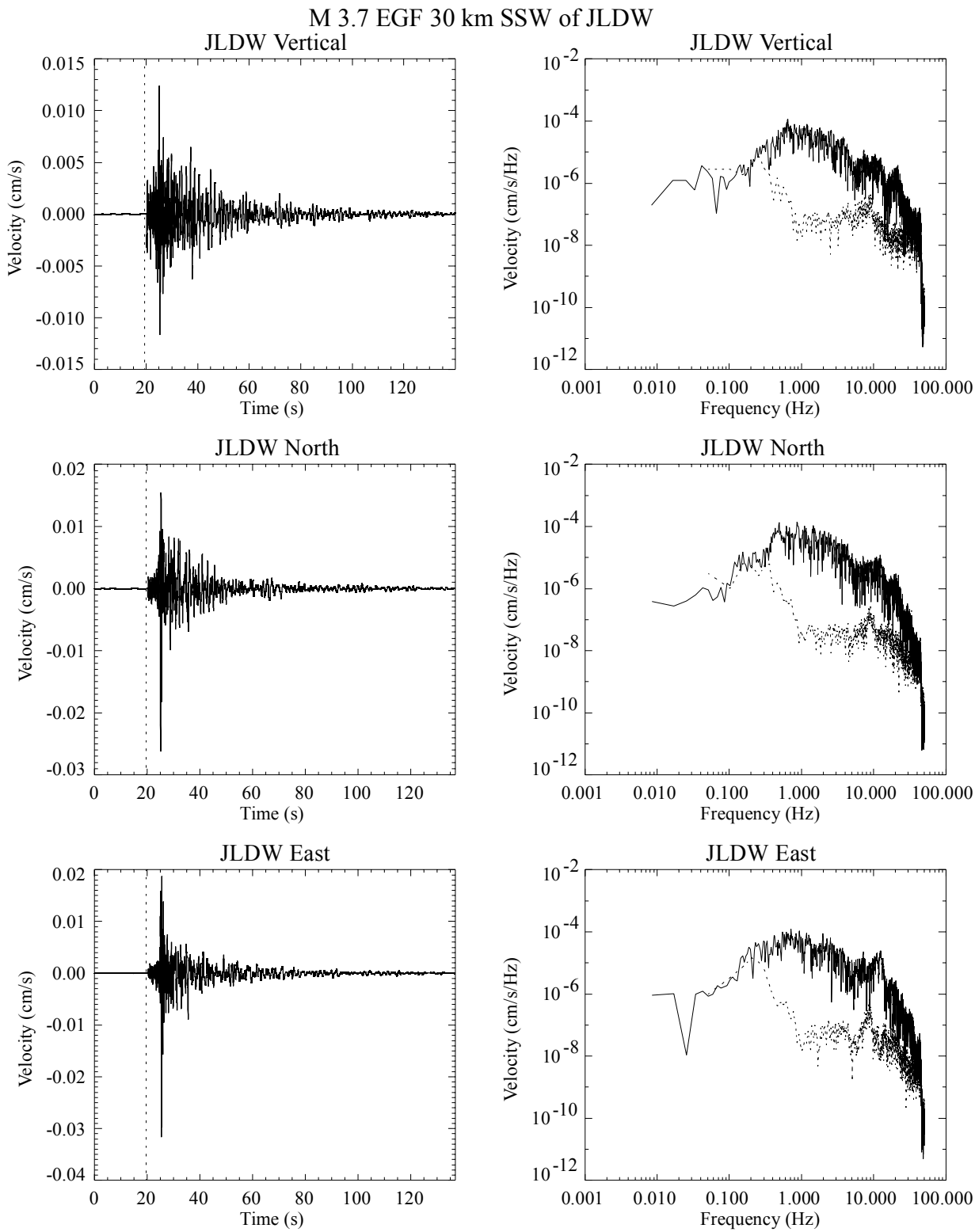

Figure 7-70: Site JLDW velocity seismograms and Fourier spectra from the **M** 3.7 29 January 2002 earthquake. The vertical dashed lines on the seismograms indicate the end time of the noise time windows (dashed curves in the Fourier spectra) and the signal windows (solid curves in the Fourier spectra). Epicenter is shown on Figure 7-67 and event information is in Table 7-4.

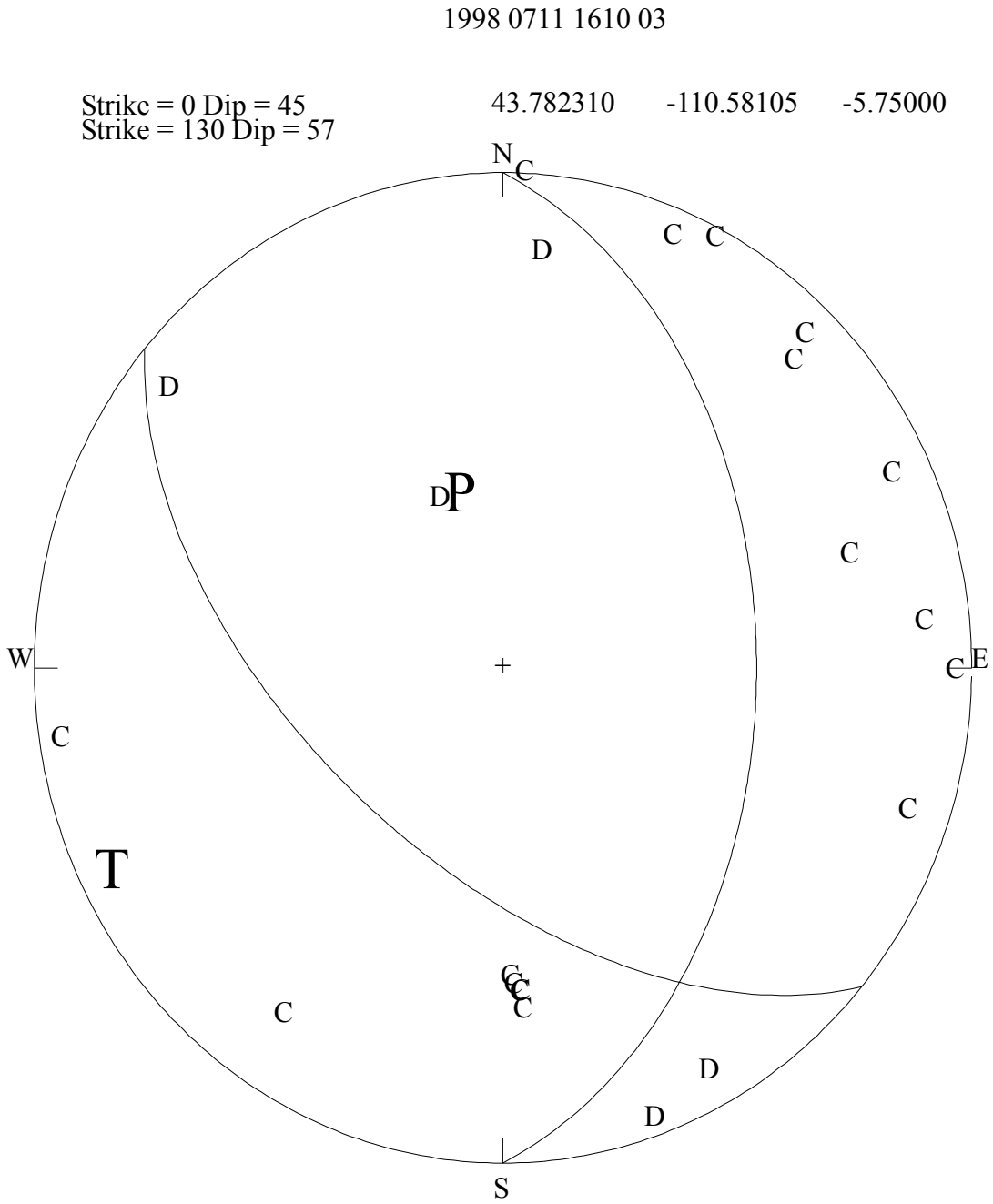

Figure 7-71: Focal mechanism for the M 2.9 EGF on 11 July 1998. Lower hemisphere projection with compressions (C) and dilatations (D), compressional (bold P) and tensile (bold T) axes, and P-wave nodal planes.

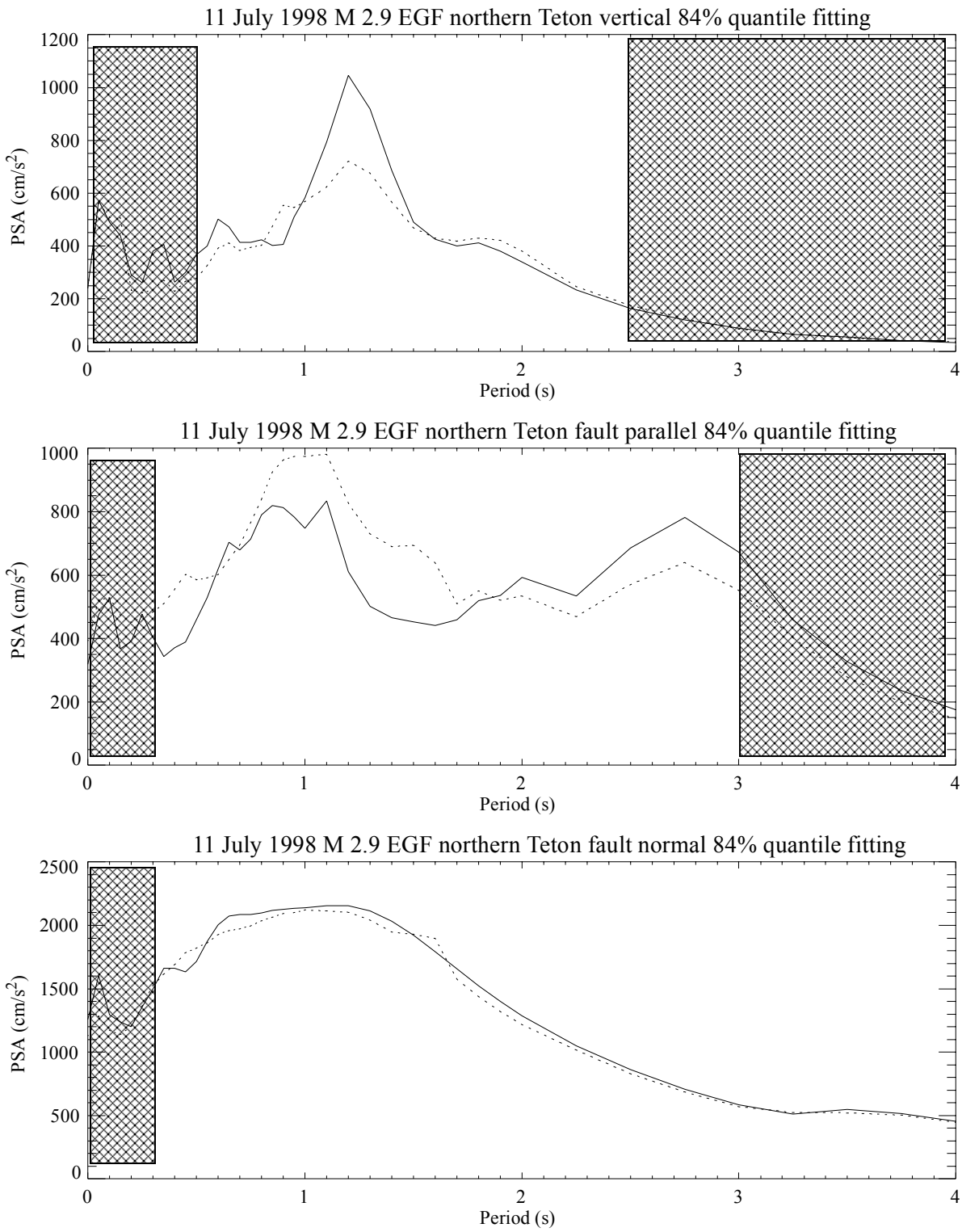

Figure 7-72: JLDW 84% quantile acceleration response spectra for the 11 July 1998 EGF. Dotted curves are 84% quantile response spectra from the 3300 northern Teton fault segment rupture simulations and solid curves are the response spectra from the best-fitting ground motion using an L1 norm for periods between 0.5 s and 3 s. Corresponding seismograms are shown in Figure 7-33 to 7-35. Hatched regions have inadequate S/N levels to interpret synthesized ground motions.

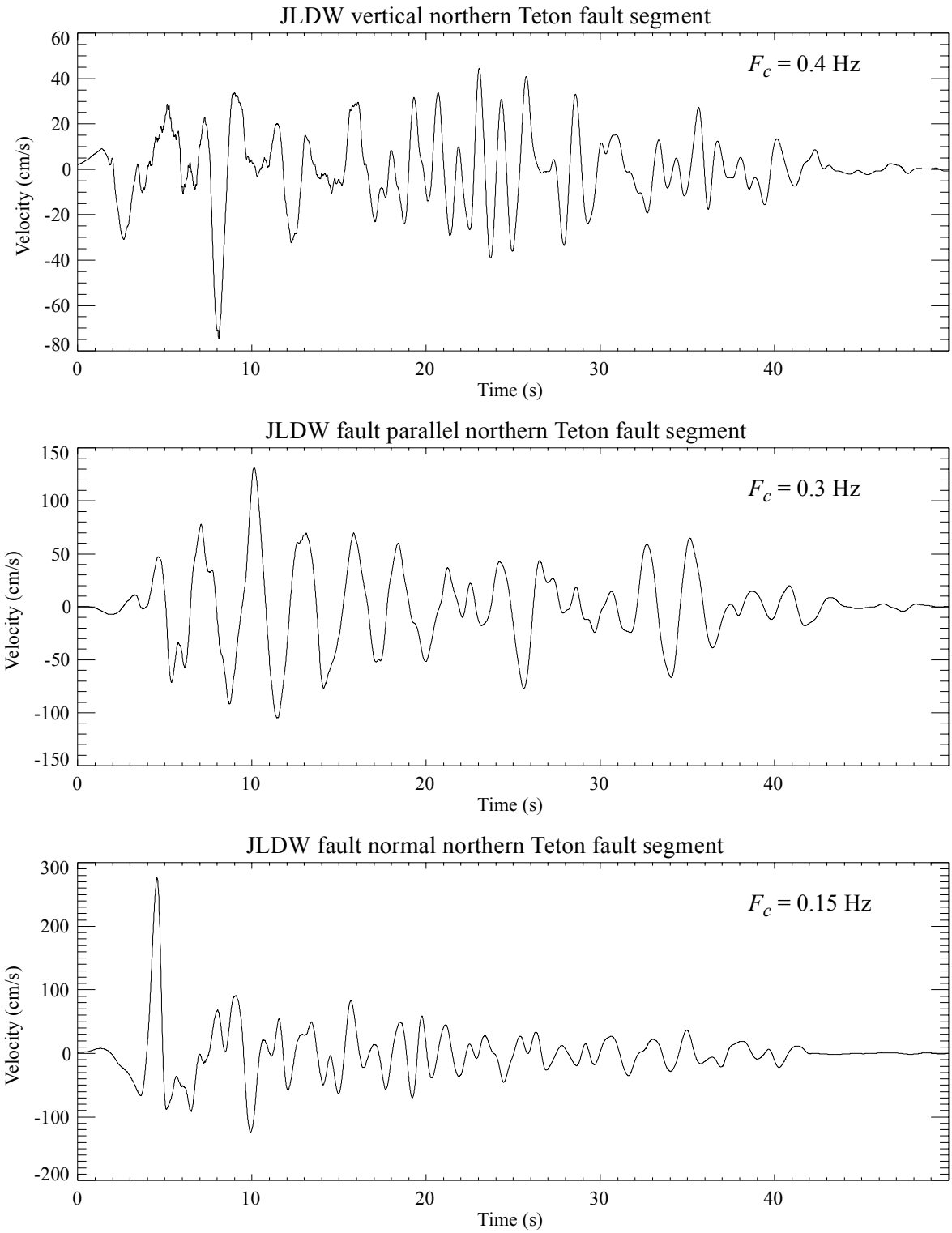

Figure 7-73: JLDW velocity seismograms for the best-fitting 84% quantile acceleration response spectra for the 11 July 1998 EGF. Note that the EGF were artificially truncated by the recording system, tapered to zero over the last 6 s of the seismograms during the simulation, and probably strongly underestimate the total duration of expected ground shaking. Also, signal-to-noise constraints dictated that the seismograms were high-pass filtered using corner frequencies as indicated on each

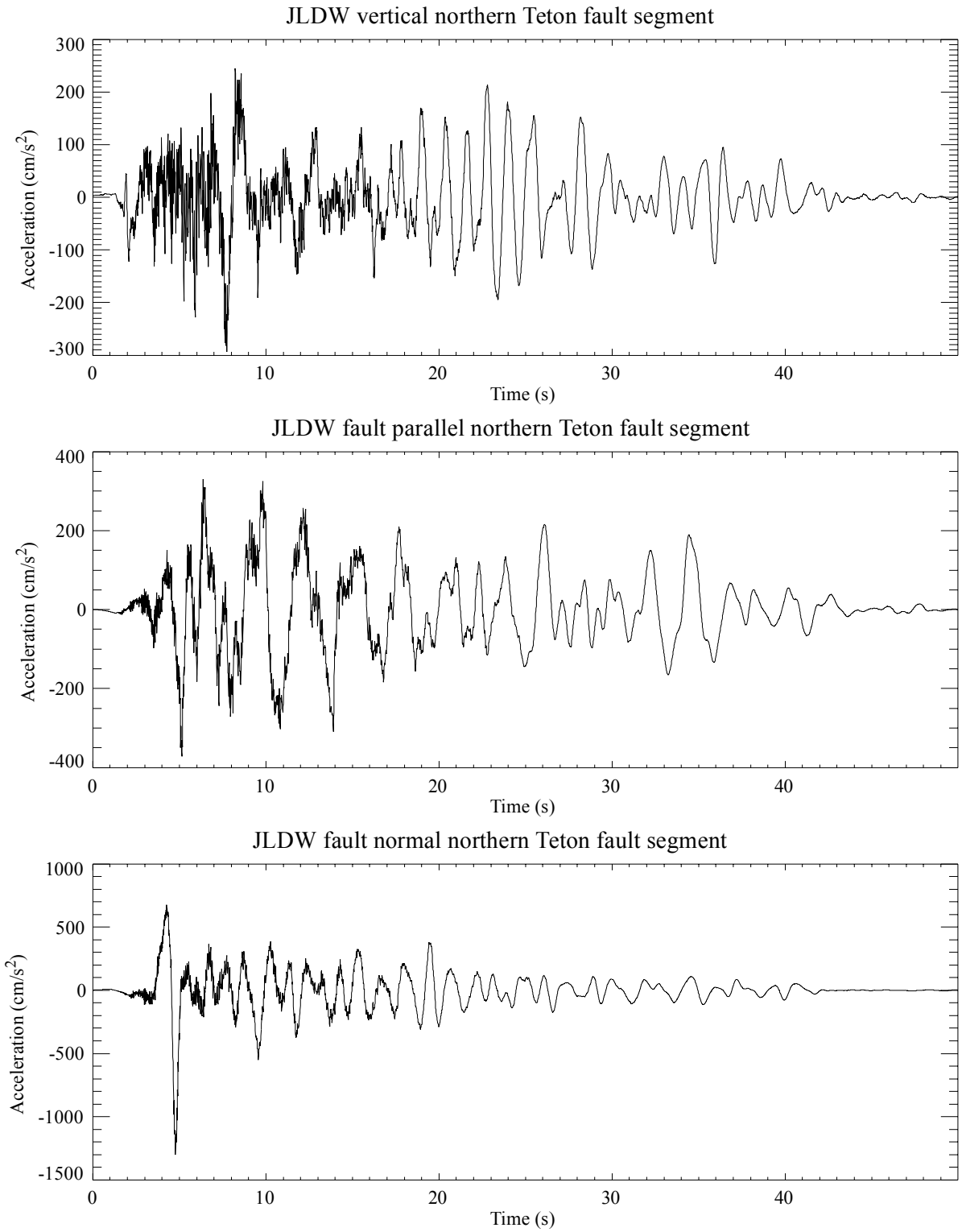

Figure 7-74: JLDW acceleration seismograms for the best-fitting 84% quantile acceleration response spectra for the 11 July 1998 EGF. Note that the EGF's were artificially truncated by the recording system, tapered to zero over the last 6 s of the seismograms during the simulation, and probably strongly underestimate the total duration of expected ground shaking.

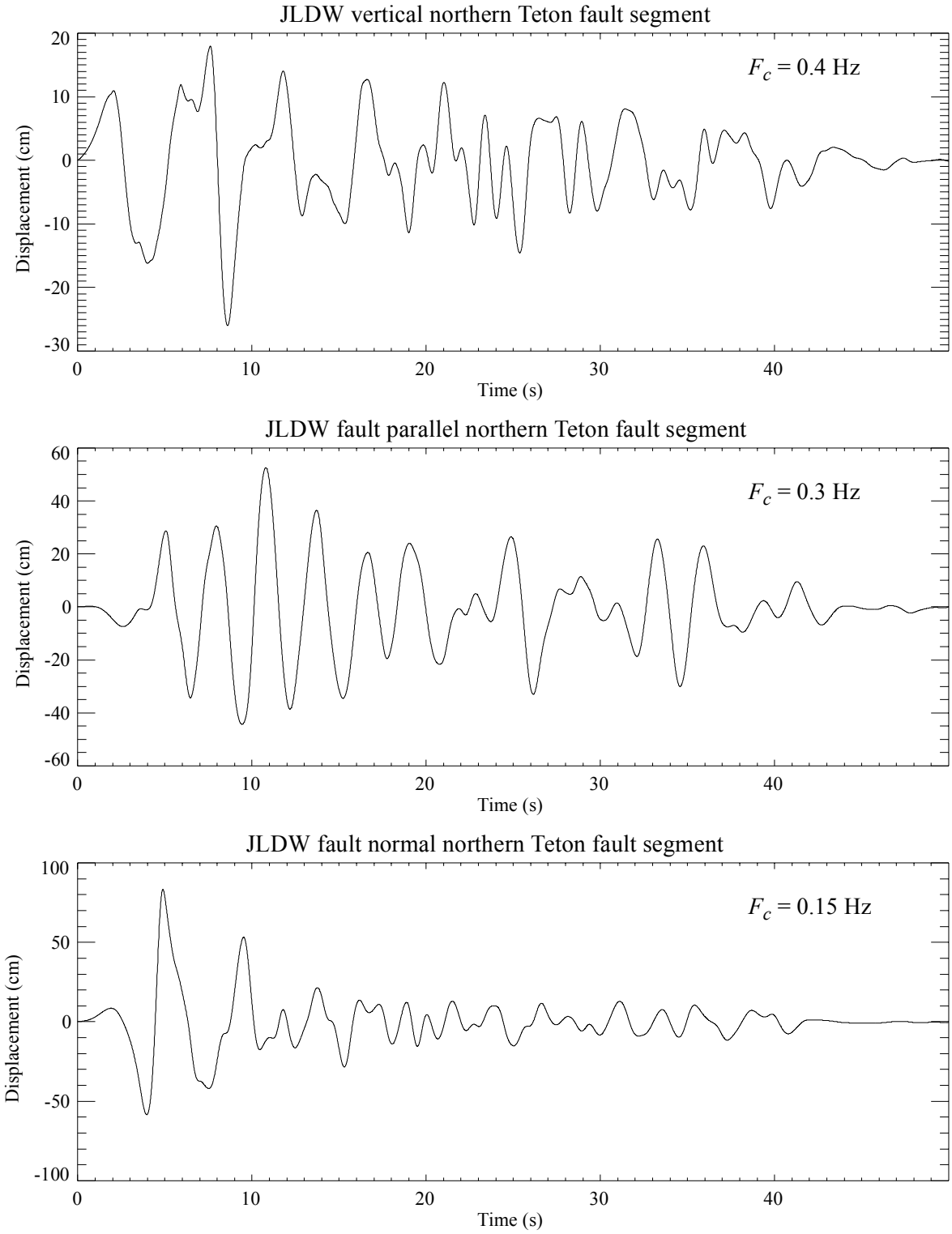

Figure 7-75: JLDW displacement seismograms for the best-fitting 84% quantile acceleration response spectra for the 11 July 1998 EGF. Static and long-period responses were eliminated by the high-pass filters. See Figure 7-73 for details.

has the largest peak velocity (Figure 7-73), but the fault-parallel and vertical components also have significant peak velocities with durations limited by the length of the EGF's. Strong accelerations associated with periods > 1 s are clearly evident throughout the acceleration seismograms, and dominate ground motions after times of about 20 s (Figure 7-74). The high-pass filtering necessitated by long-period noise limits interpretation of displacement seismograms (Figure 7-75). More detailed comparison of simulated ground motions to the hybrid ground motions of Section 6 is deferred to Section 7.5.4 below. Since the EGF's are clearly truncated, the only conclusion concerning duration is that strong ground shaking durations are likely to significantly exceed 40 s (length of the EGF's).

7.5.2 Simulated Ground Motions Using the 20 November 2002 M 3.2 EGF. This earthquake is located at the northern edge of the JLSN. Consequently, the focal mechanism is not well-constrained, but includes a normal-faulting component on planes striking roughly northeast. Constraints on focal mechanism rake are too weak to attempt to quantify shear-wave radiation, so the EGF's are used without any other scaling except simple distance corrections. Thus, it is advisable to put little credence in the absolute amplitudes, but instead limit interpretation to the general characteristics of the 0.5 s to 3 s period response range. Another significant caveat concerning this earthquake is that it is depleted of > 1 Hz shear-waves relative to all eight EGF earthquakes used in Section 6 and shown in Appendix D. Thus, the primary reason to use this earthquake's EGF's is to evaluate responses for periods > 1 s, a period range where S/N is too low to use the smaller magnitude EGF's in Appendix D.

Mean and 84% quantile acceleration responses show a strong spectral peak in the 1-2 s period range on all components (Figure 7-76) and weak acceleration responses for periods < 1 s. Shear-wave resonance within the low-velocity basin provides a possible explanation of the strong 1.3-1.8 s acceleration response in Figure 7-76. A local low-velocity basin thickness of 2-3 km and an average shear-wave velocity of 1.5 km/s could produce a quarter-wavelength resonance similar to the response in Figure 7-76, but does not explain the strong vertical component acceleration responses in the same period range. The simulated ground motions closest to the 84% acceleration response spectra (Figure 7-77) have the largest velocity responses on the north component (Figure 7-78), while vertical and fault-normal peak velocities are similar. It is possible that the fault-

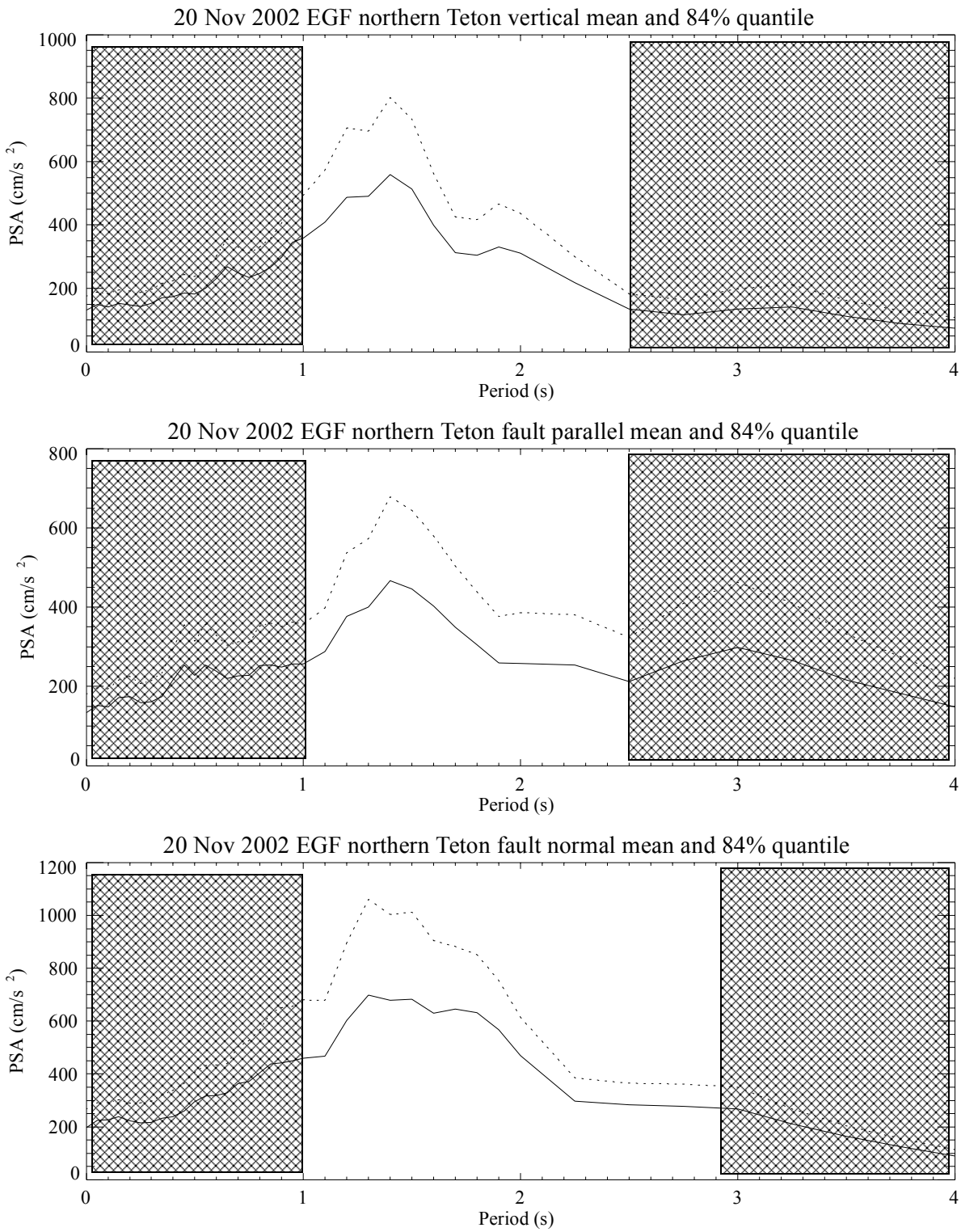

Figure 7-76: JLDW mean and 84% quantile northern Teton fault segment acceleration response spectra using the **M** 3.2 20 Nov. 2002 EGF. Dotted curves are 84% quantile response spectra and solid curves are corresponding means. Hatched areas are periods were noise levels are too large to warrant interpretation.

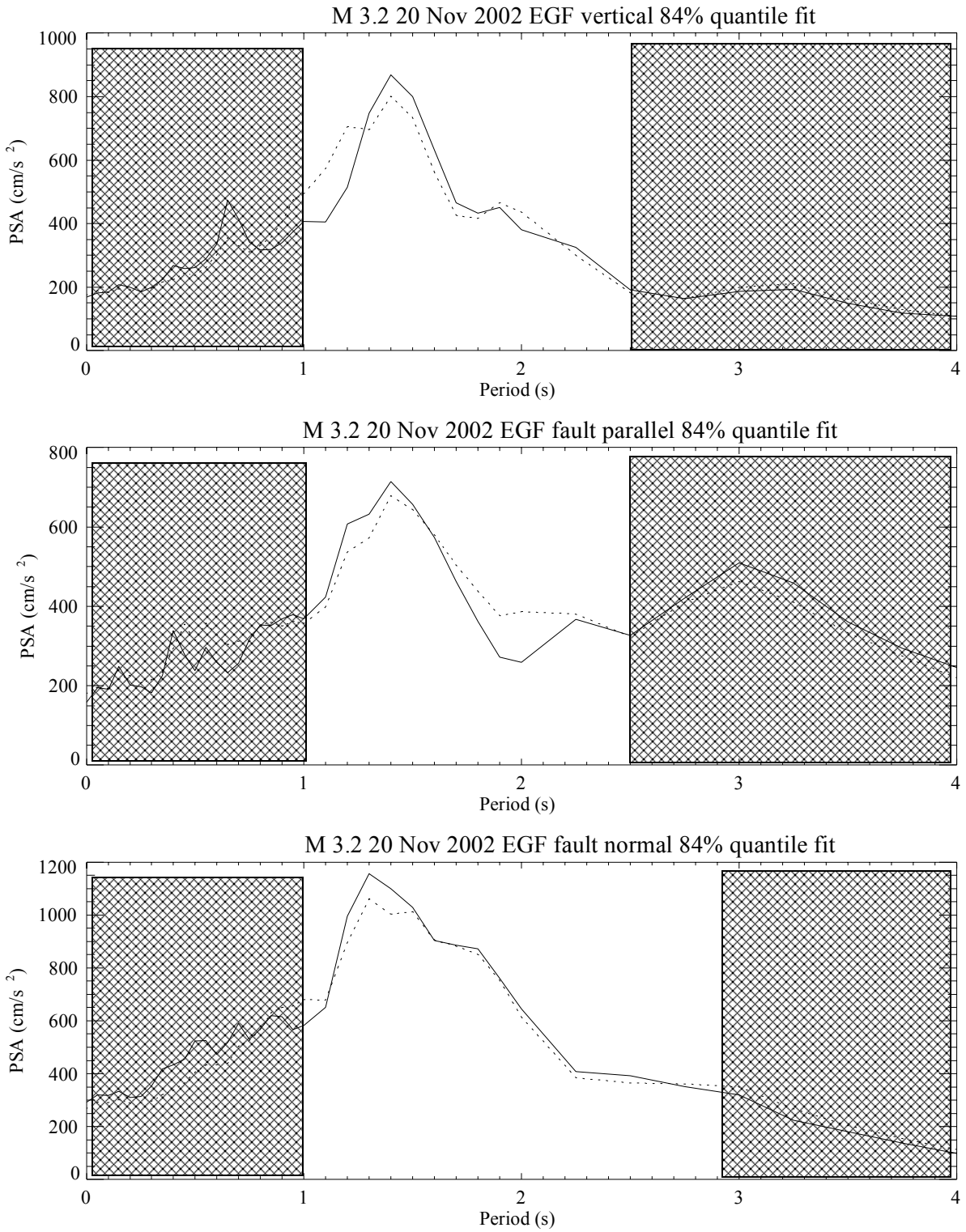

Figure 7-77: JLDW 84% quantile acceleration response spectra for the 20 Nov. 2002 EGF. Dotted curves are 84% quantile response spectra from the 3300 northern Teton fault segment rupture simulations and solid curves are the response spectra from the best-fitting ground motion using an L1 norm for periods between 0.5 s and 3 s. Corresponding seismograms are shown in Figure 7-38 to 7-40. Hatched areas are periods were noise levels are too large to warrant interpretation.

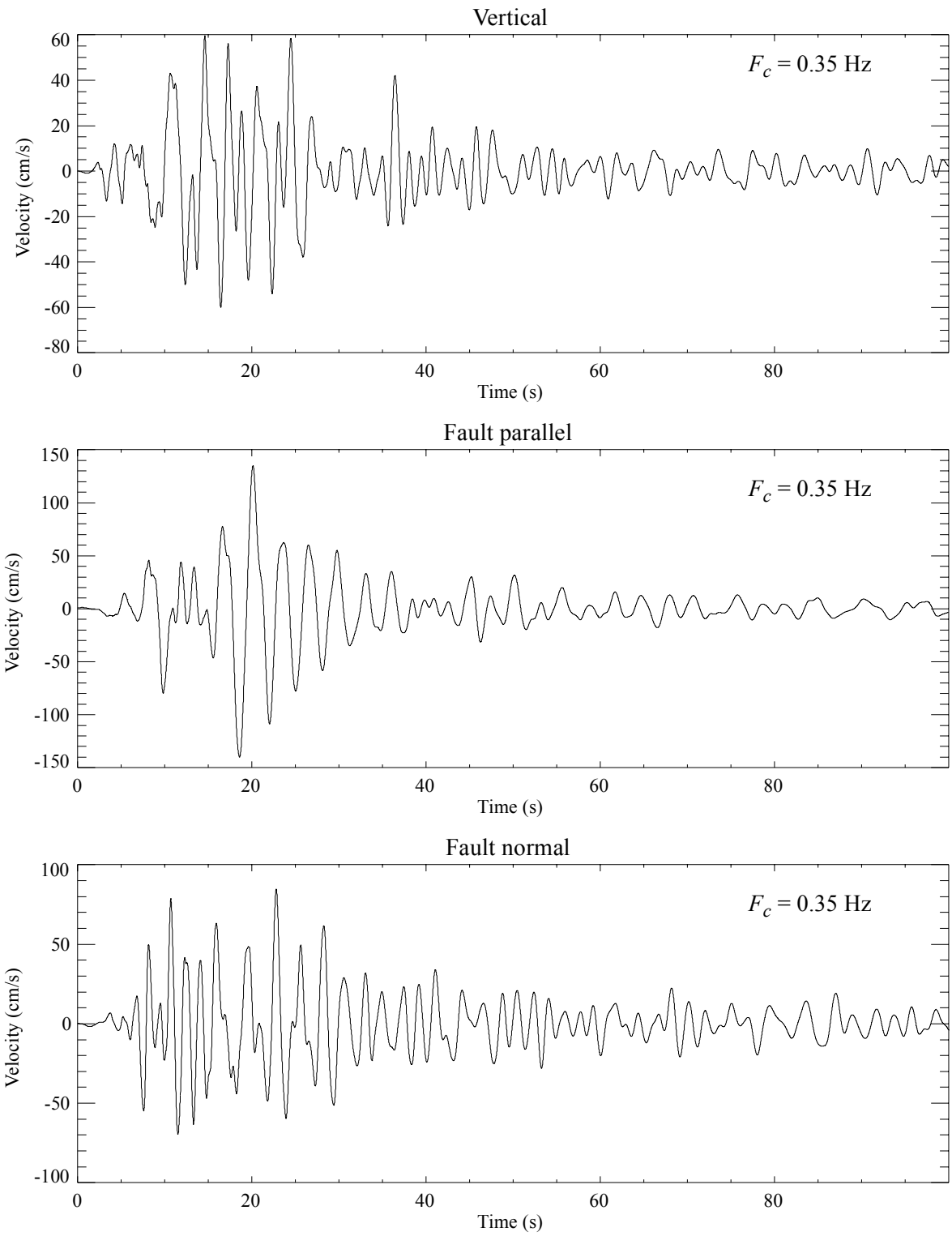

Figure 7-78: JLDW velocity seismograms for the best-fitting 84% quantile acceleration response spectra for the 20 Nov. 2002 EGF. Signal-to-noise constraints dictated that the seismograms were high-pass filtered using corner frequencies as indicated on each component.

parallel component has a significant basin-edge Love wave generated at the northwest basin boundary and that the vertical and fault-normal components are dominated by basin-edge induced Rayleigh waves. The peak acceleration responses of all the components is similar, although the fault-parallel component has a stronger response at longer periods (Figure 7-79). The ~3 s maximum period S/N-cutoff, limits interpretation of the displacement seismograms (Figure 7-80), although the lack of clear correlation between the vertical and fault-normal displacement seismograms argues against Rayleigh waves comprising a dominate phase on these ground motion components. The principal conclusion is that energy incident from the northern Teton fault segment north of the low-velocity basin appears to excite a very strong 1-2 s resonant response at the JLDW rock site. Given the already strong 1-2 s period acceleration responses observed at the JLD3 soil site associated with shallow soil resonances, this result suggests that energy from the northern end of the northern Teton fault segment may especially amplify ground motions in the 1-2 s period band for the embankment portion of the dam. Unfortunately, it appears that the fundamental resonant periods of basins at two entirely different spatial scales coincide, a situation that could produce unprecedented accelerations for periods > 1 s along the embankment section of the dam. Station JLD3 was no longer operating and did not record the 20 Nov. 2002 earthquake, so a direct estimate of the impact of overlapping multi-basin resonant responses on long-period acceleration responses for the embankment portion of the dam using EGF's is not possible.

7.5.3 Influence of EGF Location on Long-Period Responses. Another way to ascertain the influence of incident direction on ground motions at the dam is to ratio acceleration response spectra of the more distant EGF's from the dam (the **M** 3.2 and **M** 3.7 earthquakes 20 north and 30 km SSW, respectively, see Figure 7-67) using the **M** 2.9 earthquake EGF's as a reference. There are a number of ways to attempt to correct for differences in distances, radiation patterns, etc., but for the sake of simplicity each component EGF was normalized to a peak velocity of one prior to calculating the PSA ratios. This serves to illustrate the differences in long-period responses relative to consistent scaling of peak shear-wave amplitudes. All components of the **M** 3.2 earthquake north of JLDW are amplified for periods of 1-2 s (Figure 7-81), but the vertical component shows the strongest amplification. The uniform amplification of vertical motions relative to a nearby earthquake sources makes intuitive sense, since incident angles

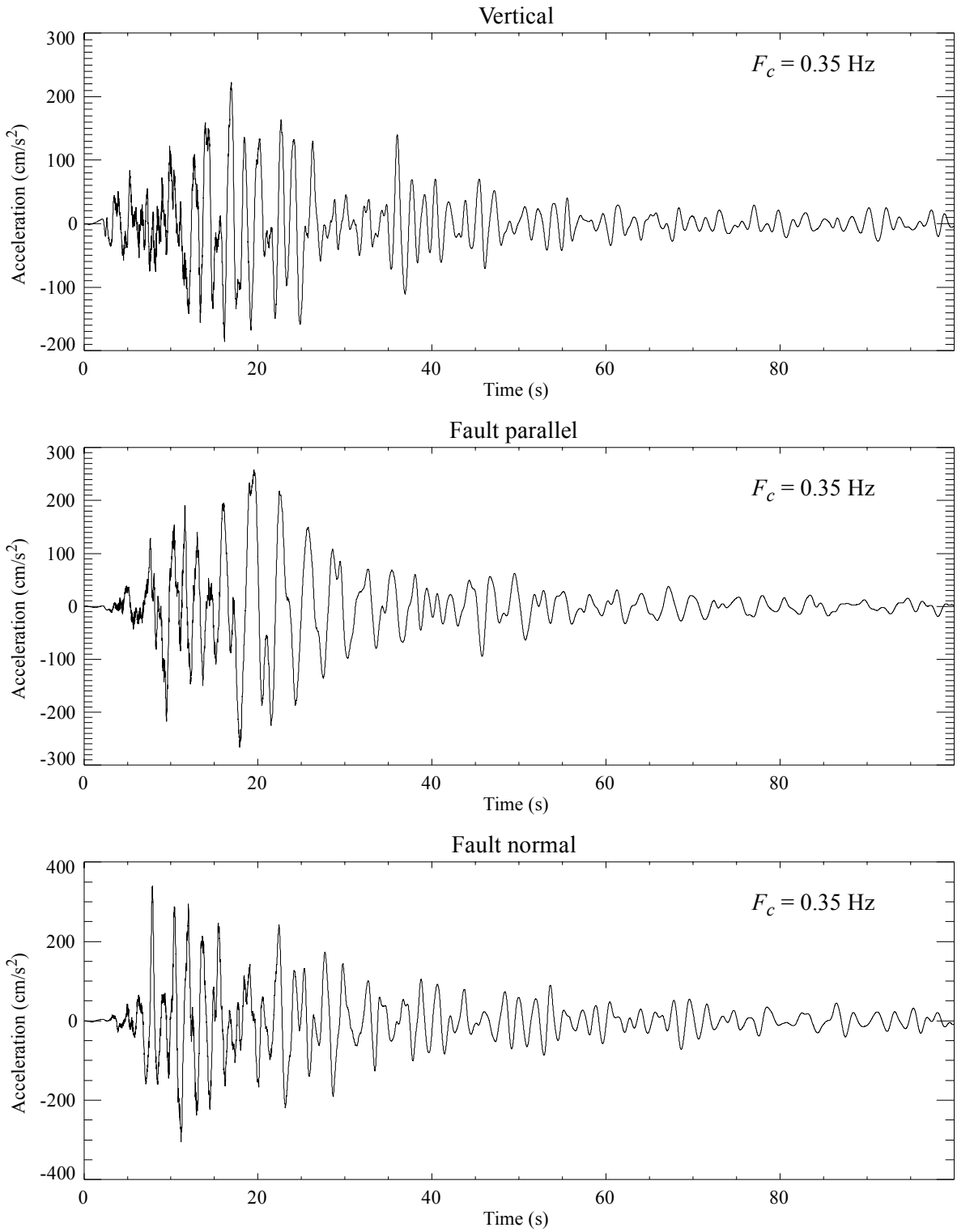

Figure 7-79: JLDW acceleration seismograms for the best-fitting 84% quantile acceleration response spectra for the 20 Nov. 2002 EGF. Signal-to-noise constraints dictated that the seismograms where high-pass filtered using corner frequencies as indicated on each component.

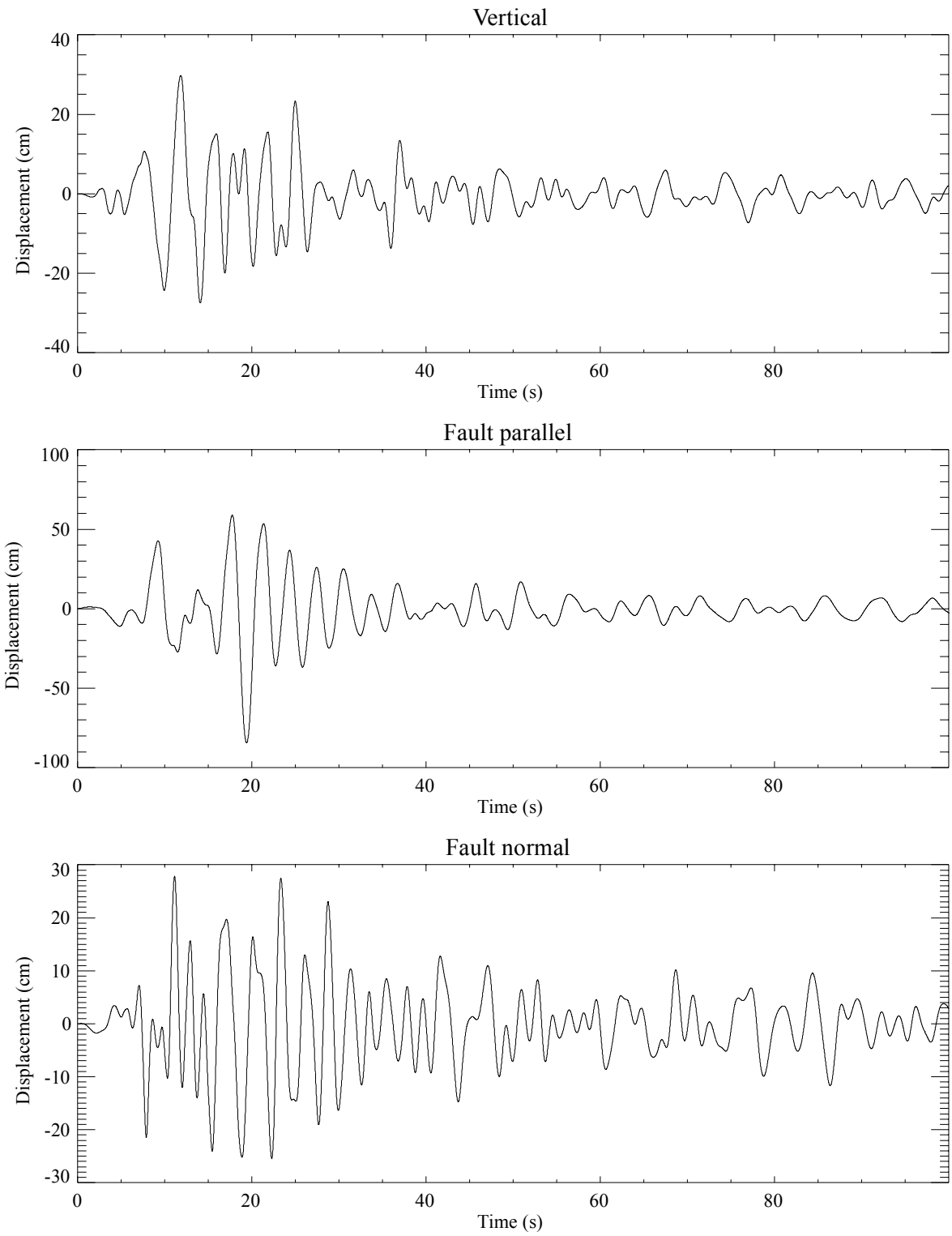

Figure 7-80: JLDW displacement seismograms for the best-fitting 84% quantile acceleration response spectra for the 20 Nov 2002 EGF. Static and long-period responses were eliminated by the high-pass filters. See Figure 7-78 for details.

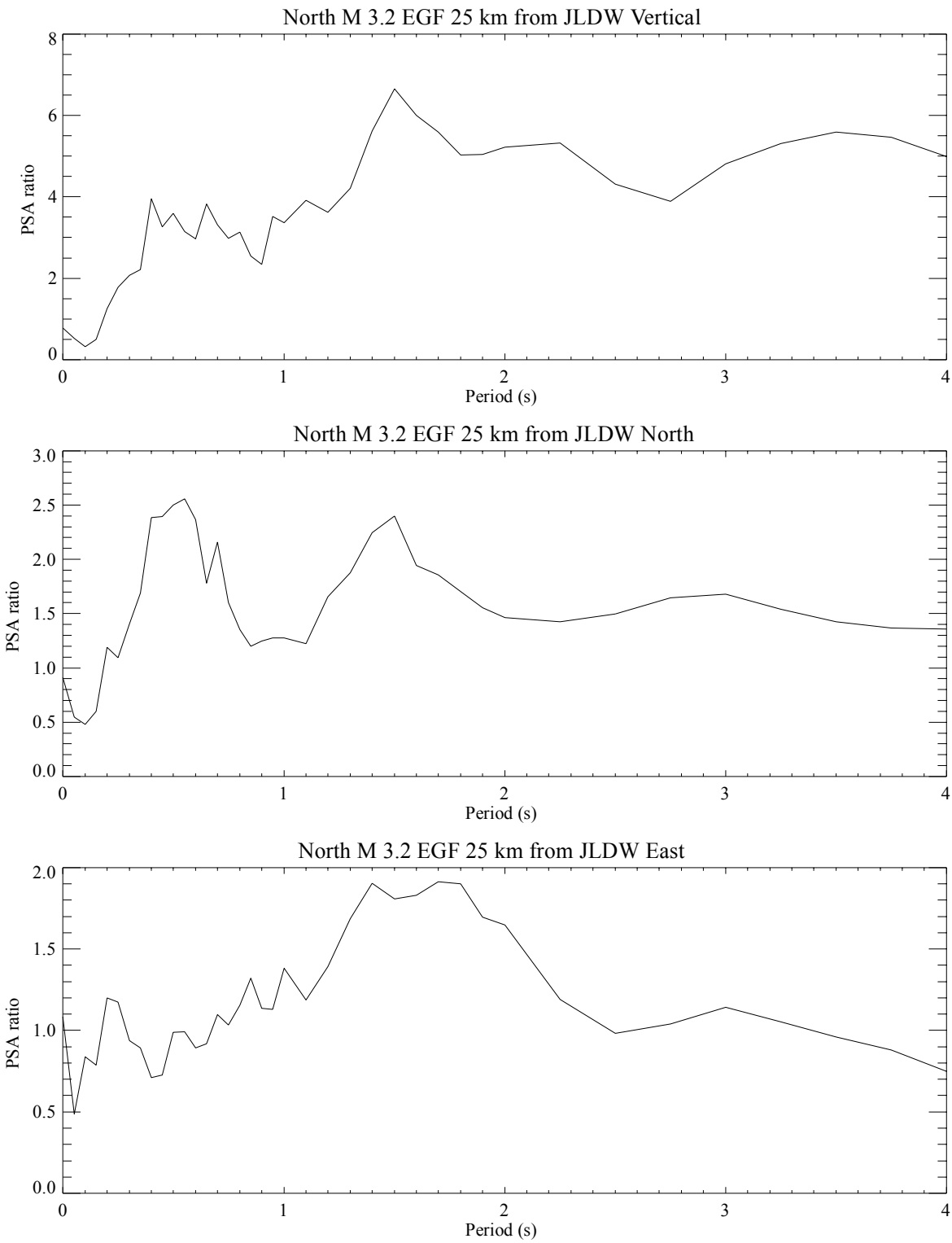

Figure 7-81: JLDW PSA ratios of the **M** 3.2 EGF ground motions to the **M** 2.9 EGF ground motions. The **M** 3.2 earthquake was located about 25 km north of site JLDW (Figure 7-67). Each component was normalized to a peak velocity of 1 cm/s prior to calculating the PSA ratios.

decrease with increasing distance and the opportunities for phase conversion between body waves and surface waves increases with distance. The north component is uniformly amplified at periods > 1 s, but the east component is only strongly amplified for periods of 1-2.4 s (Figure 7-81). In contrast, the north component from the M 3.7 earthquake to the SSW of site JLDW is only amplified for periods of 1-3 s (Figure 7-82) and the east component does not show any long-period amplification. The portion of the low-velocity basin south of the dam is postulated in Section 4 to shallow toward the south. The amplification cutoff at a period of 3 s period in Figure 7-82 is consistent with estimated basin thickness of ~ 3 km beneath the dam. The progressive shallowing of the basin to the south would reduce amplification periods which could explain the broad amplification for periods extend down to 1 s on the north component in Figure 7-82. The vertical component is amplified at all periods, consistent with expectations.

7.6 Comparison to Broadband Hybrid Ground Motions From Section 6.

For the purposes of comparison with Section 6 estimated ground motions a single dip scenario (35°) and the only broadband local earthquake EGF that could be associated with the northern Teton fault segment (the **M** 2.9 earthquake, 8 km south of JLDW in Table 7-4) were used to synthesize ground motions using the same 3300 rupture scenarios used in Section 6.4.3. Table 7-5 shows the differences in peak velocities between the hybrid Green's function estimates of Section 6 and the purely empirical Green's function estimates using the single earthquake EGF. The EGF

Table 7-5: JLDW Rock Ground Motion Parameters: 35°-Dipping Northern Teton Fault Segment.

Component	EGF peak velocity	Hybrid peak velocity
	(cm/s)	(cm/s)
fault-normal (E15S) mean	184	146
fault-normal (E15S) 84%	252	201
fault-parallel (N15E) mean	74	102
fault-parallel (N15E) 84%	108	135
Vertical mean	31	125
Vertical 84%	62	147

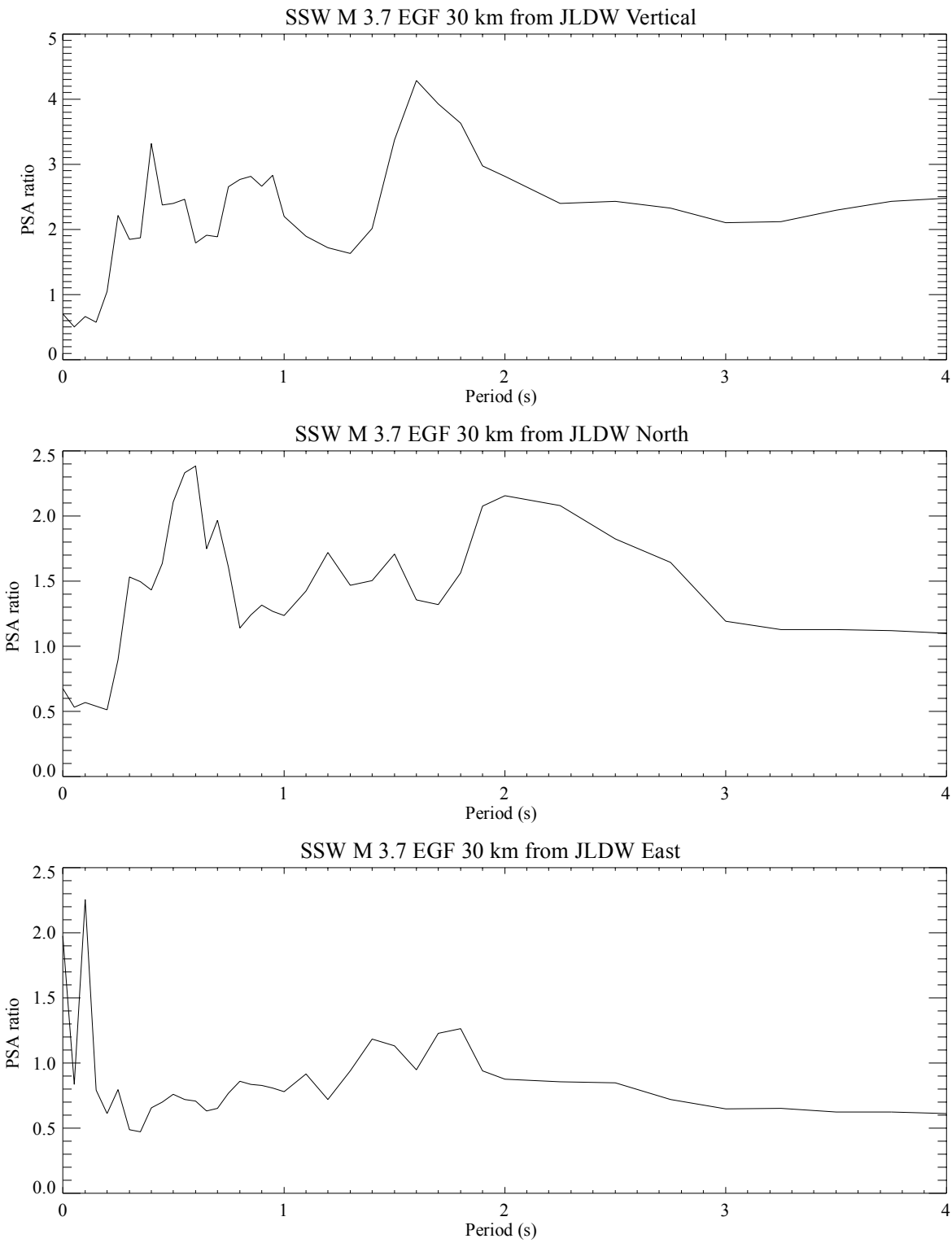

Figure 7-82: JLDW PSA ratios of the **M** 3.7 EGF ground motions to the **M** 2.9 EGF ground motions. The **M** 3.7 earthquake was located about 30 km SSW of site JLDW (Figure 7-67). Each component was normalized to a peak velocity of 1 cm/s prior to calculating the PSA ratios.

fault-normal peak velocities are somewhat larger than the hybrid fault-normal peak velocities because the EGF's indicate a stronger long-period response (Figures 7-83 and 7-84). Fault-parallel EGF peak velocities are about 30% smaller than hybrid estimates (Table 7-5). EGF vertical peak velocities are much smaller than hybrid peak velocities (Table 7-5)..

In light of the findings in Section 7.4 and 7.5 that energy from the ends of the Teton fault is likely to strongly amplify fault-parallel and vertical responses relative to energy radiated from the middle of the fault, the single-earthquake EGF estimates of fault-parallel and vertical peak velocities in Table 7-5 are probably lower bounds. Conversely, based on the results of Sections 7.4 and 7.5 it appears that the **M** 2.9 EGF will somewhat overestimate fault-normal responses for energy arriving from the ends of the northern Teton fault segment, so fault-normal single-earthquake EGF peak velocities in Table 7-5 are probably overestimated.

Even more so than the mean (Figure 7-83) and 84% (Figure 7-84) E15S Section 6 hybrid acceleration response spectra, the single-earthquake EGF spectra exhibit responses more similar to soil responses from the Spudich et al. (1999) extensional acceleration attenuation relations than rock responses. Direct comparison of the single-earthquake EGF 84% quantile spectra and the **M** 5.2 Idaho earthquake EGF spectra with the hybrid ground motion spectra from Section 6 (Figure 7-85) indicates that the hybrid ground motions probably provide realistic acceleration responses for most periods with three significant caveats. First, it appears that the hybrid ground motions overpredict vertical accelerations for periods > 2 s (Figure 7-85). Second, the hybrid horizontal acceleration responses for periods from ~0.8 s to 1.5-2 s may be underestimated. Third, hybrid ground motion durations are probably too short and lack prolonged periods (~40 s) of substantial ground shaking with sustained peak velocities > 70 cm/s and sustained peak accelerations > 0.2 g for rock site conditions and sustained peak accelerations exceeding 0.25 g along the embankment section for more than 70 s.

The very-strong acceleration responses in Figures 7-83 to 7-85 for periods of 1-3 s are consistent with trapped-wave resonances in the low-velocity basin for basin thicknesses varying between 2-4 km. Figure 7-86 provides a schematic illustration of the first-order factors influencing the how the low-velocity basins beneath Jackson Lake dam amplifies seismic energy and prolong ground-

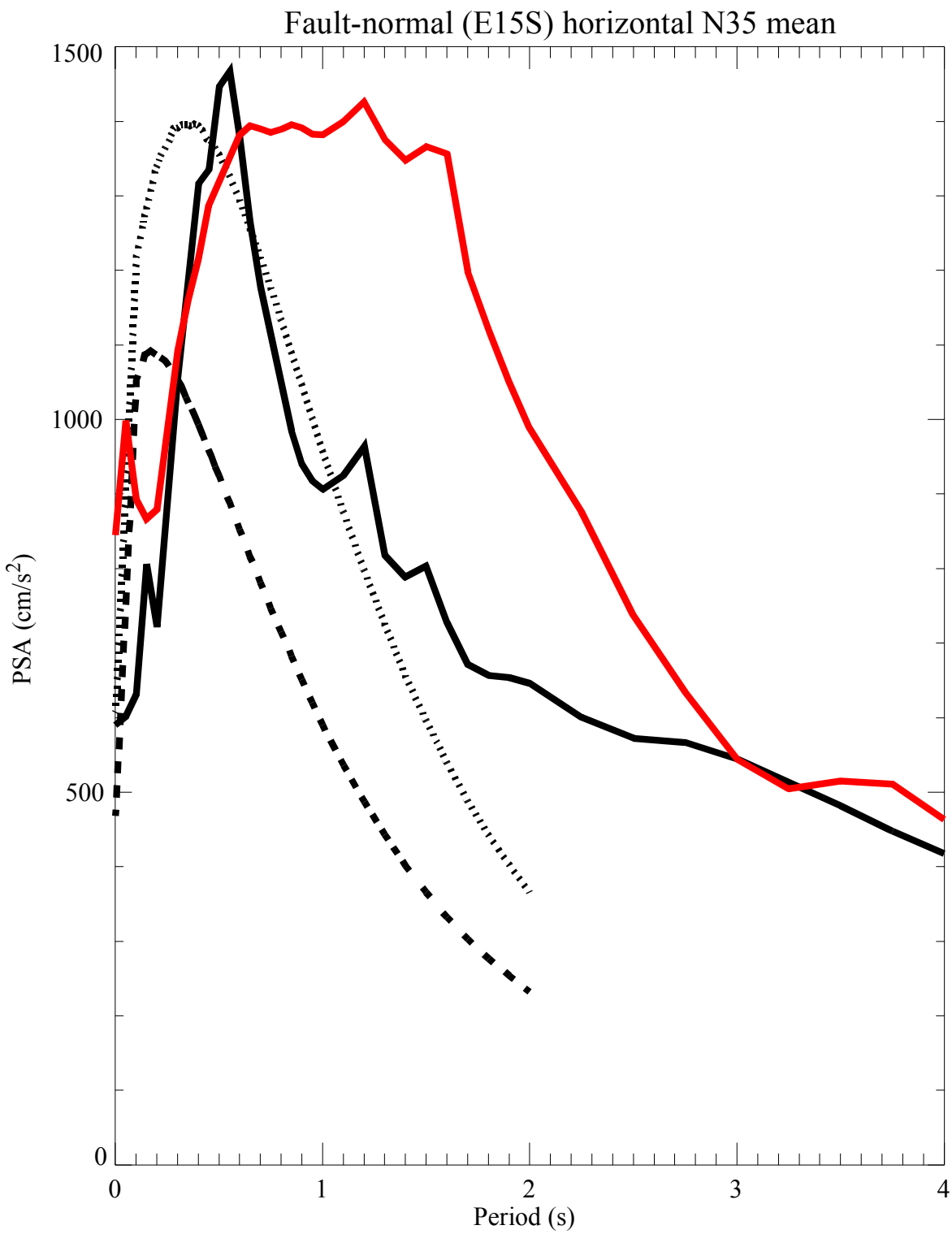

Figure 7-83: JLDW rock site mean downstream horizontal PSA response spectra for a 35°-dipping northern Teton fault segment (solid). SEA99 average horizontal component estimates for a **M** 7.0 normal-faulting earthquake are shown for soil (dotted) and rock (dashed) site conditions. Red curve are the mean spectra using the M 2.9 earthquake EGF.

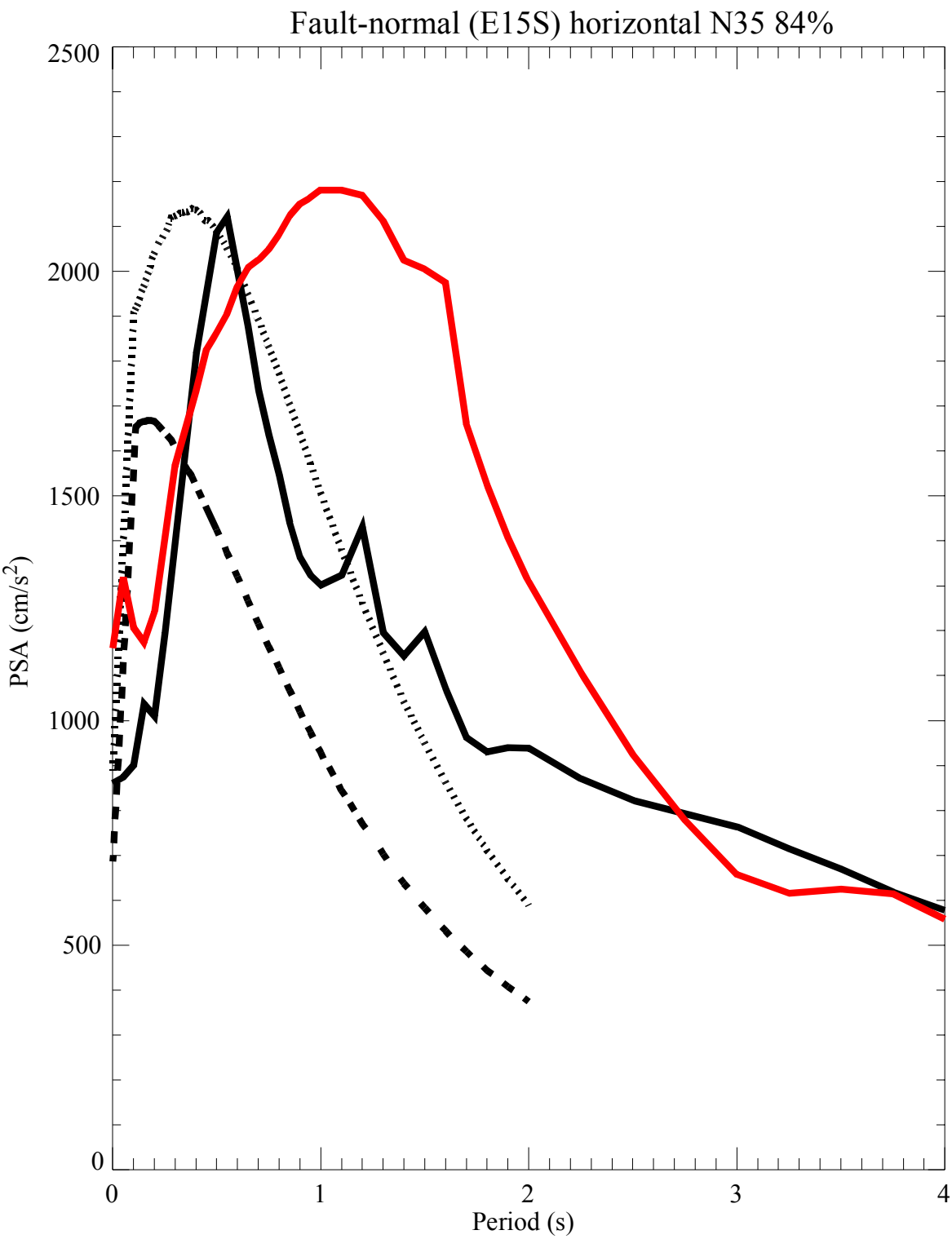

Figure 7-84: JLDW rock site hybrid Section 6 84% quantile downstream horizontal PSA response spectra for a 35°-dipping northern Teton fault segment (solid). SEA99 average horizontal component estimates for a **M** 7.0 normal-faulting earthquake are shown for soil (dotted) and rock (dashed) site conditions. Red curve are the 84% quantiles using the M 2.9 earthquake EGF.

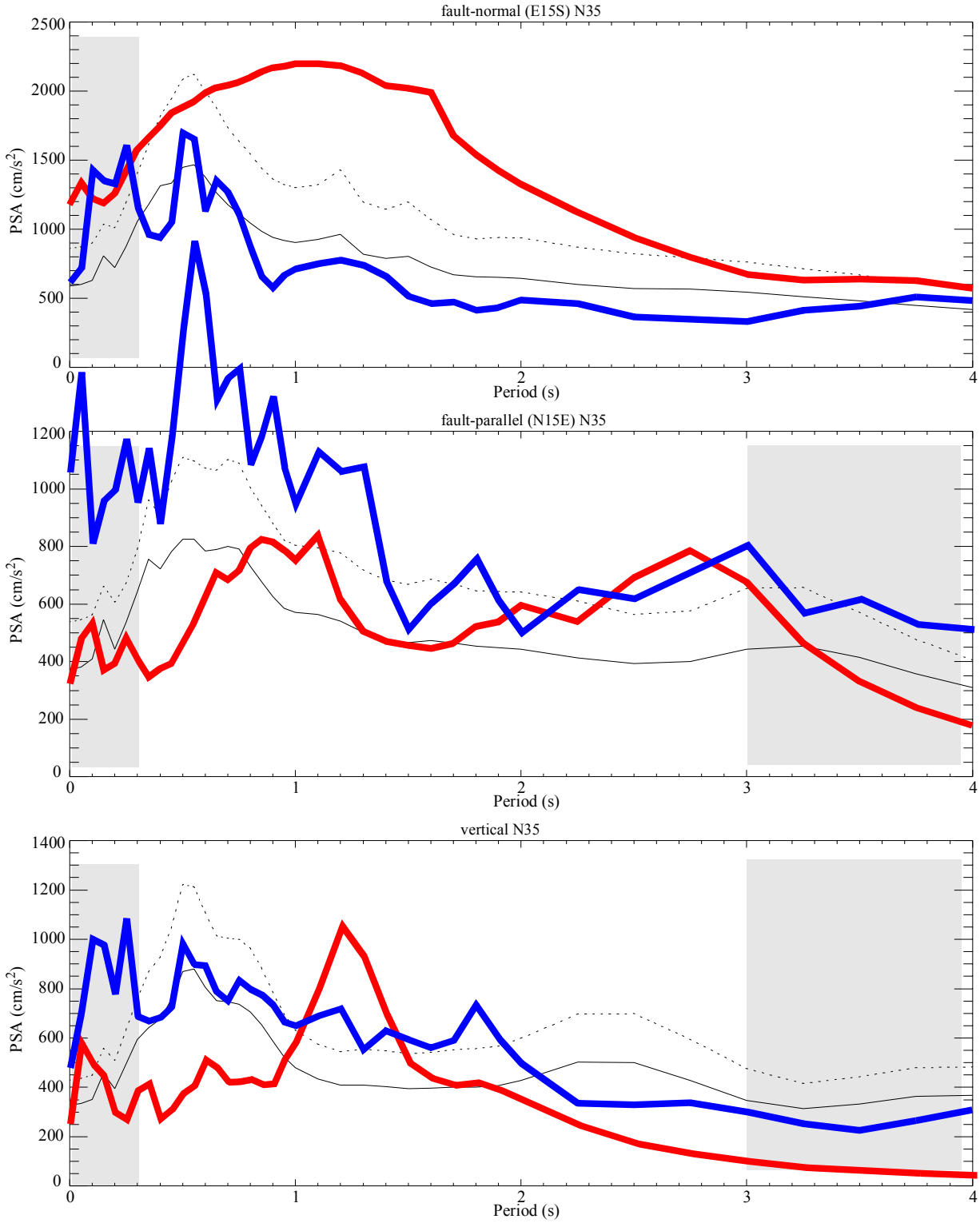

Figure 7-85: JLDW rock site hybrid Section 6 PSA response spectra for a 35°-dipping northern Teton fault segment for all hypocenters. Mean hybrid curves are solid, 84% hybrid quantile curves are dotted, local **M** 2.9 broadband EGF 84% quantile curves are red, and **M** 5.2 Idaho EGF PSA spectra are blue curves. Components are as labeled.

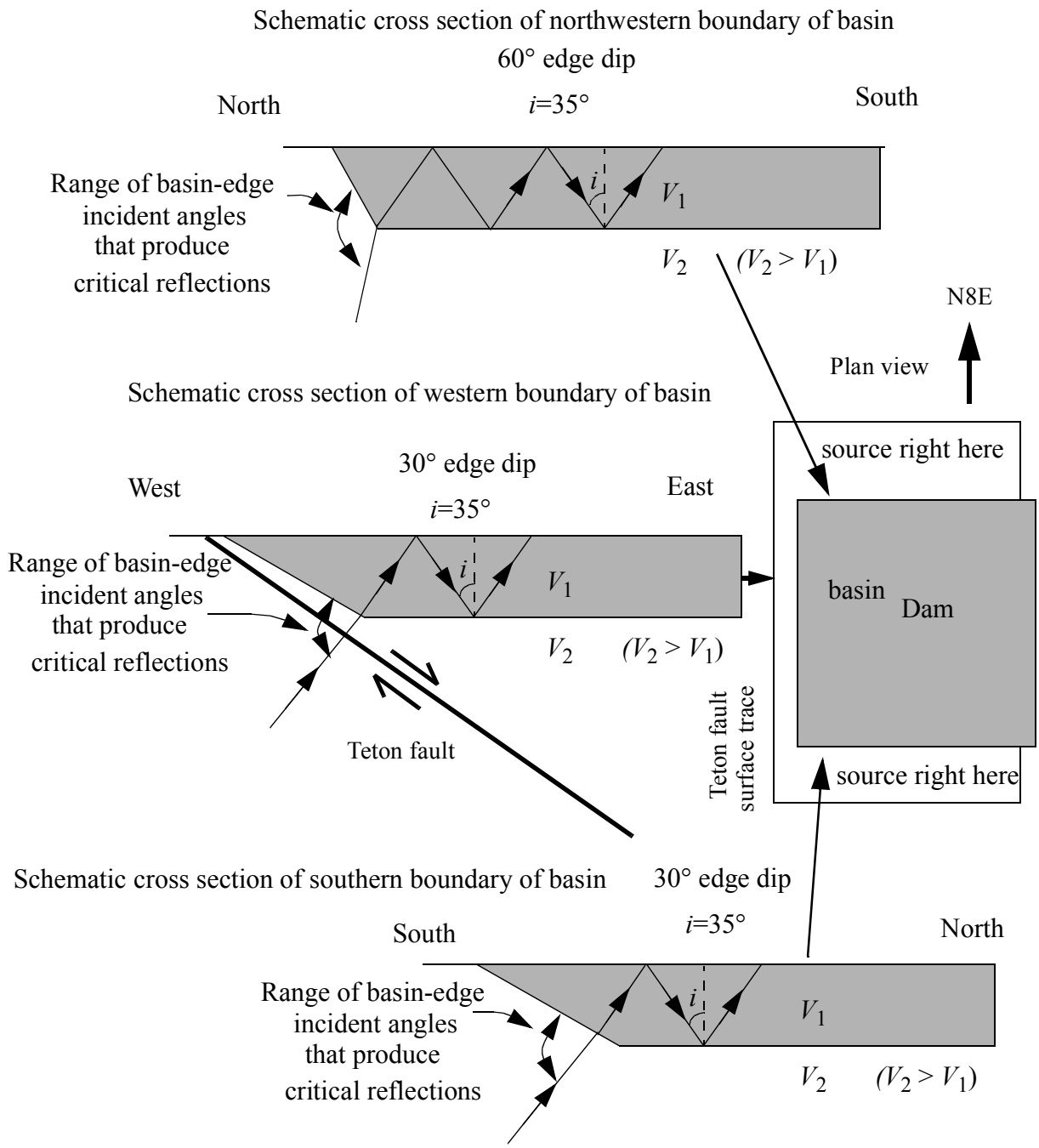

Figure 7-86: Schematic plan and cross section views of the low-velocity basin boundary configuration for Jackson Lake Dam. Basin indicated by shaded regions. Open rectangle is the outline of the northern segment of the Teton fault in the plan view. Uniform shear velocities used for illustration of V_1 = 2 km/s and V_2 = 3.5 km/s, producing a critical angle (i) of 35°. Unlike the basins considered by Somerville et al. (2003) that were generally located more than 5 km from one edge of basins, the Teton fault is in close proximity to three edges of the low-velocity basin containing Jackson Lake Dam.

shaking durations. The northwestern boundary traps nearly all the waves incident to the 60° boundary as critical reflections within the basin. This explains why the Yellowstone earthquake and **M** 3.2 earthquake 25 km north of the dam produce such strong long-period acceleration responses and long durations of strong ground shaking. The western boundary critically traps all waves incident from the nearby portion of the fault plus a portion of the fault below the basin, but does not trap steeply incident wave energy as effectively as the northwestern margin of the low-velocity basin. The southern boundary critically traps waves incident from the western portion of the Teton fault that extends south of the southern basin boundary, but does not trap steeply incident wave energy as effectively as the northwestern margin of the low-velocity basin. This partially explains why the **M** 5.2 Idaho earthquake and **M** 3.7 southern Teton fault segment earthquake produce less long-period amplification at the dam than the earthquakes north of the low-velocity basin. The situation at Jackson Lake Dam has two factors that appear to strongly influence basin amplification. The relatively high shear-wave velocity of the basement rocks (~3.5 km/s) at relatively shallow depths (2-3 km) produce a small critical angle of ~35° and a shorter period resonance (1-3 s) than comparatively deeper basins in California (San Fernando and Los Angeles). There are several significant departures of Figure 7-86 from the schematic of Somerville et al. (2003) that inspired it. First, the steep dip of the northwestern portion of the basin causes nearly all incident energy from the north at nearly all incident angles to be critically-reflected within the basin. Second, Teton fault is embedded in high-velocity rocks very close to the basin (only 1-2 km from the basin boundary) and parallels the basin edge for more than 10 km, a configuration not present in the basin configurations considered by Somerville et al. (2003). All these factors and results of the ground motion simulations in Sections 6 and 7 lead to the conclusion that basin amplification and durations effects are likely to be stronger in the low-velocity basin containing Jackson Lake Dam than any basin ground motion experience to date. This is a result of the combined compounding effects of unusually large amplification of ground motions by the low-velocity basin, basin-margin velocity structure, the location of the embankment portion of the dam in an extremely low-velocity-basin embedded in a larger basin with nearly identical fundamental mode resonant periods, the close proximity of the Teton fault to the basin, and the Teton fault extending to the surface through high-velocity rocks within 1-2 km of the western edge of the low-velocity basin.

7.7 Discussion.

Somerville (2003) identified two aspects of the simulated ground motions in Section 6 that warranted further investigation, the validity of the kinematic source model and verification of basin response and its significance to estimate ground motions. The kinematic source model in Section 6 was shown in Section 7.2 to reproduce near-source Northridge ground motions and their associated statistical properties. An alternative source model (Frankel, 1995) produced ground motions similar to Section 6. The estimated ground motions appear relatively insensitive to details of rupture model specifications. Ground motion amplitudes are most sensitive to assumed stress drop. A mean stress drop of 3.4 Mpa (34 bars) was used in Section 6 to produce rupture models for the northern Teton fault segment and are consistent with stress drops associated with Basin and Range earthquakes. Mayeda and Walter (1996) estimated stress drops in the western United States using regional coda envelopes with corrections for attenuation. Their mean dynamic stress drop for Basin and Range earthquakes was 3.0 Mpa (30 bars). Ichinose et al. (1997) found stress drops of ~ 6.0 MPa (60 bars) for a normal-faulting earthquake sequence near Reno, Nevada, that contained a **M** 4.5 mainshock. Doser (1986) estimated stress drops of 6-7 MPa (60-70 bars) for the three **M** > 6 normal-faulting earthquakes in the Fairview Peak-Dixie Valley, Nevada, earthquake sequence. Boatwright (1985) estimated dynamic stress drops 3.3 ±1.6 MPa (33 ±16 bars) and 7.7 ±5.2 MPa (77 ±52 bars) for aftershocks from two segment of the 1983 **M** 7.0 Borah Peak, Idaho, earthquake. Mayeda and Walter (1996) find a tendency for dynamic stress drops to increase with magnitude in the western United States and suggest that mean dynamic stress drops of 3.0 MPa (30 bars) may underestimate dynamic stress drops of **M** 6.6-7.3 earthquakes in the western United States. Thus, while the mean dynamic stress drop of 3.4 MPA (34 bars) used in Section 6 appears reasonable, the regional stress drop results of Boatwright (1985), Doser (1986), Mayeda and Walter (1996), and Ichonese et al. (1997) indicate that higher mean stress drops may warrant consideration for estimating ground motions at Jackson Lake Dam. Thus, stress drop and kinematic rupture models can be eliminated as potential biases that would overestimate ground motions at Jackson Lake Dam. Borah Peak eyewitnesses accounts require significant stress drops near the surface because surface-rupture rise times were 1-2 s. Near-surface stress drops comparable to the Borah Peak earthquake are likely to produce ground motions larger than estimated in this report because shallow stress drops were tapered to small values as the fault

approached the surface in the kinematic rupture models. The Teton fault is located within 1-2 km of the ~10-km-long basin-edge caustic region for the dam and slip-velocities of 50-100 cm/s would experience limited geometric spreading before entering the western edge of the low-velocity basin, where significant amplification would occur due to the extreme velocity contrast between basement rocks and low-velocity basin rocks.

The dip of the Teton fault is probably the largest remaining unresolved uncertainty in the seismic source specifications that strongly influences estimated ground motions at the dam. The spatial distribution of hypocenters favors a dip of 35° (Section 3). The few well-constrained focal mechanisms have widely ranging normal-faulting dips from 30° to 60°. The emergence of a relatively new normal fault several km west of the large-scale Teton fault with a steep dip of 60-70° (Section 2) suggests that the current large-scale Teton fault may be approaching unfavorably low dips for continued normal faulting. Thus, the only available information specific to the Teton fault argues for a fault dip of 35° to 40°. In lieu of any other specific information about the dip of the Teton fault at depth, a fault dip of 35° is considered the most reasonable estimate for the northern Teton fault segment. More specifically, higher dips are not considered reasonable estimates. Since the global normal-fault database allows for dips ranging from 25° to 70°, appealing to dips found on other normal faults as evidence for what the dip on the Teton fault "should be" are not compelling or informative. Obviously, if new information becomes available to show that the northern Teton fault segment has dips of 45° or greater, then seismic loadings for Jackson Lake Dam will need to be revised. For now the ground motions estimated using a Teton fault dip of 35° are recommended for dynamic analyses of Jackson Lake Dam.

Purely empirical Green's function approaches were used in Sections 7.4 and 7.5 to produce ground motion estimates independent of the hybrid Green's function method in Section 6. Section 7.4 and 7.5 demonstrated acceleration responses similar to those estimated in Section 6 were obtained using completely different rupture models and purely empirical Green's function. The results of Sections 6 and 7 unequivocally demonstrate that unusually large > 1 s accelerations are likely to occur at Jackson Lake Dam in response to large earthquake on the northern Teton fault segment and that such amplitudes are likely to exceed the largest > 1 s accelerations recorded to date and durations may exceed the longest durations associated with **M** ~7 earthquakes. Expected

felt durations within the low-velocity basin are likely to extend to 1.5 to 3 minutes, durations normally only associated with sites relatively close to **M** > 8 subduction zone earthquakes. Ground motions from the 1979 **M** 6.5 Imperial Valley earthquake provide empirical precedent for the large acceleration responses estimated at Jackson Lake Dam. However, the low-velocity basin and fault configuration at Jackson Lake Dam are likely to produce more extreme long-period acceleration than observed in Imperial Valley based on first-principles analyses of wave trapping (Figure 7-86).

The production of shear-waves at the basin edges, as inferred in the analyses in Sections 4 and 5, in addition to basin-edge surface waves, significantly contributes to the broadband ground motion hazard at the dam. The findings in Sections 4 and 6 are similar to Spudich and Iada (1993). They showed that shear-waves are produced at basin-edges of Coachella Valley, California, low-velocity basin and become strong secondary arrivals in the basin at a site 8 km from the basin edge. Similarly, Frankel et al. (1991) found that shear arrivals persisted for 8 s after the initial shear-wave arrival in the Santa Clara Valley low-velocity basin. The combination of strong conversion of shear-waves and surface waves at the low-velocity basin edges and likely shear-wave and surface wave resonances in the low-velocity basin, as demonstrated by the EGF ground motions simulations, suggest that the very-broad-period large amplitude acceleration responses in Figures 7-83 and 7-84 are credible expectations at Jackson Lake Dam.

Using a reference station located outside the low-velocity basin in Mexico City, Kawase and Aki (1989) showed that the inclusion of a shallow soft basin within a much larger basin ~10 km long is required to explain the extraordinary durations of ground motions observed in Mexico City from the 1985 Michoacan earthquake. The long durations were a product of two distinctive phases, the first associated with the reverberations of incident body waves, and the second phases consisting of surface waves. However, at Jackson Lake Dam the JLDW rock site inside the large-scale low-velocity basin exhibit durations only modestly less than durations at the JLDW soil site within the shallow very-low-velocity basin. Thus, there must be some fundamental differences between the physical properties of the large-scale low-velocity basins at Jackson Lake and Mexico City. More importantly, there appears to be a parasitic interaction of nearly-identical-

period resonant responses between the soil basin containing the embankment portion of the dam and the large-scale low-velocity basin for periods of 1-2 s.

The Jackson Lake low-velocity basin appears to have more abrupt basin-edges (steeper dips) than Mexico City and stronger impedance contrasts, which appears to more effectively trap energy than the large-scale basin beneath Mexico City. Thus, unlike the case found by Kawase and Aki (1989) in Mexico City, where very long-durations of > 80 s were limited to sites located in low-velocity lake sediments embedded in the larger low-velocity basin, it appears that even sites located on relatively high-velocity compacted till (~1 km/s shear-wave velocity) in the Jackson Lake low-velocity basin are likely to experience durations exceeding 80 s. The effect of the very-low-velocity basin containing the embankment section of Jackson Lake Dam is to strongly amplify accelerations for periods > 1 s, increase dynamic strains by decreasing coherence with increasing periods, and to prolong strong motion durations to several minutes. Since strong nonlinear damping of accelerations is generally limited to periods < 1 s (Archuleta, 1998; Archuleta et al., 2000; Bonilla, 2000), strong amplification of > 1 s period accelerations by the very-low-velocity shallow sedimentary basin beneath the embankment portion of Jackson Lake Dam appears likely for **M** ~7 earthquakes on the Teton fault. Phase velocities of basin-edge shear-waves and surface waves within the embankment portion of the dam are likely to be much lower than assumed in Chen and Harichandran (2001) which would lead to larger embankment stresses and foundation associated with three-dimensional variations of dynamic strains than calculated by Chen and Harichandran (2001). In particular, limited coherence calculations suggest that along-axis differential displacements between the concrete and embankment sections of > 50 cm are likely to persist for 10-20 s and that differential displacements > 20 cm may persist for > 60 s.

The broadband empirical Green's function ground motions suggest that the rock ground motions in Section 6 underestimate acceleration responses for periods ranging from 0.8-2 s on the horizontal components, overestimate vertical responses for periods > 2 s, and underestimate the total duration of strong ground shaking. The local and regional broadband EGF's identified a serious ground motion characteristic that was not revealed in the analyses in Section 6. For seismic energy incident into the low-velocity basin from azimuths north of the dam, the fundamental resonant periods are virtually identical for the large-scale low-velocity basin and the

very-low-velocity soil basin containing the embankment portion of the dam. Consequently, the long-duration resonances continuously re-energize the soil resonances for several minutes at periods > 1 s. Since accelerations for periods > 1 s are likely to be amplified by nonlinear dynamic modulus degradation of soils (Archuleta et al., 2000; Bonilla, 2000) the embankment may be subjected to several minutes of strong ground shaking. It is not possible to credibly quantify expected ground motion amplitudes or durations using the regional larger magnitude earthquakes because it was not possible to install the broadband reference seismographic stations outside the low-velocity basin necessary to identify and account for the relative proportion and amplitudes of body and surface waves incident into the low velocity basin. Consequently, considerable uncertainties remain about the expected duration and intensity of ground-shaking at Jackson Lake Dam.

Appropriate specification of soil input motions for the embankment portion of the dam is a difficult issue. The investigations in Section 5 show that 1D vertically-incident propagators will not adequately represent soil responses, so use of rock site JLDW motions as input to nonlinear calculations is inappropriate. Probably the best way to specify input motions for dynamic analyses of the embankment section of the dam is to limit engineering foundation models to a maximum depth of 30 m with no significant impedance contrasts within the foundation material, and use the JLD3 motions scaled by 0.5-0.6 as input at 30 m depth in the nonlinear engineering model. This is necessary between no 2D or even 3D FEM model of the foundation will include the 3D reverberation amplitude and duration responses using the JLDW motions as inputs. The JLD3 synthetic motions produced using the **M** 5.2 Idaho earthquake EGF's provide one reasonable ground motion scenario (Figures 7-53, 7-55, 7-57). However, it is imperative to also use a ground motion scenario that includes the double resonance responses produced by energy arriving from north of the dam. The JLD3 synthetic motions from the **M** 4.6 Yellowstone EGF's are likely corrupted by significant whole-path surface wave responses and without an broadband recordings outside the basin there is no quantitative basis to adjust the synthetic motions. The **M** 3.2 20 Nov. 2002 earthquake is close enough to the Teton fault that there are surface waves are appropriately scaled. Unfortunately station JLD3 was no longer operating when this earthquake was recorded at JLDW. Consequently, there are no empirical soil records available to represent the duration of expected ground shaking and parasitic double basin 1-2 s amplified acceleration responses along

the embankment section of Jackson Lake Dam for seismic energy incident from the north. The regional earthquake EGF's ground motion results suggest that JLD3 responses are starting to approach durations of **M** ~8-9 subduction zone earthquakes.

In principal it would be possible to calculate coherence between rock sites JLDW and JLD2, and soil sites JLD3 and JLD5. However, in practice the stations are either very close together (< 30 m) and straddle the dam, or are located more than 200 m apart. Instead of calculating coherence, the differential displacements between rock site JLD2 located near the northern end of the concrete section of the dam and soil site JLD3 using the **M** 5.2 Idaho, EGF's are shown in Figure 7-87. These difference displacements provide a rough idea of the minimum expected differential movements between the concrete section and the embankment section located about 200 m north of site JLD2 and the duration of differential movements. Positive differential displacements for the north horizontal correspond to along-axis extension. Maximum extensional along-axis differential displacements exceed 50 cm (Figure 7-87) and extensional along-axis differential displacements exceeding 20 cm persist for at least 60 s.

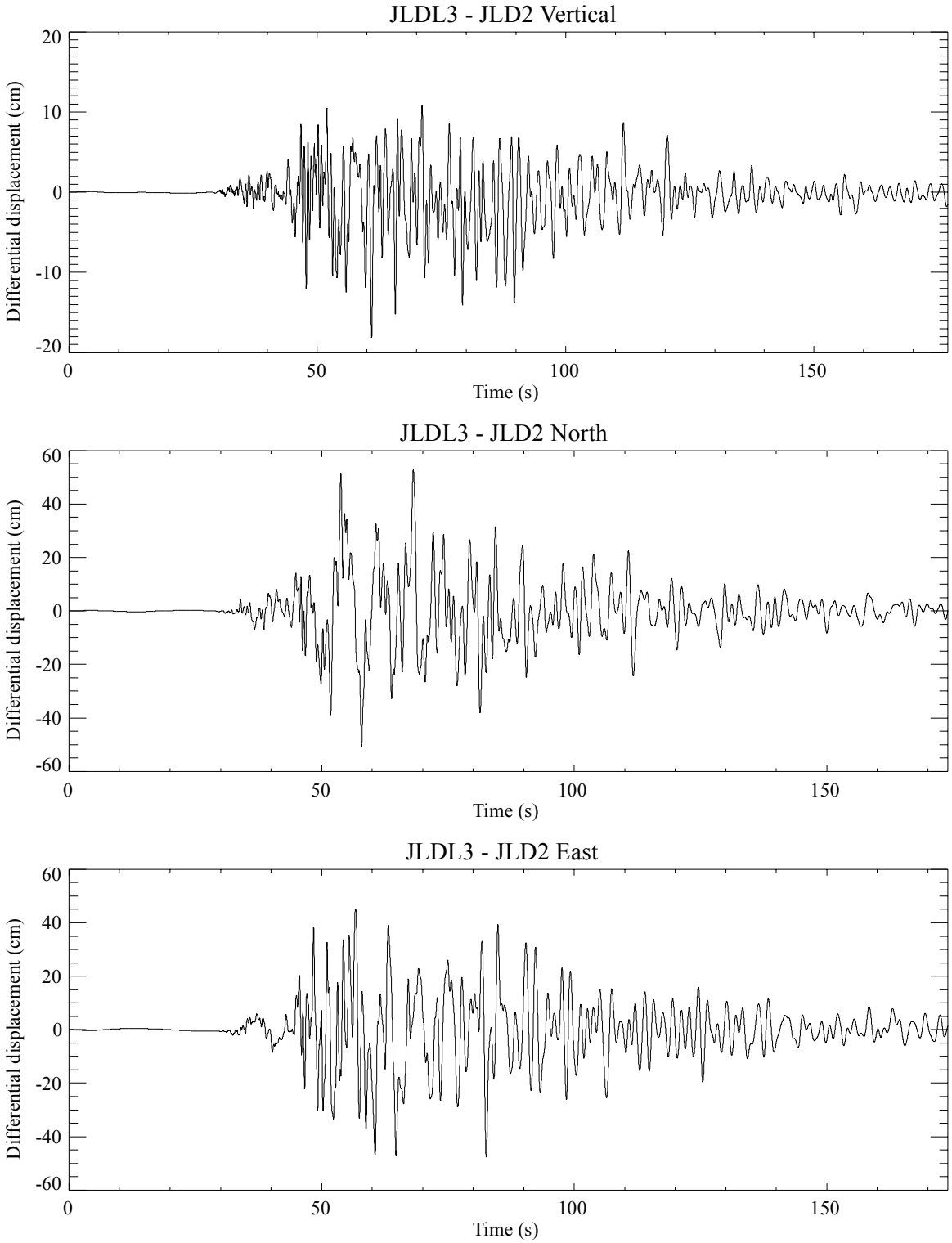

Figure 7-87: Differential displacements between sites JLD3 and JLD2 for a **M** 7.1 northern Teton fault segment earthquake. The **M** 5.2 Idaho, EGF's were used to synthesize ground motions at each site. The EGF's implicitly contain the propagation delays for the incident wavefield for azimuths near ~210°. A much wider variety of incident azimuths occur during an actual large earthquakes on the Teton fault, so this scenario likely represents lower bounds on peak differential displacement.

8.0 CONCLUSIONS

This report provides a detailed characterization of the ground motions that might affect Jackson Lake Dam due to a large earthquake on the Teton fault. These ground motion results are intended as inputs for engineering analyses of the stability of the dam during large earthquakes as part of an overall risk assessment for Jackson Lake Dam. Advances in the understanding of strong ground motions over the past decade have accrued due to the recording of several large earthquakes and research efforts to understand the seismic source, propagation, and site effects that produce and influence recorded ground motions. These efforts have lead to the development of improved methods of estimating and predicting strong ground motions at sites such at Jackson Lake Dam. These new data and approaches highlight the importance of geologic structure, basin geometry and properties, and site response to at-site ground motion estimation.

Large-scale crustal velocity structure and source radiation strongly influence the amplitudes and durations of ground motions at Jackson Lake Dam. Ground motions are synthesized for a variety of magnitudes and source geometries to quantify peak ground motions scaling and variability associated with earthquake rupture scenarios postulated for earthquakes on nearby Teton fault segments. Rupture of the northern Teton fault segment is likely to produce a **M** 6.9 earthquake for a dip of 60° and **M** 7.0 for a dip of 45° (**M** 7.0 is also used for a dip of 35°), based on moment fault area relations of Wells and Coppersmith (1994). Rupture of the northern and southern Teton fault segments in a single fault rupture increases **M** by ~ 0.2-0.3 based on moment fault area relations of Wells and Coppersmith (1994). Rupture of the northern segment for dips of 35° and 45° involves fault rupture directly beneath the dam. Impacts of 3D crustal velocity structure are substantial and much of the strong motion modeling effort was devoted to accounting for the influences of 3D velocity heterogeneity on ground motion amplitudes and durations and evaluating the influence of fault dip uncertainties on ground motion characteristics. Ground motion modeling revealed that source characterization, particularly the assumed dip of the Teton fault, strongly influenced peak ground motions and ground motion durations. Consequently, significant geological and geophysical subtasks were required to estimate ground motions at the dam. These include 1) geologic source characterization of the Teton fault, 2) analyses of seismicity in the region of the Teton fault and Jackson Lake Dam, 3) analyses of the hangingwall crustal velocity structure and seismic response, 4) empirical site response analyses based on

specific foundation conditions and recorded data at Jackson Lake Dam, and 5) development of ground motion results from the Teton fault for Jackson Lake Dam considering the integrated results of the previous tasks. As a final step, these results are portrayed in a simplified probabilistic framework to facilitate their input to Reclamation risk assessments for Jackson Lake Dam. Analyses of data from the Jackson Lake Seismic Network (JLSN) and from site-response instrumentation operated at Jackson Lake Dam between 1996-2002 in conjunction with the JLSN are major inputs of most of these subtasks.

8.1 Teton Fault Slip Rates

For the ground motion analyses, existing data have been used as the basis for defining the source characteristics of the Teton fault in the ground motion modeling and as the basis for estimating the probability of the modeled results. Fault scarps on Quaternary deposits indicate the locations of the most recently active fault traces and show the variations in slip along the length of the fault. Maximum slip rates on the Teton fault appear to be in the range of 2 to 5 mm/yr along sections of the fault that are located to the west and southwest of Jackson Lake. Estimated slip rates decrease significantly to the north along the west shore of Jackson Lake and the late Quaternary extent of the fault appears to terminate just north of Jackson Lake near Steamboat Mountain. Slip rates decrease more gradually south of Jackson Lake and the southern limit of late Quaternary fault ruptures appear to be in the Phillips Canyon area, west of the town of Jackson. The largest uncertainty in characterization of late Quaternary slip rates along the Teton fault is uncertainty in the age(s) of faulted and unfaulted deposits along the fault trace. The limited detail of the existing geomorphic mapping of the Teton fault scarps and deposits along the range front results in at least a factor of 2 uncertainty in slip rate estimates for the fault. These same limitations also mean that the existing data are not sufficient to determine whether the Teton fault is segmented or to define in detail the extent of any individual paleoseismic ruptures which could be used as proxies for slip distribution or extent in ground motion models. Because of the absence of detailed data on fault segmentation for the Teton fault, three alternative fault rupture models are considered. These models consider a range of fault rupture segmentation from a highly segmented fault which ruptures in sections that are typically 20-25 km in length to a full rupture of the entire 60-km long fault. Among these models, mean average recurrence intervals for a large surface-rupturing earthquake, **M** ~7, on the Teton fault range from about 700 years to about 2000 years. The mean

average recurrence interval for a large surface-rupturing earthquake on the Teton fault from the weighted combined models is about 1180 years.

8.2 Teton Fault Dip

The assumed dip of the seismogenic, late Quaternary Teton fault is a highly significant input to the modeled ground motions at Jackson Lake Dam. Lower fault dips result in stronger radiation of seismic energy due to the closer proximity of the rupture surface beneath the dam, greater excitation of the low-velocity crustal basin on the hangingwall of the fault, and imply potentially larger seismic moment release due to the larger areas of the fault plane within the zone of brittle fault rupture. There is little direct data to constrain the dip of the late Quaternary Teton fault in northern Jackson Hole. Most previous studies have portrayed a fault dip near 60° (see review by Byrd et al., 1994), although Behrendt et al. (1968) suggested a much lower dip. Recent analyses and compilations of data from large normal-faulting earthquakes, including the 1959 Hebgen Lake and 1983 Borah Peak earthquakes, have suggested that there is a marked preference for fault planes associated with these earthquakes to have dips near 45°, but with a significant spread over a range of 30-60° (e.g., Thatcher and Hill, 1991; Collettini and Simpson, 2001). The results of Behrendt et al. (1968), which indicate a possible intrabasin trace of the Teton fault that lies east of the late Quaternary, currently seismogenic trace, are further evidence that the lower bound for the dip range of the presently active trace is greater than about 30°.

The relative paucity of earthquakes that could be associated with the Teton fault at depth do not provide strong constraints on fault dip. Focal mechanism solutions of earthquakes located east of the surface trace of the Teton fault dips have east-dipping nodal planes that dip from 25° to 60°. There are too few earthquakes located east of the Teton fault, with far too limited spatial coverage to provide a strong constraint on fault dip, although the spatial distribution of earthquakes is consistent with dips of < 50°. 2D finite-difference modeling of two microearthquakes in Section 4 suggests that the Teton fault dips 40°-50°. Waveform modeling of more of the earthquakes located east of the Teton fault may provide better constraints on Teton fault dip at depth and 3D basin velocity structure than are currently available. The emergence of a relatively new normal fault several km west of the large-scale Teton fault with a steep dip of 60-70° (Section 2) suggests that the current large-scale Teton fault may be approaching unfavorably low dips for continued normal

faulting. Thus, the only available information specific to the Teton fault argues for a fault dip of 35° to 40°. In lieu of any other specific information about the dip of the Teton fault at depth, a fault dip of 35° is considered the most reasonable estimate for the Teton fault. Ground motions models of the Teton fault used dips of 35°, 45°, and 60° to ascertain the sensitivity of estimated ground motions to fault dip.

8.3 3D Crustal Velocity Structure

The Jackson Lake Seismic Network and Jackson Lake Dam site-response data were necessary to constrain the 3D velocity structure near the Teton fault and the dam to develop realistic ground motion estimates for the dam. These microearthquake data were used to develop a large-scale 3D velocity using P-wave arrival times in a 3D velocity-hypocenter inversion. This 3D velocity model was modified and extended to include S-wave information to reproduce site-response ground motions from three microearthquakes located near the western, northern, and southern limits of the northern Teton fault segment and the large-scale 3D low-velocity basin containing the dam. The low-velocity basin is ~3-4 km deep at its deepest point and its boundaries have large velocity discontinuities relative to the relatively high-velocity basement rocks that surround the low-velocity basin. The 3D low-velocity basin velocity structure was developed using seismic refraction data (Behrendt et al., 1968; Byrd et al., 1994) and modeling of microearthquake ground motions at the dam. It allows full development of basin edge-refracted shear wave and multiple free-surface-bounce-refracted arrivals observed in the site-response recordings at the dam. These various shear-wave arrivals form complex, long-duration wavetrains following the direct shear arrival by 3-5 s, and that persist for 15-20 s, depending on the distance of the dam from the excited margin of the basin along the great circle path to the epicenter. The relatively strong velocity discontinuities between the low basin velocities and the surrounding high velocity medium are required to reproduce strong shear-wave arrivals that follow the direct shear-wave by 3-7 s in the weak ground motions recorded at the dam. 2D viscoelastic finite-difference modeling of microearthquake ground motions and site response investigations were used to construct relationships between P- and S-wave velocities and P- and S-wave quality factors (Qp and Qs, respectively).

The seismogram modeling of microearthquakes in Section 4 showed that 3D velocity-model Green's functions are necessary to simulate ground motions within the LVB, not just to obtain realistic durations, but to include the constructive interference effects of coherent secondary sources, like LVB-edge S waves. Empirical Green's functions may underestimate 1-4 Hz responses because the coherent LVB-edge S-waves are probably not adequately represented by the eight empirical Green's functions used in Section 6. Near-surface ground motion amplitudes may be very large along the western margin of the LVB due to rupture directivity. Thus, material nonlinearity may occur at the LVB edges; nonlinearity may modify LVB-edge S-wave and surface-wave contributions to LVB ground motions. It may be important to conduct 2D P-SV plane-wave experiments using nonlinear finite-difference or finite-element codes to ascertain if near-surface, LVB-edge nonlinearity substantially influences ground motion durations and amplitudes within the LVB.

Since the majority of ground motions used to develop ground motion attenuation relations are from California, it's important to recognize the significant differences between the crustal velocity structure near the Teton fault and typical California crustal velocity structure. Near-surface P-wave velocities are ~6 km/s near the surface adjacent to the Teton fault. In southern California, P-wave velocities of 6 km/s are typically not encountered until depths of 5-10 km (Hauksson and Haase, 1997). High basement velocities extending to near the surface in the vicinity of the Teton fault translates into very large velocity contrasts between the LVB and surrounding basement rocks, particularly along the western half of the LVB. Thus, even though LVB S-wave velocities are similar to California "rock" or NEHRP site B S-wave velocities (> 720 m/s), the JLDW rock site behaves more like California stiff-soil site with S-wave velocities of 300-to-600 m/s, than a California "rock" site. The large velocity contrasts between the LVB and the basement rock makes the LVB a strong collector of radiated seismic energy (Figure 4-7a), which produces unusually long observed durations at the dam (Section 5) and amplification of ground motions within the LVB.

There are significant caveats concerning the 3D velocity model, particularly the large-scale low-velocity basin that contains the dam. First, while the strong velocity contrast between the basin and the surrounding medium reproduce overall amplitude and duration characteristics of

weak ground motions recorded at the dam, these are the only data that constrain this aspect of the velocity model. The total depth of the basin probably has at least 1 km uncertainties and the overall 3D shape and roughness of the bottom of the basin are poorly constrained by the data analyzed to date. The 2D finite-difference modeling suggested that strong correlated-random velocity variations may exist in the basin, but the velocity model used to estimate ground motions at the dam has no randomization of basin velocities. The only randomization was applied to the medium outside the low-velocity basin in the form of vertical velocity oscillations with wavelengths of ~1 km that are strongest in the highest velocity gradient portions of the model outside the low-velocity basin. More sophisticated velocity randomizations (O'Connell, 1999a) of the 3D velocity were not pursued because that would have exceeded the logistical constraints of the investigation. Since the basin strongly influences peak ground motion scaling and durations at the dam, the uncertainty in the 3D crustal velocity model may be a significant source of ground motion estimation uncertainty at the dam.

8.4 Soil Site Response

Weak-motion site response was measured at Jackson Lake Dam using an array of seven broad-band seismometers. Key observations are the presence of substantial long-period amplification and prolonged duration of shaking beyond some transition point located between stations 13+00 and 24+00; minimal long-period amplification at stations 12+00 and less, referenced to a bedrock site on the right abutment; and, high-frequency de-amplification on treated sections of the north embankment referenced to a site just outside of the treated zone.

Strong ground motions at stations 13+00 and greater are expected to behave non-linearly. The observed weak-motion site response must be modified to account for non-linear soil behavior. The observed site response at station 24+00 is consistent with the 2-D and 3-D response of a sedimentary basin, and likely results from the generation of surface waves, converted phases, and interface waves. These effects are not accounted for by 1-D models. However, available computer codes for estimating non-linear soil behavior are based on propagating an incident body wave (typically a horizontally polarized S wave) through a 1-D soil column. In order to permit use of 1-D non-linear soil response computer codes, while preserving the observed 2-D and 3-D effects of prolonged duration and long-period amplification, the weak-motion impulse response is

modified for input to the non-linear soil response codes at a selected reference depth. There is considerable uncertainty in this method because the reduction of the convolved surface motions to a reference depth cannot accurately account for the depth dependency of surface waves and converted phases.

As discussed in section 5-2, we don't know the precise location of the transition in site response observed between stations 13+00 (JLD2) and 24+00 (JLD3-5). Based on drilling and geophysical logging, we would expect the transition to be near 14+00, although this is not certain. Thus engineering analyses for stations at 14+00 or greater should use the JLD3 response, and stations less than 14+00 should use the JLD2 response.

2D synthetic seismogram modeling of the soil response data show that the extended ground motion durations observed at the surface are likely associated with a mixture of refracted S-waves, and horizontally propagating surface and interface waves. For shallow depths of 0 m to 20 m the largest accelerations after the near-vertical incidence S-wave direct and reflected arrivals consist of a mixture of refracted S-waves and broadband Rayleigh wave Airy phases. For the portion of the dam located within 1.5 km of the southern glacial scour and depths of 30 m and larger, the largest accelerations after the near-vertical incidence S-wave direct and reflected arrivals are associated with refracted S-waves. At distances > 1.5 km from the glacial scour boundary, the Stonely wave produces the largest accelerations for depths of 30 m and larger. The influence of soil nonlinearity on the amplitudes of these interface waves is unknown, although the continued existence of the free surface and internal velocity discontinuities during modulus degradation suggests that these phases will persist as soils respond nonlinearly. Since a significant amount of energy is propagating horizontally at depths of up to 50 m, it is necessary to account for this significant seismic energy in 1D vertical-incident SH nonlinear simulations of nonlinear soil effects, since the existing codes do not simulate the production of these observed phases. Consequently, it is necessary to include the extended durations in the 1D nonlinear inputs to account for observed, broadband, strong-amplitude extended soil response durations, as discussed in Section 6.

The 2D synthetic seismograms show that there is a critical distance range from the southern margin of the glacial scour where peak horizontal acceleration responses are likely to be amplified

relative to most of the embankment section of the dam. This amplification is associated with the constructive interference of the scour basin-edge interface waves, particularly the broadband Airy phases, but also the Stonely wave, with the direct, reflected, and basin-edge refracted S-waves. The critical distance of maximum amplification is a function of the sediment velocities, which limited geophysical measurements (Sirles, 1986) show vary vertically and laterally from near the southern glacial scour margin and the borehole located between stations JLD3 and JLD6. There are no geophysical velocity measurements or ground motion recordings between stations JLD2 (modest amplification) and station JLD3 (strong amplification). Although the 2D velocity model does not contain all the complex features of the glacial scour geometry inferred in Section 2, the 2D finite-difference synthetic results indicate that it is likely that amplifications stronger than those measured at stations JLD3 and JL6 probably occur somewhere between stations JLD2 and JLD3 (along the tallest portion of the embankment section of the dam). Due to the lack of sediment S-wave-velocity information between stations JLD2 and JLD3, it is not possible to indicate the position or magnitude of the additional amplification relative to station JLD3. It is important to understand that the amplification responses at JLD3 are unlikely to represent the maximum amplification along the embankment portion of the dam between stations JLD2 and JLD3.

The glacial scour S-wave velocity structure at the dam is very similar to the Valley of Mexico in Mexico City (Bodin et al., 1997), except that low-velocities extend ~20 m deeper at Jackson Lake Dam. In the Valley of Mexico, monochromatic, large-amplitude ground motions have durations of ~250 s for **M** > 6.5 seismic sources located > 200 km from the site (Lomnitz et al., 1999). In contrast, the closest portion of the Teton fault is located ~10 km from Jackson Lake Dam. However, the Valley of Mexico is probably significantly longer and wider than the glacial scour basin at Jackson Lake Dam, although the total extent of the glacial scour basin north of the dam is unknown. Consequently, it is likely that the durations in the central portion of the Valley of Mexico would be somewhat longer than at Jackson Lake Dam because the propagation times from the edges of the very-low-velocity basin to the basin interior would be longer. In contrast, the S-wave soil velocities are slower and thicker than those found in the Marina District of San Francisco, which suffered extensive damage during the **M** 6.9 1989 Loma Prieta earthquake. The earthquake was located about 90 km away, yet the Marina District exhibited amplification and

extended durations associated with shallow basin response (Graves, 1993). In the Marina District, near-surface S-wave velocities are ~200 m/s (Graves, 1993), about twice the S-wave velocities in the soil section of Jackson Lake Dam. Using a 3D basin velocity model, Graves (1993) was able to reproduce long ground motion durations and amplification of aftershocks recorded in the Marina District basin. The lower soil S-wave velocities at Jackson Lake Dam make it likely that ground motion durations at the dam will be at least double those observed in the Marina District.

8.5 Ground Motion Estimation

The viscoelastic 3D finite difference methods of Graves and Day (2003) and P.C. Liu (pers. comm.) were used to calculate ground motions for frequencies < 1 Hz and empirical Green's functions (EGF) extracted from the Jackson Lake Dam site-response array were used to simulate ground motions for frequencies > 1 Hz. Broadband strong ground motions were produced by blending the 3D finite-difference motions with the high-frequency EGF motions over transition frequency band centered at 1 Hz. Viscoelastic 3D finite difference methods are used for forward-modeling ground simulations of single and multiple segment finite-fault rupture of the Teton fault using the method of P.C. Liu (pers. comm). The reciprocity approach of Graves and Wald (2001), updated as per Graves and Day (2003) to provide a realistic approximation for damping, was used to calculate 3D Green's functions for grids of point sources distributed on the six fault segments used to evaluate ground motions associated with earthquakes on the Teton fault.

In theory there is no reason EGF's could not be used to produce broadband ground motions. In practice, ambient background noise precludes using EGF's for frequencies substantially < 1 Hz. A total of eight microearthquake three-component seismograms obtained from site-response stations in the vicinity of Jackson Lake Dam were used to produce EGF's for ground motion simulations corresponding to earthquake ruptures on the northern Teton fault segment. Seven seismograms were obtained from station JLDW, located on the south abutment of the dam. The EGF's earthquakes were selected because of their proximity to the northern segment of the Teton fault. several of the earthquakes conceivably are located on the Teton fault; the uncertainties in fault dip and hypocenter locations precludes definitive assignment of these earthquakes to the Teton fault.

Ground motion estimation efforts focused on developing ground motion estimates for rock conditions on the south abutment and soil responses at 140 m depth below the embankment section of the dam for scenario earthquakes on the northern segment of the Teton fault. A limited number of multi-segment ground motion simulations were used to establish that the southern Teton fault segment increases the duration of ground shaking at the dam by 10-20 s, but does not substantially increase ground motion amplitudes. Consequently, detailed ground motion modeling focused on ground motion associated with earthquakes on the northern Teton fault segment.

A kinematic rupture model is used that mimics the spontaneous dynamic rupture behavior of a self-similar stress distribution model. Self-similar effective stresses (and slip velocities) are generated over the fault with rise times that are inversely proportional to effective stress. The kinematic model used here produces slip models with $1/k^2$ distributions consistent with estimates of earthquake slip distributions (Somerville *et al.*, 1999) and ω^2 displacement spectra in the far-field. Effective stress correlation lengths were increased by 33% relative to the **M** 6.7 Northridge rupture simulations of O'Connell et al. (2001) to be consistent with the empirical relations of Somerville et al. (1999), that indicate that asperity size increases with magnitude. Rupture velocities were allowed to vary over a wide range (between 0.6*β to 1.05*β) to allow rupture directivity caustics to develop, and to produce variable rupture times. Effective stresses average 30-40 bars, consistent with stress drops typically associated with normal-faulting earthquakes. Rise times average 2-3 s and combined with average slips of 2-3 m, produce average slip velocities on the fault of ~ 1 m/s.

There is no direct evidence to constrain the dip of the northern segment of the Teton fault beyond placing "reasonable limits" of 35° to 60°. Consequently, ground motions were simulated for dips of 35°, 45°, and 60°. Several thousand earthquake rupture simulations were performed for each fault dip to estimate strong motion variability associated with uncertainties in earthquake rupture behavior. Resulting ground motions were sorted by response spectral ordinate, and the parameters listed in Table 8-1, to produce mean and 84 percentile ground motion estimates for each discrete value of fault dip. These results were compared to the empirical relations of Spudich et al. (1999) for strike-slip/normal faulting ground motions. A significant caveat is that there are NO strong motion recordings of **M** > 6 normal-faulting earthquakes for a hanging wall site located < 12 km

from the fault in a low-velocity basin. The "empirical relations" of Spudich et al. (1999) use reduced amplitude strike-slip data as a proxy for nonexistent normal faulting data.

A number of ground motion quantities are reported for mean and 84% results, including peak velocity, Arias Intensity, and cumulative kinetic energy. Two durations are reported both defined by the duration of motion from the 5% quantile to the 95% quantile of either Arias Intensity or cumulative kinetic energy. The ground motions from the 35° dip scenario (Table 8-1) have the largest peak motions and longest durations because this fault configuration produces the maximum fault area and the largest fault area beneath the dam. Also, the fault is closest to the dam for a dip of 35°. The peak velocities are very large reflecting a significant amount of rupture directivity compounded by the amplifying responses of the large, low-velocity basin.

Table 8-1: Ground Motion Parameters for a 35°-Dipping Northern Teton Fault Segment.

Component	Peak velocity	Arias Intensity	Cumulative energy	Arias duration	Energy duration
	(cm/s)	(m/s)	(J)	(s)	(s)
Downstream mean	146	6.2	10,928	15.1	21.2
Downstream 84%	201	9.3	15,343	17.7	27.9
Cross canyon mean	102	3.5	9,111	18.5	21.2
Cross canyon 84%	135	5.1	14,154	21.4	26.3
Vertical mean	125	2.4	11,233	16.5	14.3
Vertical 84%	147	3.4	15,709	20.1	16.9

Corresponding mean and 84% acceleration response spectra for JLDW are shown in Figures 8-1 and 8-2, respectively. The synthesized ground motions are much more similar to the Spudich et al. (1999) soil responses than the rock responses (Figures 8-1 and 8-2), both in terms of period content and amplitude. The synthesized ground motions have much stronger responses for periods > ~1.5 s than the empirical predictions, consistent with the first-order influences of the large, low-velocity basin on "rock" ground motions at the dam. Similarly, the synthesized shortest period motions (< 0.4 s) are somewhat lower than SEA99 soil responses, because even the rock conditions at Jackson Lake Dam attenuate higher frequencies more strongly than typical

California soil sites. Corresponding results for dips of 45° and 60° are shown in Tables 8-2 and 8-3.

Of particular note is that mean peak velocities exceed 90 cm/s for all dip scenarios. Mean 45°-dip response spectra are closer to SEA99 soil results than rock results (Figure 8-3), but 84% 45°-dip response spectra (Figure 8-4) and both mean and 84% 60°-dip response spectra (Figures 8-5 and 8-6) have amplitudes more similar to SEA99 rock results, than SEA99 soil results.

Table 8-2: Ground Motion Parameters for a 45°-Dipping Northern Teton Fault Segment.

Component	Peak velocity	Arias Intensity	Cumulative energy	Arias duration	Energy duration
	(cm/s)	(m/s)	(J)	(s)	(s)
Downstream mean	133	4.8	11,767	16.1	23.4
Downstream 84%	171	7.1	16,956	18.1	33.1
Cross canyon mean	111	4.0	10,063	18.5	21.8
Cross canyon 84%	155	6.1	16,010	21.1	27.4
Vertical mean	105	2.4	9,605	16.3	16.7
Vertical 84%	130	3.6	14,111	19.1	20.1

Table 8-3: Ground Motion Parameters for a 60°-Dipping Northern Teton Fault Segment.

Component	Peak velocity	Arias Intensity	Cumulative energy	Arias duration	Energy duration
	(cm/s)	(m/s)	(J)	(s)	(s)
Downstream mean	96	2.7	9,366	18.3	24.8
Downstream 84%	122	3.9	14,100	23.0	33.8
Cross canyon mean	84	2.6	5,616	19.5	26.0
Cross canyon 84%	116	3.9	8,510	22.4	36.0
Vertical mean	76	1.8	4,819	15.9	20.0
Vertical 84%	98	2.6	,7220	18.7	28.2

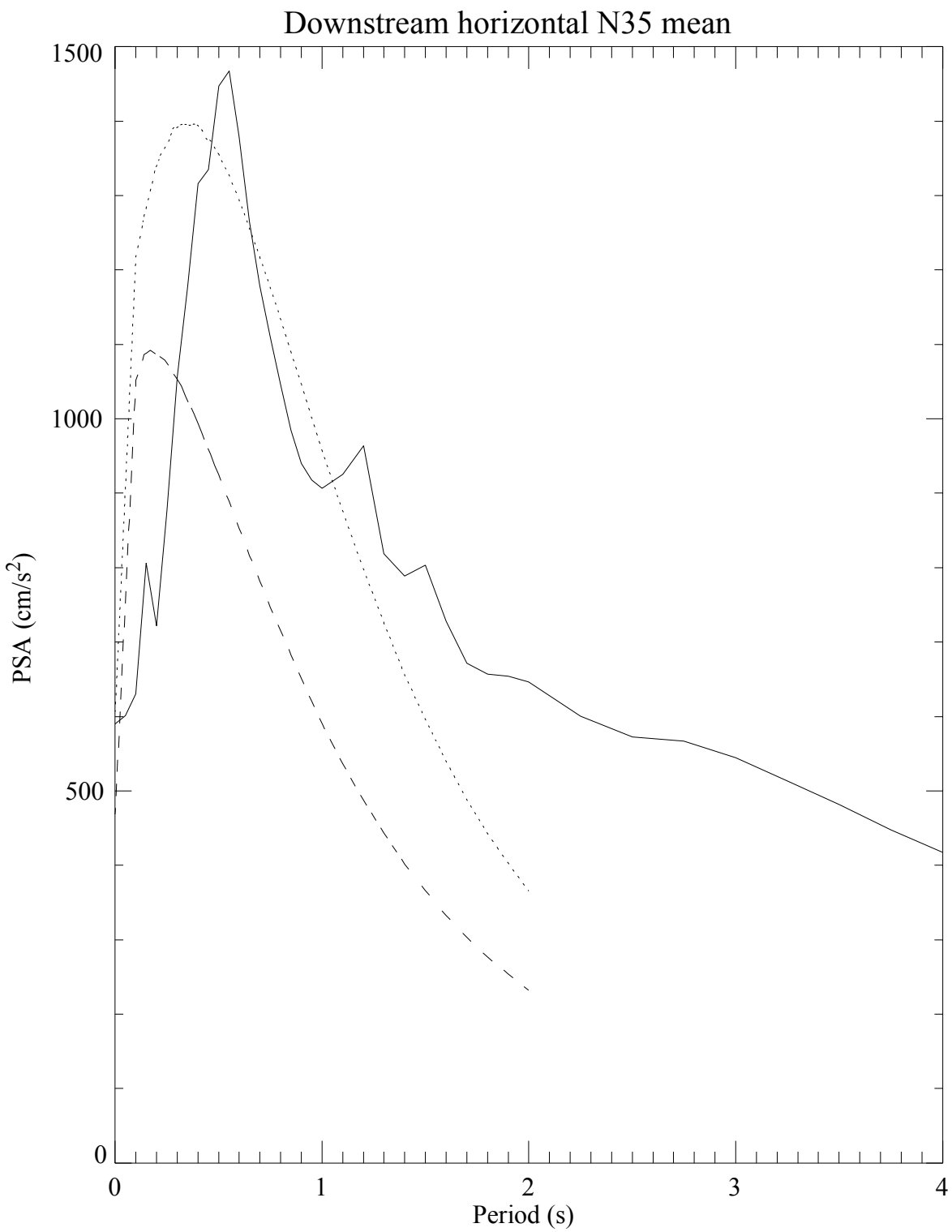

Figure 8-1: Mean downstream horizontal JLDW rock site PSA response spectra for a 35°-dipping northern Teton fault segment (solid). Mean Spudich et al. (1999) (SEA99) average horizontal component estimates for a **M** 7.0 normal-faulting earthquake are shown for soil (dotted) and rock (dashed) site conditions.

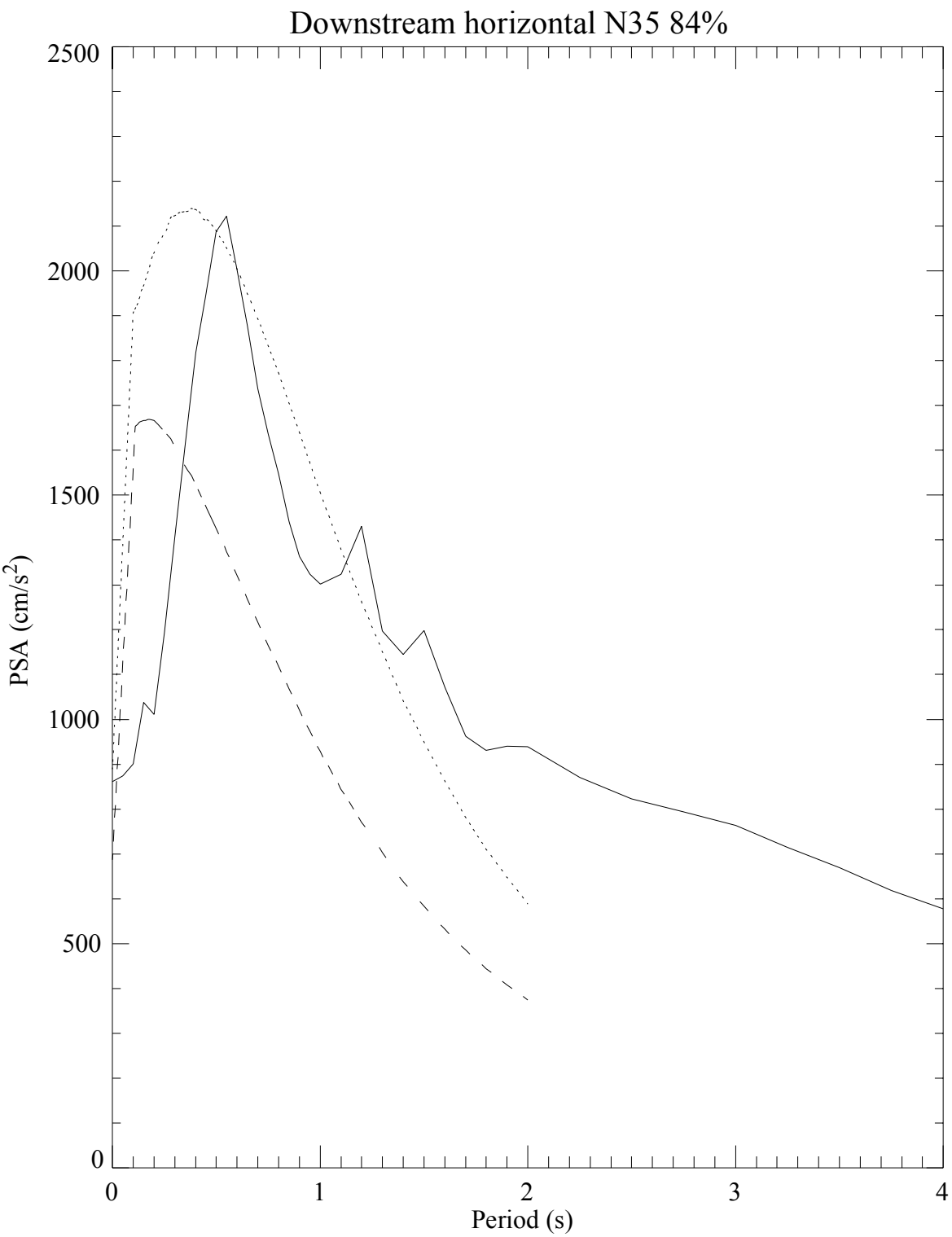

Figure 8-2: 84% quantile downstream horizontal JLDW rock site PSA response spectra for a 35°-dipping northern Teton fault segment (solid). 84% SEA99 average horizontal component estimates for a **M** 7.0 normal-faulting earthquake are shown for soil (dotted) and rock (dashed) site conditions.

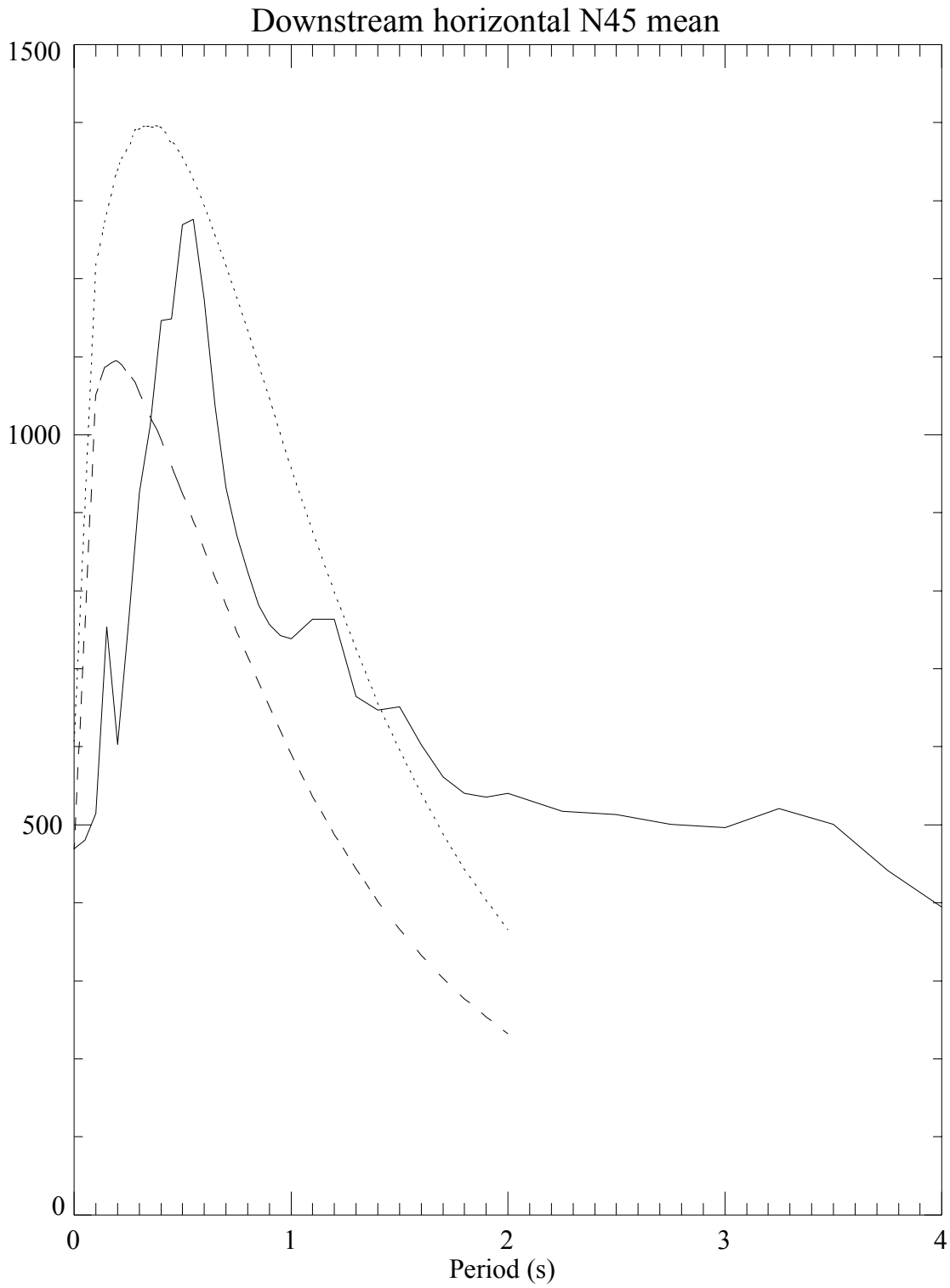

Figure 8-3: Mean downstream horizontal JLDW rock site PSA response spectra for a 45°-dipping northern Teton fault segment (solid). Mean SEA99 average horizontal component estimates for a **M** 7.0 normal-faulting earthquake are shown for soil (dotted) and rock (dashed) site conditions.

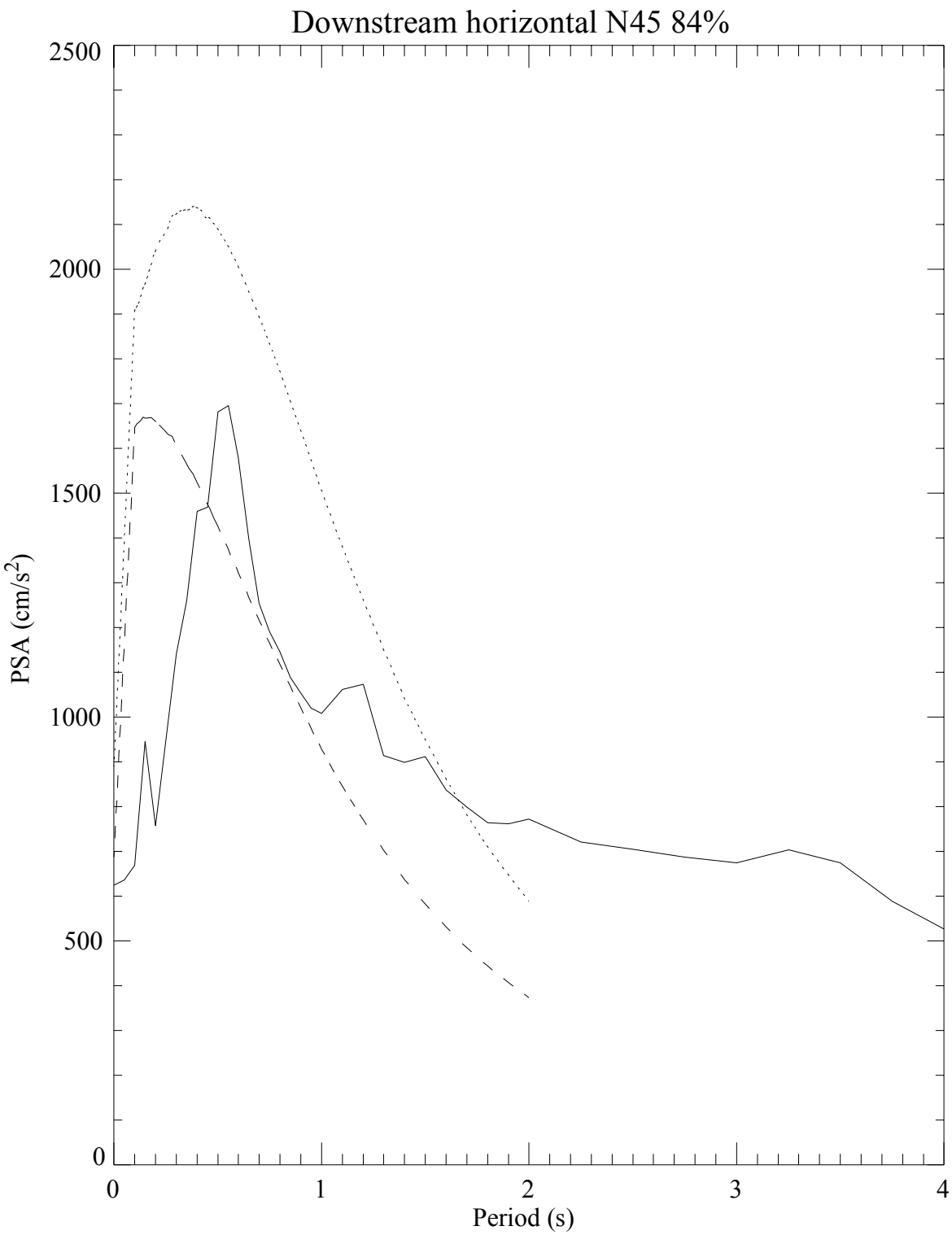

Figure 8-4: 84% quantile downstream horizontal JLDW rock site PSA response spectra for a 45°-dipping northern Teton fault segment (solid). 84% SEA99 average horizontal component estimates for a **M** 7.0 normal-faulting earthquake are shown for soil (dotted) and rock (dashed) site conditions.

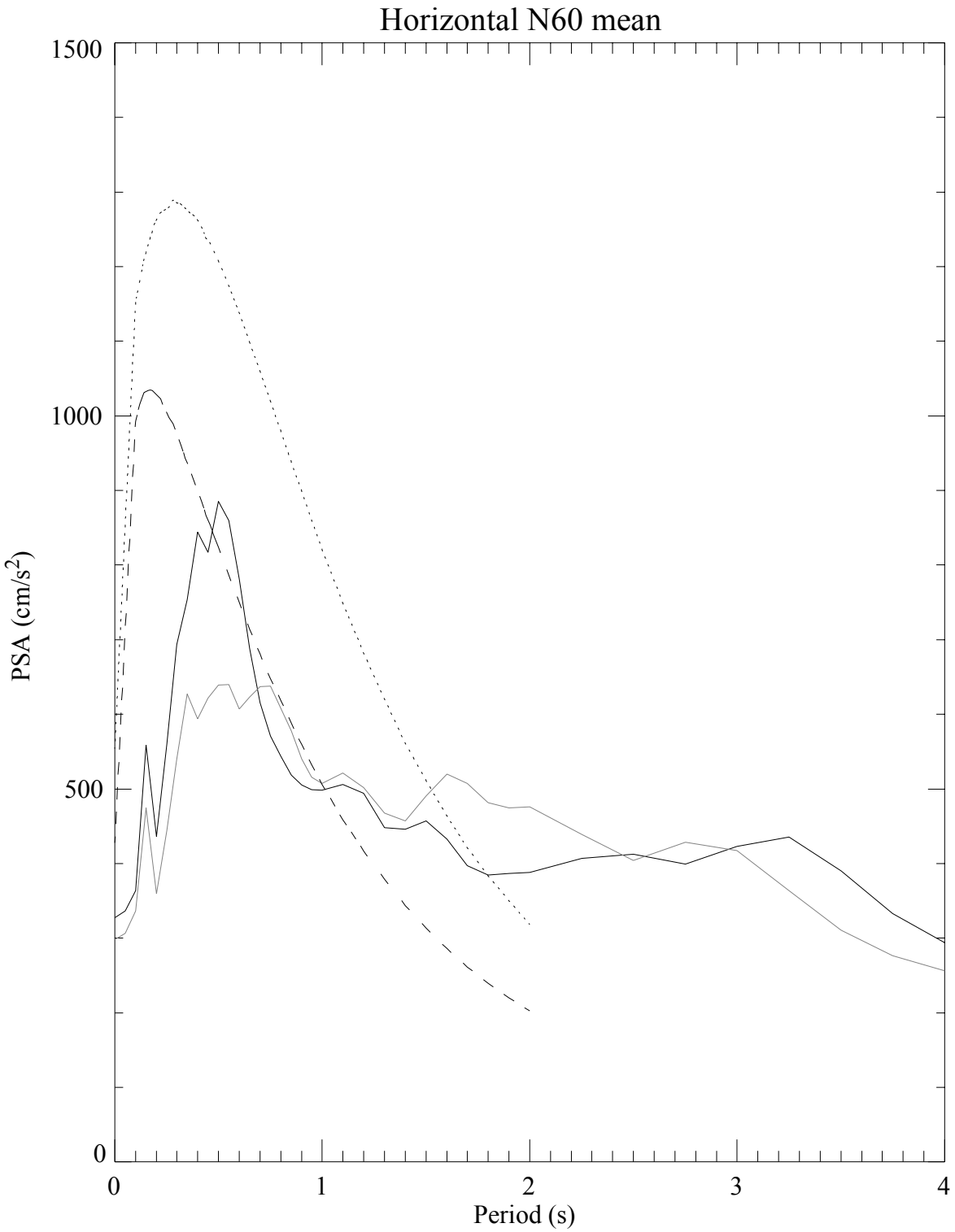

Figure 8-5: Mean JLDW rock site PSA horizontal response spectra for a 60°-dipping northern Teton fault segment. Downstream is solid and cross canyon is gray. Mean SEA99 average horizontal component estimates for a **M** 6.9 normal-faulting earthquake are shown for soil (dotted) and rock (dashed) site conditions.

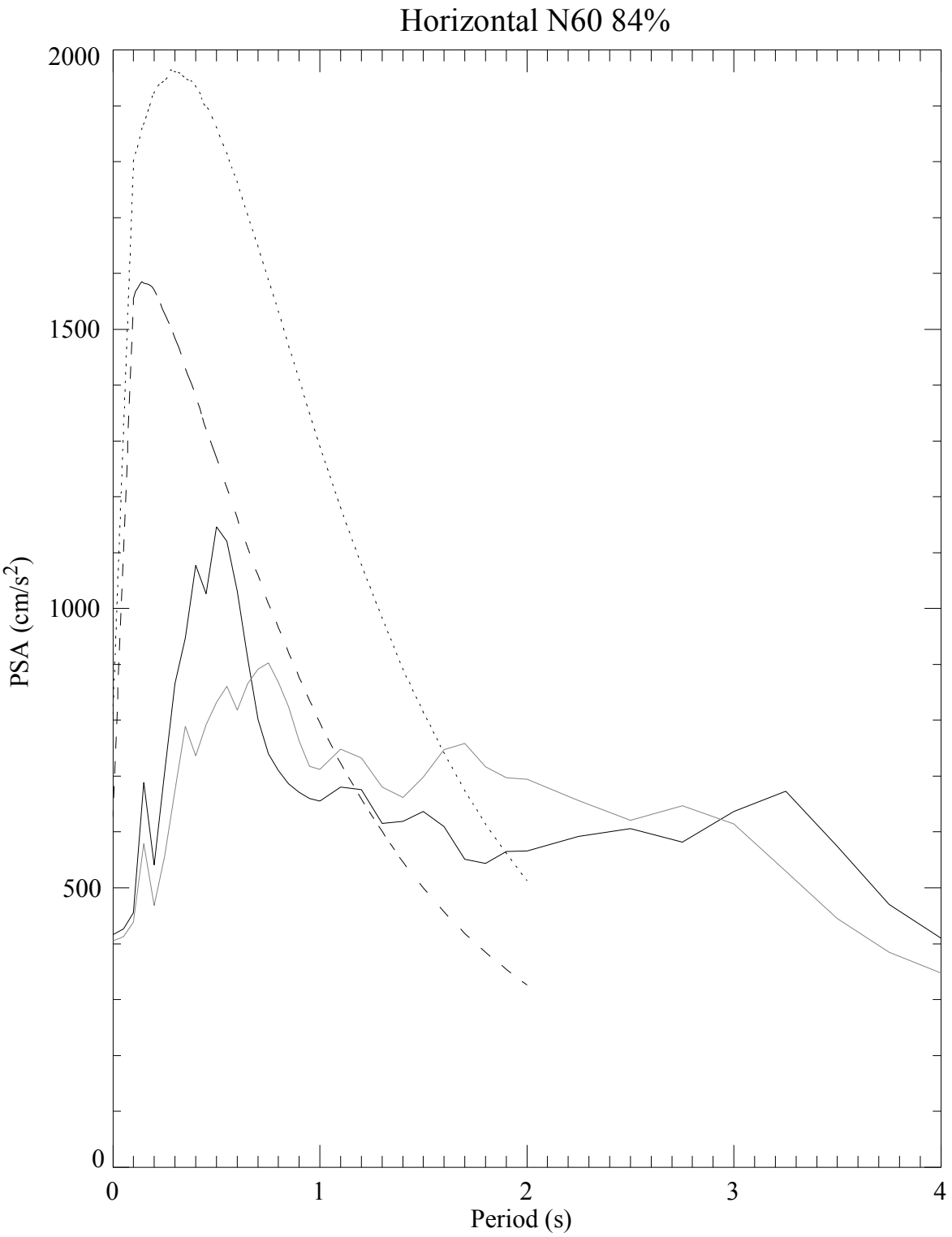

Figure 8-6: 84% quantile JLDW rock site PSA horizontal response spectra for a 60°-dipping northern Teton fault segment. Downstream is solid and cross canyon is gray. 84% SEA99 average horizontal component estimates for a **M** 6.9 normal-faulting earthquake are shown for soil (dotted) and rock (dashed) site conditions.

The ground motion simulation approach used in Section 6 was critically evaluated by using alternative ground motion estimation procedures and by confirming that the kinematic rupture model reproduces near-source ground motions from the **M** 6.7 1994 Northridge earthquake. Near-source ground motions from the **M** 6.5 1979 Imperial Valley earthquake are consistent with unusually large long-period acceleration responses predicted for Jackson Lake Dam. The > 0.4 g > 2 s period acceleration responses observed at stations in the low-velocity basin in Imperial Valley indicate that the large (> 0.5 g) > 2 s period acceleration responses predicted for Jackson Lake Dam are not without precedent. Considering the more extreme impedance contrast between the low-velocity sediments and the basement at Jackson Lake Dam relative to Imperial Valley, the large (> 0.5 g) > 2-s-period acceleration responses predicted for Jackson Lake Dam make physical sense, particularly with respect to the incidence angle criteria of Somerville et al. (2003) for predicting the amplification of long-period motions in low-velocity basin. Broadband empirical Green's function investigations in Section 7 confirmed that unusually large accelerations are likely to occur at the dam for periods > 1 s on the horizontal components and for periods extending to 2 s on the vertical component. The broadband EGF ground motions revealed a double parasitic resonance (both the soil and the low-velocity basin are resonating at the same period) for the embankment portion of the dam for periods of 1-2 s for seismic energy arriving from north of the dam. This double resonance strongly amplifies the soil accelerations for periods > 1 s and increases the duration of strong ground shaking to several minutes.

Since the peak ground motions are strongly dependent on the assumed dip of the Teton fault, it is necessary to decide which dip scenario is most representative of expected ground motions at the dam. As discussed in Section 2, worldwide **M** > 5.5 earthquake data for normal-faulting earthquakes indicate that normal-fault dips of ≤ 50° comprise 76% of the normal-faulting earthquakes (Collettini and Sibson, 2001). The focal mechanism data in Section 3 allow for a Teton fault dip of 25° to 60°, but do not place strong constraints on fault dip. As discussed in Section 4, detailed waveform modeling of two earthquakes suggest that the northern Teton fault segment dips < 50°. The local and region evidence for normal-faulting dip suggests that the 35° and 45° fault dip ground motion scenarios represent the most likely dip scenarios for the Teton fault. In view of the lack of any definitive information indicating that the northern Teton fault rupture segment dips > 50°, the 60° fault dip ground motion scenarios are discounted for the

purposes of recommending ground motions for dynamic analyses of Jackson Lake Dam. Although a fault dip of 45° is plausible, the ground motions produced using a fault dip of 35° are recommended for dynamic analyses of Jackson Lake Dam. Our judgement is that the 35°-dipping ground motions are probably most representative of expected ground motions for faults dips < 50°, the most likely range of dips for the Teton fault, based on world-wide distributions of normal fault dips (Section 2) and the limited inferences that can be made about Teton fault dip from microearthquake data (Sections 3 and 4).

8.6 Rock Ground Motions for the Concrete Section

One of the probabilistic parameters requested for use in simplified engineering analyses of the concrete section of Jackson Lake Dam was peak horizontal acceleration (PHA). Since the random seismicity did not significantly contribute to PHA exceeding 0.5 g (see Section 3 and Wong et al., 1999), only ground motions associated with the Teton fault were considered. Specifically, the mean return period for large Teton fault earthquakes of 1180 years from Section 2 was used and the median PHA (0.5 g) and 84% PHA (0.8 g) from Section 6 used to define the annual probabilities. Two different ranges of PHA were of interest for analyses related to the concrete section of the dam. The annual probabilities of PHA within specific requested ranges are provided in Tables 8-4 and 8-5. It must be emphasized that PHA is the least robust and most uncertain of all

Table 8-4: Rock PHA for the Concrete Section, PHA Range 1.

PHA interval	Annual Probability
0.2 - 0.5 g	1/2360
0.5 – 0.8 g	1/3930
> 0.8 g	1/5900

the ground motion quantities estimated for Jackson Lake Dam. There is potential for nonlinearity in the till to modify PHA. In contrast, peak velocities are little affected by nonlinear soil responses

and are robust even with substantial uncertainties in rock and soil properties. The estimates in Tables 8-4 and 8-5 are solely intended for analyses of structures on the rock section of the dam.

Table 8-5: Rock PHA for the Concrete Section, PHA Range 2.

PHA interval	Annual Probability
0.2 - 0.65 g	1/1735
0.65 – 0.8 g	1/9830
> 0.8 g	1/5900

8.7 Rock Ground Motion Time Histories

Synthetic ground motion time histories that were closest to the mean (Figures 8-7 to 8-10) and 84% quantile (Figures 8-11 to 8-14) response spectra were selected to represent mean and 84% ground motions for dynamic analyses of structures on rock. A ground motion from the **M** 7.9 March 13, 1985 Valpariso, Chile earthquake (Figures 8-15 to 8-18) was also recommended to provide sufficiently long shaking durations to correspond to multi-segment rupture of the Teton fault. While this record contains substantial peak acceleration (> 0.8 g), it has relatively small peak velocities compared to the synthetic records. It is recommended that this record be revised to remove some of the response for frequencies > 2 Hz, to produce high-frequency responses more consistent with the synthesized rock site responses in Figure 8-18.

The durations of the mean and 84% synthetic ground motions are lower bounds because the EGFs were limited to durations of 13.5 s after the direct shear-wave arrival. Also, the relatively deterministic nature of the 3D velocity model lacks correlated-random velocity variations that exist in the crust. Consequently, the synthetic low-frequency portions of the motions are also likely to be lower bounds on total ground motion durations. Multi-segment rupture on the Teton fault will likely produce ground motions with 10-15 s longer > ~0.2 g durations that the motions provided in Figures 8-7 to 8-14; this was the motivation for providing the Lleleo record.

The return periods assigned to the individual ground motion time histories reflect multiple sources of uncertainty and natural variability. The average return period for **M** ~6.9-7.1

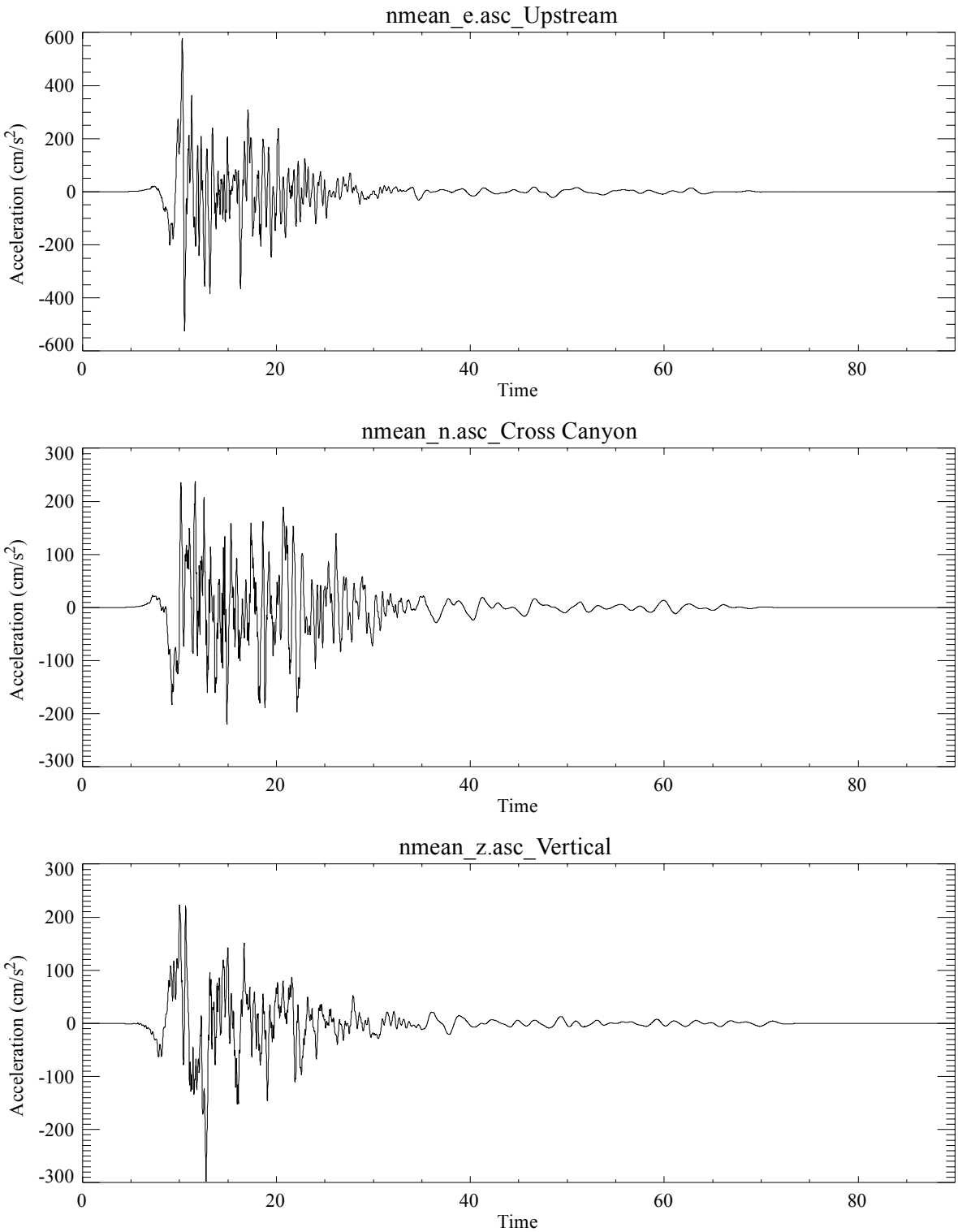

Figure 8-7: Northern Teton fault segment mean rock synthetic ground motion acceleration time histories. Components are as labeled.

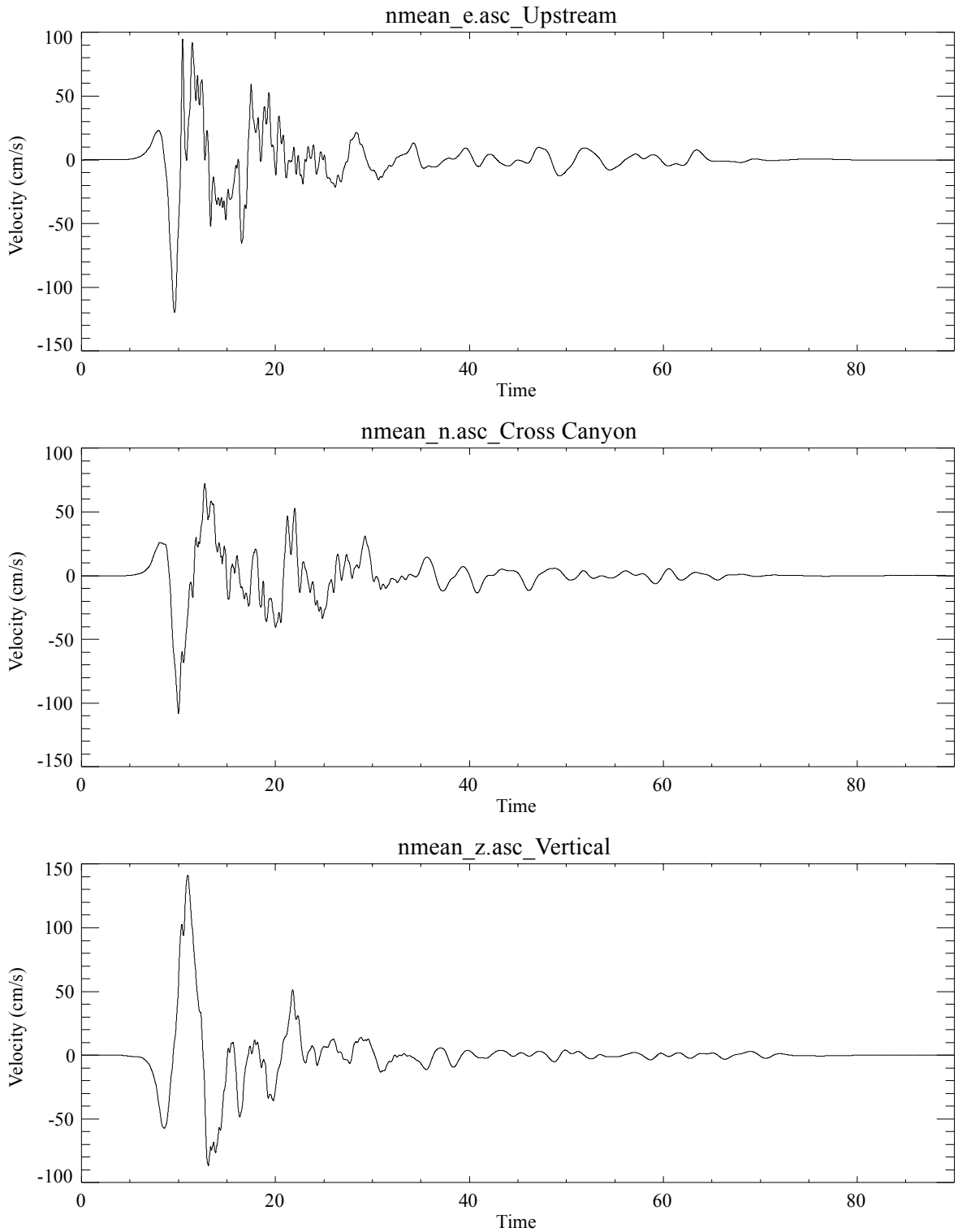

Figure 8-8: Northern Teton fault segment mean rock synthetic ground motion velocity time histories. Components are as labeled.

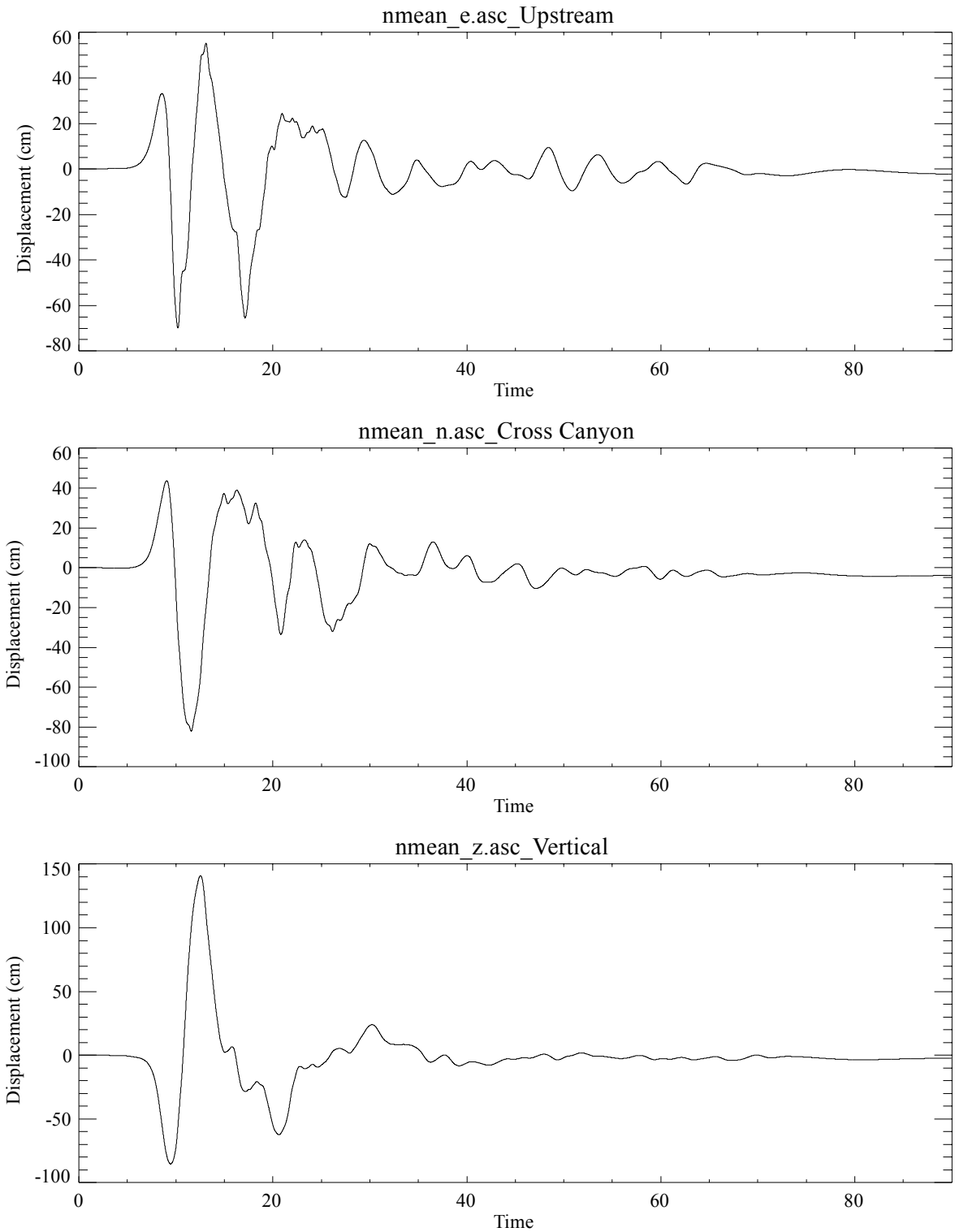

Figure 8-9: Northern Teton fault segment mean rock synthetic ground motion displacement time histories. Components are as labeled.

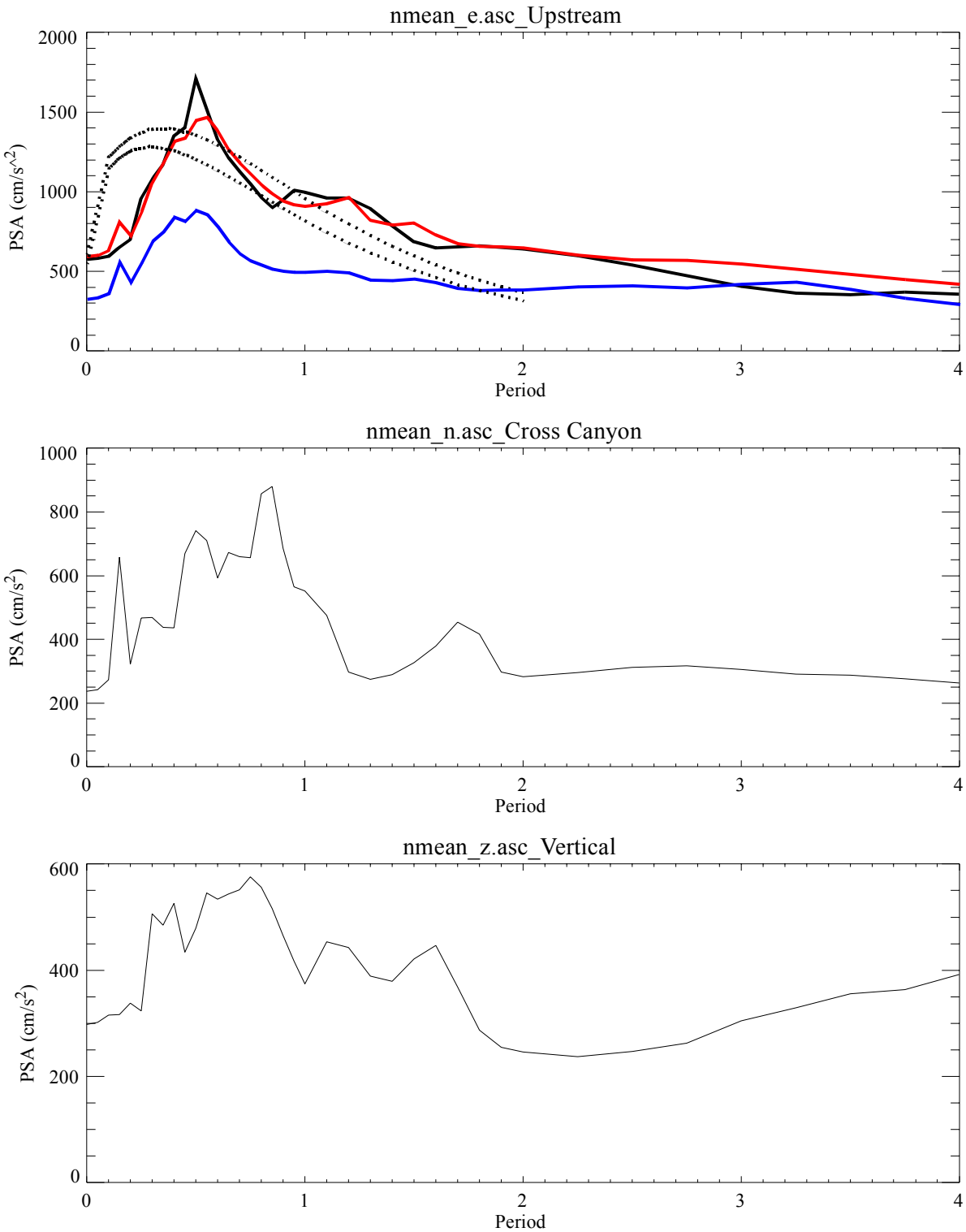

Figure 8-10: Northern Teton fault segment mean rock synthetic ground motion acceleration response spectra. Components are as labeled. Red curve is the mean 35° dip result and the blue curve is the 60° dip result. Upper dotted curve is the Spudich et al. (1999) soil estimate for the 35° dip fault and the lower dotted curve is the empirical soil estimate for the 60° dip fault.

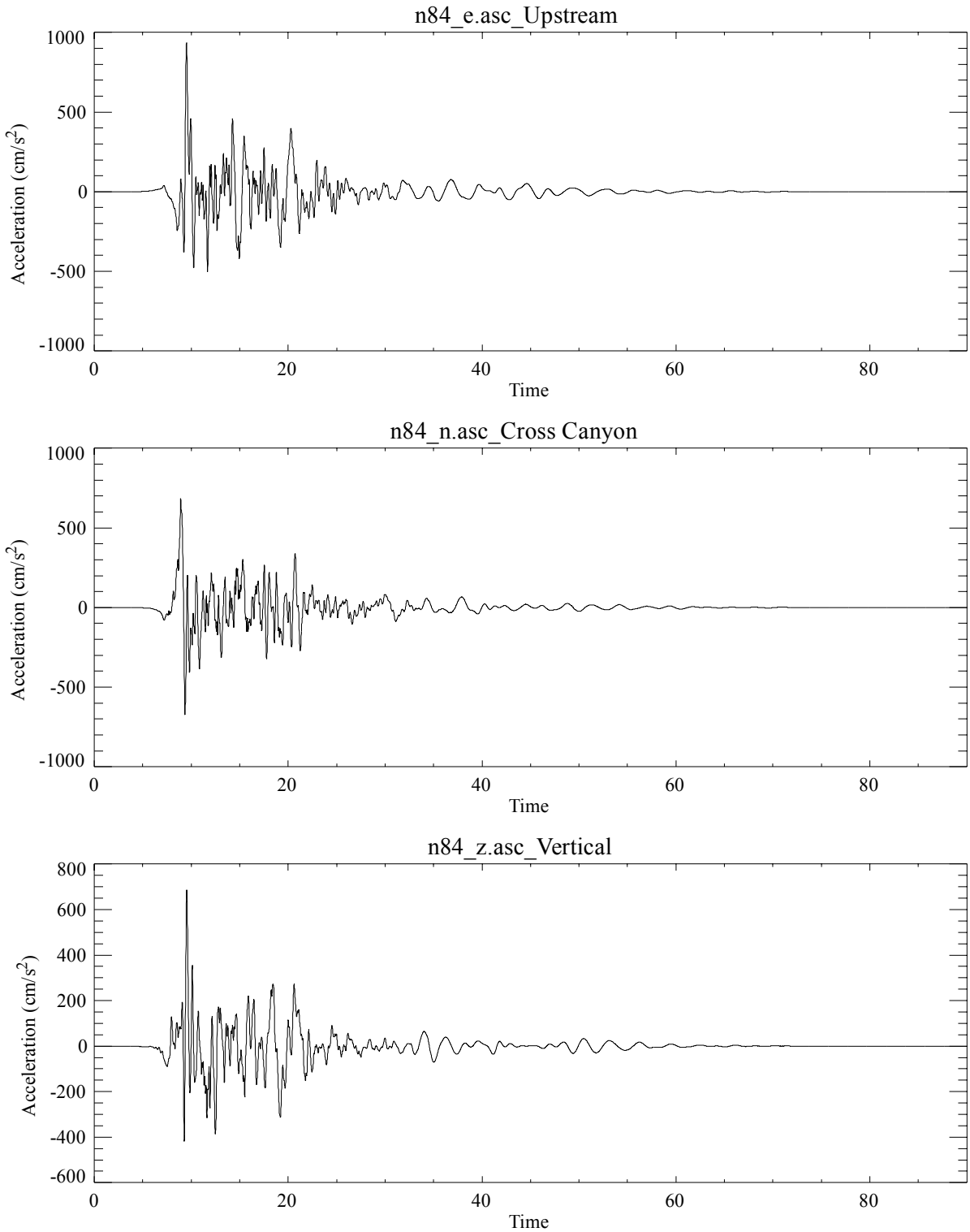

Figure 8-11: Northern Teton fault segment 84% quantile rock synthetic ground motion acceleration time histories. Components are as labeled.

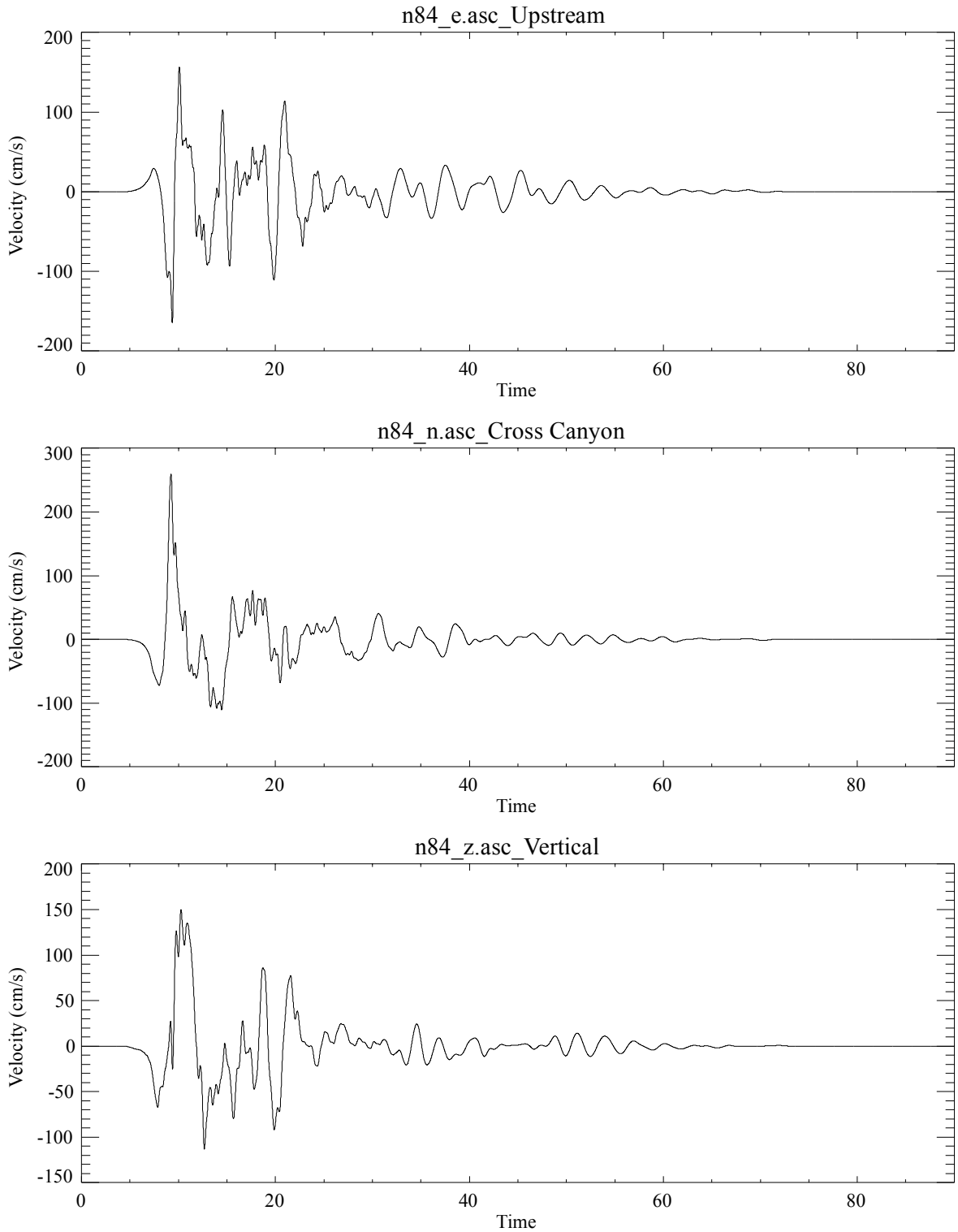

Figure 8-12: Northern Teton fault segment 84% quantile rock synthetic ground motion velocity time histories. Components are as labeled.

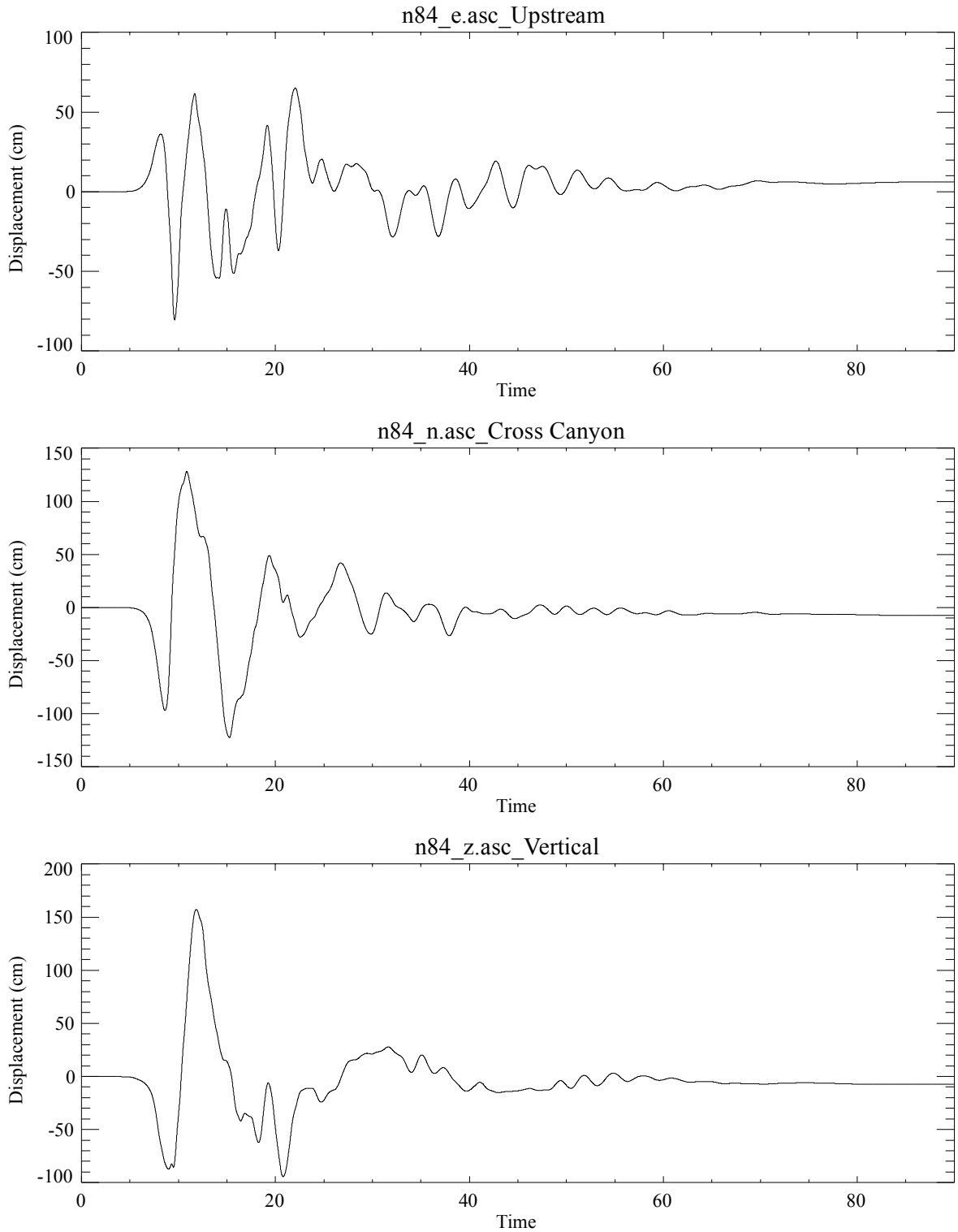

Figure 8-13: Northern Teton fault segment 84% quantile rock synthetic ground motion displacement time histories. Components are as labeled.

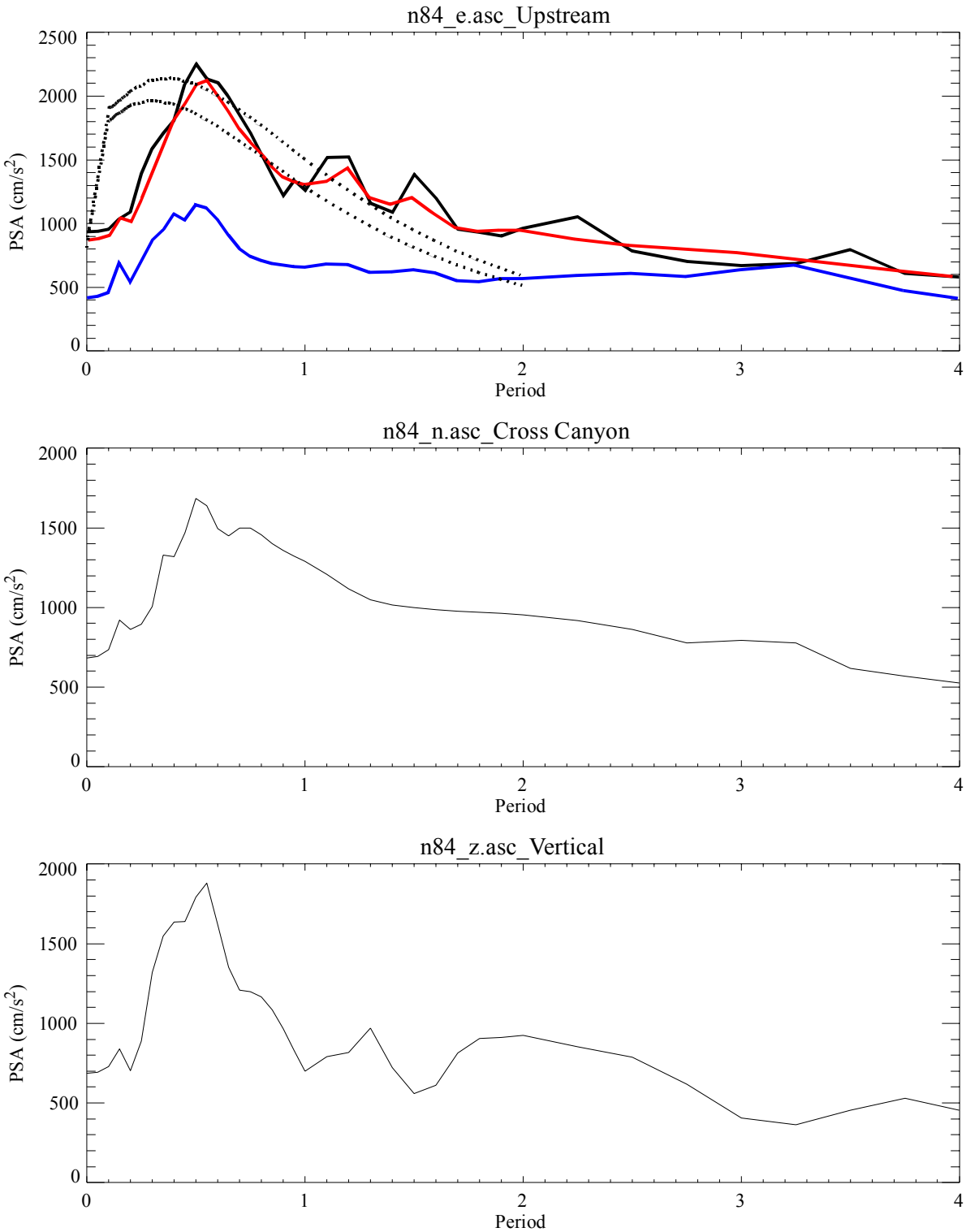

Figure 8-14: Northern Teton fault segment 84% quantile rock synthetic ground motion acceleration response spectra. Components are as labeled. Red curve is the mean 35° dip result and the blue curve is the 60° dip result. Upper dotted curve is the Spudich et al. (1999) soil estimate for the 35° dip fault and the lower dotted curve is the empirical soil estimate for the 60° dip fault.

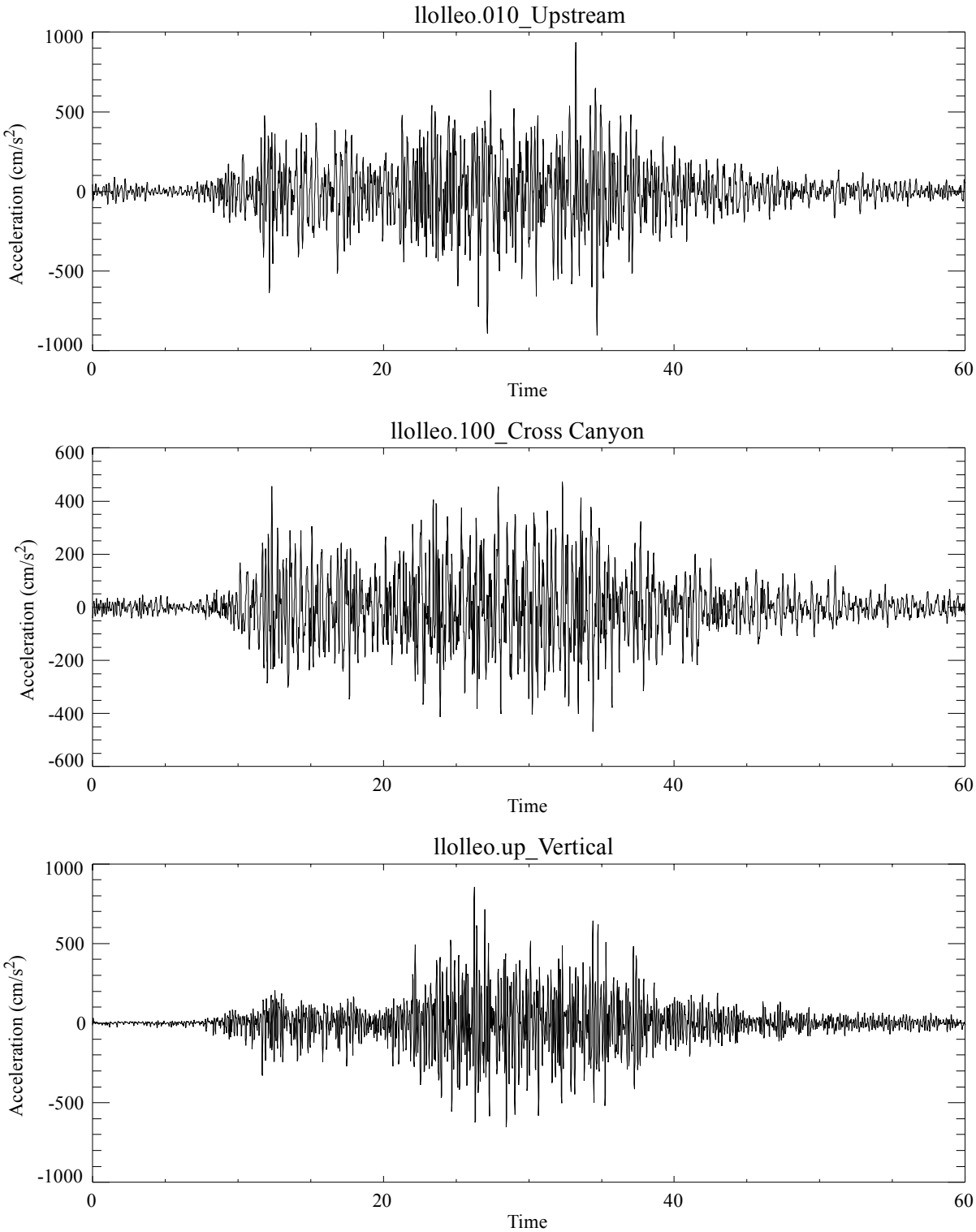

Figure 8-15: Llelleo Valparaiso, Chile, proxy for a Northern Teton fault segment rock ground motion acceleration time histories. Components are as labeled.

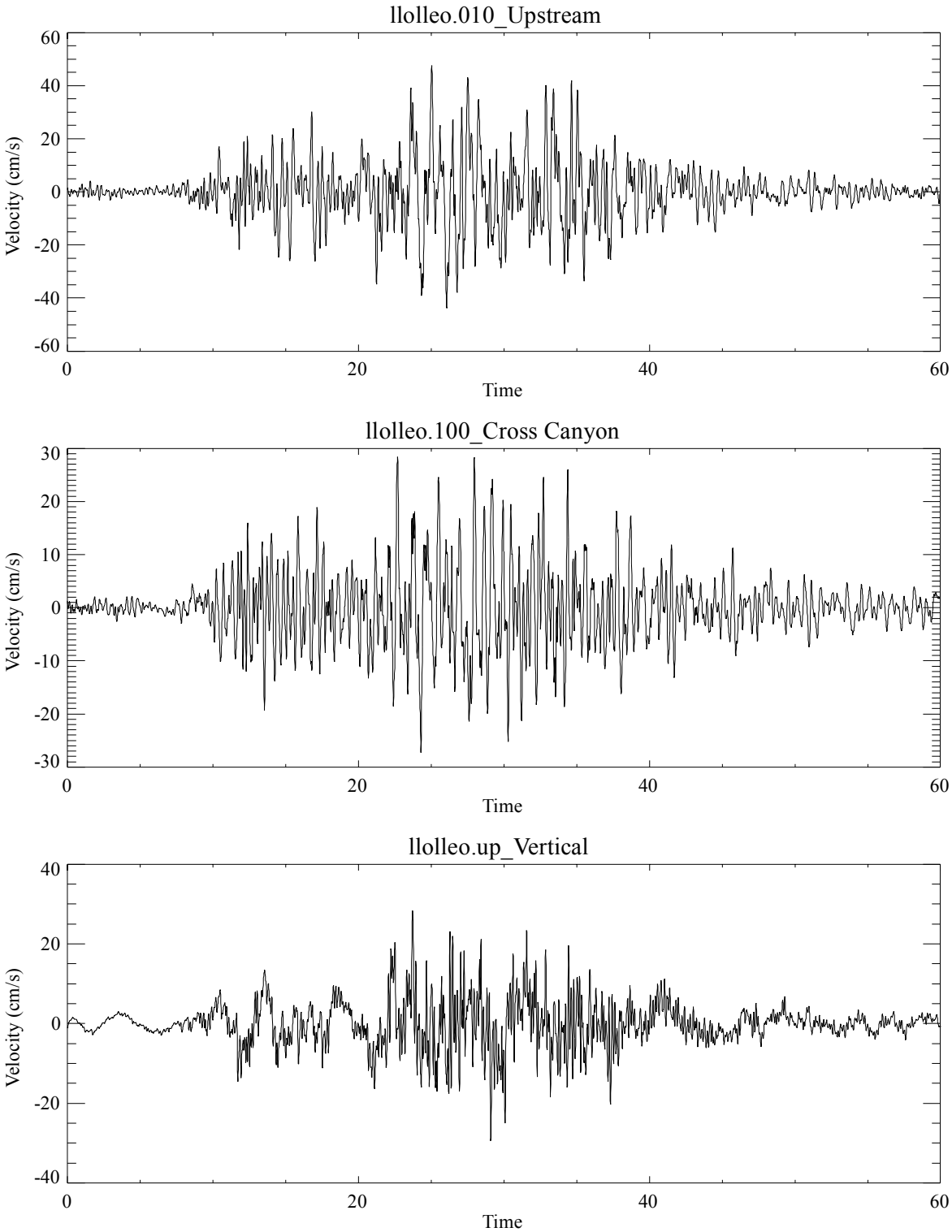

Figure 8-16: Llelleo Valparaiso, Chile, proxy for a Northern Teton fault segment rock ground motion velocity time histories. Components are as labeled.

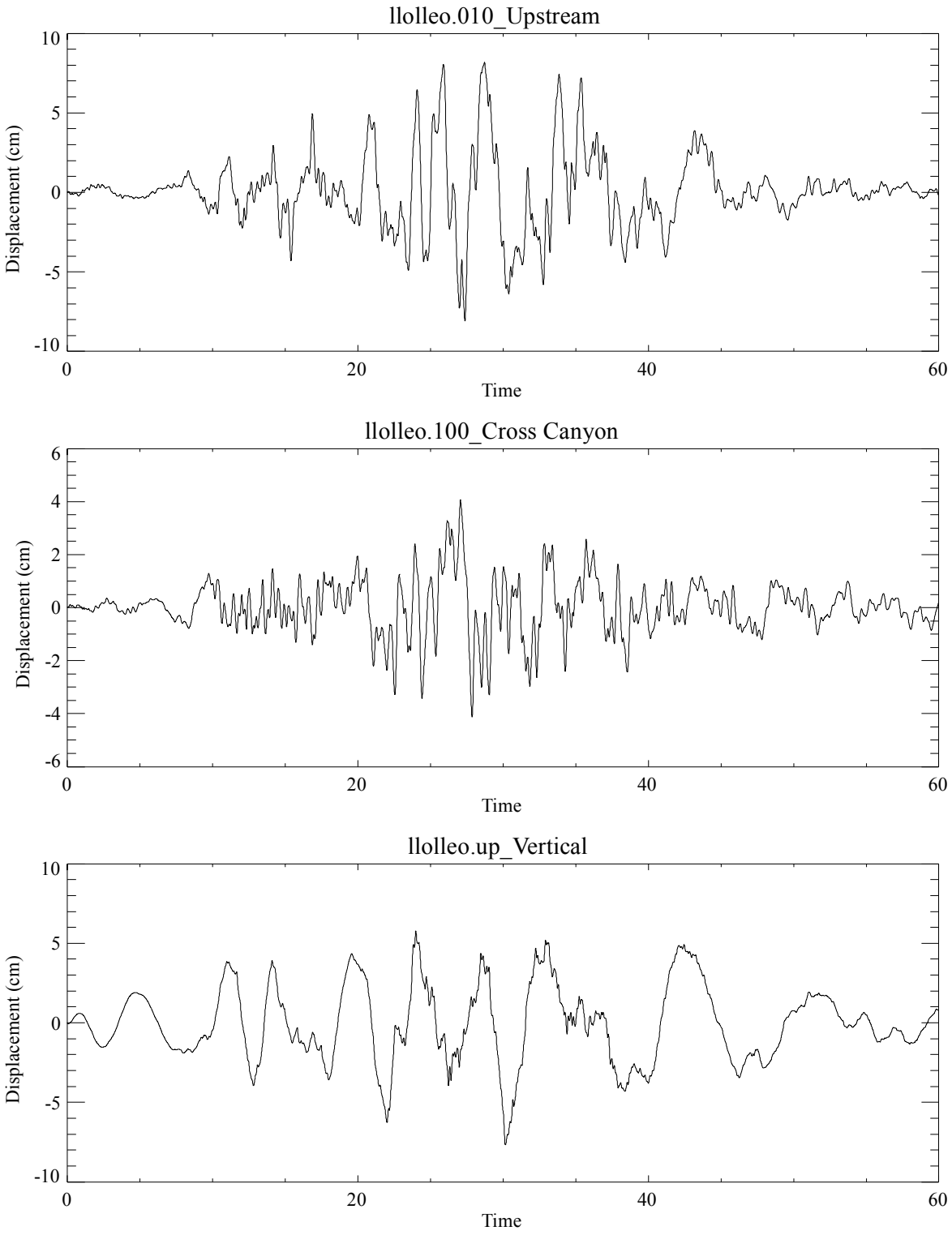

Figure 8-17: Llelleo Valparaiso, Chile, proxy for a Northern Teton fault segment rock ground motion displacement time histories. Components are as labeled.

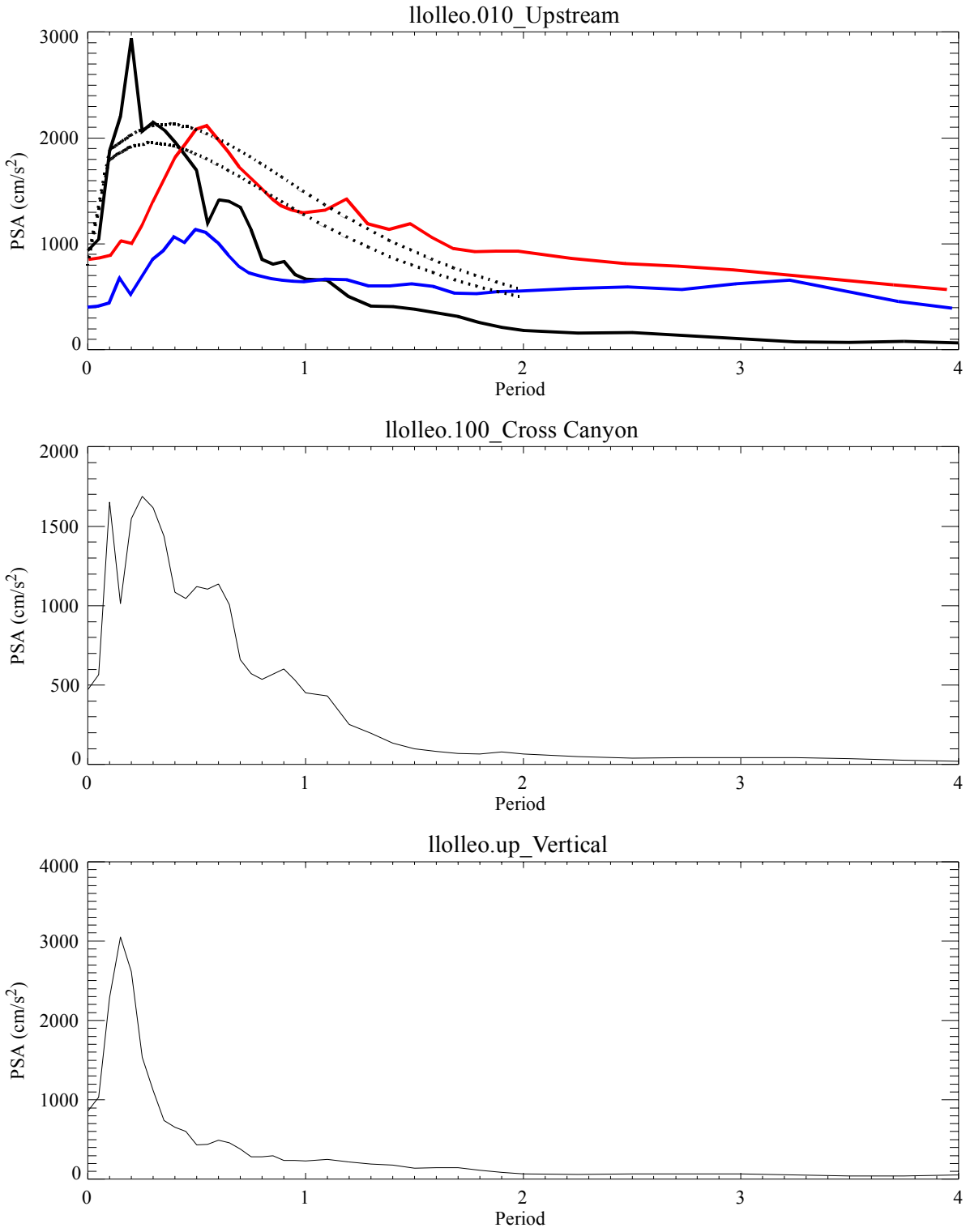

Figure 8-18: Llelleo Valparaiso, Chile, proxy for a Northern Teton fault segment rock ground motion acceleration response spectra. Components are as labeled. Red curve is the mean 35° dip result and the blue curve is the 60° dip result. Upper dotted curve is the Spudich et al. (1999) soil estimate for the 35° dip fault and the lower dotted curve is the empirical soil estimate for the 60° dip fault.

earthquakes on the northern segment of the Teton fault is ~1180 years. Estimated return periods and probability weights for the ground motion time histories are provided in Table 8-6.

Table 8-6: Ground Motion Time History Annual Exceedence Probabilities

Annual probability	Lower AEP (weight = 0.25) (1/yr)	Median AEP (weight = 0.5) (1/yr)	Upper AEP (weight = 0.22) (1/yr)
Mean synthetic (Figures 8-7 to 8-10)	1/4625	1/2950	1/2000
84% quantile (Figures 8-11 to 8-14)	1/11,560	1/7375	1/5000
Lleleo (Figures 8-15 to 8-18)*	N/A	N/A	N/A
*(after record is filtered to reduce high-frequency response)			

The Lleleo record in Table 8-6 is shaded indicated that this record is only intended for sensitivity analyses.

A fourth ground motion from Section 7 that produced using the JLDW EGF's from the **M** 5.2 Idaho, earthquake, is also recommended for dynamic analyses of the concrete section of the dam . Figures 7-35, 7-37, and 7-39 may be the only available ground motion that provides realistic durations and long-period amplitudes for dynamic analyses of the dam. The caveats are that due to a lack of reference broadband recordings outside the low-velocity basin, the appropriate scaling of the amplitudes is not known and the motions may contain overamplified surface wave components. The broadband EGF synthetic motions provide more realistic amplitude and durations responses than the Lleleo record.

8.8 Recommended Acceleration Seismograms for Nonlinear Soil Analyses

Weak-motion site response was measured at Jackson Lake Dam using an array of seven broad-band seismometers. Key observations are the presence of substantial long-period amplification and prolonged duration of shaking beyond some transition point located between stations 13+00 and 24+00; minimal long-period amplification at stations 12+00 and less, referenced to a bedrock site on the right abutment; and, high-frequency de-amplification on treated sections of the north embankment referenced to a site just outside of the treated zone.

Strong ground motions at stations 13+00 and greater are expected to behave non-linearly. The observed weak-motion site response must be modified to account for non-linear soil behavior. The observed site response at station 24+00 is consistent with the 2-D and 3-D response of a sedimentary basin, and likely results from the generation of surface waves, converted phases, and interface waves. These effects are not accounted for by 1-D models. However, available computer codes for estimating non-linear soil behavior are based on propagating an incident body wave (typically a horizontally polarized S wave) through a 1-D soil column. In order to permit use of 1-D non-linear soil response computer codes, while preserving the observed 2-D and 3-D effects of prolonged duration and long-period amplification, the weak-motion impulse response is modified for input to the non-linear soil response codes at a selected reference depth. There is considerable uncertainty in this method because the reduction of the convolved surface motions to a reference depth cannot accurately account for the depth dependency of surface waves and converted phases.

The observed site responses between the rock south abutment and the deep soil portion of the embankment portion of the dam were combined with geophysical information linear 2D finite-difference modeling and nonlinear 1D modeling to estimate horizontal acceleration time histories at 140 m depth. The objective was to produce representative soil ground motion scenarios and provide acceleration time histories at ~140 m depth for use in 1D nonlinear analyses of the soil foundation. Three scenarios were used to construct ground motions for use in nonlinear soil calculations to bracket the ranges of possible ground motion inputs into nonlinear soils (Table 6-5). The most likely case is a scenario where the rock responses were convolved with JLD3 responses to obtain reasonable soil durations. However, the appropriate scaling of the resulting responses is uncertain. Consequently, two scaling scenarios with the JLD3 responses in Section 6 are recommended to facilitate sensitivity testing for nonlinear soil analyses. Table 8-6 provides probabilities to associate with the mean and 84% quantile ground motions. Probabilities were not assigned to the Tabas record, which has peak velocities comparable to the mean record and peak accelerations comparable to the 84% record and is provided for sensitivity testing between the mean and 84% ground motions.

Nonlinear effective-stress soil response calculations with NOAH show that near-surface Arias Intensities and peak acceleration responses, and their associated durations are very sensitive to input motion peak amplitudes and durations. Certain combinations of input motions produced nonlinear soil Arias Intensity and Arias duration responses that exceeded corresponding rock responses by a factor of six. Nonlinear soil response (modulus reduction) may increase ground motions durations because interface phase velocities will be reduced, increasing the time required for Airy phases to propagate from the boundaries of the glacial scour to the dam.

Probably the best way to specify input motions of dynamic analyses of the embankment section of the dam is to limit engineering foundation models to a maximum depth of 30 m with no significant impedance contrasts within the foundation material. Then, use simulated JLD3 motions produced using broadband EGF's, scaled by 0.5-0.6 as input at 30 m depth in the nonlinear engineering model. This is necessary between no 2D or even 3D FEM model of the foundation will include the 3D reverberation amplitude and duration responses using the JLDW motions as inputs. The JLD3 synthetic motions produced using the **M** 5.2 Idaho earthquake EGF's provide the only available ground motion scenario (Figures 7-53, 7-55, 7-57) for the embankment section of the dam. However, it is imperative to also use a ground motion scenario that includes the double resonance responses produced by energy arriving from north of the dam. The JLD3 synthetic motions from the **M** 4.6 Yellowstone EGF's are likely corrupted by significant whole-path surface wave responses and without an broadband recordings outside the basin there is no quantitative basis to adjust the synthetic motions. The **M** 3.2 20 Nov. 2002 earthquake is close enough to the Teton fault that there are surface waves are appropriately scaled. Unfortunately station JLD3 was no longer operating when this earthquake was recorded at JLDW. Consequently, there are no empirical soil records available to represent the duration of expected ground shaking and parasitic double basin 1-2 s amplified acceleration responses along the embankment section of Jackson Lake Dam for seismic energy incident from the north. The regional earthquake EGF's ground motion results suggest that JLD3 responses are starting to approach durations of **M** ~9 subduction zone earthquakes.

8.9 Appropriate Use of Ground Motions

Earthquake magnitude is sometimes used as a proxy for ground motion duration in engineering analyses of soils. The earthquake magnitudes used to simulate ground motions at Jackson Lake Dam from earthquakes on the Teton fault should *not* be used for this purpose. Due to the proximity of the Teton fault to the LVB and glacial scour very-low-velocity basin, and the resulting peak ground motion amplifications, extended durations, and increased Arias Intensities of ground motions at the dam, effective magnitudes for geotechnical analyses of the seismic loads are 7 1/2-8 for the rock ground motions, and are 8-9 for the soil ground motions. These recommended magnitudes for soil analyses are 0.25-0.75 to 0.5-1.5 magnitude units larger than the moment magnitudes of all-segment and northern segment rupture scenarios of the Teton fault, specifically to account for the extended durations and amplifications of ground motions observed at the dam (Sections 5 and 7). The most likely scenarios for soil response based on Sections 5 and 7 and nonlinear soil calculations using NOAH indicate ground motion durations of at least 80 seconds and possibly as long as 180 s for the embankment portion of the dam.

Jackson Lake Dam is > 1.5 km long and spans a wide variety of foundation materials with widely varying S-wave velocities and straddles a region with > 10:1 S-wave velocity contrasts. These large velocity contrasts occur between the overcompacted till (Vs ~ 1 km/s) and the soils in the glacial scour (Vs ~ 0.1 km/s). S-wave velocities also vary both laterally and vertically within the glacial scour region that is composed of fluvial-lacustrine deposits with Vs varying from to 0.09 km/s to 0.2 km/s (Sirles, 1986). Ground motions are likely to vary substantially, both along the dam's axis and in the upstream-downstream direction, because the low soil S-wave velocities result in wavelengths nearly equal to the dam's width at 1 Hz. Chen and Harichandran (2001) showed that spatially varying ground motions are likely to substantially increase shear stresses in foundation materials at the toes of an embankment dam, particularly when spatial coherence is significantly < 1 for low frequencies. Santa-Cruz et al. (1999) showed that for low-velocity basins, the absolute value of coherency can be substantially less than 1 for frequencies as low as 0.3 Hz, for separation distances as low as 800 m, and for frequencies as low as 1 Hz, for separation distances as low as 100 m. Given the results of Santa-Cruz et al. (1999), and the substantial and variable thickness of low S-wave velocity materials in the glacial scour that comprises the foundation for the embankment section of the dam, and the strongly varying site

responses noted in Chapter 5 from the Jackson Lake Dam site response stations, it is likely that ground motions coherency will be substantially < 1 for frequencies as low as 0.3 Hz along the embankment portion of the dam. Estimated differential displacements between the concrete section and the soil section are likely to exceed 50 cm both along the dam's axis and in downstream shear, although the length scale over which the differential displacements will occur is unknown.

The southern portion of the dam, consisting primarily of the concrete section, is founded on ~1 km/s S-wave velocity till and tuff. The rest of the dam is founded on ~0.1 km/s S-wave fluvial-lacustrine deposits that increase in thickness towards the northern end of the dam. The southern portion of the dam will shake less strongly and for shorter durations than the rest of the dam. Consequently, the largest strains resulting from differential motions along the axis of the dam are likely to be located in the embankment section extending from the concrete section to station 32, where Sirles (1986) found a ~140 m thick section of fluvial-lacustrine deposits below the ground surface. The distances between stations JLD2 near the northern end of the concrete section and station JLD3 near station 24+00 is 356 m. For a vertically-incident shear wave, the propagation delay at station JLD3 relative to JLD2 due to ~140 m of fluvial-lacustrine fill with an average S-wave velocity of ~140 m/s is 0.87 s (1 s travel-time through the last 140 m for JLD3 and 0.13 s travel time through the last 140 m for JLD2). This yields a S-wave apparent velocity of 0.41 km/s, which will likely reduce S-wave coherency at low frequencies, based on the results of Santa-Cruz et al. (1999). This is an apparent velocity 10 times *smaller* than considered by Chen and Harichandran (2001) in their analyses of the influence of coherency on the dynamic analysis of embankment dams. Since the peak velocity loads at Jackson Lake Dam are substantially larger than considered by Chen and Harichandran (2001), and apparent velocities are much lower, differential displacements, and correspond strains and stresses are likely to be larger at Jackson Lake Dam than those considered in Chen and Harichandran (2001). S-wave apparent velocities will decrease for S-waves arriving from the south (about half of the northern Teton rupture segment, and the entire southern Teton rupture segment). S-wave apparent velocities will be increased slightly for S-wave arrivals from north of station JLD3, but the increases in apparent velocity will be modest.

Uncertainties about the velocity structure and spatial extent of the glacial scour produce uncertainties of about a factor of two in peak soil ground motions, and factor of four uncertainties in soil ground motion durations. It is necessary to determine the wave-types that comprise the long duration soil ground motions to determine the appropriate methods to calculate nonlinear soil responses. Synthetic calculations in Section 5 indicate that a significant fraction of the long-duration high-amplitude soil motions at the dam may be produced by S-waves and horizontally propagating interface waves occurring at depth in the glacial scour basin.

Consistent with past approaches to reduce ground motion estimation biases and uncertainties (Anderson and O'Connell, 1998; Anderson and O'Connell, 1993; O'Connell and Unruh, 2000; Ake et al., 2002) microearthquake data from the Jackson Lake Seismic Network provided the crucial information about the subsurface fault geometries, particularly dip of faults at depth, and seismotectonic constraints on state-of-stress and fault kinematics, information necessary to estimation ground motions at Jackson Lake Dam. The combination of broadband site response stations at Jackson Lake Dam and the short-period JLSN provided empirical Green's functions and the ability to estimate site responses in the same manner as the site response stations in previous studies (O'Connell and Ake, 1995; O'Connell, 1999b; O'Connell and Unruh, 2000; O'Connell, 2001), where local seismographic networks such as the short-period Southern California Seismic Network and the Northern California Seismic Network provided crucial information necessary to convert site response recordings into empirical Green's functions. The development of site-specific ground motions using empirical Green's functions substantially reduced ground motion biases in several previous studies (O'Connell, 1999a, 1999b; O'Connell and Unruh, 2000; O'Connell, 2001). For instance, site-response recordings used in conjunction with short-period data from the Southern California Seismic Network showed that convention approaches to estimating near-source ground motions at stiff-soil sites in southern California were likely to strongly overpredict peak ground motions (O'Connell, 1999a). At a high-velocity hard-rock site, broadband site-response data in conjunction with short-period data from the Northern California Seismic Network showed that source characterization of blind thrust faults in the western Sacramento Valley were incorrect (O'Connell and Unruh, 2000; O'Connell et al., 2001) and that peak acceleration loads would likely be about 2/3 empirical predictions, resulting in substantially lower final peak ground motion estimates (LaForge, 1999). Estimation of the 3D

velocity structure of the crust and discovery of the significant impacts of 3D velocity structure on peak ground motions and ground motion durations were made possible by the earthquake data from the JLSN and the broadband site response seismographs at Jackson Lake Dam. The earthquake data provided by the JLSN were necessary to fully exploit the site response earthquake recordings to develop empirical Green's functions and site response information for nonlinear soil analyses. At Jackson Lake Dam, development of site-specific ground motions increases confidence that estimated ground motions are not likely to be significantly biased. The fact that alternative ground motion synthesis methods in Section 7 produced similar ground motion estimates, suggests that the ground motions recommended for dynamic analyses of Jackson Lake Dam are reasonable.

The stochastic characteristics of earthquake occurrence means that seismic monitoring may or may not record additional earthquakes on the Teton fault. However, in previous studies the operation of two three-component broadband instruments on the hanging wall of the Red Mountain fault in the Transverse Ranges of southern California for less than one year produced valuable data for constraining the downdip dip geometry of the Red Mountain fault (Anderson and O'Connell, 1998). Adding these two three-component stations to a predominantly short-period vertical seismographic network reduced hypocenter depth uncertainties on the Red Mountain fault to < 1 km (Anderson and O'Connell, 1998). Of particular interest, was the recording of numerous earthquakes < **M** 1.5 by these stations that went unrecorded by most of the more distant stations in the network, and thus were not included in the earthquake catalog. Near the Ortigalita fault along the western margin of the San Joaquin Valley, California, < 1 year of earthquake recordings from four broadband three-component stations located near the dams provided valuable constraints on the depth and dip of blind thrust faults below the dams that was not available from the local short-period seismographic network operated by the California Department of Water Resources.

Based on the significantly longer rock site durations at Jackson Lake Dam indicate that there must be some fundamental differences between the physical properties of the large-scale low-velocity basins at Jackson Lake and Mexico City. More importantly, at Jackson Lake Dam soil sites there appears to be a parasitic interaction of nearly-identical-period resonant responses between the soil

basin containing the embankment portion of the dam, and the large-scale low-velocity basin for periods of 1-2 s, which produces unusually long sustained peak accelerations of ~0.25 g lasting up to 70 s. The Jackson Lake Dam site responses instruments were necessary to discover the range of ground motion responses likely to occur in a such a complex geological and geophysical setting, particularly for the wide range of incidence angles and azimuths associated with seismic energy radiated by the Teton fault. The value of broadband site response recordings of small earthquakes was also demonstrated in investigations of anomalously-large peak accelerations in Santa Monica, California, in response to the 1994 **M** 6.7 Northridge earthquake (Davis et al., 2000). Davis et al. (2000) discovered a relatively small-scale crustal velocity lens that substantially amplifies ground motions for a limited range of azimuths, including azimuths associated with wave arrivals from the Northridge earthquake. It would be difficult and expensive to discover such a small velocity structure using exploration geophysics methods; the earthquake recordings were clearly the most efficient and compelling means to discover important ground motion anomalies. An importance difference between Santa Monica and Jackson Lake Dam, is that at Jackson Lake Dam, the broadband site-response recordings and local seismic network afforded the opportunity to identify significant ground motion characteristics prior to the occurrence of a large, nearby earthquake. It appears that there may be other low-velocity basins in the ISB with characteristics similar to Jackson Lake (Zoback, 1983). Studies in other low-velocity basins in the ISB would likely benefit from a combination of the approach used in the study and the approach of Davis et al. (2000), by combining broadband recordings of local and regional earthquakes from sites inside the basin and from sites located on high-velocity portions of the footwall outside the low-velocity basin, to facilitate deconvolution of the basin responses from incident seismic energy.

9.0 REFERENCES

Abbott, R.E., Louie, J.N., Caskey, S.J., and Pullammanappallil, S., 2001, Geophysical confirmation of low-angle normal slip on the historically active Dixie Valley fault, Nevada, *J. Geophys. Res.*, v. 106, p.4169-4181.

Abercrombie, R. E., 1995, Earthquake source scaling relationships from -1 to 5 M_L, using seismograms recorded at 2.5 km depth, J. Geophys. Res., v. 100, p. 24015-24036.

Abrahamson, N. A. and W. J. Silva, 1997, Empirical response spectral attenuation relations for shallow crustal earthquakes, *Seismol. Res. Lett.*, v. 68, p. 94-127.

Ake, J.P., Ostenaa, D., Mahrer, K., Sneddon, C., and Block, L., 2001, Seismotectonic evaluation and probabilistic seismic hazard analysis for Ridgway Dam, Dallas Creek Project, Colorado, U.S. Bureau of Reclamation Seismotectonic Report 2001-4, Denver, Colorado.

Anders, M.H., Geissman, J.W., Piety, L.A., and Sullivan, J.T., 1989, Parabolic distribution of circumeastern Snake River Plain seismicity and latest Quaternary faulting: Migratory pattern and association with the Yellowstone hotspot, *J. Geophys. Res.*, v. 94, p. 1589-1621.

Anderson, E.M., 1951, The Dynamics of Faulting (2nd edition), Edinburgh, Oliver, and Boyd, 206 pp.

Anderson, J.G., Zeng, Z., and Sucuoglu, H., 2001, Analysis of accelerations from the 1 October 1995 Dinar, Turkey, earthquake, *Bull. Seism. Soc. Am.*, v. 91, p. 1433-1445.

Anderson, L.W., and O'Connell, D.R.H., 1993, Seismotectonic study of the northern portion of the lower Colorado River, Arizona, California, Nevada, U.S. Bureau of Reclamation Seismotectonic Report 93-4, Denver, Colorado.

Anderson, L.W., and O'Connell, D.R.H., 1998, Seismotectonic evaluation for Casitas Dam, Ventura River Project, California, U.S. Bureau of Reclamation Seismotectonic Report 98-3, Denver, Colorado, 72 pp.

Andrews, D.J., 1980, A stochastic fault model, 1, static case, *J. Geophys. Res.*, v. 85, p. 3867-3877.

Andrews, D.J., 1986, Objective determination of source parameters and similarity of earthquakes of different size, *in* Earthquake Source mechanics, Das, S., Boatwright, J., and Scholz, C.H., eds., American Geophysical Union, Washington, D.C., p. 259-268.

Andrews, D. J. and J. Boatwright, 1998, Dynamic simulation of spontaneous rupture with heterogeneous stress drop, *Seism. Res. Lett.*, v. 69, p. 143.

Andrews, D.J., 1999, Test of two methods for faulting in finite-difference calculations, *Bull. Seism. Soc. Am.*, v. 89, p. 931-937.

Arabasz, W.J. and S.J. Hill, 1996, Applying Reasonberg's cluster-analysis algorithm to regional earthquake catalogs outside California (abstract), *Seism. Res. Lett.*, v. 67, no. 2, p. 30.

Arabasz, W.J., R.B. Smith, and W.D. Richins (1980), Earthquake studies along the Wasatch front, Utah: Network monitoring, seismicity, and seismic hazards, Bulletin of the Seismological Society of America, 70, 1479-1499.

Archuleta, R. J. and S. H. Hartzell, 1981, Effects of fault finiteness on near-source ground motion, *Bull. Seism. Soc. Am.*, v. 71, p. 939-957.

Archuleta, R.J., 1984, A faulting model of the 1979 Imperial Valley earthquake, *J. Geophys. Res.*, v. 89, p. 4559-4585.

Archuleta, R. J., 1998, Direct observation of nonlinearity in accelerograms, *in* "The Effects of Surface Geology on Seismic Motion", K. Irikura, K. Kudo, H. Okada and T. Sasatani (eds), Vol.2, p. 787-792, A. A. Balkema, Rotterdam.

Archuleta, R.J., L. F., Bonilla, and D. Lavallée, 2000, Nonlinearity in observed and computed accelerograms, in Proceeding of the 12th World Conference on Earthquake Engineering, Aston Koedyk Ltd (pub). Paper reference number 0338.

Behrendt, J.S., Tibbetts, B.L., Bonini, W.E., and Lavin, P.M., 1968. A geophysical study in Grand Teton National Park and vicinity, Teton County, Wyoming, *U.S. Geol. Surv. Prof. Pap., 516-E*, 23 pp.

Ben-Zion, Y., 2001, Dynamic ruptures in recent models of earthquake faults, *J. Mech. Phys. Solids*, v. 49, p. 2209-2244.

Beresnev, I. A., and G. M. Atkinson, 1997, Modeling finite-fault radiation from the ω^n spectrum, *Bull. Seism. Soc. Am.*, v. 87, p. 67-84.

Bizzarri, A., Cocco, M., Andrews, D.J., and Boschi, E., 2001, Solving the dynamic rupture problem with different numerical approaches and constitutive laws, Geophys. J. Int., v. 144, p. 656-678.

Boatwright, J., 1982, A dynamic model for far-field acceleration, Bull. Seism. Soc. Am., v. 72, p. 1049-1068.

Bodin, P., Gomberg, J., Singh, S.K., and Santoyo, 1997, Dynamic deformations of shallow sediments in the Valley of Mexico, part I: Three-dimensional strains and rotations recorded on a seismic array, *Bull. Seism. Soc. Am.*, v. 87, p. 528-539.

Bommer, J.J., and Martinez-Pereira, A., 1999, The effective duration of earthquake strong motion, J. Earthquake Eng., v. 3, p. 127-172.

Bonilla, L. F., D. Lavallee, and R. J. Archuleta, 1998, Nonlinear site response: Laboratory modeling as a constraint for modeling accelerograms, in The Effects of Surface Geology on Seismic Motion, Vol. 2, K. Irikura, K. Kudo, H. Okada, and T. Sasatani (Editors), Balkema, Rotterdam, p. 793–800.

Bonilla, L. F., 2000, Computation of linear and nonlinear response for near field ground motion, Ph.D. Dissertation, University of California, Santa Barbara.

Borcherdt, R.D., 1970, Effects of local geology on ground motions near San Francisco Bay, Bull. Seism. Soc. Am., v. 60, p. 29-61.

Boore, D.M., 1970, Love waves in non-uniform wave guides: finite difference calculations, *J. Geophys. Res.*, v. 75, p. 1512-1527.

Boore, D.M., Larner, K.L., and Aki, K., 1971, Comparison of two independent methods for the solution of wave-scattering problems: response of a sedimentary basin to vertically incident SH waves: Journal of Geophysical Research, v. 76, p. 558-569.

Bouchon, M., Bouin, H. Karabulut, M.N.Toksoz, M. Dietrich, A.J. Rokasis, 2001, How fast is rupture during an earthquake? New insight from the 1999 Turkey earthquakes, Geophys. Res. Lett., v. 28, p. 2723-2726.

Buck, W.R., 1993. Effect of lithospheric thickness on the formation of high- and low-angle normal faults, *Geology,* v. 21, p. 933-936.

Byrd, J.O.D., Smith, R.B., and Geissman, J.W., 1994, The Teton fault, Wyoming: Topographic signature, neotectonics, and mechanism of deformation: *Jour. Geophys. Res.*, v. 99, no. B10, p. 20,095-20,122.

Byrd, J.O.D., 1995, Neotectonics of the Teton fault, Wyoming: [unpub] PhD dissertation, Department of Geology and Geophysics, Univ. of Utah, Salt Lake City, UT, Aug. 1995, 214 p.

Chen, M.-T., and Harichandran, R.S., 2001, Response of an earth dam to spatially varying earthquake ground motion, J. Eng. Mech., v. 127, p. 932-939.

Claerbout, J.F., 1976, *Fundamentals of Geophysical Data Processing*, McGraw-Hill, New York.

Collettini, C., and Sibson, R.H., 2001, Normal faults, normal friction?, *Geology*, v. 29, p. 297-930.

Connor, M.A., 1998, Final report on the Jackson Lake archeologal project, Grand Teton National Park, Wyoming: Report prepared for Bureau of Reclamation, Pacific Northwest Office, Boise, ID, with contributions by K.L. Pierce, S. Lundstrom, and J.M. Good, Technical Report No. 46, Department of the Interior, National Park Service, Midwest Archeological Center, Lincoln, Nebraska, 278 p.

Dahlen, F. A., 1974, On the ratio of P-wave to S-wave corner frequencies for shallow earthquake sources, *Bull. Seism. Soc. Am.*, v. 64, p. 1159-1180.

Davis, P. M., J. L. Rubinstein, K. H. Liu, S. S. Gao, L. Knopoff, 2000, Northridge earthquake damage caused by geologic focusing of seismic waves, *Science*, v. 289, p. 1746-1750.

Doser, D.I., 1986, Earthquake processes in the Rainbow Mountain-Fairview Peak-Dixie Valley, Nevada, region 1954-1959, J. Geophys. Res., v. 91, p. 12,572-12,586.

Doser, D.I., and Smith, R.B., 1989, An assessment of source parameters of earthquakes in the cordillera of the western United States, Bull. Seism. Soc. Am., v. 79, p. 1383-1409.

Field, E.H., Jacob, K.H., and Hough, S.H., 1992, Earthquake site response estimation: a weak-motion case study, Bull. Seism. Soc. Am., v. 82, p. 2283-2307.

Field, E.H., and Jacob, K.H., 1995, A comparison and test of various site-response estimation techniques, including three that are not reference-site dependent, Bull. Seism. Soc. Am., v. 85, p. 1127-1143.

Field, E. H., P. A. Johnson, I. A. Beresnev, and Y. Zeng, 1997, Nonlinear ground-motion amplification by sediments during the 1994 Northridge earthquake, *Nature*, v. 390, p. 599-602.

Frankel, A., and Clayton, R. W., 1986, Finite difference simulations of seismic scattering: implications for the propagation of short-period seismic waves in the crust and models of crustal heterogeneity, *J. Geophys. Res.*, v.91, p. 6465-6489.

Frankel, A., S. Hough, P. Friberg, and R. Busby, 1991, Observations of Loma Prieta aftershocks from a dense array in Sunnyvale, California, *Bull. Seism. Soc. Am.*, v. 81., p. 1900-1922.

Frankel, A., 1993, Three-dimensional simulations of ground motions in the San Bernardino Valley, California, for hypothetical earthquakes on the San Andreas fault, *Bull. Seism. Soc. Am.*, v. 83, p. 1020-1041.

Frankel, A., 1995, Simulating strong motions of large earthquakes using recordings of small earthquakes: The Loma Prieta mainshock as a test case, *Bull. Seism. Soc. Am.*, v. 85., p. 1144-1160.

Frankel, A.D., Carver, D.L., and Williams, R.A., 2002, Nonlinear and linear site response and basin effects in Seattle for the **M** 6.8 Nisqually, Washington, earthquake, *Bull. Seism. Soc. Am.*, v. 92., p. 2090-2109.

Fuis, G.S., Mooney, W.D., Healy, J.H., McMechan, G.A., and Lutter, W.J., 1982, Crustal structure of the Imperial Valley region, *in* The Imperial Valley, California, Earthquake, October 15, 1979, *U.S. Geol. Surv. Prof. Pap., no. 1254*, p. 25-50.

Gilbert, J.D., Ostenaa, D., and Wood, C., 1983, Seismotectonic study, Jackson Lake Dam and Reservoir, Minidoka Project, Wyoming: Seismotectonic Report 83-8, US Bureau of Reclamation, Boise, ID and Denver, CO, 122 p. and appendices.

Good, J.M., and Pierce, K.L., 1996, Interpreting the landscapes of Grand Teton and Yellowstone National Parks, recent and ongoing geology: Grand Teton Natural History Association, Grand Teton National Park, Moose, Wyoming, 58 p.

Guatteri, M., Mai, P.M., Beroza, G.C., and Boatwright, J., 2003, *Bull. Seism. Soc. Am.*, v. 93, p. 301-313.

Graves, R.W., 1993, Modeling three-dimensional site responses effects in the Marina District basin, San Francisco, California, *Bull. Seism. Soc. Am.*, v. 83, p. 1042-1063.

Graves, R.W., 1996, Simulating seismic wave propagation in 3D elastic media using staggered-grid finite differences, *Bull. Seism. Soc. Am.*, v. 86, p. 1091-1106.

Graves, R. W. and Wald, D. J., 2001, Resolution analysis of finite fault source inversion using one- and three-dimensional Green's functions: 1, Strong motions. J. Geophys. Res., v. 106, p. 8745-8766.

Graves, R.W., and Day, S.M., 2003, Stability and accuracy analysis of course-grain viscoelastic simulations, Bull. Seism. Soc. Am., v. 93., p. 283-300.

Hartzell, S., 1978, Earthquake aftershocks as Green's functions, *Geophys. Res. Lett*., v. 5, p. 1-4.

Hartzell, S., Liu, P., and Mendoza, C., 1996, The 1994 Northridge, California, earthquake: Investigations of rupture velocity, risetime, and high-frequency radiation, *J. Geophys. Res.*, v. 101, p. 20,091-20,108.

Hartzell, S., Leeds, A., Frankel, A., Williams, R.A., Odum, J., Stephenson, W., and Silvea, W., 2002, Simulation of broadband ground motion including nonlinear soil effects for a magnitude 6.5 earthquake on the Seattle fault, Seattle, Washington, *Bull. Seism. Soc. Am.*, v. 92, p. 831-853.

Hauksson, E., and Haase, J.S., 1997, Three-dimensional Vp and Vp/Vs velocity models of the Los Angeles and central Transverse Ranges, California, *J. Geophys. Res*., v. 102, p. 5423-5443.

Heaton, T. H., J. F. Hall, D. J. Wald, and M. W. Halling, 1995, Response of high-rise and base-isolated buildings to a hypothetical Mw 7.0 blind thrust earthquake, *Science*, v. 267, p. 206-211.

Herrero A. and P. Bernard, 1994, A kinematic self similar rupture process for earthquakes, *Bull. Seism. Soc. Am.*, v. 84, p. 1216-1228.

Hole, J. A., and B. C. Zelt, 1995, 3-D finite-difference reflection traveltimes, Geophys. J. Int., v. 121, p. 427-434.

Holzer, T. L., T. L. Youd, and T. C. Hanks, 1989, Dynamics of liquefaction during 1987 Superstition Hills, California, earthquake, Science, v. 244, p. 56–59.

Hutchings, L., 1994, Kinematic earthquake models and synthesized ground motions using empirical Green's functions, *Bull. Seism. Soc. Am.*, v. 84, p. 1028-1050.

Iai, S., Y. Matsunaga, and T. Kameoka, 1990a, Strain Space Plasticity Model for Cyclic Mobility, Report of the Port and Harbour Research Institute, v. 29, p. 27-56.

Iai, S., Y. Matsunaga, and T. Kameoka (1990b). Parameter Identication for Cyclic Mobility Model, Report of the Port and Harbour Research Institute, v. 29, p. 57-83.

Iai, S., T. Morita, T. Kameoka, Y. Matsunaga, and K. Abiko, 1995, Response of a dense sand deposit during 1993 Kushiro-Oki earthquake, *Soils Found.*, v. 35, p. 115–131.

Ichinose, G.A., Smith, K.D., and Anderson, J.G., 1997, Source parameters of the 15 November 1995 Border Town, Nevada, earthquake sequence, *Bull. Seism. Soc. Am.*, v. 87, p. 652-667.

Ishihara, K., 1985, Stability of natural deposits during earthquakes, in Proceedings, 11th International Conference on Soil Mechanics and Foundation Engineering, Balkema Publishers, Rotterdam, v.1, p. 321–376.

Jarpe, S. P. and P. W. Kasameyer, 1996, Validation of a procedure for calculating broadband strong-motion time histories with empirical Green's functions, *Bull. Seism. Soc. Am.*, v. 86, p. 1116-1129.

Joyner, W. B. and D. M. Boore, 1993, Methods for regression analysis of strong-motion data, *Bull. Seism. Soc. Am.*, v. 83, p. 469-487.

Kanamori, H., and D.L. Anderson, 1975, Theoretical basis for some empirical relations is seismology, *Bull. Seism. Soc. Am.*, v. 65, pp. 1073-1079.

Kawase, H. and K. Aki, 1989, A study of the response of a soft basin for incident *S*, *P*, and Rayleigh waves with special reference to the long duration observed in Mexico City, *Bull. Seism. Soc. Am.*, v. 79, p. 1361-1382.

Kayen, R.,E., and Mitchell, J.K., 1997. Assessment of liquefaction potential during earthquakes by Arias intensity, *J. Geotechnical Geoenvironmental Eng.*, v. 12, p.1162-1174.

Kisslinger, C., 1980, Evaluation of S to P amplitude ratios for determining focal mechanisms from regional network observations, *Bull. Seism. Soc. Am.*, v. 70, p. 999-1014.

Kisslinger, C., Bowman, J.R., and Koch, K., 1981, Procedures for computing focal mechanisms from local $(SV/P)_Z$ data, *Bull. Seism. Soc. Am.*, v. 71, p. 1719-1729.

Kramer, S. L., and P. Arduino, 1999, Constitutive modeling of cyclic mobility and implications for site response, in Proceedings, Second International Conference on Earthquake Geotechnical Engineering, Lisbon, Portugal, Balkema Publishers, Rotterdam, v. 3, p. 1029–1034.

LaForge, R., 1999, Probabilistic ground motions for Monticello Dam, Solano Project, California, U.S. Bureau of Reclamation Technical Memorandum D8330-99-14, Denver, Colorado.

Lageson, D.R., 1987, Laramide uplift of the Gros Ventre Range and implications for the origin of the Teton fault, Wyoming: Wyoming Geol. Assoc., 38th Annual Field Conf. Guidebook, p. 78-89.

Lageson D.R. 1992, Possible Laramide influence on the Teton normal fault, western Wyoming, *in:* Link, P.K, Kuntz, M.A., and Platt, L. B., editors, Regional Geology of eastern Idaho and western Wyoming: Geological Society of America Memoir 179, p. 183-196.

Larsen, S., and Grieger, J., 1998, Elastic modeling initiative, part III: 3-D computational modeling, Expanded Abstracts, 68th Annual SEG meeting, p.1803-1806.

Lavin, P.M., and Bonini, W.E., 1957, Detailed gravity measurements in the Teton Range and Jackson Hole, Wyoming, *Geol. Soc. Am. Bull.*, v. 68. p. 1760.

Lavier, L.L., Buck, W.R., and Pliakov, A.N.B., 1999, *Geology,* v. 27, no. 12, p. 1127-1130.

Leopold, E.B., and Love, J.D., 2002, Plio-Pleistocene sediments indicate a Pleistocene uplift of Grand Tetons [abstr]: Geol. Soc. Amer. Abstracts with Programs, v. 34, no. 6, p. 409.

Liu, H. L., and D. V. Helmberger, 1985, The 23:19 aftershock of the 15 October 1979 Imperial Valley earthquake: More evidence for an asperity, *Bull. Seism. Soc. Am.*, v. 75, p. 689-709.

Lockhart, A.C., et al., 1986, Geologic report for final design, Jackson Lake Dam Modification, Jackson Lake Dam, Minidoka Project, Wyoming, Pacific Northwest Regional Office, Boise, Idaho.

Lomnitz, C., J. Flores, O. Novaro, T. H. Seligman, and R. Esquivel, 1999, Seismic coupling of interface modes in sedimentary bains: A recipe for distaster, *Bull. Seism. Soc. Am.*, v. 89, p. 14-21.

Love, J.D., and J. de la Montagne, 1956, Pleistocene and Recent tilting of Jackson Hole, Teton County, Wyoming: Guidebook Wyoming Geol. Asso., 11th Ann. Field Conf., p 169-178.

Love, J.D., and Reed, J.C., 1971, Creation of the Teton landscape, the geological story of rand Teton National Park: Grand Teton Natural History Association, Moose, WY, 120p.

Love, J.D., Reed, J.C., Jr., 1992, Geological map of Grand Teton National Park: U.S. Geological Survey Miscellaneous Investigations Map I-2031, scale 1:62,500, 1 sheet.

Love, J.D., and Christiansen, A.C., 1985, Geologic map of Wyoming: U.S. Geological Survey, Scale 1:500,000, 3 sheets.

Machete, M.N., Pierce, K.L., MacCalpin, J.P., Haller, K.M., and Dart, R.L, in prep, Map and data for Quaternary faults and folds in Wyoming: US Geol. Surv., Open-File Report, review draft dated May 31, 2001.

Madariaga, R., 1977, High-frequency radiation from crack (stress-drop) models of earthquake faulting, Geophys. J., v. 51, p. 625-652.

Mandl, G., 2000, Faulting in Brittle Rocks: An Introduction to the Mechanics of Tectonic Faults, Springer-Verlag, Berlin, 434 pp.

Mayeda, K. and W. R. Walter, 1996, Moment, energy, stress drop, and source spectra of western United States earthquakes from regional coda envelope, *J. Geophys. Res.*, v. 101, p. 11,195-11,208.

McGarr, A., 1984, Scaling of ground motion parameters, state of stress, and focal depth, *J. Geophys. Res.*, v. 89, p. 6969-6979.

McGuire, J.J., Zhao, L., and Jordan, T.H., 2002. Predominance of unilateral rupture for a global catalog of large earthquakes. Bull. Seism. Soc. Am., v. 92, p. 3309-3317.

Mendoza, C., and Hartzell, S.H., 1988, Inversion for slip distribution using teleseismic P waveforms: North Palm Springs, Borah Peak, and Michoacan earthquakes, *Bull. Seism. Soc. Am.*, v. 78, p. 1092-1111.

Miller, D. S. and R. B. Smith, 1999, P and S velocity structure of the Yellowstone volcanic field from local earthquake and controlled-source tomography, *J. Geophys. Res.*, v. 104, p. 15,105-15,121.

Moczo, P., Kristek, J., and Halada, L., 2000, 3D 4th-order staggered-grid finite-difference schemes: Stability and grid dispersion, *Bull. Seism. Soc. Am.*, v. 90, p. 587 - 603.

O'Connell, D.R., and Ake, J.P., 1995, Ground motion analysis for Hoover Dam, Boulder Canyon Project, U.S. Bureau of Reclamation Seismotectonic Report 94-1, Denver, Colorado, 114 pp.

O'Connell, D. R. H., 1999a, Replication of apparent nonlinear seismic response with linear wave propagation models, *Science*, v. 283, p. 2045-2050.

O'Connell, D. R. H., 1999b, Possible super-shear rupture velocities during the 1994 Northridge earthquake, *EOS*, v. 80, p. F941.

O'Connell, D.R.H., 1999c, Ground motion evaluation for Casitas Dam, Ventura River Project, California, U.S. Bureau of Reclamation Seismotectonic Report 99-4, Denver, Colorado, 113 pp.

O'Connell, D.R.H., and Unruh, J.R., 2000, Updated seismotectonic evaluation of faults within 10 km of Monticello Dam, Solano Project, California, U.S. Bureau of Reclamation Seismotectonic Report 99-5, Denver, Colorado, 101 pp., two appendices.

O'Connell, D.R.H., and Unruh, J.R., and Block, L.V., 2001, Source characterization and ground-motion modeling of the 1892 Vacaville–Winters earthquake sequence, California, *Bull. Seism. Soc. Am.*, v. 91, p. 1471-1497.

O'Connell, D.R.H., 2001, Ground motion analyses for Stony Gorge Dam, Orland Project, California, U.S. Bureau of Reclamation Seismotectonic Report 2001-3, Denver, Colorado, 212 pp., one appendix.

O'Connell, D.R.H., and Ake, J.P., in press, Earthquake ground motion estimation, in: Earthquakes: Two-Volume Set (Hazards and Disasters), C. Rodrigue and E. Rovai, eds., Routledge, New York, 760 pp.

Oglesby, D.D.; Archuleta, R.J., and Nielsen, S. B., 1998, Earthquakes on dipping faults: The effects of broken symmetry, *Science*, v. 280, p.1055-1059.

Oglesby, D.D.; Archuleta, R.J., and Nielsen, S. B., 2000, The three-dimensional dynamics of dipping faults, *Bull. Seism. Soc. Am.*, v. 90, p. 616 - 628.

Oglesby, D.D., and Day, S.M., 2002. Stochastic fault stress: Implications for fault dynamics and ground motions, *Bull. Seism. Soc. Am.*, v. 92, p. 3006-3021.

Oreskes, N., Shrader-Frechett, K., and Belitz, K., 1994, Verification, validation, and confirmation of numerical models in the earth sciences, *Science,* v. 263, no. 5147, p. 641-646.

Osborne, N.M., and Taber, J.J., 2000, Observation of basin edge effects in the Hutt Valley, New Zealand from weak ground motion recordings, *in*, Proceedings, Sixth International Conference on Seismic Zonation, Managing Earthquake Risk in the 21st Century, November 12-15, 2000, Palm Springs, California, USA, v. I, p. 393-398.

Ostenaa, D.A., and Gilbert, J.D., 1988, Late Quaternary behavior of the Teton fault, Wyoming [abstr]: Geol. Soc. Amer. Abstracts with Programs, v. 20, p. A14.

Ostenaa, D.A., Wood, C., and Gilbert, J.D., 1993, Seismotectonic study for Grassy Lake Dam - Minidoka Project, Wyoming: Seismotectonic Report 93-3, US Bureau of Reclamation, Denver, CO, 68 p. and plate.

Pakiser, L.C., Jr., and Black, R.A., 1957, Exporing for ancient channels with the refraction seismograph [Arizona - Utah], *Geophysics*, v. 22, p. 32-47.

Pierce, K.L., and Good, J.D., 1992, Field guide to the Quaternary geology of Jackson Hole, Wyoming: US Geol. Surv. Open-File Report 92-504, 54 p.

Piety, L.A., C.K. Wood, J.D. Gilbert, J.T. Sullivan, and M.H. Anders (1986), Seismotectonic study for Palisades Dam and Reservoir, Seismotectonic Report 86-3, U.S. Bureau of Reclamation, Denver, CO, 198 pp.

Porcella, R. L., 1980, Atypical accelerograms recorded during recent earthquakes, seismic engineering report, May–August 1980, U.S. Geol. Surv. Circ. 854-B, 1–7.

Press, W.H., Teukolsky, S.A., Vetterling, W.T., Flannery, B.P., 1992, Numerical recipes in FORTRAN: The art of scientific computing, Cambridge University Press, New York, 963 p.

Reasenberg, P., 1985, Second-order moment of Central Californian seismicity, 1969-1982, *J. Geophys. Res.*, v. 90, p. 5479-5495.

Richards, P. G., 1976, Dynamic motions near an earthquake fault: A three-dimensional solution, *Bull. Seism. Soc.Amer.*, v. 60, p. 1-32.

Robertsson, J. 0. A., Blanch, J. 0., and Symes, W. W., 1994, Viscoelastic finite-difference modcling, *Geophysics*, v. 59, p. 1444-1456.

SAC Joint Venture Steel Project Phase 2, 1997, Develop Suites of Time Histories, http://nisee.berkeley.edu/data/strong_motion/sacsteel/draftreport.html

Sadigh, K., C.-Y. Chang, J. A. Egan, F. Makdisi, and R. R. Youngs, 1997, Atenuation relationships for shallow crustal earthquakes based on California strong motion data, *Seism. Res. Lett.*, v. 68, no. 1, p. 180-189.

Safak, E., 1991, Problems with using spectral ratios to estimate site amplification, *in* Proceedings, Fourth International Conference on Seismic Zonation, August 26-29, Stanford, California, USA, v. 2, p. 227-284.

Safak, E., 1997, Models and methods to characterize site amplification from a pair of records, Earthquake Spectra, v. 13, p. 97-129.

Santa-Cruz, S., Heredia-Zavoni, E., and Harichandran, R.S., 1999, Low-frequency behavior of coherency for strong ground motions in Mexico City and Japan, Proc. 12th ASCE Engineering Mech. Conf., N. Jones and R.G. Ghanem, eds., ASCE, Reston, Va.

Savage, M.K. and . Depolo, M.,1993, Foreshock probabilities in the western Great-Basin Eastern Sierra Nevada, *Bull. Seism. Soc. Am.*, v. 83, p. 1910-1938.

Schnabel, P.B., J. Lysmer, and H.B. Seed, 1972,"SHAKE - A Computer Program for Earthquake Response Analysis of Horizontally Layered Sites, Earthquake Engineering Research Center, Report No. UCB/EERC-72/12. University of California, Berkeley, December.

Schneider, J. F., W. J. Silva, and C. Stark, 1993, Ground motion model for the 1989 **M** 6.9 Loma Prieta earthquake including effects of source, path, and site, Earthquake Spectra, v. 9, p. 251-287.

Selma, D.N., with contributions by Wirkus, K.E., and Roser, D.W., Final Construction Geology Report, Jackson Lake Dam, Safety of Dams Modifications, Specification DC-7665 and -7695, Minidoka Project, Idaho-Wyoming, Bend Construction Office, Bend, Oregon, December, 1996.

Silva, W. J. and K. Lee, 1987, WES RASCAL code for synthesizing earthquake ground motions: State-of-the-Art for Assessing Earthquake Hazards in the United States, Report 24, U.S. Army Corps of Engineers Waterways Experiment Station, Miscellaneous Paper S-73-1, 120 pp.

Sirles, P., 1986. In situ compressional and shear wave velocity investigations, Jackson Lake Dam, Minidoka Project, Wyoming, Bureau of Reclamation, Geophysics Section report of October, 1986, Denver, Colorado.

Smith, R.B., and Arabasz, W.J., 1991, Seismicity of the Intermountain Seismic Belt, *in:* Slemmons, D.B., Engdahl, E.R., Zoback, M.D., and Blackwell, D.D., eds., Neotectonics of North America: Decade Map vol. 1., Geological Society of America, Boulder, CO, p. 185-228.

Smith, R.B., Pierce, K.L., and Wold, R.J., 1993a, Seismic survey and Quaternary history of Jackson Lake, Wyoming , *in* Snoke, A.W., Steidtmann, J.R., and Roberts, S.M., eds., Geology of Wyoming: Geological Survey of Wyoming Memooir No. 5, p. 668-693.

Smith, R.B., Byrd, J.O.D., Susong, D.D., 1993b, The Teton fault, Wyoming - Seismotecontics, Quaternary history, and earthquake hazards, *in* Snoke, A.W., Steidtmann, J.R., and Roberts, S.M., eds., Geology of Wyoming: Geological Survey of Wyoming Memooir No. 5, p. 628-667.

Somerville, P., M. Sen, and B. Cohee, 1991, Simulations of strong ground motions recorded during the 1985 Michoacan, Mexico and Valparaiso, Chile, earthquakes, *Bull. Seism. Soc. Am.*, v. 81, p. 1-27.

Somerville, P., K. Irikura, R. Graves, S. Sawada, D. Wald, N. Abrahamson, Y. Iwasaki, T. Kagawa, N. Smith, and A. Kowada, 1999, Characterizing crustal earthquake slip models for the prediction of strong ground motion, *Seism. Res. Lett.*, v. 70, p. 59-80.

Somerville, P., N. Collins, R. Graves, and A. Pitarka, 2003, Development of an engineering model of basin-generated surface waves, Proceedings SMIP03 Seminar on Utilization of Strong-Motion Data, May 22, 2003, Oakland, California, M. Huang, ed., California Strong Motion Instrumentation Program, California Geological Survey, California Department of Conservation.

Spetzler, J., and Snieder, R., 2001. The formation of caustics in two- and three-dimensional media, *Geophys. J. Int.*, v. 144, p. 175-182.

Spudich, P., and Archuleta, R. J., 1987, Techniques for earthquake ground-motion calculation with applications to source parameterization to finite faults, in "Seismic Strong Motion Synthesis," (B. A. Bolt, ed.), Academic Press, Orlando, Florida, pp. 205-265.

Spudich, P. and Iida, M., 1993, The seismic coda, site effects, and scattering in alluvial basins studied using aftershocks of the 1986 Palm Springs, California, earthquake as source arrays, *Bull. Seism. Soc. Am.*, v. 83, p. 1721-1743.

Spudich, P., Fletcher, J. B., Hellweg, M., Boatwright, J., Sullivan, C., Joyner, W. B., Hanks, T. C., Boore, D. M.,. McGarr, A, Baker, L. M,. and Lindh, A. G.,1997, SEA96 - A new predictive relation for earthquake ground motions in extensional tectonic regimes, *Seism. Res. Lett.,* v. 68, no. 1, p. 190-198.

Spudich, P., Joyner, W.B., Lindh, A.G., Boore, D.M., Margaris, B.M., and Fletcher, J.B., 1999, SEA99: A revised ground motion prediction relation for use in extensional tectonic regimes, *Bull. Seism. Soc. Am.*, v. 89, p. 1156-1170.

Stirling, M.W., Anooshehpoor, A., Brune, J.N., Biasi, G., Wesnousky, S.G., 2002, Assessment of the site conditions of precariously balanced rocks in the Mojave Desert, southern California, *Bull. Seism. Soc. Am.*, v. 92, p. 2139-2144.

Susong, D.D., Smith, R.B., and Bruhn, R.L., 1987, Quaternary fualting and sementation of the Teton fault zone, Grand Teton National Park, Wyoming [abstr]: Eos, Trans. Amer. Geophys. Union, v. 68, p. 1452.

Sylvester, A.G., Byrd, J.O.D., and Smith, R.B., 1991, Geodectic evidence for aseismic reverse creep across the Teton normal fault: *Geophys. Res. Letters*, v. 18, p. 1083-1086.

ThatcherW., and Hill, D.P., 1991, Fault orientations in extensional and conjugate strike-slip environments and their implications: *Geology*, v. 19, p. 1116-1120.

Tibbetts, B.L., Behrendt, J.C., and Love, J.D., 1969, Seismic-refraction measurements in Jackson Hole, Wyoming, *Geol. Soc. Am. Bull.*, v. 80, p. 1109-1122.

Towhata, I. and Ishihara, K., 1985, Shear work and pore water pressure in undrained shear, *Soils and Foundations*, v. 25, No.3, pp.73-84.

USBR (Bureau of Reclamation), 1987, Design Summary, Jackson Lake Dam Modification, Minidoka Project, Wyoming (for Specifications no. DC-7665 (Stage I) and DC-7695 (Stage II)): prepared by Bureau of Reclamation, Assistant Commissioner - Engineering and Research Center, Denver, CO, 2 vol., variously paginated.

Vidale, J.E., and Helmberger, D.V., 1987, Path effects in strong motion seismology, in "Seismic Strong Motion Synthesis," (B. A. Bolt, ed.), Academic Press, Orlando, Florida, pp. 267-319.

Vidale, J. E., 1989, Influence of focal mechanism on peak accelerations of strong motions of the Whittier Narrows, California, earthquake and an aftershock, *J. Geophys. Res.*, v. 94, p. 9607-9613.

Wald, D. J, T. H. Heaton, and K. W. Hudnut, 1996, The slip history of the 1994 Northridge, California, earthquake determined from strong-motion, teleseismic, GPS, and leveling, *Bull. Seism. Soc. Am.*, v. 86, p. S49-S70.

Weichert, D., 1980, Estimation of the earthquake recurrence parameters for unequal observation periods for different magnitudes, *Bull. Seism. Soc. Am.*, v. 70, p. 1337-1347.

Wells, D.L. and K. J. Coppersmith, 1994, New empirical relationships among magnitude, rupture length, rupture width, rupture area, and surface displacement, *Bull. Seism. Soc. Am.*, v. 84, p. 974-1002.

Wernicke, B., 1995, Low-angle normal fault seismicity: A review: *J. Geophys. Res.*, v. 100, p. 20,159-20,174.

Wolf, J.P., and Song, C., 1996, Finite-Element Modeling of Unbounded Media, John Wiley & Sons, New York, 331 pp.

Wong, I., Olig, S., and Dober, M., 2000, Preliminary probabilistic seismic hazard analyses, Island Park, Grassy Lake, Jackson Lake, Palisades, and Ririe Dams: contract report to US Bureau of Reclamation, Denver, CO prepareed by Seismic Hazards Group, URS Greiner Woodward-Clyde, Oakland, CA, variously paginated.

Wong, J., and Nelson, J.S., 1989, Seismic tomography survey, Jackson Lake Dam, Jackson Hole, Wyoming, contained in USBR Technical Memorandum No. 3610-90-JL2.

Wood, C., 1988, Earthquake Data - 1986, Jackson Lake Seismograph Network, Jackson Lake Dam, Minidoka Project, Wyoming, Seismotectonic Report 88-1, Bureau of Reclamation, Denver, Colorado.

Wright, J., 1990, SMW quality assurance geophysical tomography testing and interpreted results in SMW columns and cutoff wall, U.S. Bureau of Reclamation, Division of Geotechnical Engineering and Geology Technical Memorandum 3610-90-JL2, Denver, Colorado.

Yoshida, N., Kobayashi, S., Suetomi, I., and Miura, K., 2002, Equivalent linear method considering frequency dependent characteristics of stiffness and damping, Soil Dynamics Earthquake Eng., v. 22, p. 203-222.

Zeghal, M., and A.-W. Elgamal, 1994, Analysis of site liquefaction using earthquake records, *J. Geotech. Eng.*, v. 120, p. 996–1017.

Zeng, Y., J. G. Anderson, and G. Yu, 1994, A composite source model for computing realistic strong ground motions, Geophys. Res. Lett., v. 21, p. 725-728.

Zeng, Y., and J. Anderson, 2000. Evaluation of numerical procedures for simulating near-fault long-period ground motions using the Zeng method, Pacific Earthquake Engineering Res. Center Utilities Program Report 2000/01.

Zoback, M.L., 1983, Structure and Cenozoic tectonism along the Wasatch fault zone, Utah, in "Tectonic and Stratigraphic Studies in the Eastern Great Basin", Miller, D.M., Todd, V.R., and Howard, K.A., eds., *Geol. Soc. Am. Memoir 157*, p. 3-27.